

Pretest Round Robin Analysis of a Prestressed Concrete Containment Vessel Model

Sandia National Laboratories

**U.S. Nuclear Regulatory Commission
Washington, DC 20555-0001**

**Nuclear Power Engineering Corporation
Tokyo, Japan**



**AVAILABILITY OF REFERENCE MATERIALS
IN NRC PUBLICATIONS**

NRC Reference Material

As of November 1999, you may electronically access NUREG-series publications and other NRC records at NRC's Public Electronic Reading Room at www.nrc.gov/NRC/ADAMS/index.html.

Publicly released records include, to name a few, NUREG-series publications; *Federal Register* notices; applicant, licensee, and vendor documents and correspondence; NRC correspondence and internal memoranda; bulletins and information notices; inspection and investigative reports; licensee event reports; and Commission papers and their attachments.

NRC publications in the NUREG series, NRC regulations, and *Title 10, Energy*, in the Code of *Federal Regulations* may also be purchased from one of these two sources.

1. The Superintendent of Documents
U.S. Government Printing Office
P. O. Box 37082
Washington, DC 20402-9328
www.access.gpo.gov/su_docs
202-512-1800
2. The National Technical Information Service
Springfield, VA 22161-0002
www.ntis.gov
1-800-533-6847 or, locally, 703-805-6000

A single copy of each NRC draft report for comment is available free, to the extent of supply, upon written request as follows:

Address: Office of the Chief Information Officer,
Reproduction and Distribution
Services Section
U.S. Nuclear Regulatory Commission
Washington, DC 20555-0001

E-mail: DISTRIBUTION@nrc.gov
Facsimile: 301-415-2289

Some publications in the NUREG series that are posted at NRC's Web site address www.nrc.gov/NRC/NUREGS/indexnum.html are updated periodically and may differ from the last printed version. Although references to material found on a Web site bear the date the material was accessed, the material available on the date cited may subsequently be removed from the site.

Non-NRC Reference Material

Documents available from public and special technical libraries include all open literature items, such as books, journal articles, and transactions, *Federal Register* notices, Federal and State legislation, and congressional reports. Such documents as theses, dissertations, foreign reports and translations, and non-NRC conference proceedings may be purchased from their sponsoring organization.

Copies of industry codes and standards used in a substantive manner in the NRC regulatory process are maintained at—

The NRC Technical Library
Two White Flint North
11545 Rockville Pike
Rockville, MD 20852-2738

These standards are available in the library for reference use by the public. Codes and standards are usually copyrighted and may be purchased from the originating organization or, if they are American National Standards, from—

American National Standards Institute
11 West 42nd Street
New York, NY 10036-8002
www.ansi.org
212-642-4900

The NUREG series comprises (1) technical and administrative reports and books prepared by the staff (NUREG-XXXX) or agency contractors (NUREG/CR-XXXX), (2) proceedings of conferences (NUREG/CP-XXXX), (3) reports resulting from international agreements (NUREG/IA-XXXX), (4) brochures (NUREG/BR-XXXX), and (5) compilations of legal decisions and orders of the Commission and Atomic and Safety Licensing Boards and of Directors' decisions under Section 2.206 of NRC's regulations (NUREG-0750).

DISCLAIMER: This report was prepared as an account of work sponsored by an agency of the U.S. Government. Neither the U.S. Government nor any agency thereof, nor any employee, makes any warranty, expressed or implied, or assumes any legal liability or responsibility for any third party's use, or the results of such use, of any information, apparatus, product, or process disclosed in this publication, or represents that its use by such third party would not infringe privately owned rights.

**NUREG/CR-6678
SAND 00-1535**

Pretest Round Robin Analysis of a Prestressed Concrete Containment Vessel Model

**Manuscript Completed: June 2000
Date Published: August 2000**

**Prepared by
V.K. Luk**

**Sandia National Laboratories
Albuquerque, NM 87185-0744**

Prepared for

**Systems Safety Department
Nuclear Power Engineering Corporation
Tokyo 105, Japan
Under Funds-in-Agreement
No. DE-F104-91AL73734**

**Office of Nuclear Regulatory Research
U.S. Nuclear Regulatory Commission
Washington, DC 20555-0001 USA
Under Containment Integrity Under
Extreme Loads JCN A1401**

NUPEC Project Manager: S. Shibata

NRC Project Manager: J.F. Costello

**NUREG/CR-6678 has been
reproduced from the best available copy.**

ABSTRACT

The Nuclear Power Engineering Corporation of Japan and the U.S. Nuclear Regulatory Commission, Office of Nuclear Regulatory Research, are co-sponsoring and jointly funding a Cooperative Containment Research Program at Sandia National Laboratories in Albuquerque, New Mexico. As a part of the program, a prestressed concrete containment vessel model will be tested to failure at Sandia in September 2000. The model, uniformly scaled at 1:4, is representative of the containment structure of an actual pressurized-water reactor plant (OHI-3) in Japan. The objectives of the internal pressurization test are to obtain data on the structural response of the model to pressure loading beyond design basis accident in order to validate analytical modeling, to find the model's pressure capacity, and to observe its response and failure mechanisms.

Seventeen organizations participated in a pretest Round Robin analysis to predict the structural response of the model under overpressurization. Each organization was supplied with the same basic information to use in its analysis. This information included the design drawings of the prestressed concrete containment vessel model and the material properties of the structural components. Each organization worked independently, using its own analytical methods, to produce analysis results for 55 specified locations on the model. The Round Robin analysis provides a forum for participants to discuss pretest predictions of the deformation behavior of the prestressed concrete containment vessel model, as well as to compare them to the test data.

This report contains the analytical modeling procedures and the pretest predictions submitted by each organization. This report also includes composite plots of participants' analysis results at the 55 specified locations on the model. These plots, which were discussed among participants at the pretest analysis meeting, held October 12-14, 1999, in Albuquerque, will be compared to the test data generated during the internal pressurization test.

CONTENTS

Abstract.....	iii
Executive Summary.....	ix
Abbreviations	xiii
1. INTRODUCTION	1
1.1 Background	1
1.2 Program Description.....	1
1.3 Report Organization	2
2. DESIGN OF THE PRESTRESSED CONCRETE CONTAINMENT VESSEL MODEL.....	3
2.1 Model Design	3
2.2 Material Properties	5
3. INSTRUMENTATION.....	7
3.1 Model Instrumentation	7
3.1.1 Strain Measurements.....	7
3.1.1.1 Reinforcing Bar Strain.....	7
3.1.1.2 Liner and Liner Anchor Strain.....	7
3.1.1.3 Concrete Strain	10
3.1.2 Displacement Measurements	10
3.1.3 Pressure Measurements.....	10
3.1.4 Temperature Measurements.....	10
3.1.5 Tendon Measurements.....	10
3.1.5.1 Tendon Prestress Force (at ends).....	10
3.1.5.2 Local Tendon Strain (along length).....	10
3.1.6 Acoustic Monitoring System	10
3.1.7 Video and Still Cameras	10
3.2 Standard Output Locations	10

4.	PRESSURE TESTING	13
4.1	System Functionality Test (SFT)	13
4.2	Structural Integrity Test and Integrated Leak Rate Test	13
4.3	Limit State Test	13
5.	PRETEST ANALYSIS	15
6.	SUMMARY	23
7.	REFERENCES	25
Appendix A	Composite Plots	A-1
Appendix B	AECL Atomic Energy of Canada Limited Canada	B-1
Appendix C	ANL Argonne National Laboratory U.S.	C-1
Appendix D	CEA Commissariat a l'Énergie Atomique France	D-1
Appendix E	EDF Électricité de France France	E-1
Appendix F	Glasgow University of Glasgow U.K.	F-1
Appendix G	HSE Health and Safety Executive U.K.	G-1
Appendix H	IBRAE Nuclear Safety Institute Russia	H-1
Appendix I	INER Institute of Nuclear Energy Research Republic of China..	I-1
Appendix J	IPSN Institut de Protection et de Sûreté Nucléaire France	J-1
Appendix K	JAERI Japan Atomic Energy Research Institute Japan	K-1
Appendix L	JAPC The Japan Atomic Power Company Japan	L-1
Appendix M	KINS Korea Institute of Nuclear Safety Korea	M-1
Appendix N	KOPEC Korea Power Engineering Company Korea	N-1
Appendix O	NUPEC Nuclear Power Engineering Corporation Japan	O-1
Appendix P	PRIN Principia Spain	P-1
Appendix Q	RINSC Russia International Nuclear Safety Center Russia	Q-1
Appendix R	SNL/ Sandia National Laboratories/ANATECH U.S.	R-1
	ANATECH	

Figures

2.1	Outline Sketch of the Prestressed Concrete Containment Vessel (PCCV) Model	4
3.1	Prestressed Concrete Containment Vessel (PCCV) Model Coordinate System and Cardinal Lines	7
3.2	Developed Elevation of the Prestressed Concrete Containment Vessel (PCCV) Model and Standard Output Locations.....	8
4.1	Pressurization Sequence for the Prestressed Concrete Containment Vessel (PCCV) Model Test.....	14

Tables

3.1	Prestressed Concrete Containment Vessel (PCCV) Model Standard Output Locations	11
5.1	Finite Element Codes Used by Round Robin Participants.....	16
5.2	Modeling Approaches Used in the Pretest Analyses.....	17
5.3	Material Properties used in the Pretest Analyses	18
5.4	Standard Output Location Matrix for Round Robin* Pretest Analysis of a Prestressed Concrete Containment Vessel (PCCV) Model	20
5.5	Pretest Analysis Results (MPa).....	21
5.6	Failure Criteria	22

EXECUTIVE SUMMARY

Sandia National Laboratories^a (SNL) has tested and analyzed numerous scale models of containment vessels that were pressurized to failure as part of the Containment Integrity Programs sponsored by the U.S. Nuclear Regulatory Commission (NRC). The overall objective of the programs has been to develop test-validated analytical methods that can be used to predict the performance of light-water reactor (LWR) containment vessels subject to loads beyond the design basis. Five scale models of steel containments and a 1:6-scale model of a reinforced concrete containment were tested. Accompanying the reinforced concrete containment model test, a number of organizations in the United States and Europe, performed pretest and posttest Round Robin analyses of the model subjected to static internal pressurization [1,2].

SNL is currently conducting a Cooperative Containment Integrity Program under the joint sponsorship of the Nuclear Power Engineering Corporation (NUPEC)^b of Japan, and the NRC Office of Nuclear Regulatory Research. The purpose of the program is to investigate the response of representative models of nuclear containment structures to pressure loading beyond the design basis accident and to compare analytical predictions to measured behavior.

The first test in this program was of a mixed-scale model of the steel containment of an Improved Mark-II boiling-water reactor nuclear power plant in Japan. This test was conducted in December 1996. Three reports were issued on this test [3,4,5].

The second test in this program consists of pressure testing a uniform 1:4-scale model of a prestressed concrete containment vessel (PCCV). This model is representative of the containment structure of an actual pressurized-water reactor plant in Japan. The design pressure for the prototype and model is 0.4 MPa. The model was designed by Mitsubishi Heavy Industries (MHI) and Obayashi Corporation. The 1.6mm liner was fabricated by MHI in Japan and was shipped to the United States in segments. On-site construction of the model by Hensel Phelps Construction Co. commenced on January 3, 1997, under the general supervision of MHI and Taisei Corporation and was completed in 2000. Concurrently, Sandia installed more than 1700 channels of instrumentation on the model, including strain gages on the reinforcing steel, prestressing tendons and steel liner, displacement transducers, temperature sensors, pressure sensors, concrete crack transducers, as well as visual monitoring. Model testing will commence in mid-2000 with a series of low pressure tests including an Integrated Leak Rate Test (ILRT) at 0.9 P_d, a Structural Integrity Test (SIT) at 1.125 P_d, and, finally, a test to failure.

This report presents the results of the pretest Round Robin analysis of the PCCV model. Seventeen organizations performed calculations to predict the structural response of the PCCV model to static overpressurization. The participating organizations are:

AECL	Atomic Energy of Canada Limited	Canada
ANL	Argonne National Laboratory	U.S.
CEA	Commissariat a l'Énergie Atomique	France
EDF	Électricité de France	France
Glasgow	University of Glasgow	U.K.
HSE	Health and Safety Executive	U.K.
IBRAE	Nuclear Safety Institute	Russia
INER	Institute of Nuclear Energy Research	Republic of China
IPSN	Institut de Protection et de Sûreté Nucléaire	France
JAERI	Japan Atomic Energy Research Institute	Japan
JAPC	The Japan Atomic Power Company	Japan

^a Sandia is a multiprogram laboratory operated by Sandia Corporation, a Lockheed Martin Company, for the United States Department of Energy under Contract DE-AC04-94AL85000.

^b The work of the Nuclear Power Engineering Corporation is performed under contract to the Ministry of International Trade and Industry, Japan.

KINS	Korea Institute of Nuclear Safety	Korea
KOPEC	Korea Power Engineering Company	Korea
NUPEC	Nuclear Power Engineering Corporation	Japan
PRIN	Principia	Spain
RINSC	Russia International Nuclear Safety Center	Russia
SNL	Sandia National Laboratories/ANATECH	U.S.

NUPEC and the NRC jointly invited these organizations in spring of 1995, to participate in a pretest Round Robin analysis, and SNL coordinated the effort. Each participant was provided the same basic information in December 1997, including design drawings of the PCCV model and material properties of the structural components, and participants were asked to submit their results to SNL by the end of June 1999. A meeting was held October 12-14, 1999, in Albuquerque, which allowed most of the participants to present their analyses and to compare analysis results for 55 specified locations on the PCCV model. Composite plots of participants' analysis results at these locations, prepared to facilitate discussion at the meeting, will be compared to data from the internal pressurization test, scheduled to be conducted in September 2000.

The Round Robin analysis had several objectives. First, it provides a forum to compare pretest response predictions, applying different modeling approaches and finite element codes to the same model description, and, later, to compare these pretest predictions to the test data. Second, it is hoped that by comparing analysis methodologies and results, it may be possible to identify improvements that will increase reliability and confidence in the prediction of capacity calculations for actual nuclear power plant containments.

While no final conclusions can be drawn until the PCCV model tests are completed, it is possible to make a few observations regarding the response predictions:

- Predictions of elastic response were, for the most part, very similar up to the onset of global yielding (hoop), which appears to occur around $2.5 P_d$. Predictions of response diverge significantly beyond this point with responses varying by more than a factor of three to five or more at a given pressure.
- The predicted capacity of the model is fairly consistently bounded at 4 to 5 P_d . For failure predictions based on material failure of the steel components (liner, rebar, or tendons) the average predicted pressure at failure is 3.6 P_d .
- Approximately half the participants predicted failure based on structural failure, i.e., rupture of rebar or tendons, while approximately half the participants predicted functional failure from excessive leakage through a tear in the liner and/or cracks in the concrete.

ACKNOWLEDGMENTS

This effort would not have been possible without the cooperation and support of many individuals and groups. The Nuclear Power Engineering Corporation (NUPEC) of Tokyo, Japan, the U.S. Nuclear Regulatory Commission (NRC), and Sandia National Laboratories (SNL) are pleased to have had the participation of the following organizations in the pretest Round Robin analysis activities. While there were many other individuals who contributed to this effort, only the principal correspondents are listed below.

AECL	Lester S.S. Lee	Atomic Energy of Canada Limited	Canada
ANL	Phillip A. Pfeiffer	Argonne National Laboratory	U.S.
CEA	Alain Millard	Commissariat a l'Énergie Atomique	France
EDF	Laurent Granger	Électricité de France	France
Glasgow	Nenad Bicanic	University of Glasgow	U.K.
HSE	David Shepherd	Health and Safety Executive	U.K.
IBRAE	Valerii Strizhov	Nuclear Safety Institute	Russia
INER	Chin-Cheng Huang	Institute of Nuclear Energy Research	Republic of China
IPSN	Georges Nahas	Institut de Protection et de Sûreté Nucléaire	France
JAERI	Kazuichiro Hashimoto	Japan Atomic Energy Research Institute	Japan
JAPC	Yukio Watanabe	Japan Atomic Power Co.	Japan
KINS	Sung-Kyu Lee	Korea Institute of Nuclear Safety	Korea
KOPEC	Nam Ho Lee	Korea Power Engineering Company	Korea
NUPEC	Takako Kashiwase	Nuclear Power Engineering Corporation	Japan
PRIN	Francisco Martinez	Principia	Spain
RINSC	Sergei E. Bougaenko	Russia International Nuclear Safety Center	Russia
SNL/ ANATECH	Robert A. Dameron	ANATECH	U.S.

The author also wishes to acknowledge the guidance, support, and encouragement of NUPEC's Dr. Hideo Ogasawara, Director and General Manager, Systems Safety Department; and the NRC's Dr. James F. Costello, Engineering and Research Applications Branch, Division of Engineering Technology, Office of Reactor Research.

ABBREVIATIONS

A/L	(personnel) airlock
AECL	Atomic Energy of Canada Limited
ANL	Argonne National Laboratory
BWR	boiling-water reactor
CEA	Commissariat a l'Énergie Atomique
CL	centerline
CPOT	cable potentiometer
E/H	equipment hatch
EDF	Électricité de France
F/W	feedwater (penetration)
HSE	Health and Safety Executive
IBRAE	Nuclear Safety Institute
ILRT	Integrated Leak Rate Test
INER	Institute of Nuclear Energy Research
IPSN	Institut de Protection et de Sûreté Nucléaire
JAERI	Japan Atomic Energy Research Institute
JAPC	The Japan Atomic Power Company
JIS	Japanese Industrial Standard
KINS	Korea Institute of Nuclear Safety
KOPEC	Korea Power Engineering Company
LST	Limit State Test
LVDT	linear variable differential transformer
M/S	main stream (penetration)
MHI	Mitsubishi Heavy Industries
NRC	U.S. Nuclear Regulatory Commission
NUPEC	Nuclear Power Engineering Corporation
PCCV	prestressed concrete containment vessel
PRIN	Principia
PWR	pressurized-water reactor
RINSC	Russia International Nuclear Safety Center
RTD	resistance temperature detector
SCV	steel containment vessel
SFT	System Functionality Test
SIT	Structural Integrity Test
SNL	Sandia National Laboratories
TLDT	temposonic linear displacement transducer

1. INTRODUCTION

1.1 Background

Sandia National Laboratories (SNL) is conducting a Cooperative Containment Research Program that is co-sponsored and jointly funded by the Nuclear Power Engineering Corporation (NUPEC) of Japan and the U.S. Nuclear Regulatory Commission (NRC), Office of Nuclear Regulatory Research. The purpose of the program is to investigate the response of representative scale models of nuclear containments to pressure loading beyond the design basis accident and to compare analytical predictions to measured behavior. This objective is accomplished by conducting static, pneumatic overpressurization tests of scale models at ambient temperature. This research program consists of testing two scale models: a steel containment vessel (SCV) model (tested in 1996) and a prestressed concrete containment vessel (PCCV) model, which is the subject of this report.

Prior to pressure testing the scale models, a number of regulatory and research organizations were invited to participate in a pretest Round Robin analysis to perform predictive modeling of the response of scale models to overpressurization. Luk and Klamerus reported the results of the pretest (1998) and posttest (2000) SCV Round Robin analyses.

1.2 Program Description

The second test in this program consists of pressure testing a uniform 1:4-scale model of a PCCV, whose design was reported by Matsumoto et al. (1995). This model is representative of the containment structure of an actual pressurized-water reactor plant in Japan. The design pressure for the prototype and model is 0.4 MPa. The model was designed by Mitsubishi Heavy Industries (MHI) and Obayashi Corporation. The 1.6mm liner was fabricated by MHI in Japan and was shipped to the United States in segments. On-site construction of the model by Hensel Phelps Construction Co. commenced on January 3, 1997, under the general supervision of MHI and Taisei Corporation and was completed in 2000. Concurrently, Sandia installed more than 1700 channels of instrumentation on the model, including of strain gages on the reinforcing steel, prestressing tendons and steel liner, displacement transducers, temperature sensors, pressure sensors, concrete crack transducers as well as visual monitoring. Model testing will commence in mid-2000 with a series of low pressure tests including an Integrated Leak Rate Test (ILRT) at 0.9 P_d, a Structural Integrity Test (SIT) at 1.125 P_d, and, finally, a test to failure.

Seventeen international regulatory and research organizations participated in the pretest Round Robin analysis activities:

AECL	Atomic Energy of Canada Limited	Canada
ANL	Argonne National Laboratory	U.S.
CEA	Commissariat a l'Énergie Atomique	France
EDF	Électricité de France	France
Glasgow	University of Glasgow	U.K.
HSE	Health and Safety Executive	U.K.
IBRAE	Nuclear Safety Institute	Russia
INER	Institute of Nuclear Energy Research	Republic of China
IPSN	Institut de Protection et de Sûreté Nucléaire	France
JAERI	Japan Atomic Energy Research Institute	Japan
JAPC	The Japan Atomic Power Company	Japan
KINS	Korea Institute of Nuclear Safety	Korea
KOPEC	Korea Power Engineering Company	Korea
NUPEC	Nuclear Power Engineering Corporation	Japan
PRIN	Principia	Spain
RINSC	Russia International Nuclear Safety Center	Russia
SNL	Sandia National Laboratories/ANATECH	U.S.

Each participant was supplied with the same basic information, including the design drawings of the PCCV model and the material properties of the structural components. Each participant used his own chosen analytical methods and performed independent analyses.

1.3 Report Organization

This report presents the pretest analysis results provided by the Round Robin participants. These results include predictions of the response of the PCCV model in terms of 55 measurements (strain, displacement, force) at specified locations throughout the model, the pressure capacity of the

PCCV model, and the failure mode and mechanisms. Section 2 summarizes the design of the PCCV model and the material properties of the structural components. Section 3 summarizes instrumentation on the PCCV model. Special attention is focused on the instruments installed at the 55 response locations; results will be compared to the pretest predictions. The pressurization sequence of the PCCV model is described in Section 4. Section 5 describes the composite plots presented in Appendix A and summarizes the PCCV pretest Round Robin analysis presented in Appendices B-R. Section 6 summarizes the pretest Round Robin analysis effort and provides some observations from this exercise.

2. DESIGN OF THE PRESTRESSED CONCRETE CONTAINMENT VESSEL MODEL

2.1 Model Design

The prestressed concrete containment vessel (PCCV) model is a uniform, 1:4-scale model of the containment structure of Unit 3 of the Ohi Nuclear Power Station in Japan. Ohi Unit 3 is a 1180 MWe pressurized-water reactor (PWR) plant designed and constructed by Mitsubishi Heavy Industries (MHI) and operated by Kansai Electric Power Company. The Ohi-3 containment vessel is a steel-lined, prestressed concrete cylinder with a hemispherical dome and two vertical buttresses. The design pressure is 0.4 MPa.

The model was designed by MHI and Obayahsi Corporation. The approach to designing the model was to scale the design of the Ohi-3 containment to the extent possible and include as many representative features of the prototype as practical. Specific considerations in designing the model are summarized below.

- **Geometry:** The configuration and overall dimensions (height, radius, thickness) were scaled 1:4 from the prototype. While the basemat thickness was scaled from the prototype, the footprint of the basemat was selected so that the bending stiffness of the basemat at the junction with the containment wall was preserved. The overall geometry is shown in Figure 2.1.
- **Liner:** The liner thickness was scaled directly from the prototype resulting in a liner thickness of 1.6 mm. In the prototype, the

liner anchorage consists of meridional T-anchors throughout the cylinder and dome. Anchorage of the model liner consists of scaled T-anchors in the cylinder portion and stud-type anchors in the dome. Circumferential spacing of the vertical anchors was expanded in the model by a factor of three to simplify fabrication, except in areas around penetrations and other discontinuities. To the extent practical, all liner details were similar to the prototype.

- **Penetrations:** All penetrations were scaled from the prototype (geometry, thickness), and the equipment hatch (E/H), and personnel airlock (A/L) are functional with pressure seating covers. The main steam (M/S) and feedwater (F/W) penetration sleeves are scaled but are terminated with heavy, bolted, pressure seating blind flanges and covers which are used for instrumentation, power, and gas feed-throughs.
- **Concrete:** There was no scaling of the concrete for the model; however, maximum aggregate size was limited to 10 mm to facilitate placement.
- **Reinforcing Steel:** All reinforcing ratios in the prototype are maintained in the model. Rebar areas were scaled, but there was no attempt to match individual bars. Bars ranging in size from 2 mm to 16 mm in diameter were placed in two orthogonal layers on each face, and shear reinforcing was included.

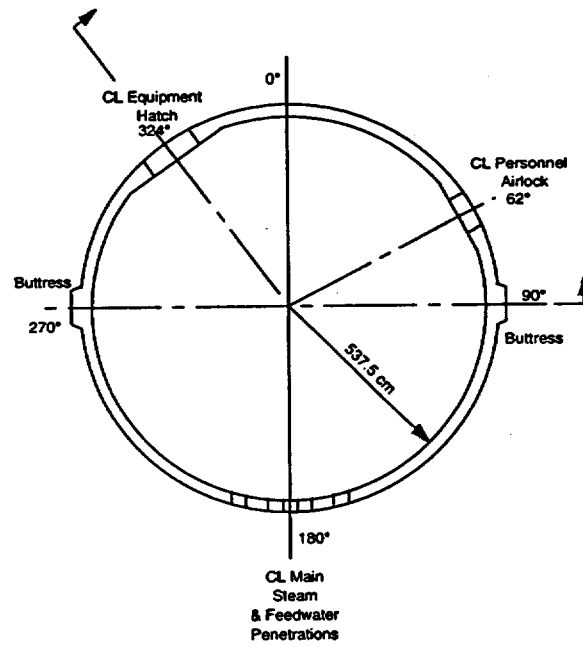
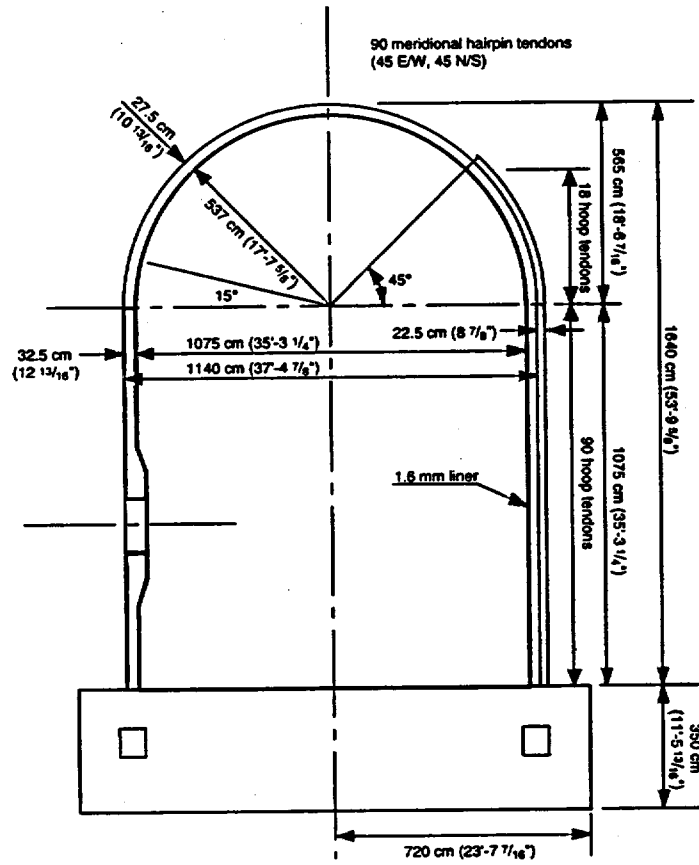


Figure 2.1 Outline Sketch of the Prestressed Concrete Containment Vessel (PCCV) Model

- Tendons: Each tendon in the prototype was matched in the model, 90 meridional hairpin tendons and 108 360° hoop tendons. Individual tendon areas were scaled, resulting in three 13.7 mm seven-wire strands per tendon.

Details of the design, including the design drawings, and construction are reported in the PCCV test report.^c

Prestressing levels for the model tendons were selected so that the net anchor forces (considering all losses due to anchor seating, elastic deformation, creep, shrinkage and relaxation) at the time of the Limit State Test matched those expected in the prototype after 40 years of service. One further adjustment was made by increasing the vertical tendon stress level to account for the additional gravity load in the prototype, which is lost in the geometric scaling.

2.2 Material Properties

The material specifications for the model components are the same as for the prototype and are summarized below.

Liner:	Japanese Industrial Standard (JIS) SGV410
Liner Anchors:	JIS SS400
Basemat Rebar:	JIS G3112, SD490 and SD390

Shell Rebar: JIS G3112, SD390 and SD345

Tendons: JIS G3536

Concrete: 450 kg/cm² and 300 kg/cm² at 91 days

Actual properties for all components were obtained from standard tests of samples of the construction materials. Standard coupons of the liner and liner anchor material were tested in uniaxial tension. Both full-sized and machined specimens of each size of rebar were tested in uniaxial tension. Separate tension tests of individual strands and the full tendon system (including anchorage hardware) were conducted. The results of these tests are reported in the PCCV test report^c and were made available to all the Round Robin participants.

Because pretest analyses and model construction occurred simultaneously, actual properties of the concrete were not available to the Round Robin participants. Compression tests of a trial mix, using the identical specifications and component materials (cement, aggregate, admixtures) as the concrete in the model, were conducted and provided to the Round Robin participants for pretest analysis. Subsequent to these tests, standard tests of concrete specimens obtained from batches of the model concrete were conducted for quality control purposes and to obtain estimates of properties at the time of prestressing and the Limit State Test. Results of all the material property tests are included in the PCCV test report.^c

^c Hessheimer, M. F. "Overpressurization Test of a Prestressed Concrete Containment Vessel Model. To be published.

3. INSTRUMENTATION

3.1 Model Instrumentation

Consistent with the objectives of the prestressed concrete containment vessel (PCCV) model test, the instrumentation suite was designed to provide information on the overall response of the model as well as areas that were expected to exhibit significant local response modes. The data collected from these transducers will be compared to the pretest analyses and, it is hoped, will lead to improvements in analysis methodologies. The instrumentation is not designed to "capture" specific failure events or rapid changes in the response variables, although the data, coupled with posttest analysis and physical inspection, should allow a reconstruction of the events resulting in the failure of the model.

A total of 1493 transducers, consisting of strain gages, displacement transducers, load cells, and pressure and temperature sensors, were installed on the model. The placement of these instruments was based on experience from previous model tests and preliminary analyses. In addition to these discrete response measurements, an acoustic monitoring system along with a suite of video and still cameras will be used to monitor the overall response of the model.

The global coordinate system and cardinal azimuths and elevations used to describe the model and the instrumentation suite are shown in Figure 3.1. The model global coordinate system is left-handed and originates at the center-top of basemat with the Z-axis (vertical) up and counterclockwise from 0°, as shown in the figure. The cardinal elevations are numbered 1 (top of basemat) through 13 (apex), and the cardinal azimuths, typically at 30° intervals, are labeled A (0°) through L (324°). One additional cardinal azimuth, Z, was introduced at 135° to represent the axisymmetric response of the model. (This azimuth was assumed to be relatively unaffected by structural discontinuities and a reasonable location for comparison with axisymmetric analyses.) Given this coordinate system, the buttresses are located at 90° (D) and 270° (J), the personnel airlock (A/L) at 62° (C), the main steam and feedwater line penetrations at 180° (G), and the equipment hatch (E/H) at 324° (L).

Both labeling systems appear in the stretched layout of the model in Figure 3.2. The solid dots in this figure represent the standard output locations for which participants are requested to provide the pretest analysis predictions of the deformation behavior of the model under pressurization. The detailed description of these locations is available in Section 3.2. The azimuth of 135° has been selected by Sandia National Laboratories as the location to best describe the free-field behavior of the model, because it is not close to any penetrations.

Brief descriptions of the types of measurements and data objectives for each type follow.

3.1.1 Strain Measurements

3.1.1.1 Reinforcing Bar Strain

Bonded, electrical resistance gages were installed on selected rebar to measure meridional, hoop, and transverse strains throughout the basemat, cylinder wall and dome. These gages are to determine the global and near-field membrane, bending and through-thickness strains as a function of location and pressure. Strain gages were not placed in areas of highly congested reinforcing or potentially high-strain concentrations. In these areas, rebar strains are measured at the "perimeter" of the zone of interest to provide the boundary conditions for comparison to analyses.

3.1.1.2 Liner and Liner Anchor Strain

Bonded, electrical resistance gages were installed on the liner and liner anchors to measure membrane and bending strains. These gages were located to measure both free-field and local strains. At several locations where high strains are expected, multiple gages were installed to obtain information about the strain distribution in the vicinity of the discontinuities and, it is hoped, to gain some insight into the mechanisms leading up to failure, should it occur at these locations. Measurements on the liner anchor are intended to provide some insight into shear transfer and pullout behavior of the liner anchor.

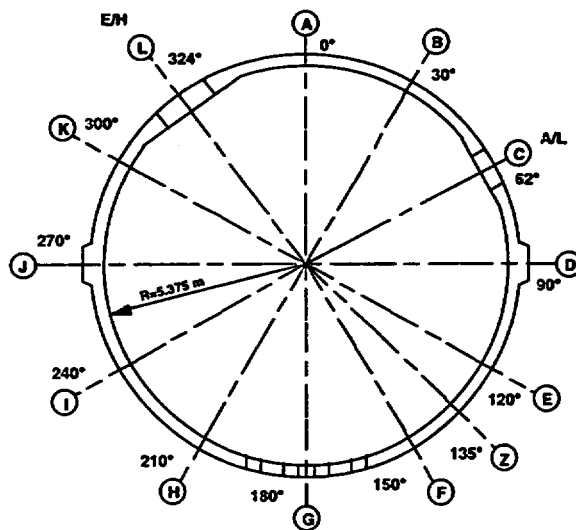
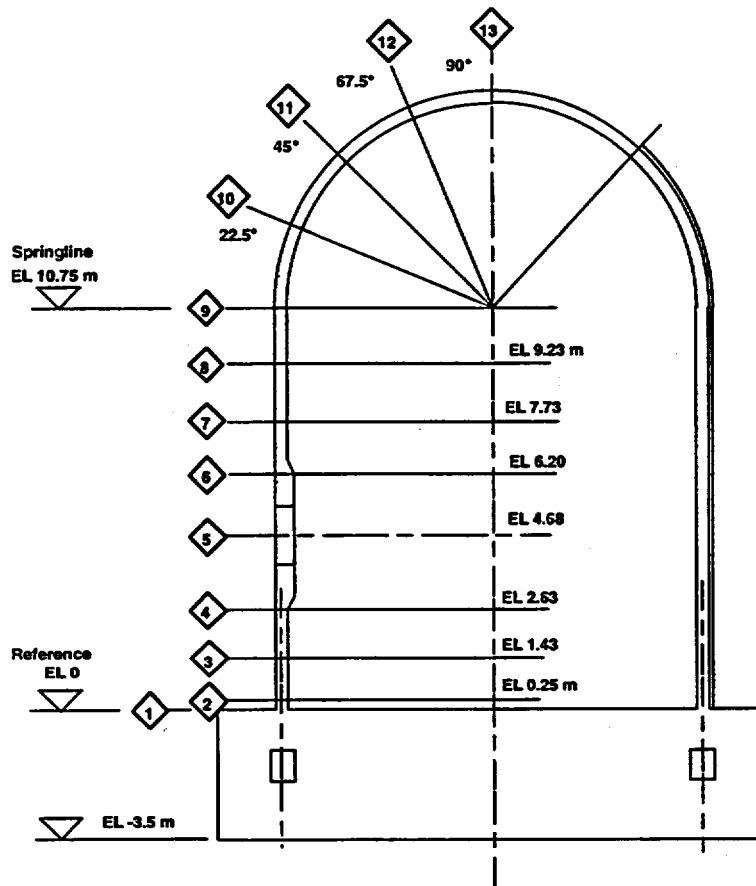


Figure 3.1 Prestressed Concrete Containment Vessel (PCCV) Model Coordinate System and Cardinal Lines

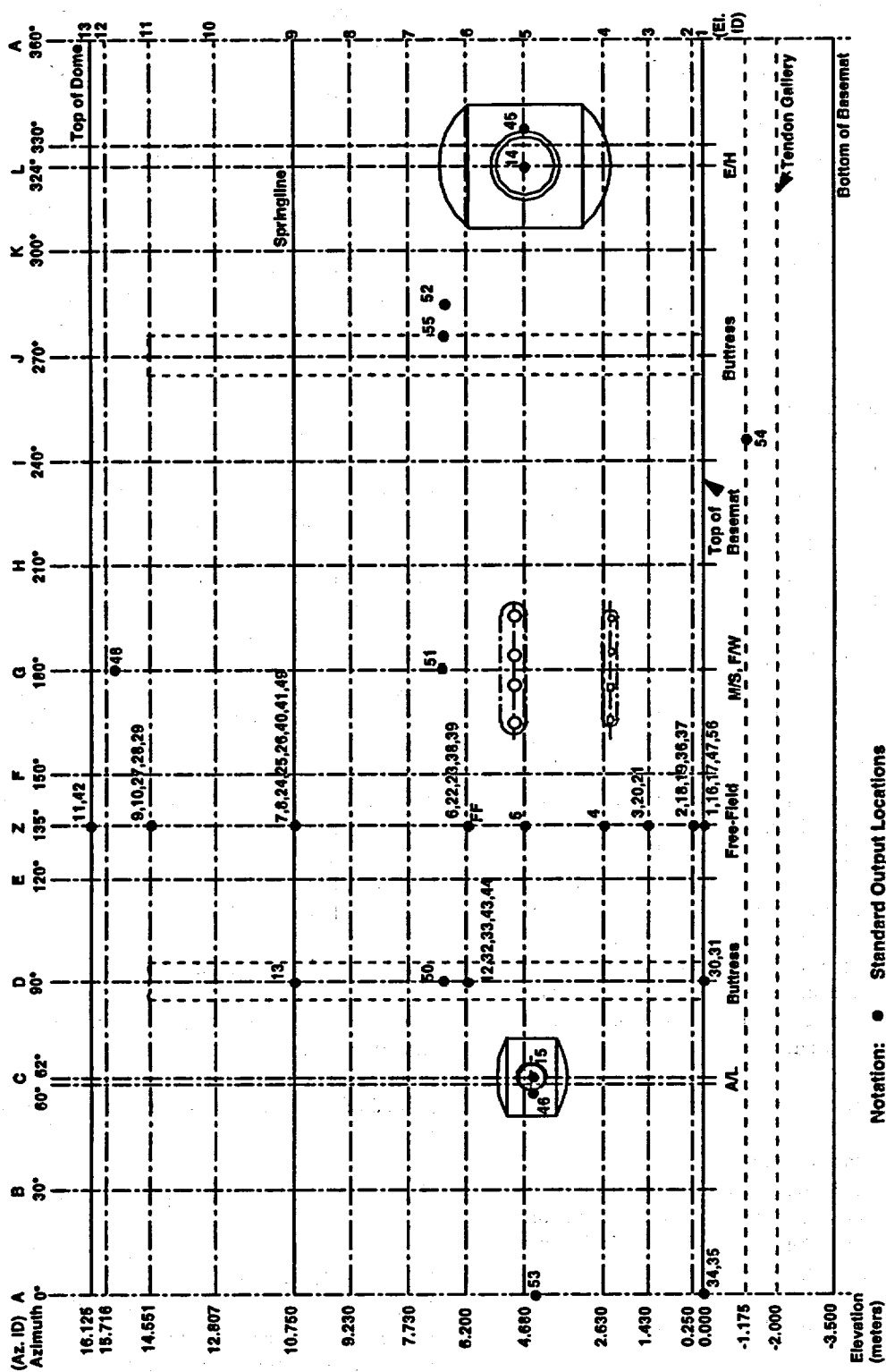


Figure 3.2 Developed Elevation of the Prestressed Concrete Containment Vessel (PCCV) Model and Standard Output Locations

3.1.1.3 Concrete Strain

Long gage-length fiber optic gages were imbedded in the concrete to obtain a direct measurement of concrete strains for comparison to the rebar strain measurements. Gages were placed where large free-field membrane strains are expected and at the wall-basemat junction where large tensile and compressive strains are expected to develop from bending.

3.1.2 Displacement Measurements

Three types of displacement transducers, with varying degrees of sensitivity and range, are used to measure displacements. Cable potentiometers (CPOTs) with a large range and medium accuracy are used to measure global deformations. Linear variable differential transformer (LVDT) transducers, with ranges less than 10 cm and relatively high accuracy, measure deformations around discontinuities where more accurate measurements are required. Where the overall displacements are small, a few temposonic linear displacement transducers (TLDTs) are used to measure displacements at locations requiring both high range and high accuracy. Most displacements are measured radially or vertically relative to an internal reference frame, which is assumed to remain fixed relative to the global coordinate system. (This assumption will be verified by monitoring the motion of the reference frame and, if necessary, correcting the model displacements by correcting for the frame deformation.) Local diametric displacements of the E/H and personnel A/L barrels and uplift of the basemat will also be measured.

3.1.3 Pressure Measurements

Two pressure transducers will record the internal pressure during the tests as a function of time. In addition to providing control feed back, the pressure data will be used to detect leaks and estimate the integrated gross leak.

3.1.4 Temperature Measurements

Thermocouples embedded in the concrete and installed on the inside surface of the liner will be used to correlate model response to ambient temperature variations and provide data for thermal compensation of all strain gages inside

the model. Resistance temperature detectors (RTDs) located inside the model will measure gas temperatures for estimating leak rates during the pressurization tests.

3.1.5 Tendon Measurements

3.1.5.1 Tendon Prestress Force (at ends)

Load cells at each end of every sixth tendon will be used to record tendon forces during prestressing operations and pressure testing.

3.1.5.2 Local Tendon Strain (along length)

Two types of electrical resistance strain gages, mounted along eight tendons, will measure the variation of strains along the tendon during tensioning and pressure testing.

3.1.6 Acoustic Monitoring System

An acoustic monitoring system, consisting of an array of 16 internal and 32 external accelerometers coupled with an independent data acquisition and processing computer, will record the acoustic output of the model during prestressing and pressure testing. The acoustic system is capable of locating the source of acoustic emissions and discriminating between acoustic events to identify cracking in the concrete, breakage of tendon wires or rebar and, it is hoped, tearing of the liner.

3.1.7 Video and Still Cameras

Four pressure-rated video cameras inside the model and four video cameras and two still cameras outside the model will provide a visual record of the model response during the pressure tests.

3.2 Standard Output Locations

Reporting and comparison of the pretest Round Robin analyses was standardized by specifying fifty-five (55) response variables (displacement, strain, etc.) corresponding to specific transducers on the PCCV model. These response variables were selected to provide a comparison of the predictions of the global and local response of the model based on engineering judgment, past experience, and preliminary analysis results. The participants were asked to submit response

predictions as a function of gage pressure at each of these Standard Output Locations (SOL). The SOL responses are defined in Table 3.1, and the locations are illustrated in Figure 3.2. The

preliminary and pretest analyses performed by Dameron et al. [6, 7] provided results that guided the selection of these locations.

**Table 3.1 Prestressed Concrete Containment Vessel (PCCV) Model
Standard Output Locations**

Loc. #	Type	Orientation	Az. (deg)	EL. (m)	Comments	General Location
1	Displacement	Vertical	135	0.00	Outside Cylinder	Top of Basemat
2	"	Radial	135	0.25	Inside Liner Surface	Base of Cylinder
3	"	Radial	135	1.43	"	"
4	"	Radial	135	2.63	"	"
5	"	Radial	135	4.68	"	E/H elev.
6	"	Radial	135	6.20	"	Approximate Midheight
7	"	Radial	135	10.75	"	Springline
8	"	Vertical	135	10.75	"	"
9	"	Horiz. (Rad)	135	14.55	"	Dome 45 deg
10	"	Vertical	135	14.55	"	"
11	"	Vertical	135	16.13	"	Dome apex
12	"	Radial	90	6.20	"	Midheight @ Buttress
13	"	Radial	90	10.75	"	Springline @ Buttress
14	"	Radial	324	4.675	"	Center of E/H
15	"	Radial	62	4.525	"	Center of A/L
16	Rebar Strain	Meridional	135	0.05	Inner Rebar Layer	Base of Cylinder
17	"	Meridional	135	0.05	Outer Rebar Layer	"
18	"	Meridional	135	0.25	Inner Rebar Layer	"
19	"	Meridional	135	0.25	Outer Rebar Layer	"
20	"	Meridional	135	1.43	Inner Rebar Layer	"
21	"	Meridional	135	1.43	Outer Rebar Layer	"
22	"	Hoop	135	6.20	Outer Rebar Layer	Midheight
23	"	Meridional	135	6.20	Outer Rebar Layer	"
24	"	Hoop	135	10.75	Outer Rebar Layer	Springline
25	"	Meridional	135	10.75	Inner Rebar Layer	"
26	"	Meridional	135	10.75	Outer Rebar Layer	"
27	"	Hoop	135	14.55	Outer Rebar Layer	Dome 45 deg
28	"	Meridional	135	14.55	Inner Rebar Layer	"
29	"	Meridional	135	14.55	Outer Rebar Layer	"
30	"	Meridional	90	0.05	Inner Rebar Layer	Base of Cylinder @ Buttress
31	"	Meridional	90	0.05	Outer Rebar Layer	"
32	"	Hoop	90	6.20	Outer Rebar Layer	Midheight @ Buttress
33	"	Meridional	90	6.20	Outer Rebar Layer	"
34	Liner Strain	Meridional	0	0.010	Inside Liner Surface	Base of Cylinder
35	"	Meridional	0	0.010	Outside Liner Surface	"
36	"	Meridional	135	0.25	Inside Liner Surface	"
37	"	Hoop	135	0.25	"	"
38	"	Meridional	135	6.20	"	Midheight
39	"	Hoop	135	6.20	"	"
40	"	Meridional	135	10.75	"	Springline
41	"	Hoop	135	10.75	"	"
42	"	Meridional	135	16.13	"	Dome apex
43	"	Meridional	90	6.20	"	Midheight @ Buttress
44	"	Hoop	90	6.20	"	"
45	"	Hoop	332	4.675	"	10 mm from thickened plate
46	"	Hoop	59	4.525	"	10 mm from thickened plate
47	Base Liner	Radial	135	0.00	100 mm Inside Cylinder	Basemat Liner Strain
48	Tendon Strain	Hairpin	180	15.60	Tendon - V37	Tendon Apex
49	"	Hairpin	135	10.75	Tendon - V46	Tendon Springline
50	"	Hoop	90	6.58	Tendon - H53	Mid Tendon
51	"	Hoop	180	6.58	Tendon - H53	1/4 - Tendon
52*	"	Hoop	280	6.58	Tendon - H53	Tendon Near Buttress
53	"	Hoop	0	4.57	Tendon - H35	Tendon between E/H and A/L
54	Tendon Force	Hairpin	241	-1.16	Tendon - V37	Tendon Gallery
55	"	Hoop	275	6.58	Tendon - H53	@ Buttress

4. PRESSURE TESTING

The prestressed concrete containment vessel (PCCV) model will be subjected to a series of quasi-static pressurization tests leading to functional failure or rupture during the Limit State Test. Figure 4.1 illustrates the nominal pressure time history, and each phase is summarized below. The model will be depressurized between each test. Nitrogen gas at ambient temperature (nominally 21°C) will be used as the pressurization medium for each test. All pressure tests will be conducted in a quasi-static manner by pressurizing the model in increments and holding pressure until the model response and pressure reach equilibrium. The pressurization system is designed to maintain the model at a constant pressure (within $\pm 3\text{kPa}$) up to a maximum leak rate of 1000% mass/day.

4.1 System Functionality Test (SFT)

The model will be pressurized to $0.1 P_d$ (0.04 MPa) in two increments of $0.05 P_d$ (0.02 MPa) holding pressure for one hour or longer at each step, depending on the duration needed to perform all system functionality and leak checks.

4.2 Structural Integrity Test and Integrated Leak Rate Test

The Structural Integrity Test (SIT) and the Integrated Leak Rate Test (ILRT) will be conducted as one continuous test, following a sequence that combines Japanese and U.S. standards for each test. First, during the SIT, the model is pressurized in five equal increments at a rate of 20 percent of the test pressure per hour up to the maximum test pressure of $1.125 P_d$ (0.44 MPa). The SIT pressure will be maintained for

one hour, then the model is depressurized to the ILRT pressure of $0.9 P_d$ (0.35 MPa). The model will be held at the ILRT pressure for a minimum of four hours to allow the model atmosphere to stabilize before the start of the leakage rate test, which will last for 24 hours. After the ILRT is completed, the model will be depressurized in steps matching the initial SIT-pressurization phase to allow for comparison of the response at each increment of pressure.

4.3 Limit State Test

The Limit State Test (LST) fulfills the primary objectives of the PCCV test program, i.e., to investigate the response of representative models of nuclear containment structures to pressure loading beyond the design basis accident and to compare analytical predictions to measured behavior.

Initially, the model pressurization sequence will match the pressurization sequence followed for the SIT to allow comparison of the model response to two cycles of loading. As the model pressure increases, the dwell time between pressure steps is expected to increase because the model takes longer to achieve its equilibrium state in the plastic domain. The high pressure test will be terminated when the model fails or the internal pressure reaches the operational limit of the pressurization system, $5.2 P_d$ (2.0 MPa). Model failure can be a structural failure, including a catastrophic rupture, or a functional failure that occurs when the pressurization system can no longer maintain pressure because of excess leakage ($>1000\%$ mass/day).

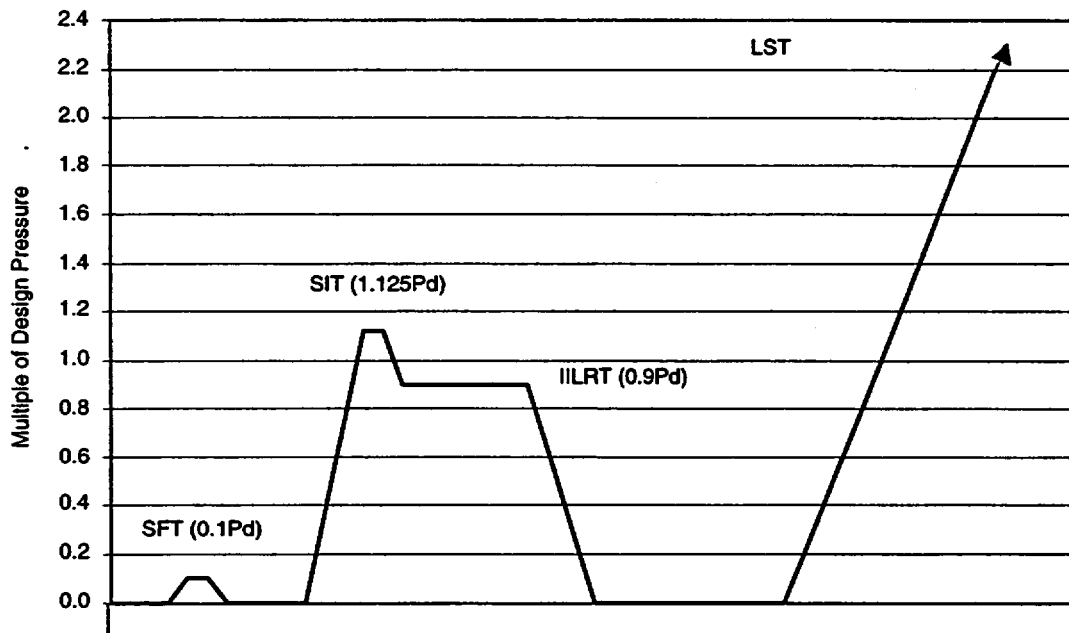


Figure 4.1 Pressurization Sequence for the Prestressed Concrete Containment Vessel (PCCV) Model Test

5. PRETEST ANALYSIS

Each Round Robin participant developed an approach to the pretest analysis, including selection of models and codes, application of the design information provided and criteria for interpreting or evaluating the results. Although each participant was asked to predict the response at each of the 55 Standard Output Locations (SOL), the majority of participants submitted predictions only at a subset of locations because of limitations in the analysis approach used. These results were compiled into composite plots for each SOL. These composite plots are provided in Appendix A. Congested sections of the composite plots were enlarged to provide an expanded view for clarity.

Every participant was asked to provide a report summarizing their analysis, and these are reproduced in Appendices B–R. Tables 5.1, 5.2, and 5.3 provide a brief summary of the codes, modeling approaches, and material models used by each participant to facilitate comparison of the analyses.

In addition to submitting response predictions at the SOLs, each participant was asked to provide a best estimate of failure pressure and mechanisms of the PCCV model. These are summarized in Table 5.5. Table 5.5 also summarizes predictions of the pressure for various milestones (onset of cracking, yielding, etc.) leading up to failure. Comments on the failure criteria applied by each participant are provided in Table 5.6.

Table 5.1 Finite Element Codes Used by Round Robin Participants			
AECL	Atomic Energy of Canada Limited	Canada	ABAQUS
ANL	Argonne National Laboratory	U.S.	TEMP-STRESS and NEPTUNE
CEA	Commissariat a l'Énergie Atomique	France	CASTEM 2000
EDF	Électricité de France	France	ASTER
Glasgow	University of Glasgow	U.K.	Research Code Univ. of Glasgow
HSE	Health and Safety Executive	U.K.	ABAQUS
IBRAE	Nuclear Safety Institute	Russia	CONT-2D and CONT-3D
INER	Institute of Nuclear Energy Research	Republic of China	ABAQUS
IPSN	Institut de Protection et de Sûreté Nucléaire	France	CASTEM 2000
JAERI	Japan Atomic Energy Research Institute	Japan	ABAQUS
JAPC	The Japan Atomic Power Company	Japan	FINAL
KINS	Korea Institute of Nuclear Safety	Korea	DIANA 7.1
KOPEC	Korea Power Engineering Company	Korea	ABAQUS
NUPEC	Nuclear Power Engineering Corporation	Japan	ABAQUS
PRIN	Principia	Spain	ABAQUS
RINSC	Russia International Nuclear Safety Center	Russia	DANCO
SNL	Sandia National Laboratories/ANATECH	U.S.	UMAT/ABAQUS

Table 5.2 Modeling Approaches Used In the Pretest Analyses

Participant	Model					Concrete	Liner	Rebar	Tendon	Cylinder Prestress Avg. or @ 135 (MPa)	
	General	Basemat	Penetrations	Buttress	# Elements					Hoop	Meridional
ANL	2D Axisym; shell	no	no	no	650	shell	offset membrane	embedded bars in shell	Hoop: ring Merid: truss, sliding no friction	350 kN (245 kN 30% red.)	470 kN
AECL	2D Axisym	yes		yes	85,000			rebar subelement	truss, no friction	Uniform initial stress	
	3D	no	E/H, A/L			8-node solid	4-node membrane	rebar subelement	truss, no friction	927	1272
CEA	Axisym @ 135	yes	no	no	5105	4-node solid	shell	Hoop: ring Merid: shell	Hoop: ring & shell Merid: shell tied to concrete	Uniform 269 kN	470 kN
EDF	1/8 w/ sym. multi-layer shell	yes	no	no	6120 DOF	multi-layer shell	shell layer	smearred shell layer	smearred shell layer tied to concrete	Uniform 513 174 kN	844 286 kN
Glasgow	3D	mp	no	yes		8-node solid		smearred tied to concrete	smearred tied to concrete		1377 467 kN
INER	3D slice (45° (135° - 180°)	yes	no	no	n/a	3D solid element, C3D20	3D shell element S8R	r/a	r/a	1185 MPa	1436 MPa
IPSN	3D slice (2 deg)	yes	no	no	2,513	solid	shell	discrete	truss	453 kN	303 kN
JAERI	3D symmetric shell model (90° - 180°)	yes	no	yes	8,237	shell	shell	rebar subelement	bar element	350 kN	470 kN
	2D Axisym shell	no	no	no	382	shell	shell	rebar subelement	merid: rebar subelement hoop: shell	350 kN	470 kN
JAPC	Global (Axisym, 3D)	yes		yes	2,000	multi-layer shell	shell	shell	truss	Friction loss considered	
	Local (3D)		E/H, A/L		20,000	8-node solid	anchor as springs	truss	w/ friction element		
	Local (liner)		M/S								
KINS	3D multi-layer shell	yes	E/H, A/L	yes	2,000	shell	shell	smearred layer	bar, bonded	Friction and setting loss calculated by code	
KOPEC	3D multi-layer shell	yes	E/H, A/L	yes	1,720	4-node shell	shell	bar, bonded	bar, bonded	724	varies
	2D Axisym	soil			209	8-node solid	3-node shell				
HSE	3D global	yes	E/H, A/L	yes	140,662	8-node solid	Membrane	rebar subelement	Merid: truss w/ sliding	1031	1386
	3D slice	soil				3 thickness	anchor as spring		initial stress	350 kN	471 kN
	2D liner										
NUPEC	Axisym	yes	no	no	1,279	4-node solid	shell	rebar subelement	Hoop: rebar subelement Merid: shell	991	503-470 kN @ loading end
	Axisym	yes	no	no	2,194	4-node solid (duplicate)	shell	rebar subelement	rebar	991	470 kN
	3D local	no	no	yes	15,810	8-node solid (duplicate)	shell	rebar subelement	beam w/ friction	453-394 kN	470 kN
	3D local	no	E/H	yes	16,567	8-node solid (duplicate)	shell	rebar subelement	beam w/ friction	453-394 kN	470 kN
	3D local	no	A/L	yes	16,425	8-node solid (duplicate)	shell	rebar subelement	beam w/ friction	453-394 kN	470 kN
	3D local	no	M/S	yes	13,081	8-node solid (duplicate)	shell	rebar subelement	beam w/ friction	453-394 kN	470 kN
IBRAE	2D Axisym	no	no	no	2,700	4-node solid	4-node solid	Thin layers	Distributed load		
	3D	yes	yes	yes	24,508	8-node solid	8-node solid	Thin layers	Distributed load	331.5 kN	467.5 kN
PRINCIPIA	2D Axisym solid	yes soil	no	no	510	8-node solid	3-node shell	rebar	Hoop: rebar Merid: truss w/ friction	829	1142
RINSC	3D (90 deg)	no	E/H	no		shell		thin wall layers	shell ribbons	350 kN	470 kN
SNL/	2D Axisym	yes	E/H	yes	4,000	solids	shell/membrane	rebar subelement	truss w/ friction tie	797	1334
ANATECH	3D R-Theta		A/L		60,000					1109	
	3D Local		M/S								

Table 5.3 Material Properties used in the Pretest Analyses

Participant	Cylinder/Dome Concrete			Liner			Cylinder/Dome Rebar				Tendons		
	E (MPa)	f _c (MPa)	f _t (MPa)	E (MPa)	f _y (MPa)	Strain	Grade	E (MPa)	f _y (MPa)	Strain	E (MPa)	f _y (MPa)	Strain
ANL				Best fit			Average of 390&490				Best fit		
	27,000	47.3	3.45	240,900	386	33%	SD 390	210,500	422	6.90%	206,120	1,604	3.25%
AECL													
	26,790	44.13	3.45 e _{cr} =60*	198,389	383	5%		166,194	364	7%	217,672	1,750	3%
CEA	Otosen						Average for each size and type				191,000 1,703 5%		
	27,000	44 • ρ=-0.9%	3.45	183,000	457	14%							
EDF	Nadal B with fixed crack @ 90 deg												
	29,470	54.52 • u=0.005	2.55 • u=0.0005	232,000	383	30%		190,000	439.00 445.00	20%	200,000	1,750	3.4%
Glasgow													
	38,100	44.13	3.4 4.06 (?)	224,000	398			183,000	470		200,000	1,750	
INER							Data fit						
	32,552 29,619	44.13 39.16	2.284 2.078	228,000	375	(perfectly plastic)					211,784	1,482.5	2.5%
IPSN	Otosen			n/a			n/a				n/a		
	27,000	44	3.45										
JAERI							Multi-linear elasto plastic for each size						
	29,100	617	3.82	217,000	381	5%					210,000	1,594	2.5%
JAPC	Darwin-Pecknold, shear retention			Multi-linear			Multi-linear elasto plastic				Multi-linear		
	29,400	44	3.33	215,745	382	0.177%		185,082	459	0.25%	196,132	1,520	0.78%
					382	2.00%			459	1.53%		1,746	1.10%
					408	2.44%			554	4.00%		1,902	3.70%
					436	3.60%			589	6.00%		1,912	0.08%
					457	5.00%			644	21.29%		1,940	20.00%
					500	33.00%							
KINS	Hognested, tension stiffening			Multi-linear elasto plastic			Multi-linear elasto plastic				Multi-linear elasto plastic		
	29,500	54.3	3.83	210,000	383	33%		210,000	482	8%			3.5%
									490	9%			
KOPEC	(Avg. SC & FC)												
	Menetrey-William						Bi-linear approximation for each size and type						
	26,970 27,950	47.3 39.16	3.45 3.37	218,700	376	33%					191,000	1,691	3.51%

Table 5.3 Material Properties used in the Pretest Analyses (continued)

Participant	Cylinder/Dome Concrete			Liner			Cylinder/Dome Rebar				Tendons		
	E (MPa)	fc' (MPa)	ft (MPa)	E (MPa)	fy (MPa)	Strain	Grade	E (MPa)	fy (MPa)	Strain	E (MPa)	fy (MPa)	Strain
HSE	Chen-Chen (smeared crack) + damaged			Elastic plastic (mean value)			Elastic plastic (mean value)				Elastic plastic (mean value)		
	27,950	88	4.4	219,850	382	11%	SD345-D8	169,000	370	30%	224,230	1,740	4%
							SD345-D10	182,000	370	24%			
							SD390-D10	183,000	477	21%			
							SD390-D13	183,000	440	24%			
							SD390-D16	183,000	450	22%			
							SD390-D19	184,000	470	22%			
							SD390-D22	191,000	465	26%			
							SD490-D10	187,000	500	21%			
							SD490-D13	184,000	548	16%			
						SD490-D16	185,000	490	17%				
						SD490-D19	186,000	514	18%				
NUPEC	Smeared Crack			Average of test data									
	27,000 28,000	49 42	3.45 3.37	219,000	377	8%		185,000	459	12% 18%	194,000	1,470	3%
IBRAE													
	27,000 26,970	40 44.13	3.45 3.84	210,000	380	33%		18,500	450	33%	200,000	1,700	3.3%
PRINCIPIA	Chen-Chen with strain softening			Elastic-plastic									
	27,000 28,000	44 55	3.6 3.6	219,000	384	28%	SD390 SD490	186,000 185,000	460 526	19% 17%	220,000	1,742	8%
RINSC													
	27,000	49	3.5	n.a.	n.a.	n.a.	Both	200,000	400	n.a.	210,000	1,690	n.a.
SNL/ ANATECH	ANACAP-U, smeared crack			Data Fit			Data Fit				Data Fit		
	33,000		2.64 (80μ)										

fc' = uniaxial strength
fy = yield strength

Table 5.5 Pretest Analysis Results (MPa)

Participant	Cracking		Liner Yield	Rebar Yield		Hoop Tendon Stress				Pressure @ Failure	Free-Field Hoop Strain	Mode
	Hoop	Meridional		Hoop	Meridional	Yield	1%	2%	3%			
ANL	0.68	0.64	1.00	1.07	1.35	1.23	1.37	1.53	1.61	1.51 1.62	1.69% 3.31%	local liner tear (El. 6.4 m) midheight hoop tendon failure at El. 6.4 m
AECL (3D) (Axi)	0.97 0.87	0.85 0.78	— 1.06	— —	— —	— —	— —	— —	— —	0.94 1.24		complete cracking axisymmetric yield
CEA	0.70	0.50								1.60 1.70		numerically unstable
EDF	0.47	0.86		0.88	1.03	1.30	1.34	1.38	1.91	1.95		
Glasgow	0.95		1.00 1.10		0.87 1.60							
INER	0.69	n/a	n/a	n/a	n/a	n/a	n/a	n/a	n/a	0.81	n/a	n/a
IPSN	n/a	n/a	n/a	n/a	n/a	n/a	n/a	n/a	n/a	n/a	n/a	n/a
JAERI	0.92	0.74	1.20	n/a	n/a	n/a	n/a	n/a	n/a	n/a	1.24	buckling at dome portion or local fracture by bending in cylinder portion
JAPC	0.60	0.65	0.96	0.98	1.25	1.15	1.25	1.37	1.42	1.45 1.55		Rupture of structural elements (tendon, rebar, or liner) placed in the hoop direction at a wall height of about El. 7 m.
KINS	0.39	0.62		0.86	1.27		1.25	1.33	1.37	1.25 1.44		tendon rupture
KOPEC (2D) (3D)	0.64 0.61		1.01 0.94	1.20 1.08		1.03 1.41	1.32	1.36	1.39	1.30 1.51		tendon @ 3.55%
HSE/NNC	0.57	0.57			1.70	1.60	1.60	1.75	1.75	1.98	3%	Liner tear with extensive concrete cracking at buttress region.
NUPEC	0.82	0.59	1.02	1.25	1.45		1.33	1.49	1.57	1.49 1.57	3%	tendon rupture
IBRAE	0.70	0.78	1.15	1.22	0.90	1.01	1.15	1.21	1.25	1.26		tendon rupture
PRINCIPIA	0.58	0.92		0.96	1.00	1.30				1.30		tendon yielding
RINSC	n.a.	1.00	n.a.	n.a.	n.a.	n.a.	n.a.	n.a.	n.a.	1.50	n.a.	hoop failure of vessel
SNL/ ANATECH	0.59	0.57		0.86	1.10		1.18	1.27	1.32	1.18 1.25 1.40 1.42		local liner strain (lower bound) 16% liner strain @ E/H-best guess tendon rupture 2% global strain (upper bound)

Table 5.6 Failure Criteria

Participant	Comments on Failure Criteria
ANL	Effective plastic strain exceeds uniaxial strain limits for rebar and tendons, Rebar failure strain \approx 7.0% and Tendon failure strain = 3.25% Local "knockdown" and triaxiality consideration on uniaxial strain failure for liner, failure strain = 1.69% (using global strain in liner from axisymmetric analysis)
AECL	"Capacity failure" means that both through-wall concrete cracks and the ultimate strength/strain of any steel component (liner, rebar, post-tension tendons) have occurred. In view of the complexity and uncertainties involved in this type of analysis (and perhaps testing also), some sort of "fragility capacity" should be defined, e.g. 90% or 95% of confidence of non-exceedance.
CEA	Cracking of concrete leading to the yielding of tendons and rebars
EDF	Hoop tendon yielding @ 3% (1.41 for ASTER, 1.45 for hand calculations)
Glasgow	Define more precisely failure indicators.
INER	n/a
IPSN	n/a
JAERI	Buckling at dome portion at 1.24 MPa or local fracture by bending in the cylinder portion at 1.27 MPa
JAPC	Equivalent average strain of rebar exceeds 6% around rebar cut-off sections and buttresses. Hoop tendon strain exceeds 3.75% at fixed end or 8.0% at regular region. Liner strain exceeds 20% at buttresses because of out-of-plane bending.
KINS	Hoop tendons in cylinder portion reach a rupture strain of 3.35% at 1.38 MPa
KOPEC	Tendon strain 3.51% Liner tearing strain 33%
HSE/NNC	Liner: 11% at joint, 3% @ free field
NUPEC	Liner: 8%; Rebar: 12-18%; Tendon: 3% at loading end; Concrete: 34 MPa after cracking
IBRAE	Hoop tendon yielding 3.3%
PRINCIPIA	Effective material stress exceeds material stress limits
RINSC	Penetrating cracks appear in concrete and loss of air-tightness occurs at 1.5 MPa
SNL/ANATECH	"Damage that leads to leakage"; Concrete cracking is <i>not</i> failure; Rebar e_u = 5%, Liner e_u = 16%

6. SUMMARY

The work reported herein represents, arguably, the state of the art in the numerical simulation of the response of a prestressed concrete containment vessel (PCCV) model to pressure loads up to failure. A significant expenditure of time and money on the part of the sponsors, contractors, and Round Robin participants was required to meet the objectives. While it is difficult to summarize the results of this extraordinary effort in a few paragraphs, the following observations are offered for the reader's consideration:

(Note: These observations by the Round Robin Analysis Coordinator, Sandia National Laboratories, do not represent a consensus by the participants.)

- Almost half the participants used ABAQUS as the primary computational tool for performing the pretest analyses. The other participants used a variety of codes, most of which were developed "in house."
- Only a few participants reported on "hand calculations" used to corroborate the finite element calculations, although it is suspected many more participants performed checks that they did not include in their reports.
- Almost every participant performed some type of simplified analysis that "smeared" or omitted spatial discontinuities before proceeding to more-detailed three-dimensional analyses.
- The majority of participants tried to account for some "slip" between the tendons and the concrete, although most also chose to assume that tendon forces were uniform along the length of the tendon.
- All participants used the material property test data provided as the basis for their material models, although there was some variation in how the material data were used. Some participants chose to average the data for a group of materials while others chose to define subsets of material properties that more closely matched the test data.
- Predictions of elastic response were, for the most part, very consistent up to the onset of global yielding (hoop) which appears to occur around $2.5 P_d$ or about 0.8 to 1.3 MPa. Predictions of response diverge significantly beyond this point with responses varying by a factor of three to five or more at a given pressure.
- There are considerable differences in the predictions of some local strains, such as those close to a penetration, after global yielding has occurred.
- Nevertheless, the predicted capacity of the model is fairly consistently bounded at 4 to 5 P_d . For failure predictions based on material failure of the steel components (liner, rebar or tendons), the average predicted pressure at failure is $3.6 P_d$ or 1.46 MPa.
- Approximately half the participants predicted failure based on structural failure, i.e., rupture of rebar or tendons, while approximately half the participants predicted functional failure from excessive leakage through a tear in the liner and/or cracks in the concrete. No one predicted failure from a shear failure or by leakage through the penetrations.

7. REFERENCES

1. Clauss, D.B. *Round Robin Pretest Analyses of a 1:6-Scale Reinforced Concrete Containment Model Subject to Static Internal Overpressurization*. NUREG/CR-4913, SAND87-0891. Albuquerque, NM: Sandia National Laboratories. 1987.
2. Clauss, D.B. *Round Robin Analysis of the Behavior of a 1:6-Scale Reinforced Concrete Containment Model Pressurized to Failure: Posttest Evaluations*. NUREG/CR-5341, SAND89-0349. Albuquerque, NM: Sandia National Laboratories. 1989.
3. Luk, V.K., M.R. Hessheimer, G.S. Rightley, L. Dwight Lambert, E.W. Klamerus. *Design, Instrumentation, and Testing of a Steel Containment Vessel Model*. NUREG/CR-5679, SAND98-2701. Albuquerque, NM: Sandia National Laboratories. 2000.
4. Luk, V.K., and E.W. Klamerus. *Round Robin Pretest Analyses of a Steel Containment Vessel Model and Contact Structure Assembly Subject to Static Internal Pressurization*. NUREG/CR-6517, SAND96-2899. Albuquerque, NM: Sandia National Laboratories. 1998.
5. Luk, V.K., and E.W. Klamerus. *Round Robin Posttest Analysis of a Steel Containment Vessel Model*. NUREG/CR-5678, SAND98-2700. Albuquerque, NM: Sandia National Laboratories. 2000.
6. Dameron, R.A., Y.R. Rashid, V.K. Luk, and M.F. Hessheimer. "Preliminary Analysis of a 1:4 Scale Prestressed Concrete Containment Vessel Model," *Proceedings of the 14th International Conference on Structural Mechanics in Reactor Technology*, Vol. 5, pp. 89-96, Lyon, France, August 17-22, 1997.
7. Dameron, R.A., Y.R. Rashid, V.K. Luk, and M.F. Hessheimer. 1998. "Investigation of Radial Shear in the Wall-Base Juncture of a 1:4 Scale Prestressed Concrete Containment Vessel Model," *Proceedings of 1998 ASME/JSME Joint Pressure Vessels and Piping Conference*, PVP-Vol. 362, pp. 189-198, San Diego, California, July 26-30, 1998.

APPENDIX A

COMPOSITE PLOTS

This page intentionally left blank to facilitate plot comparison.

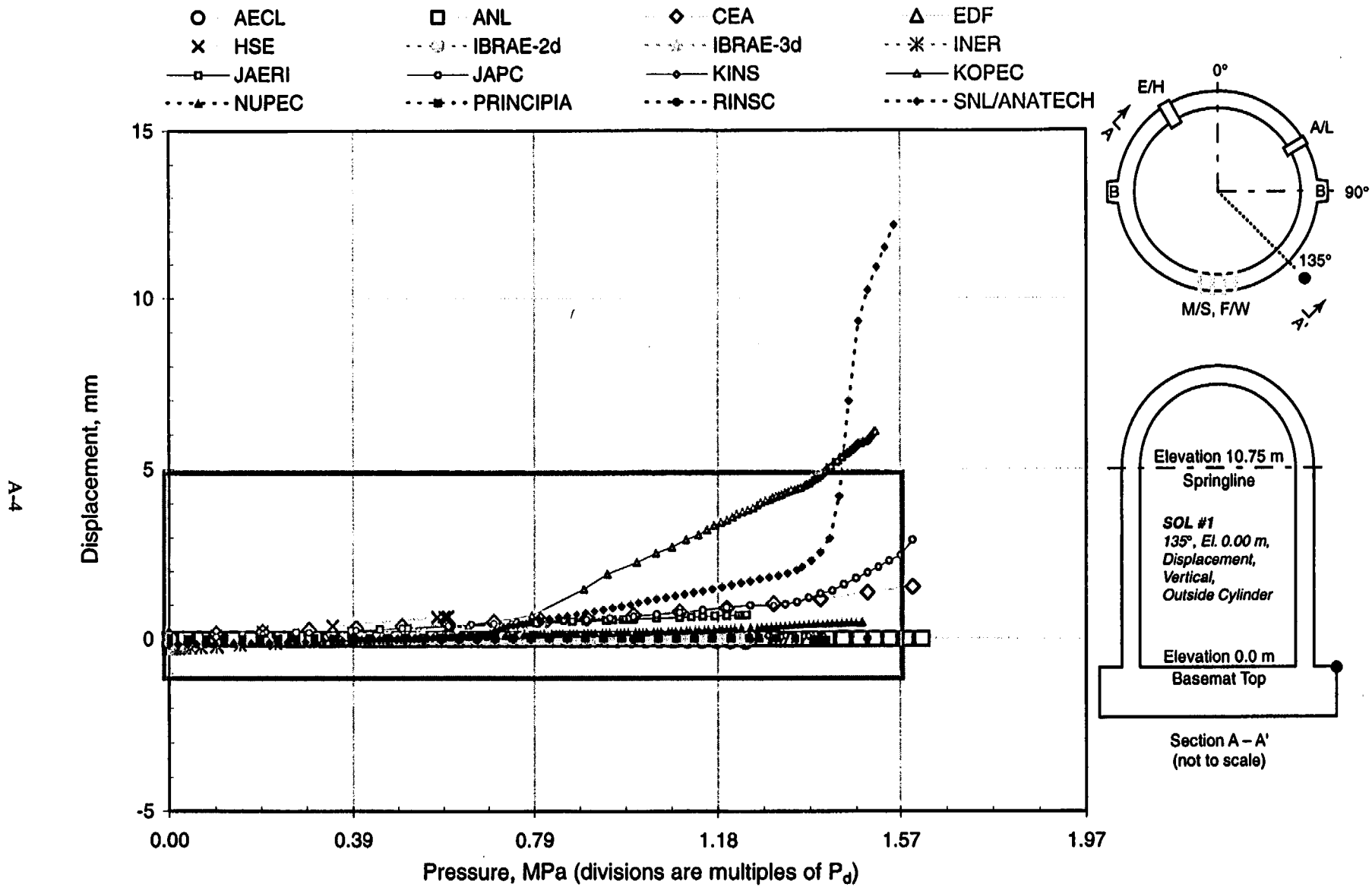


Figure A-1a. PCCV Standard Output Location (SOL) #1.

A-5

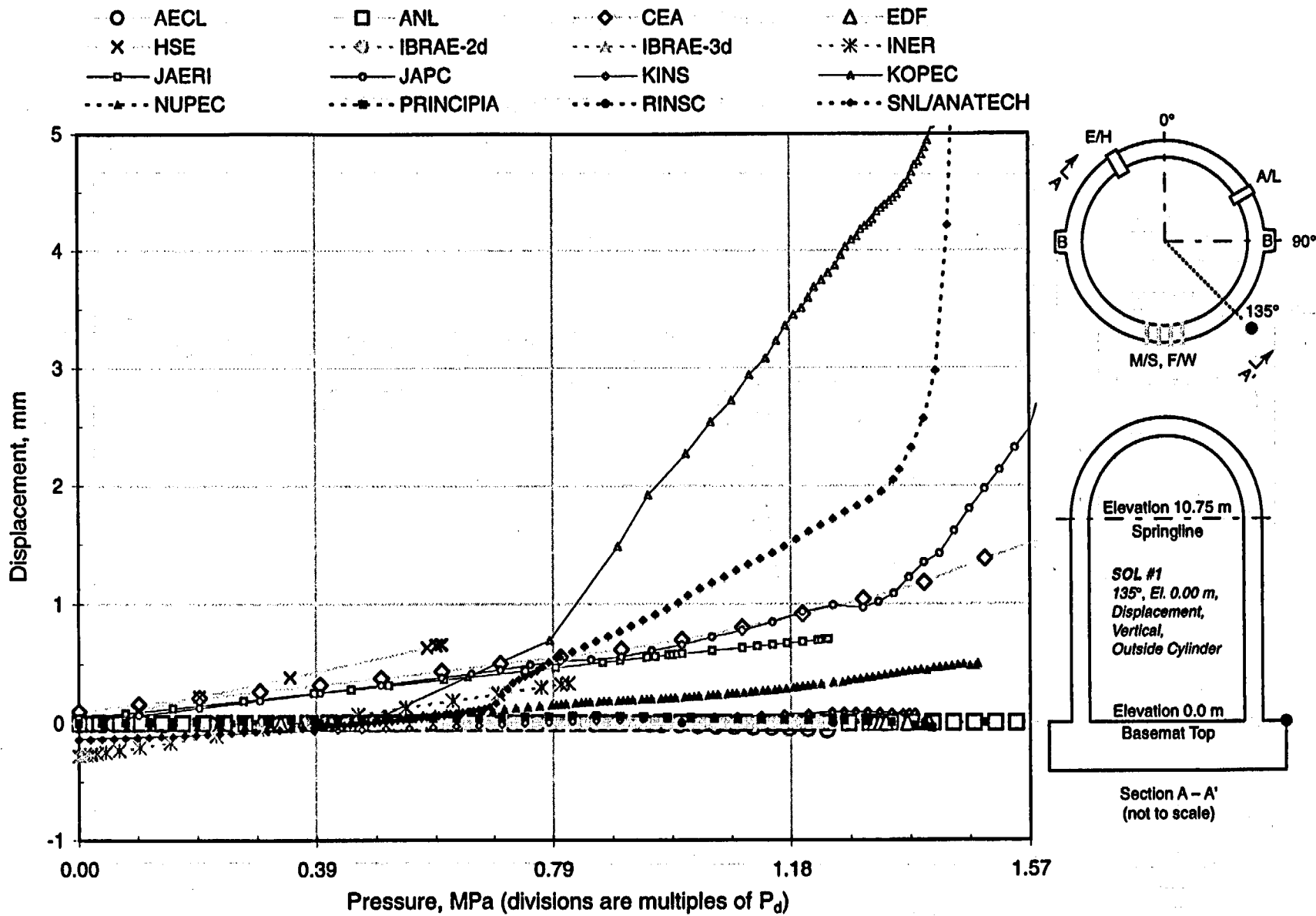


Figure A-1b. PCCV Standard Output Location (SOL) #1, enlarged.

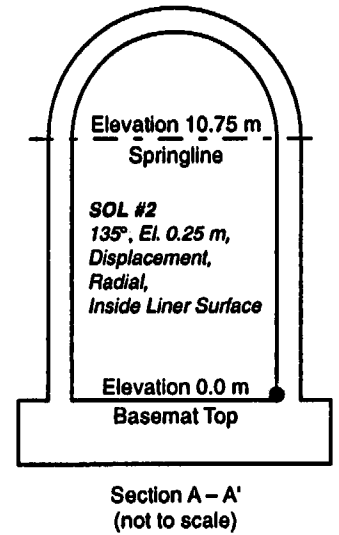
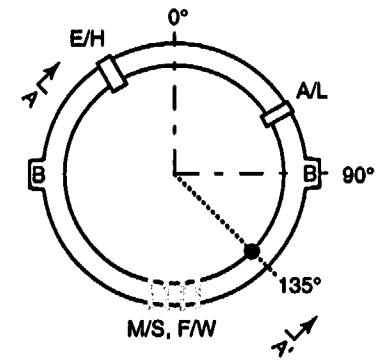
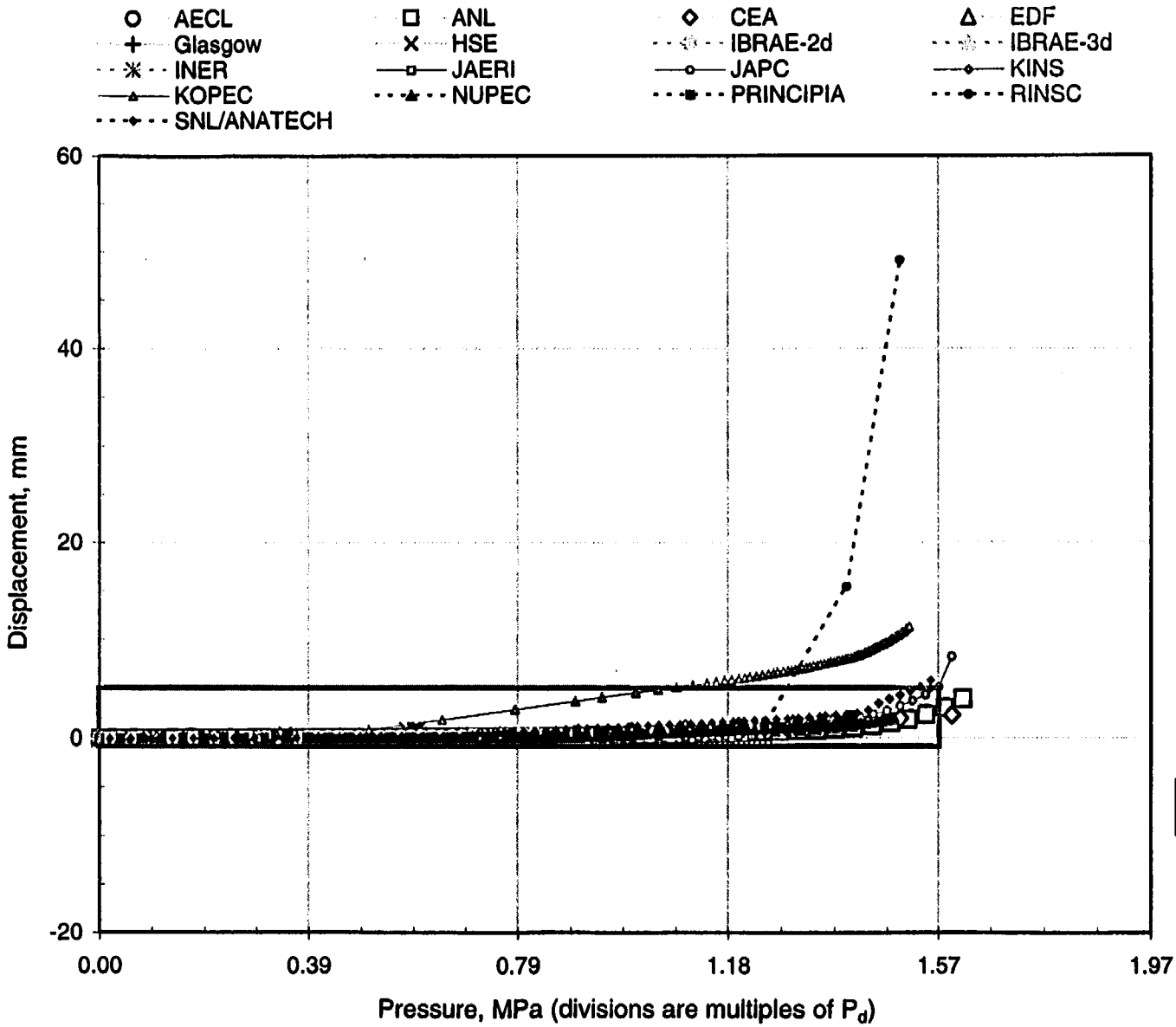


Figure A-2a. PCCV Standard Output Location (SOL) #2.

A-7

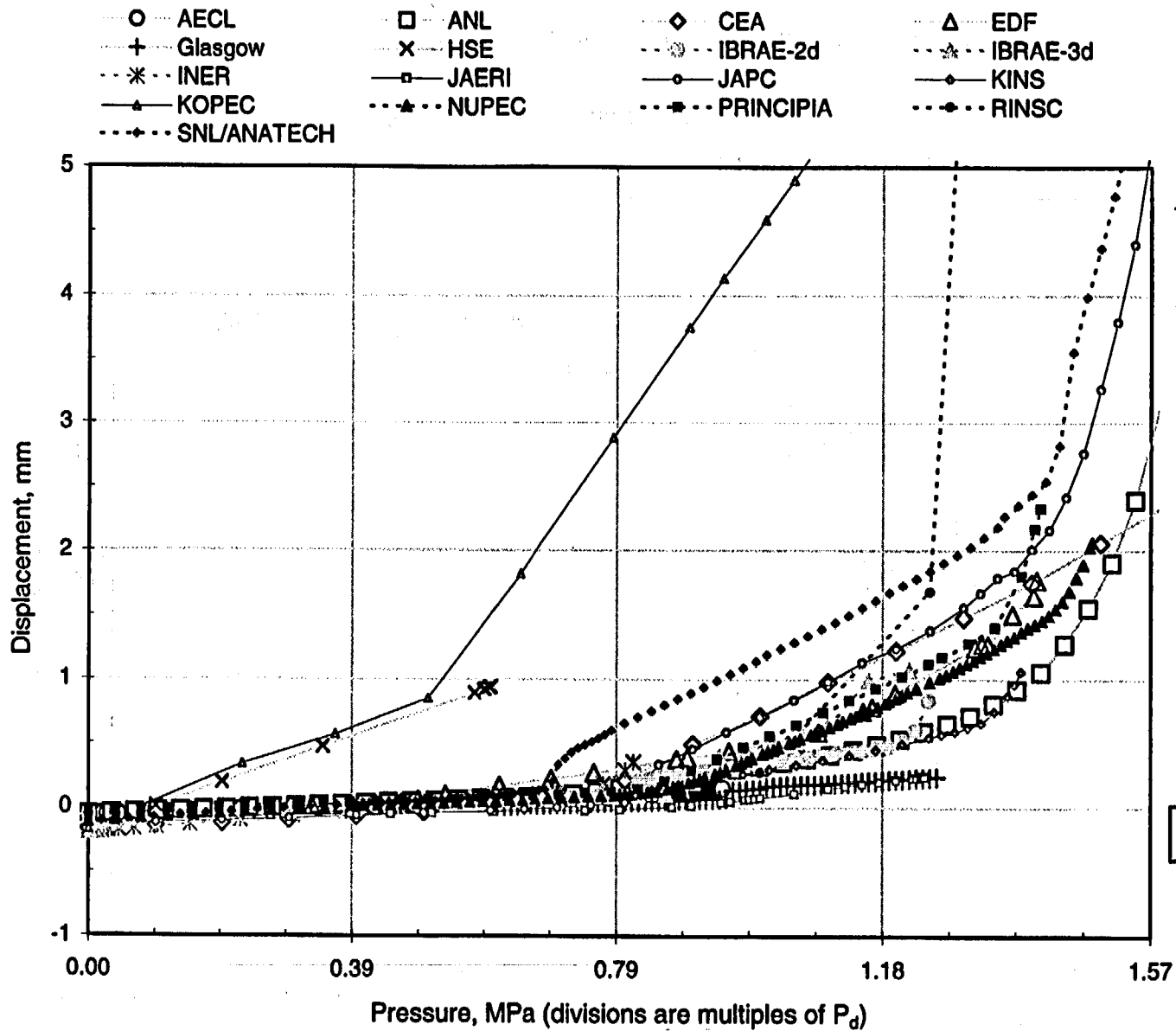


Figure A-2b. PCCV Standard Output Location (SOL) #2, enlarged.

A-8

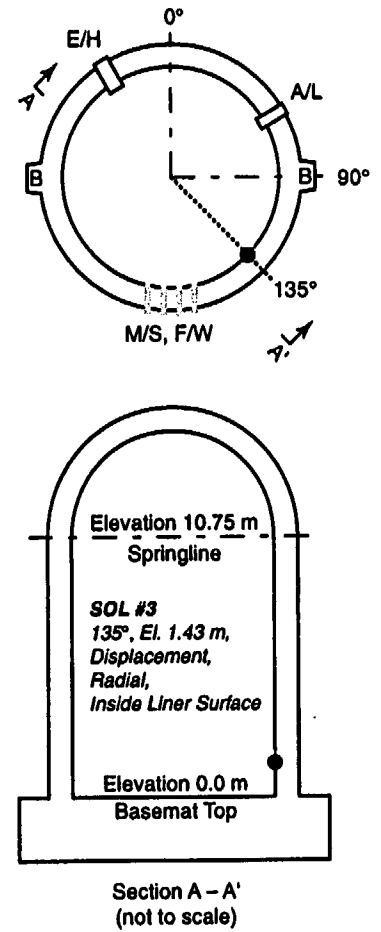
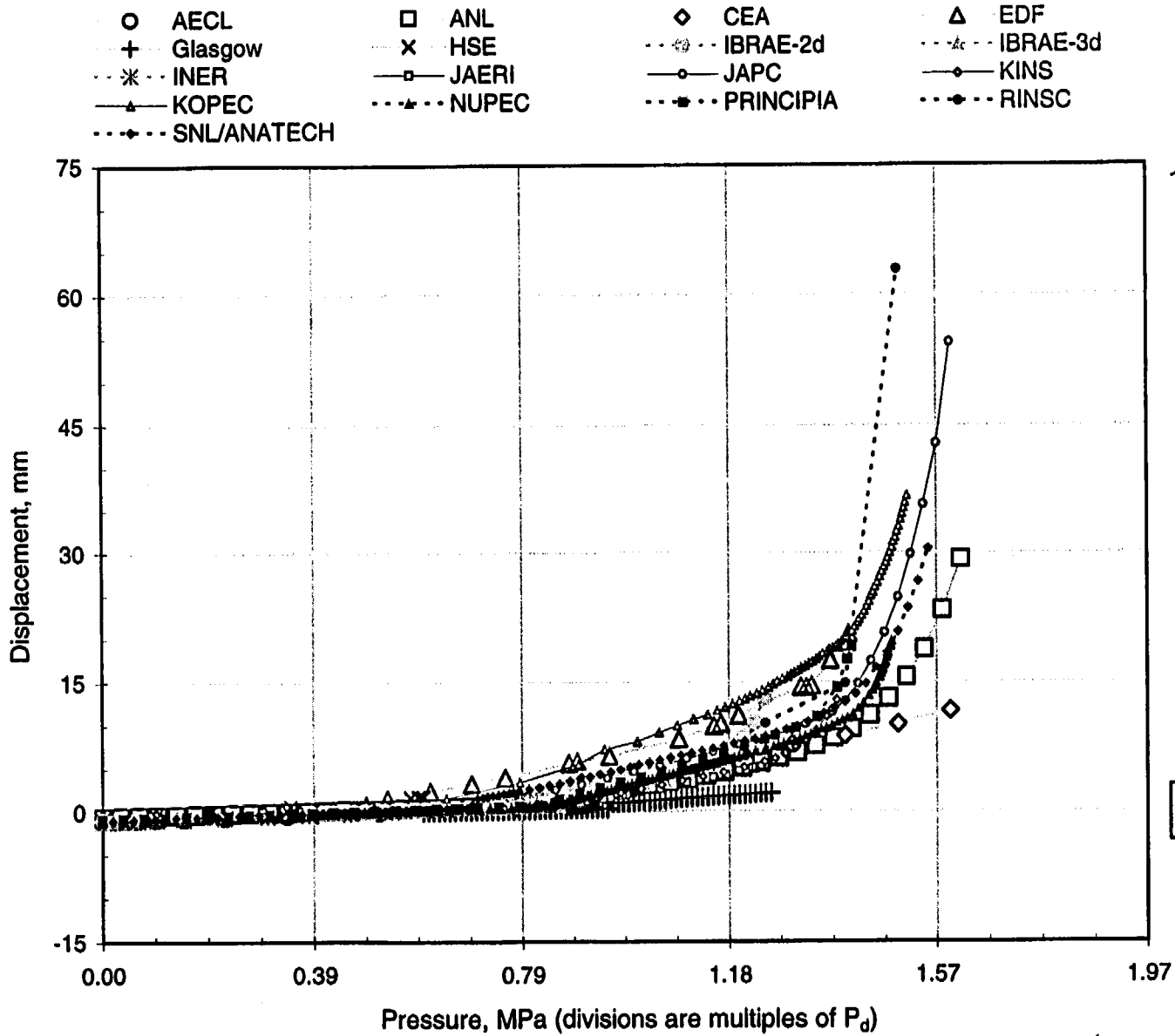


Figure A-3. PCCV Standard Output Location (SOL) #3.

This page intentionally left blank to facilitate plot comparison.

A-10

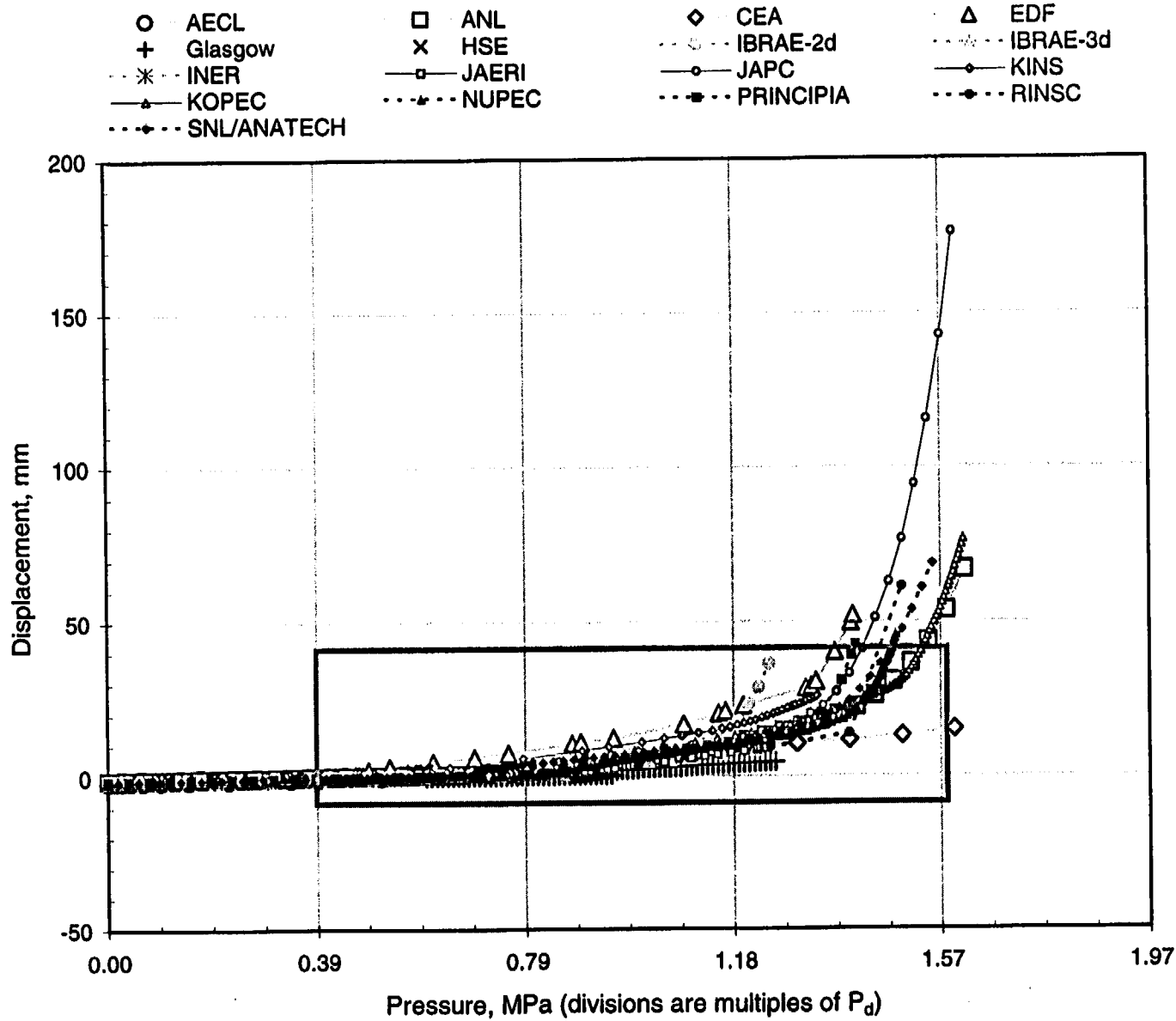


Figure A-4a. PCCV Standard Output Location (SOL) #4.

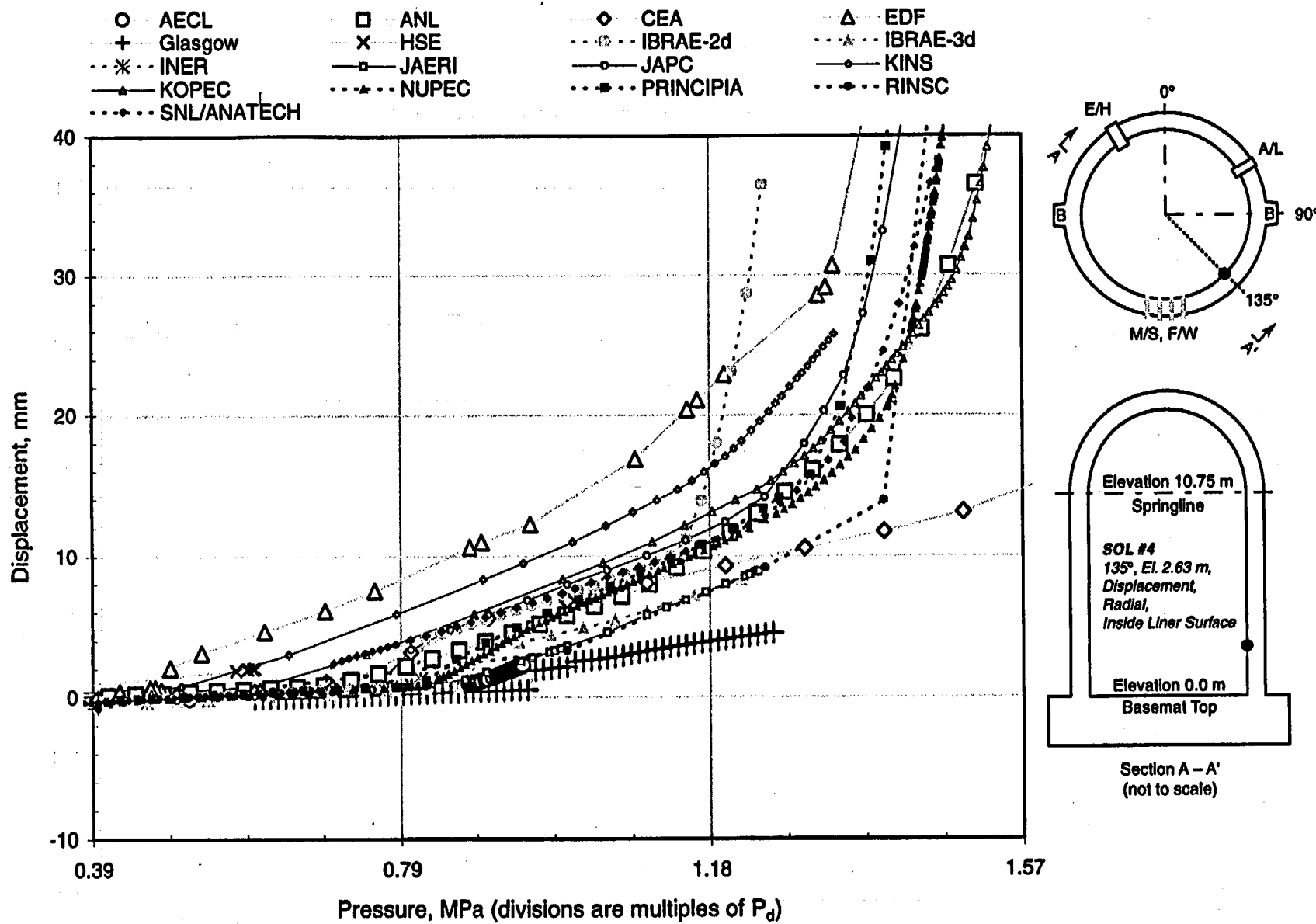


Figure A-4b. PCCV Standard Output Location (SOL) #4, enlarged.

A-12

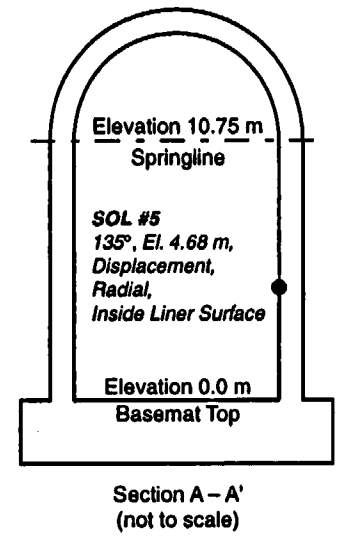
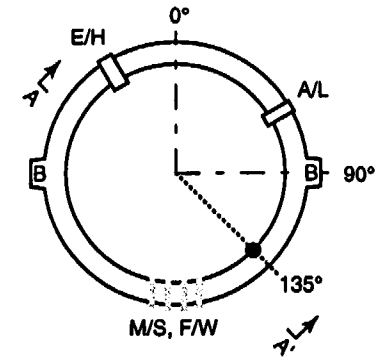
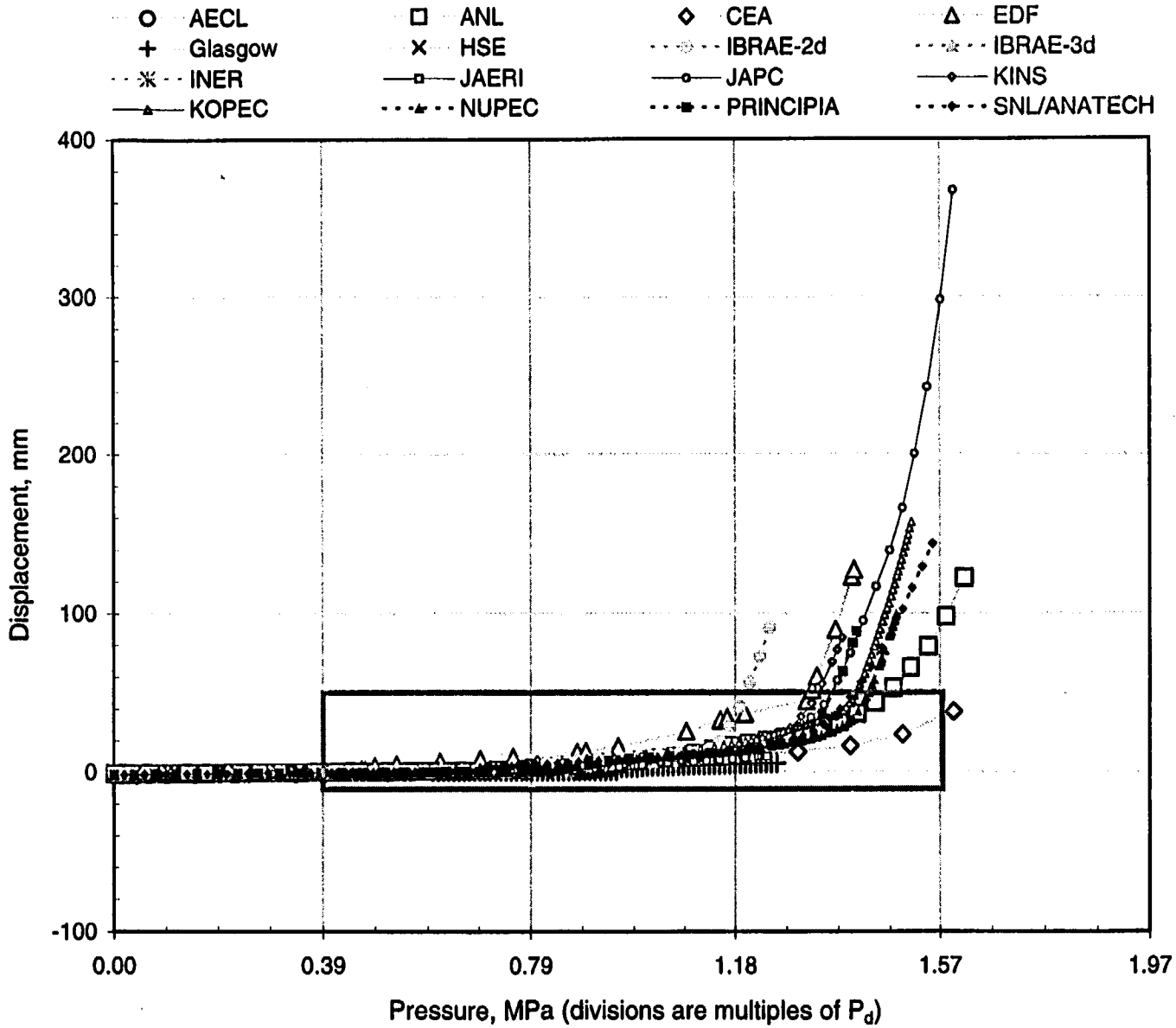


Figure A-5a. PCCV Standard Output Location (SOL) #5.

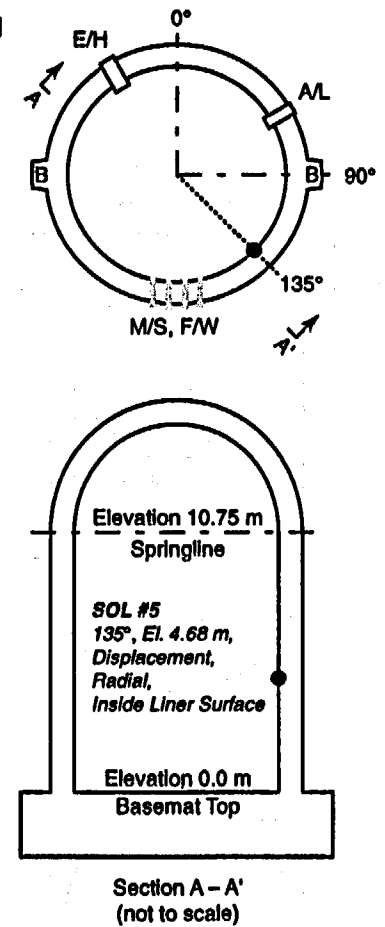
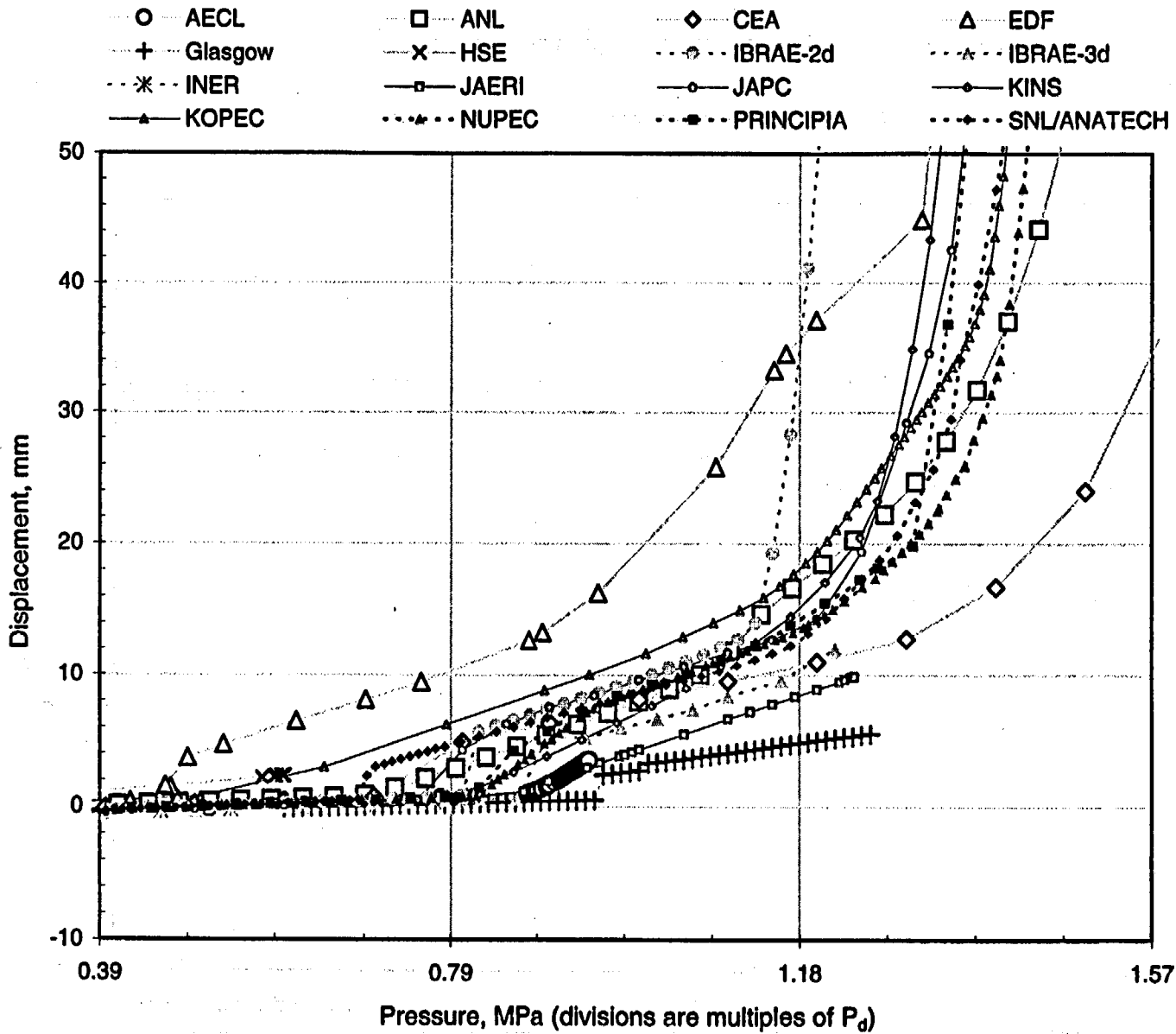


Figure A-5b. PCCV Standard Output Location (SOL) #5, enlarged.

A-14

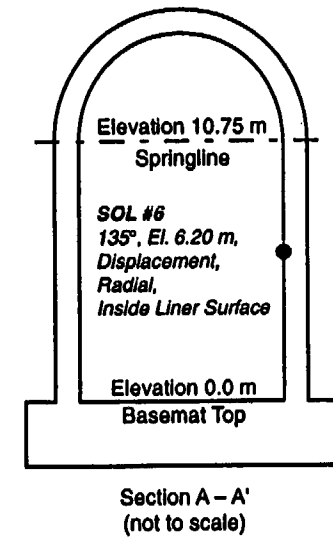
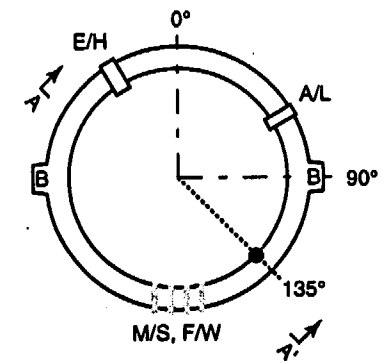
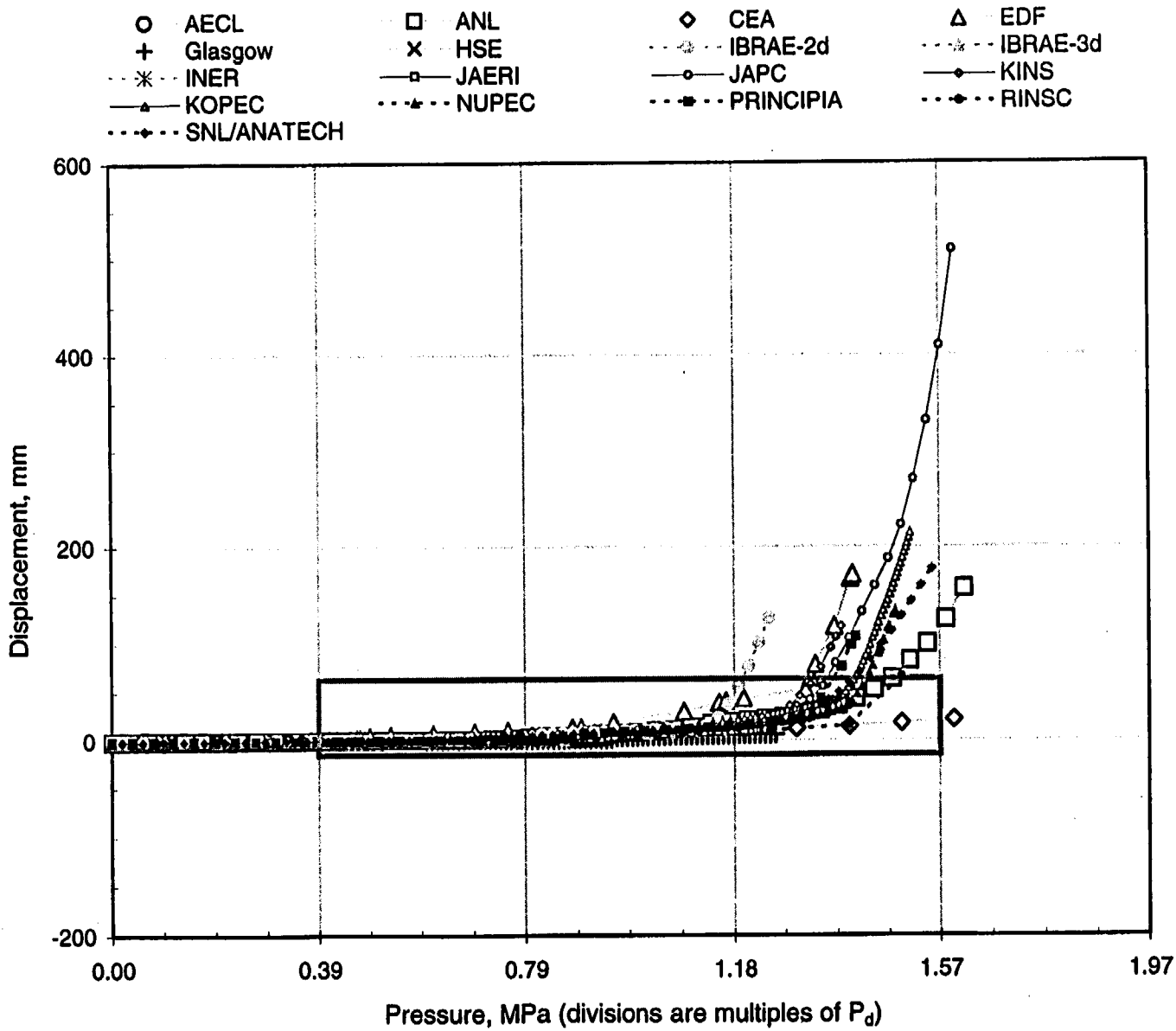
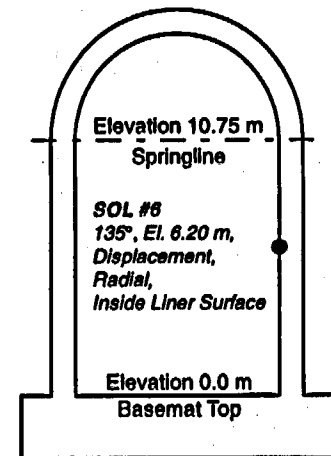
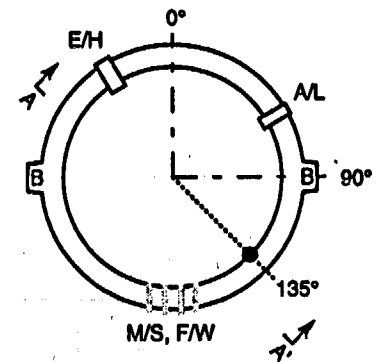
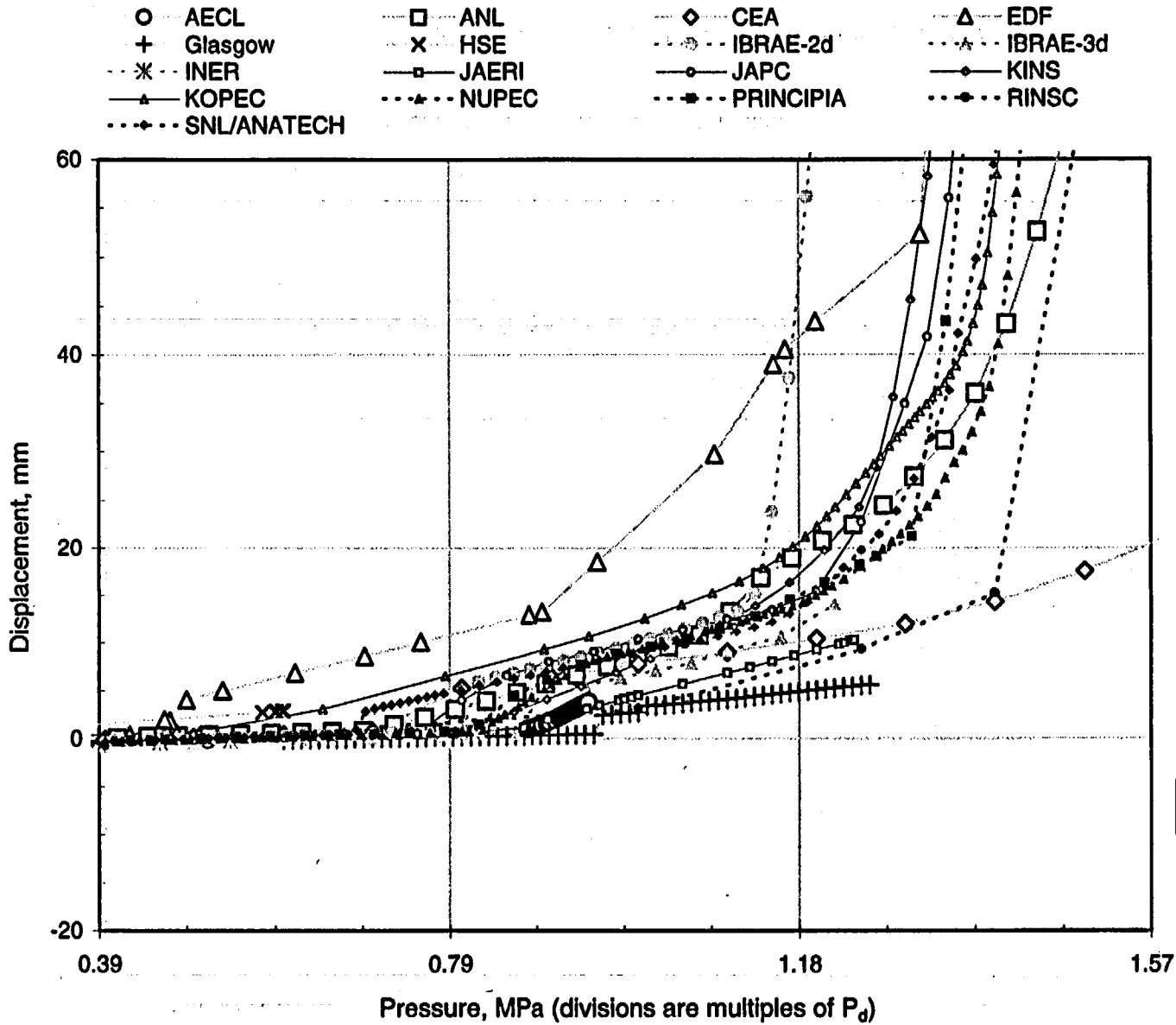


Figure A-6a. PCCV Standard Output Location (SOL) #6.



Section A - A'
(not to scale)

Figure A-6b. PCCV Standard Output Location (SOL) #6, enlarged.

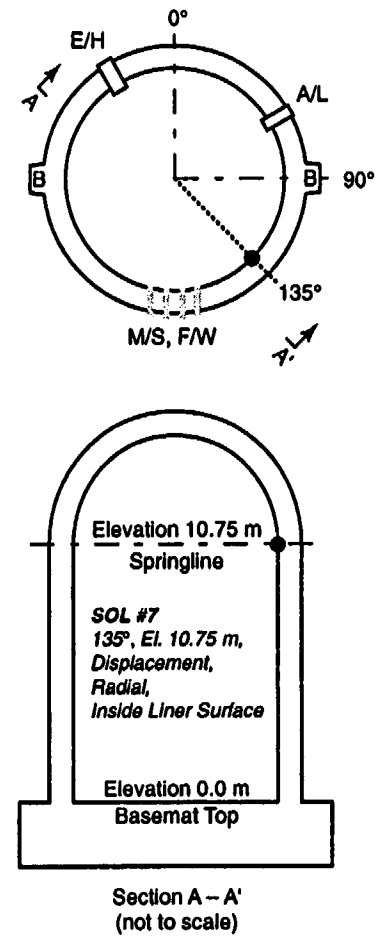
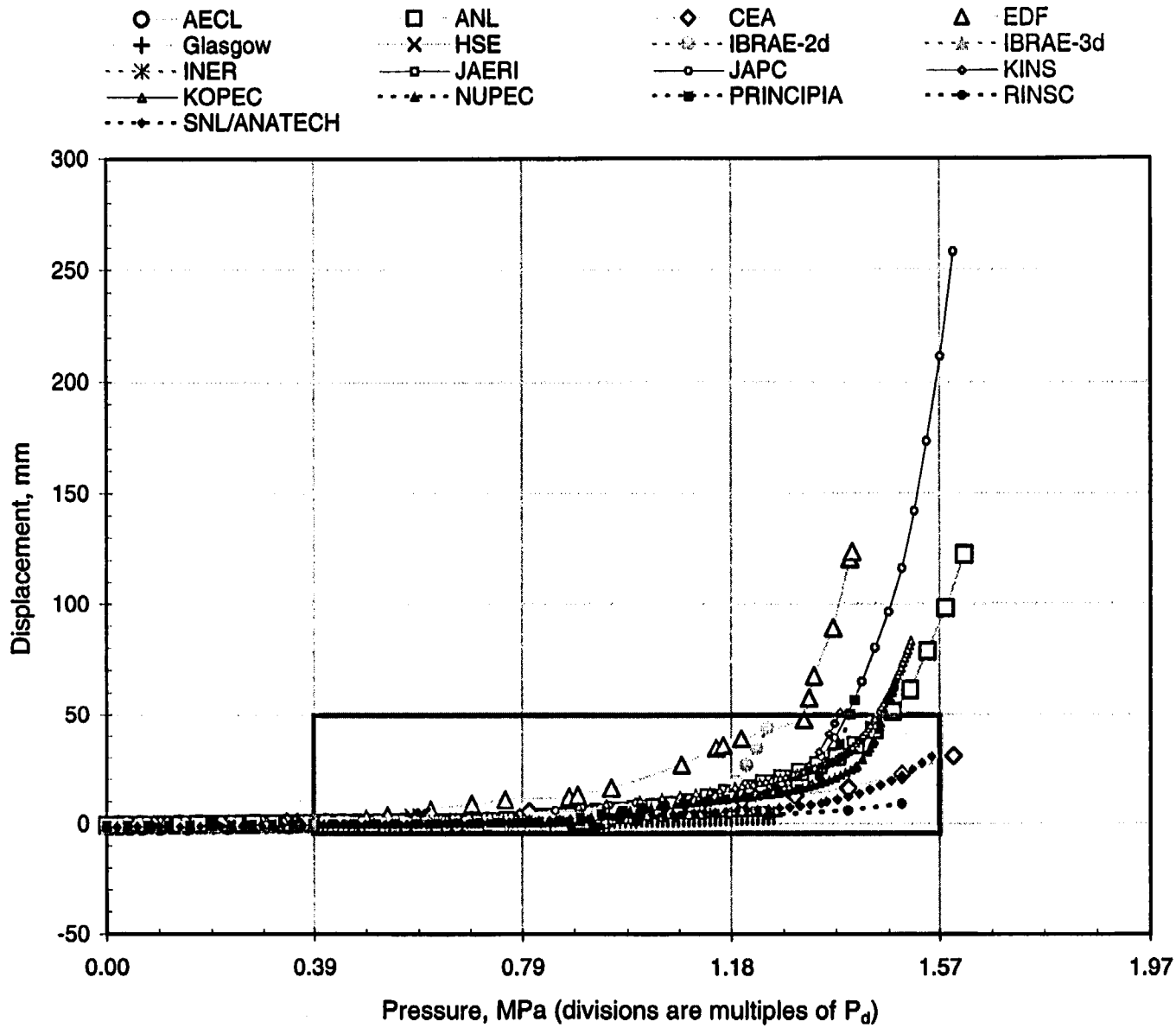
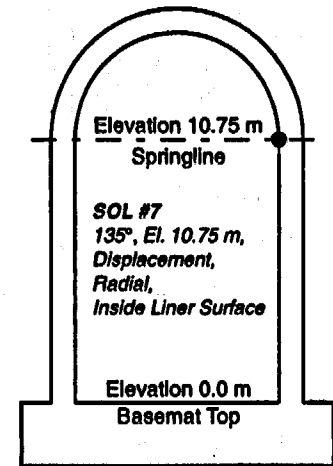
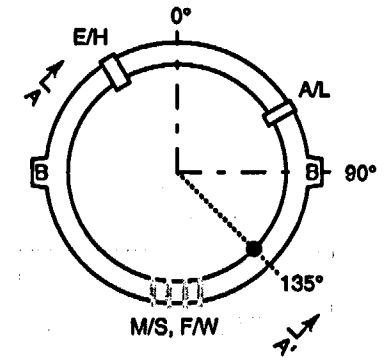
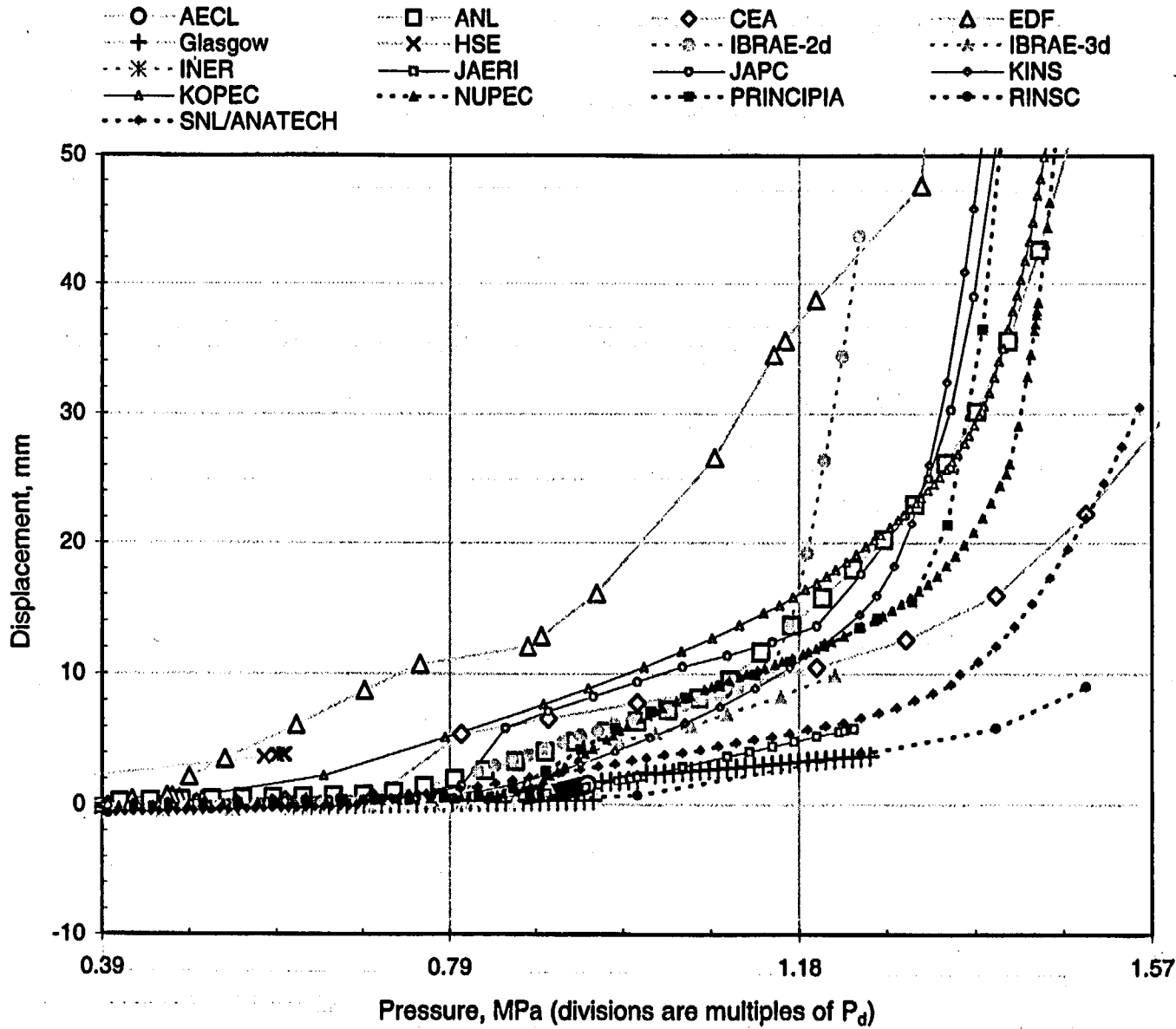
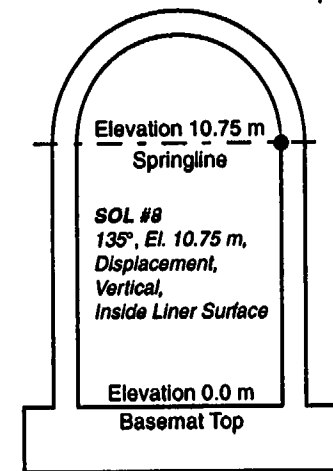
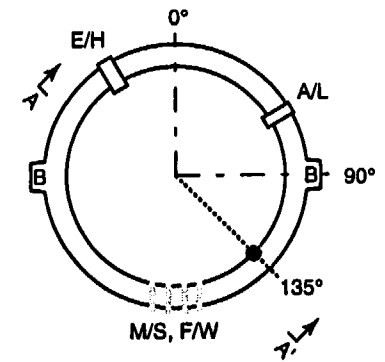
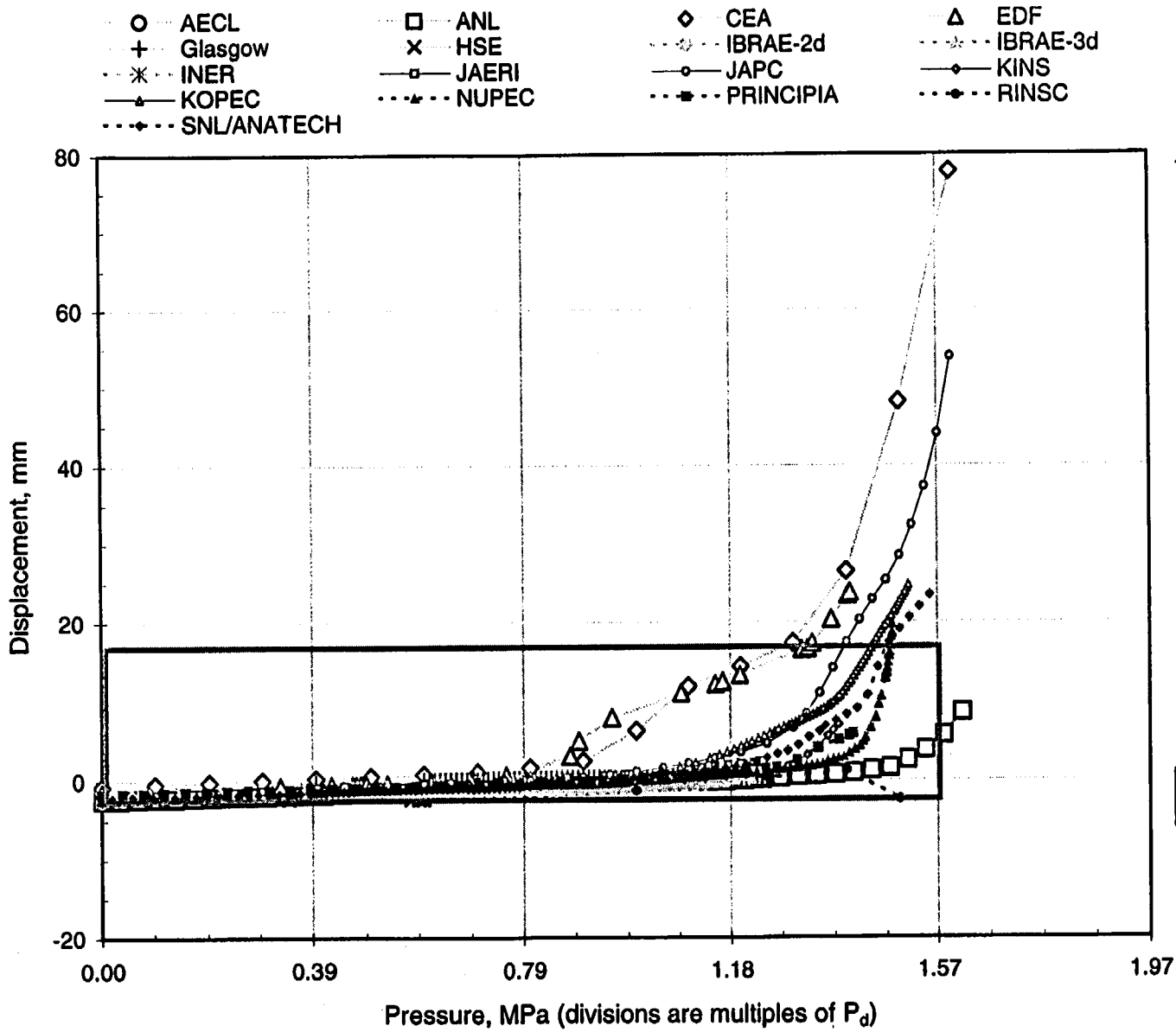


Figure A-7a. PCCV Standard Output Location (SOL) #7.



Section A - A'
(not to scale)

Figure A-7b. PCCV Standard Output Location (SOL) #7, enlarged.



Section A - A'
(not to scale)

Figure A-8a. PCCV Standard Output Location (SOL) #8.

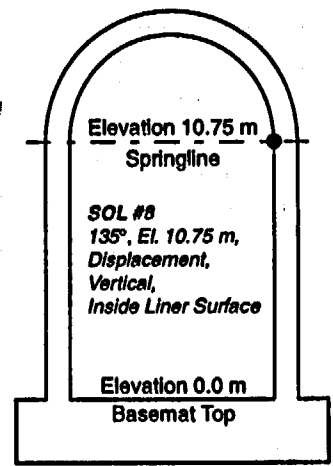
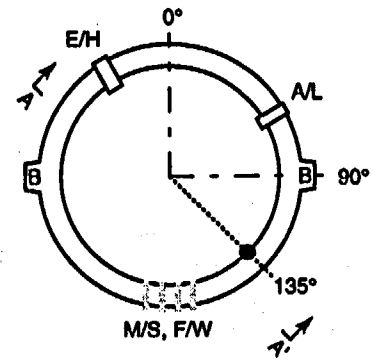
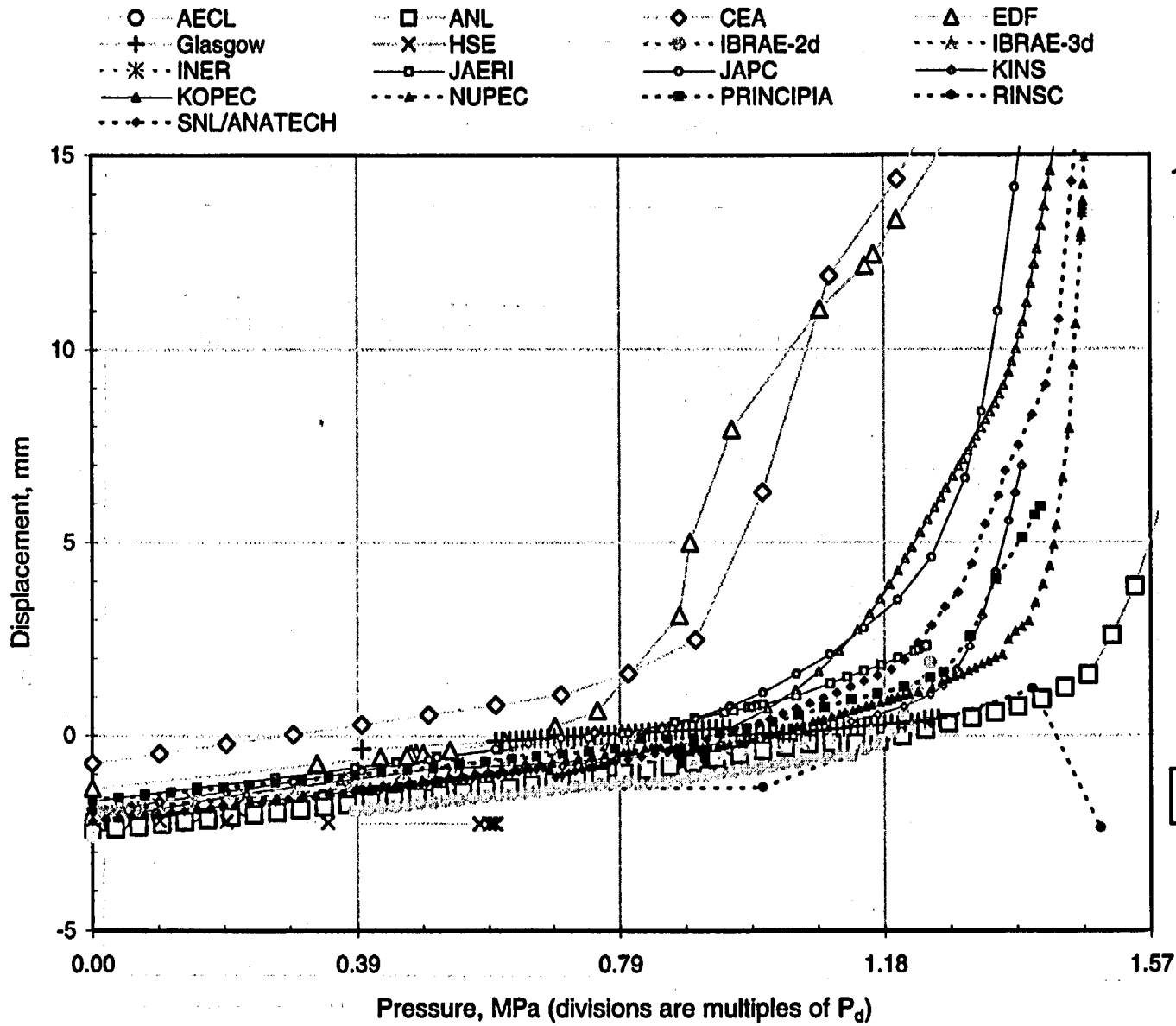
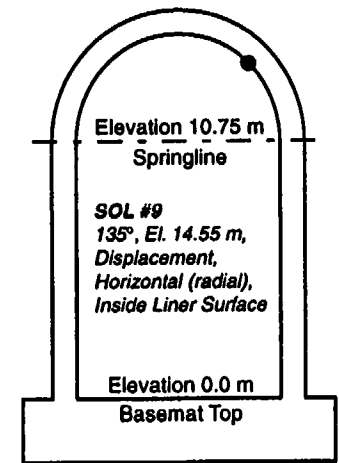
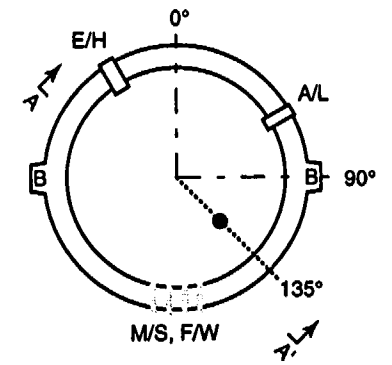
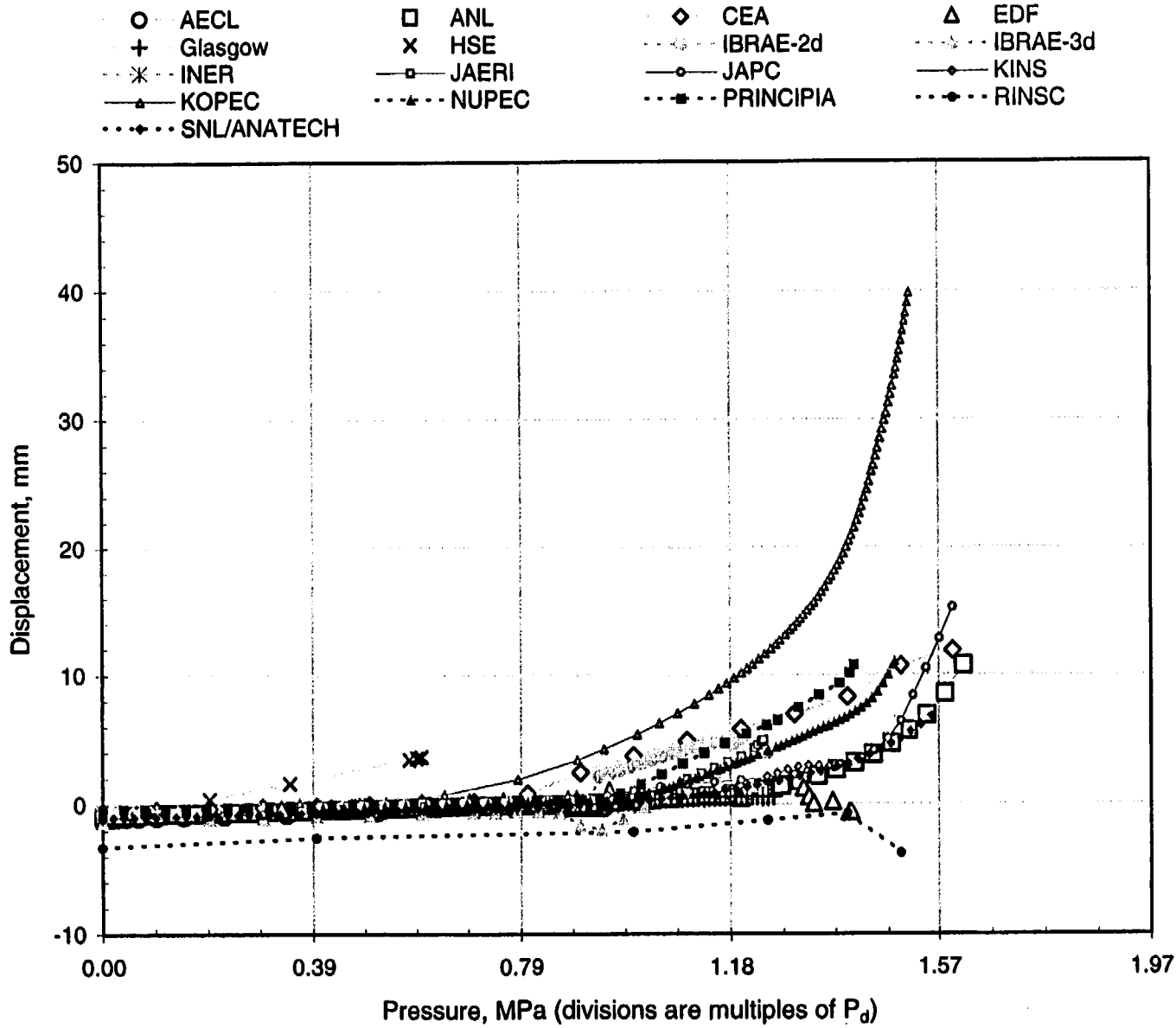


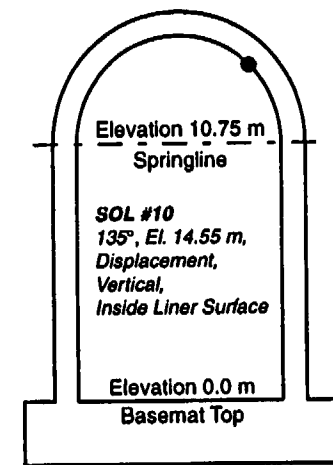
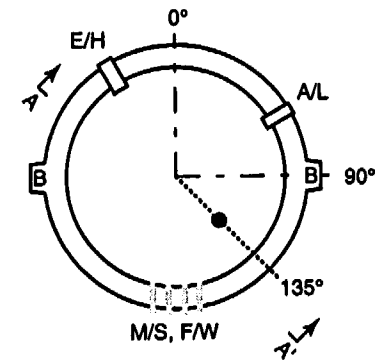
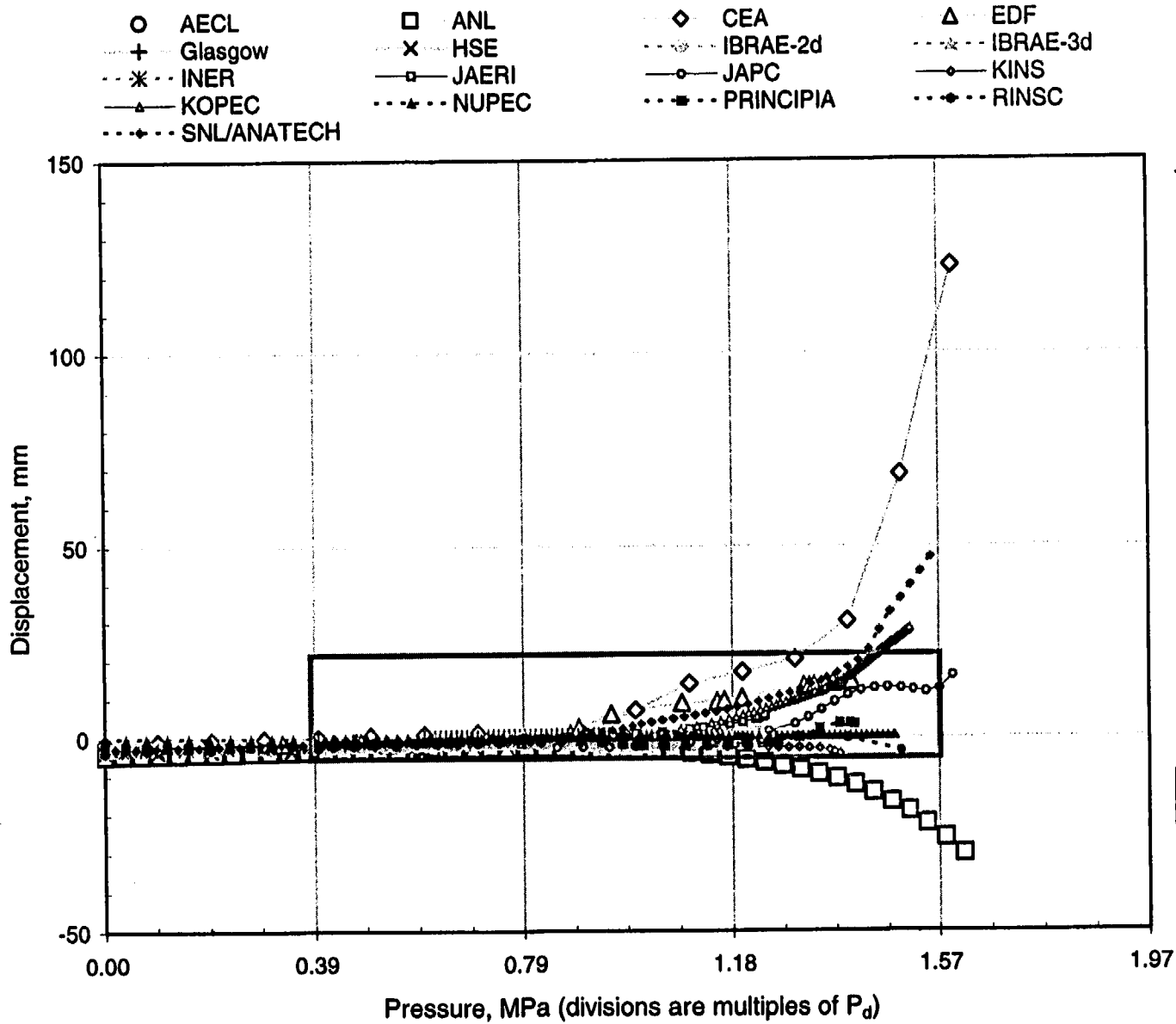
Figure A-8b. PCCV Standard Output Location (SOL) #8, enlarged.



Section A - A'
(not to scale)

Figure A-9. PCCV Standard Output Location (SOL) #9.

This page intentionally left blank to facilitate plot comparison.



Section A - A'
(not to scale)

Figure A-10a. PCCV Standard Output Location (SOL) #10.

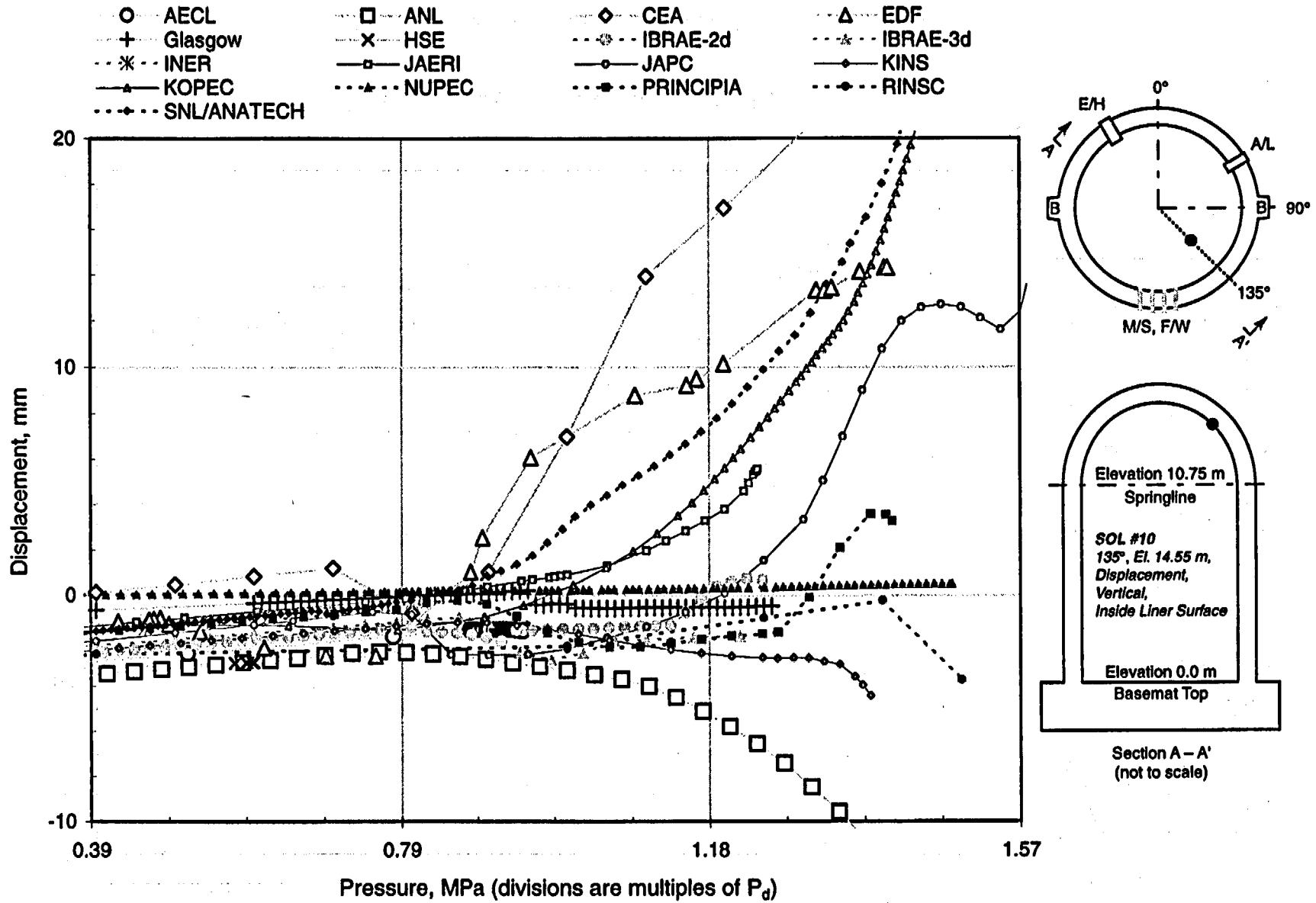


Figure A-10b. PCCV Standard Output Location (SOL) #10, enlarged.

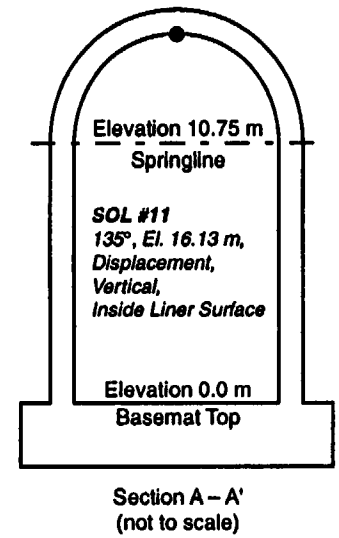
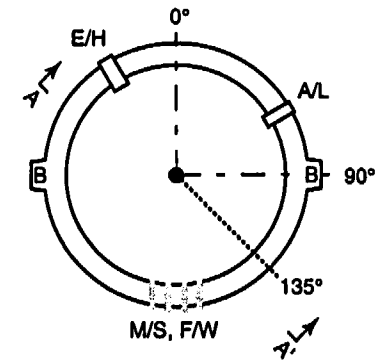
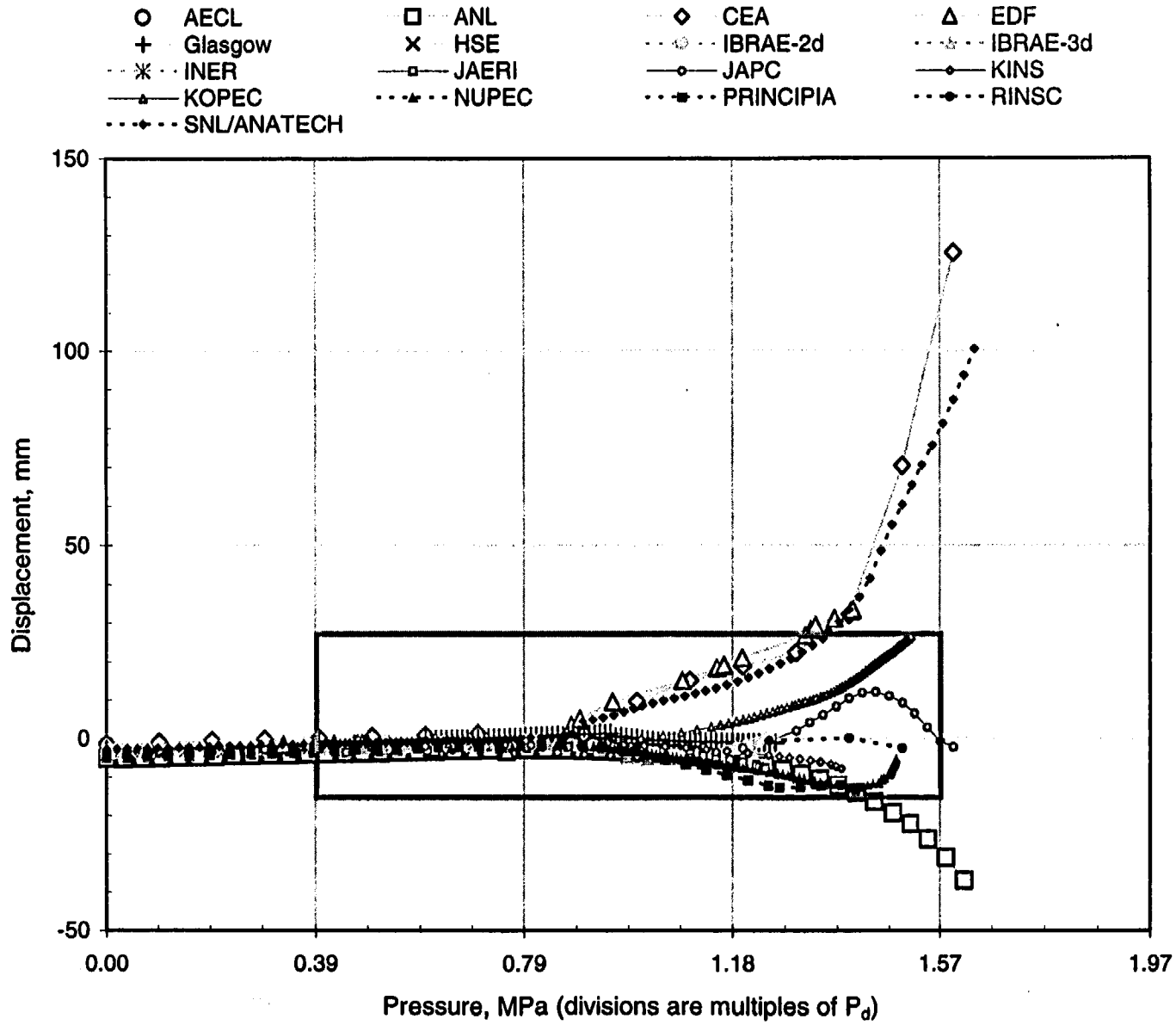


Figure A-11a. PCCV Standard Output Location (SOL) #11.

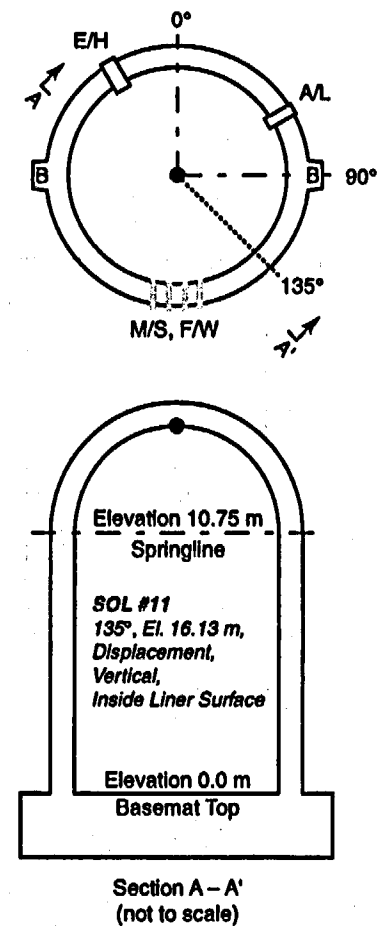
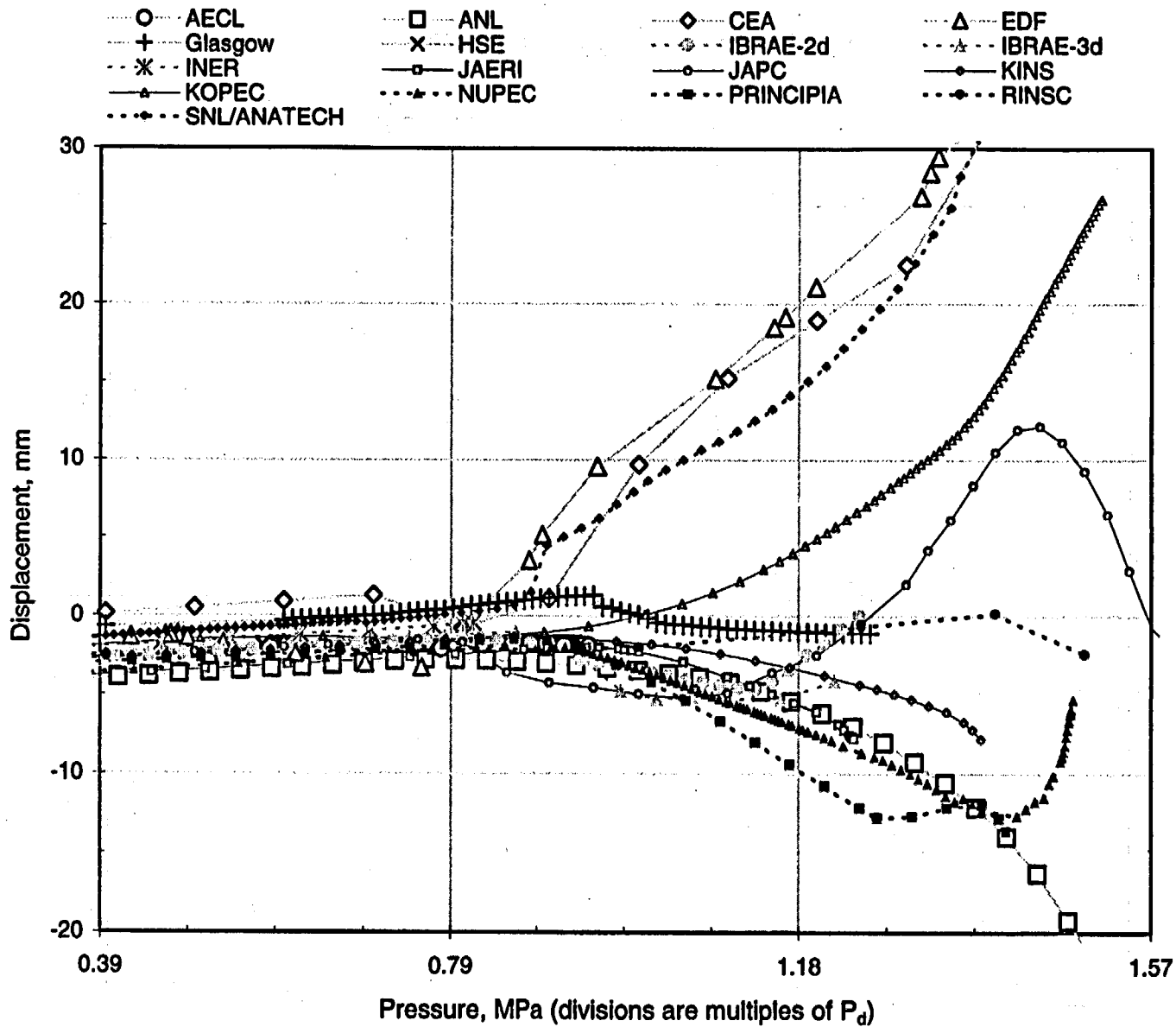


Figure A-11b. PCCV Standard Output Location (SOL) #11, enlarged.

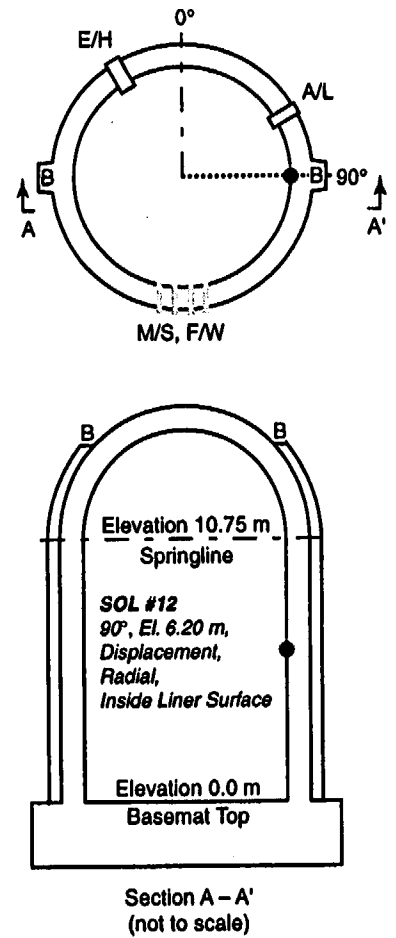
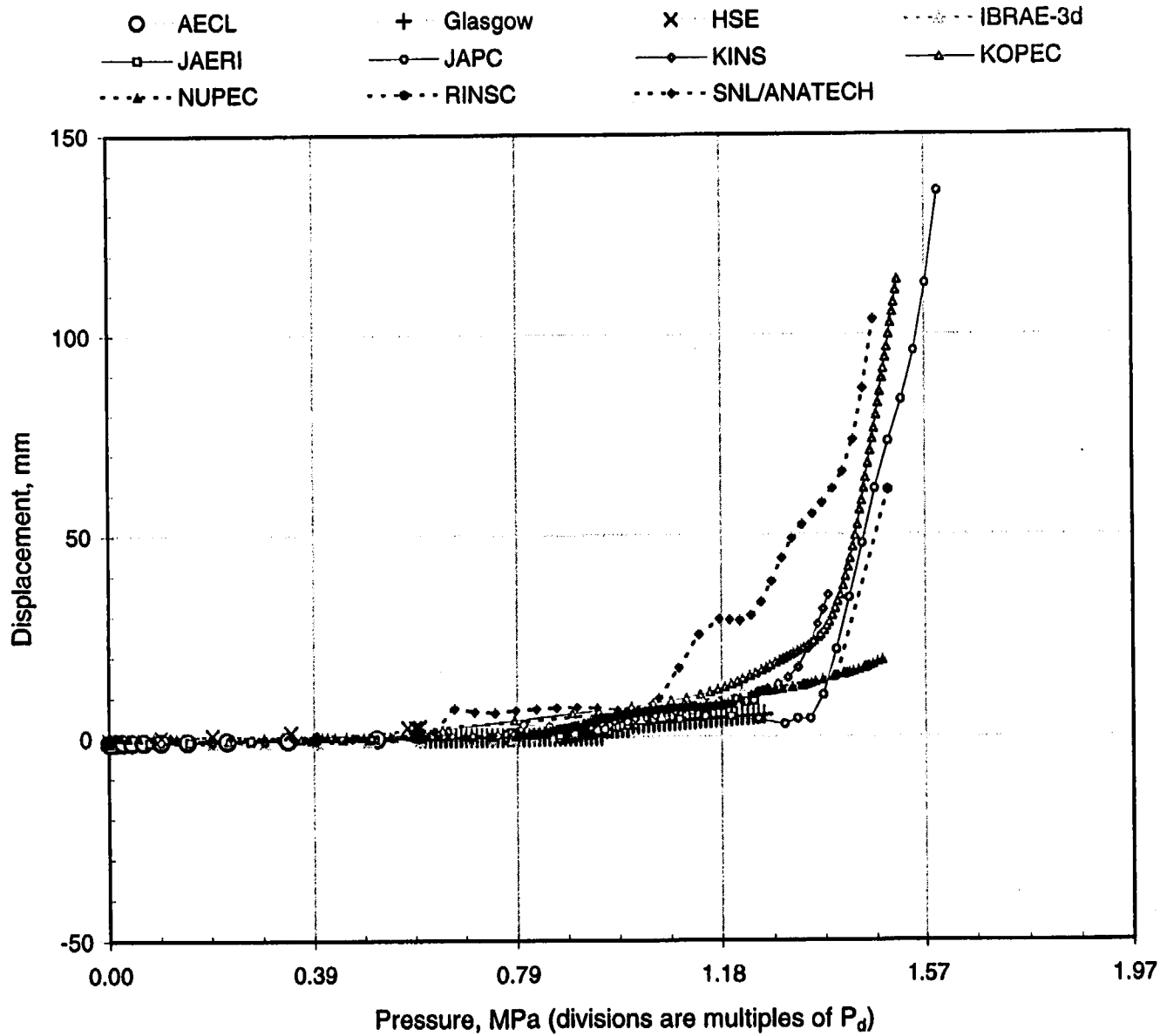


Figure A-12. PCCV Standard Output Location (SOL) #12.

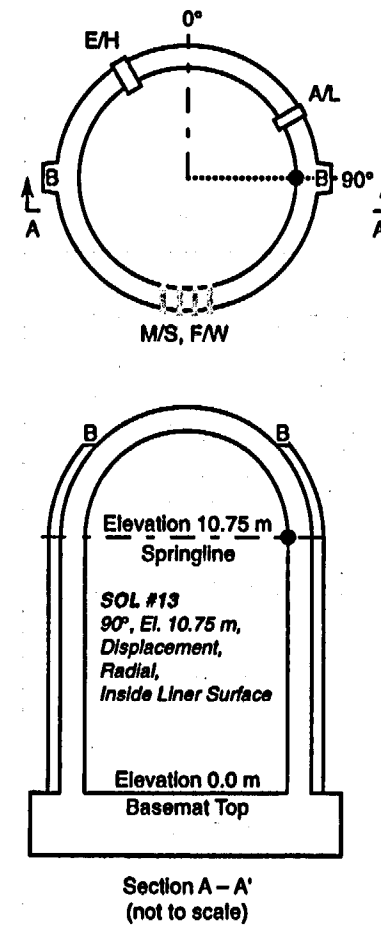
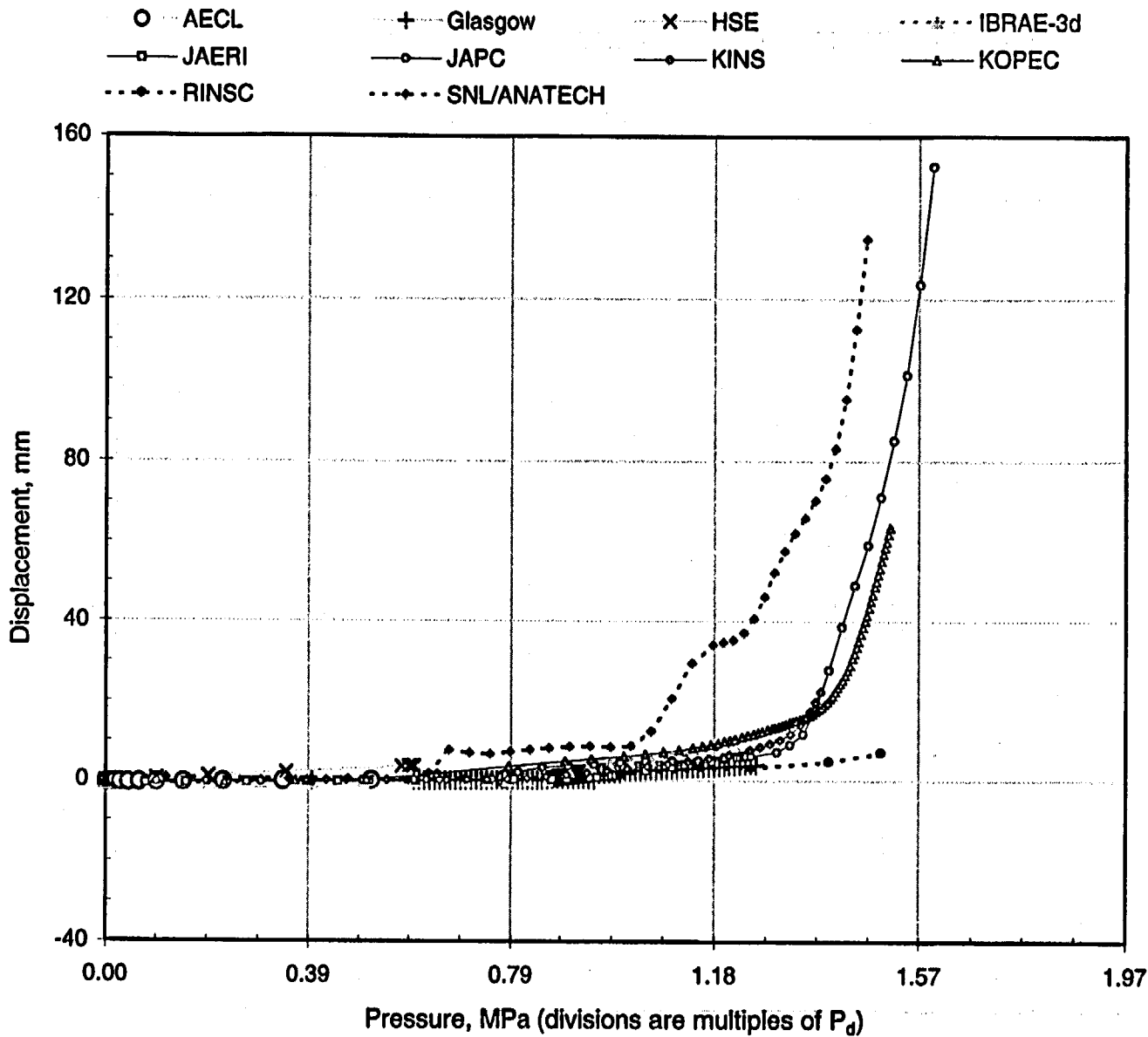


Figure A-13. PCCV Standard Output Location (SOL) #13.

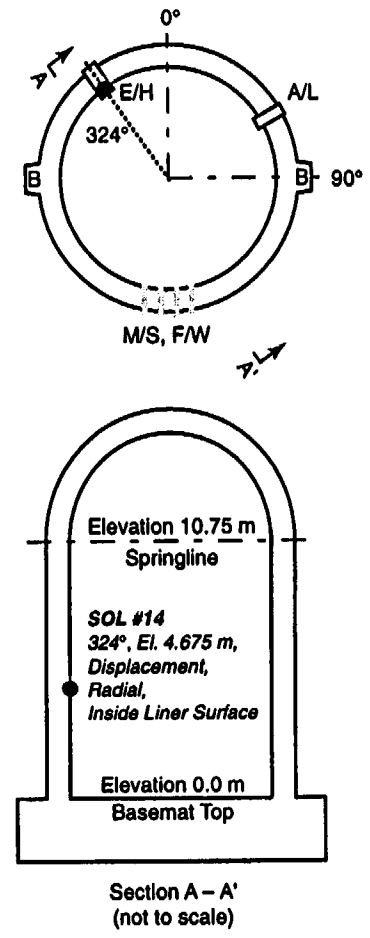
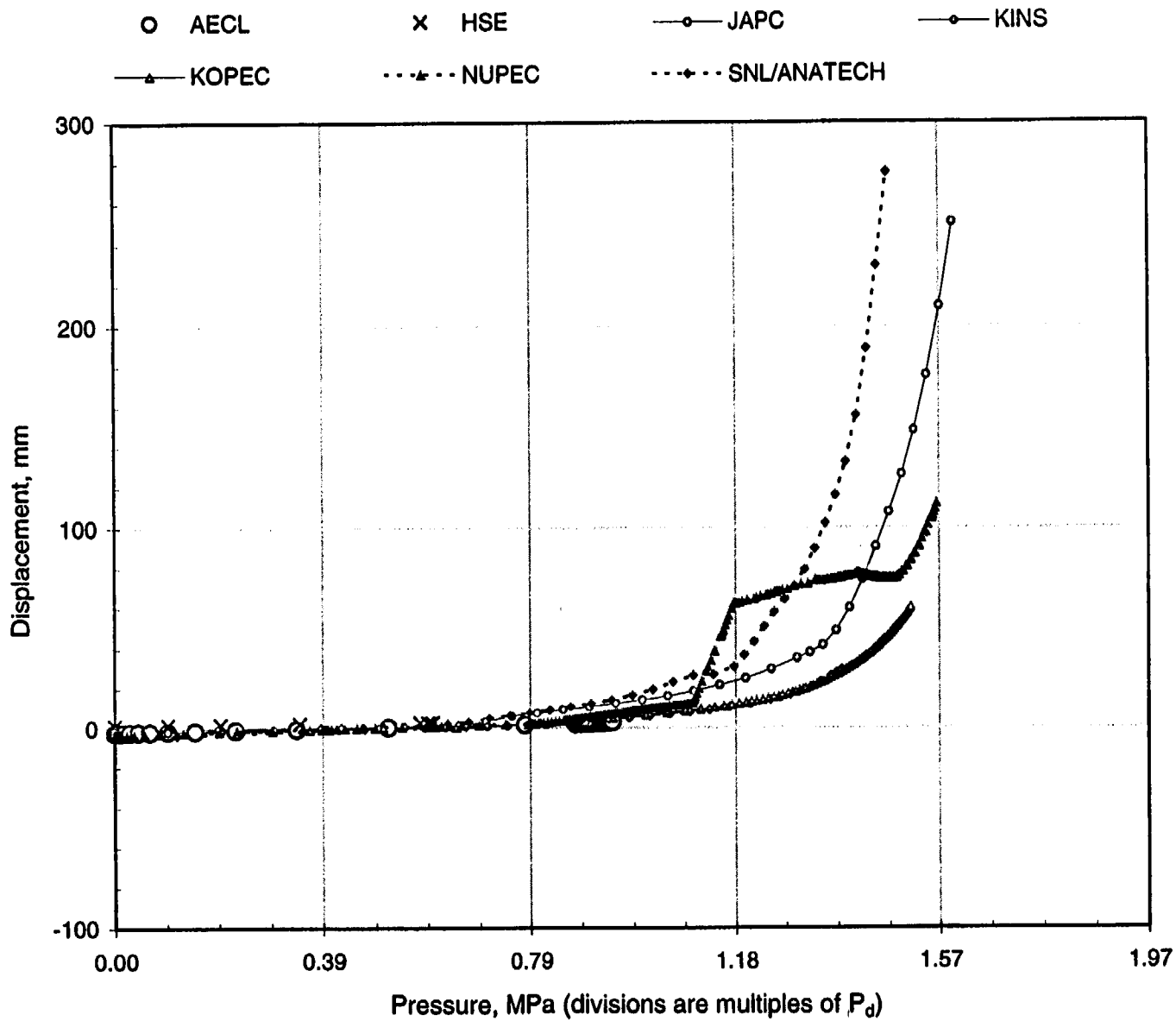


Figure A-14. PCCV Standard Output Location (SOL) #14.

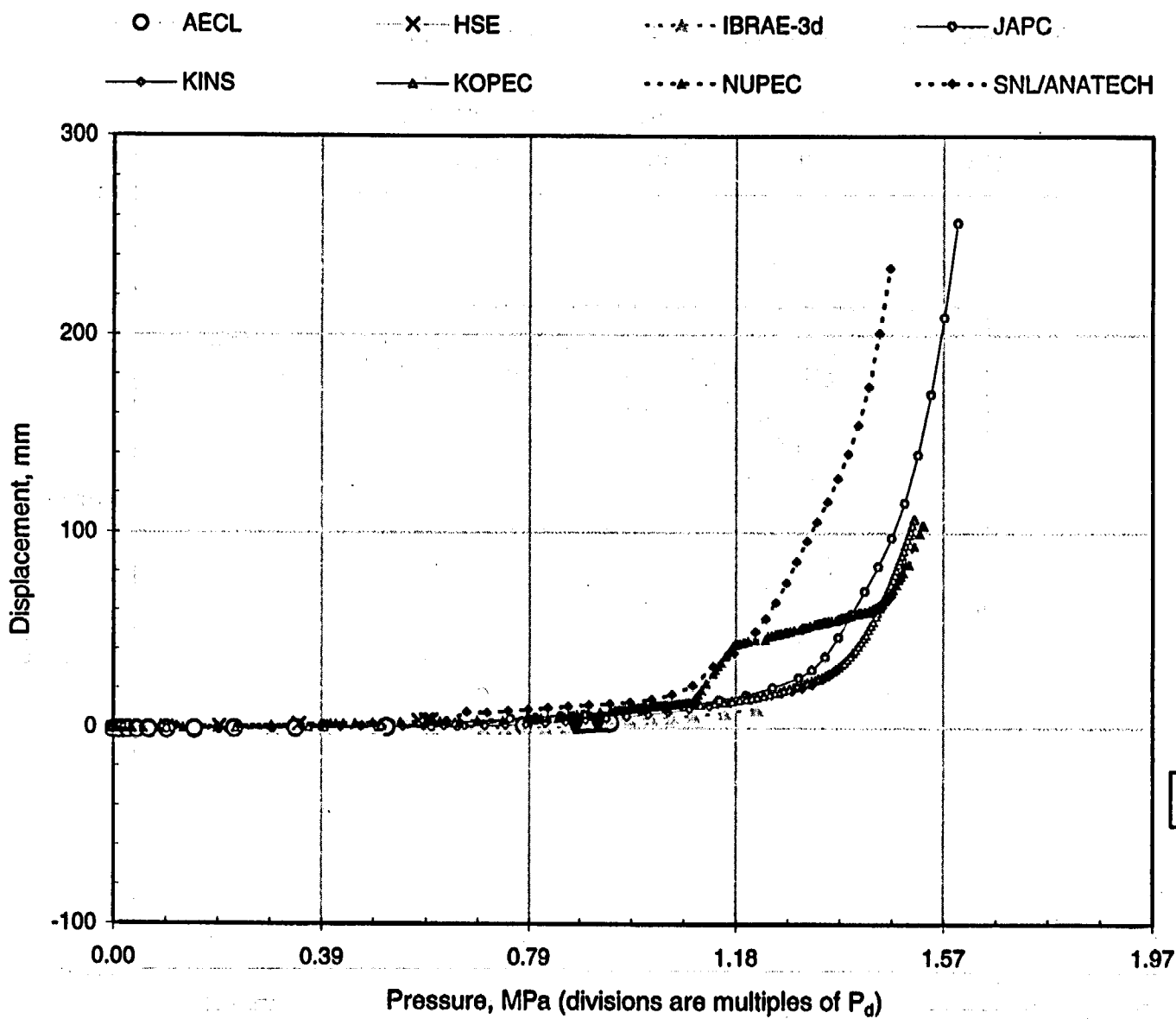
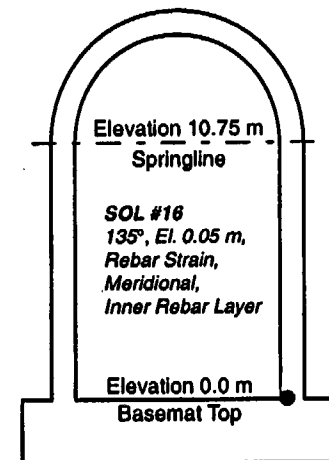
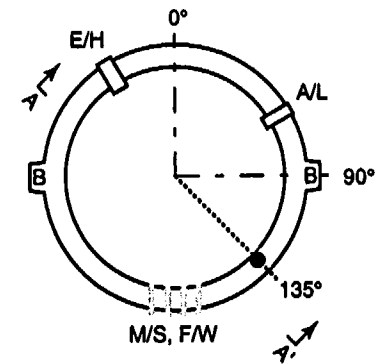
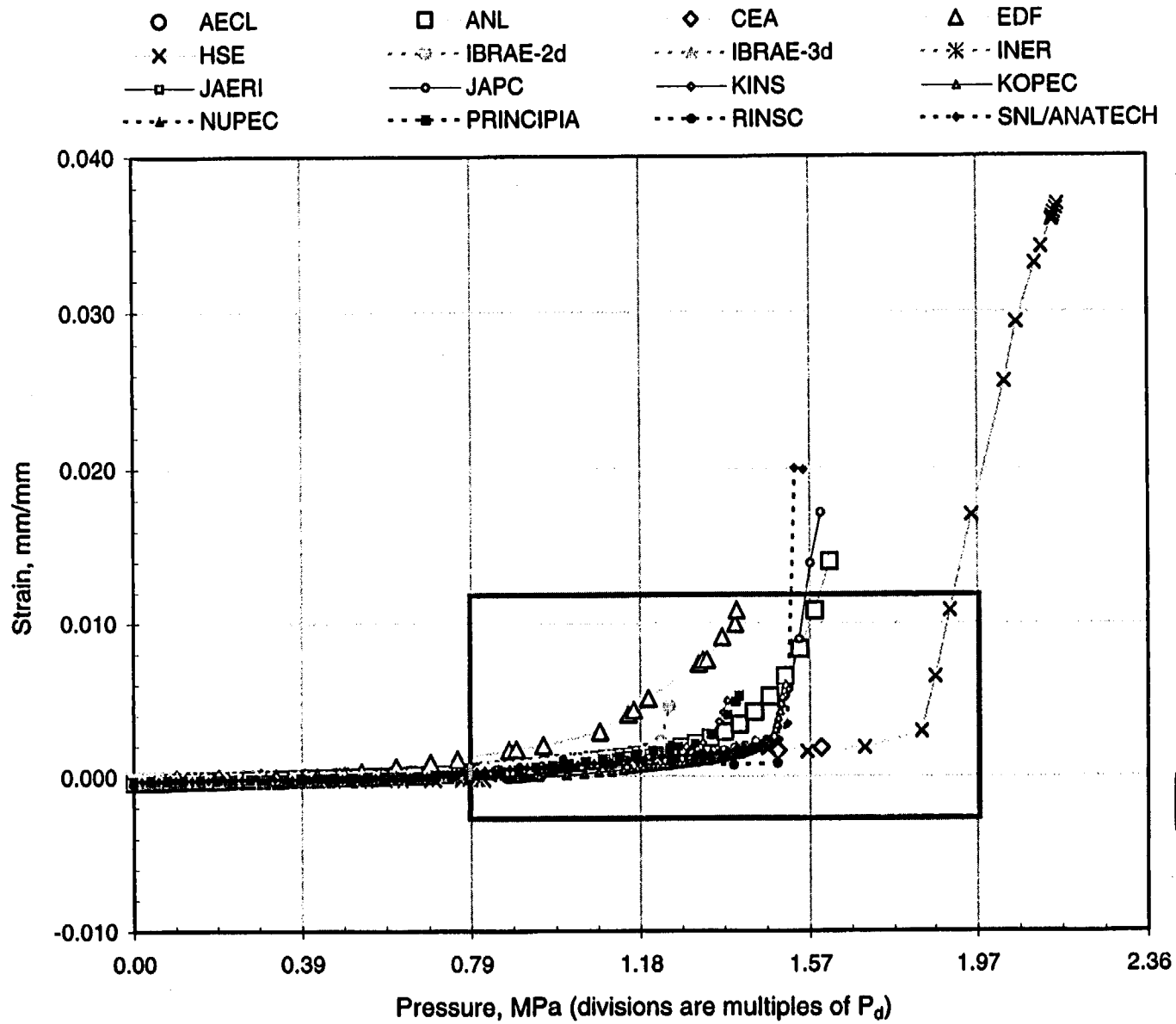


Figure A-15. PCCV Standard Output Location (SOL) #15.

A-30



Section A - A'
(not to scale)

Figure A-16a. PCCV Standard Output Location (SOL) #16.

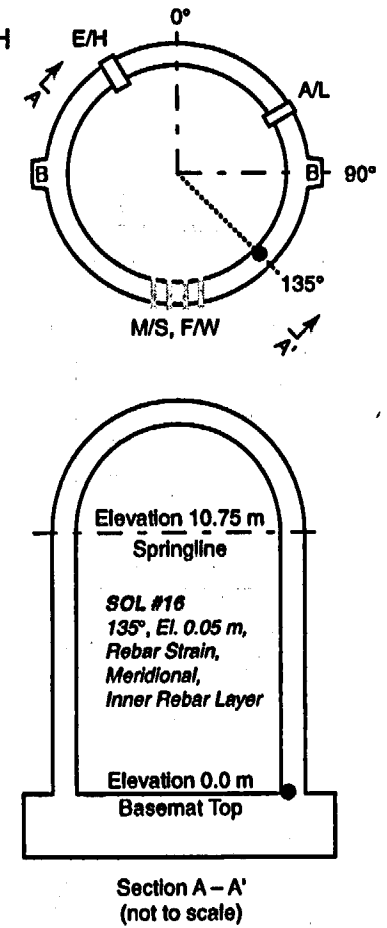
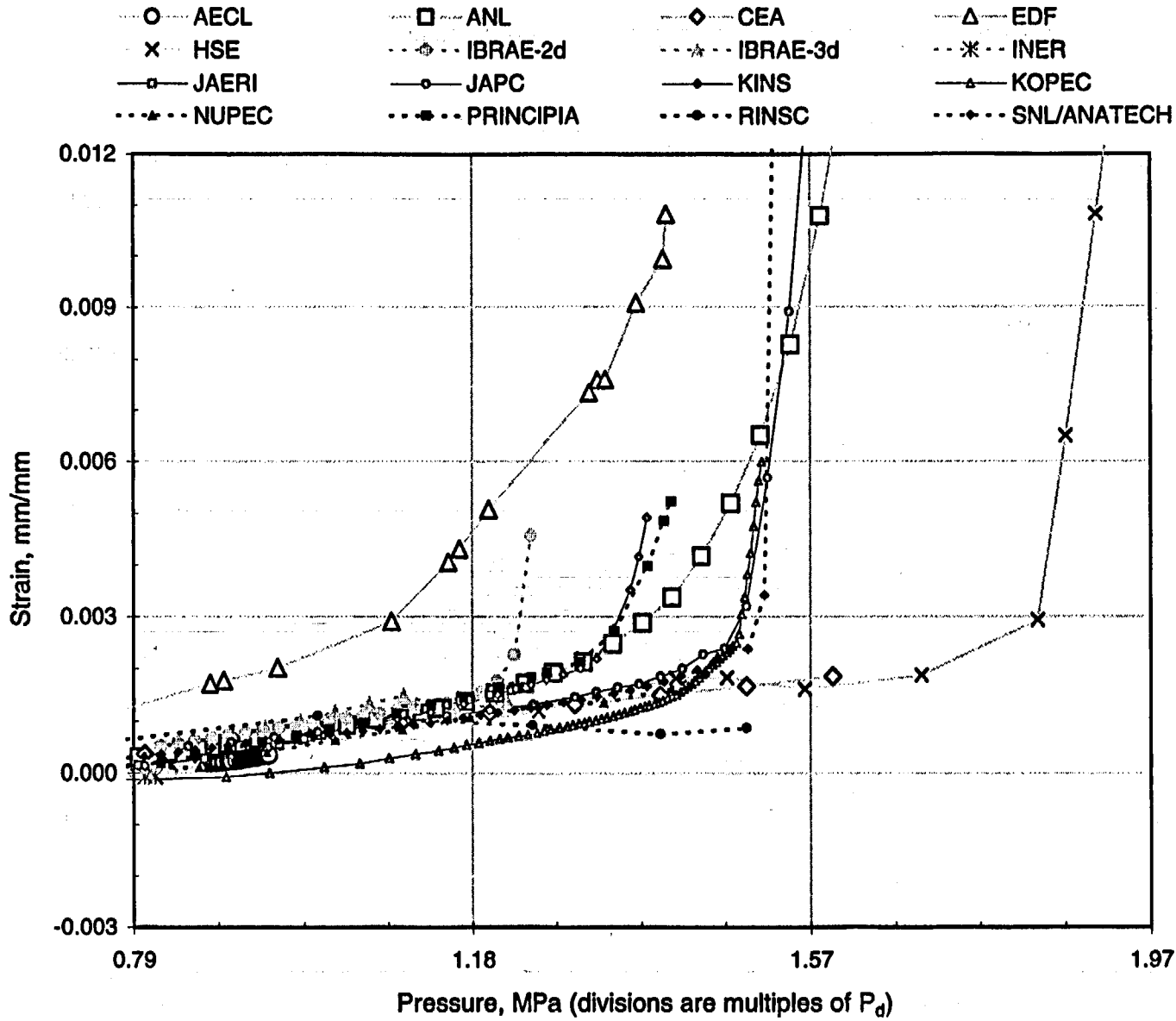


Figure A-16b. PCCV Standard Output Location (SOL) #16, enlarged.

A-32

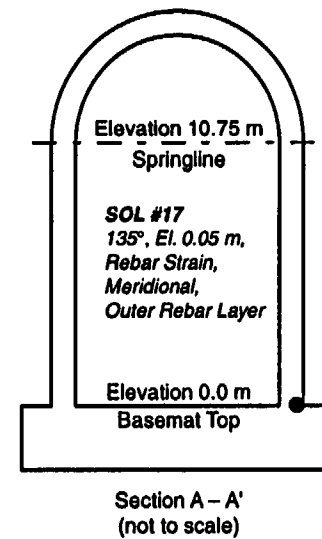
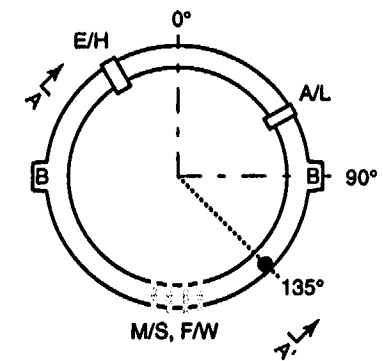
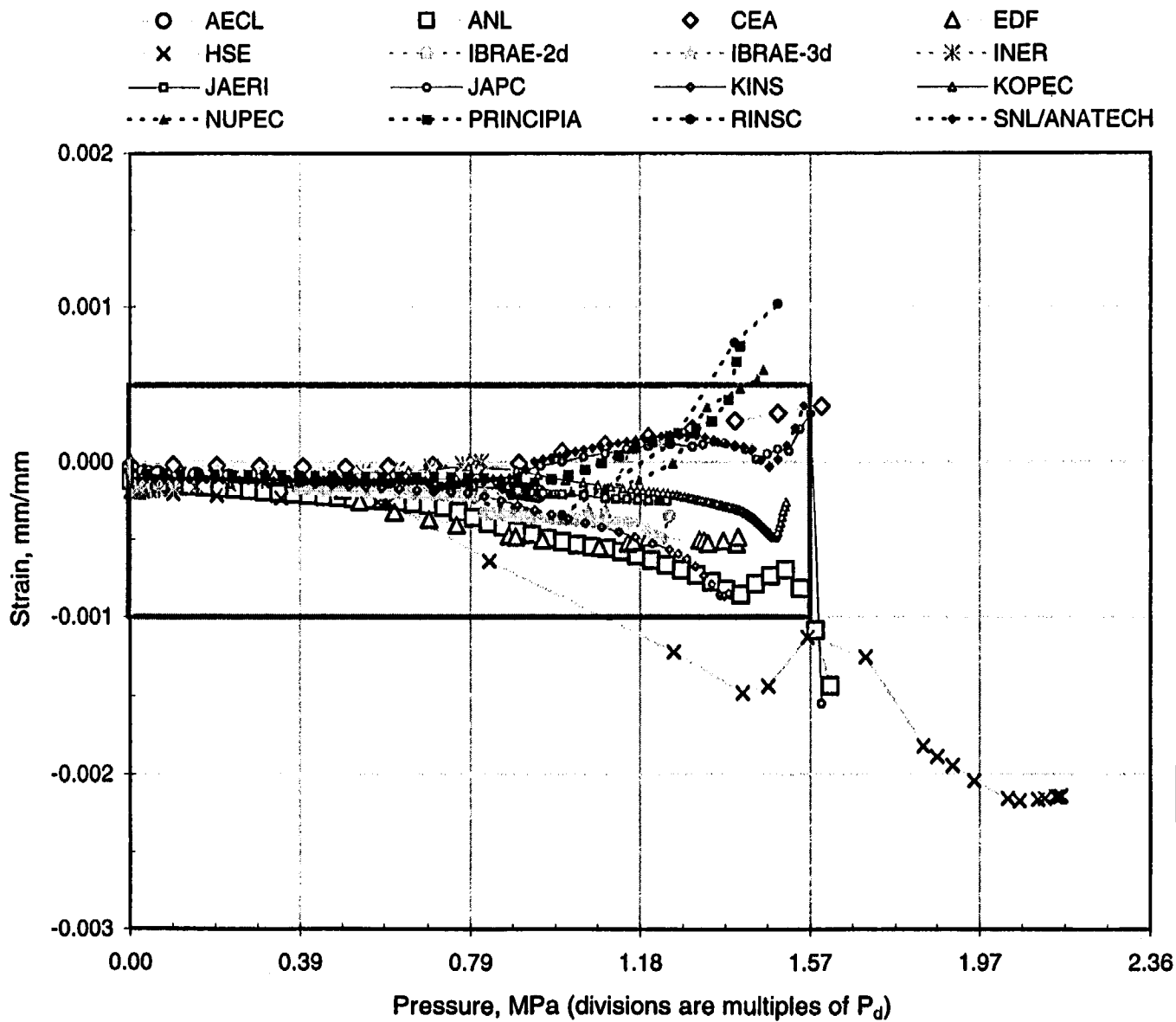


Figure A-17a. PCCV Standard Output Location (SOL) #17.

A-33

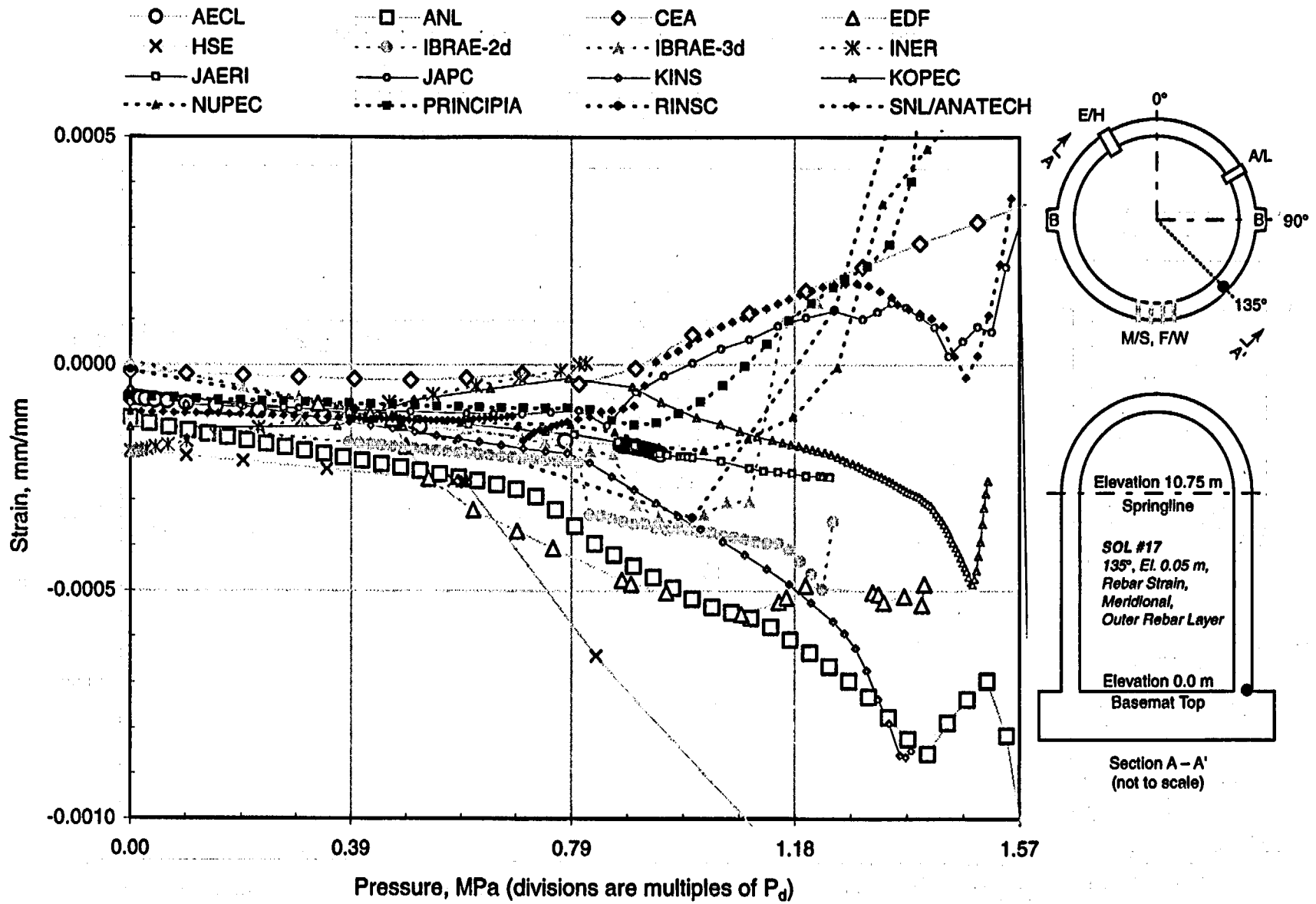
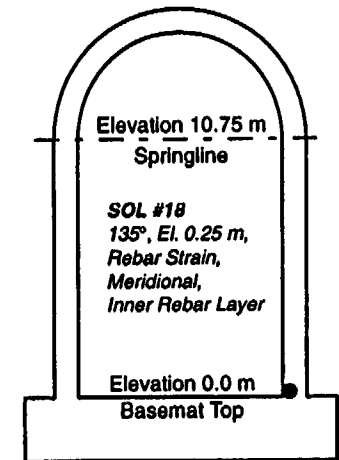
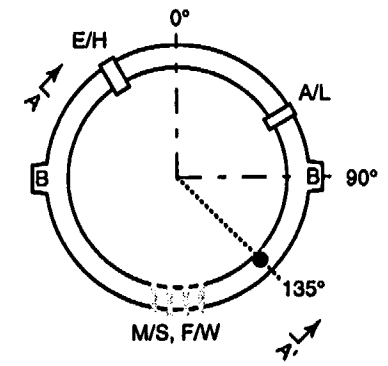
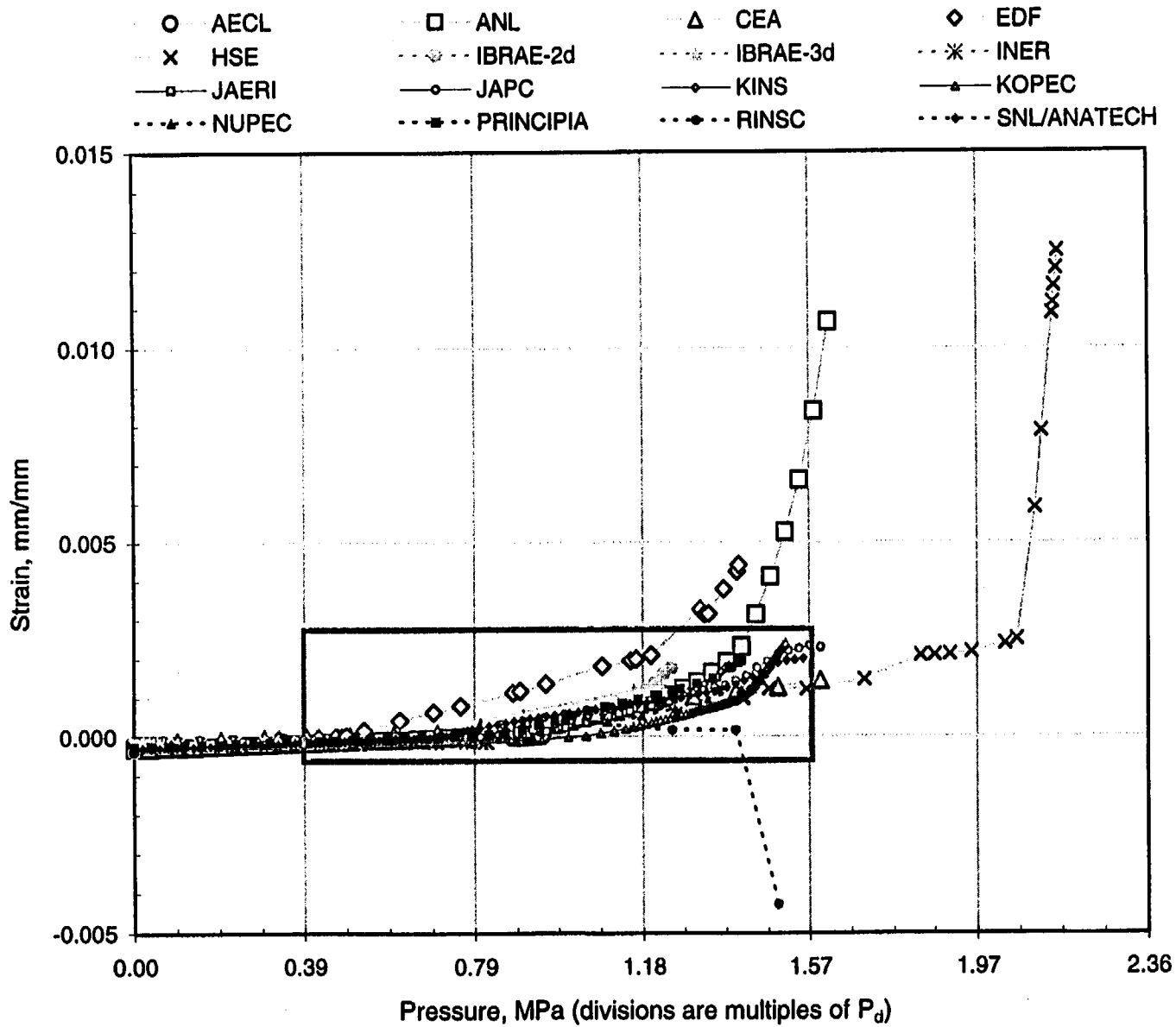


Figure A-17b. PCCV Standard Output Location (SOL) #17, enlarged.

A-34



Section A - A'
(not to scale)

Figure A-18a. PCCV Standard Output Location (SOL) #18.

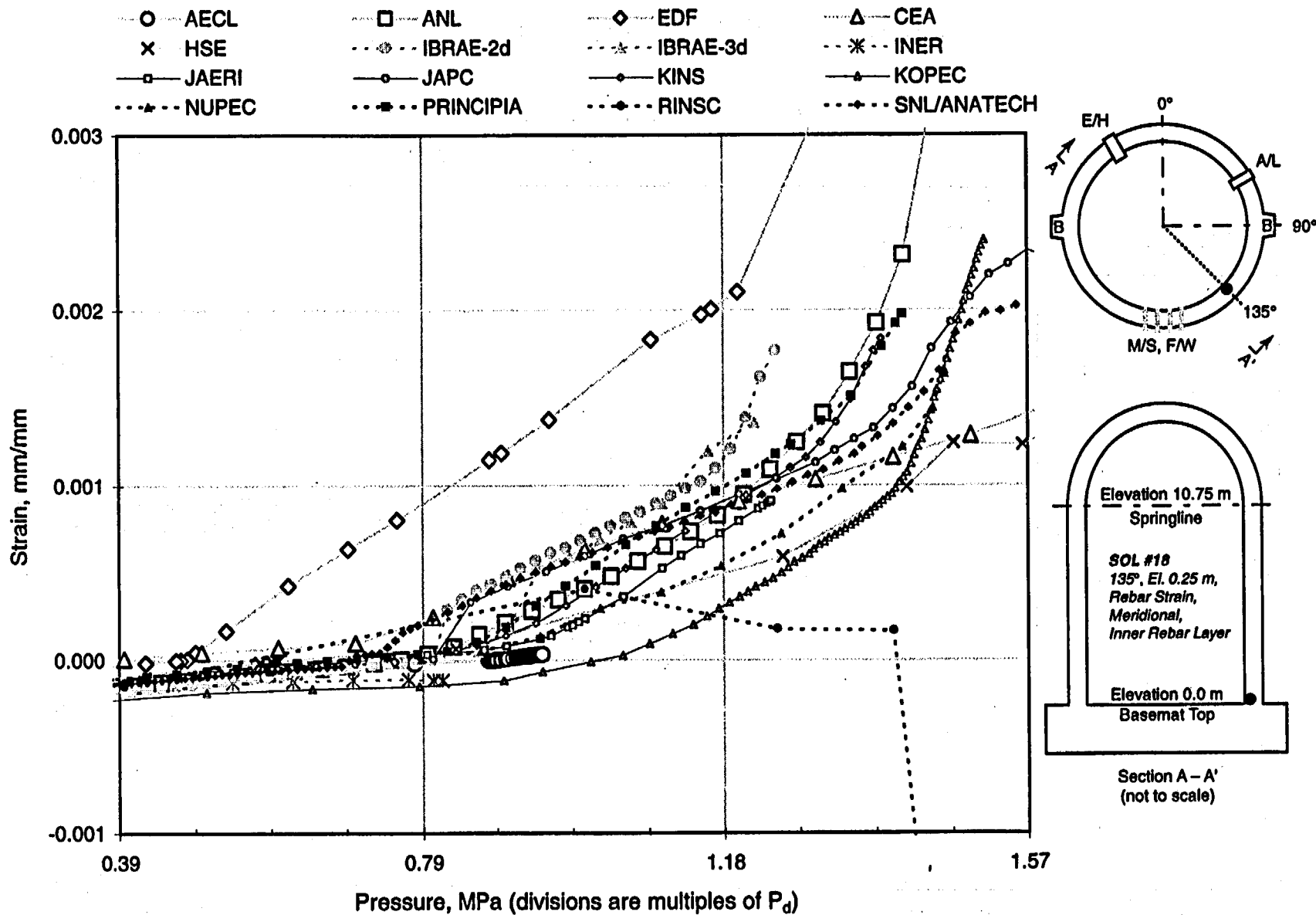
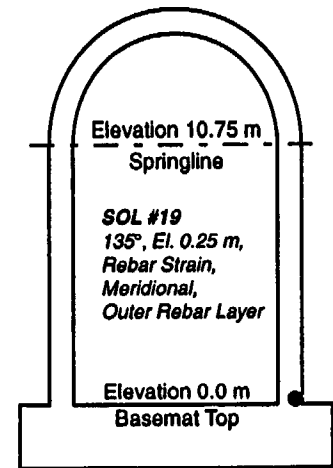
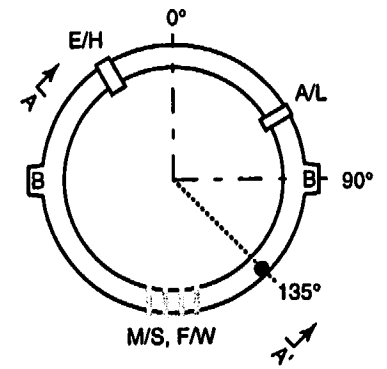
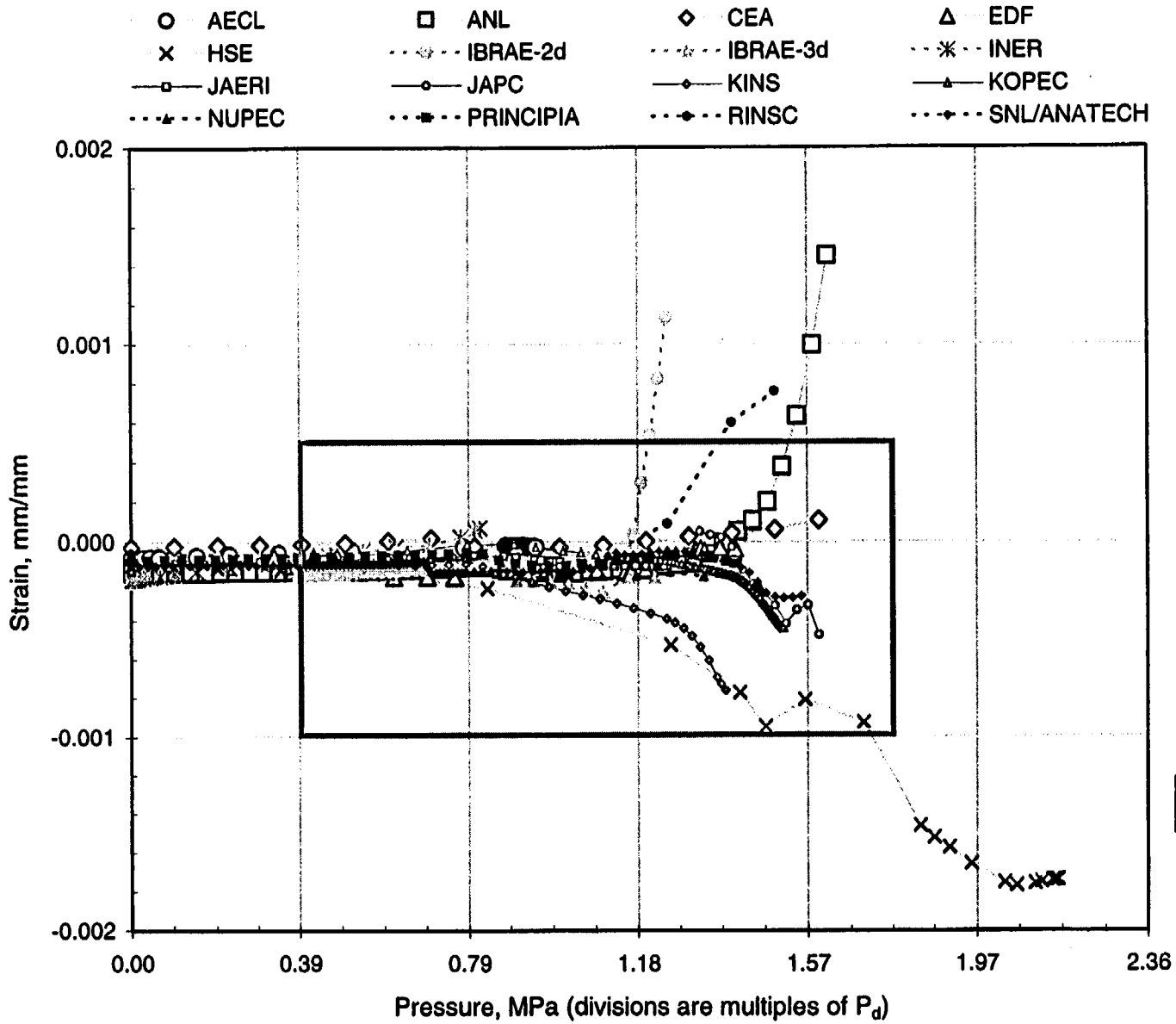


Figure A-18b. PCCV Standard Output Location (SOL) #18, enlarged.

A-36



Section A - A'
(not to scale)

Figure A-19a. PCCV Standard Output Location (SOL) #19.

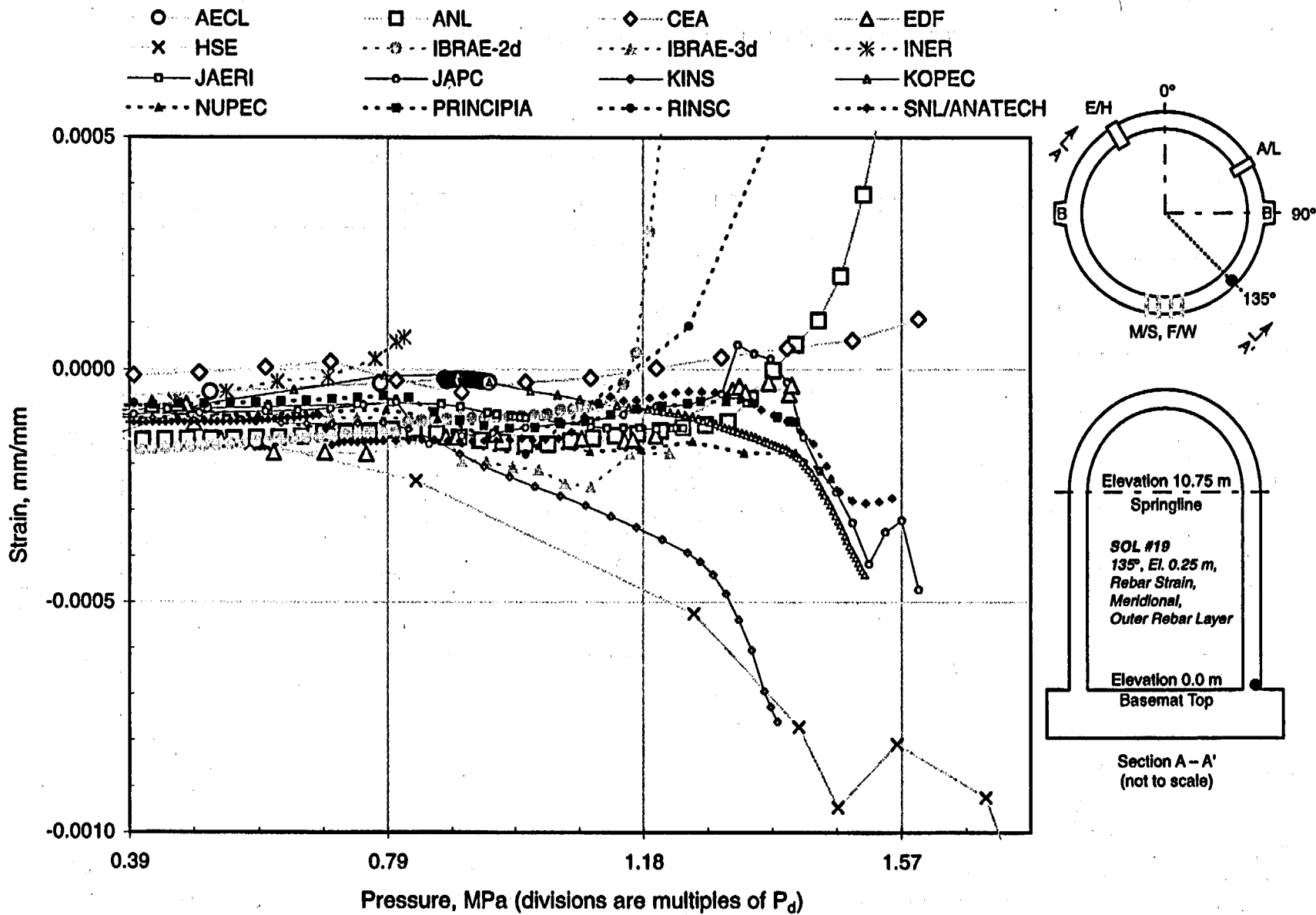
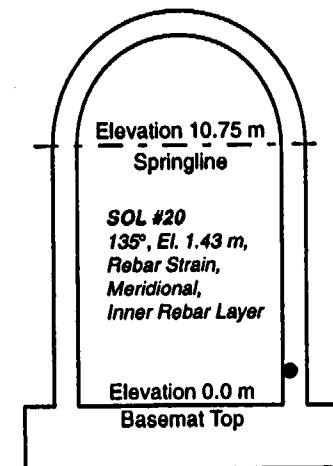
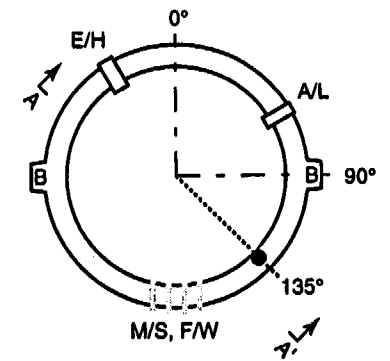
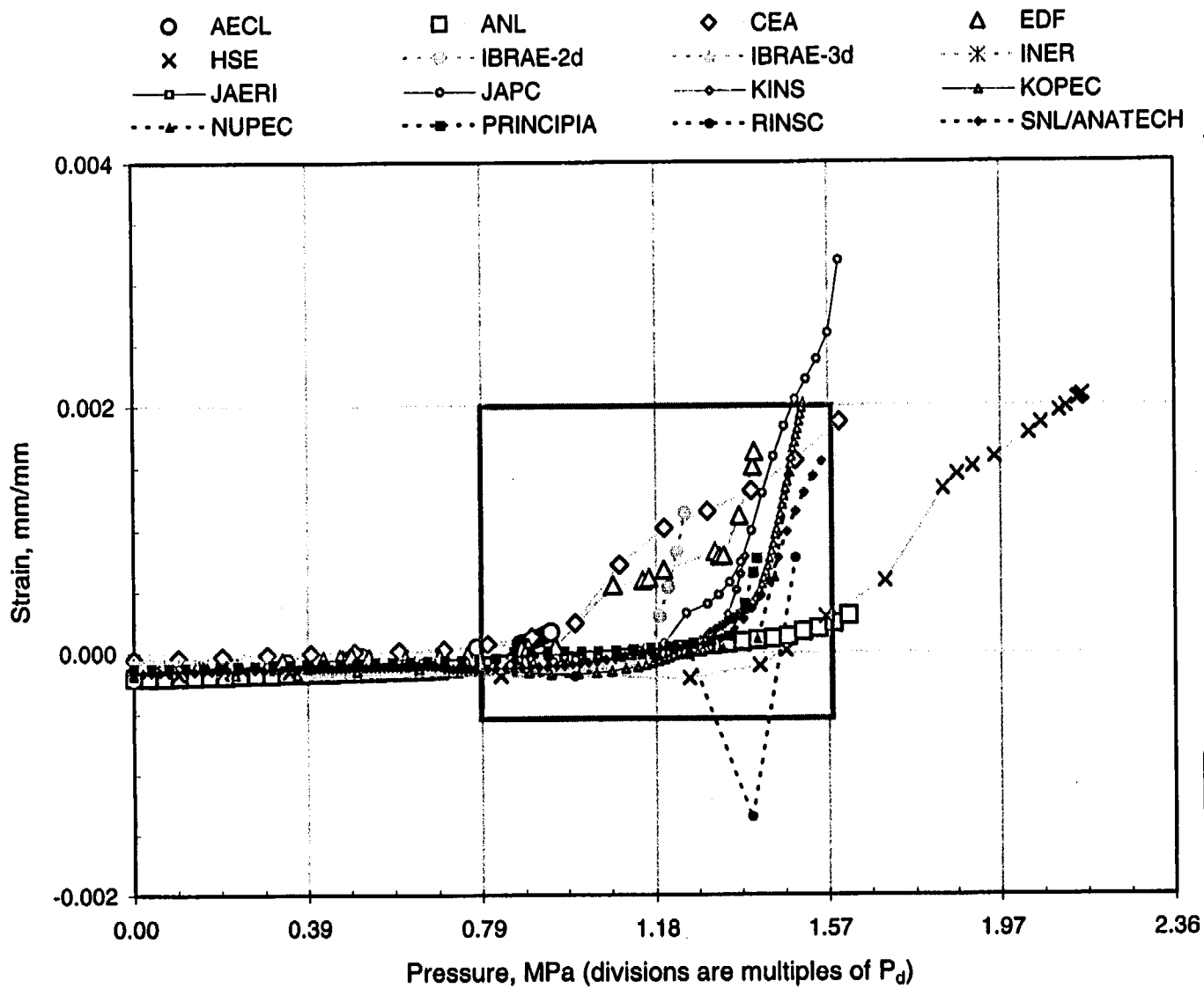


Figure A-19b. PCCV Standard Output Location (SOL) #19, enlarged.



Section A - A'
(not to scale)

Figure A-20a. PCCV Standard Output Location (SOL) #20.

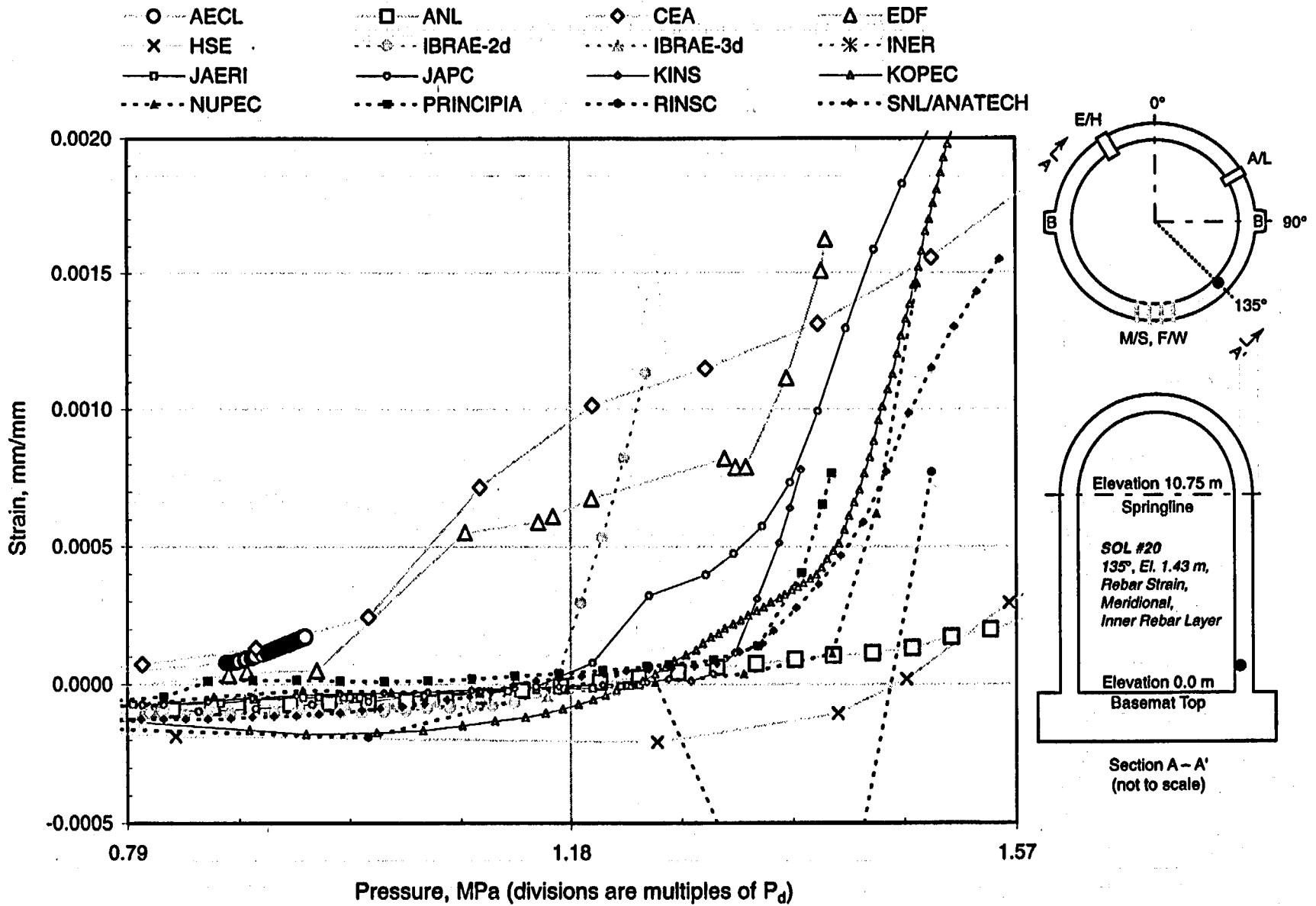


Figure A-20b. PCCV Standard Output Location (SOL) #20, enlarged.

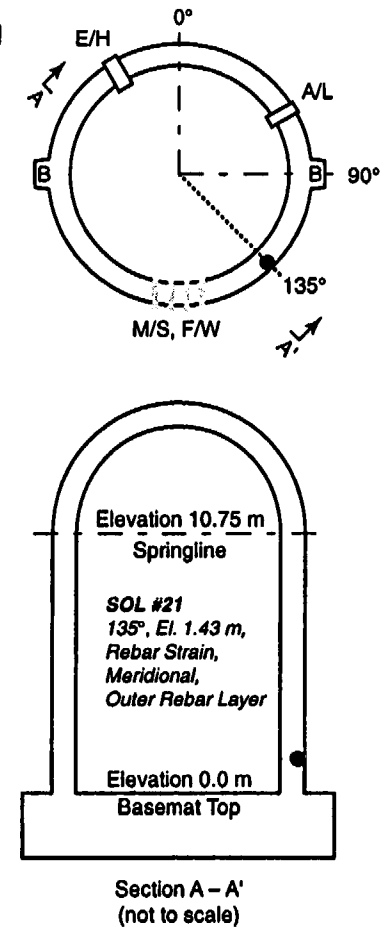
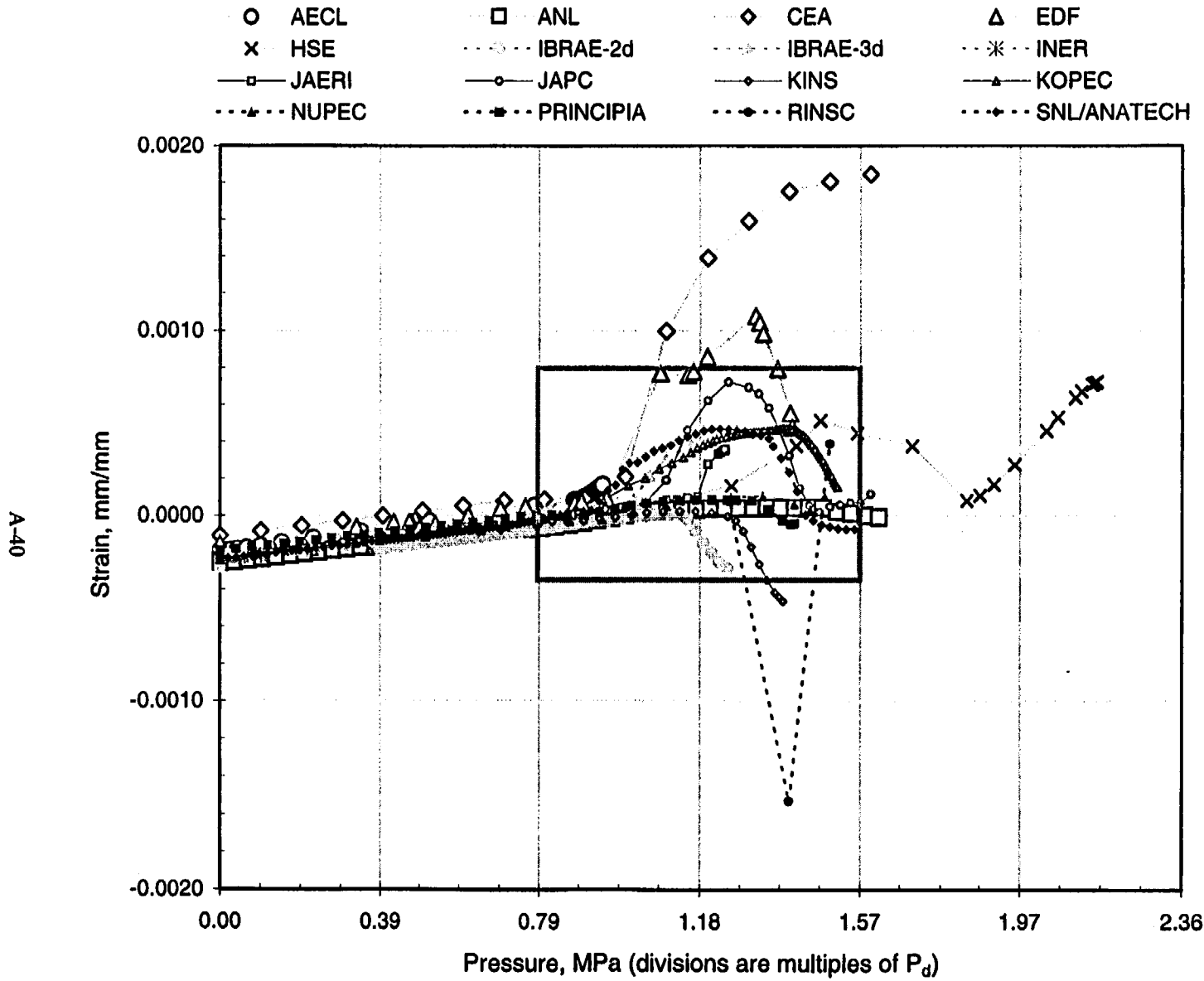


Figure A-21a. PCCV Standard Output Location (SOL) #21.

A-41

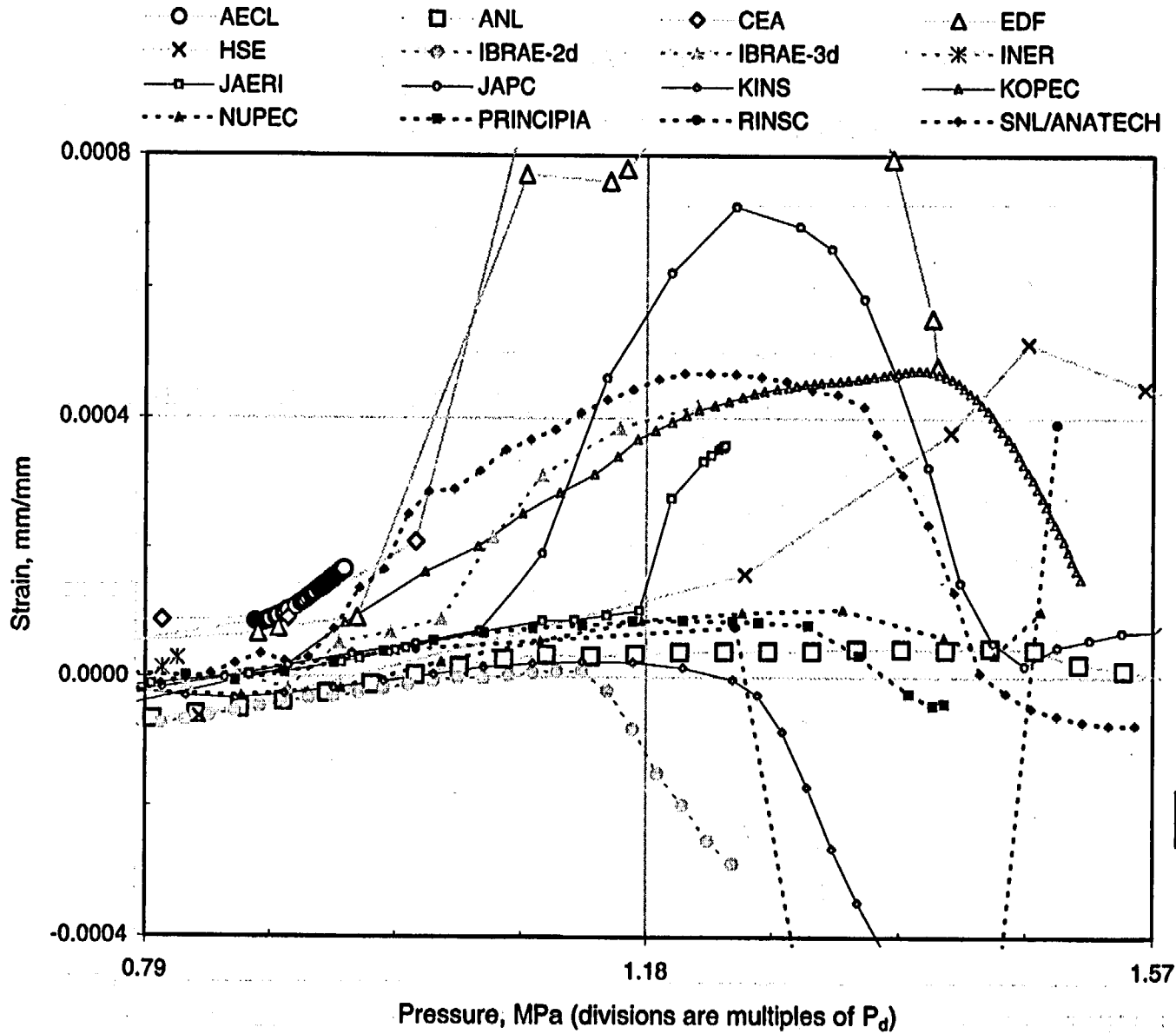


Figure A-21b. PCCV Standard Output Location (SOL) #21, enlarged.

A-42

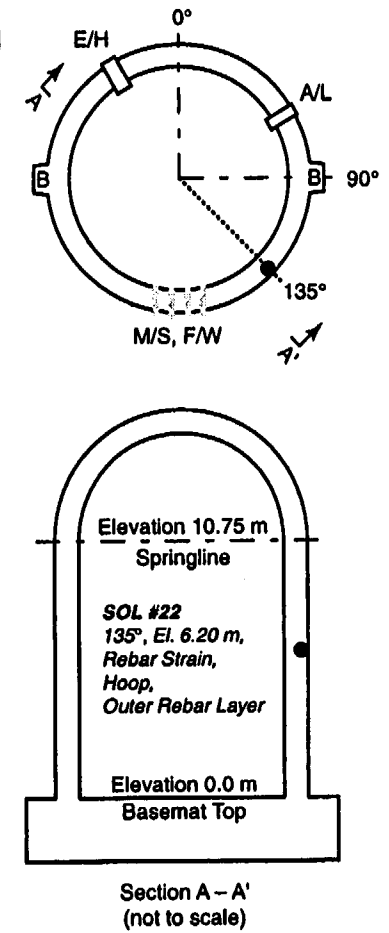
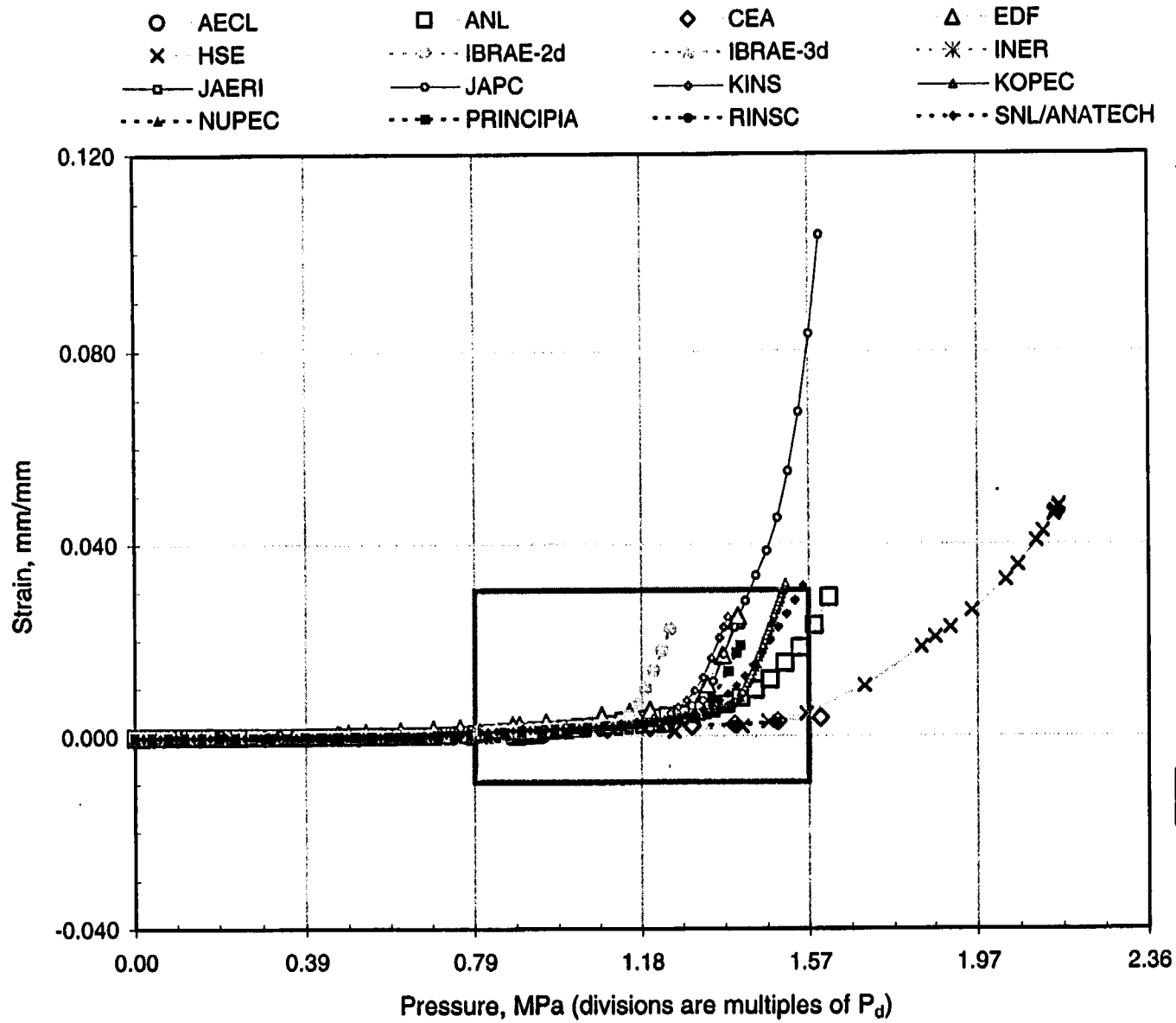


Figure A-22a. PCCV Standard Output Location (SOL) #22.

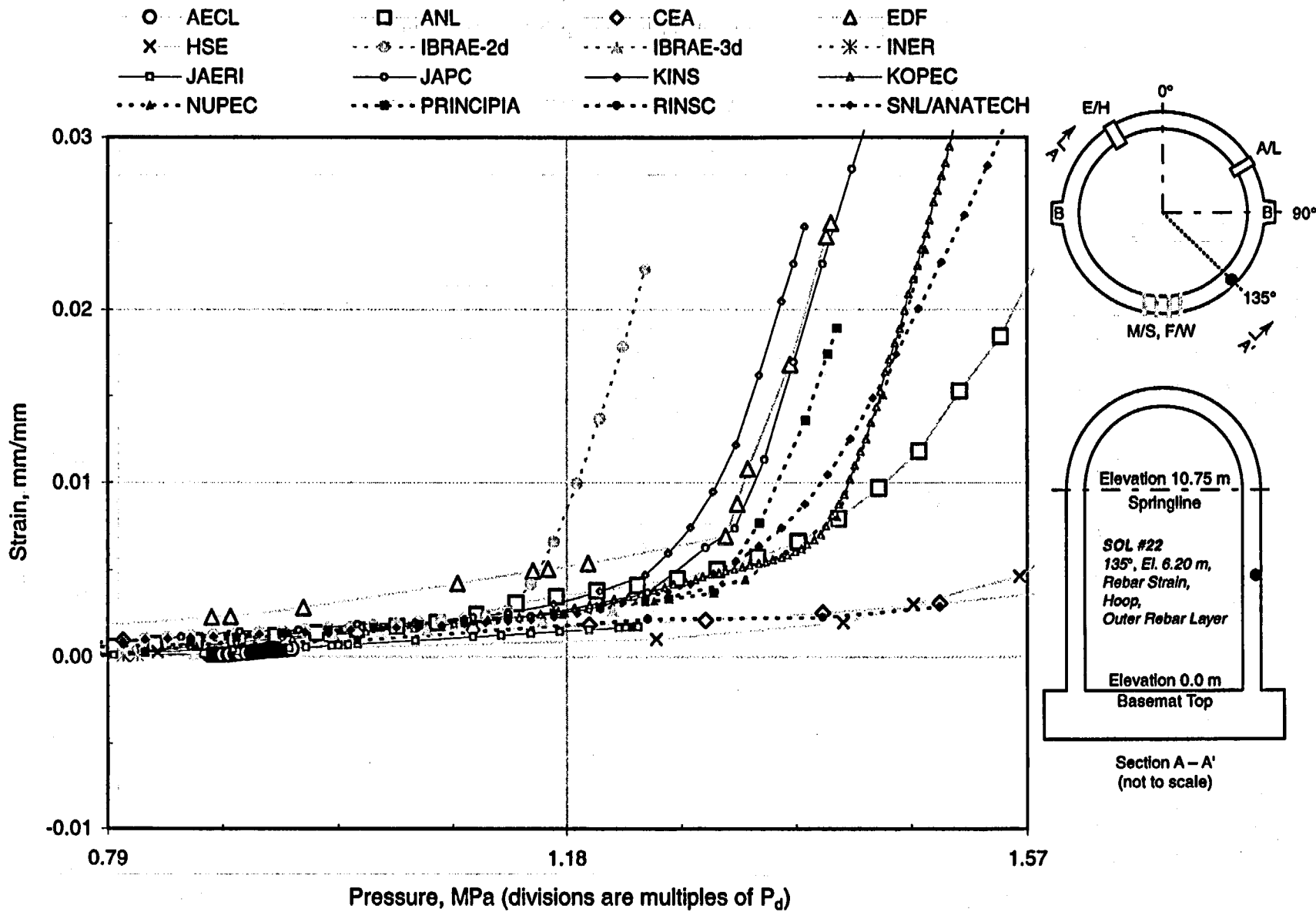


Figure A-22b. PCCV Standard Output Location (SOL) #22, enlarged.

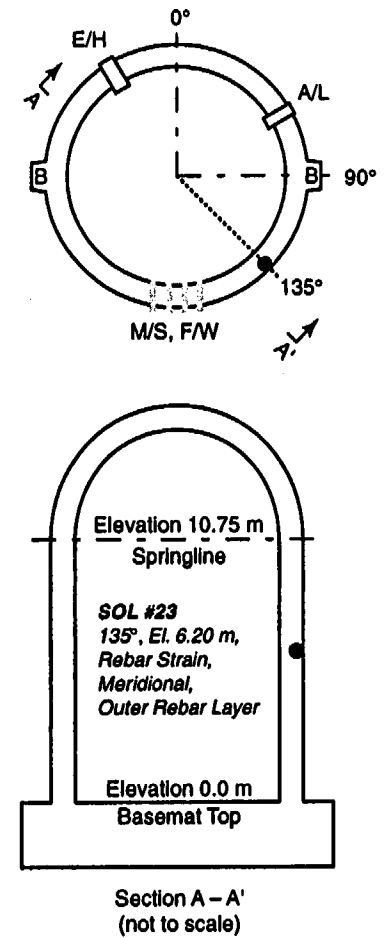
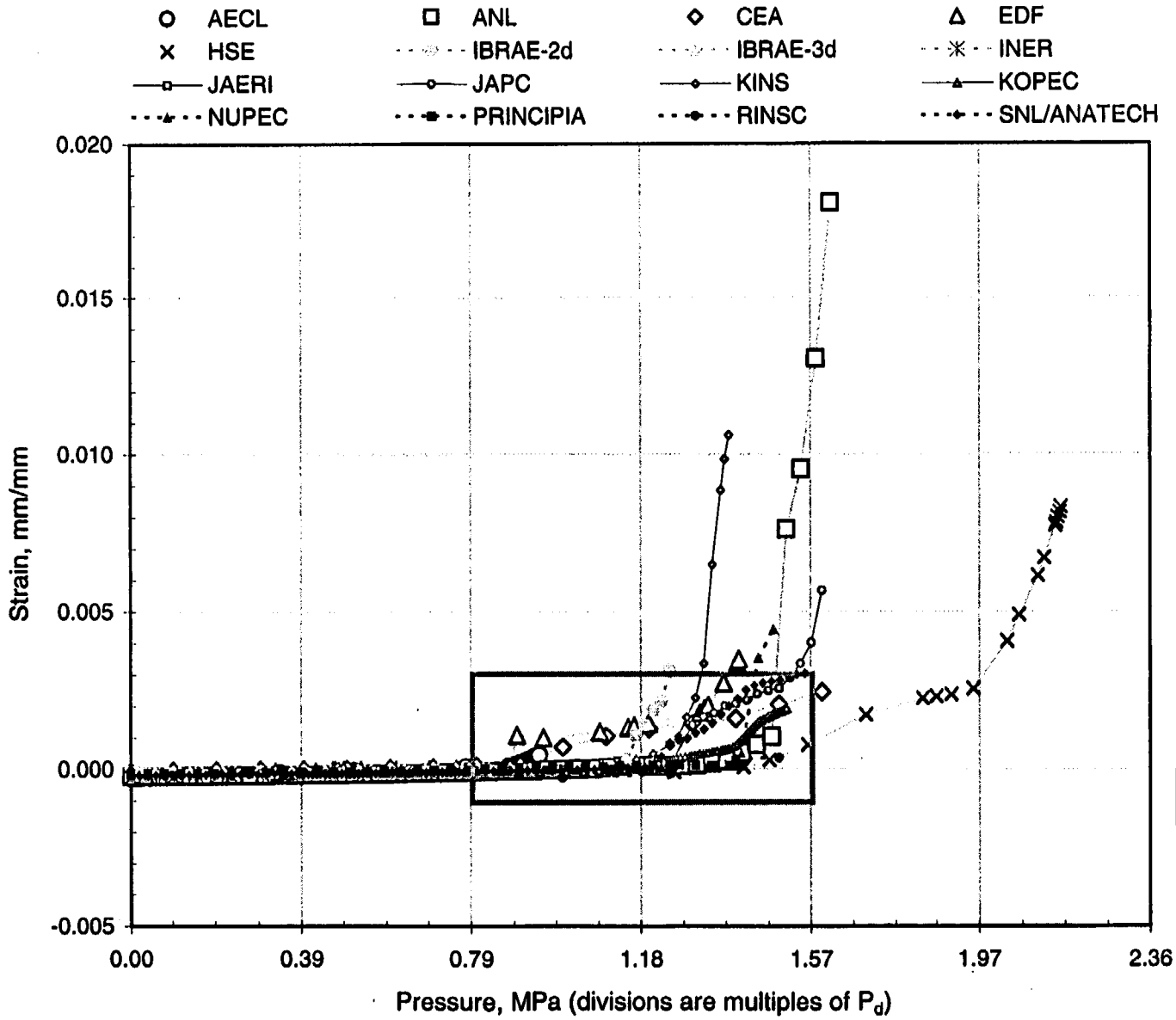


Figure A-23a. PCCV Standard Output Location (SOL) #23.

A-45

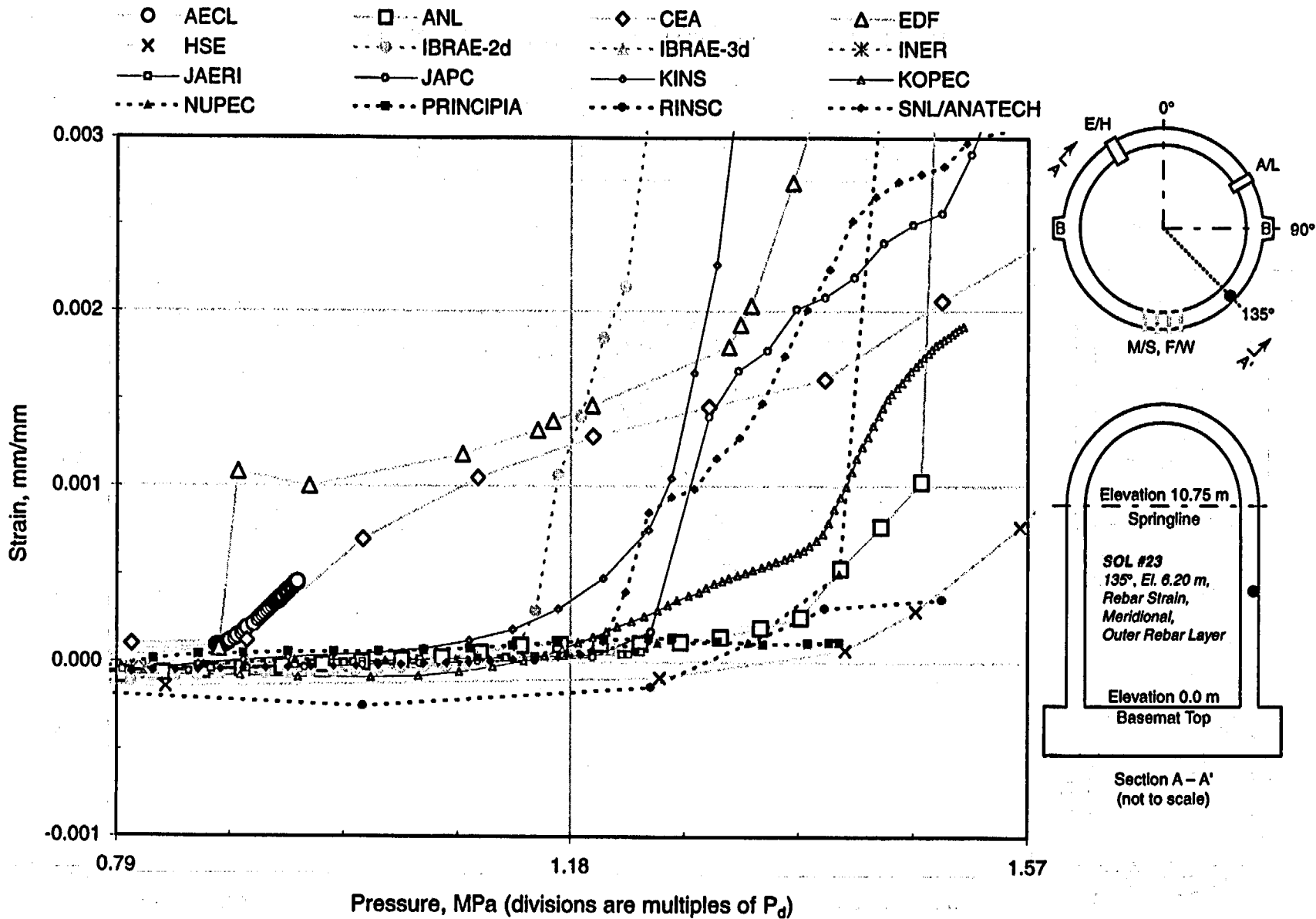


Figure A-23b. PCCV Standard Output Location (SOL) #23, enlarged.

A-46

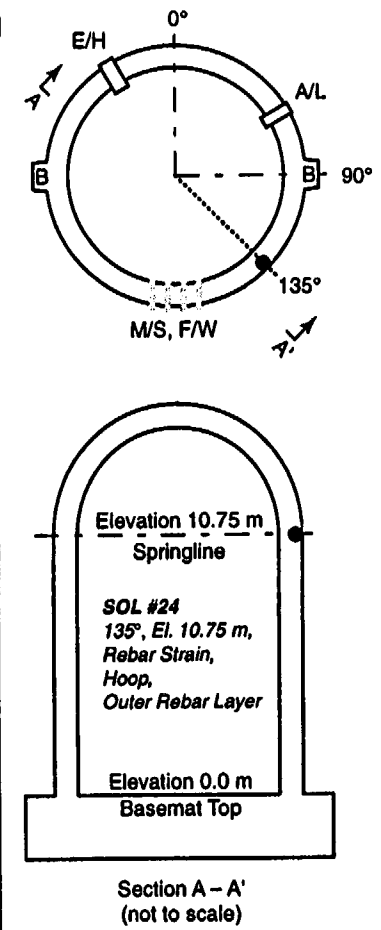
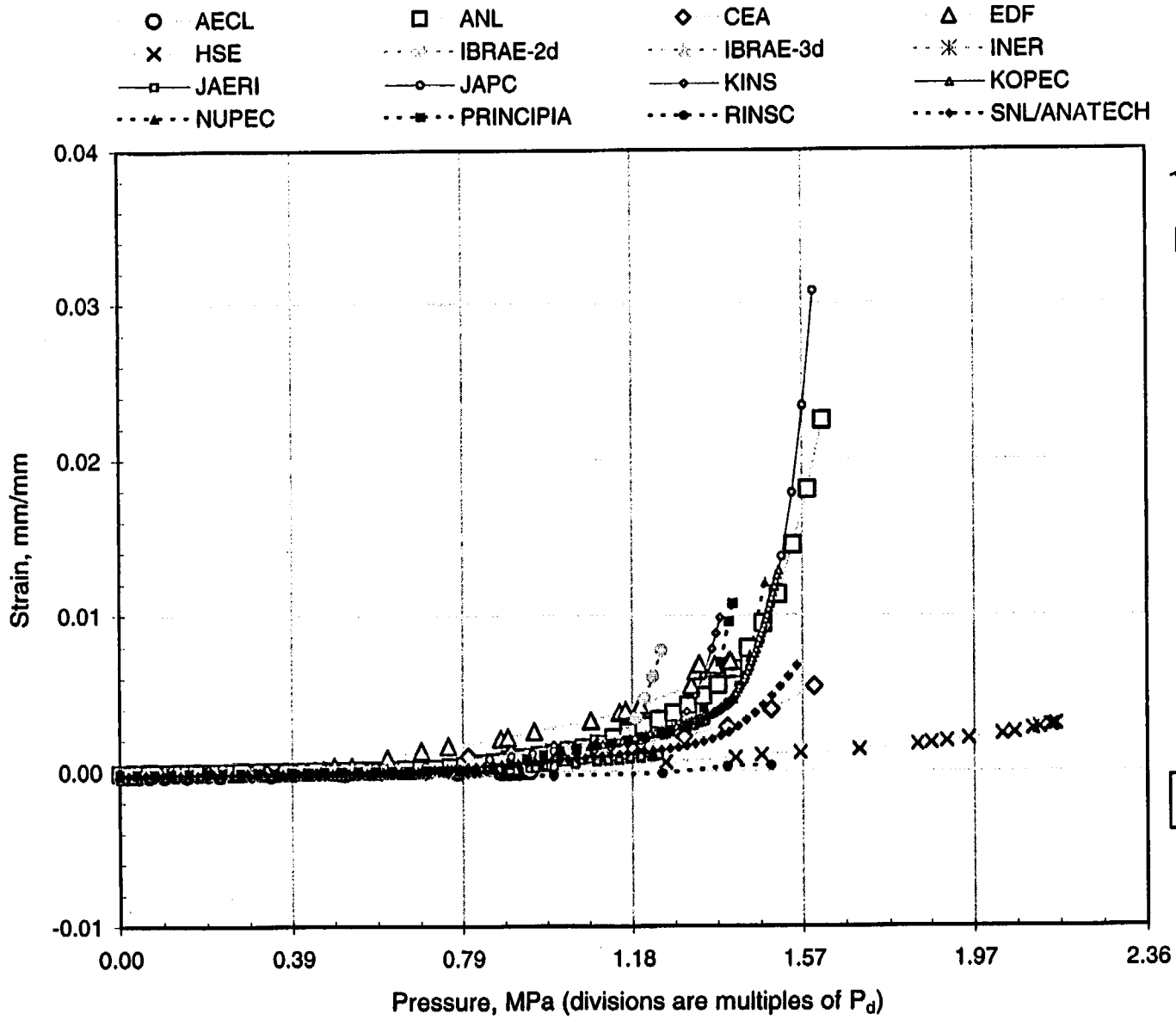


Figure A-24a. PCCV Standard Output Location (SOL) #24.

A-47

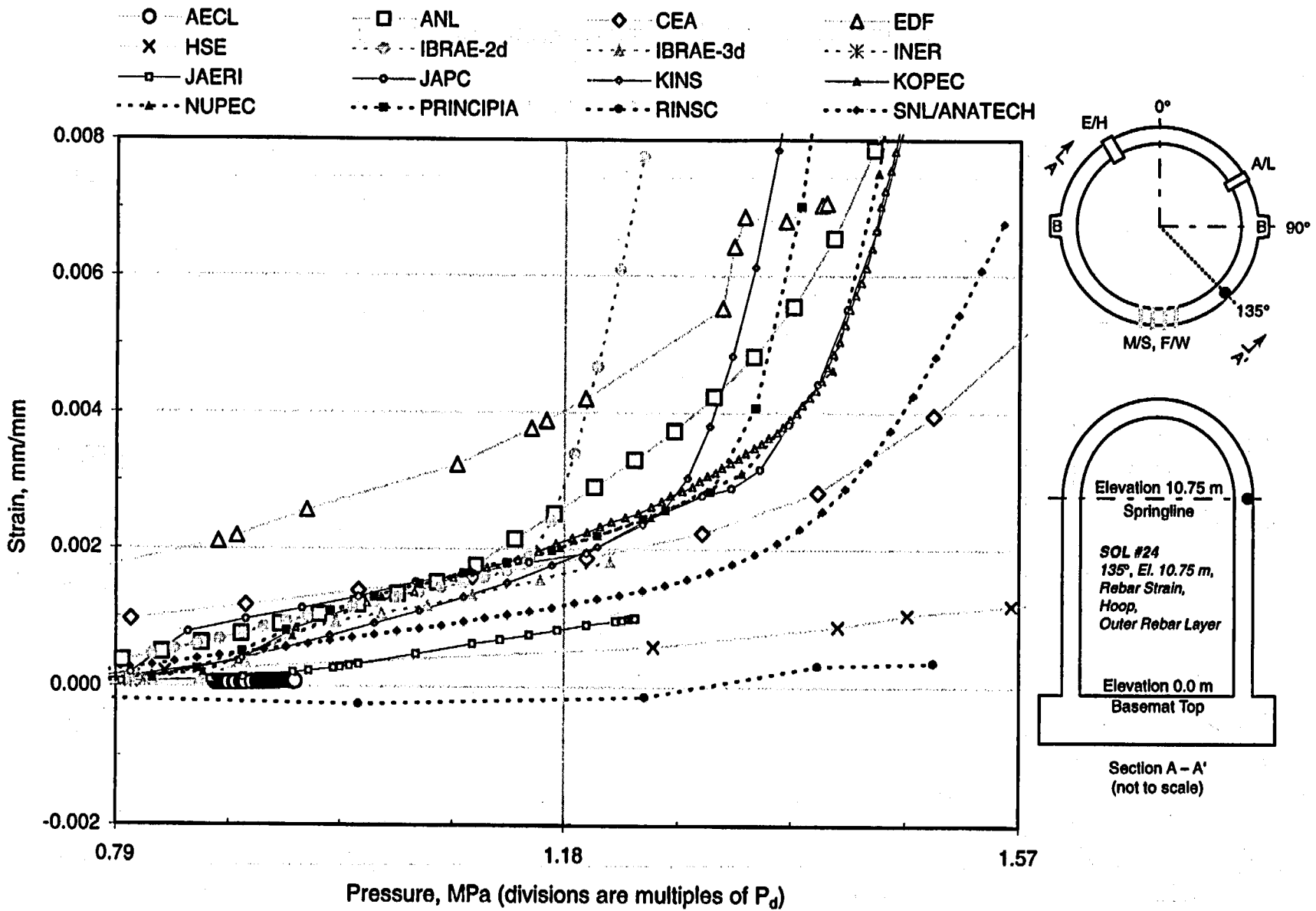


Figure A-24b. PCCV Standard Output Location (SOL) #24, enlarged.

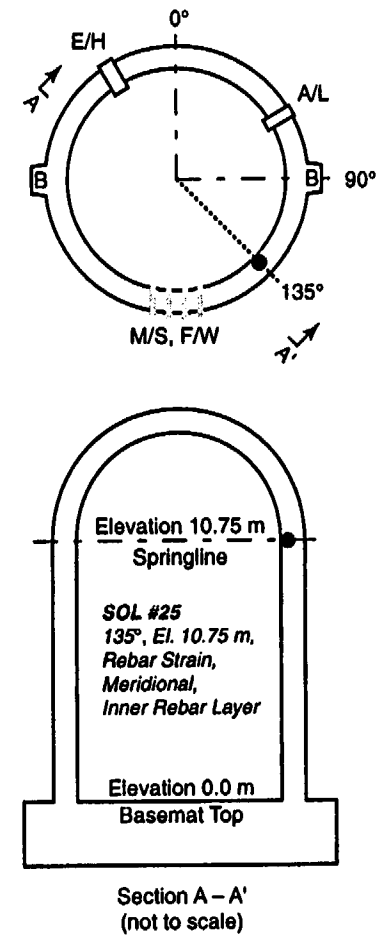
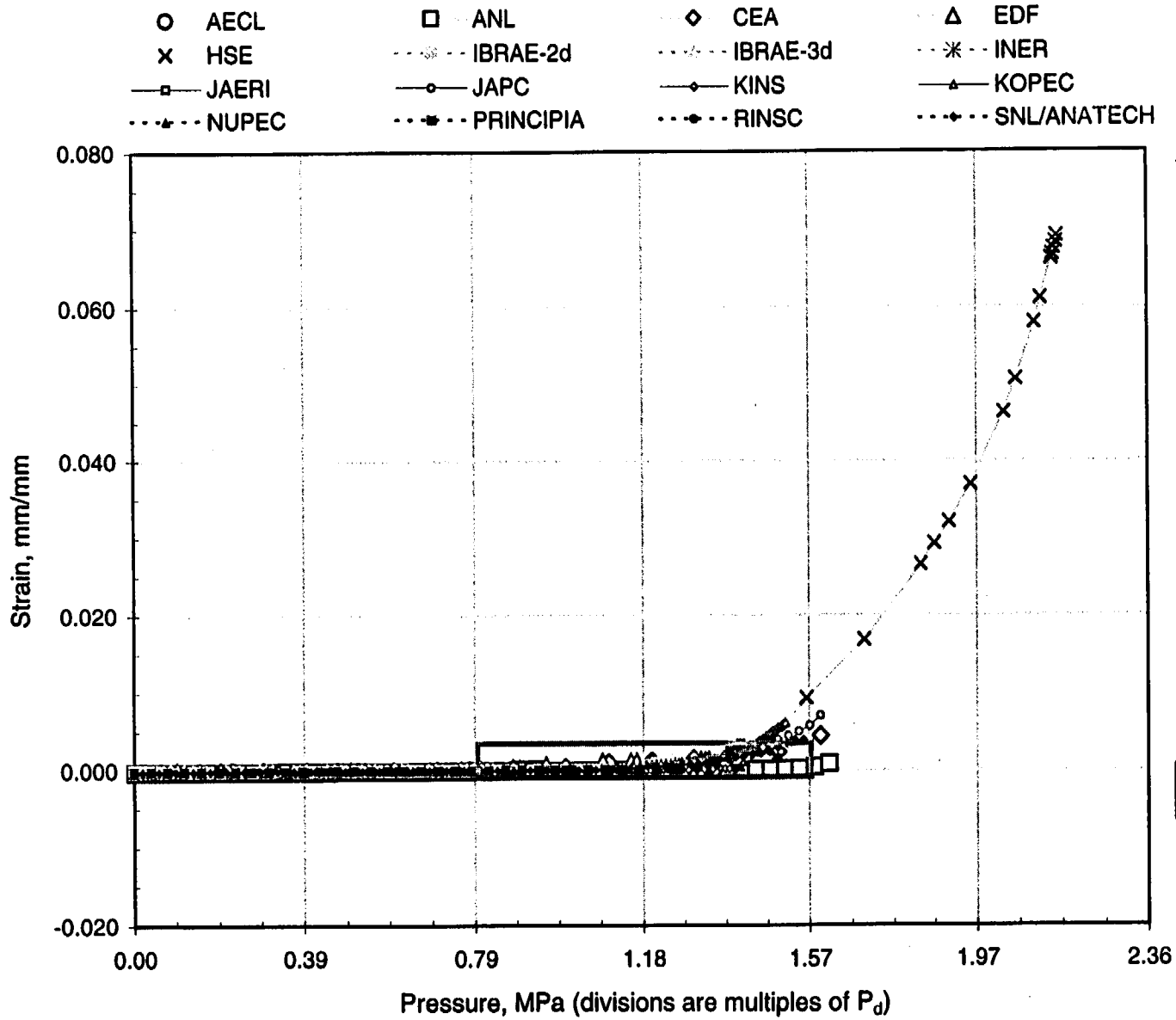


Figure A-25a. PCCV Standard Output Location (SOL) #25.

A-49

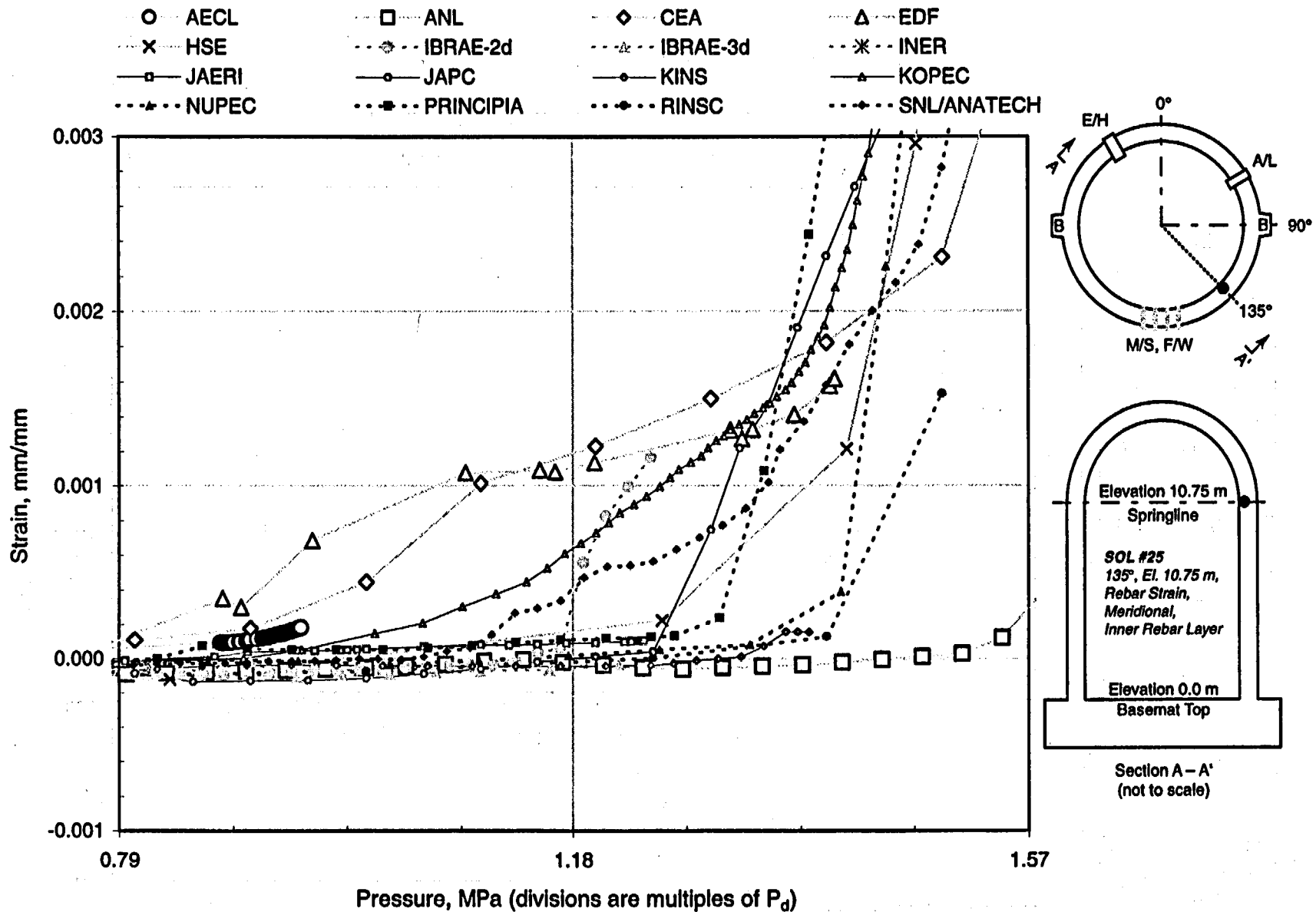


Figure A-25b. PCCV Standard Output Location (SOL) #25, enlarged.

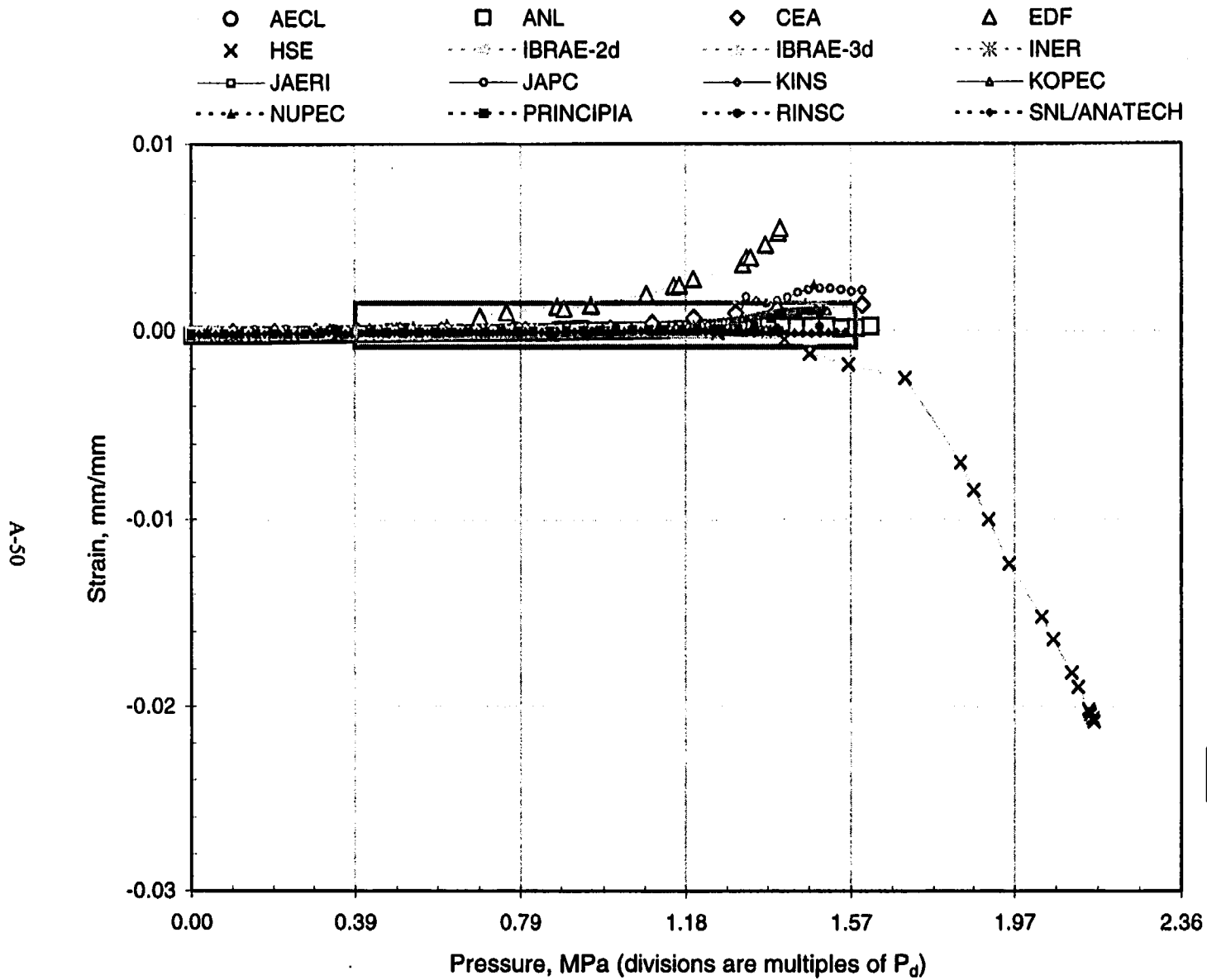


Figure A-26a. PCCV Standard Output Location (SOL) #26.

A-51

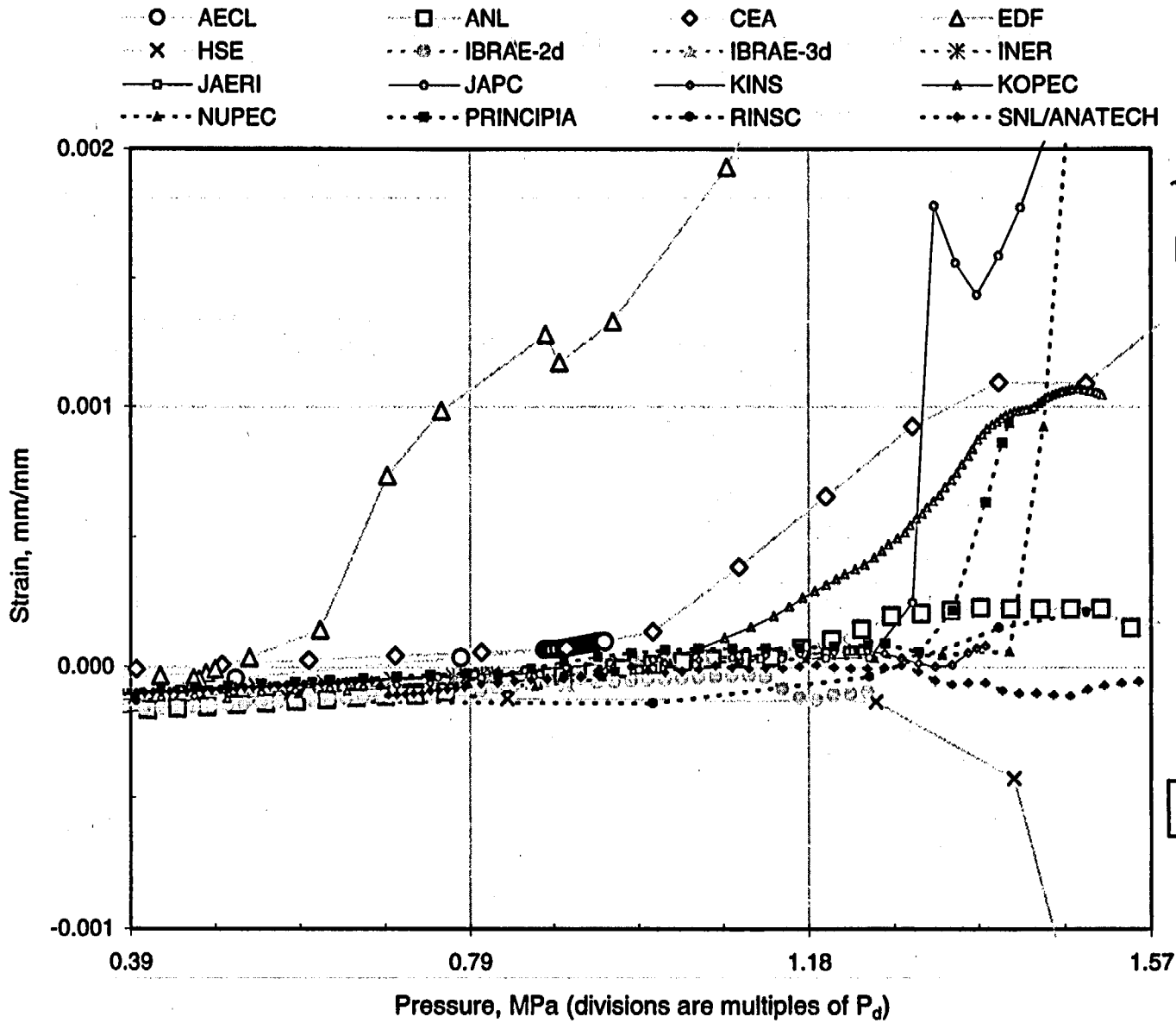


Figure A-26b. PCCV Standard Output Location (SOL) #26, enlarged.

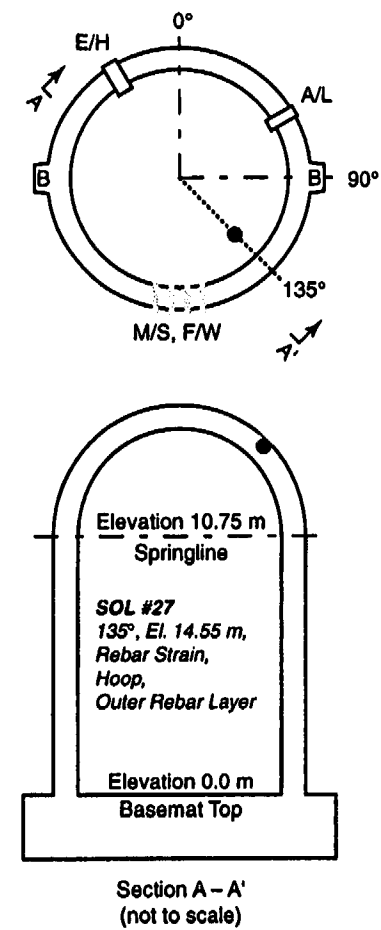
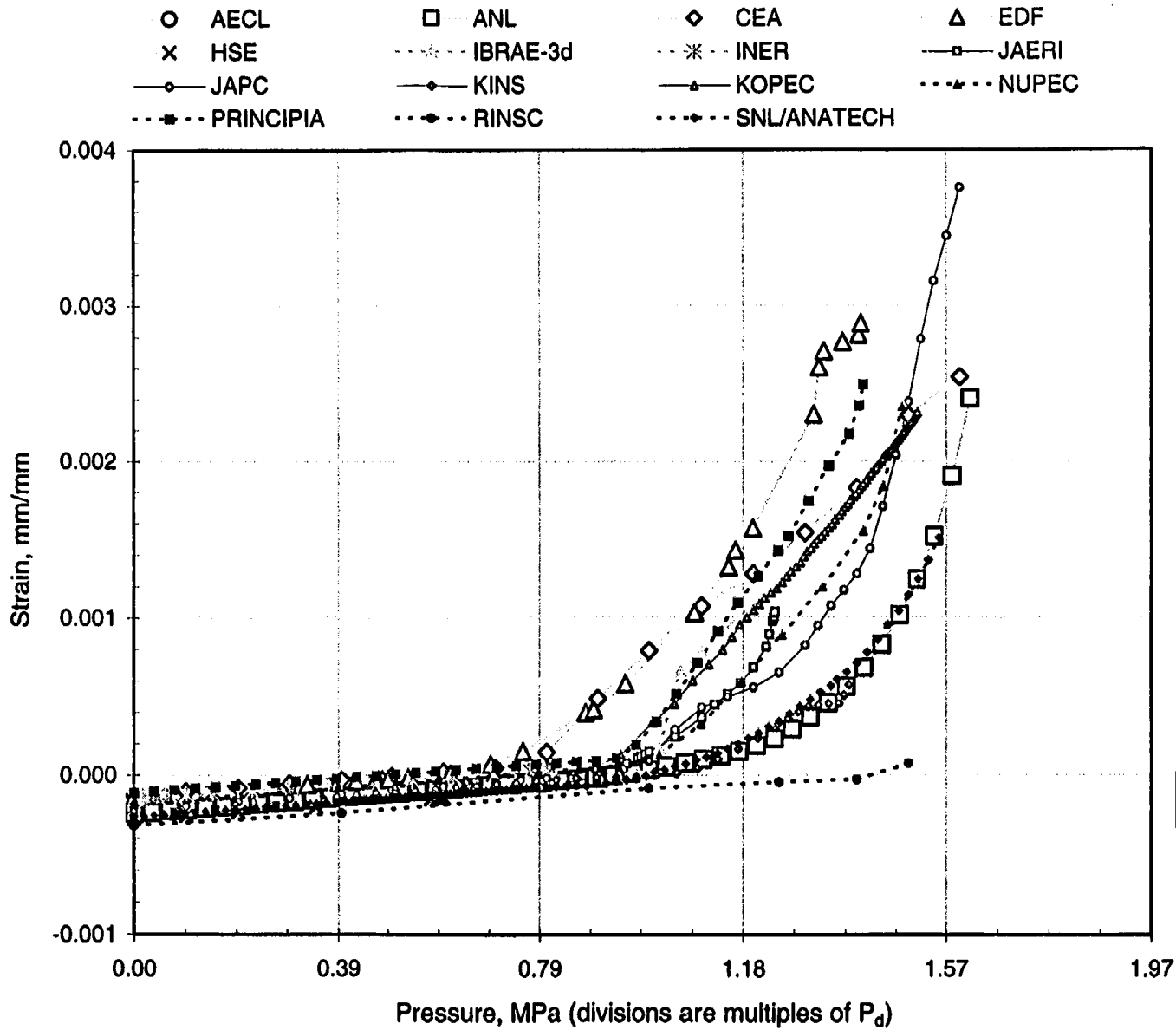


Figure A-27. PCCV Standard Output Location (SOL) #27.

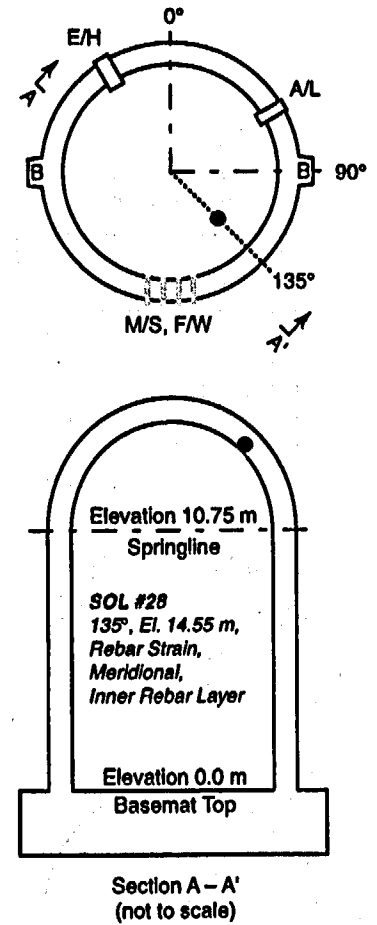
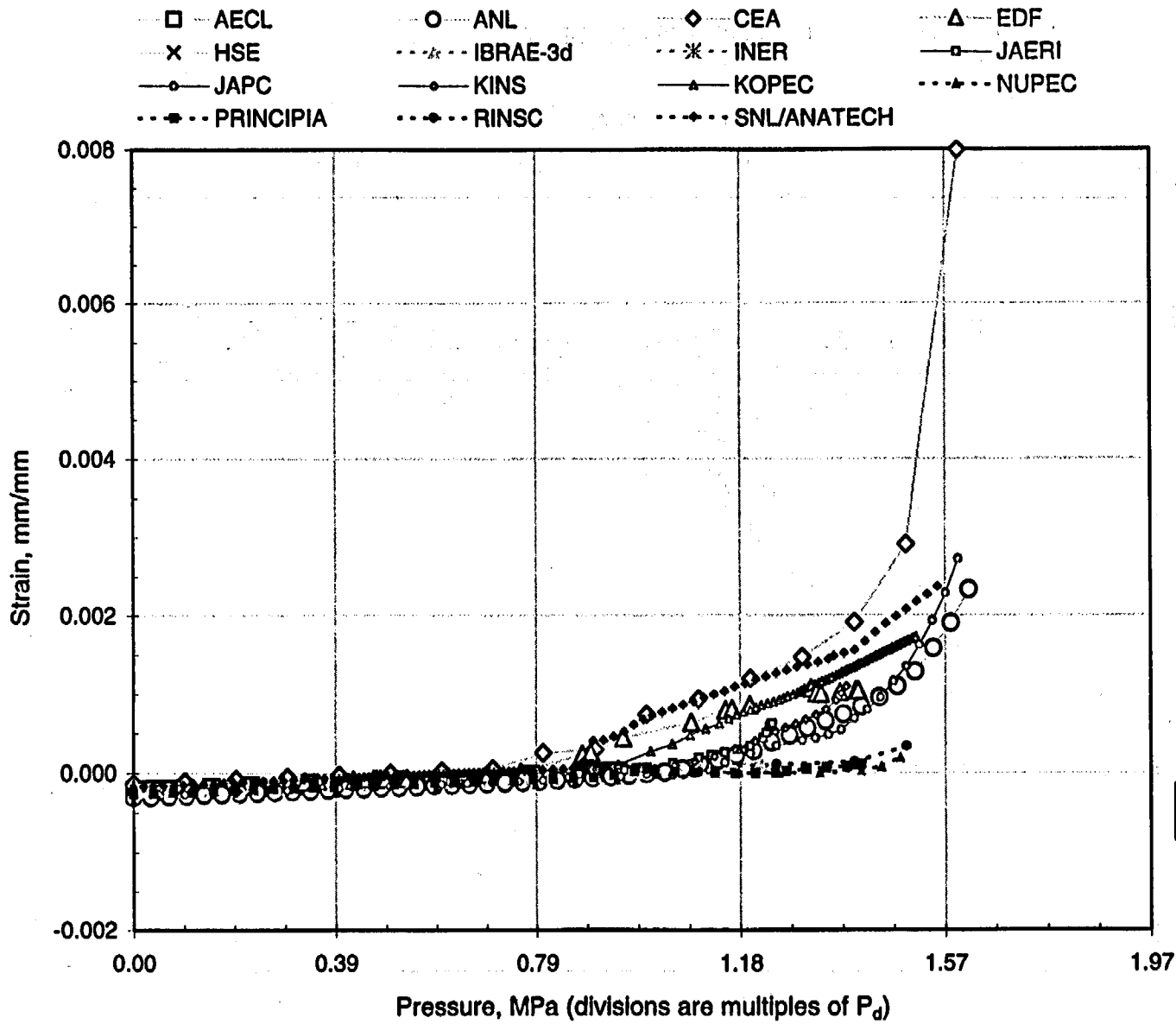
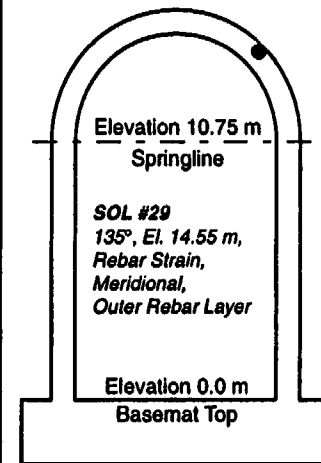
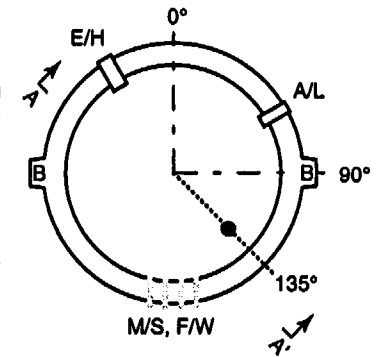
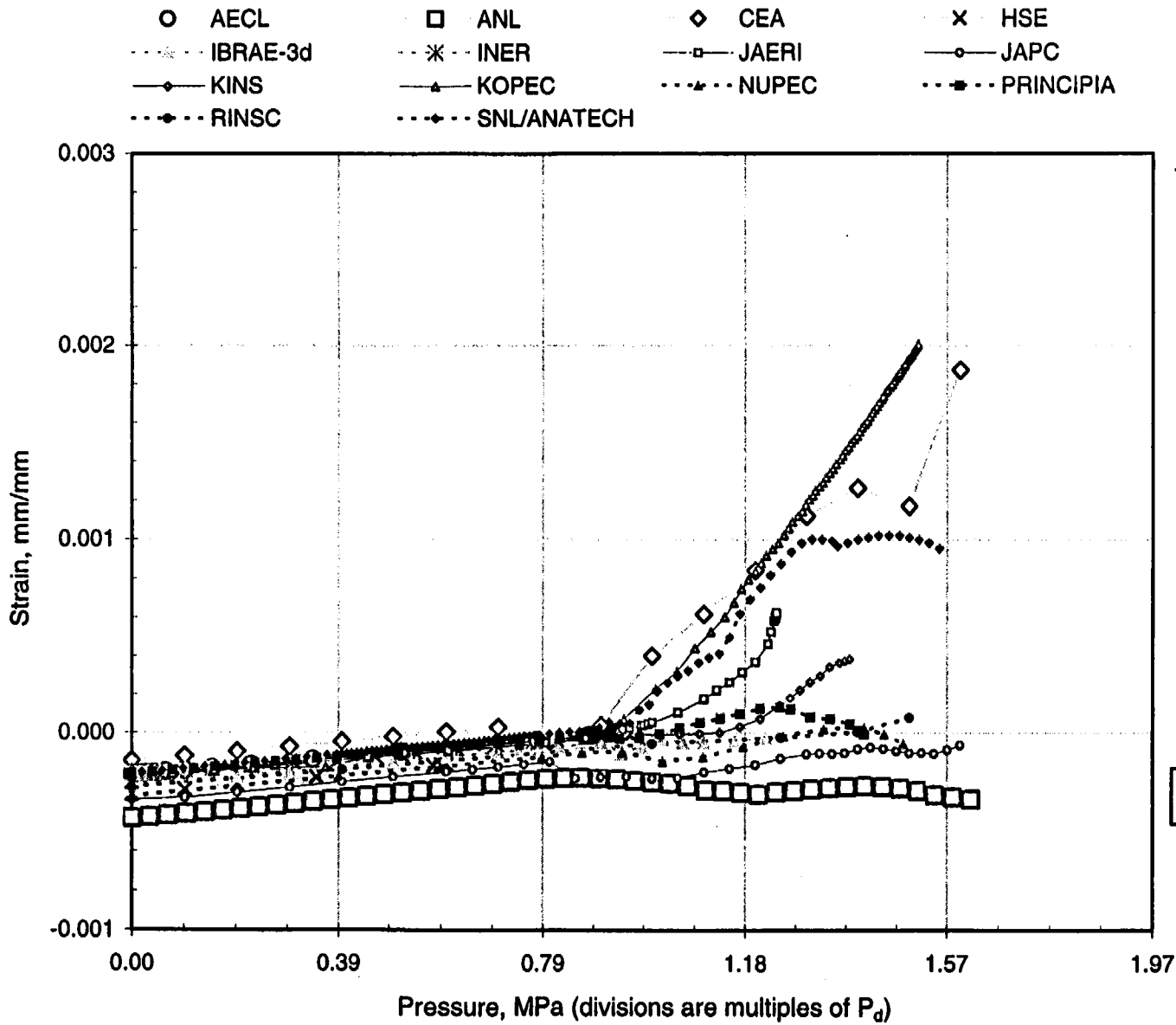


Figure A-28. PCCV Standard Output Location (SOL) #28.



Section A - A'
(not to scale)

Figure A-29. PCCV Standard Output Location (SOL) #29.

This page intentionally left blank to facilitate plot comparison.

95-V

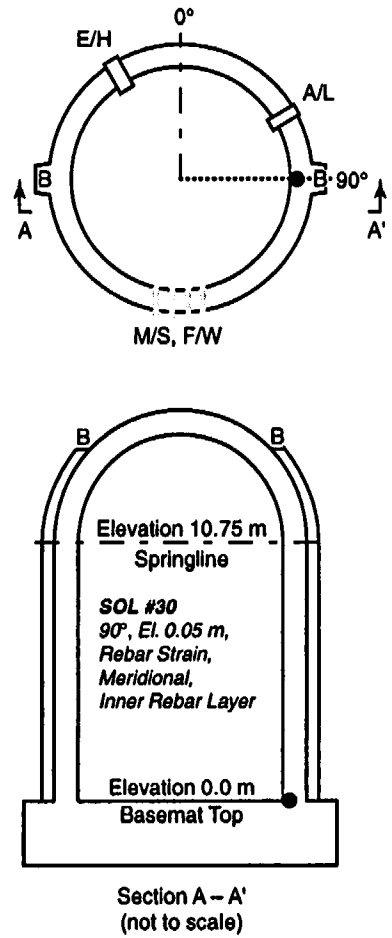
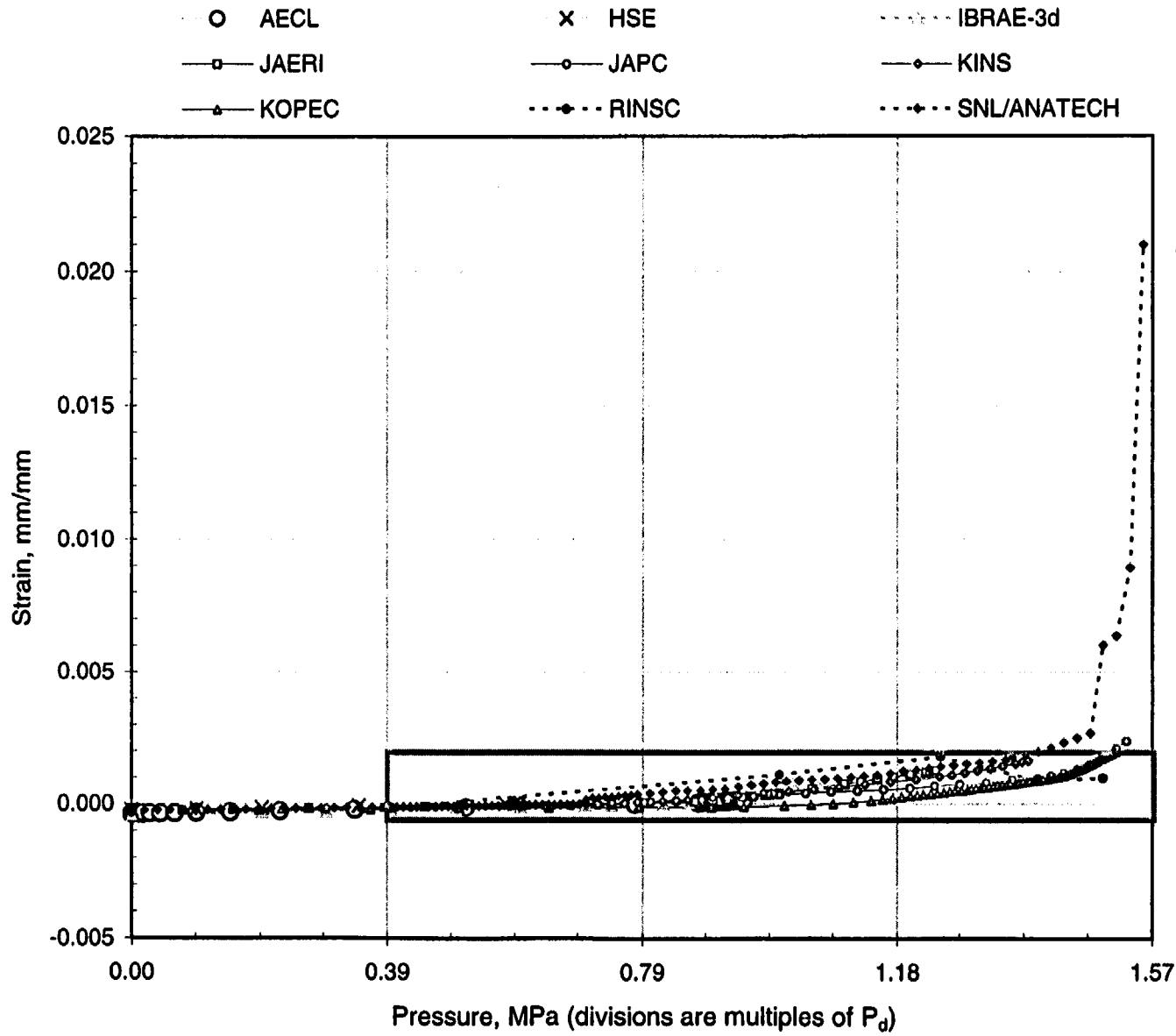
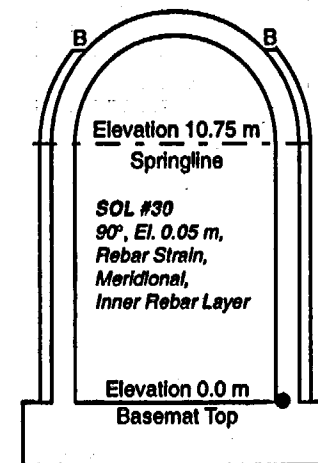
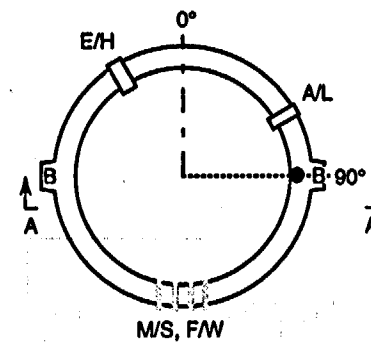
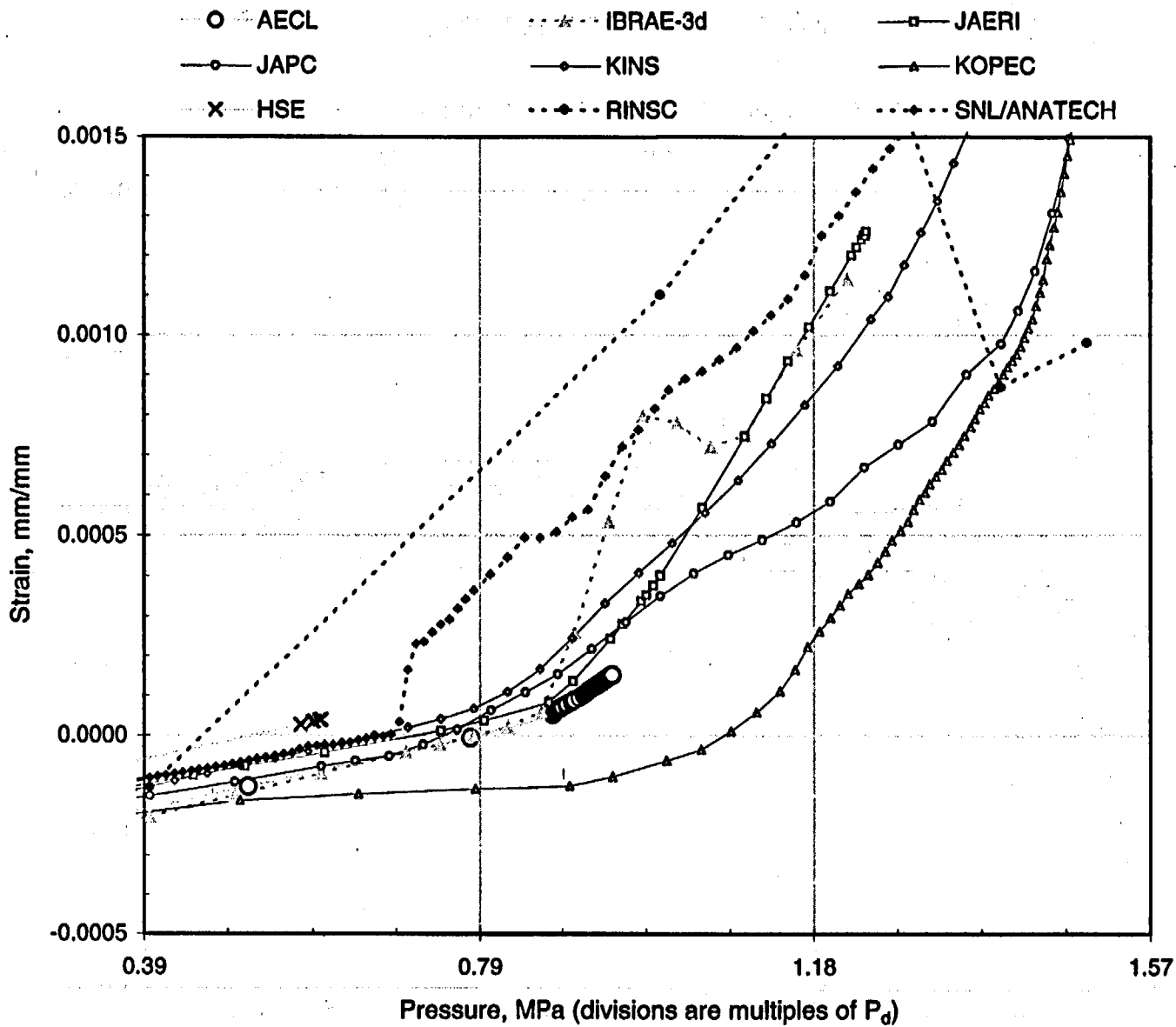


Figure A-30a. PCCV Standard Output Location (SOL) #30.

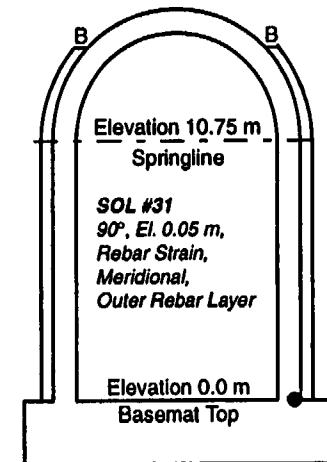
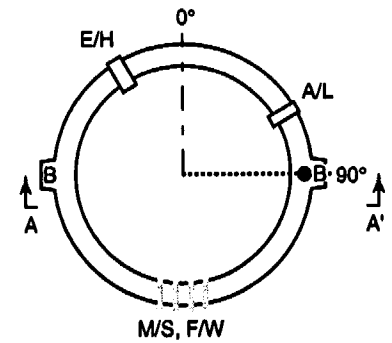
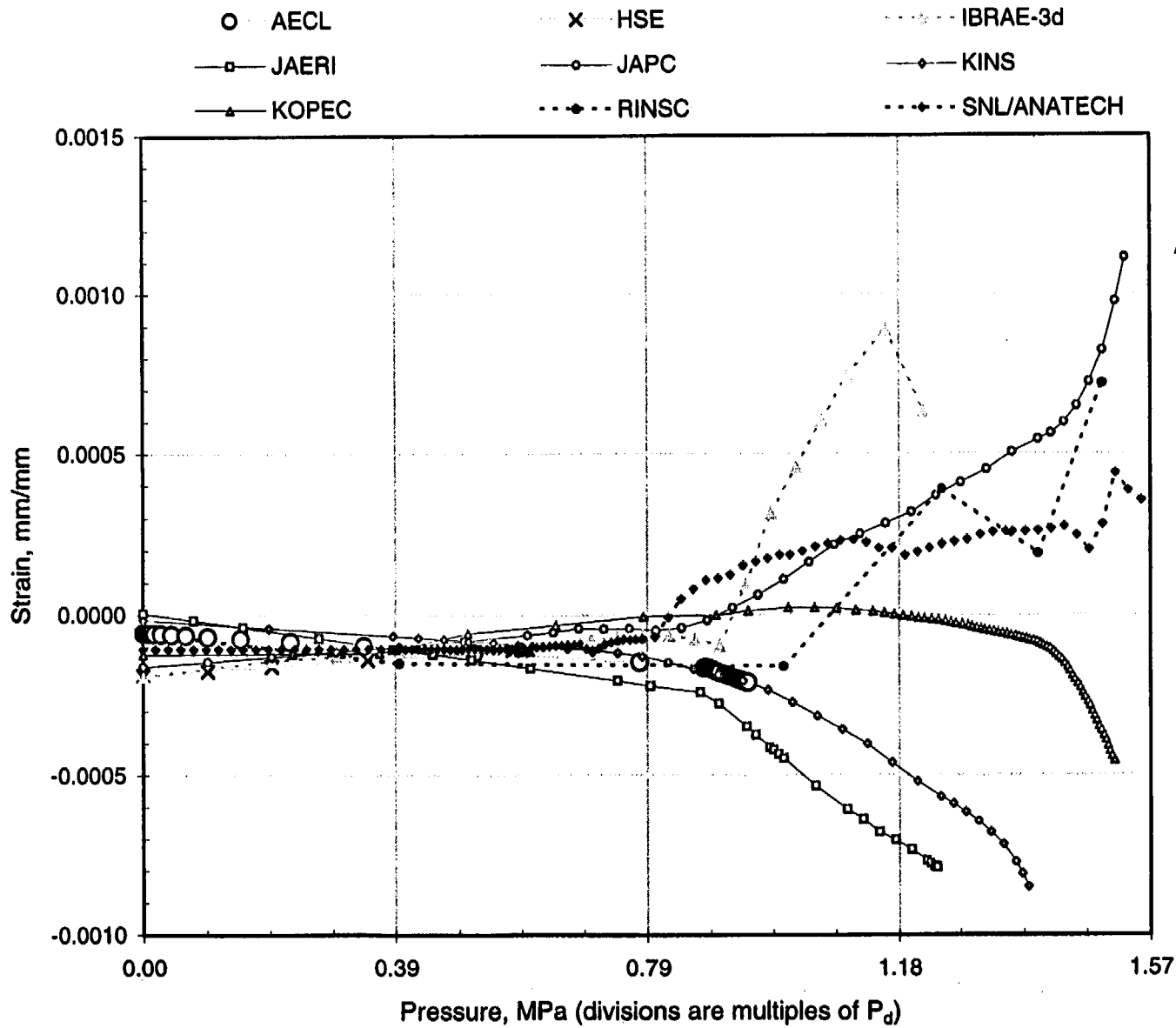
A-57



Section A - A'
(not to scale)

Figure A-30b. PCCV Standard Output Location (SOL) #30, enlarged.

A-58



Section A - A'
(not to scale)

Figure A-31. PCCV Standard Output Location (SOL) #31.

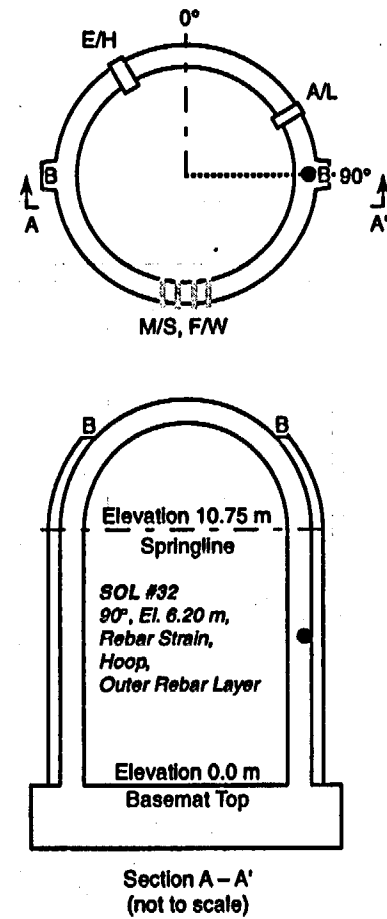
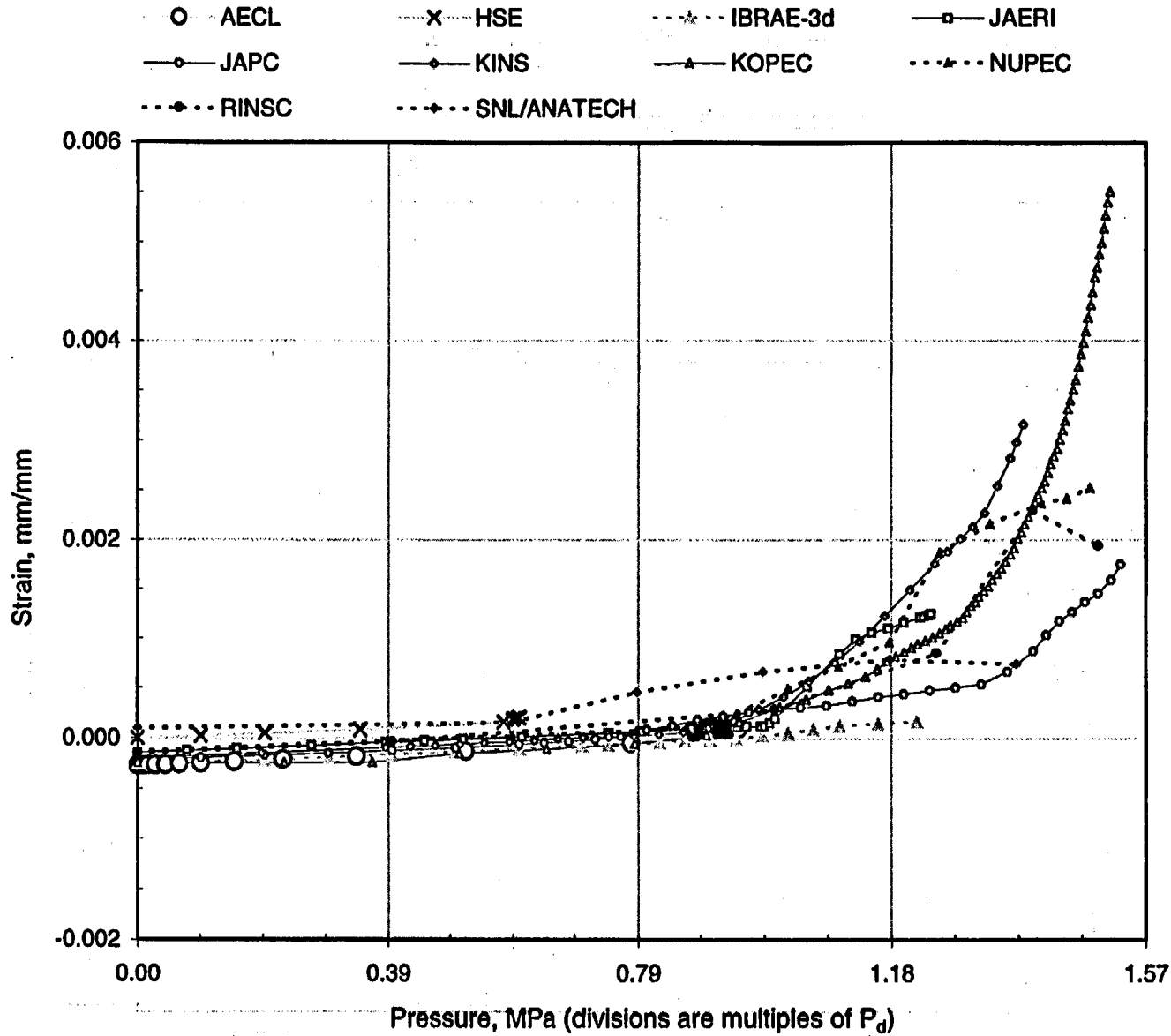


Figure A-32. PCCV Standard Output Location (SOL) #32.

A-60

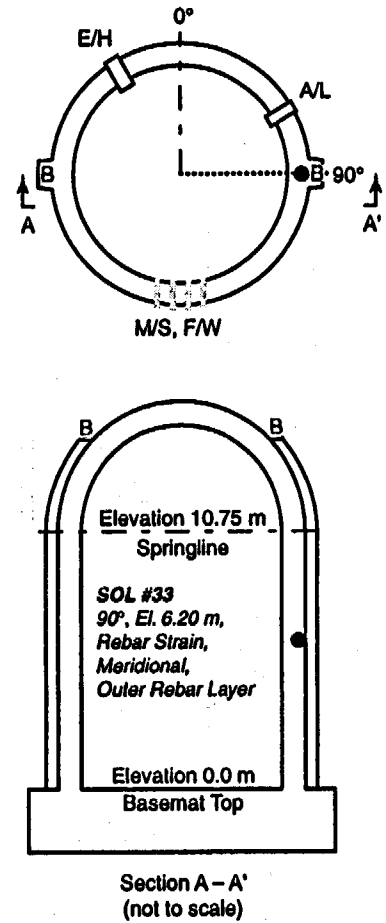
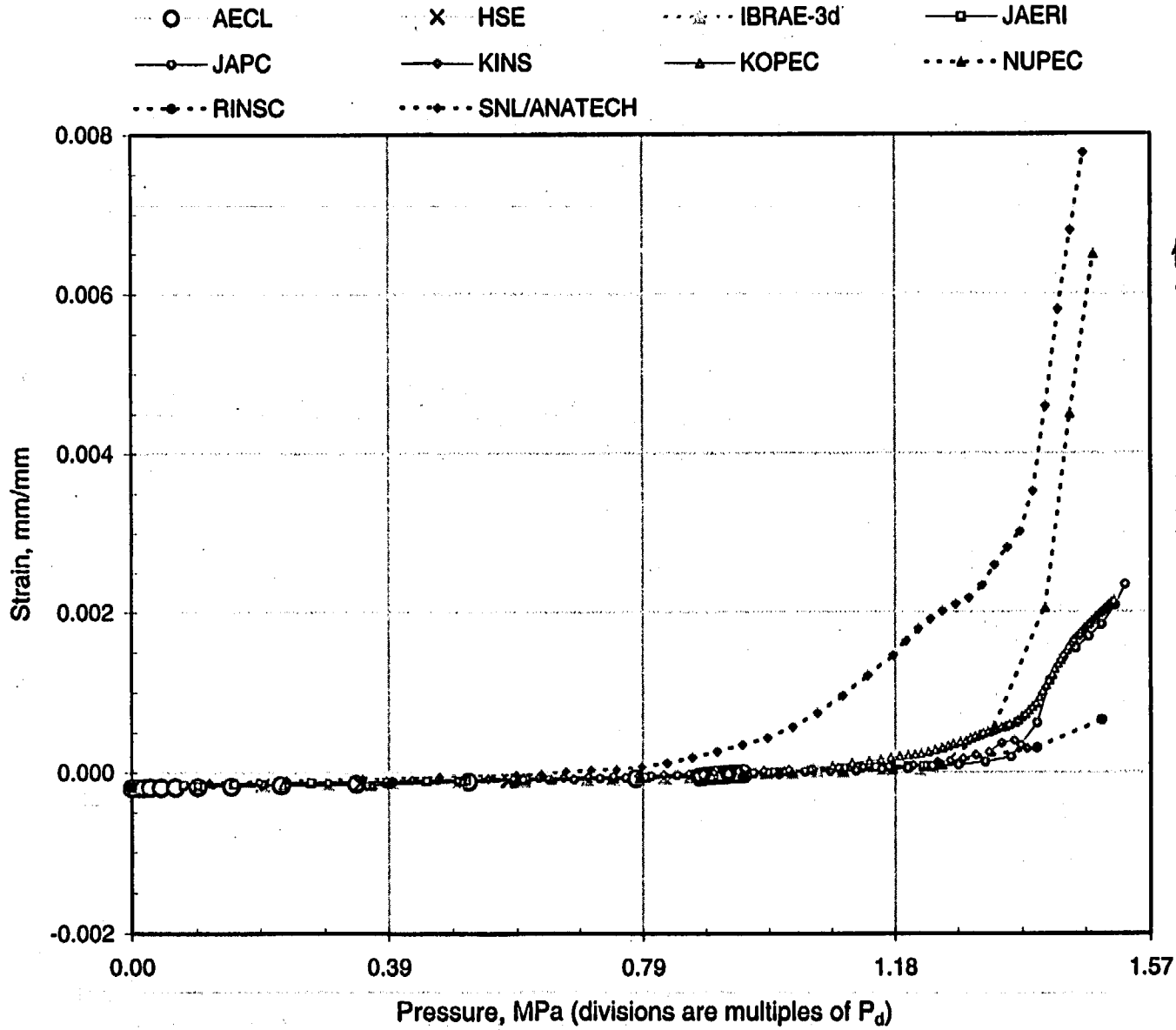


Figure A-33. PCCV Standard Output Location (SOL) #33.

This page intentionally left blank to facilitate plot comparison.

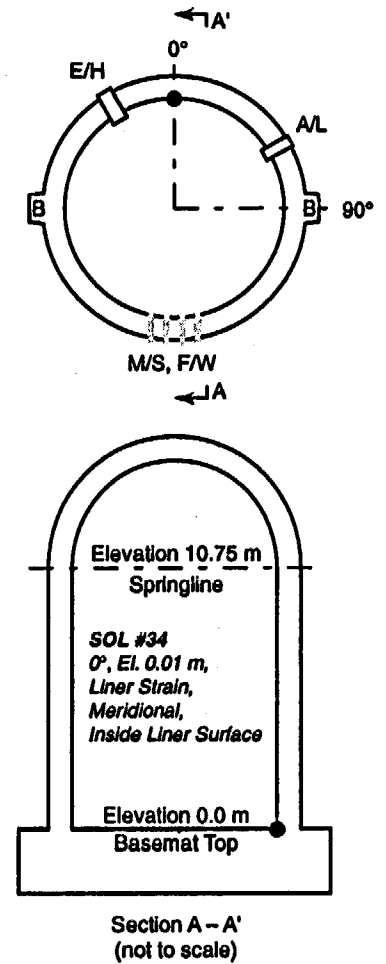
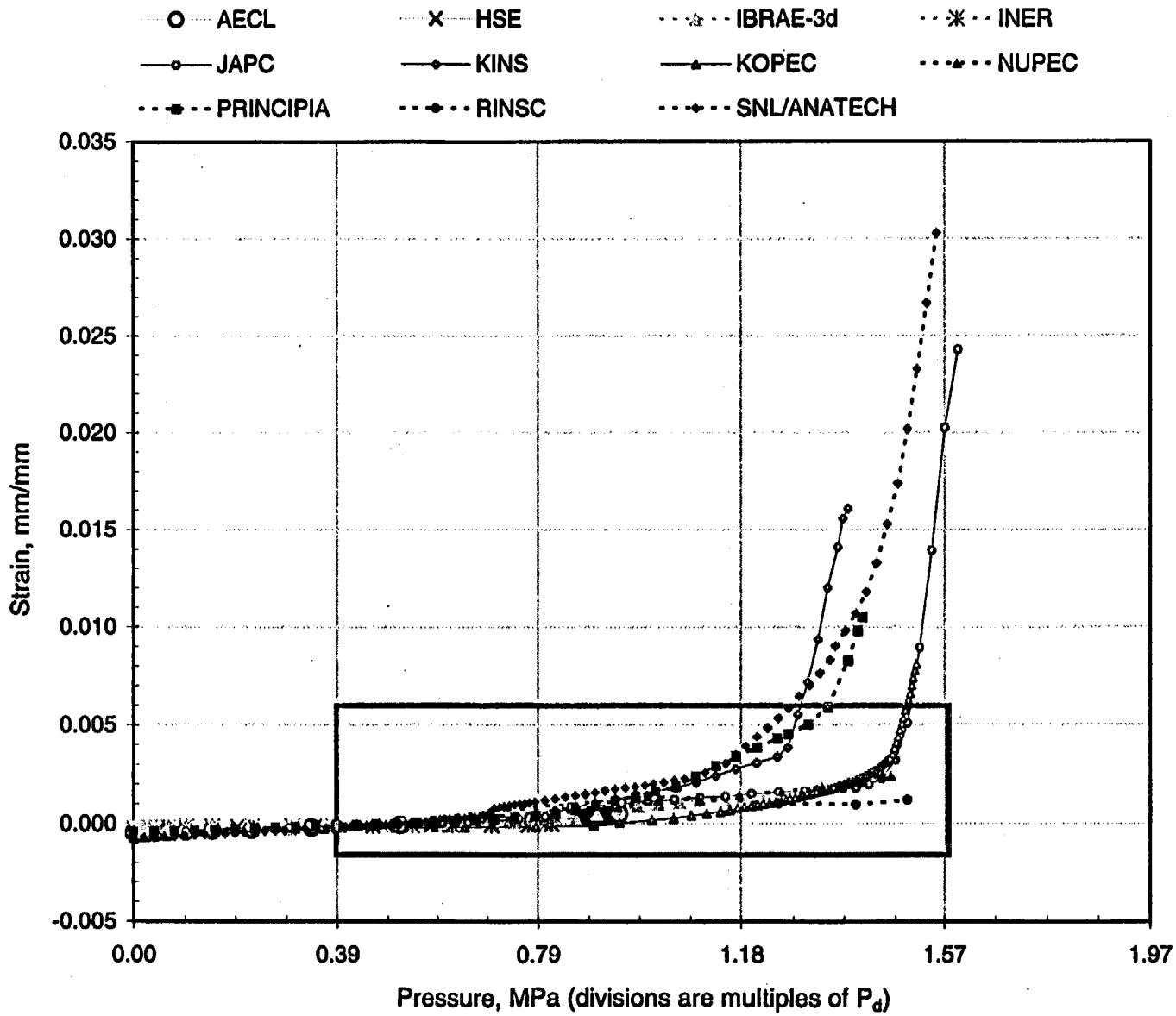


Figure A-34a. PCCV Standard Output Location (SOL) #34.

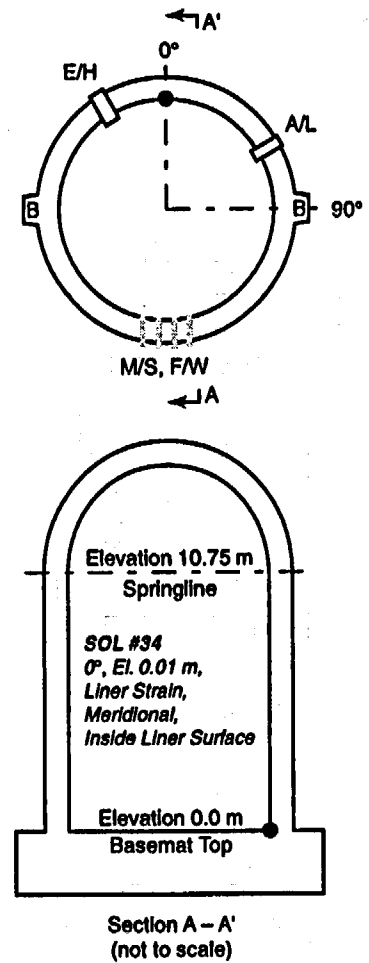
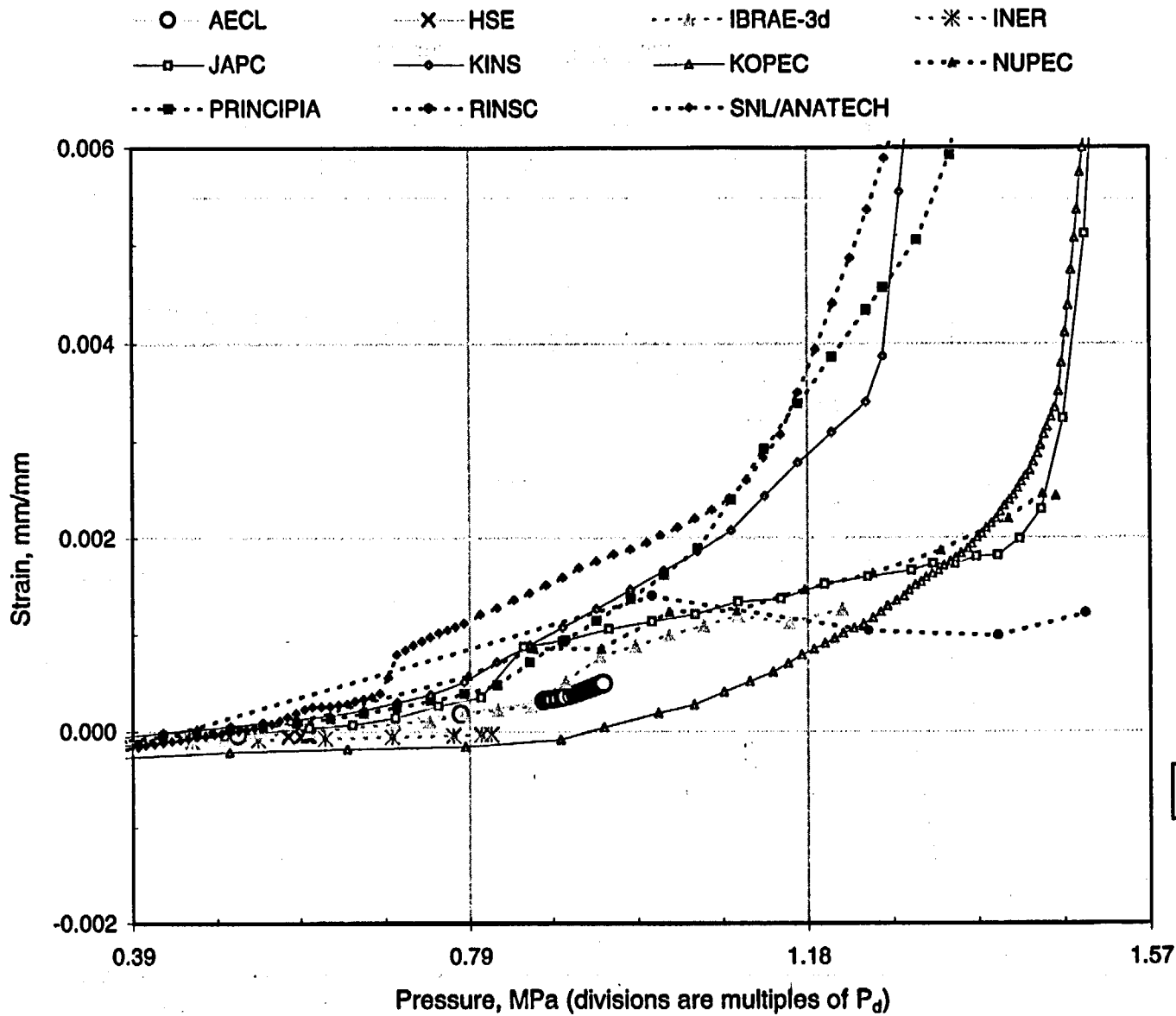


Figure A-34b. PCCV Standard Output Location (SOL) #34, enlarged.

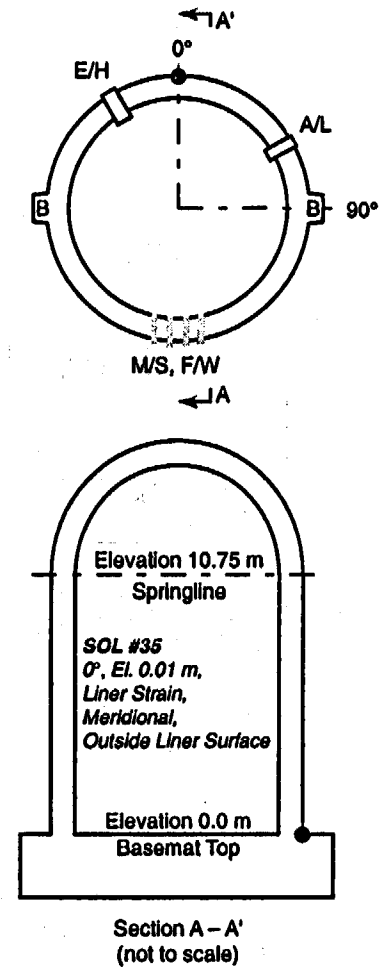
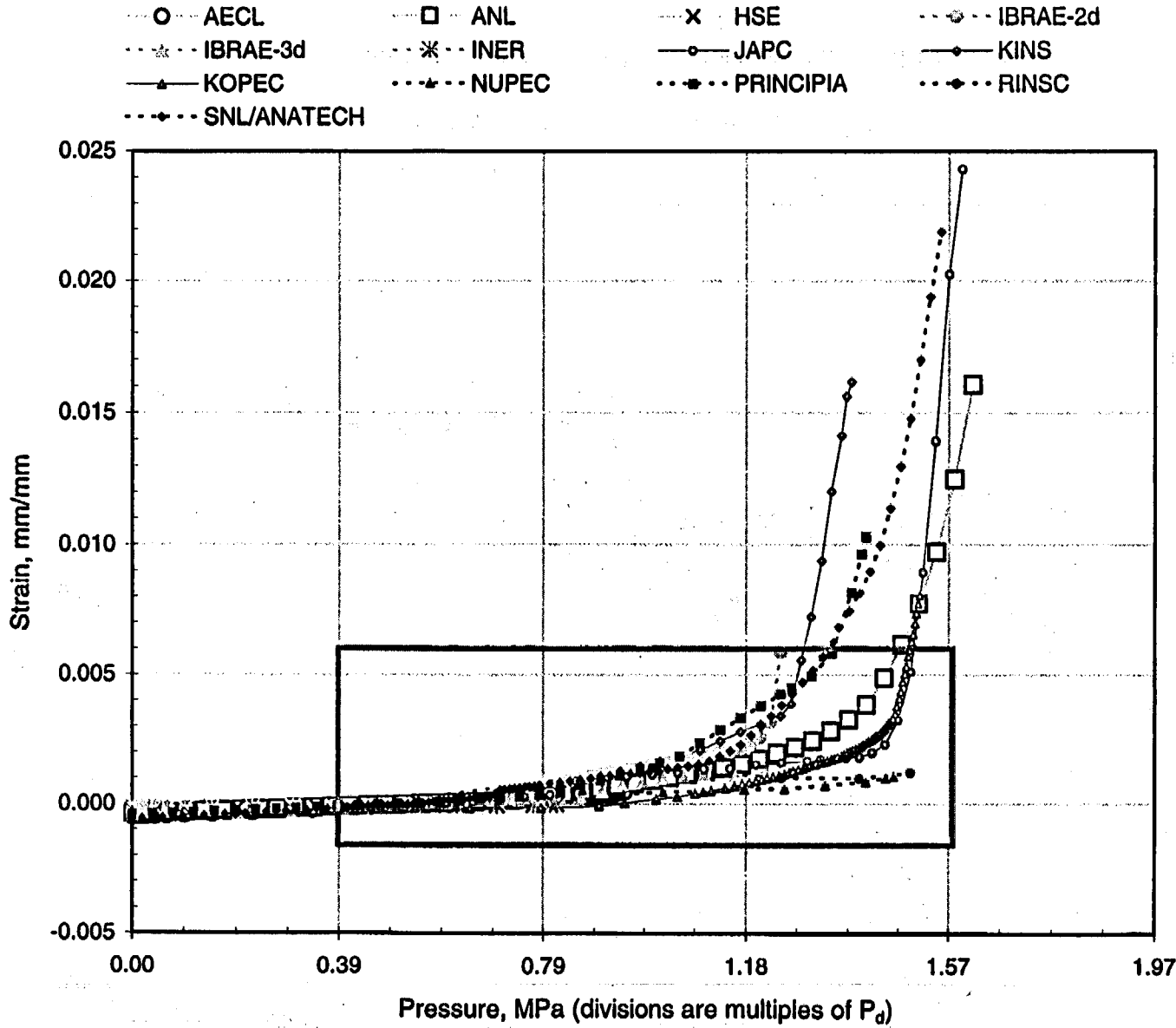


Figure A-35a. PCCV Standard Output Location (SOL) #35.

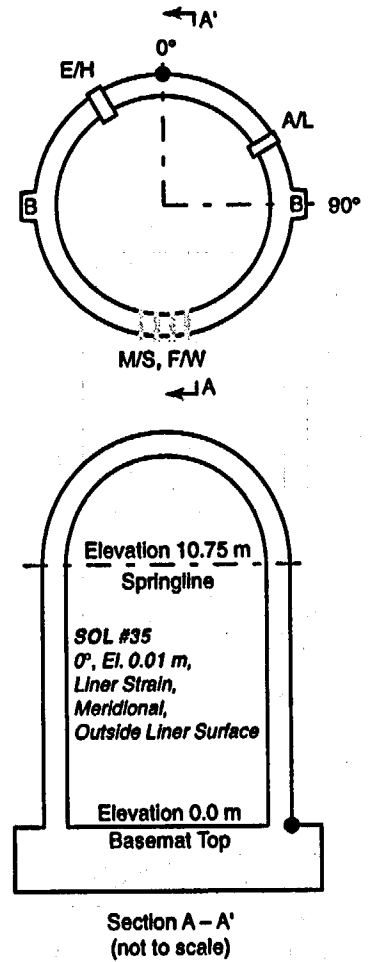
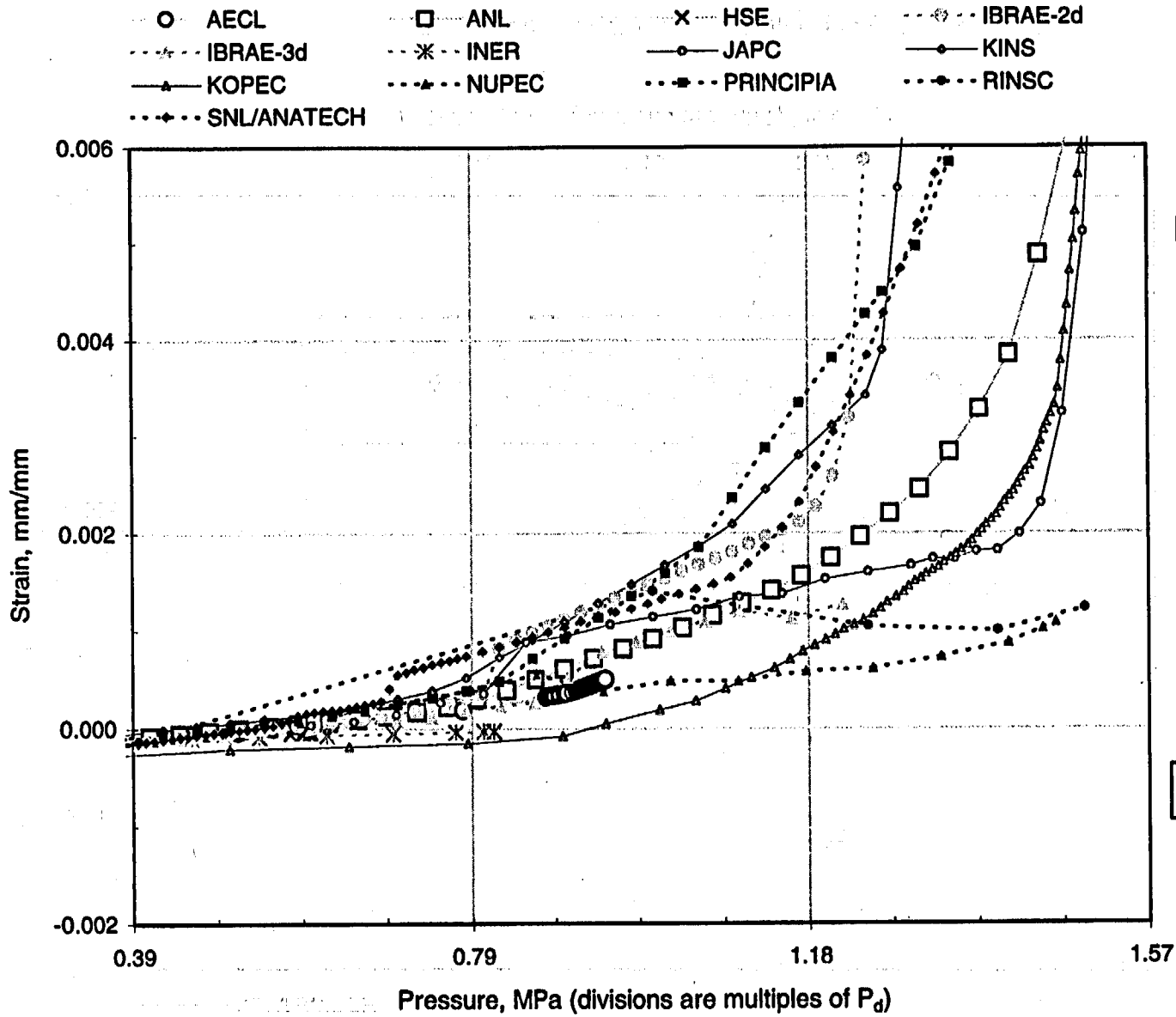
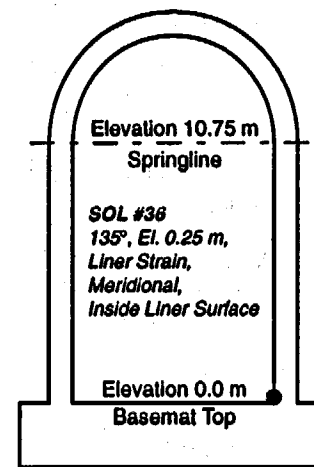
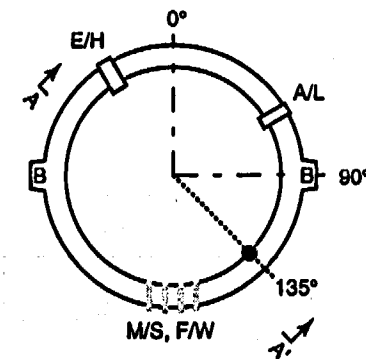
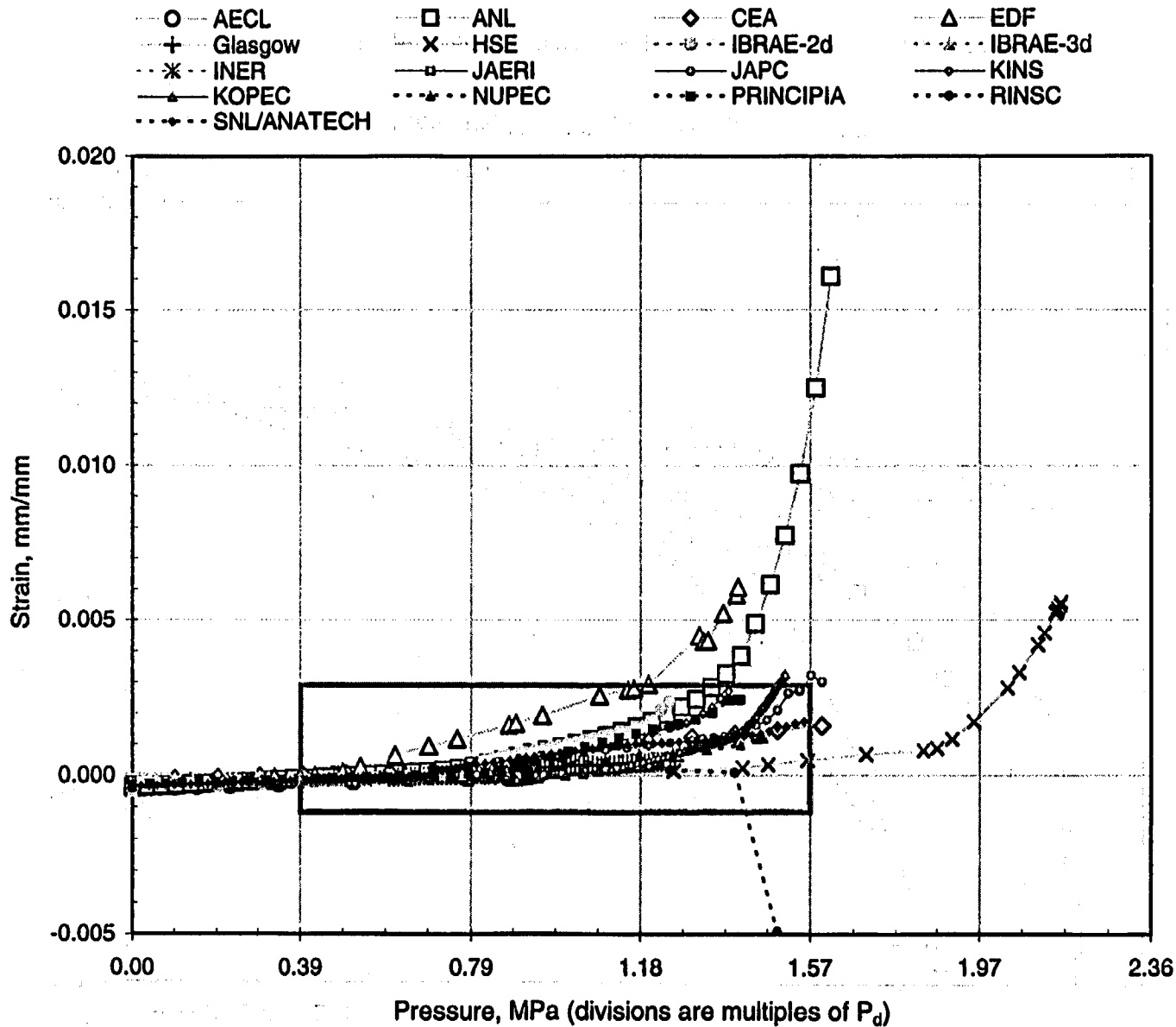


Figure A-35b. PCCV Standard Output Location (SOL) #35, enlarged.

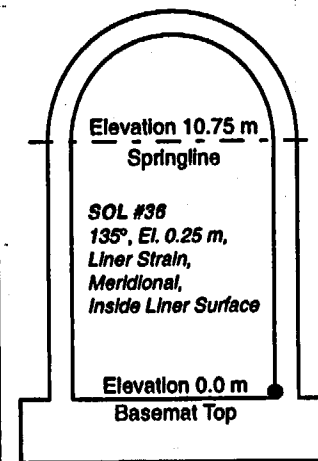
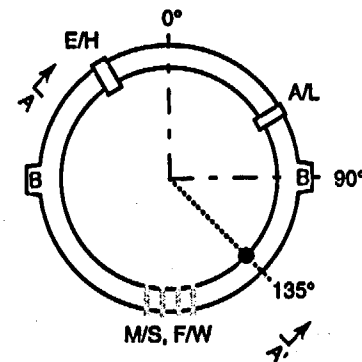
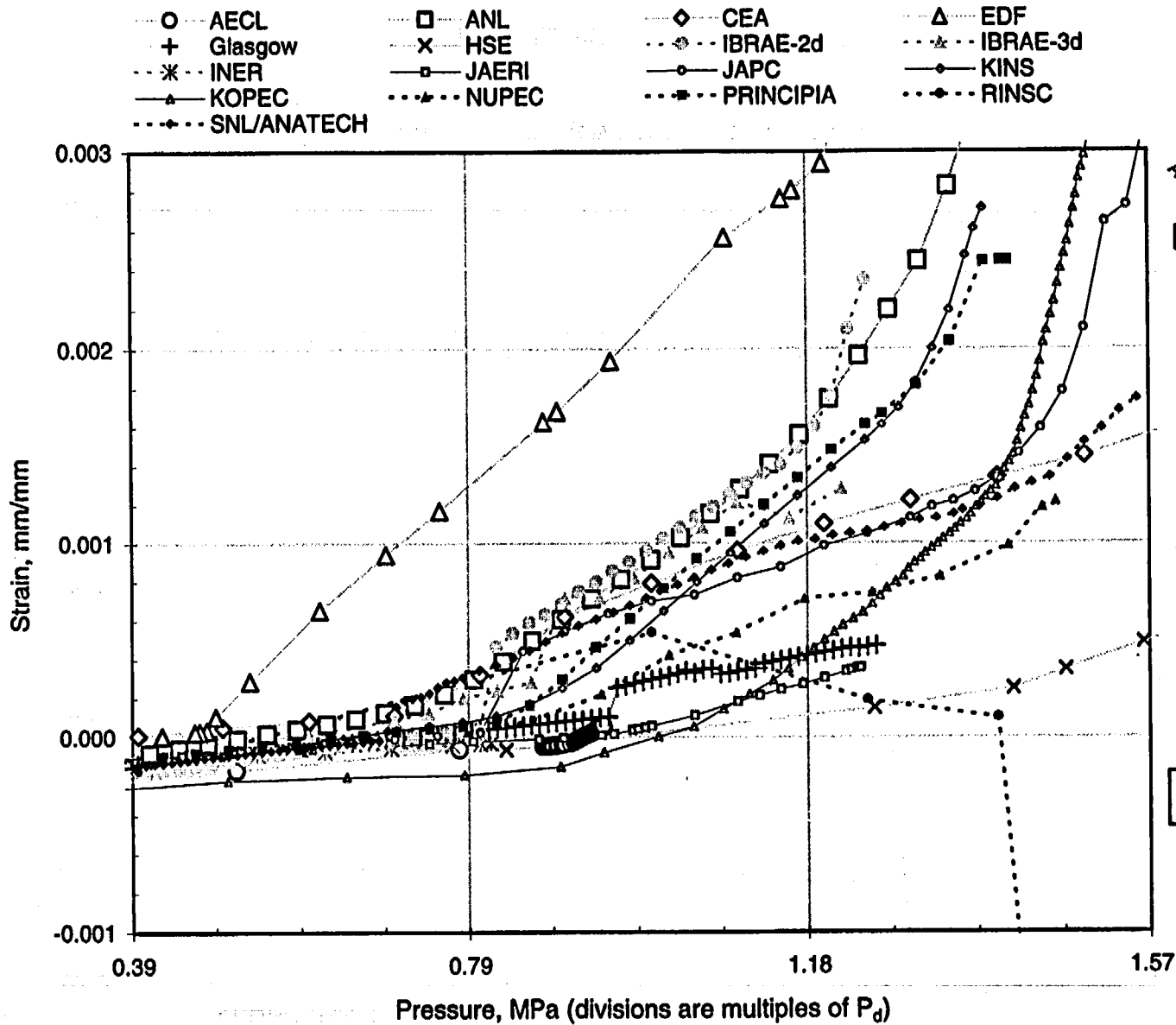
99-V



Section A - A'
(not to scale)

Figure A-36a. PCCV Standard Output Location (SOL) #36.

A-67



Section A - A'
(not to scale)

Figure A-36b. PCCV Standard Output Location (SOL) #36, enlarged.

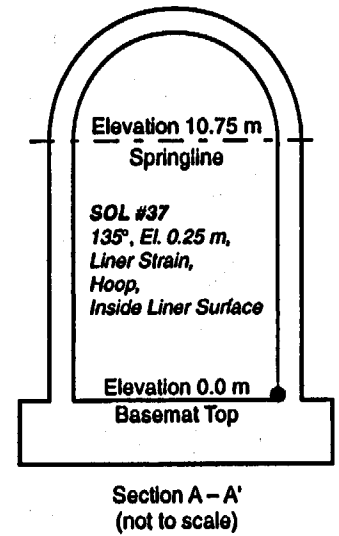
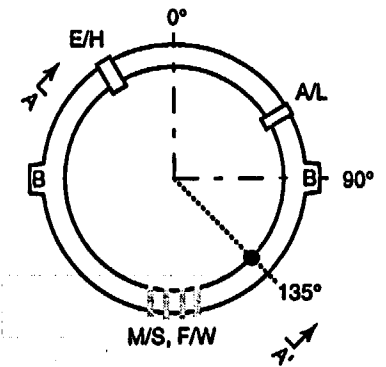
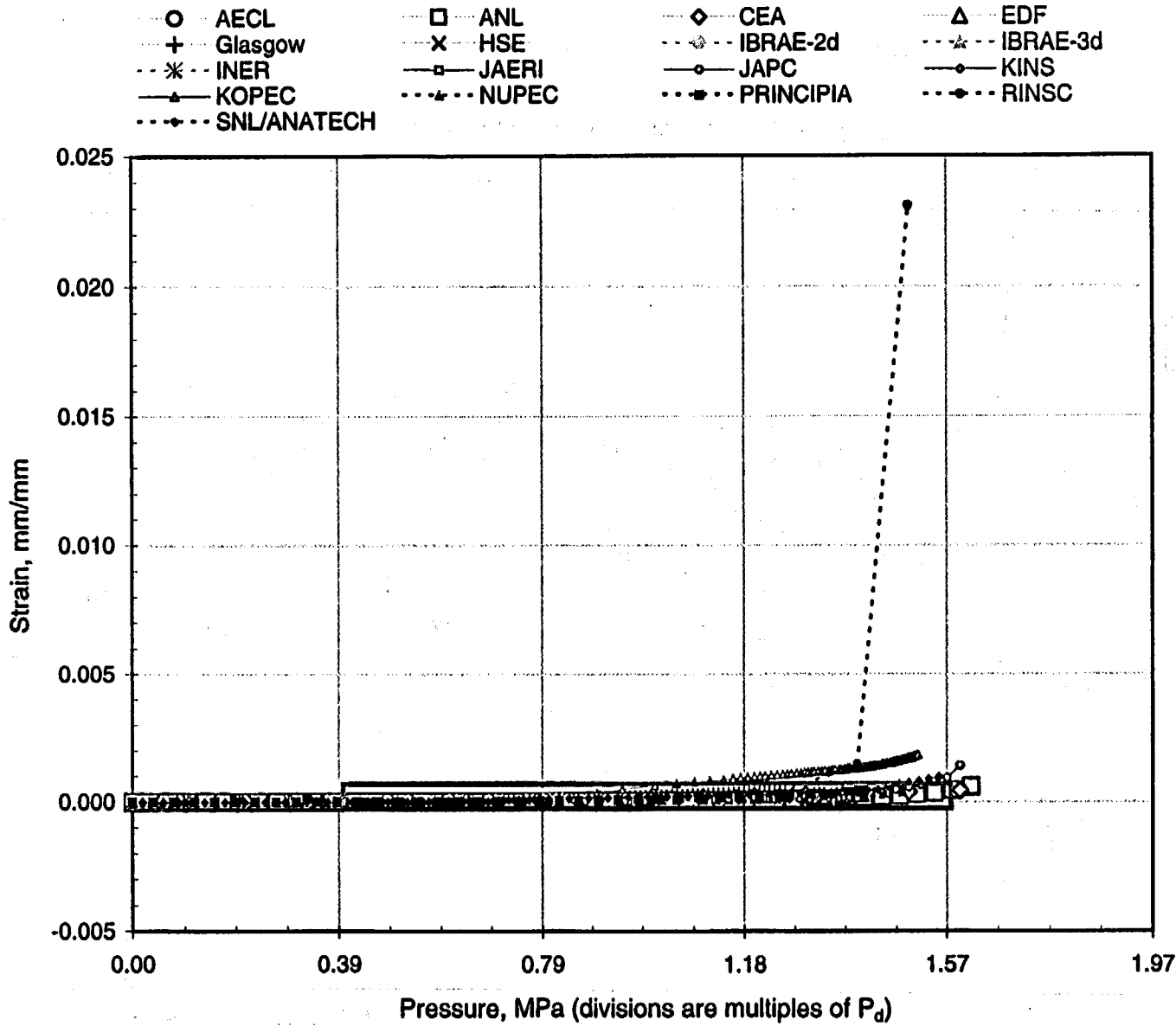
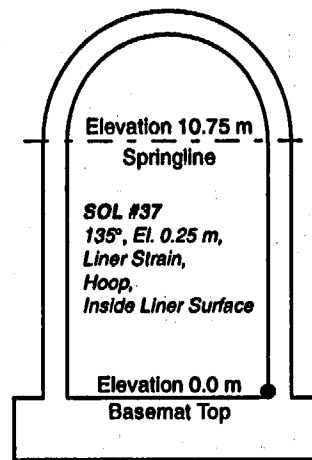
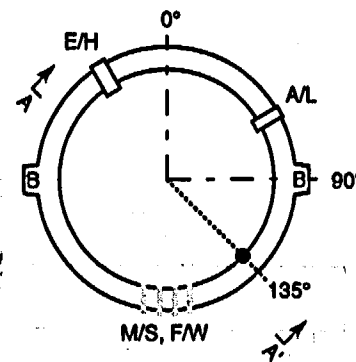
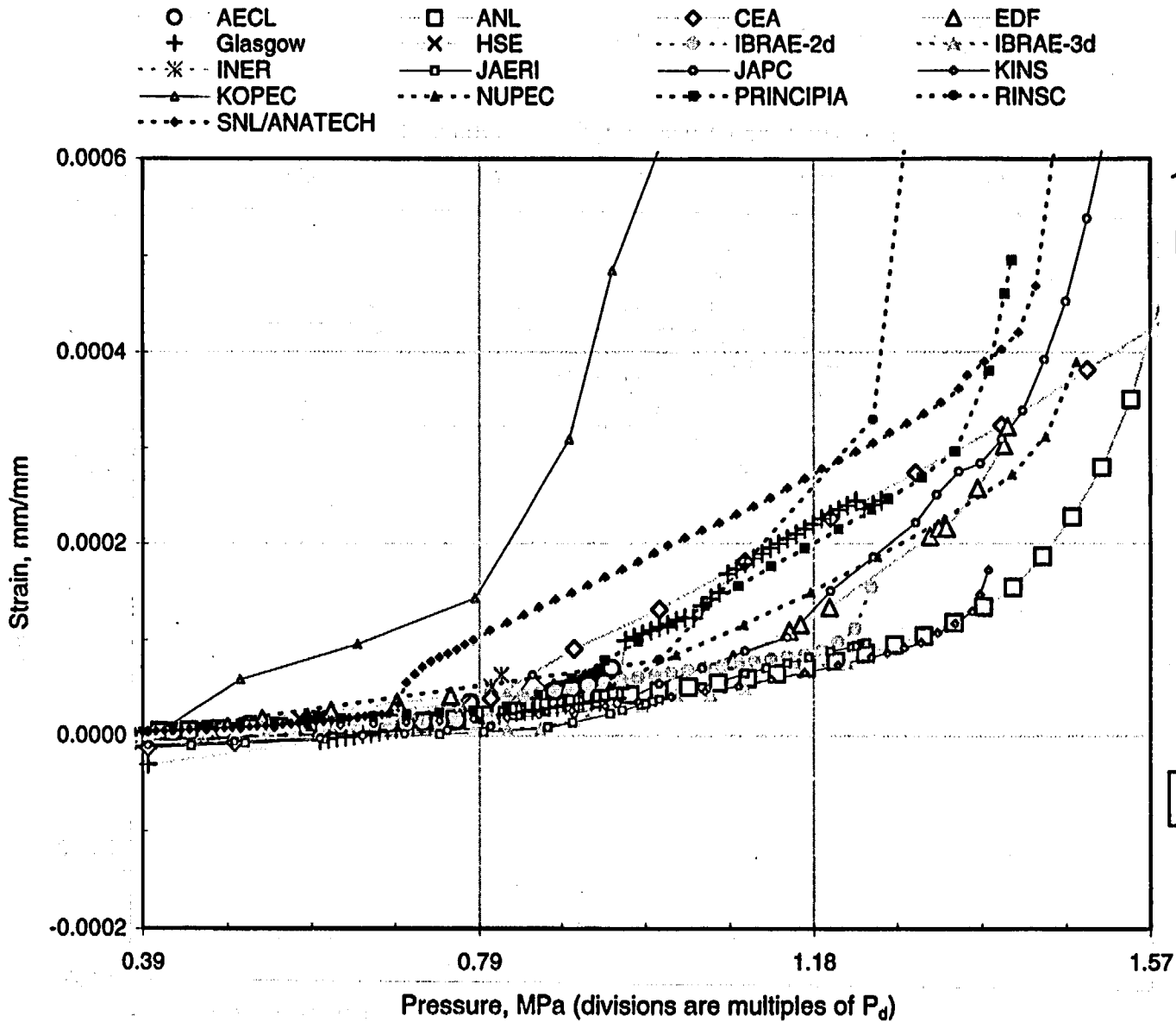


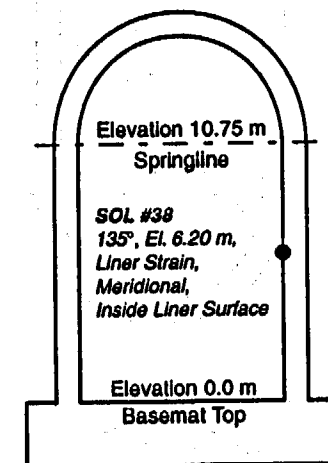
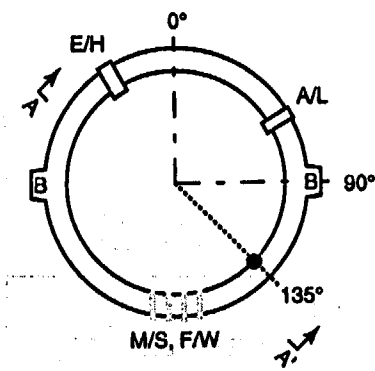
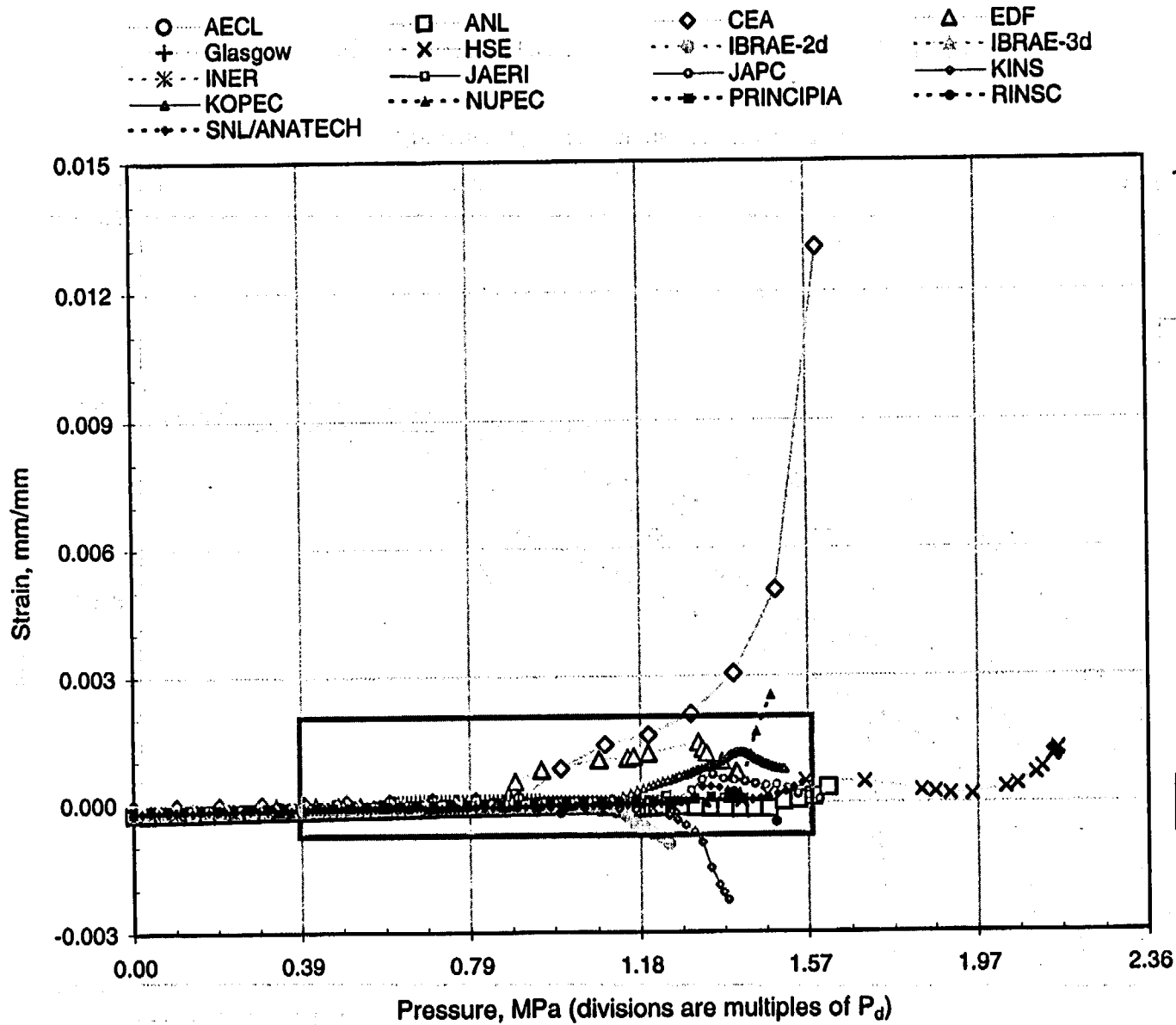
Figure A-37a. PCCV Standard Output Location (SOL) #37.



Section A - A'
(not to scale)

Figure A-37b. PCCV Standard Output Location (SOL) #37, enlarged.

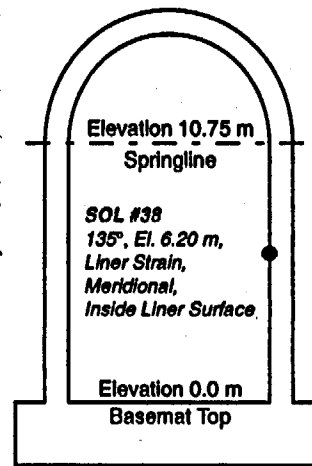
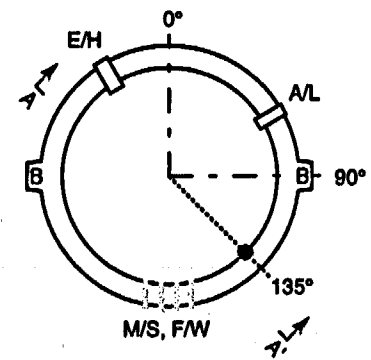
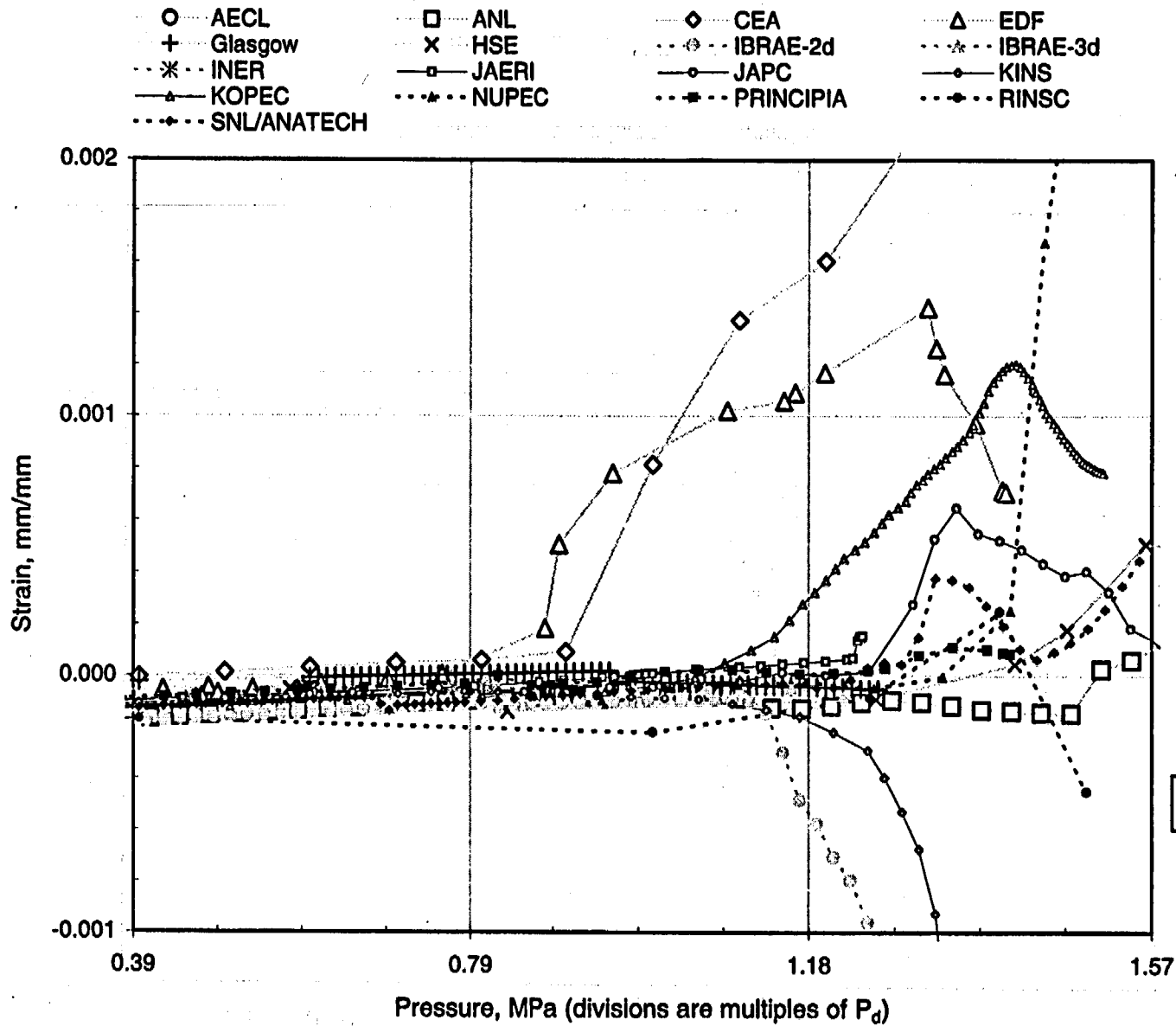
A-70



Section A - A'
(not to scale)

Figure A-38a. PCCV Standard Output Location (SOL) #38.

A-71



Section A - A'
(not to scale)

Figure A-38b. PCCV Standard Output Location (SOL) #38, enlarged.

A-72

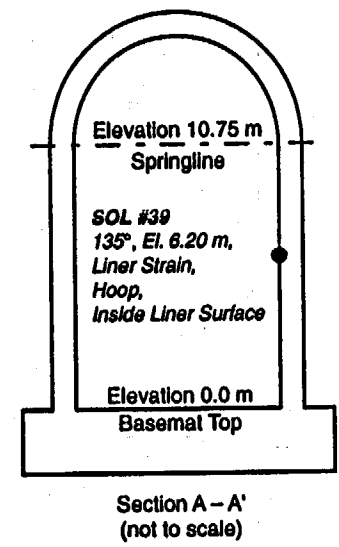
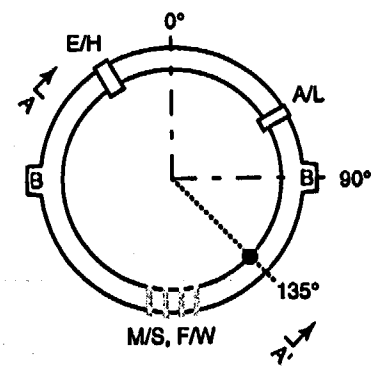
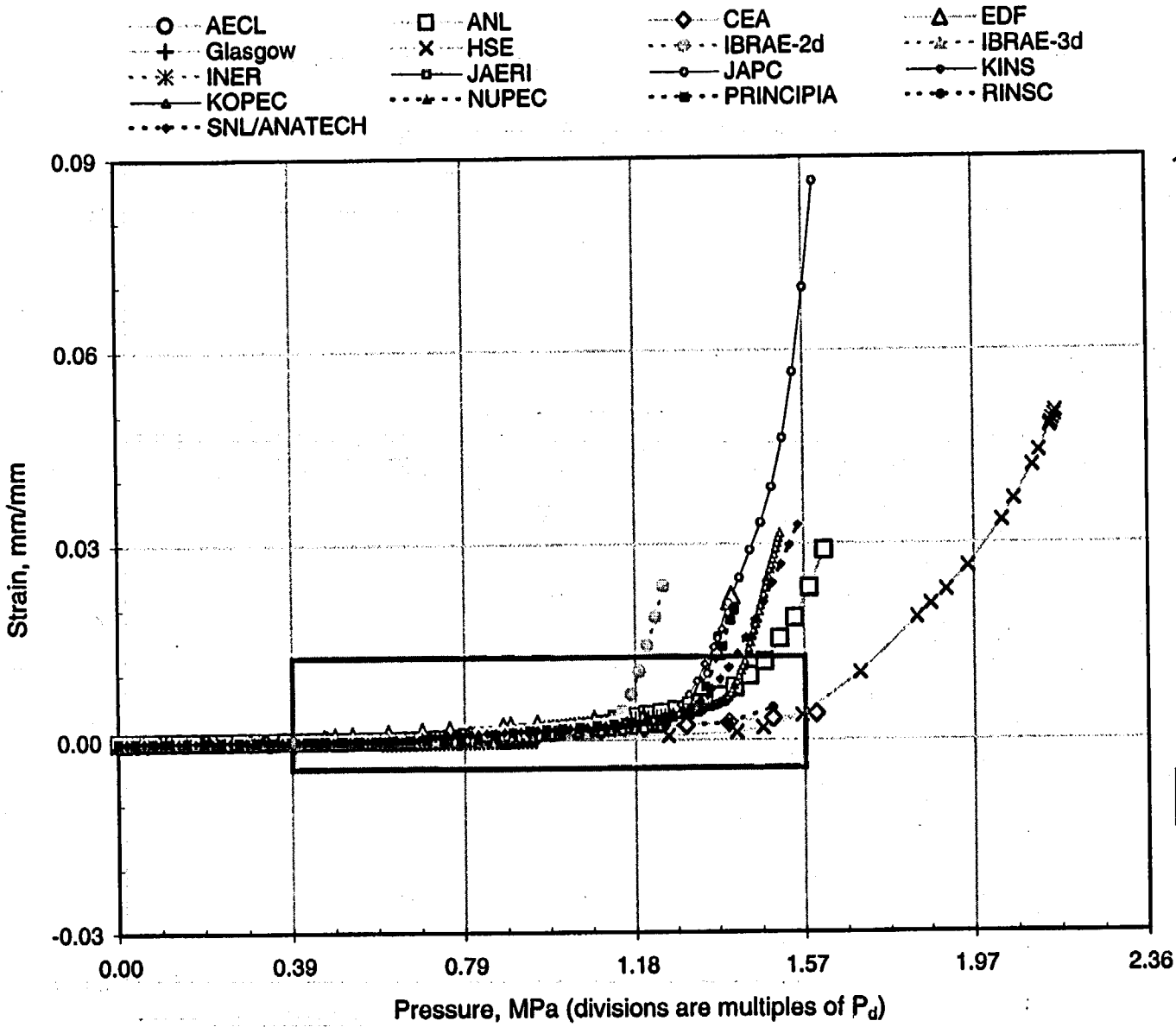
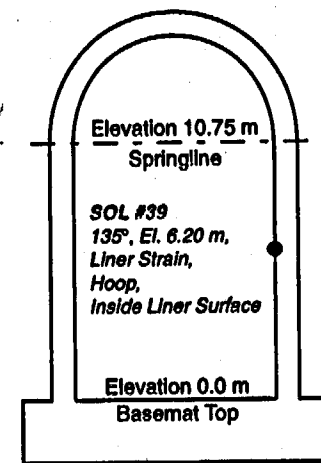
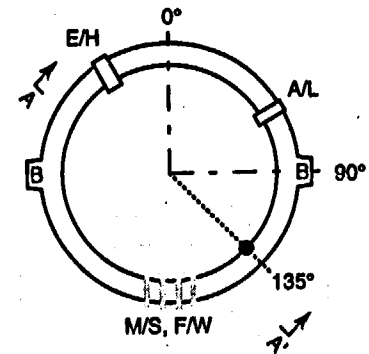
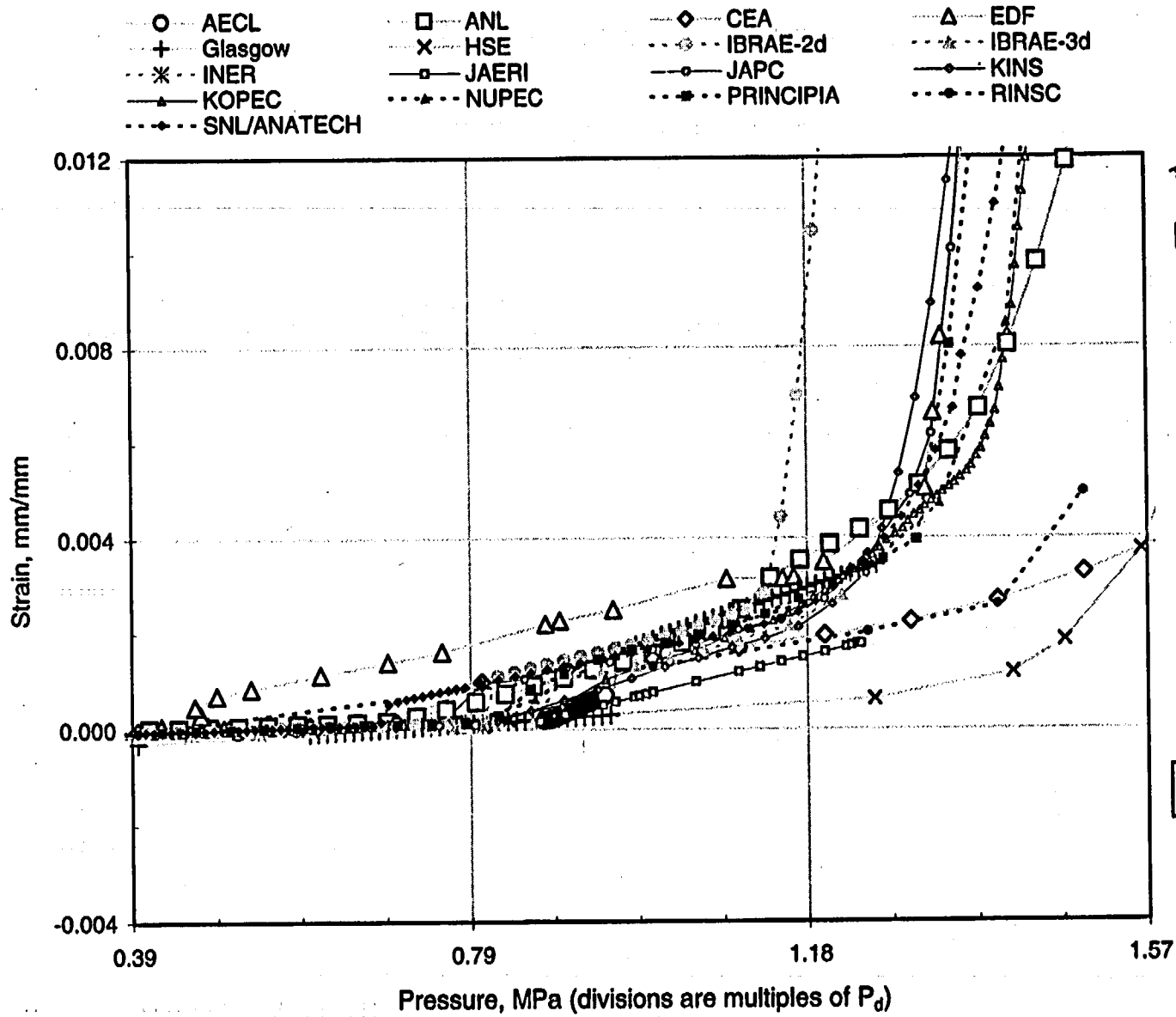


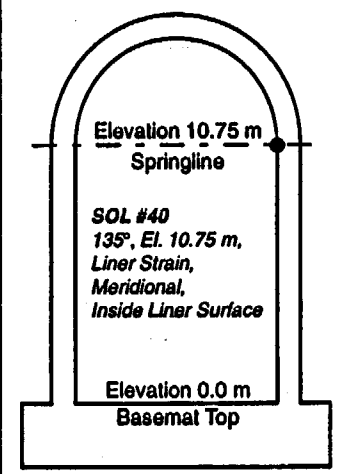
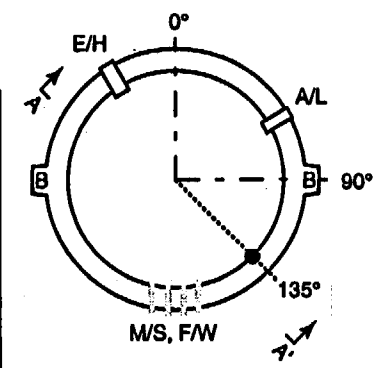
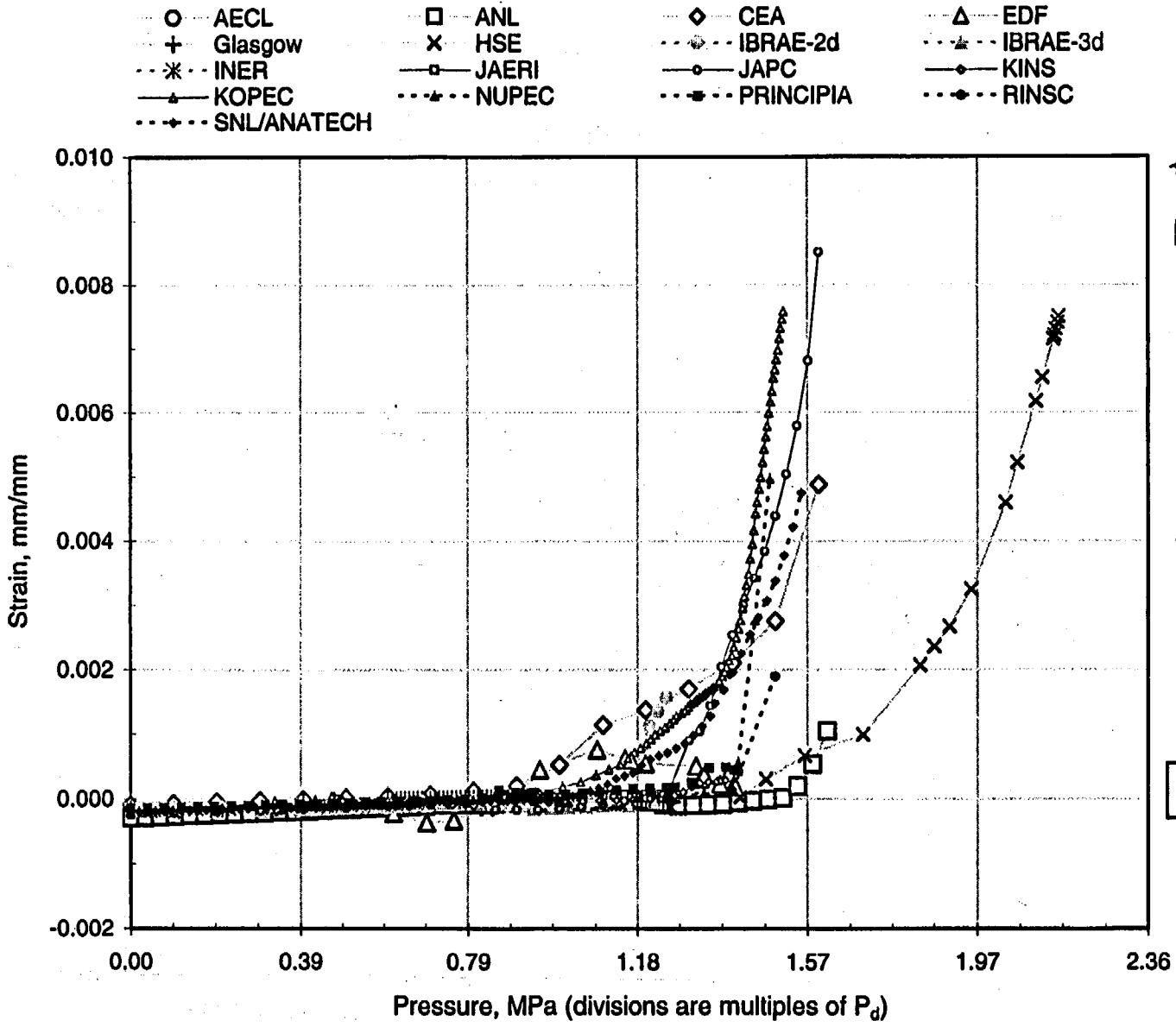
Figure A-39a. PCCV Standard Output Location (SOL) #39.



Section A - A'
(not to scale)

Figure A-39b. PCCV Standard Output Location (SOL) #39, enlarged.

A-74



Section A - A'
(not to scale)

Figure A-40. PCCV Standard Output Location (SOL) #40.

This page intentionally left blank to facilitate plot comparison.

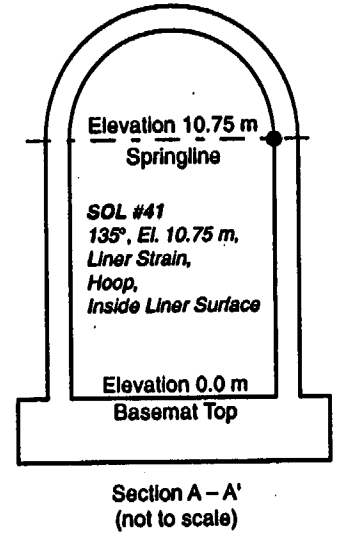
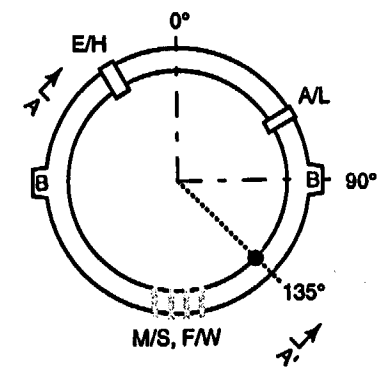
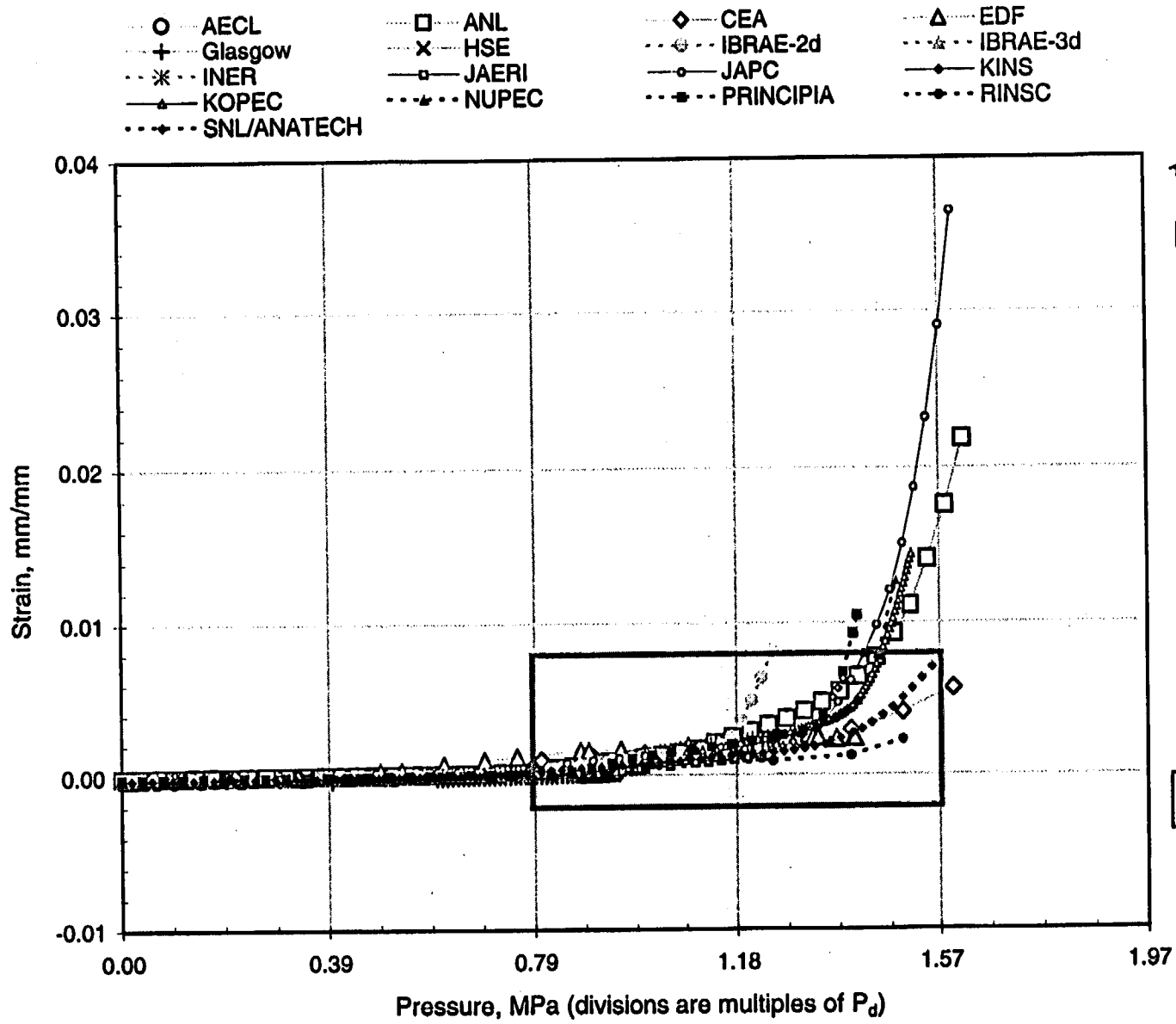
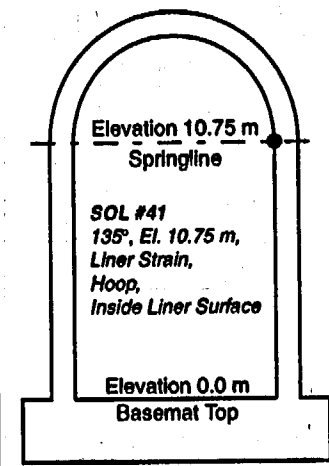
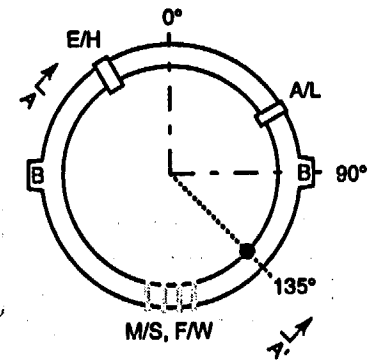
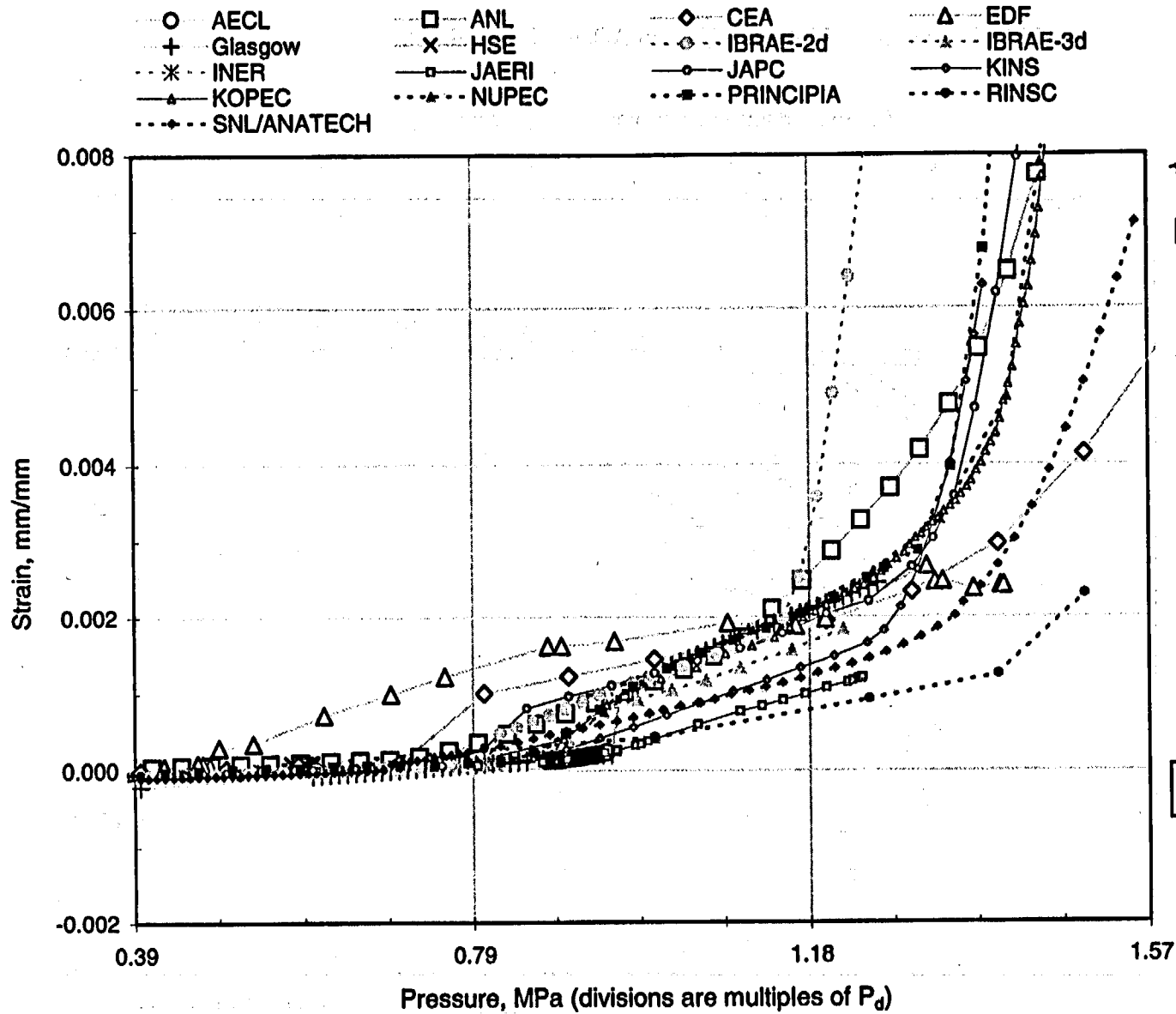


Figure A-41a. PCCV Standard Output Location (SOL) #41.

A-77



Section A - A'
(not to scale)

Figure A-41b. PCCV Standard Output Location (SOL) #41, enlarged.

A-78

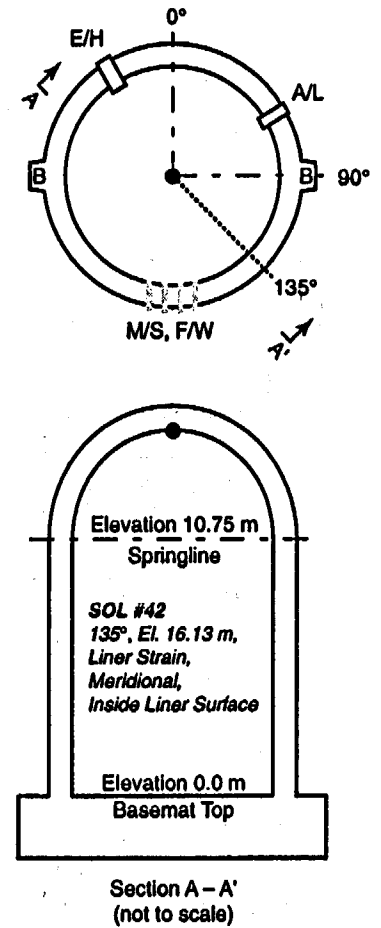
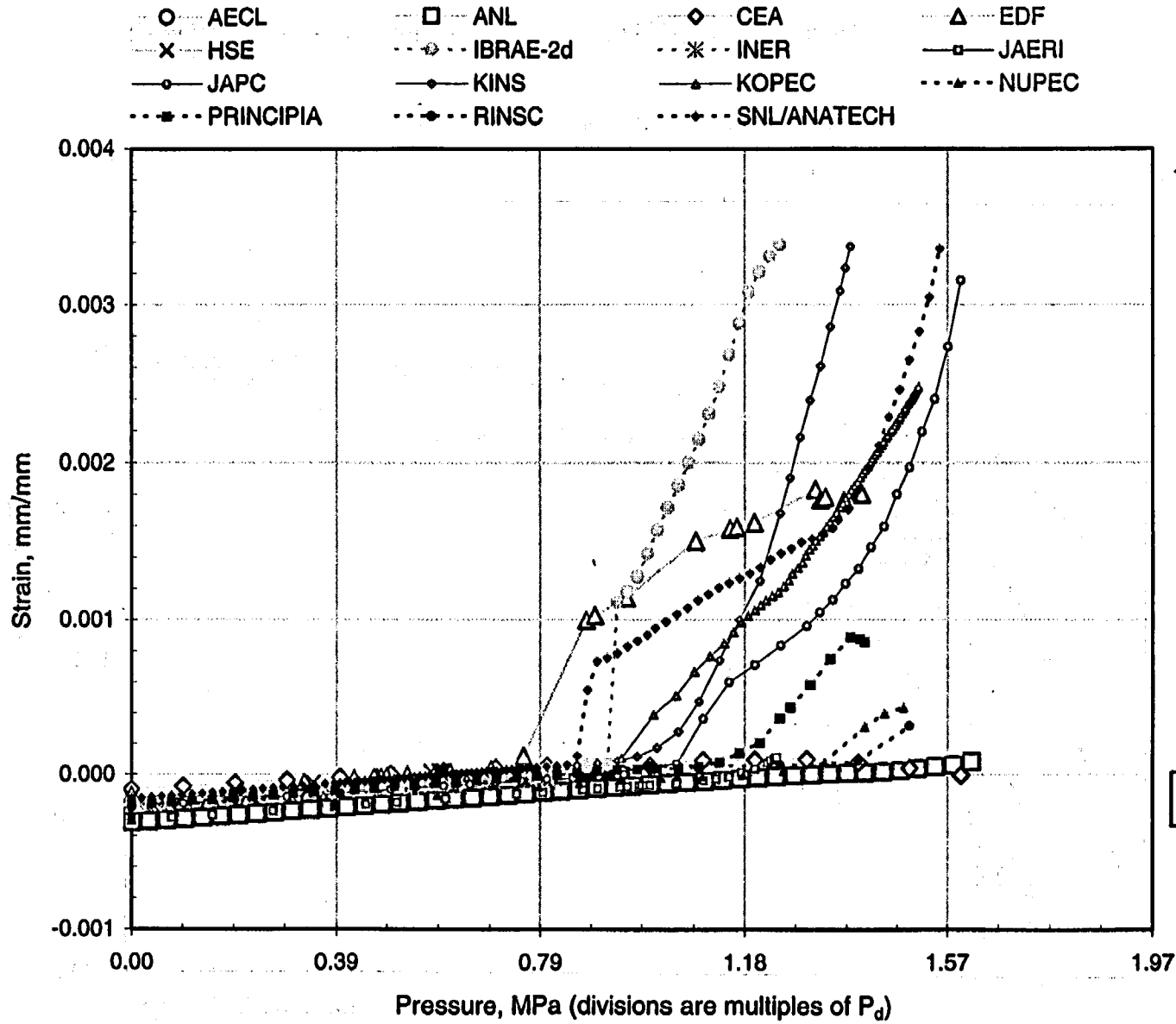


Figure A-42. PCCV Standard Output Location (SOL) #42.

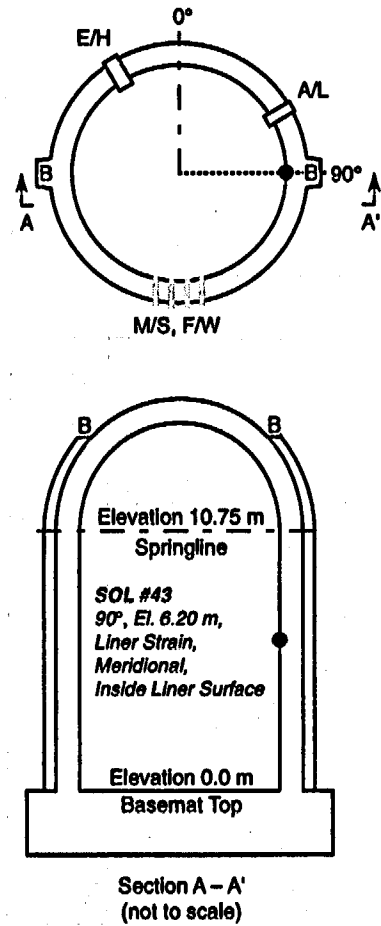
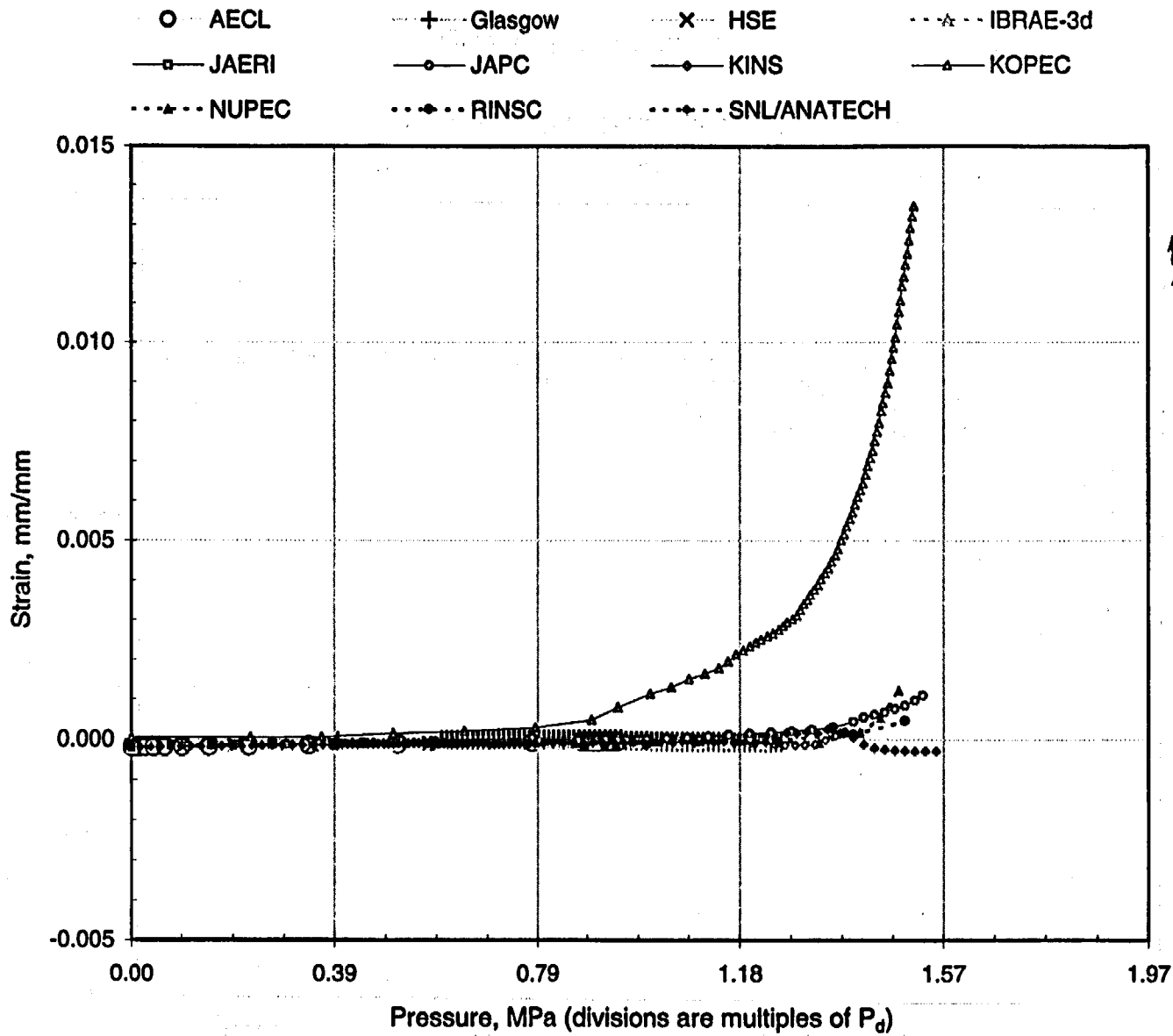


Figure A-43. PCCV Standard Output Location (SOL) #43.

A-80

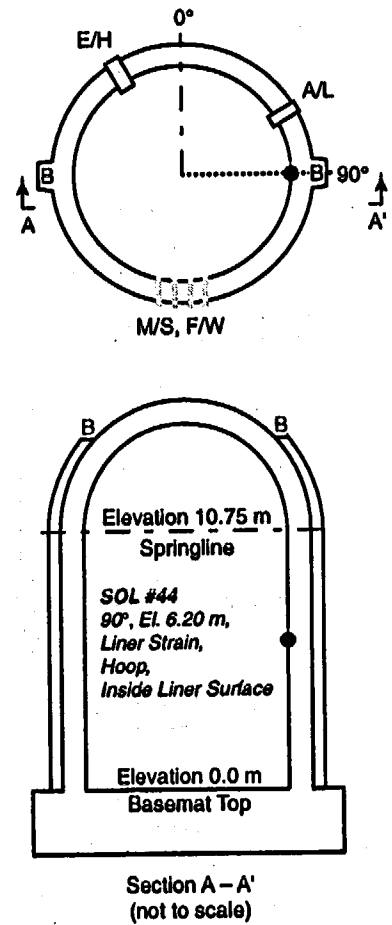
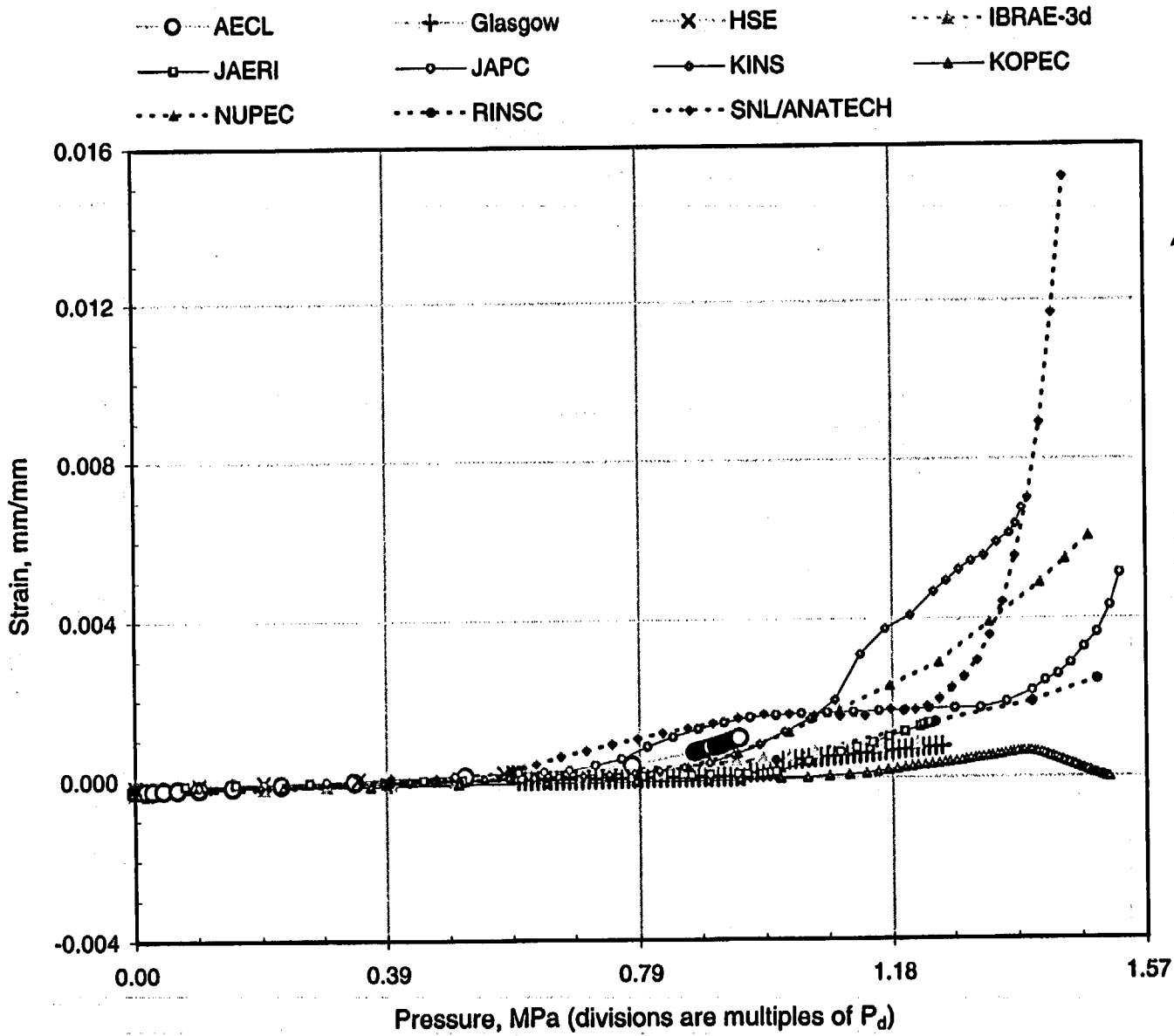
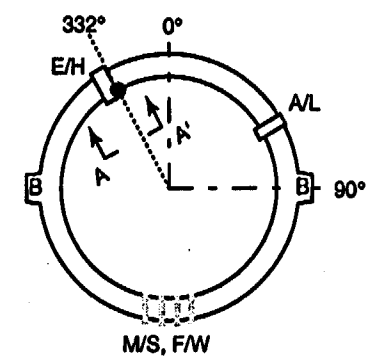
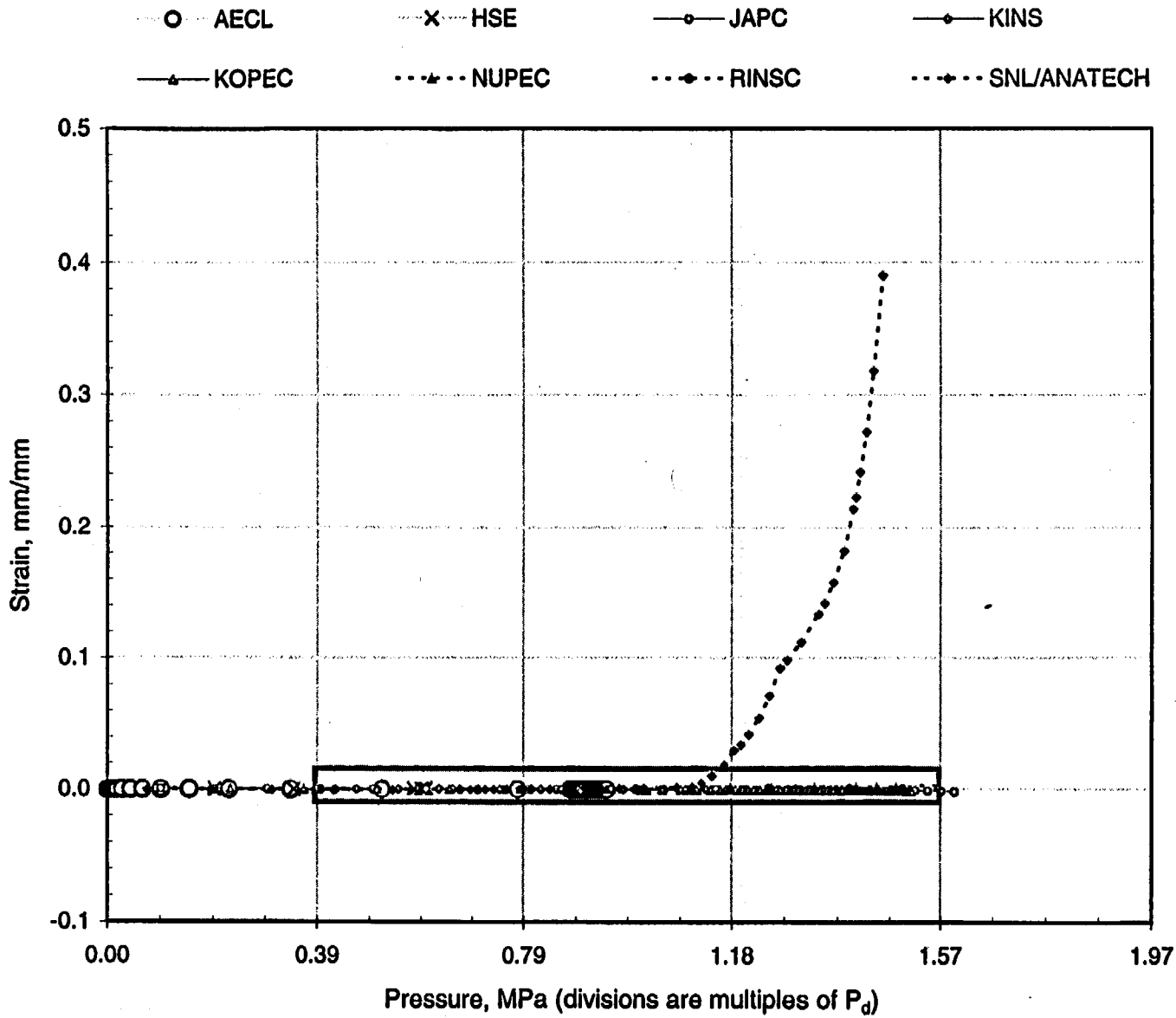


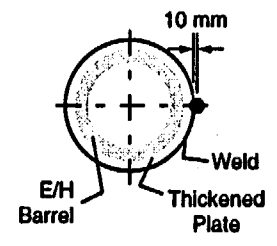
Figure A-44. PCCV Standard Output Location (SOL) #44.

This page intentionally left blank to facilitate plot comparison.

A-82



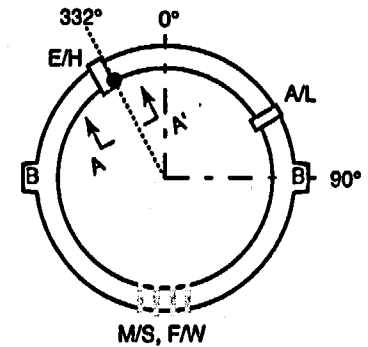
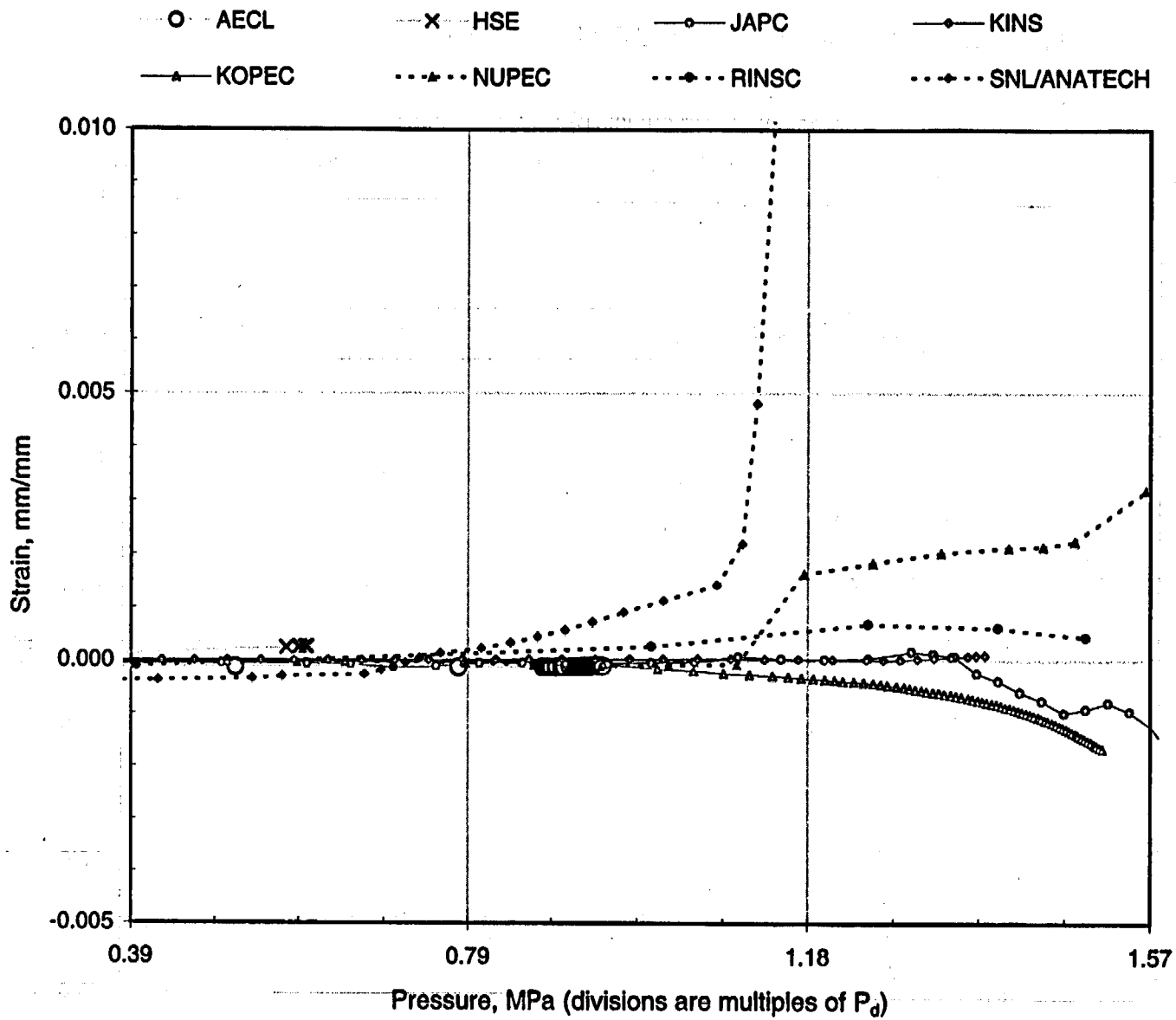
SOL #45 - 332°, El. 4.675 m,
Liner Strain, Hoop,
Inside Liner Surface



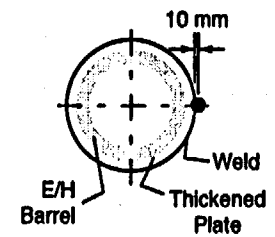
Section A - A'
(not to scale)

Figure A-45a. PCCV Standard Output Location (SOL) #45.

A-83



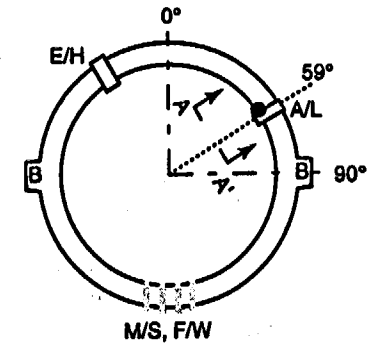
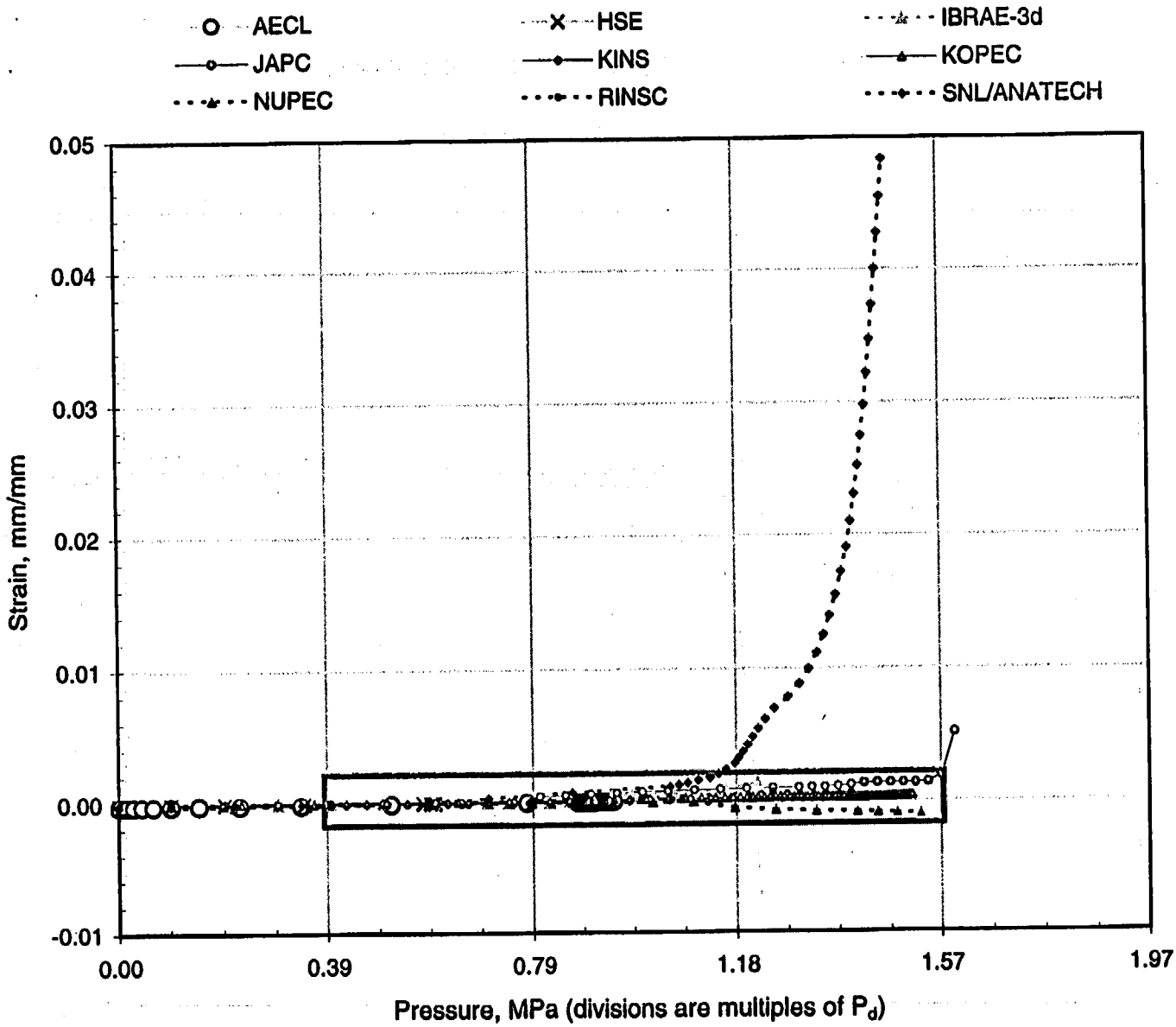
SOL #45 - 332°, El. 4.675 m,
Liner Strain, Hoop,
Inside Liner Surface



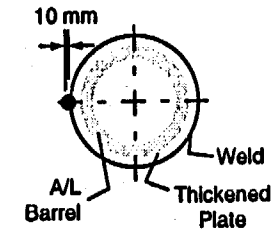
Section A - A'
(not to scale)

Figure A-45b. PCCV Standard Output Location (SOL) #45, enlarged.

A-84



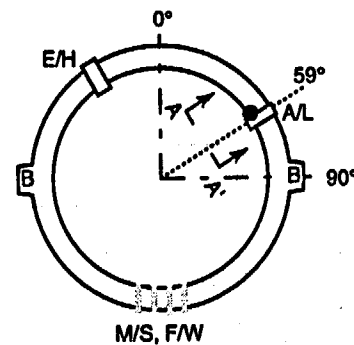
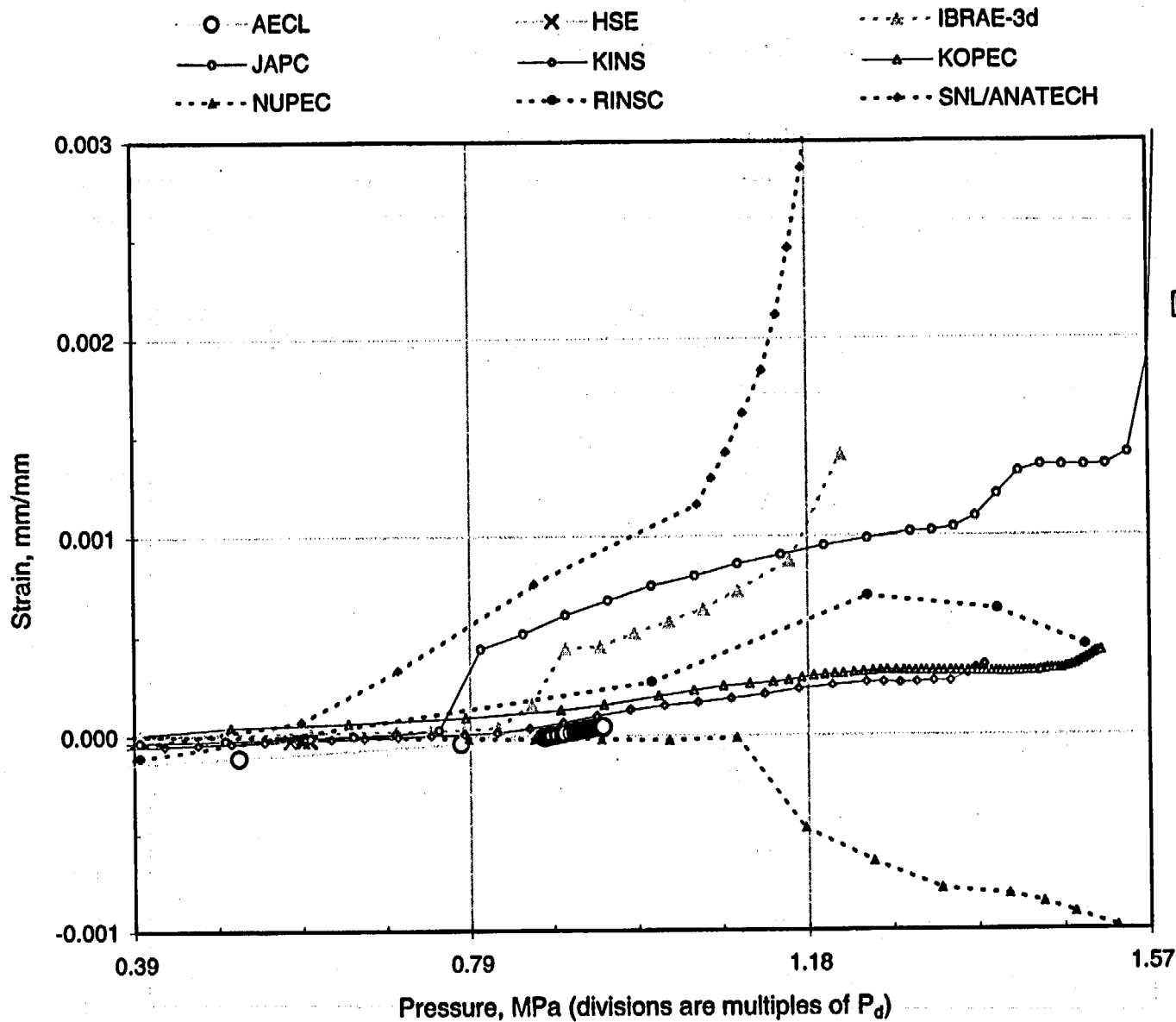
SOL #46 - 59°, El. 4.525 m,
Liner Strain, Hoop,
Inside Liner Surface



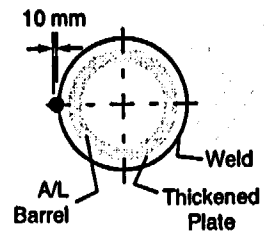
Section A - A'
(not to scale)

Figure A-46a. PCCV Standard Output Location (SOL) #46.

A-85



SOL #46 - 59°, El. 4.525 m,
Liner Strain, Hoop,
Inside Liner Surface



Section A - A'
(not to scale)

Figure A-46b. PCCV Standard Output Location (SOL) #46, enlarged.

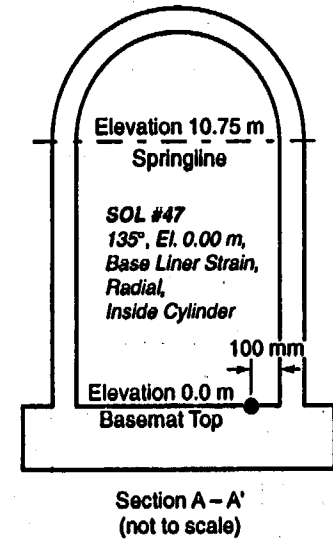
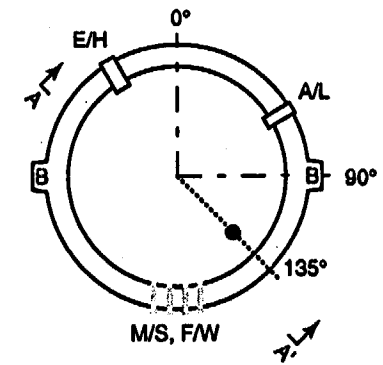
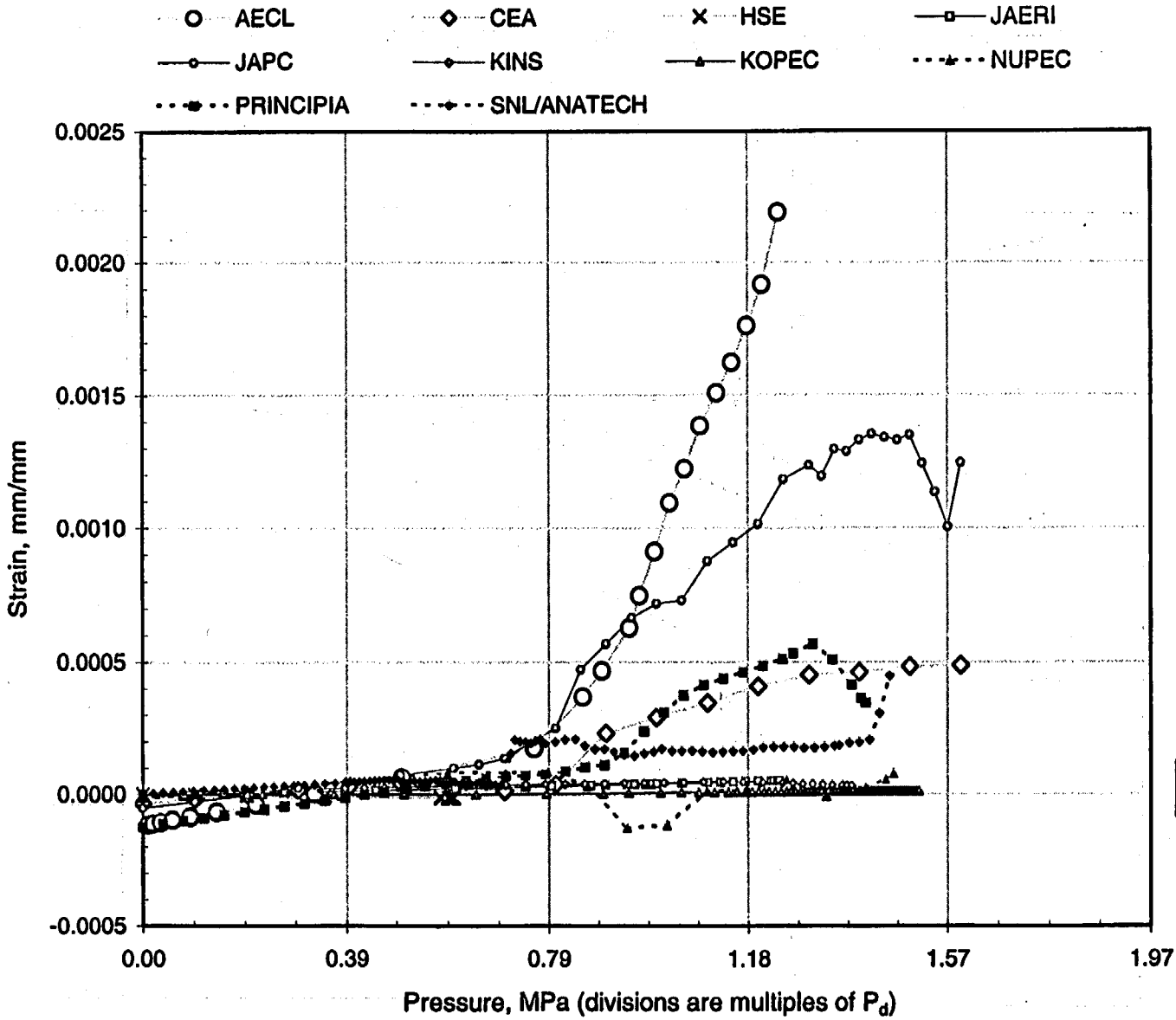
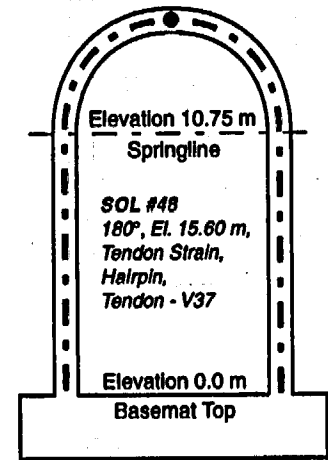
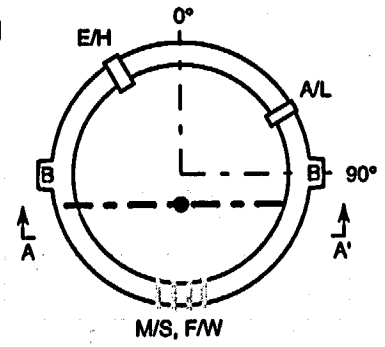
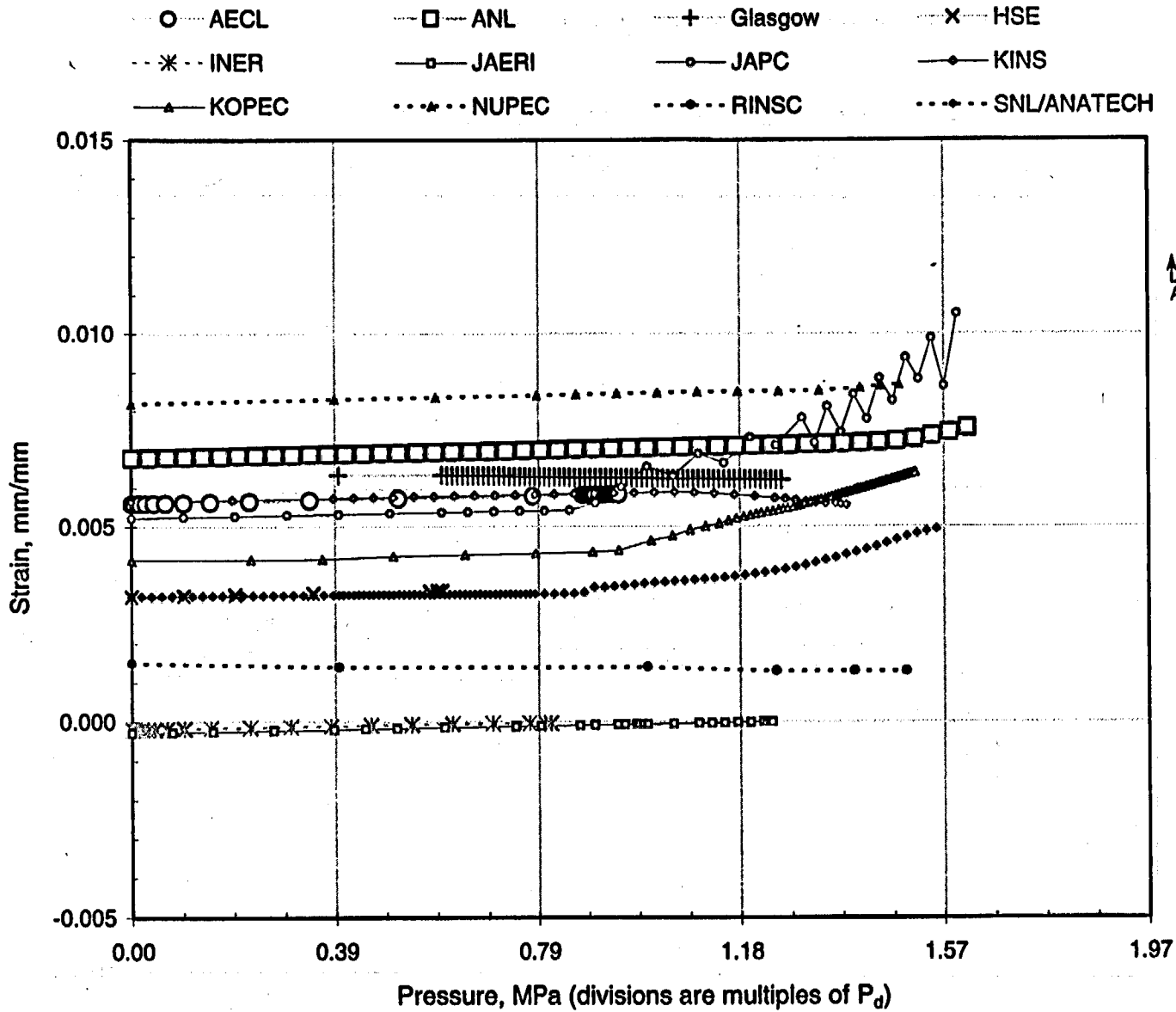


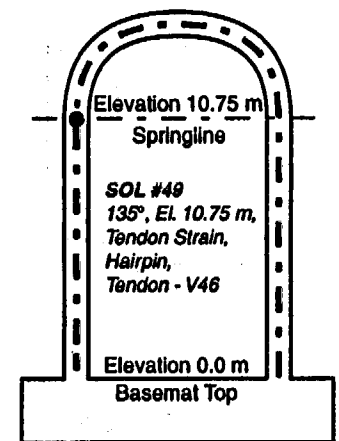
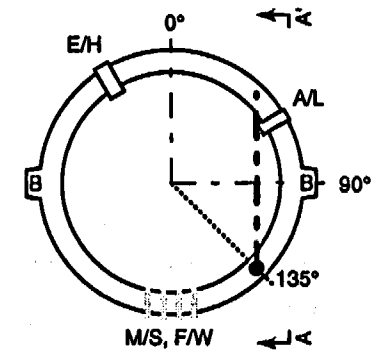
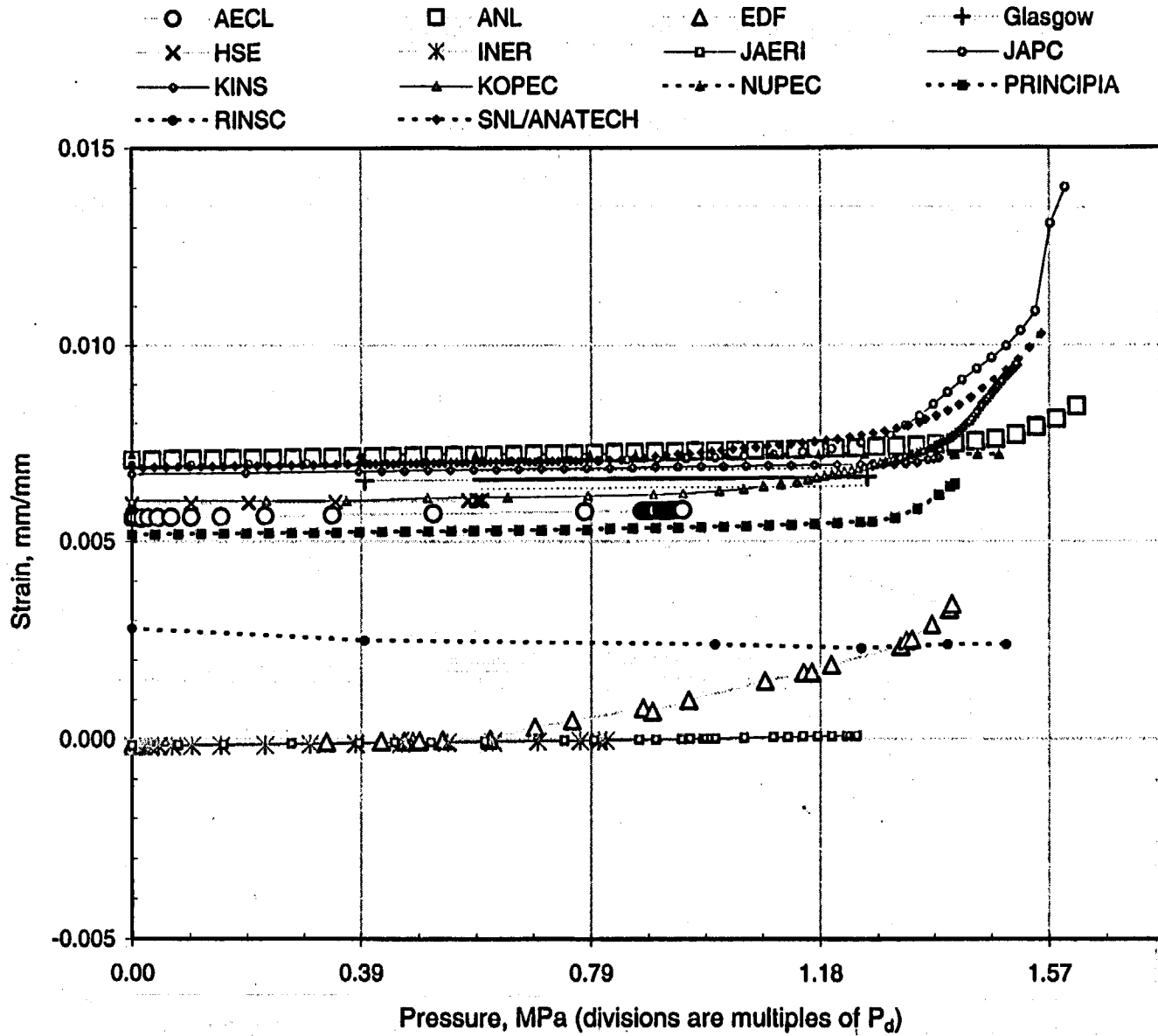
Figure A-47. PCCV Standard Output Location (SOL) #47.



Section A - A'
(not to scale)

Figure A-48. PCCV Standard Output Location (SOL) #48.

A-88



Section A - A'
(not to scale)

Figure A-49. PCCV Standard Output Location (SOL) #49.

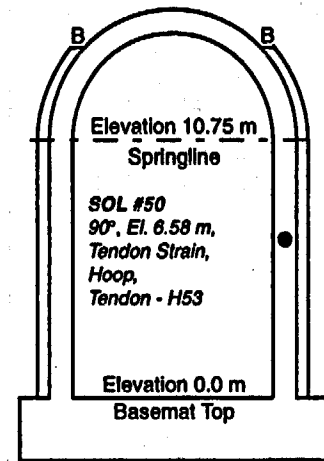
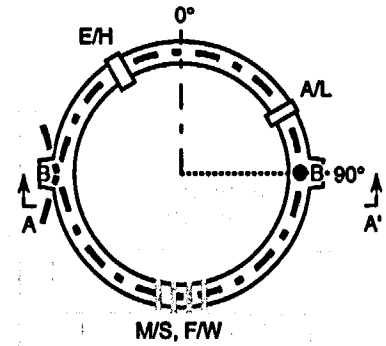
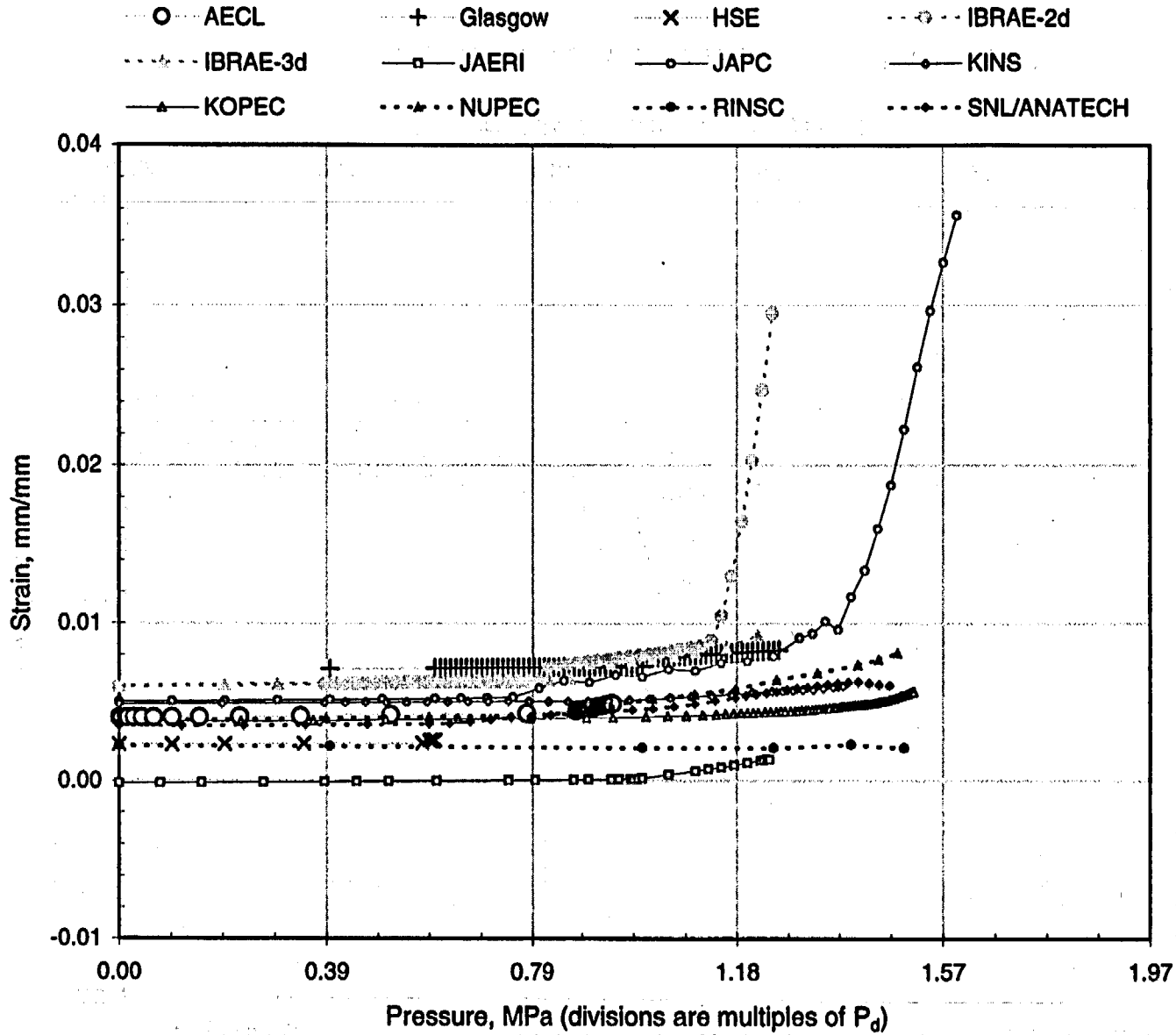
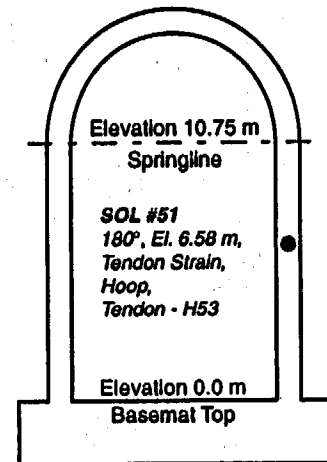
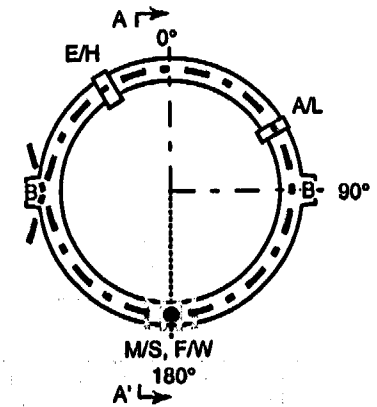
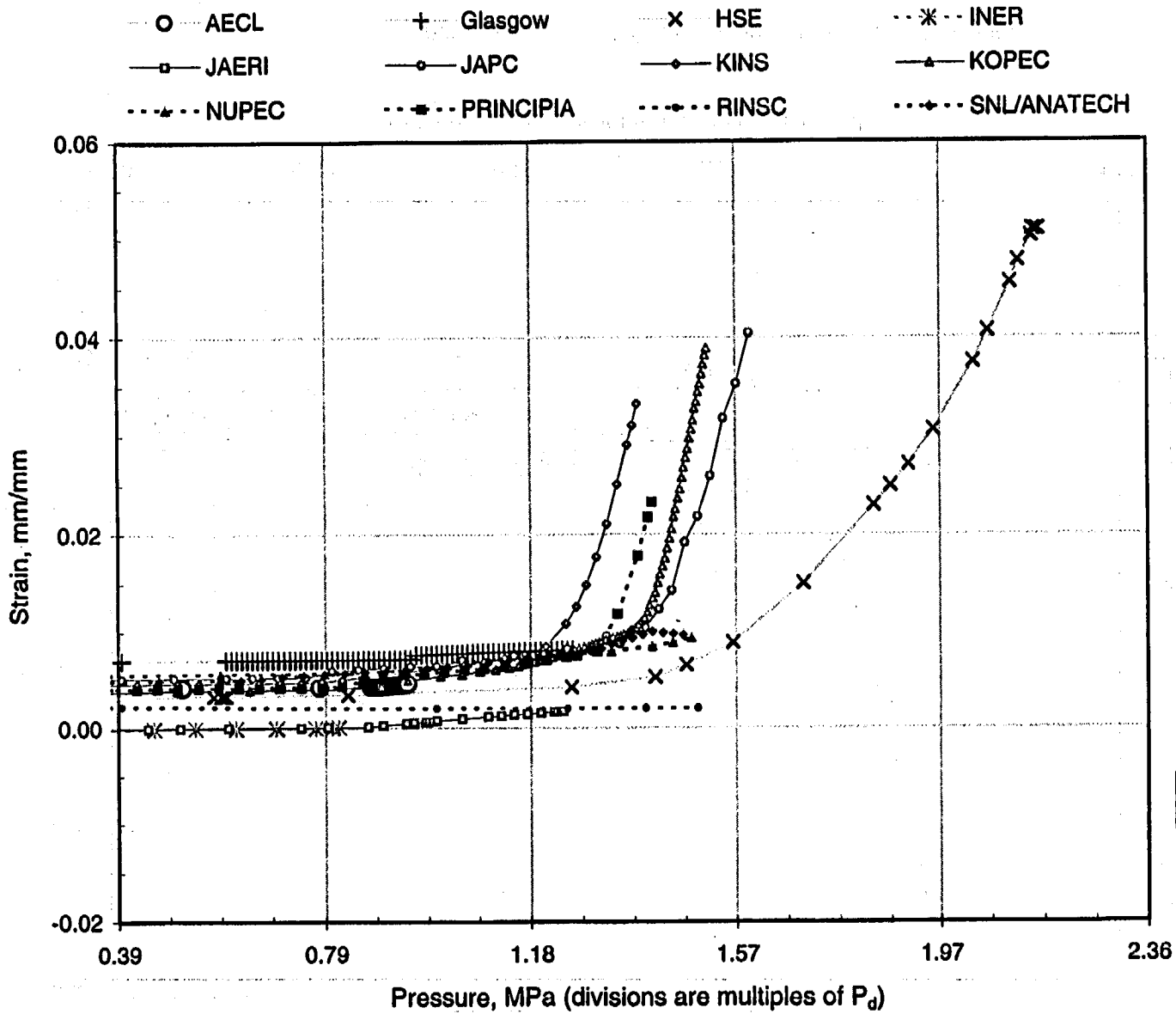


Figure A-50. PCCV Standard Output Location (SOL) #50.

A-90



Section A - A'
(not to scale)

Figure A-51. PCCV Standard Output Location (SOL) #51.

A-91

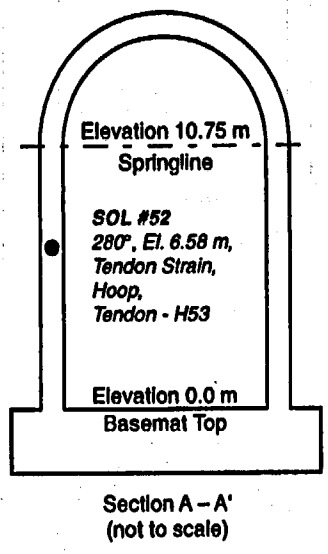
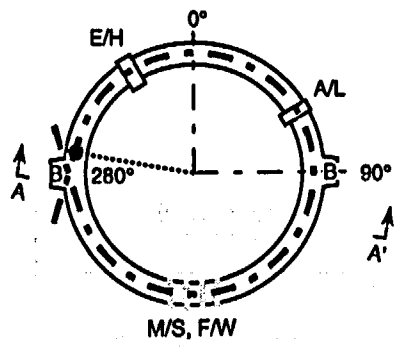
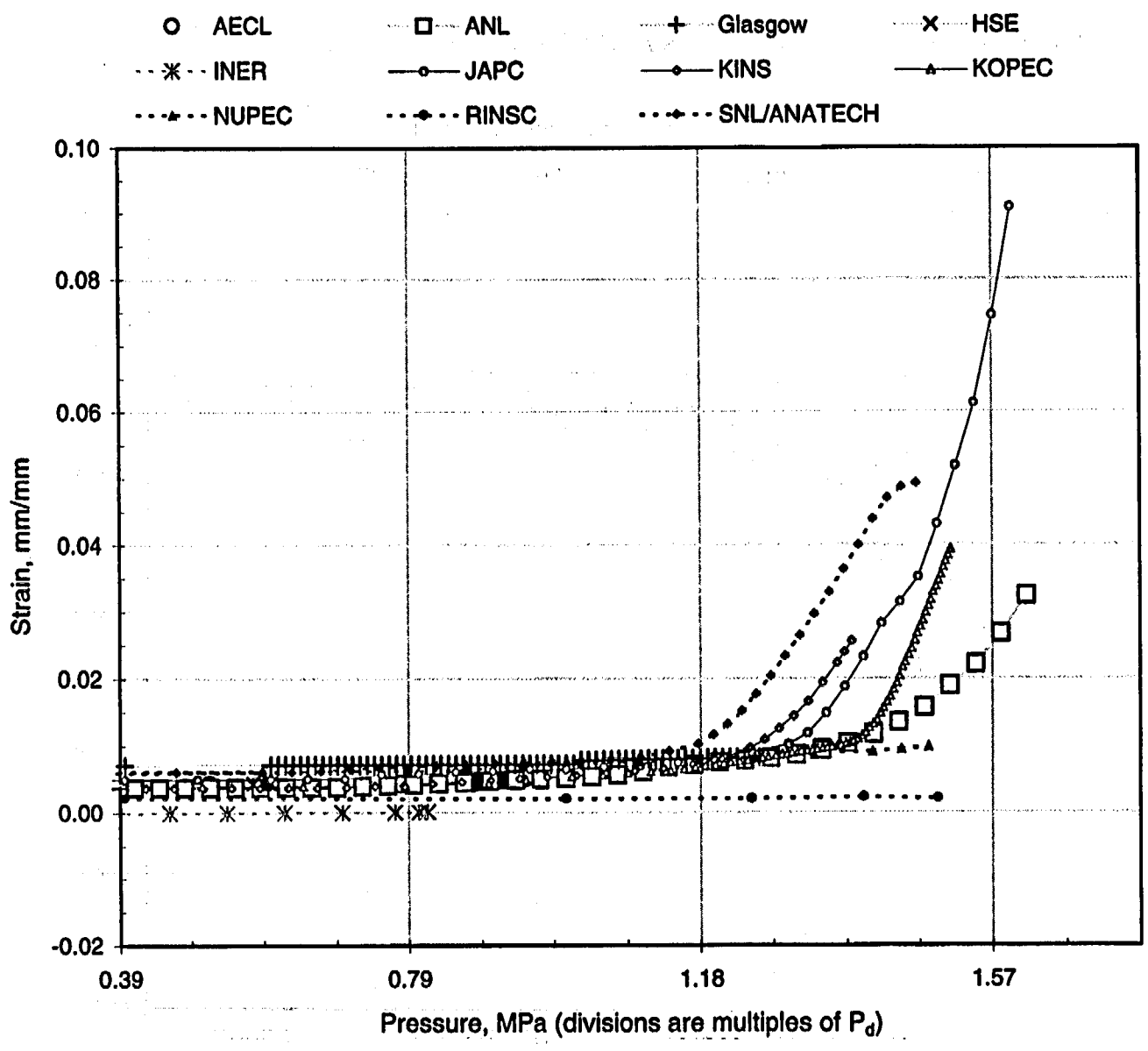


Figure A-52. PCCV Standard Output Location (SOL) #52.

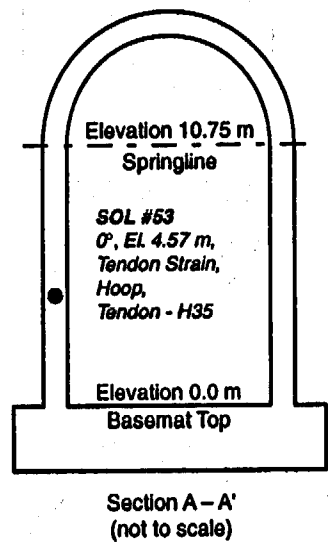
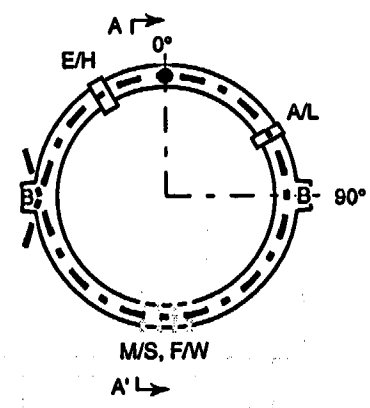
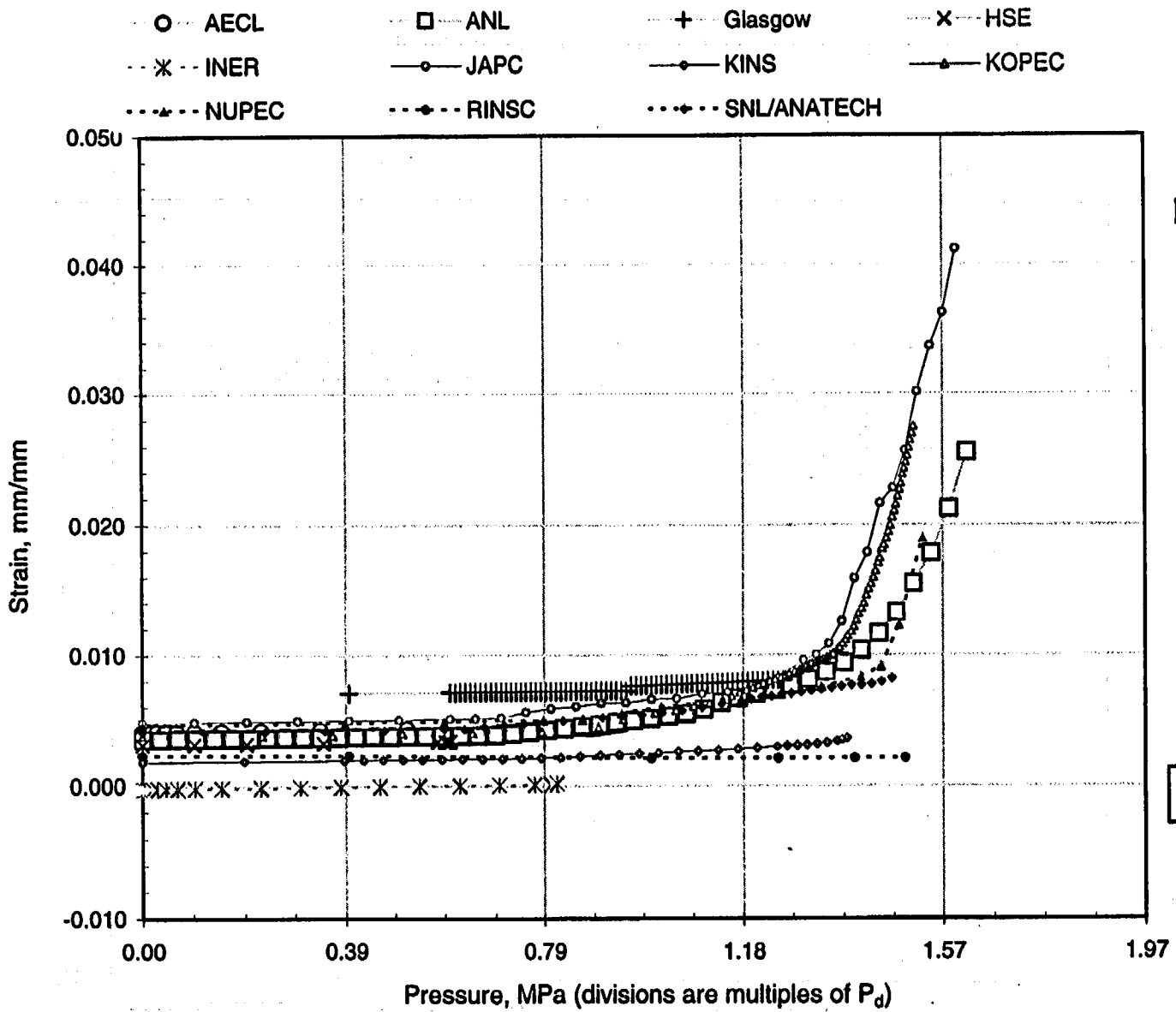
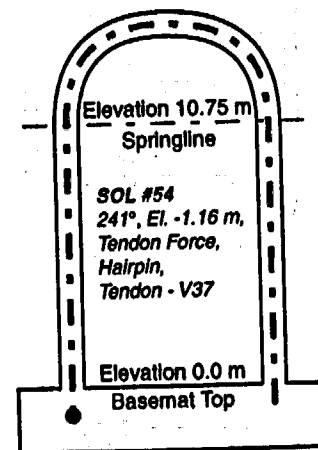
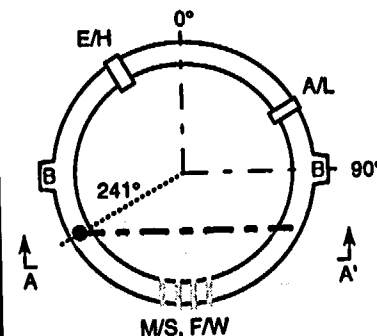
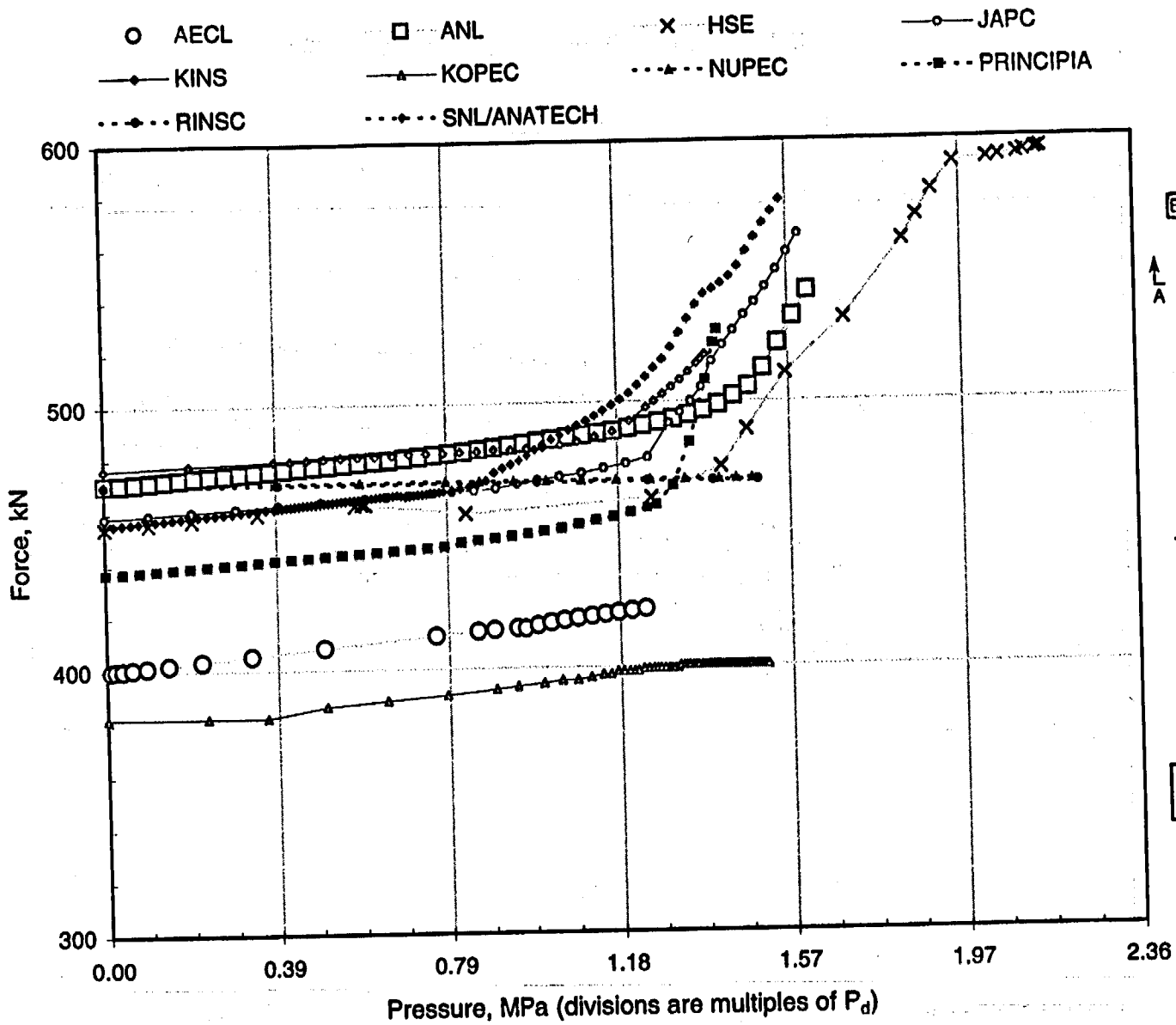


Figure A-53. PCCV Standard Output Location (SOL) #53.



Section A - A'
(not to scale)

Figure A-54. PCCV Standard Output Location (SOL) #54.

A-94

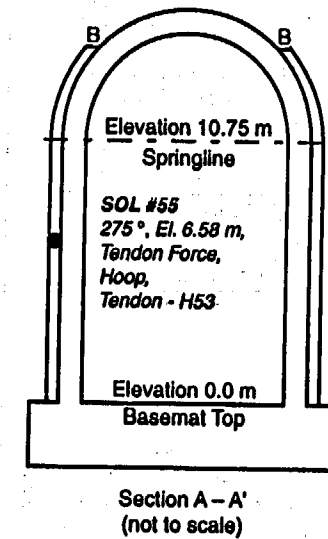
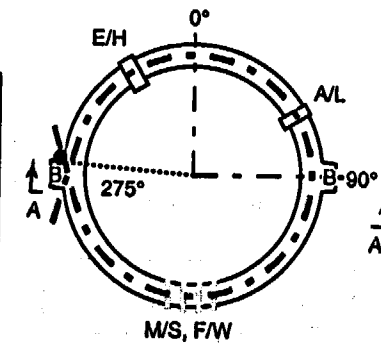
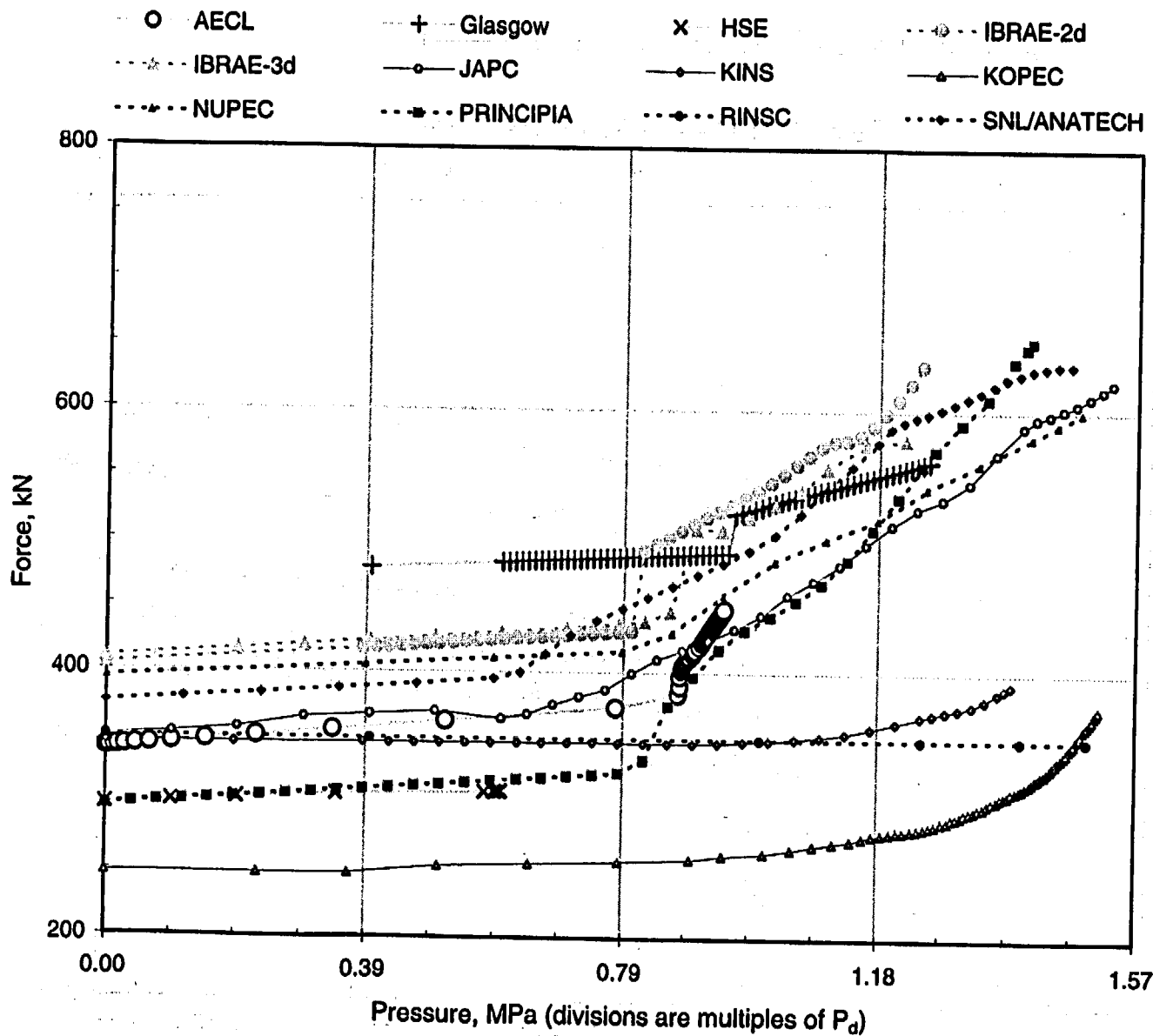


Figure A-55. PCCV Standard Output Location (SOL) #55.

APPENDIX B

AECL

**ATOMIC ENERGY OF CANADA LIMITED
CANADA**

Appendix A, Composite Plots, comprises test data compiled and plotted from all organizations that participated in the Prestressed Concrete Containment Vessel (PCCV) Round Robin Pretest Analysis. To avoid duplicating the composite information, individual sets of data and/or plots have been omitted from participants' reports. In some cases this action resulted in disconnects between callouts and content and in the numbering of figures, tables, and pagination in some reports.

In Appendix B, "AECL, Atomic Energy of Canada Limited, Canada," discontinuity arises from omitting the following material:

Figure 34

Figure 35

Appendix A, "Output at Specified Locations"

Table of Contents

1. INTRODUCTION	1
2. ANALYSIS MODEL	1
2.1 Axi-symmetric Finite Element Model	2
2.2 3D Finite Element Model	2
2.3 Material Models	3
2.3.1 Concrete Material Model	3
2.3.2 Reinforcement Material Model	5
2.3.3 Post-Tension Tendon Material Model	5
2.3.4 Steel Liner Material Model	5
3. ANALYSIS LOADS	5
3.1.1 Dead Load	6
3.1.2 Pre-stressing Load	6
3.1.3 Internal Pressure Load	6
4. ANALYSIS RESULTS	6
4.1 General Response	7
4.1.1 Axi-symmetric Analysis Results	7
4.1.2 3D Analysis Results	8
4.2 Response at Specified Locations	8
4.0 CONCLUSIONS	9
5.0 REFERENCES	9
TABLES	
Table 1: Normal Strength Concrete Material Model	10
Table 2: High Strength Concrete Material Model	10
Table 3: Special Concrete Material Model	11
Table 4: Modulus of Elasticity for Rebar Material Models	11
Table 5: Post-Tension Tendon Material Model	12
Table 6: Steel Liner Material Model	12
FIGURES	
Figure 1: Overall geometry of the 1:4 scale PCCV test model	13
Figure 2: Axi-symmetric finite element model of the PCCV	14
Figure 3: Element mesh of both the dome and the wall of the PCCV	15
Figure 4: Three-dimensional finite element model of the PCCV	16

Figure 5: Membrane elements of the steel liner	17
Figure 6: Continuum elements of the concrete containment	18
Figure 7: Truss elements of the vertical post-tension tendons	19
Figure 8: Truss elements of the hoop post-tension tendons	20
Figure 9: Details of the steel liner at major openings	21
Figure 10: Details of the hoop and vertical post-tension tendons	22
Figure 11: Details at major openings of the PCCV	23
Figure 12: Plastic stress-strain relation for Type SD345 rebars	24
Figure 13: Plastic stress-strain relation for Type SD390 rebars	25
Figure 14: Plastic stress-strain relation for Type SD490 rebars	26
Figure 15: Plastic stress-strain relation for the tendons	27
Figure 16: Plastic stress-strain relation for the steel liner	28
Figure 17: Deformed shape of the PCCV at many stages of the applied load	29
Figure 18: Pressure vs. spring line radial displacement for the PCCV	30
Figure 19: Cracking in the PCCV at different stages of the applied load	31
Figure 20: Stress-strain relation for the vertical post-tensioned tendon at the spring line	32
Figure 21: Stress-strain relation for the inner meridional rebar at the wall/basemat joint	33
Figure 22: Stress-strain relation for the inner hoop rebar at the wall/basemat joint	34
Figure 23: Stress-strain relation for the outer hoop rebar at the mid-height of the wall	35
Figure 24: Hoop stress-strain relation for the steel liner at the mid-height of the wall	36
Figure 25: Pressure vs. wall mid-height radial displacement for the PCCV	37
Figure 26: Deformed shape of the PCCV due to dead and prestressing loads	38
Figure 27: Deformed shape of the PCCV at pressure load of 944 kPa	39
Figure 28: Cracking strain in concrete elements at pressure load of 944 kPa	40
Figure 29: Cracking strain in concrete layers at pressure load of 944 kPa	41
Figure 30: Mises stress in liner elements at pressure load of 944 kPa	42
Figure 31: Stress-strain behavior for outer rebars at the PCCV wall mid-height	43
Figure 32: Stress-strain behavior for steel liner at the PCCV wall mid-height	44

APPENDIX Output at Specified Locations

1. INTRODUCTION

A joint model test project is sponsored by the Nuclear Power Engineering Corporation (NUPEC) of Japan and the U.S. Nuclear Regulatory Commission (NRC), References 1 to 4. The test model is a prestressed concrete containment vessel (PCCV) and is a 1:4 scale model of a pressurized water reactor (PWR) containment. The test model will be constructed and tested at Sandia National Laboratories, Albuquerque, New Mexico, USA, who is coordinating the Round Robin analysis activity. Organizations from many nations are participating in the Round Robin analysis activity for the PCCV test model. Atomic Energy of Canada Limited (AECL) is one of the participants.

The overall geometry of the 1:4-scale PCCV test model is shown in Figure 1. The test model consists of reinforced concrete basemat and post-tensioned concrete cylindrical wall and dome. The wall and the dome are reinforced with steel rebars as well. A steel liner is placed on the inside surface of the basemat, the wall and the dome. In addition, the test model has scaled representation of the equipment hatch, personnel airlock, and main steam and feedwater line penetrations. The model construction and instrumentation of the PCCV test model is scheduled to be completed by the mid of year 2000.

One of the objectives of the PCCV test project is to validate and improve existing numerical simulation methods for predicting the responses of containment structures to loading conditions beyond the design basis accident.

To predict the structural responses accurately, it involves at least two critical features: the structural idealization by geometry models and material property models, and the solution algorithm used in the analysis. Concrete structures with reinforcements and post-tension tendons behave in a highly non-linear manner and exhibit a complex response when cracks initiate and propagate. All these uncertainties combined pose great challenges to the goals of the PCCV Round Robin Analysis.

This report documents the pretest analysis carried out by AECL using an axi-symmetric finite element model and a three-dimensional finite element model. ABAQUS, the general non-linear computer program, is used in the analysis, Reference 5. The modeling approaches of geometry and materials and the analysis results are summarized in the following sections.

2. ANALYSIS MODEL

The analysis of the PCCV test model is carried out using an axi-symmetric finite element model and a three-dimensional finite element model. The two models are based on the geometry, material properties and applicable boundary conditions of the PCCV test model. In case of the axi-symmetric model, the PCCV is assumed to be a body of revolution. Therefore, the effects due to the presence of the openings and the buttresses in the PCCV are not considered in this model. However, these effects are accounted for in the three-dimensional analysis model.

2.1 Axi-symmetric Finite Element Model

Figure 2 illustrates the axi-symmetric finite element model of the containment structure. The axi-symmetric model consists of four main parts. These are: the dome, the wall, the basemat, and the steel liner. Six elements are defined across the thickness of both the wall and the dome of the PCCV, Figure 3.

The boundary conditions for the axi-symmetric model are defined to be consistent with the symmetry assumption of the loads to be applied to the model. Gravity load, pre-stressing load, and the internal pressure load are axi-symmetric with respect to the model geometry. Therefore, symmetric boundary conditions are used. All nodes located on the axis of symmetry are restrained in the radial direction, and all nodes located on the lower surface of the basemat are restrained in all three directions.

Elements CAX4 and MAX1 of the ABAQUS element library are used to model the concrete parts and the steel liner of the PCCV respectively. CAX4 is a 4-node bilinear axi-symmetric solid (continuum) element and MAX1 is a 2-node linear axi-symmetric membrane element. Two degrees of freedom are active at each node: translations in the radial and axial directions. No twist degree of freedom is represented in both elements. The theoretical formulation of both elements can be found in ABAQUS manual.

Steel reinforcement in concrete is modeled as rebars that are one-dimensional strain theory elements. The rebars are defined as layers of uniformly spaced reinforcing bars and are superposed on the axi-symmetric concrete elements. Each layer is treated as a smeared layer with a constant thickness equal to the area of each reinforcing bar divided by the reinforcing bar spacing. With this modeling approach, the rebar behavior is considered independently of the concrete. Effects associated with the rebar/concrete interface, such as bond slip and dowel action, are modeled approximately to simulate load transfer across concrete cracks through the rebar. Post-tension tendons are modeled using rebars in a similar manner to the steel reinforcements in the concrete elements. The pre-stressing loads in the tendons are defined as stress initial conditions in the rebars. Detailed design of the steel reinforcements, the post-tensioning tendons and the steel liner are given in the design drawings of Reference 1.

2.2 3D Finite Element Model

The PCCV three-dimensional finite element model, Figure 4, can be divided into three parts according to the used element type. On the inside surface, the liner is modeled by membrane elements, Figure 5. Continuum elements are used for the prestressed concrete containment, Figure 6. The hoop and vertical post-tensioned tendons are modeled by truss elements, Figures 7 and 8.

Based on the preliminary axi-symmetric analysis of the PCCV, the basemat is not included in the three-dimensional model. The boundary conditions for the PCCV three-dimensional model are defined such that all nodes at the cylindrical wall/basemat junctions are restrained in all three translational degrees of freedom. Therefore, no rotation is allowed at the PCCV wall end at the base.

Elements C3D8R, M3D4 and T3D2 of the ABAQUS element library are used to model the concrete containment, steel liner, and post-tension tendons of the PCCV, respectively. C3D8R is an 8-node linear brick (continuum) element with reduced integration and hourglass control. M3D4 is a 4-node quadrilateral membrane element. T3D2 is a 2-node linear displacement truss element. Three translational degrees of freedom are active at each node. The theoretical formulation of these elements can be found in ABAQUS manual.

There are four solid elements across the thickness of the containment shell. All post-tension tendons (90 vertical tendons and 108 hoop tendons) are individually modeled. Due to their curvature, the tendons are modeled as grouted. Therefore, the tendons truss elements share their nodes with the concrete nodes. The steel liner elements share their nodes with the inside layer of concrete elements. The steel liner model includes two bulkheads for the airlock and equipment hatches that represent the two major openings in the PCCV. Figures 9, 10 and 11 illustrate the details of the three-dimensional model at the two major openings.

Steel reinforcement in the concrete elements is modeled as rebars that are one-dimensional strain-theory elements. The rebars are defined as layers of uniformly spaced reinforcing bars and are superposed on the concrete elements. Each layer is treated as a smeared layer with a constant thickness equal to the area of each reinforcing bar divided by the reinforcing bar spacing. With this modeling approach, the rebar behavior is considered independently of the concrete. Effects associated with the rebar/concrete interface, such as bond slip and dowel action, are modeled approximately to simulate load transfer across concrete cracks through the rebar. Detailed design of the steel reinforcements, the post-tensioning tendons and the steel liner are given in the design drawings of Reference 1.

2.3 Material Models

The material models for concrete, steel rebars, post-tensioned tendons and steel liner are defined using different material models in ABAQUS. Some material test results are provided in Reference 1 to 4, from which the parameters of the ABAQUS material models are derived. The material models are briefly described below.

2.3.1 Concrete Material Model

The concrete model is intended for concrete behavior under relatively monotonic loading with fairly low confining pressures, such as the PCCV limit state pressure test. Two types of concrete are used for the PCCV test model: a normal strength concrete, and a high strength concrete. For each strength type of concrete, the material data are given in References 1 to 4. In this analysis study, the field curing condition and strength at 13 weeks are considered. The cracking strain for the high strength concrete is 60μ mm/mm. The concrete material parameters for both the normal strength concrete and the high strength concrete are given in Tables 1 and 2 respectively.

In the case of the three-dimensional, a revised concrete properties are used for the concrete elements surrounding the two major opening. In order to surmount numerical problems during the analysis, the cracking strain for the revised concrete is increased from 60μ mm/mm to 150μ mm/mm. The concrete material parameters for the revised concrete are given in Tables 3.

The ABAQUS concrete material model used in the analysis is described below.

a) Linear Elastic Model

When the concrete stress is within the elastic range, whether under compression or tension, the stress-strain relationship is assumed to be linear. The material properties are defined by the modulus of elasticity (E), Poisson's ratio (ν), the compressive yield strength (f_c), and the tensile strength (f_t).

b) Compressive Stress-Strain Model

When concrete is loaded in compression, it initially exhibits elastic response. As the stress increases, some inelastic hardening occurs and the response of the material softens. When the principal stress components are dominantly compressive, the response of the concrete is modeled by an elastic-plastic theory using a simple form of yield surface in terms of the equivalent pressure stress and the Mises equivalent deviatoric stress. Associated flow and isotropic hardening are used.

A uni-axial stress-strain relationship outside elastic range is assumed. In this part, the stress-strain behavior of plain concrete in uni-axial compression outside the elastic range is specified by stress as a function of plastic strain.

In addition, a failure surface for multi-axial stresses is assumed. This surface predicts the response to occasional strain reversals and strain trajectory direction changes by the isotropic hardening of the compressive yield surface when the principal stresses are dominantly compressive. This failure surface are defined in ABAQUS by the following four constants:

- The ratio of the ultimate bi-axial compressive stress to the ultimate uni-axial compressive stress (r_1). This ratio is assumed 1.16 for both types of concrete.
- The absolute value of the ratio of the uni-axial tensile stress at failure to the ultimate uni-axial compressive stress ($r_2 = f_t / f_c$). This ratio equals 0.08085 and 0.07064 for normal strength concrete, and high strength concrete respectively.
- The ratio of the magnitude of a principal component of plastic strain at ultimate stress in bi-axial compression to the plastic strain at ultimate stress in uni-axial compression (r_3). This ratio is assumed 1.28 for both types of concrete.
- The ratio of the tensile principal stress at cracking, in plane stress, when the other principal stress is at the ultimate compressive value, to the tensile cracking stress under uni-axial tension (r_4). This ratio is assumed 0.333 for both types of concrete.

c) Tensile Stress-Strain Model

When a uni-axial concrete specimen is loaded in tension, it responds elastically until cracks form at the tensile strength (f_t). For multi-axial behavior, an independent "crack detection surface" that determines if a point fails by cracking. It uses oriented damaged elasticity concepts to describe the reversible part of the material response after cracking failure.

The cracking is assumed to occur when the stress reaches a failure surface that is called "cracking detection surface." This failure surface is a linear relationship between the equivalent pressure

stress and the Mises equivalent deviatoric stress. Cracks are irrecoverable, but may open and close. Following crack detection, the crack affects the calculations because a damaged elasticity model is used. The strain-softening behavior for cracked concrete is represented by a post-failure stress-strain relation which shows the effects of reinforcement interaction with concrete. The strain-softening after failure reduces the stress linearly to zero at a total strain for direct straining across cracks. A strain of 0.001 is assumed for the effect of tension stiffening for both types of concrete.

As the concrete cracks, its shear stiffness is diminished. This effect is specified by the reduction in the shear modulus as a function of the opening strain across the crack. The modulus for shearing of cracks can be defined as a fraction of the elastic shear modulus of the un-cracked concrete. In this preliminary analysis, full shear retention of concrete is assumed; i.e. the shear modulus is unaffected by cracking.

2.3.2 Reinforcement Material Model

Rebars are used with metal elasticity and plasticity models to describe the behavior of the rebar material. The plastic behavior is modeled by the relationship between the true stress and the log plastic strain.

The test results provided in References 1 to 3 are used to derive the rebar material properties. For each rebar type, the stress-strain behavior is different for various sizes (diameters). Figures 12, 13, and 14 presents the stress-strain relation for Rebar types SD345, SD390 and 490, respectively. Table 4 presents the modulus of elasticity for each type and each size of the reinforcement steel.

2.3.3 Post-Tension Tendon Material Model

The test results provided in References 1 to 3 are used to derive the post-tension tendon material properties. Figure 15 and Table 5 give the parameter values for the elasto-plastic behavior of post-tension tendon material model.

2.3.4 Steel Liner Material Model

The test results provided in References 1 to 3 are used to derive the material properties for the steel liner. Isotropic material is assumed for the steel liner, so that the test samples for the X-direction and the Y-direction are combined. The averaged material properties for the steel liner material model are given in Table 6. The stress-strain relationship the steel liner material is shown in Figure 16.

3. ANALYSIS LOADS

The main goal of the PCCV experiment is to determine its ultimate pressure capacity. Therefore, each of the two analysis models of the PCCV is subjected to three loading conditions. The loading conditions include the dead load of the PCCV, the pre-stressing forces of the tendons, and the internal pressure. Both the dead load and the pre-stressing load are applied in one load

step. The internal pressure load is applied to the inside surface of the steel liner model in many load increments. Since the pressure is applied in a monotonic manner in one direction only, the direct non-linear solution technique is chosen. The automatic time-stepping feature of ABAQUS is invoked to march to a solution at each load increment. The convergence criteria are selected to meet the concrete cracking model requirements and to allow for its discontinuous numerical behavior. The radial degree of freedom at the spring line is selected to monitor the solution progress in the axi-symmetric analysis. The radial degree of freedom at the mid-height of the PCCV wall is selected to monitor the solution progress in the axi-symmetric analysis.

3.1.1 Dead Load

For both the axi-symmetric model and the three-dimensional model, the gravitational acceleration is applied to the whole analysis model.

3.1.2 Pre-stressing Load

For the axi-symmetric model, the pre-stressing load is defined as stress initial conditions in the rebars representing the post-tension tendons. The specified initial pre-stress loads are assumed to remain constant during the equilibrium solution.

For the three-dimensional model, the pre-stressing load is defined as stress initial conditions in the truss elements representing the post-tension tendons. The pre-stressing load is applied uniformly over the post-tension tendon, then, the structure is brought to a state of equilibrium as part of the solution. Thus, the actual stresses in the tendons are determined.

3.1.3 Internal Pressure Load

For the axi-symmetric model, the inside faces of the membrane elements representing the steel liner are loaded with a uniform pressure. The internal pressure load is applied incrementally with an initial load increment of 10 kPa up to the maximum pressure which is more than three times the PCCV design pressure.

For the three-dimensional model, the faces of the liner membrane elements representing the inside surface of the steel liner are loaded with a uniform pressure. The internal pressure load is applied incrementally with an initial load increment of 2 kPa. This load represents 0.5% of the PCCV design pressure of 390 kPa.

4. ANALYSIS RESULTS

The analysis results of the PCCV are divided into two groups. The first group summarizes the general behavior of the model under the three loading conditions. The second group summarizes the results at the specified instrument locations.

4.1 General Response

4.1.1 Axi-symmetric Analysis Results

Figure 17 shows the deformed shape of the PCCV at different loading increments of the analysis. A load-displacement curve is presented in Figure 18. The load variable represents the internal pressure and the displacement variable represents the monitored degree of freedom; i.e. the radial displacement at the spring line. The load-displacement curve indicates a linear response up to a pressure of 854 kPa. This pressure level is about 2.2 times the design pressure of the PCCV. Beyond this pressure level, the deformation significantly increases with a marginal increase in the pressure. This transition might indicate the structure is softening; i.e. cracking. At pressure level of about 970 kPa, a very small increase in the model stiffness is observed. The analysis is stopped at a pressure level of 1240 kPa since cracks are spread over almost the whole structure.

Figure 19 shows the plastic strain of the concrete elements at different loading increments and in selected radial, axial and/or hoop directions. The plastic strain indicates the zones where concrete cracks have occurred.

The first crack in the model occurs at a pressure level of 854 kPa and is located at the inside surface of the wall at the wall/basemat joint. One element only is cracked at this pressure level and this crack takes place in the radial, axial and hoop directions.

At the end of the subsequent load increment, at a pressure level of 892 kPa, the cracking in the wall starts at two other regions: the lower and upper thirds of the wall. The cracking in the lower regions is limited to the outside surface of the wall while the cracking in the upper region occurs across the whole thickness of wall. In both regions, the cracking takes place in the radial and axial directions only.

The first crack in the dome takes place at pressure level of 966 kPa and is located at the inside surface of the dome at spring line. One element only is cracked at this pressure level and this crack takes place in the radial, axial and hoop directions. At the wall, the cracking in the two regions extends to most of the wall elements.

At pressure level of 1026 kPa all elements of the wall are cracked in both the radial and axial directions. At the same pressure level, the cracking in the dome extends beyond the spring line location towards the dome apex. By the end of the analysis, at pressure level of 1240 kPa, all elements of the dome are cracked in both the radial and axial directions. In addition, most of the element are cracked in the hoop direction.

The stress-strain relation for the wall vertical tendon at the spring line throughout the loading history is shown in Figure 20. The stress-strain relation history for the inner and outer meridional rebars at the wall/basemat joint are shown in Figures 21 and 22. Figure 23 presents the stress-strain relation history for the outer hoop reinforcement at the mid-height of the wall. The stress-strain relation history for the hoop stresses in the wall steel liner at the mid-height of the wall is shown in Figure 24. These stress-strain relation histories indicate the linear behavior of the post-tension tendon, the steel rebars and the steel liner during the application of the internal pressure.

4.1.2 3D Analysis Results

A load-displacement curve is presented in Figure 25. The load variable represents the internal pressure and the displacement variable represents the monitored degree of freedom; i.e. the radial displacement at the mid-height of the PCCV wall. The load-displacement curve indicates a linear response up to a pressure of 874 kPa. This pressure level is about 2.24 times the PCCV design pressure. Beyond this pressure level, the deformation significantly increases with a marginal increase in the pressure. This transition indicates the structure is softening including cracking of concrete. The analysis is stopped at a pressure level of 944 kPa as concrete cracks are spread over almost the whole height of the PCCV wall.

Figure 26 shows the deformed shape of the PCCV due to both the dead load and the prestressing load. The deformed shape of the PCCV concrete elements at the last increment of the internal pressure load is shown in Figure 27.

Figure 28 shows the cracking strain of the concrete elements at the last increment of the internal pressure load. The cracking strain for each layer of elements are shown in Figure 29. Figure 30 illustrates the Mises stresses in the steel liner at the last increment of the internal pressure load.

The first concrete crack in the model occurs at a pressure level of 776 kPa and is located at the inside surface of the wall at approximately the middle of the height. At a pressure level of 874 kPa, the cracking in the wall extends in two regions: the lower and upper thirds of the wall. The cracking propagates from the inside surface to the outside surface of the wall. At pressure level of 994 kPa all elements of the wall are cracked. At the same pressure level, the cracking in the dome extends beyond the springline location towards the dome apex.

The stress-strain relation history for the outer hoop and meridional rebars at the mid-height of the wall and at azimuth 135 degrees are shown in Figure 31. Figure 32 presents the stress-strain relation history for the hoop stresses in the wall steel liner at the mid-height of the wall and at azimuth 135 degrees. These stress-strain relation histories indicate the linear behavior of the post-tension tendon, the steel rebars and the steel liner during the application of the internal pressure upto 944 kPa.

4.2 Response at Specified Locations

The PCCV standard output locations are listed in Reference 2. The 3D analysis results at the specified instrument locations are grouped into four sets. The first set represents the displacement history at specified locations on the three-dimensional model of the PCCV. The second set represents the strain history at specified rebar locations. The third set represents the strain history at specified liner locations. The last set represents strain and force histories in the vertical and hoop wall tendons. For Locations 1, 47 and 54, the output from the axi-symmetric analysis is included since the 3D analysis does not include the basemat of the PCCV. The appendix includes the four sets of the analysis results.

4.0 CONCLUSIONS

The analysis reported here aims to predict the responses of the PCCV to internal pressure beyond the design basis accident. Two finite element models are developed for the analysis: an axisymmetric model and a three-dimensional model. Non-linear materials models are used to describe the behavior of different components of the PCCV. The internal pressure load is applied incrementally and the structural response of the PCCV is determined.

From the analysis results, key milestones during pressurization of the PCCV can be observed as follows.

- The first crack in the axisymmetric model occurs at a pressure of 854 kPa and is located at the inside surface of the wall at the wall/basemat joint. The first crack in the 3D model occurs at a pressure of 776 kPa and is located at the inside surface of the wall at approximately the mid-height.
- At a pressure of 892 kPa, the lower third of the wall region in the axisymmetric model is cracked at the outside surface of the wall and the whole section in upper third of the wall is cracked. At a pressure of 874 kPa, cracking extends in the 3D model to the upper and lower thirds of the wall.
- At a pressure of 944 kPa, most of wall elements in the 3D model are cracked and the dome cracks extends beyond the springline towards the dome apex.
- Based on the 3D model results, the steel liner develops stress concentrations close to the air lock and equipment hatch. However, the overall behavior of the liner remains linear upto pressure load of 944 kPa.
- Based on the 3D model, the overall behavior of the prestressing tendons and the rebars remains linear upto pressure load of 944 kPa.
- Based on the axisymmetric results, the first crack in the dome occurs at pressure level of 966 kPa and is located at the inside surface of the dome at the spring line. At a pressure of 1060 kPa, all elements of the wall are cracked and the dome cracks extends beyond the spring line towards the dome apex. At a pressure of 1240 kPa, all elements of the wall and most elements of the dome are cracked.

5.0 REFERENCES

1. Letter from V. K. Luk to M. N. Gray, "PCCV Round Robin Analysis - Release of Design Package", File SO-97-047 (f), June 18, 1998.
2. Letter from V. K. Luk to M. N. Gray, "PCCV Round Robin Analysis - Updated Information Package", File SO-98-052, August 27, 1998.
3. Letter from V. K. Luk to L. S.S. Lee, File SO-99-001, January 8, 1999.
4. Letter from V. K. Luk to L. S.S. Lee, "Concrete Properties for Pretest Analysis," File SO-99-007, March 30, 1999.
5. ABAQUS User's Manual, by Hibbitt, Karlsson & Sorensen, Inc.

Table 1: Normal Strength Concrete Material Model

Mass Density (ton/m ³)	2.21
Linear Elastic Model	
Modulus of Elasticity (MPa)	27950
Poisson Ratio	0.18
Compressive yield strength (Mpa)	20.68
Compressive ultimate strength (MPa)	41.68
Tensile strength (MPa)	3.37
Compressive Stress-Strain Model (Uni-axial Stress-Strain Relationship Outside Elastic Range)	
Stress (MPa)	Plastic Strain (%)
20.68	0.0
41.68	0.0015
Compressive Stress-Strain Model (Multi-axial Stress-Strain Relationship)	
Failure Ratios	see Section 2.3.1
Cracking Tension stiffness	see Section 2.3.1
Shear Retention	see Section 2.3.1

Table 2: High Strength Concrete Material Model

Mass Density (ton/m ³)	2.19
Linear Elastic Model	
Modulus of Elasticity (MPa)	26790
Poisson Ratio	0.18
Compressive yield strength (MPa)	20.68
Compressive ultimate strength (MPa)	44.13
Tensile strength (MPa)	1.617
Compressive Stress-Strain Model (Uni-axial Stress-Strain Relationship Outside Elastic Range)	
Stress (MPa)	Plastic Strain (%)
20.68	0.0
44.68	0.0015
Compressive Stress-Strain Model (Multi-axial Stress-Strain Relationship)	
Failure Ratios	see Section 2.3.1
Cracking Tension stiffness	see Section 2.3.1
Shear Retention	see Section 2.3.1

Table 3: Special Concrete Material Model

Mass Density (ton/m ³)	2.19
Linear Elastic Model	
Modulus of Elasticity (MPa)	26970
Poisson Ratio	0.18
Compressive yield strength (MPa)	20.68
Compressive ultimate strength (MPa)	44.13
Tensile strength (MPa)	4.14
Compressive Stress-Strain Model (Uni-axial Stress-Strain Relationship Outside Elastic Range)	
Stress (MPa)	Plastic Strain (%)
20.68	0.0
44.13	0.0015
Compressive Stress-Strain Model (Multi-axial Stress-Strain Relationship)	
Failure Ratios	see Section 2.3.1
Cracking Tension stiffness	see Section 2.3.1
Shear Retention	see Section 2.3.1

Table 4: Modulus of Elasticity for Rebar Material Models

Rebar Type - Rebar Size	E (MPa)
SD345 - # 6	166194
SD345 - # 10	181667
SD390 - # 10	179996
SD390 - # 13	173232
SD390 - # 16	209940
SD390 - # 19	174954
SD390 - # 22	198383
SD490 - # 10	181597
SD490 - # 13	182199
SD490 - # 16	210539
SD490 - # 19	182977

Table 5: Post-Tension Tendon Material Model

Mass Density (ton/m ³)	7.80
Linear Elastic Model	
Modulus of Elasticity (MPa)	217672
Poisson Ratio	0.3
Yield strength (MPa)	1750

Table 6: Steel Liner Material Model

Mass Density (ton/m ³)	7.80
Linear Elastic Model	
Modulus of Elasticity (MPa)	198389
Poisson Ratio	0.3
Yield strength (MPa)	383.46

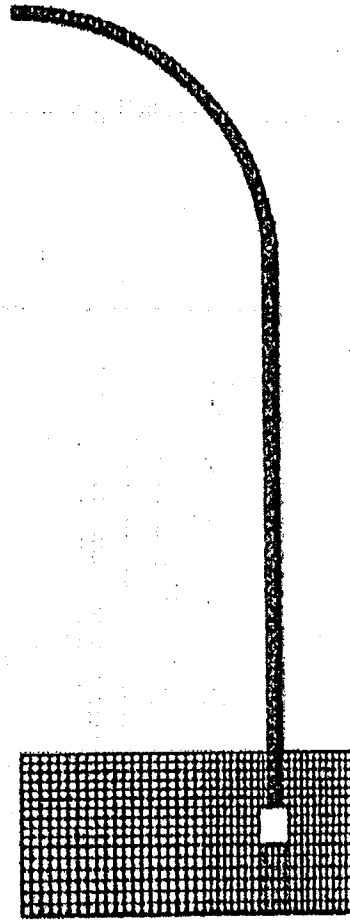


Figure 2: Axi-symmetric finite element model of the PCCV

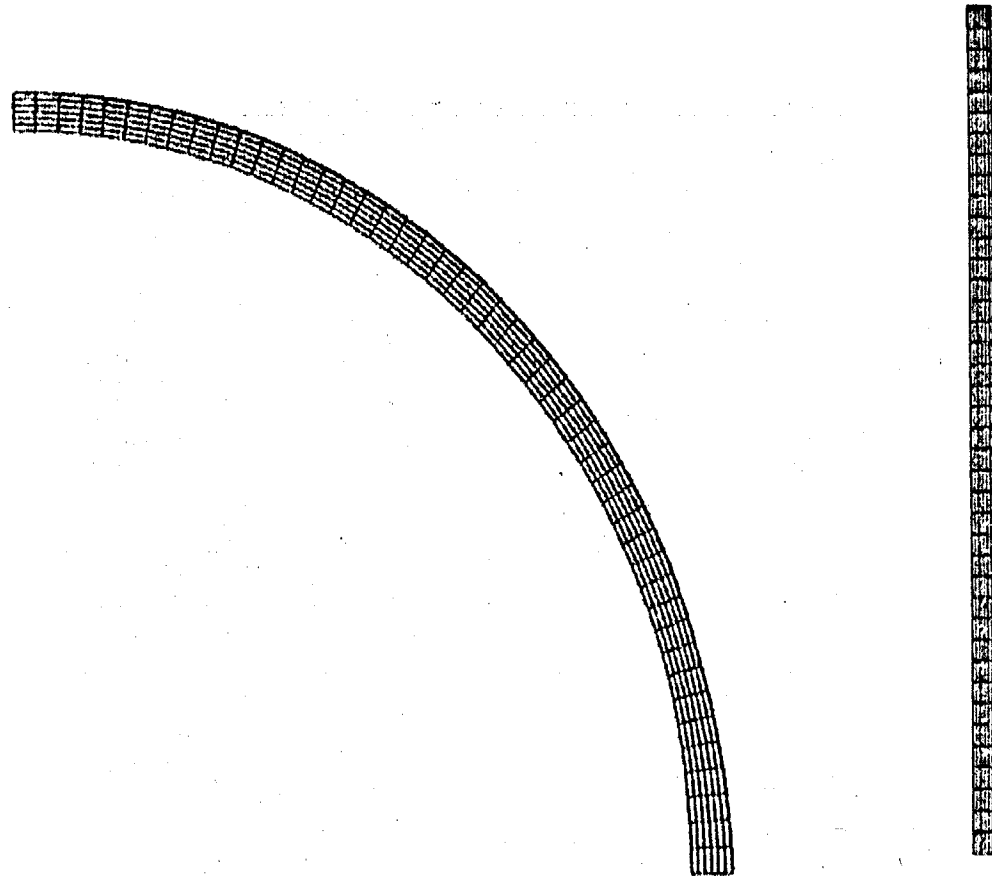


Figure 3: Element mesh of both the dome and the wall of the PCCV

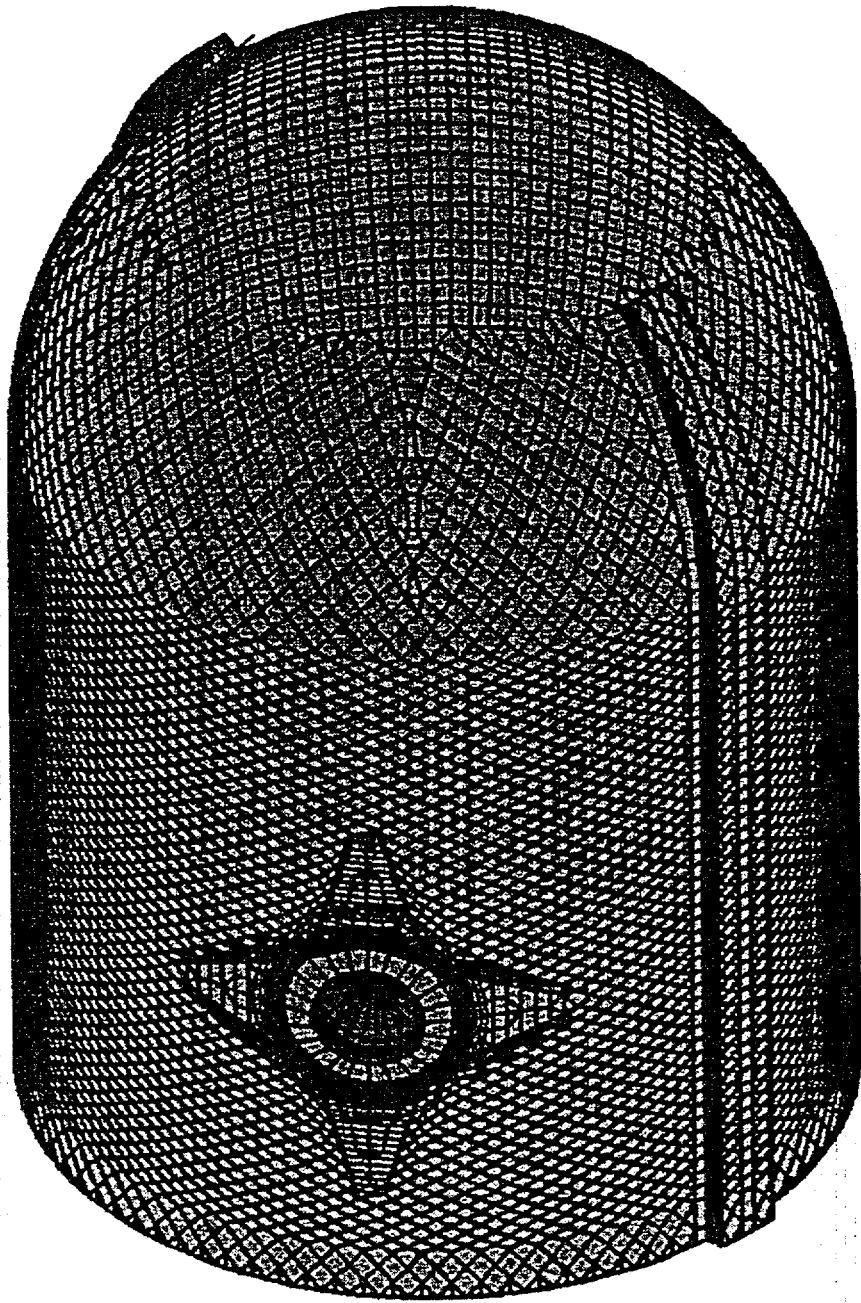


Figure 4: Three-dimensional finite element model of the PCCV

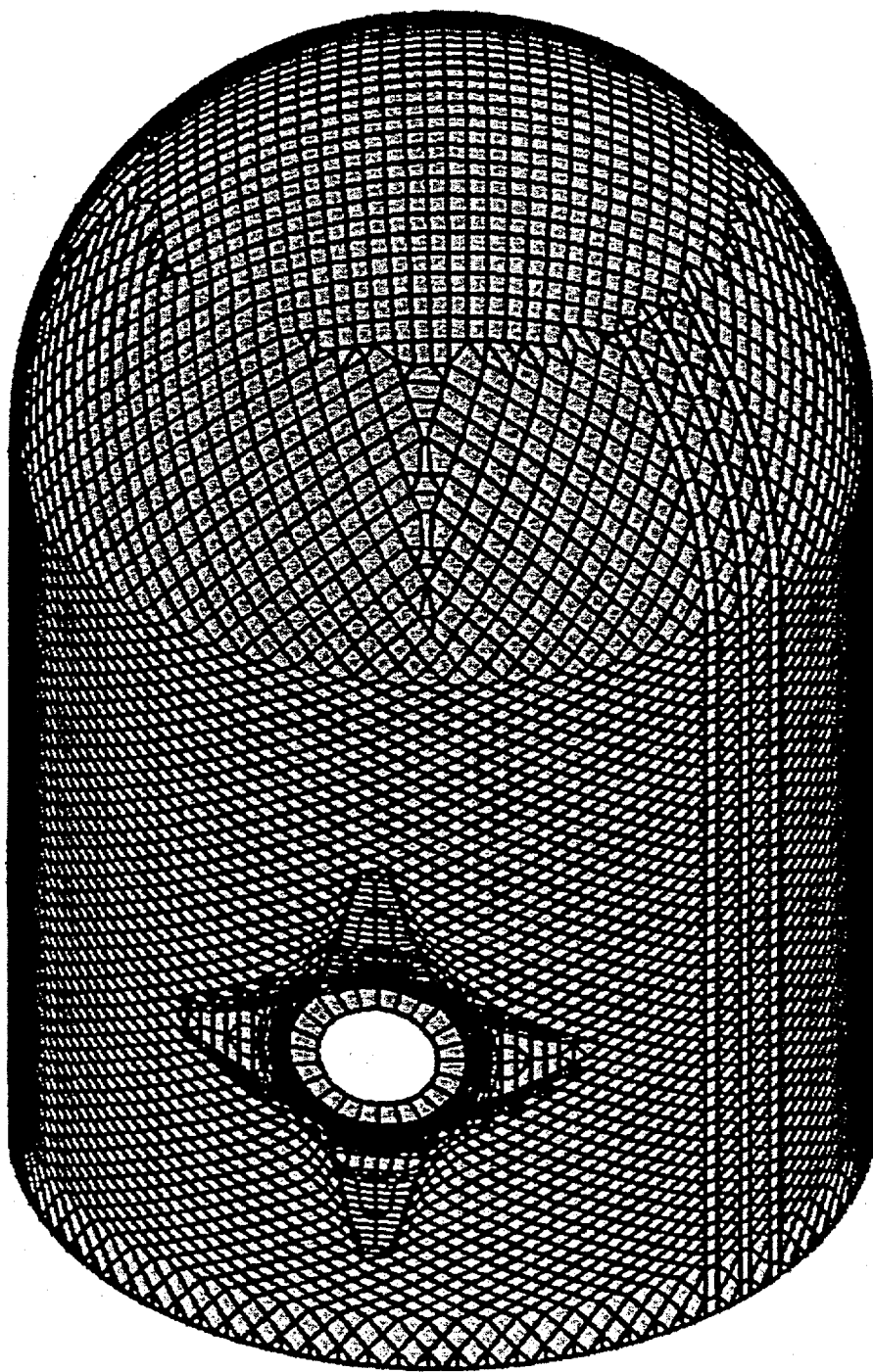


Figure 5: Membrane elements of the steel liner

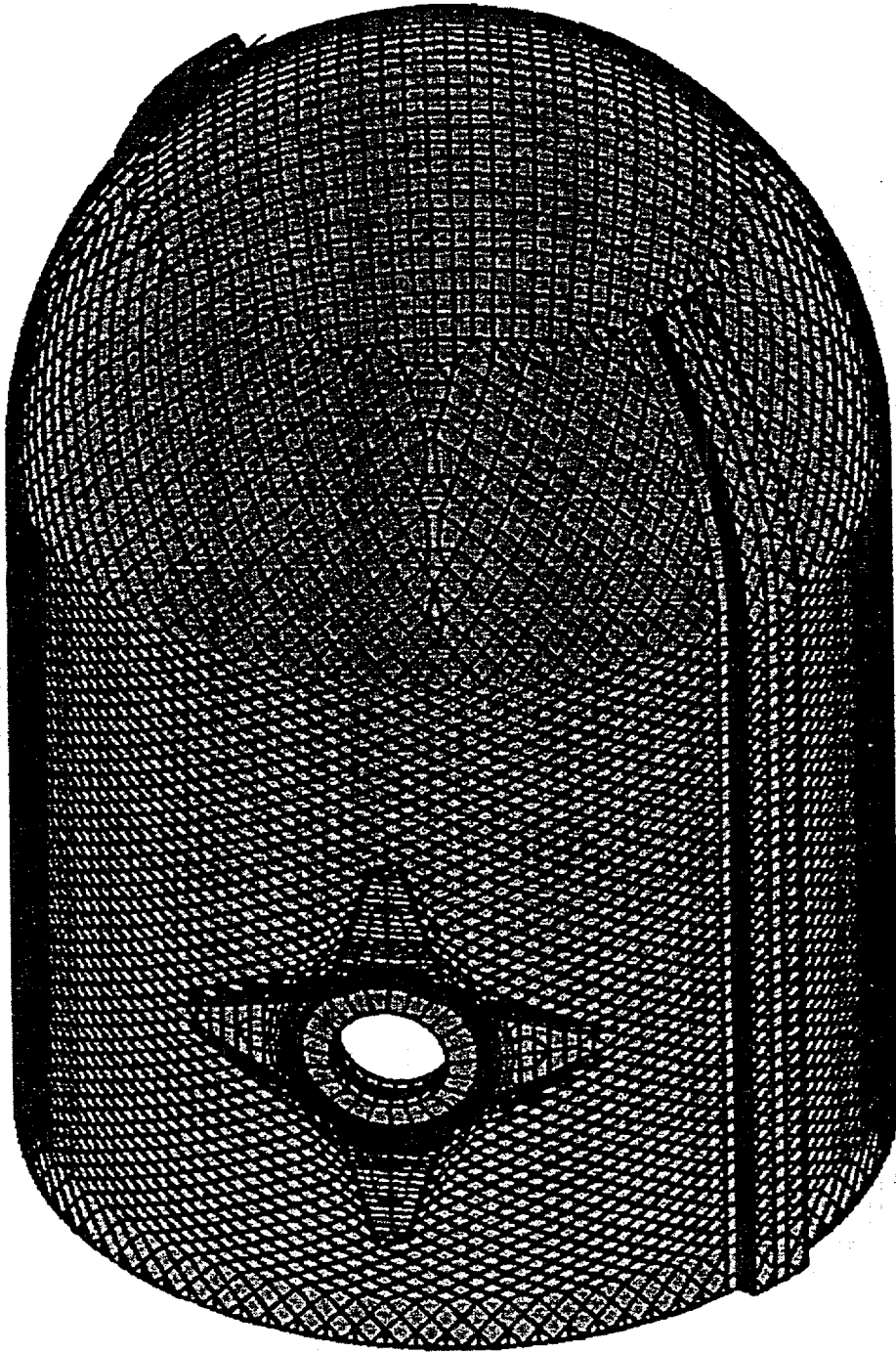


Figure 6: Continuum elements of the concrete containment

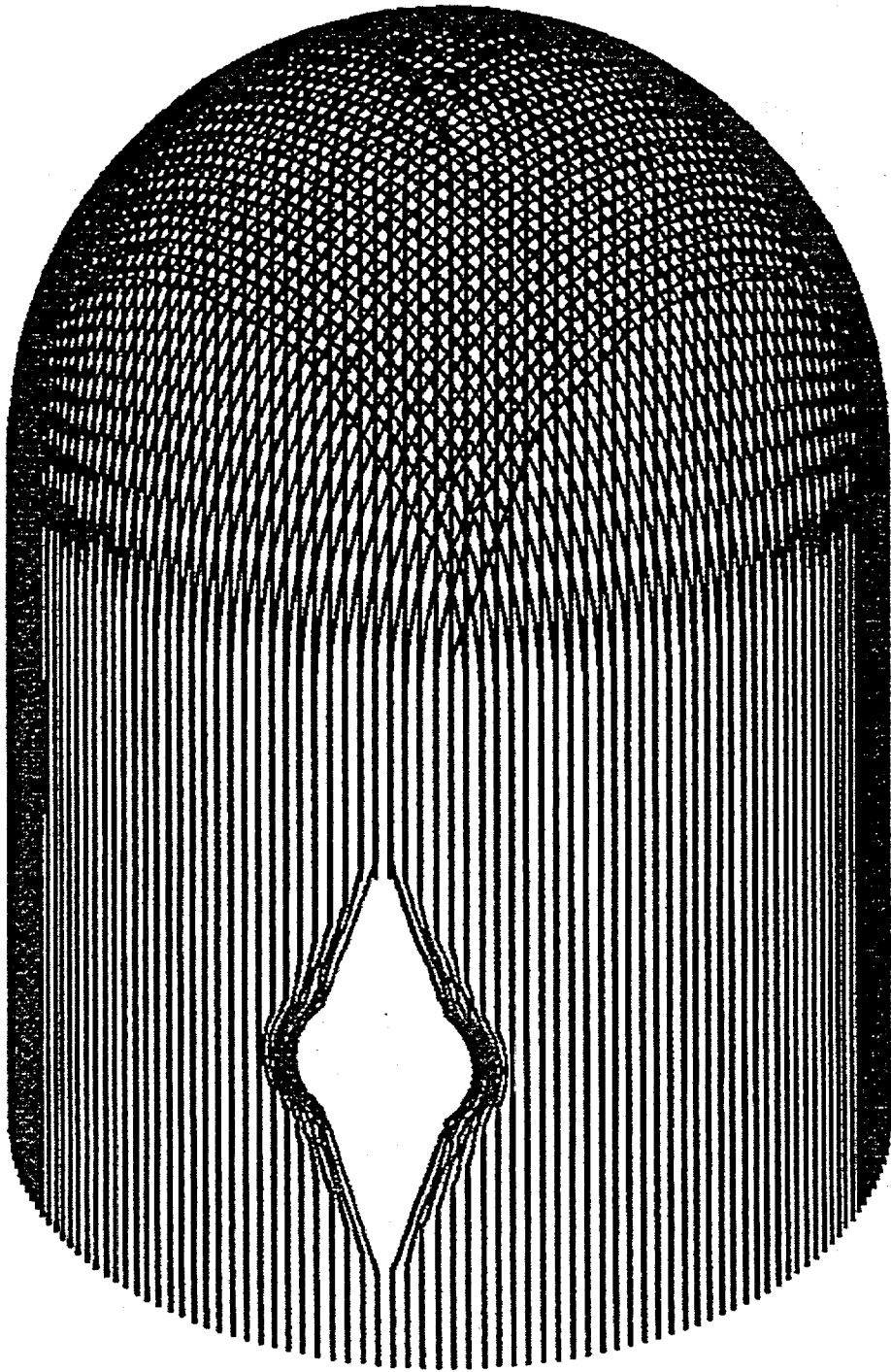


Figure 7: Truss elements of the vertical post-tension tendons

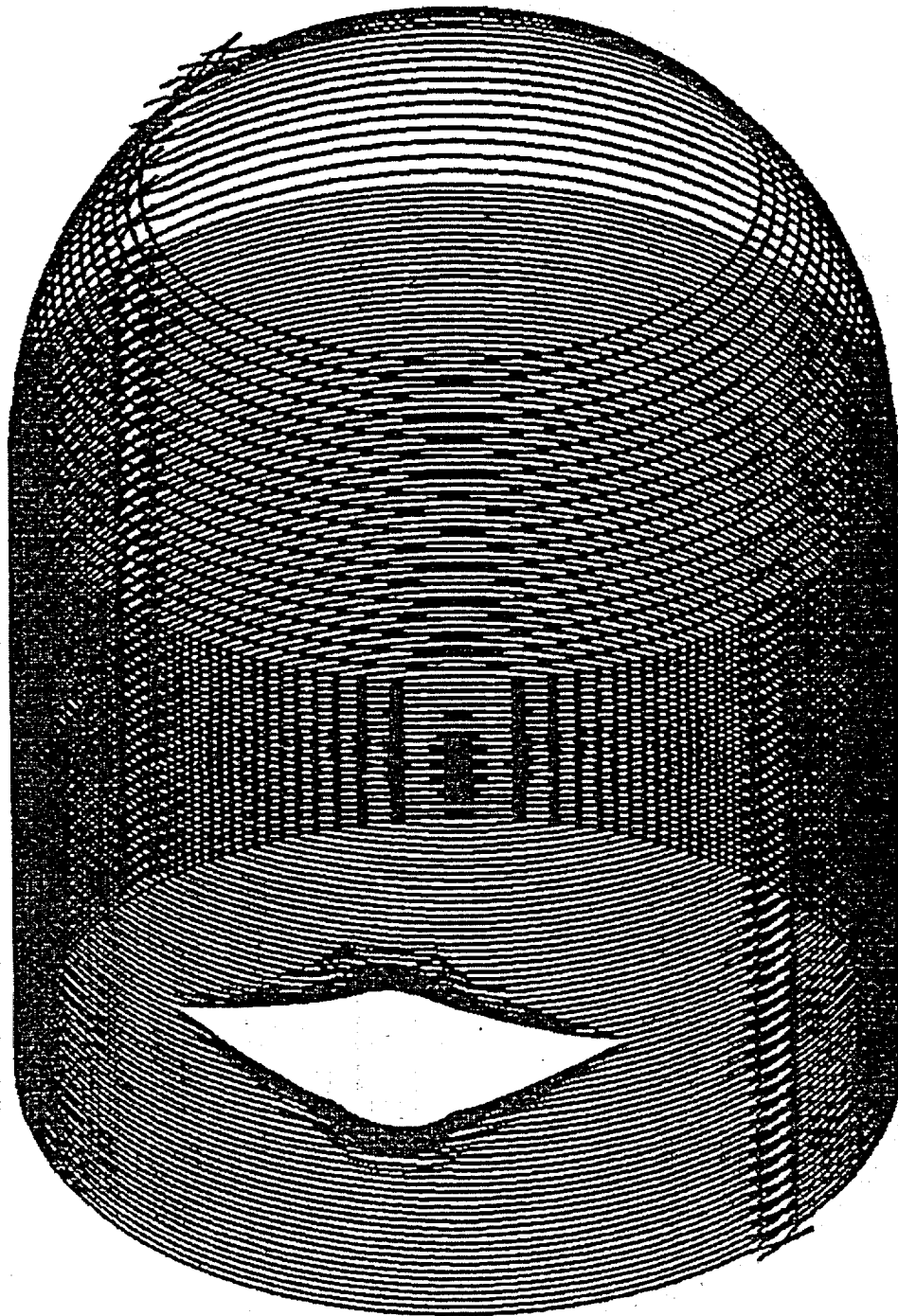
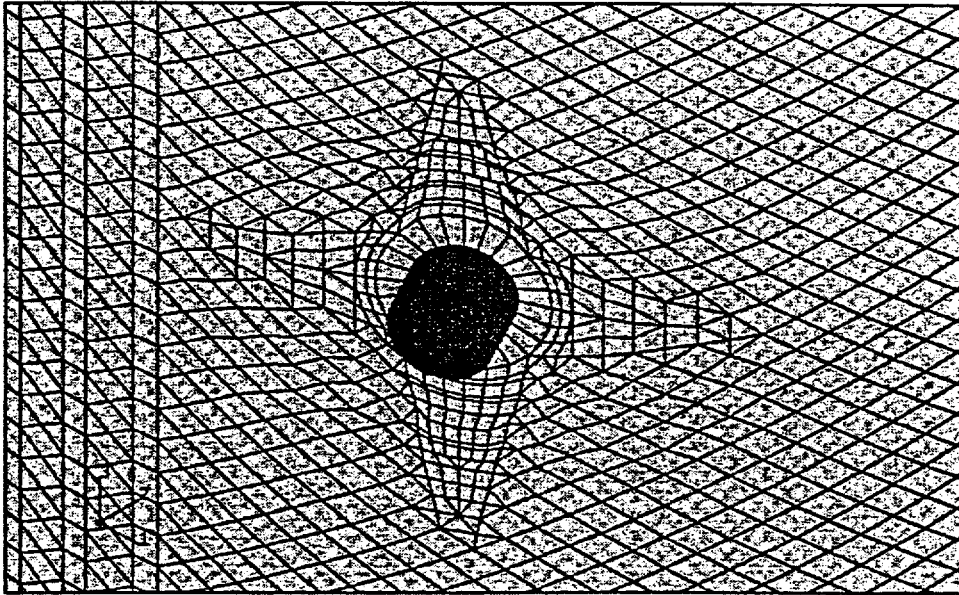
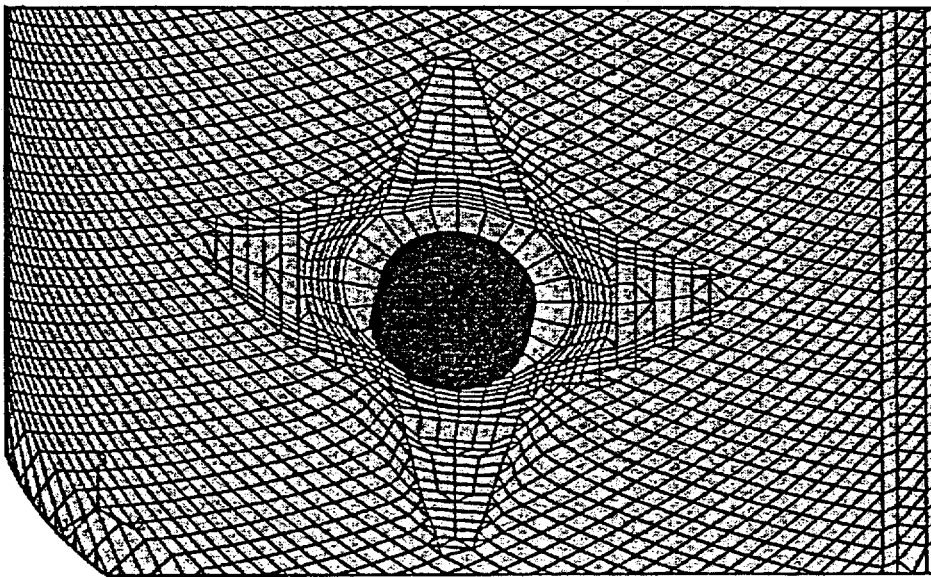


Figure 8: Truss elements of the hoop post-tension tendons

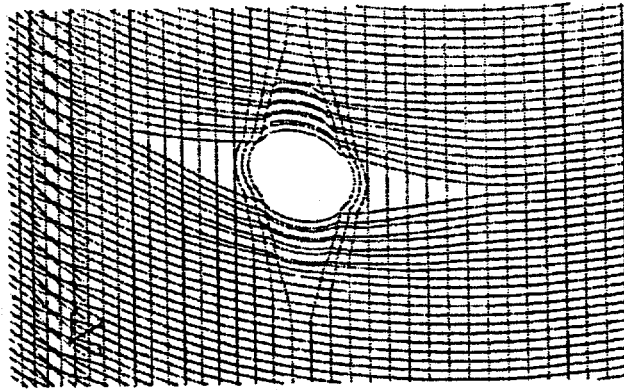


(a) Bulkhead at The Airlock

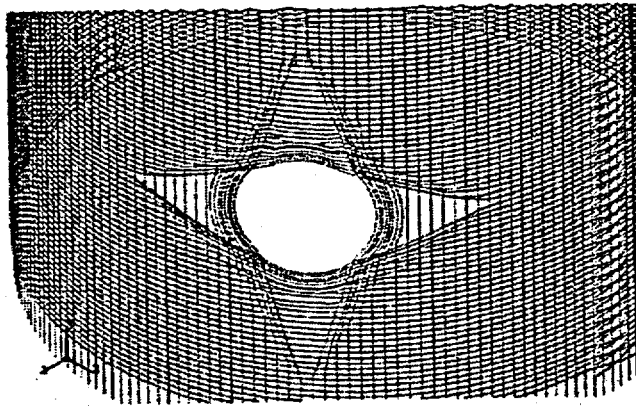


(b) Bulkhead at The Equipment Hatch

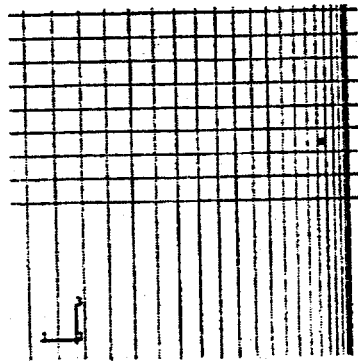
Figure 9: Details of the steel liner at major openings



(a) Post-tension Tendons at The Airlock

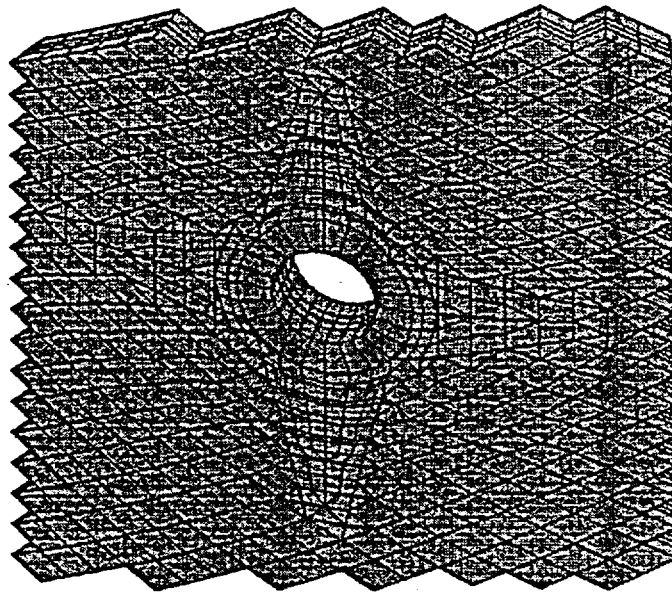


(b) Post-tension Tendons at The Equipment Hatch

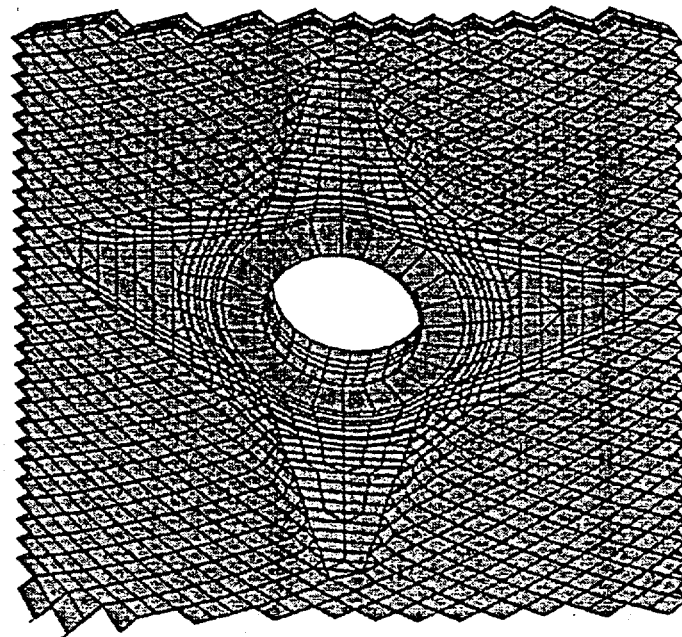


(c) Hoop and Vertical Post-tension Tendons in General Area

Figure 10: Details of the hoop and vertical post-tension tendons



(a) at Airlock



(b) at Equipment Hatch

Figure 11: Concrete elements at major openings of the PCCV

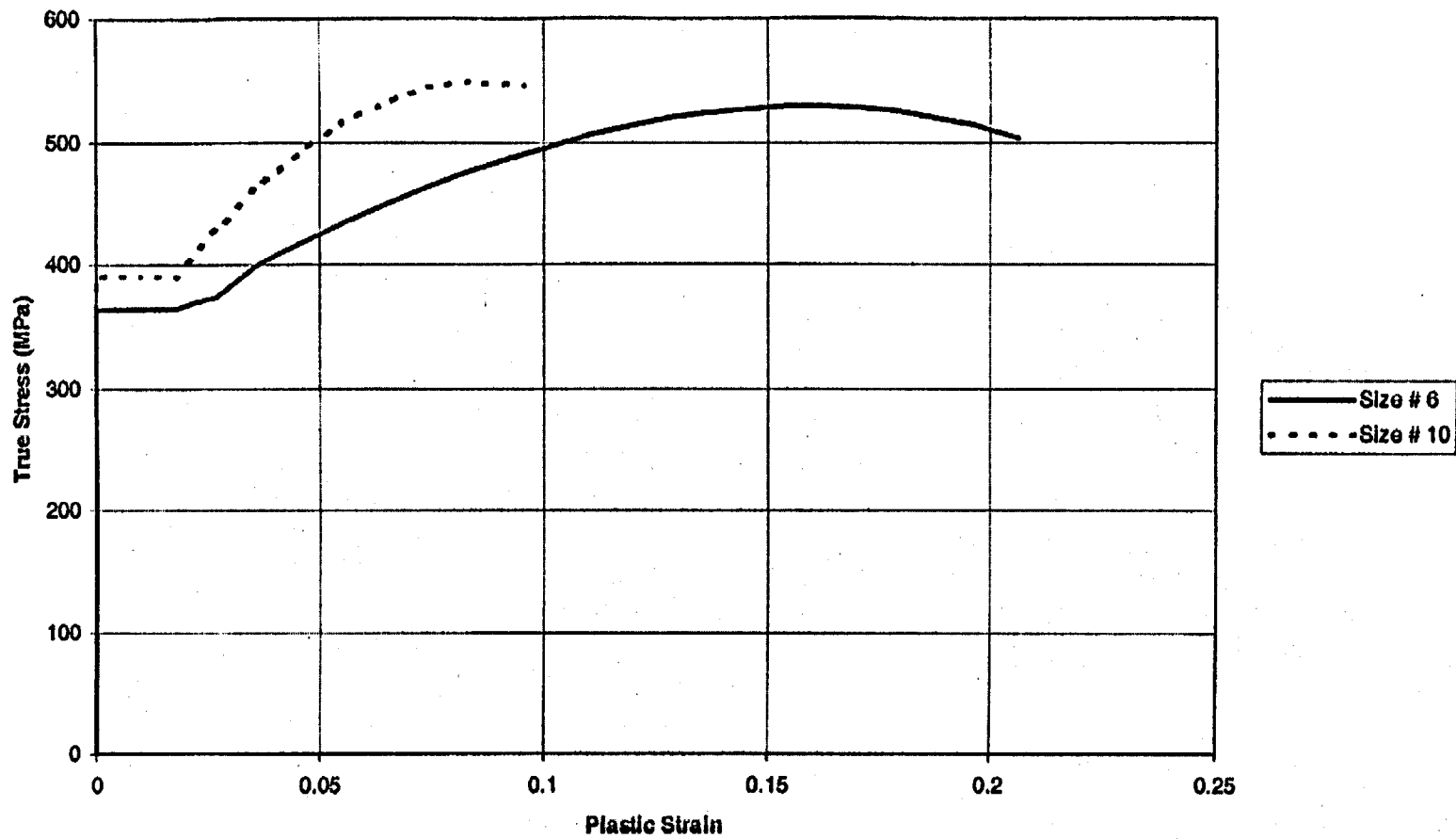


Figure 12: Plastic stress-strain relation for Type SD345 rebar

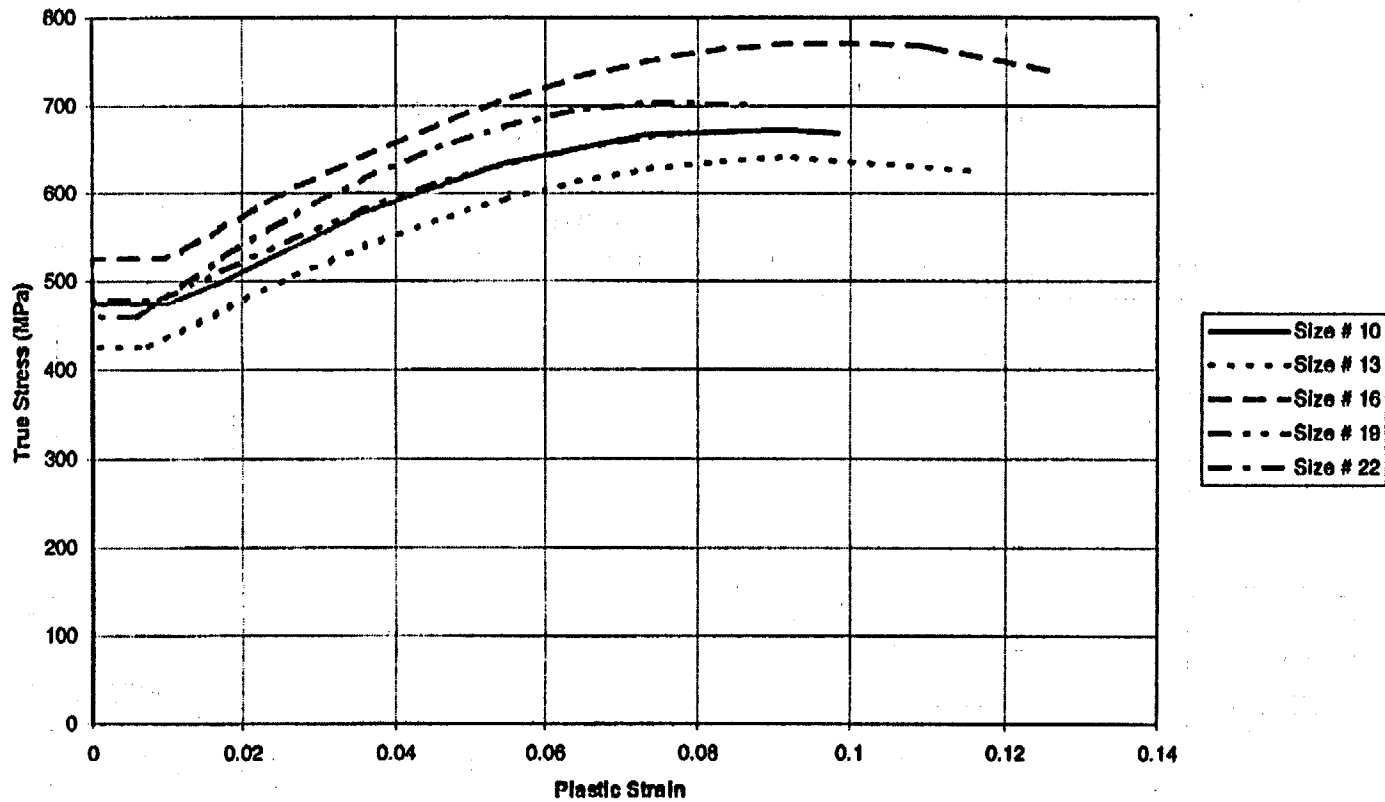


Figure 13: Plastic stress-strain relation for Type SD390 rebar

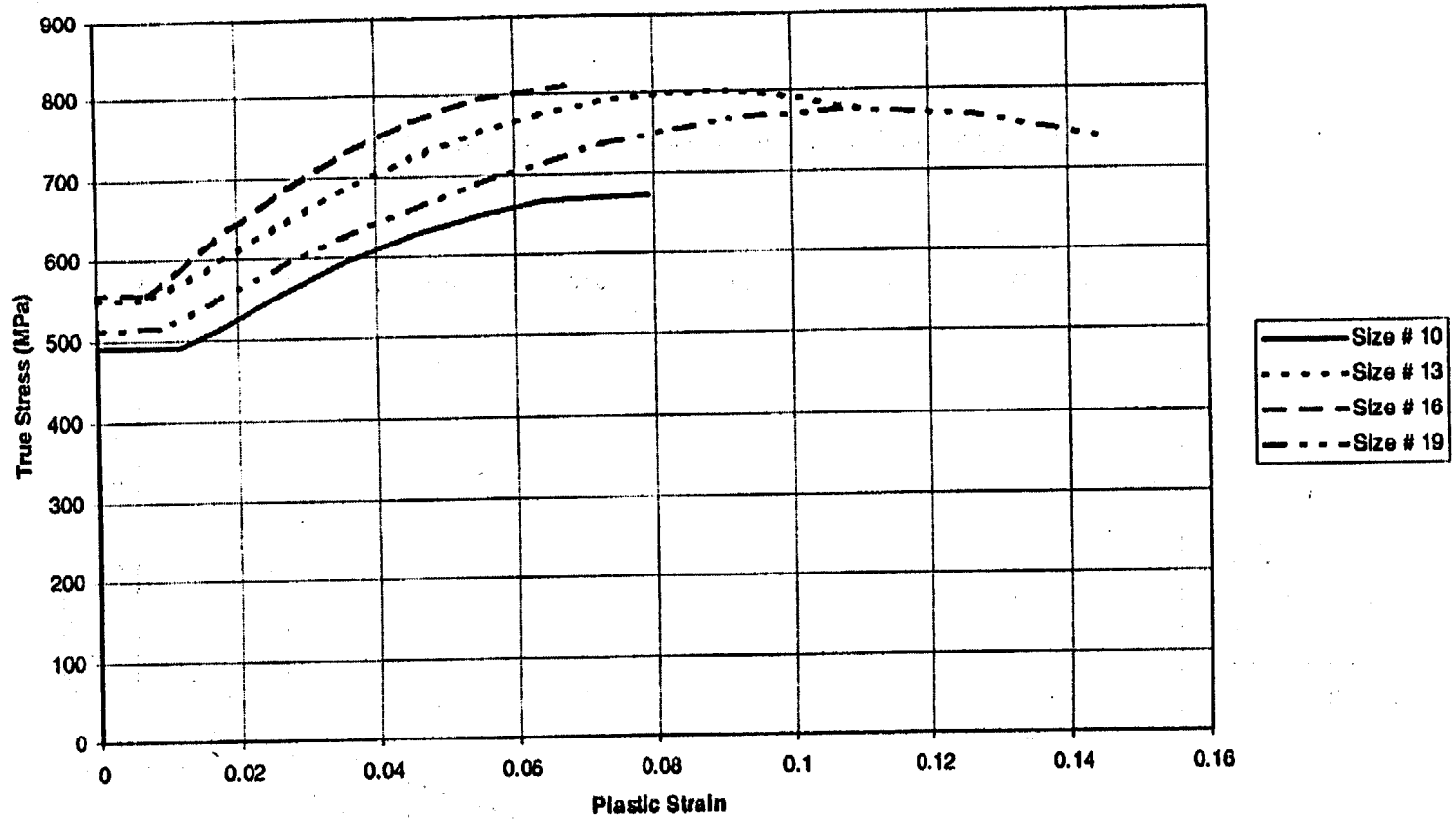


Figure 14: Plastic stress-strain relation for Type SD490 rebar

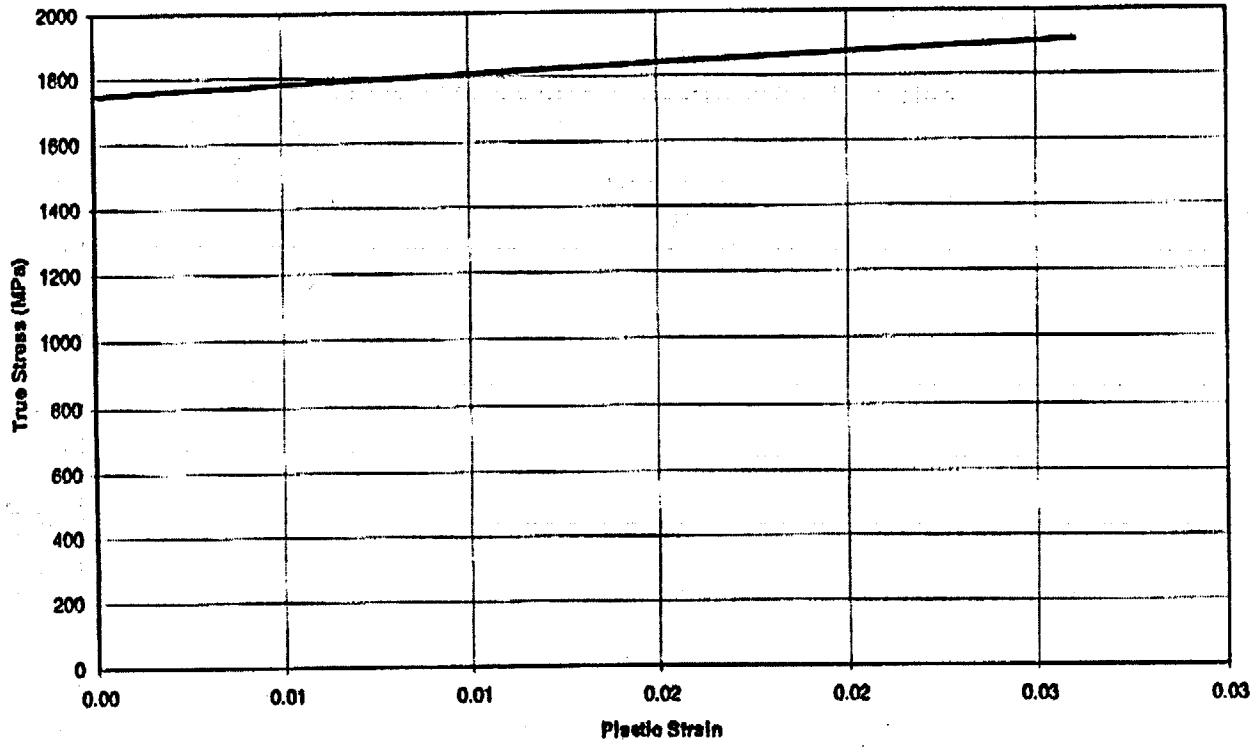


Figure 15: Plastic stress-strain relation for the tendons

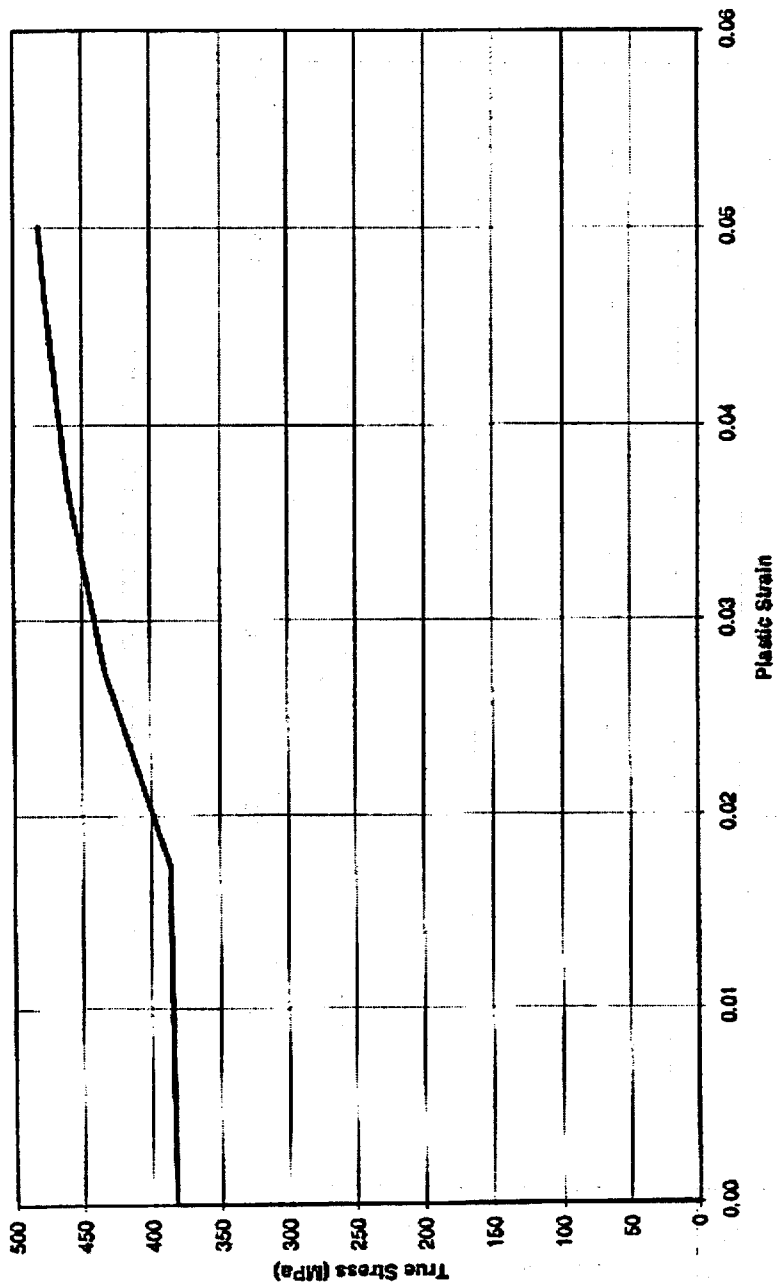
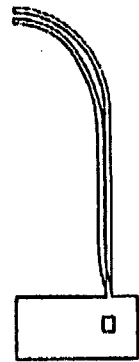
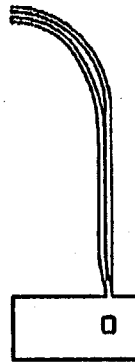


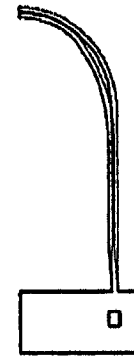
Figure 16: Plastic stress-strain relation for the steel liner



(i) due to pre-stressing load alone



(ii) due to dead and pre-stressing loads



(iii) at pressure of 390 kPa



(iv) at pressure of 854 kPa



(v) at pressure of 966 kPa



(vi) at pressure of 1240 kPa

Figure 17: Deformed shape of the PCCV at many stages of the applied load

Load-Displacement Curve

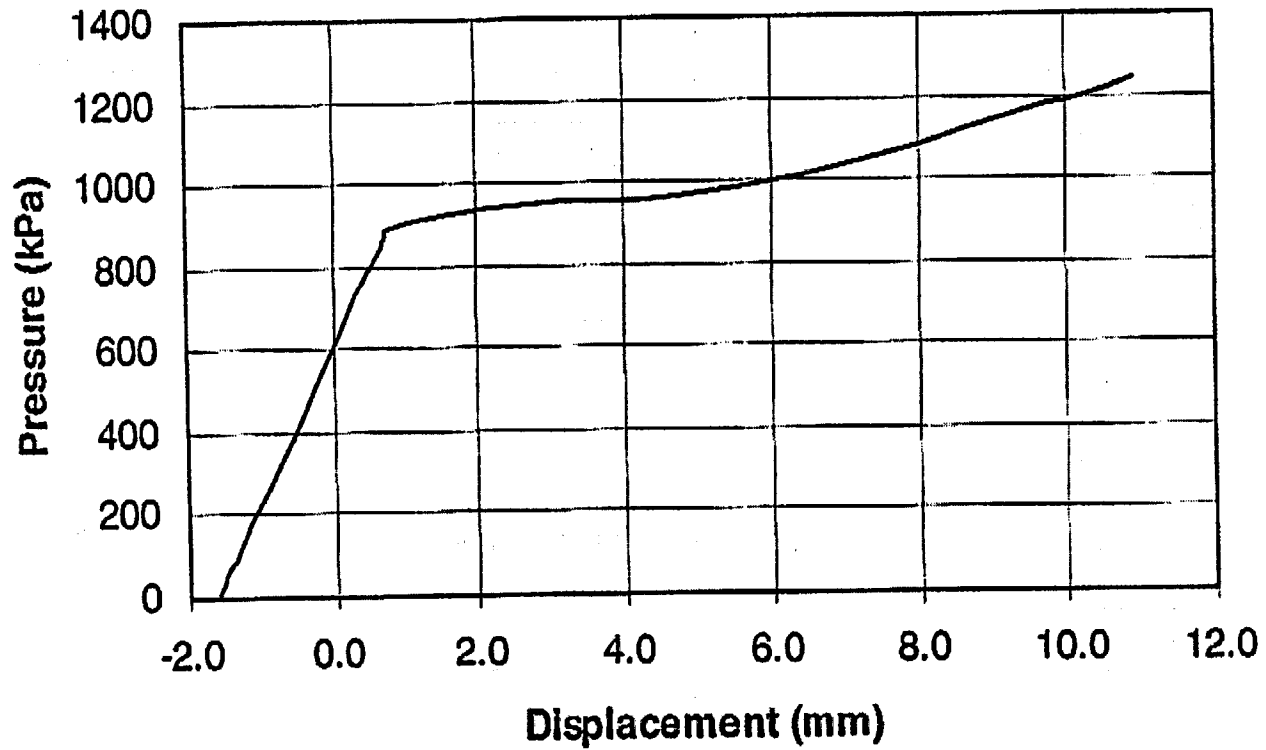


Figure 18: Pressure vs. spring line radial displacement for the PCCV

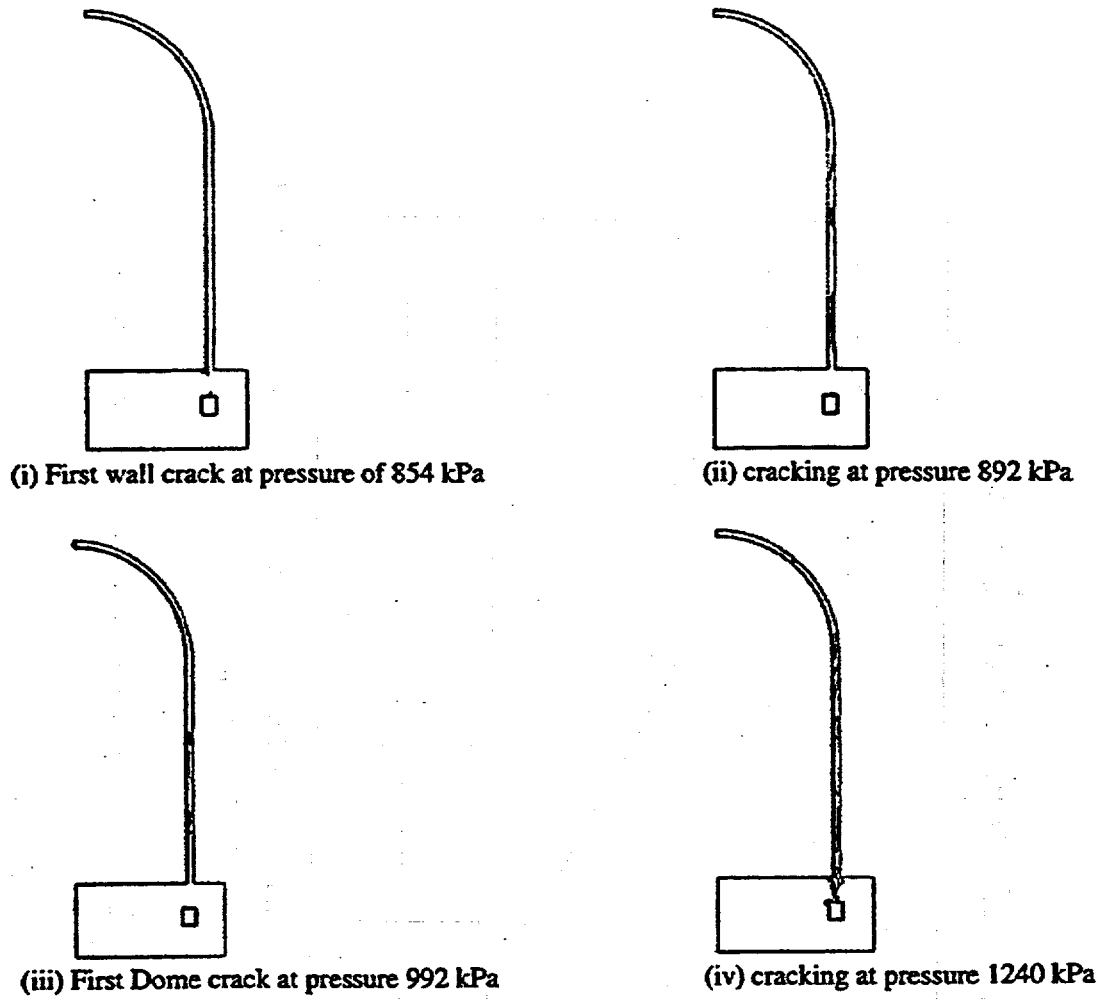


Figure 19: Cracking in the PCCV at different stages of the applied load

Tendon Stress-Strain Curve

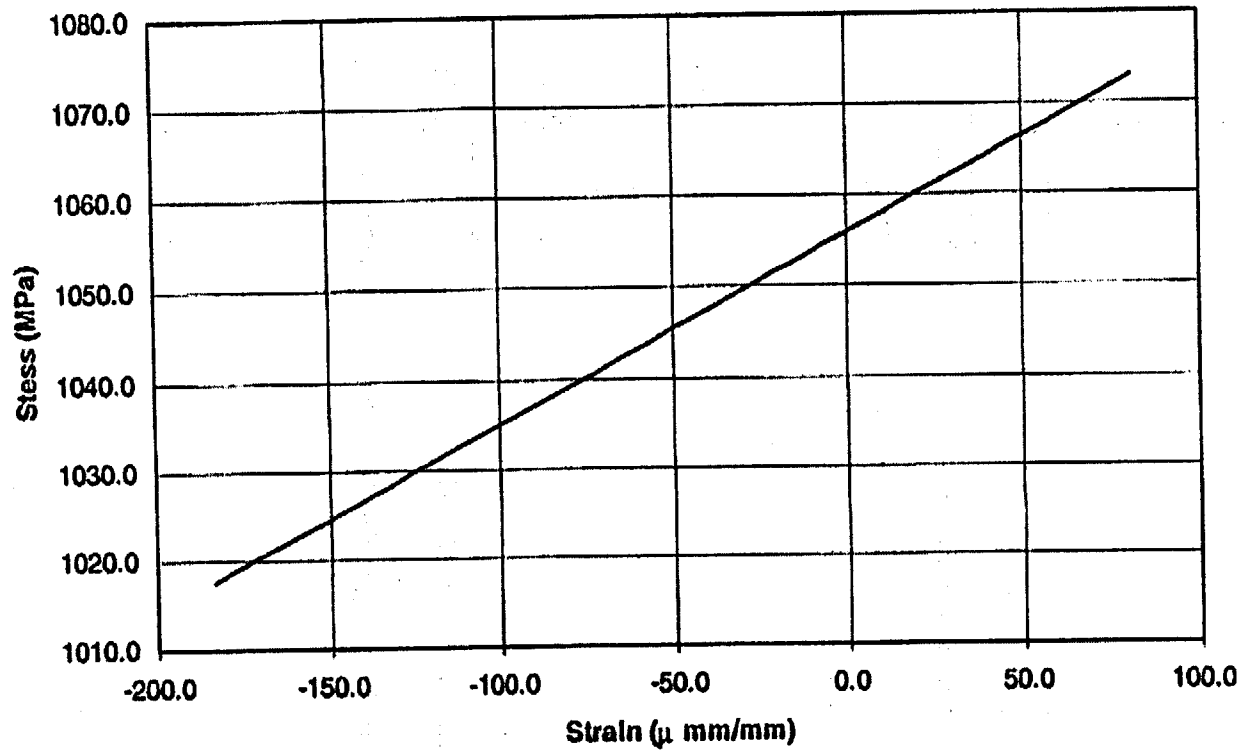


Figure 20: Stress-strain relation for the vertical post-tensioned tendon at the spring line

Inner Meridional Rebar Stress-Strain Curve

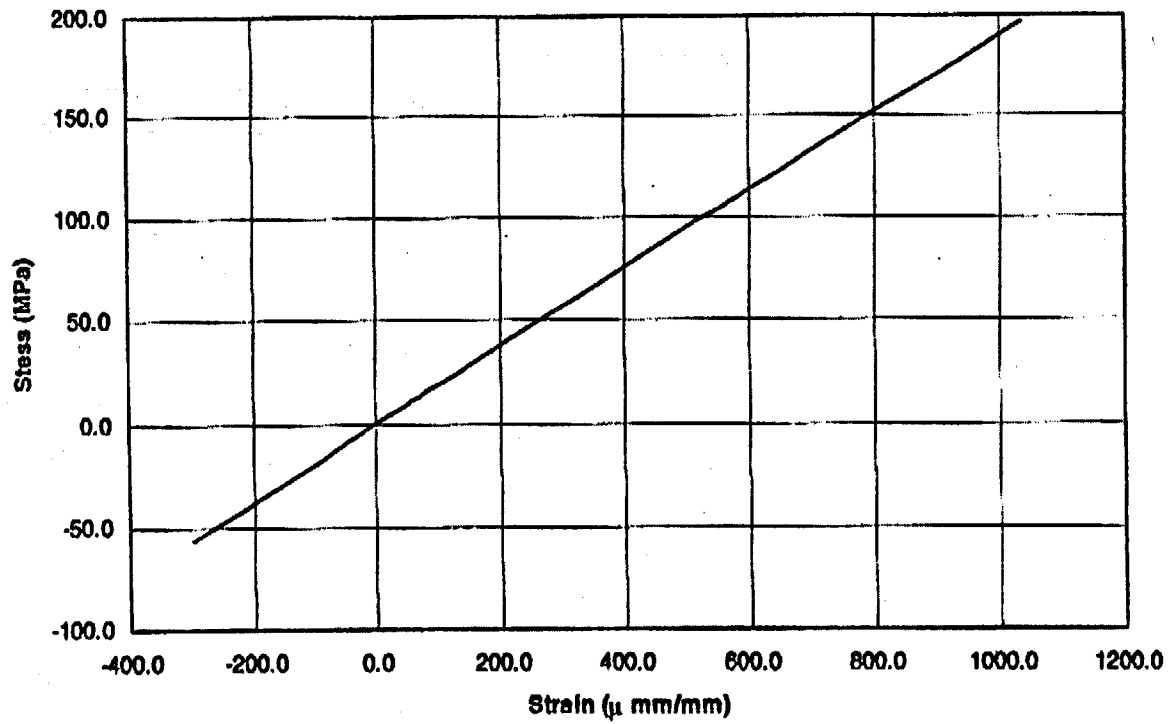


Figure 21: Stress-strain relation for the inner meridional rebar at the wall/basemat joint

Outer Meridional Rebar Stress-Strain Curve

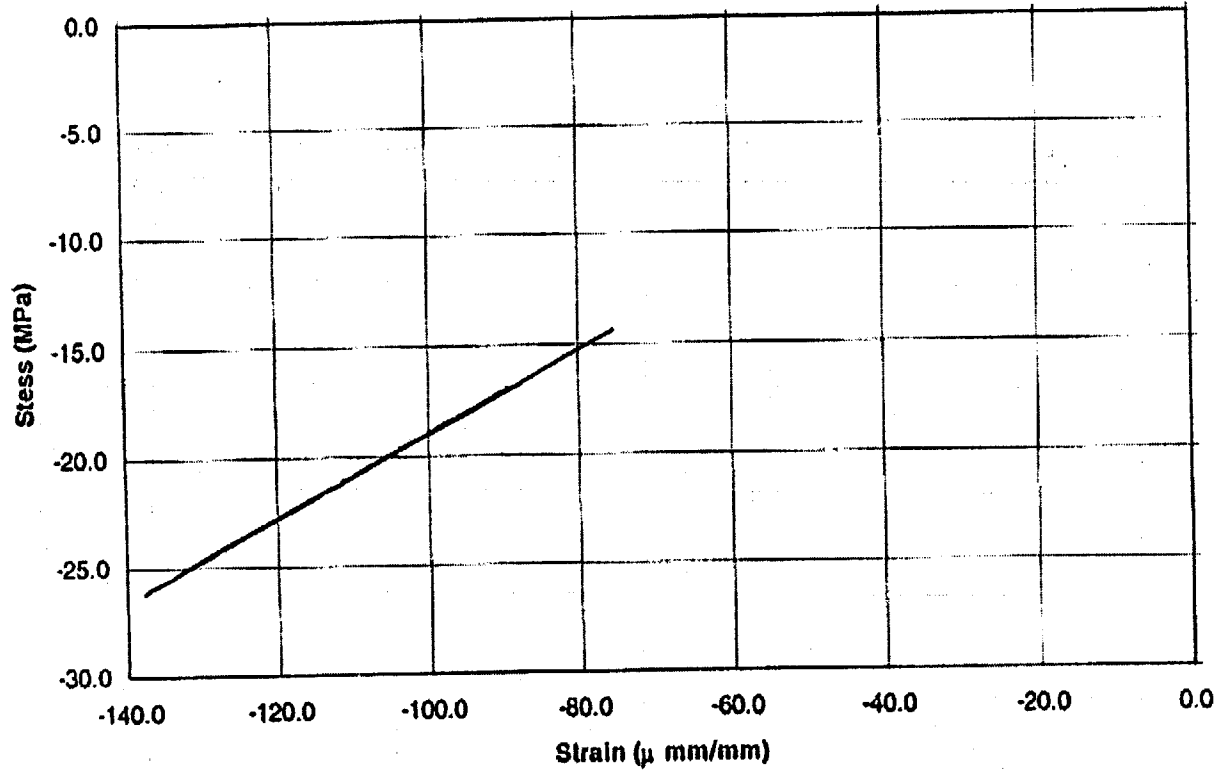


Figure 22: Stress-strain relation for the inner hoop rebar at the wall/basemat joint

Outer Hoop Rebar Stress-Strain Curve

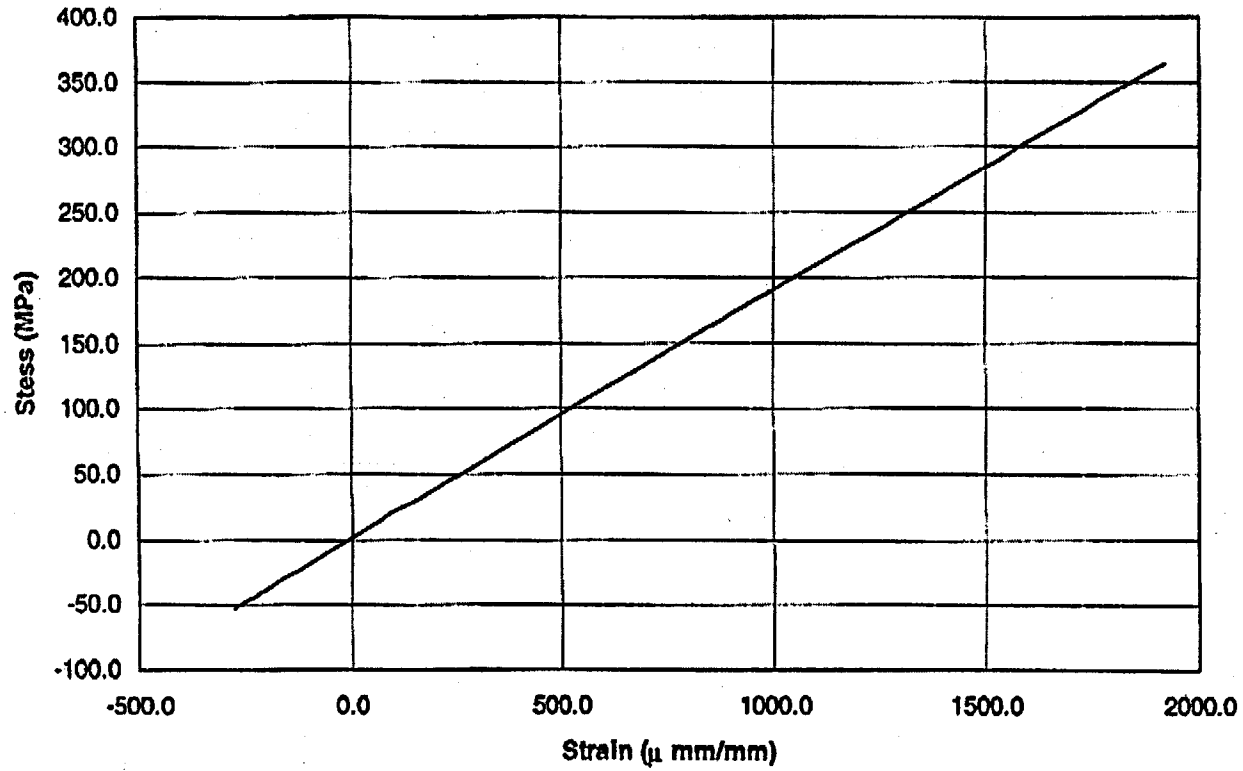


Figure 23: Stress-strain relation for the outer hoop rebar at the mid-height of the wall

Liner Hoop Stress-Strain Curve

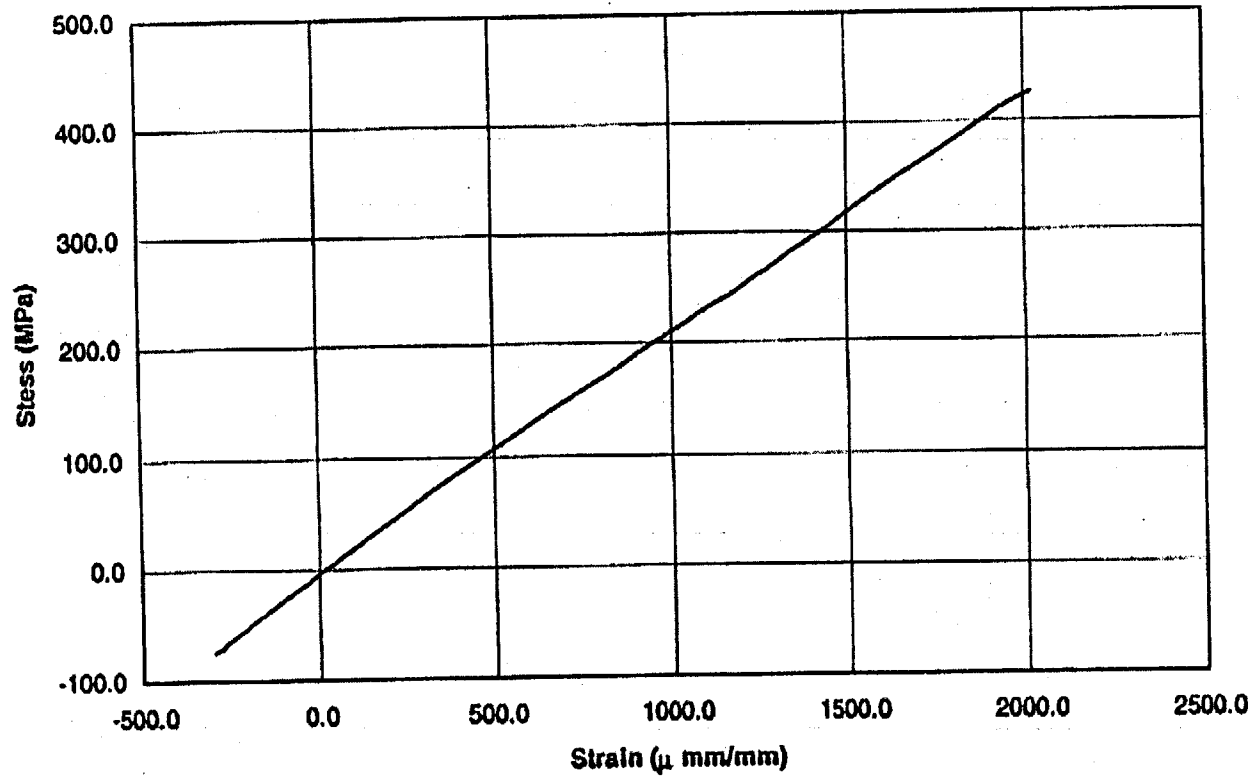


Figure 24: Hoop stress-strain relation for the steel liner at the mid-height of the wall

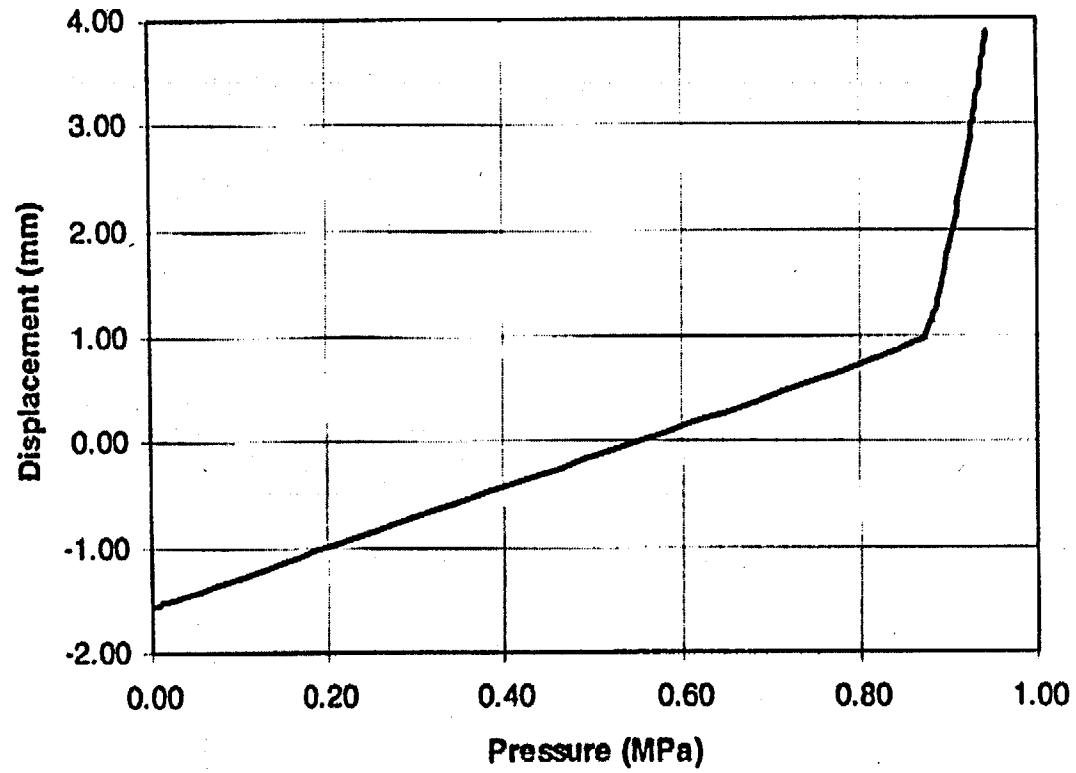


Figure 25: Pressure vs. wall mid-height radial displacement for the PCCV

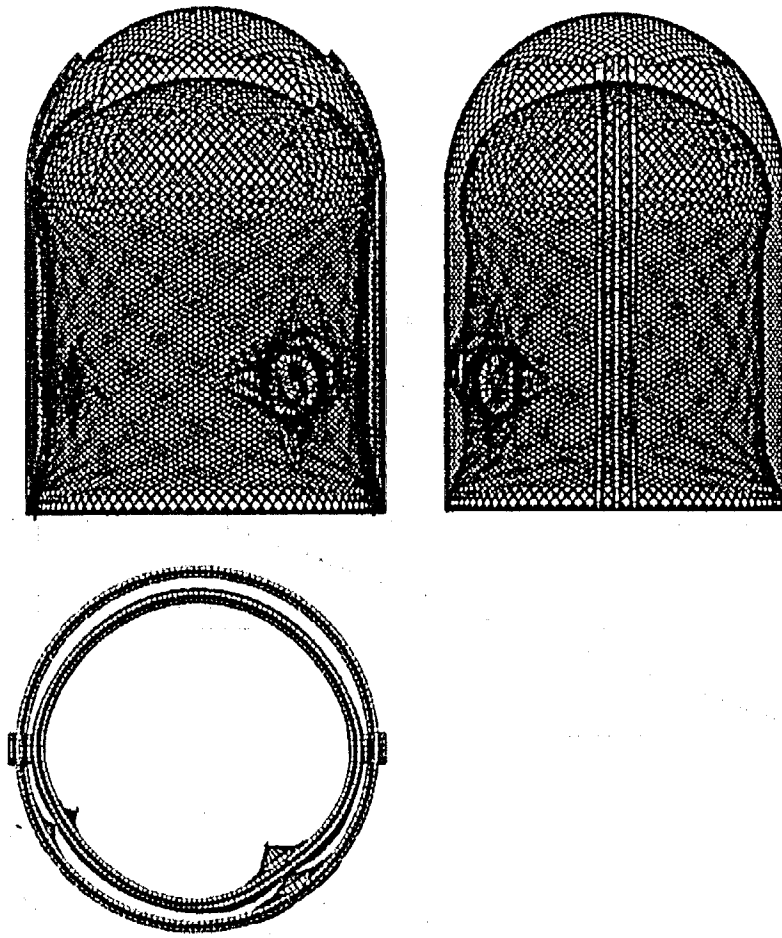


Figure 26: Deformed shape of the PCCV due to dead and prestressing loads

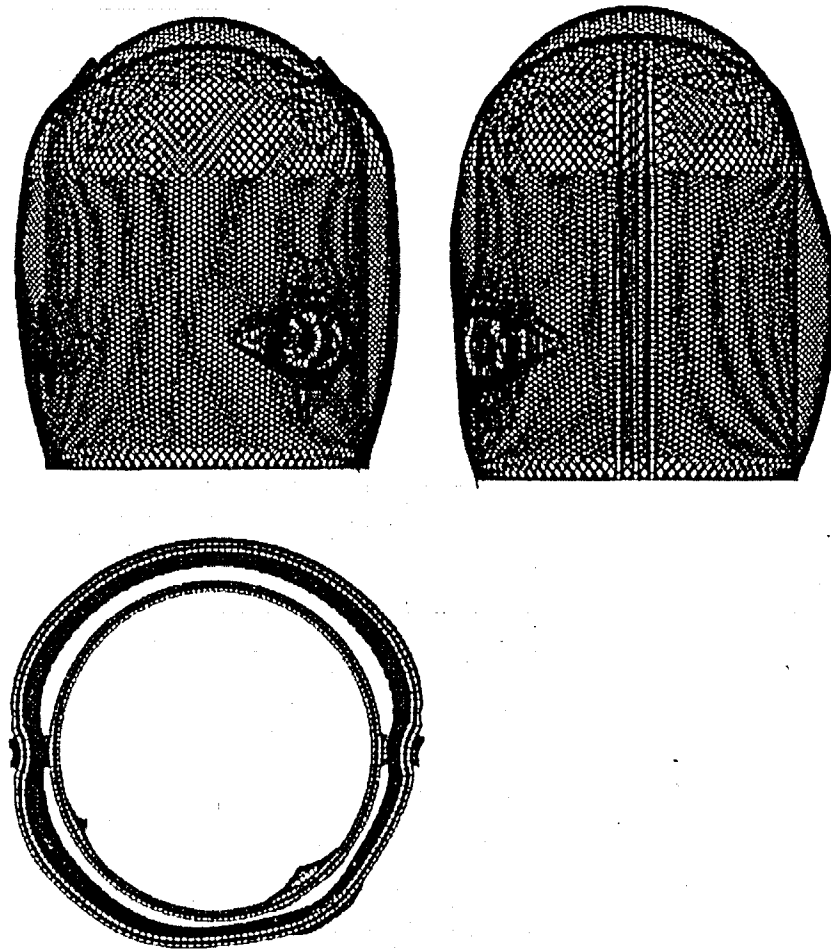
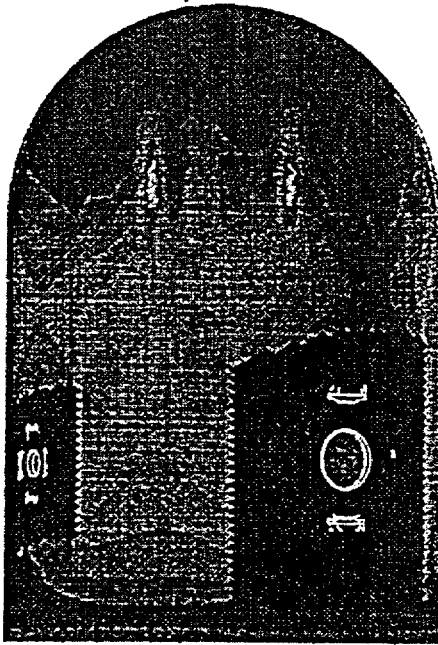
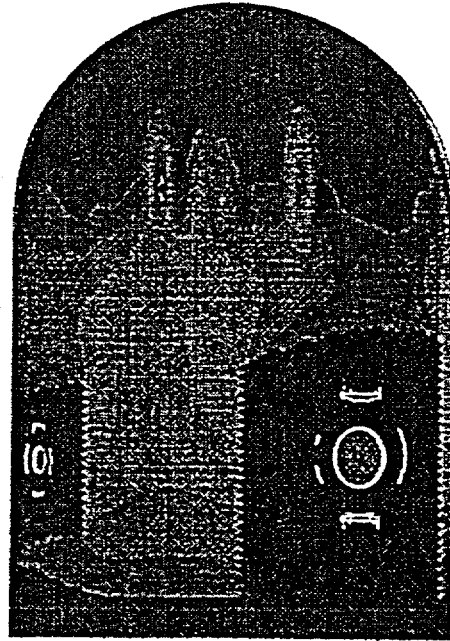


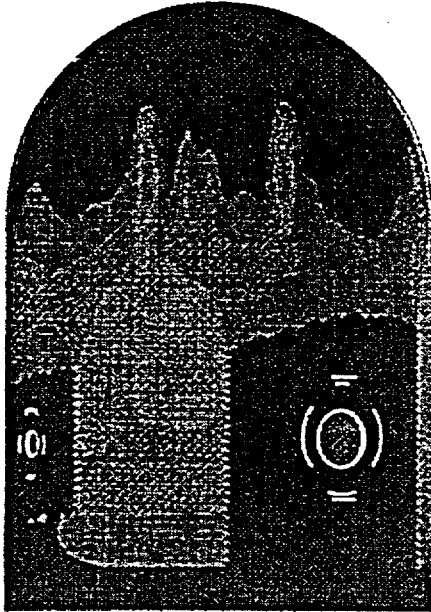
Figure 27: Deformed shape of the PCCV at pressure load of 944 kPa



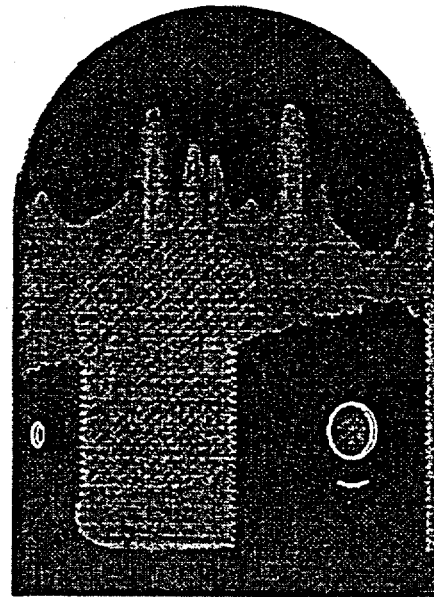
(a) Inside layer of elements



(b) Second layer of elements



(c) Third layer of elements



(d) Outside layer of elements

Figure 29: Cracking strain in concrete layers at pressure load of 944 kPa

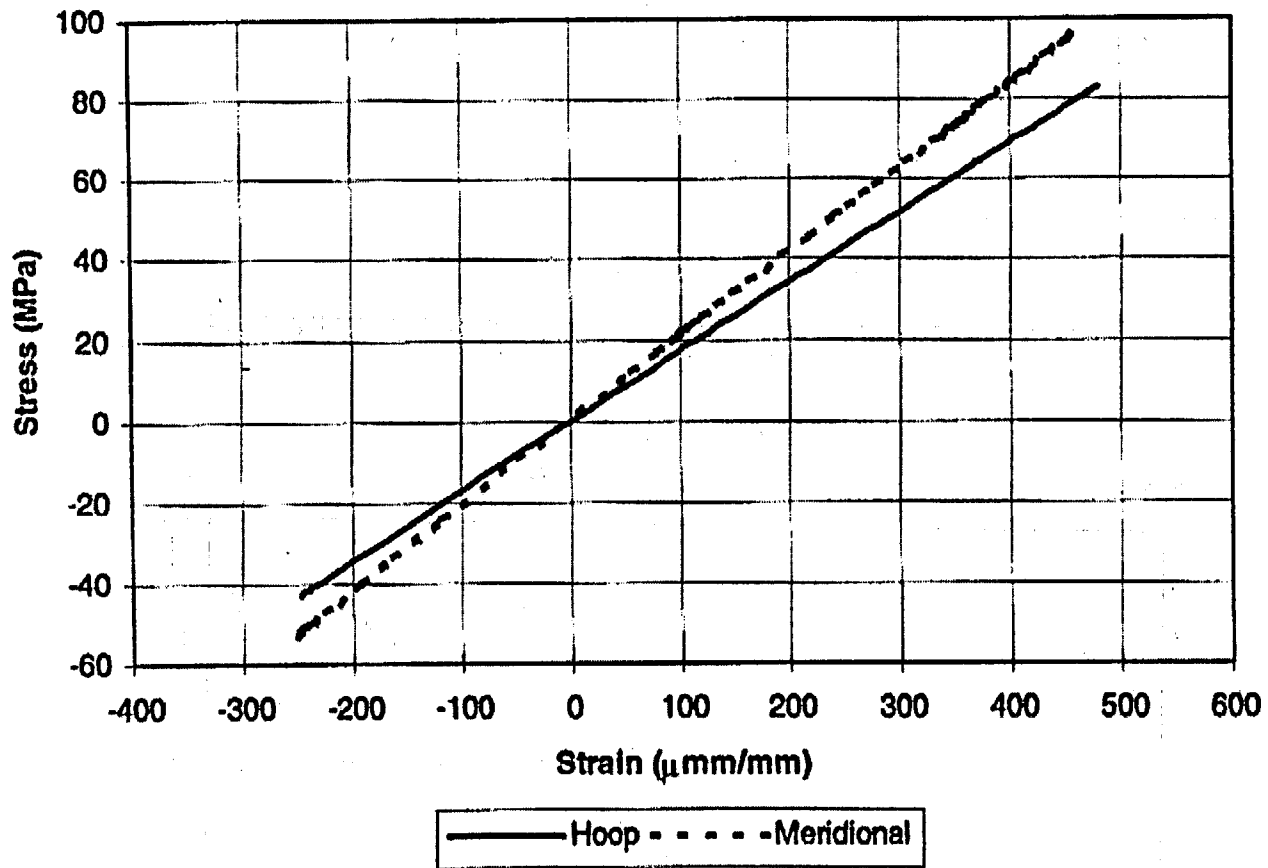


Figure 31: Stress-strain behavior for outer rebar at the PCCV wall mid-height

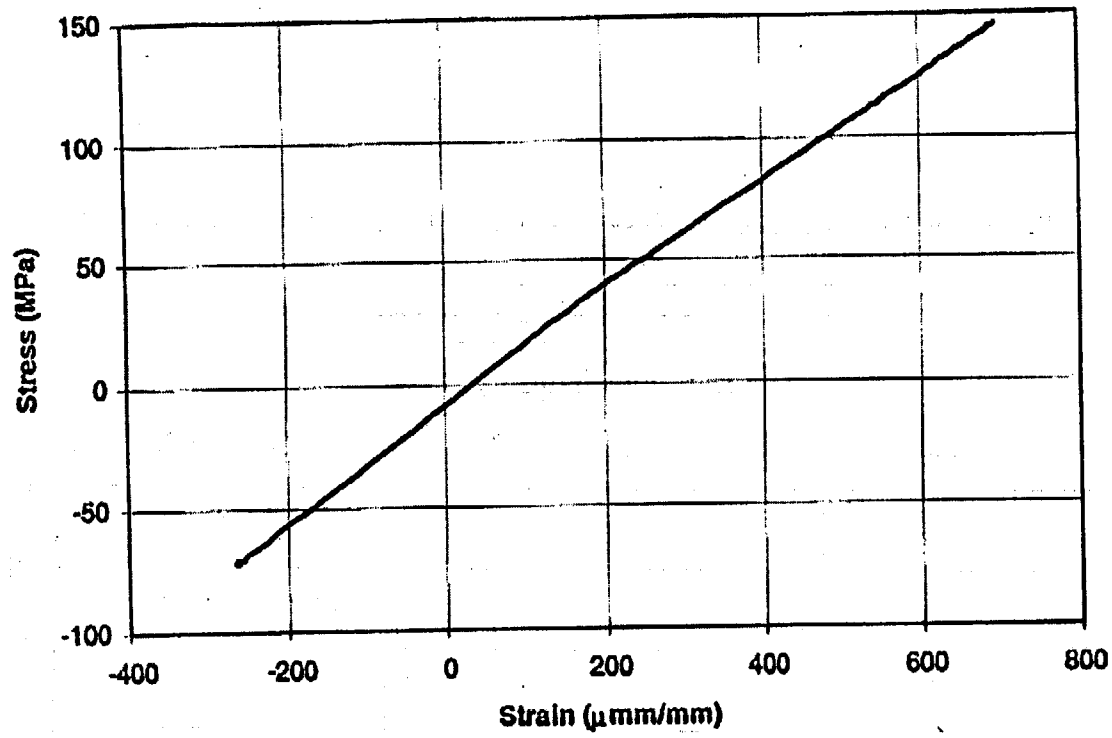


Figure 32: Stress-strain behavior for steel liner at the PCCV wall mid-height

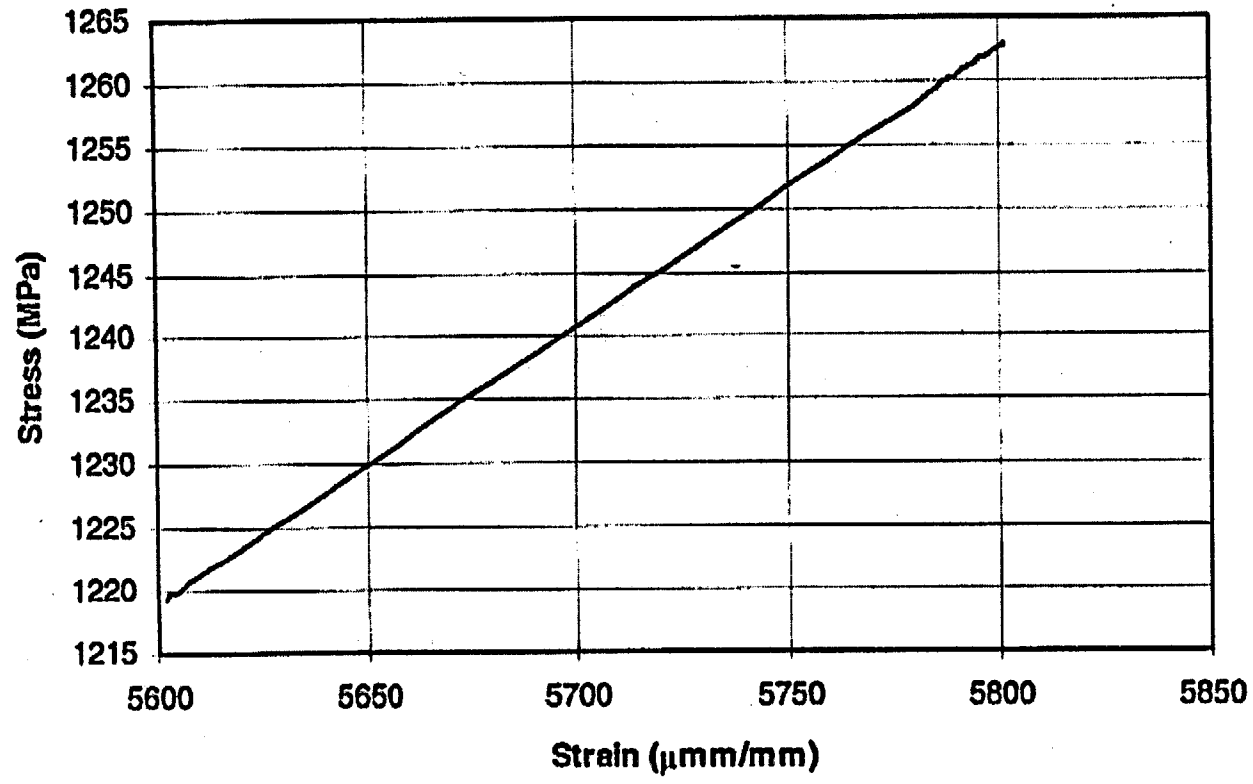


Figure 33: Stress-strain behavior for vertical tendon at the PCCV springline

APPENDIX C

ANL

**ARGONNE NATIONAL LABORATORY
UNITED STATES**

Appendix A, Composite Plots, comprises test data compiled and plotted from all organizations that participated in the Prestressed Concrete Containment Vessel (PCCV) Round Robin Pretest Analysis. To avoid duplicating the composite information, individual sets of data and/or plots have been omitted from participants' reports. In some cases this action resulted in disconnects between callouts and content and in the numbering of figures, tables, and pagination in some reports.

However, Appendix C, "ANL, Argonne National Laboratory, United States," contains none of these discontinuities.

Argonne National Laboratory
Round-Robin Pretest Analyses of a 1:4-Scale Prestress Concrete Containment
Vessel

INTRODUCTION

Pretest predictions were made by the Engineering Mechanics section of the Reactor Engineering Division at Argonne National Laboratory (ANL) for the response of the 1:4 scale Prestress Concrete Containment Vessel (PCCV) to be tested by Sandia National Laboratories (SNL). The PCCV model is scaled 1:4 uniformly in geometry of an existing water reactor (PWR) prestressed concrete containment vessel located in Japan. The model includes a steel liner with various penetrations (i.e. equipment hatch, personnel airlock, main steam and feed water lines). The design pressure of this prototype containment is 57 psi (0.39 MPa) gage.

SOLUTION METHOD

The computer code, TEMP-STRESS, was utilized in the pretest analyses and has been fully developed at ANL. TEMP-STRESS [1,2,3,4,5 and 6] is a two-dimensional finite element program that was developed for stress analysis of plane and axisymmetric 2-D metal and reinforced concrete structures under various thermal conditions. The code has evolved over the years to address safety issues. Since the code was developed to solve a variety of problems, the current version is a general purpose 2-D finite element code primarily suited for nonlinear problems. An important feature of TEMP-STRESS is its ability to handle nonlinear problems, which often occur during beyond-design basis loads. The element formulations can properly treat large deformations (i.e. geometric nonlinearities), and the rate-type material models can handle large material strains (i.e. material nonlinearities). A Von Mises elastic-plastic constitutive material law is utilized for yielding and post yielding of material. The failure model used is based on a Davis triaxial factor for a multi-axial state of stress, in combination with Von Mises elastic-plastic constitutive law. Explicit solution algorithms are used to economically solve short duration transient problems, and a dynamic relaxation (DR) method is utilized to simulate quasi-static problems.

The explicit time integration scheme is used in the TEMP-STRESS code. The numerical algorithm for the explicit time integration is based on the solution of the following equation of motion

$$m_u \ddot{u}_u + f_u^{int} = f_u^{ext}, \text{ (no sum)} \quad (1)$$

Where m_u is a diagonal mass matrix, u_u is a nodal displacement, f_u^{int} and f_u^{ext} are the internal and external nodal forces, respectively, of node I in the i th direction. Superscript dots are used to denote temporal derivatives. The equations of motion are solved using the central difference formulas. For static analysis the equilibrium equations are given by

$$f_u^{int} = f_u^{ext} \quad (2)$$

There are various methods available for obtaining static solutions, TEMP-STRESS uses the dynamic relaxation (DR) method. Details are provided in Ref. [3] on the numerical algorithm utilized for the DR method. The main problem associated with the DR algorithm, as well as other iterative techniques, is whether the current solution vector is close enough to the true solution so that the iteration process can be terminated. Premature termination will result in an incorrect solution, whereas excessive iterations will increase the time of the solution. An effective and efficient way to determine when the iteration process should cease is utilized in the code. The dual criteria used are

$$\frac{\|f_u^{ext,n} - f_u^{int,n}\|_2}{\|f_u^{ext,n}\|_2} \times 100 \leq \epsilon_f \quad (3)$$

$$\frac{\|u_u^{n+1/2} \Delta t\|_2}{\|u_u^{n+1}\|_2} \times 100 \leq \epsilon_u \quad (4)$$

where $\| \cdot \|_2$ indicates the Euclidean norm. Accurate results without excessive computations are usually obtained with $\epsilon_f = 0.25$ (i.e. 0.25% error) and $\epsilon_u = 0.02$ (0.02% change) in Eqs. (3) and (4). Equation (3) is a global force balance check of external and internal forces at an iteration step. Equation (4) is global displacement change at an iteration step. Once these equations are satisfied, the iteration process is terminated, a load increment is applied, and the iteration process is restarted. The DR method does not change the basic architecture of the central difference scheme, but enhances it so that static problems can be solved.

MODEL DESCRIPTION

TEMP-STRESS is a 2-D code for the stress analysis of plane and axisymmetric reinforced/prestressed concrete problems. A flexural element (axisymmetric shell) with two-point integration along its length and five integration points through the depth is used for the concrete cylinder and dome of the structure. The rebars are modeled by what is known as

“homogenization”: the stress-strain law for the rebars is embedded in the stress-strain response of the elements. This approach can account for the direction, position and amount of reinforcement. The rebars are assumed to remain rigidly bonded to the concrete; debonding of the rebars with the concrete is not considered.

Reinforcement in the flexural element can be specified at arbitrary layers measured from the neutral axis and spanning from the axial (meridional) direction through the hoop direction. Inclined reinforcement through the depth of the cross-section, representing the connecting ties, can also be treated. Reinforcement options in the flexural element are shown in Figure 1. The flexural elements account for cracking in the concrete, two orthogonal cracks may occur in the axisymmetric shell element at each integration point: one in the hoop direction and one in the meridional direction. In addition to reinforcement specified within the concrete element, reinforcement/prestressing can also be modeled by means of discrete rod and ring elements. The combination of homogenized and discrete elements can this be used to represent the details of reinforcement in the containment structures.

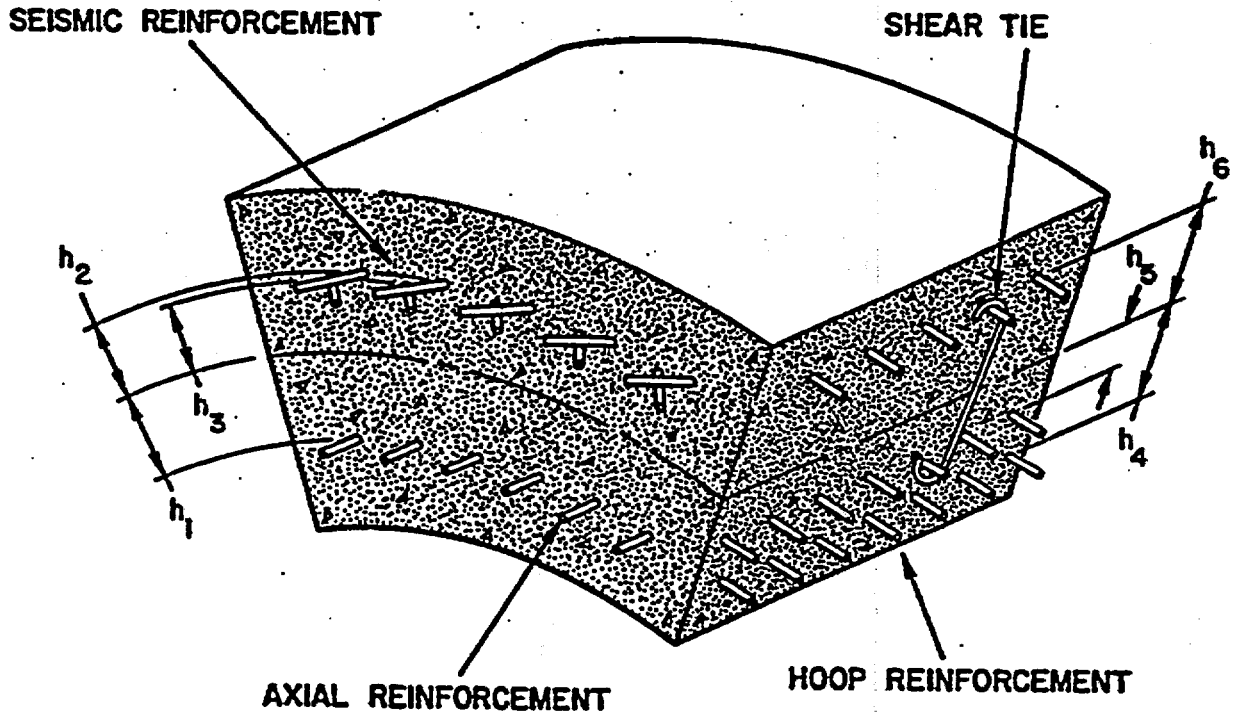


Figure 1. Representation of Reinforcement in Concrete for the Axisymmetric Shell Element

The axisymmetric finite element model is depicted in Figure 2. The numerical model consists of the reinforced concrete, meridional prestress tendons, hoop prestress tendons and the liner. Nominal thicknesses for the concrete wall and liner plate were used, and nominal areas for the reinforcement and tendons were used. The centerline mesh of the reinforced concrete wall is the outer mesh and the inside mesh is the liner as shown in the Fig. 2. Boundary conditions of the finite element model are as follows: 1) at the bottom ($Y = 0$), where the cylinder wall meets the basemat, the rotation, x displacement, and y displacement are restrained, and 2) at the top ($X = 0$) a symmetry boundary condition is applied, which means the rotation and x displacement are restrained. The reinforced concrete wall is modeled by 50 axisymmetric shell elements, with 32 elements in the cylinder and 18 elements in the dome. The liner is modeled by 50 axisymmetric membrane elements, with 32 elements in the cylinder and 18 elements in the dome. The prestressing bar elements for the meridional tendons are overlaid on the reinforced concrete elements.

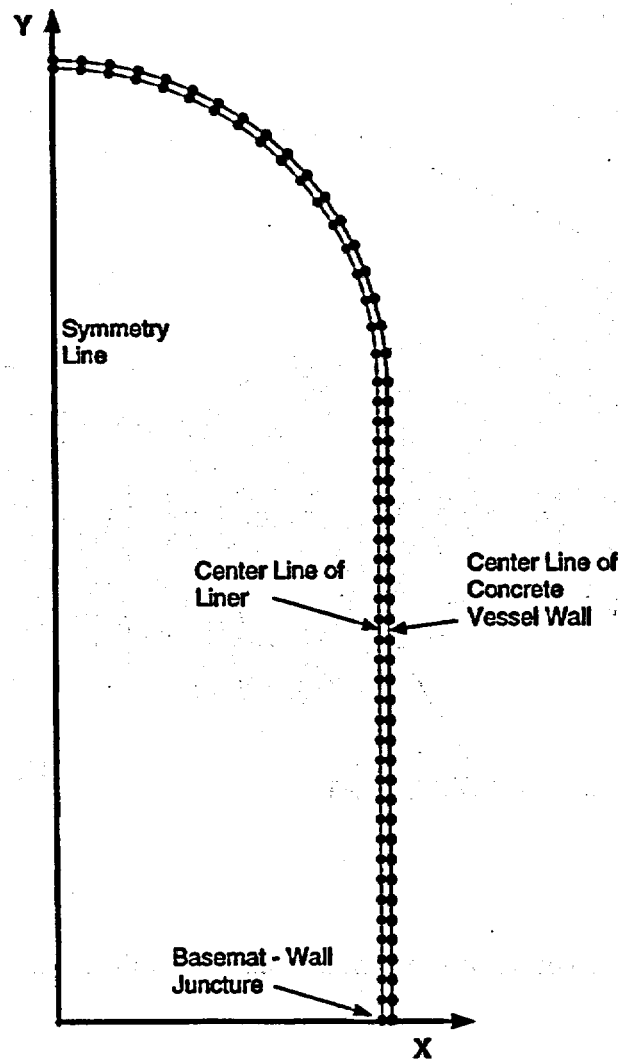


Figure 2. Axisymmetric Finite Element Mesh of PCCV

The nodes for the prestressing bar elements are, thus, overlaid on the nodes for the concrete elements. A slide line is provided to simulate the tendon and duct interface (at this time no friction was assumed). The hoop prestressing ring elements utilize the same nodes of the reinforced concrete element nodes, a total of 40 ring elements (31 in the cylinder and 9 in the lower half of the dome) were used to model the hoop prestressing. The concrete shell and liner used 51 nodes each and the slider uses 49 nodes over the concrete nodes (the apex and the basemat-wall juncture nodes of the concrete shell tie into the slider).

The hairpin prestressing cables use in the actual containment model were modeled as meridional tendons in the cylinder and lower half of the dome ($< 45^\circ$), and a combination of hoop tendons and meridional tendons were used in the upper half of the dome ($> 45^\circ$). This avoids having the entire hairpin prestressing tendons passing over the apex of the dome. Originally, the entire hairpin tendons were modeled as meridional tendons and this caused the dome concrete to crack and the dome rebars to yield (several elements near the dome apex). Thus, in the numerical model of one radian (i.e. axisymmetric), 9 layers of partial meridional prestressing were utilized from the mesh size in the dome. This method provides only one tendon, which passes over the dome apex, and as each meridional layer (equivalent to approximately 3 tendons in cross-sectional area) is terminated it is replaced with a hoop tendon (of the same equivalent area) in the upper half of the dome. A total of 455 bar elements were used to model the hairpin cables and 9 ring elements were used to model the equivalent hoop tendons in the upper half of the dome (i.e. converted meridional bar elements).

In summary, a total of 604 elements and 151 nodes (51 concrete, 51 liner and 49 slider nodes) were utilized in the finite element model of the PCCV in Fig. 2.

MATERIAL MODELS

Both the steel and the concrete are modeled as nonlinear materials. The constitutive equations for these materials are based on elastic-plastic law with initial yielding and the subsequent loading surface described by the von Mises condition.

The uniaxial strength data for the materials is given in Figures 3, 4, 5 and 6 for the reinforcing bars (rebar), concrete, prestressing cables and liner material, respectively. The rebar material properties are modified to take into account the strength of the couplers (i.e. splicing of rebar). The strength of the rebar is assumed to be the failure strain of the couplers, for SD390 it was 7.1% strain and for the SD490 it was 7.8%. The failure strain values used are approximately the average from the test data provided by SNL[11]. The values depicted in Fig. 3 are true stress-true strain for the rebar response.

The strength capacity of the concrete in multiaxial stress space is characterized by the so-called Hsieh-Ting-Chen [7] four-parameter failure surface. The concrete response after failure is simulated using the element size independent cracking criterion established by Bazant and Oh [8]. In the uniaxial tensile stress-strain relationship, a linear reduction of strength is specified from the cracking strength down to zero. The maximum strain in tension, where the cracking stress is specified as zero, is approximately 0.6 % strain for the fracture energy used and the

mesh size chosen. The input data required to define the failure surface is given in Table 1. The values of Young's modulus, Poisson's ratio and the tensile strength were based on the material data from the trial mix concrete provided by SNL in Ref. [11] on page 32, Table 4 "Material data for the trial mix concrete" for field curing of $f_c' = 44.13$ MPa concrete. The compression stress-strain input for 44 MPa (6480 psi) compressive strength concrete is shown in Figure 4, the actual strength of 47.3 MPa (6860 psi) is based on the 13-week strength provided by SNL in Ref. [11] on page 32, Table 5 "Concrete strengths of concrete for pours to date" for field curing of $f_c' = 44.13$ MPa concrete. As indicated in Fig. 4, the concrete is assumed to fail at 0.3% strain under uniaxial compression. The fracture energy of the concrete was determined from the empirical formula given in Ref. [8], which is based on the tensile strength ($f_t' = 500$ psi) and maximum aggregate size (d_a was assumed to be 0.375 inch) of the concrete.

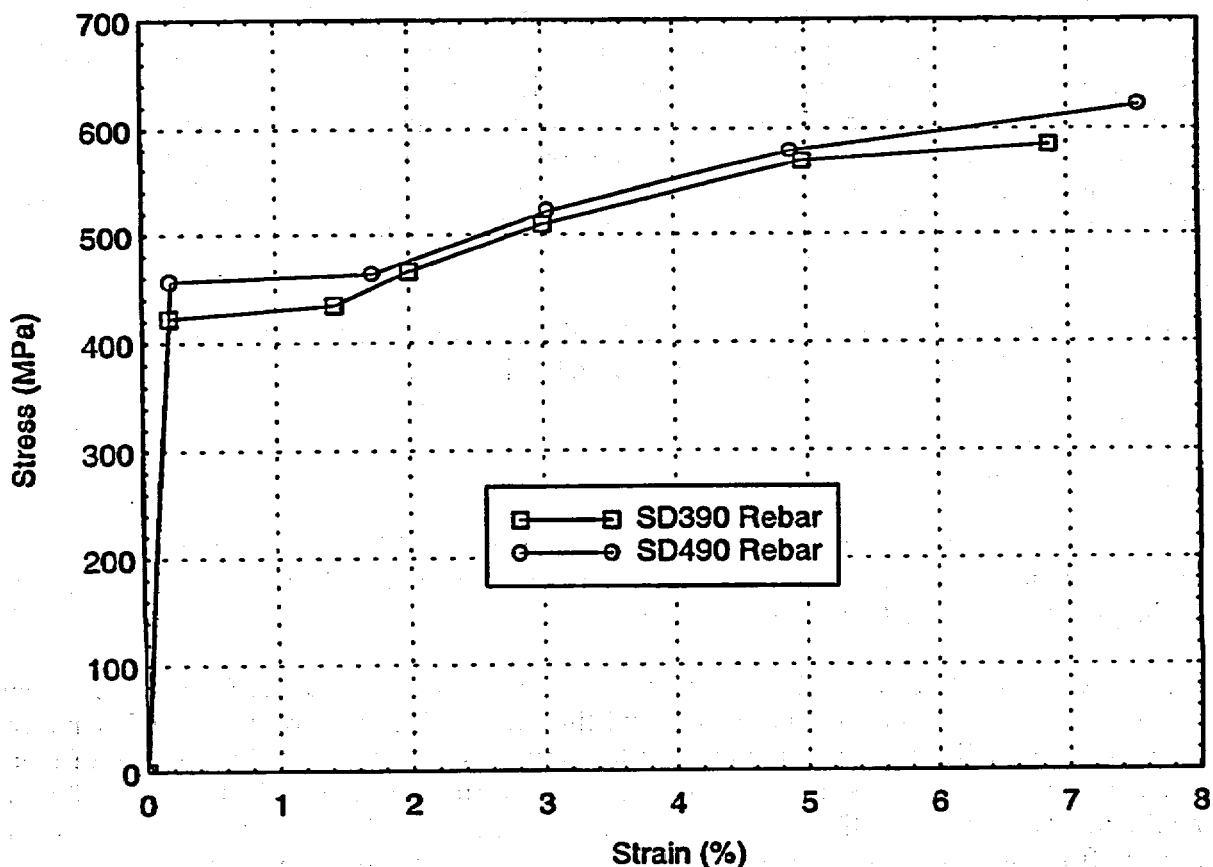


Figure 3. Reinforcement Bar True Stress - True Strain Response

With: Young's modulus = 210481 MPa (30.0×10^6 psi)
 Poisson's ratio = 0.3
 (in Figure 3)

Table 1 Concrete Material Properties

Property	Value
Young's Modulus	27000 MPa (3900 ksi)
Poisson's Ratio	0.18
Compressive Strength	47.3 MPa (6860 psi)
Biaxial Compressive Strength	54.4 MPa (7890 psi)
Tensile Strength	3.45 MPa (500 psi)
Fracture Energy, G_f	54.6 N/m (0.31 lbf/in)

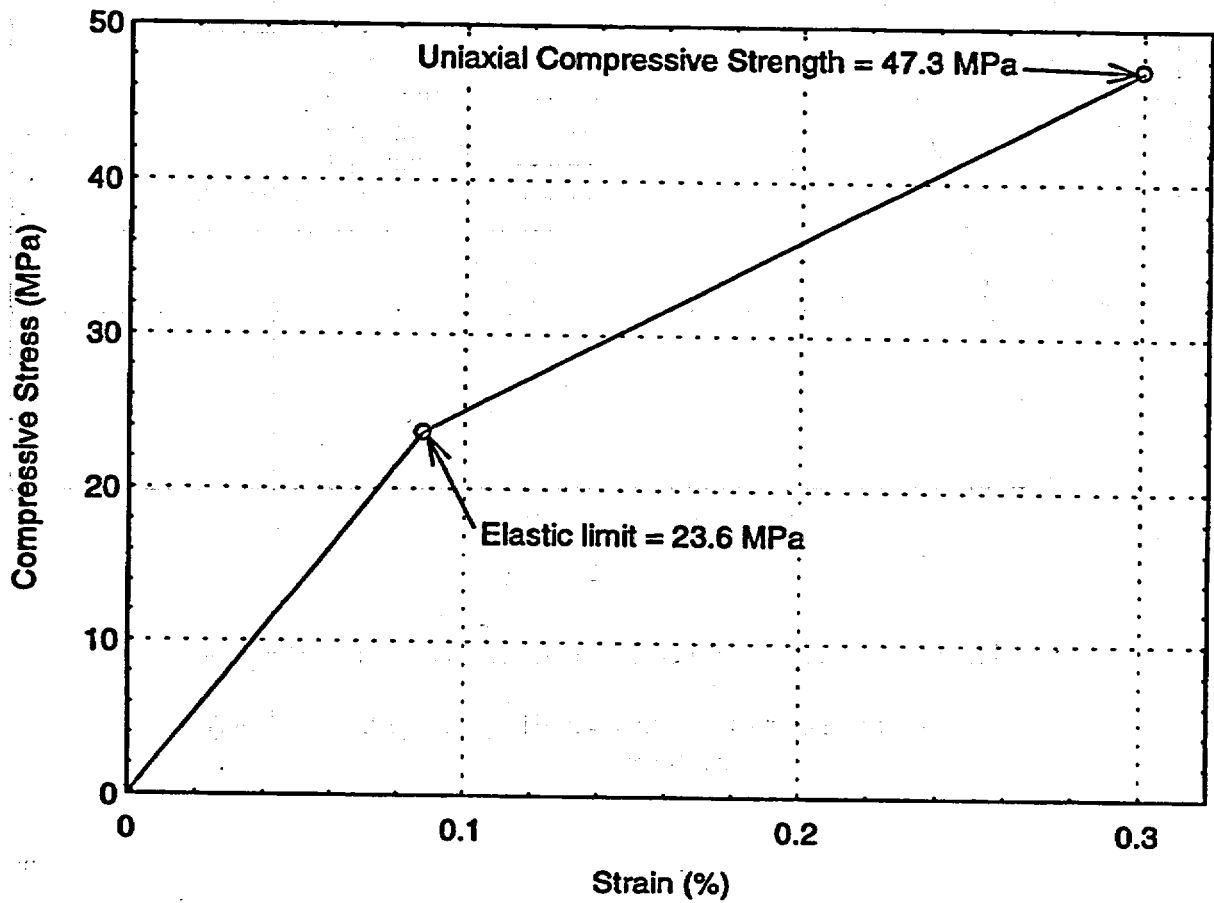


Figure 4. Concrete Uniaxial Compressive Stress - Strain Response

The true stress - true strain for the prestressing tendons is depicted in Figure 5 and is based on a best fit of the supplied data from SNL. Note that the test data is given in engineering stress-strain and the input for TEMP-STRESS requires true stress - true strain data.

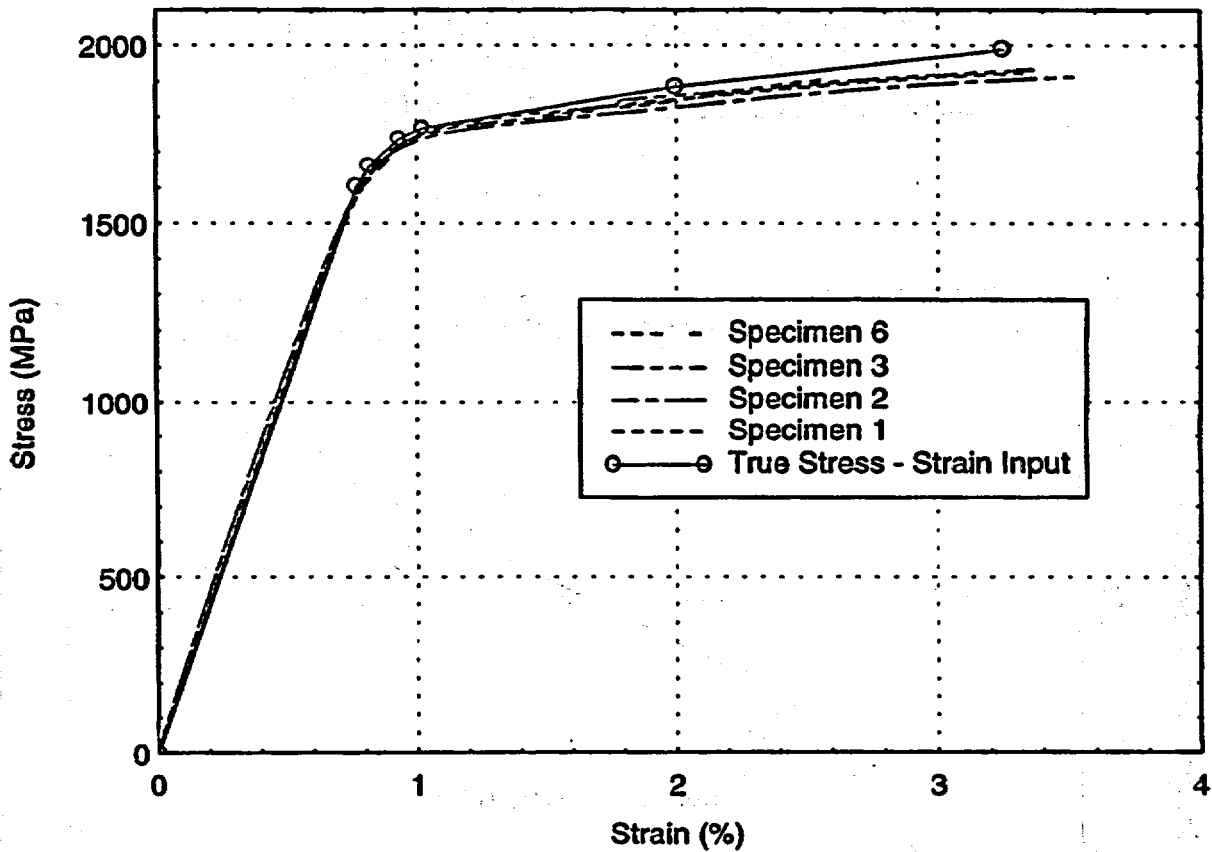


Figure 5. Prestressing Tendon True Stress - True Strain Response

With: Young's modulus = 206120 MPa (29.9×10^6 psi)
Poisson's ratio = 0.3
(in Figure 5)

The true-stress - true-strain for the liner plate is shown in Figure 6 and is based on a best fit of the data supplied by SNL[11], the test data is given in terms of engineering stress - strain. The failure strain and failure stress for the liner is shown in Figure 7, with the TEMP-STRESS input listed as true stress - true strain.

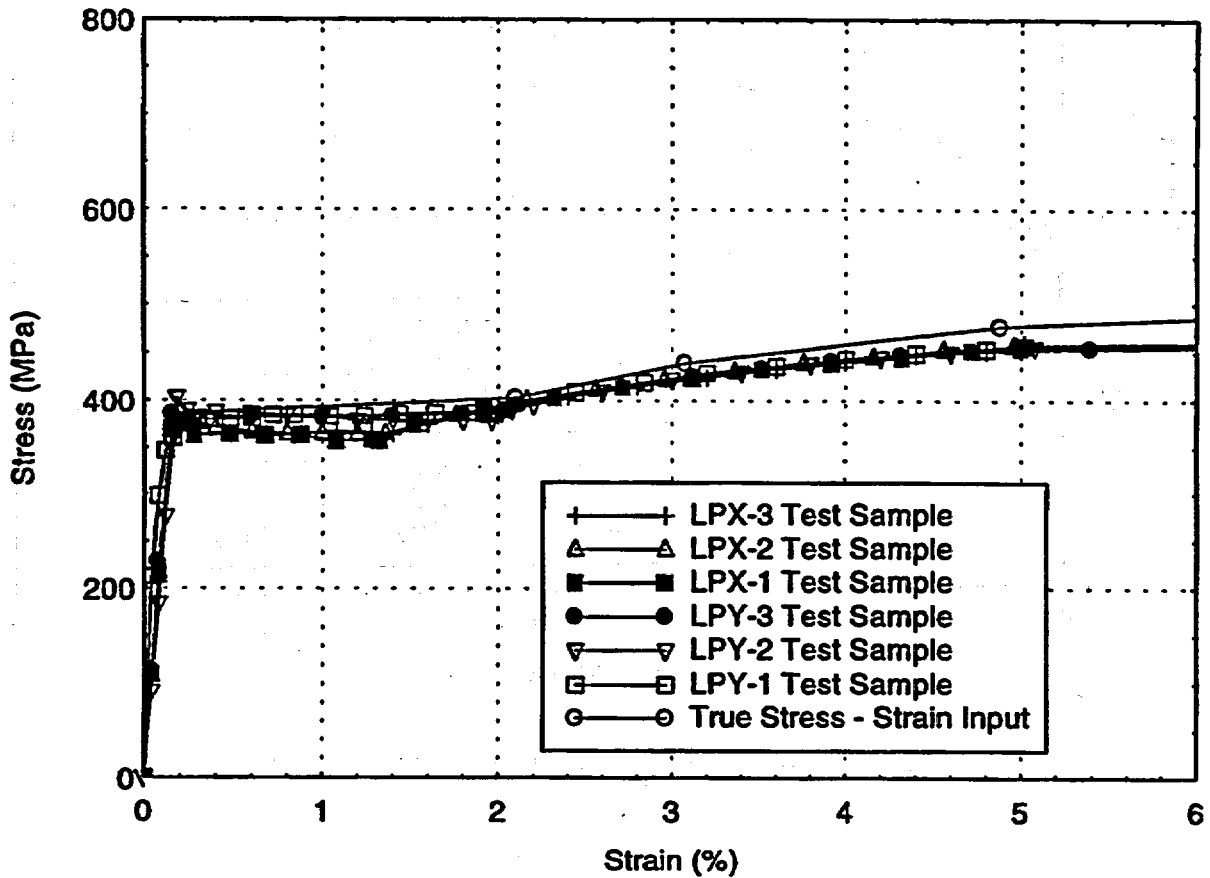


Figure 6. Liner Stress - Strain Response for Low Strain

With: Young's modulus = 240875 MPa (34.9×10^6 psi)
 Poisson's ratio = 0.3
 (in Figure 6)

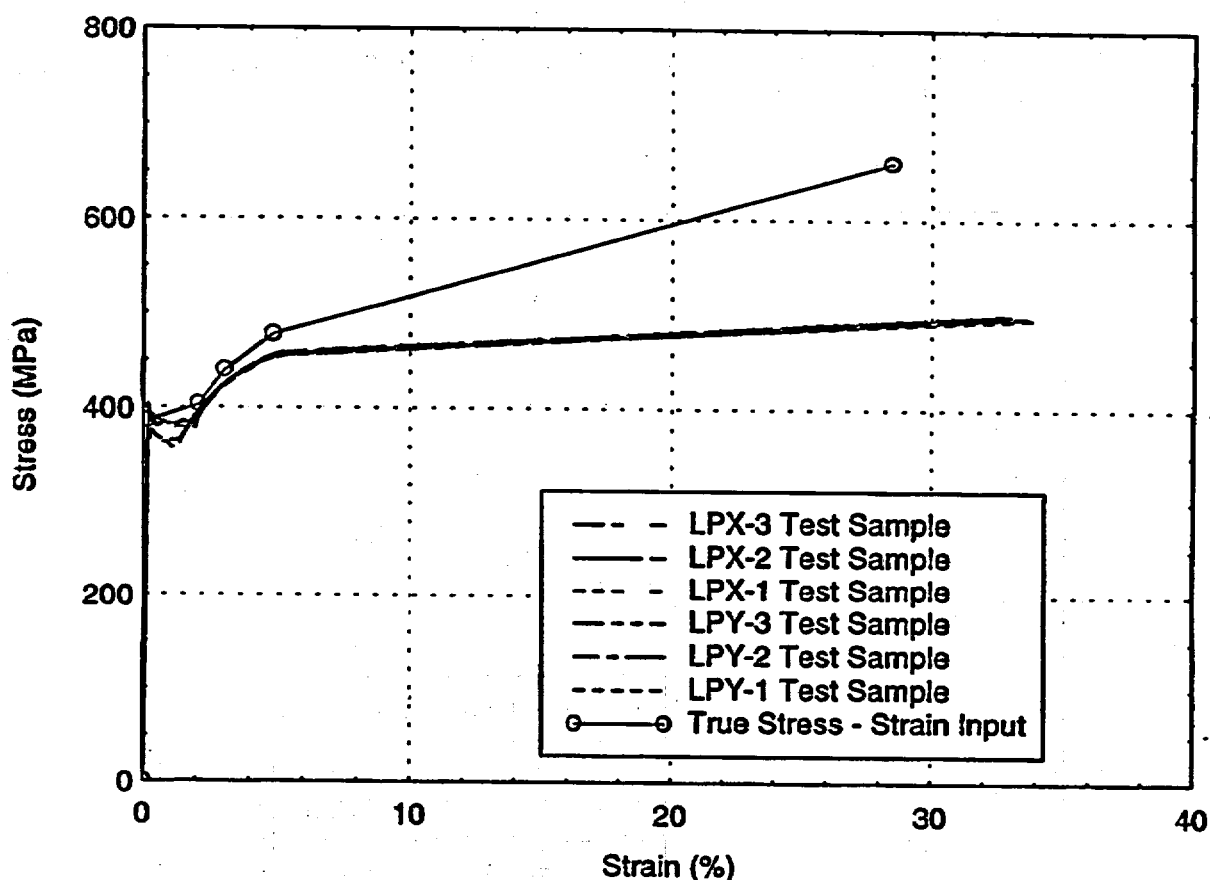


Figure 7. Liner Stress - Strain Response up to Failure

FAILURE MODELS

Both structural and local failure modes are addressed in the analysis. The structural failure modes are element failures that arise from exceeding the allowable strain from the uniaxial stress-strain response input. This includes rebar couplers, prestressing cables and liner plates. Structural failure of rebar couplers and prestressing cables are based on uniaxial tension strain exceeding the failure strain. Structural failure of the liner plates is considered as a local failure mode and is described below.

The local failure modes are difficult to obtain with an axisymmetric model due to the level of analysis sophistication, unknown as-built conditions, material conditions and triaxial stress effects on the uniaxial failure strain. The local failure mode investigated in this pretest analysis was liner tearing. The liner will most likely fail before a structural failure will occur. This will occur due to the welding of liner plates, thickened liner sections and liner studs that attach the liner to the concrete. Reference [9] addresses this type of failure and the procedure to predict the

failure strain. The failure mode associated with plastic failure arises from the global primary plastic strains. These global strains produce gross structural distortions or peak plastic strains that do not produce significant distortions. The proposed failure criterion in Ref. [9] is expressed as:

$$\varepsilon_c \leq \frac{\varepsilon_u}{KF_T} \quad (5)$$

Where:

ε_c = Maximum calculated equivalent strain

ε_u = Maximum uniform strain from uniaxial stress-strain data

$K = K_1 K_2 K_3$: Combined knockdown factor

K_1 : Knockdown factor for analysis sophistication

K_2 : Knockdown factor for as-built configuration

K_3 : Knockdown factor for material considerations

F_T : Triaxial ductility reduction factor

The ductility reduction in the material, which is a decrease in the failure strain level, due to multiaxial loading effects is addressed by using the triaxiality factor approach. The triaxiality factor is expressed as:

$$F_T = \frac{\sqrt{2}(\sigma_1 + \sigma_2 + \sigma_3)}{\sqrt{(\sigma_1 - \sigma_2)^2 + (\sigma_2 - \sigma_3)^2 + (\sigma_3 - \sigma_1)^2}} \quad (6)$$

Where:

σ_i = Principal stresses ($i = 1, 2, 3$)

Typical values for the above knockdown factors are as follows.

The K_1 knockdown factor was developed to account for the level of sophistication of the finite element model. A finite element model review that identifies the detail and completeness of the geometry, element refinement, boundary conditions and assumptions made or implied by the model. Any differences between the finite element model and the actual structure are quantified and related to the calculated strain, are used to determine the value of K_1 . The range of K_1 varies from 1 to 5; this range is based on the refinement of the finite element model and how well it

addresses global strains as well as strain gradients and concentrations due to structural discontinuities. The upper limit of 5 is based on ASME code criteria (Section III and VIII) which states that 5 is the largest concentration factor to be used for any configuration designed and fabricated.

The K_2 knockdown factor was developed to account for as-built configurations and is based on the difference between the structural information available to the analyst and the actual construction configuration. Typical values range from 1 to 1.25, which is based on the parameters of construction materials, weld quality, fabrication tolerances, post weld heat treatment, fabrication residual stresses and details, and plate thickness or bar areas.

The K_3 knockdown factor was developed to account for material degradation and is based upon the effect of material property degradation on the strain at failure and the structural loading of the component. Typical values range from 0.85 to 1.15, which is based on the parameters of corrosion, pitting, cracking, aging, etc. A factor of 1.0 would represent a mean value of material properties.

The F_T reduction factor was developed to account for multiaxial strain effect on the strain level at failure. Manjoine [10] determined empirically that the maximum principal strain at failure under a multiaxial load can be approximated as the maximum principal strain at failure under a uniaxial load divided by the triaxiality factor. Reference [9] modified Eq. (6) to ensure a reasonable limiting value based on Manjoine use of the minimum strain limit, and is given by:

$$F_T = \text{MAX} \left[F_T; \frac{1}{2^{1-F_T}}; 1 \right] \quad (7)$$

RESPONSE OF MODEL TO PRESSURIZATION

The axisymmetric finite element model was first prestressed by using 10 load increments, to avoid any damage (cracking and steel yielding) to the PCCV numerical model. Afterwards, the numerical model was pressurized in steps of 0.5 psi (3447.4 Pa) to obtain the vessel response. At each load step described above, static equilibrium was assured by a force balance described in Eq. 3 and a displacement change limit described in Eq. 4. Additionally, an energy balance check (i.e., internal strain energy balance with external work of the applied forces) was done to ensure static equilibrium was obtained. Since the numerical model is axisymmetric, only the response of the PCCV in the free field can be determined; three-dimensional models are needed to capture the effects around penetrations. Two analyses were completed with the finite element model. The first analysis used a nominal prestress load and the second analysis used a lowered hoop prestress load.

Analysis 1: No Prestress Loss

The analysis assumes that no prestress loss was present in the model at the free field location, i.e. friction loss was neglected and the full prestressing as given in the design drawing specification

was applied. The pressure history plots at the standard plot locations are given in Figures 8 through 17 for the free field response (i.e. azimuth angle of 135 degrees in the PCCV model).

The radial displacements for standard output locations 2, 3, 4, 5, 6, 7 and 9 are shown in Figure 8.

Location 2 is at:	0.25 m	base of cylinder
Location 3 is at:	1.43 m	base of cylinder
Location 4 is at:	2.63 m	base of cylinder
Location 5 is at:	4.68 m	E/H elevation
Location 6 is at:	6.20 m	Midheight of cylinder
Location 7 is at:	10.75 m	springline
Location 9 is at:	14.55 m	dome at 45°

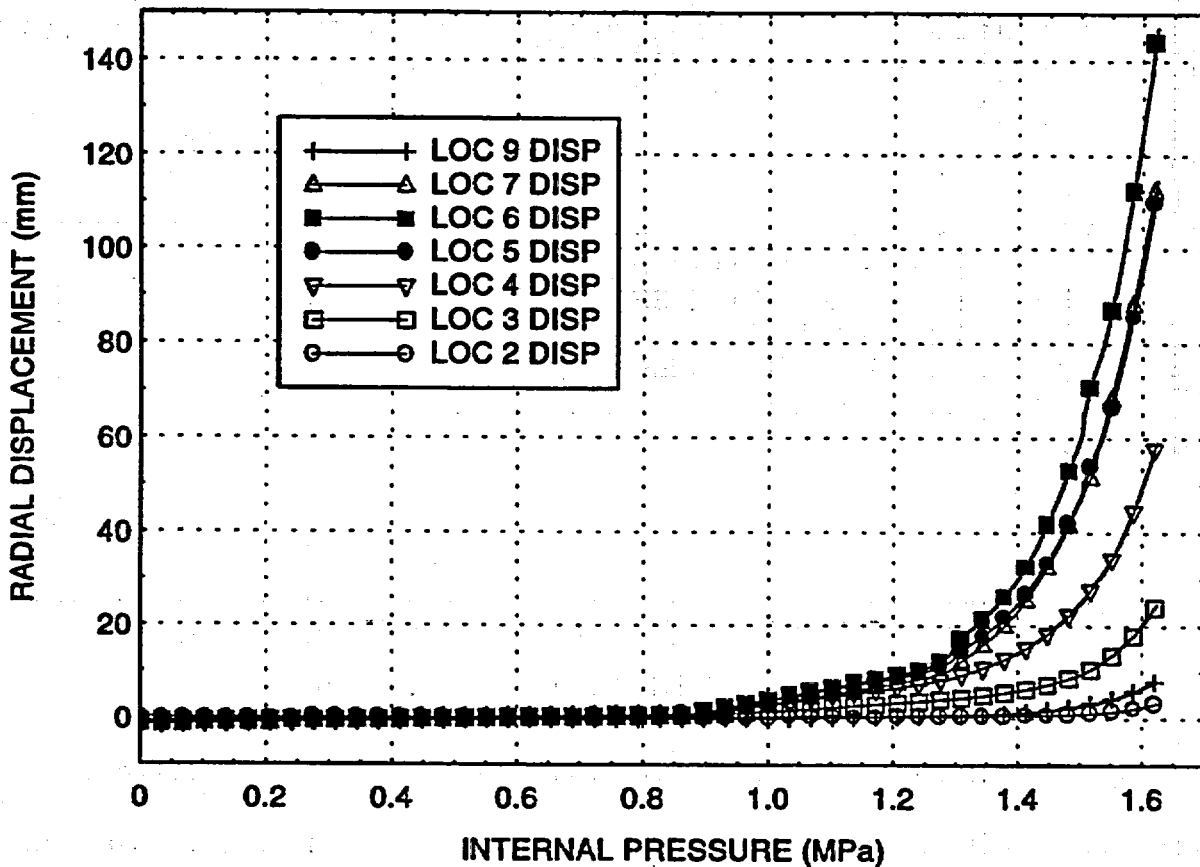


Figure 8. Radial Displacements versus Internal Pressure at Standard Output Locations

The results in Fig. 8 indicate the maximum radial displacement occurs at midheight of the cylinder and reduce substantially near the basemat-wall juncture.

The vertical displacements for standard output locations 1, 8, 10 and 11 are shown in Figure 9.

Location 1 is at:	0.0 m	top of the basemat
Location 8 is at:	10.75 m	springline
Location 10 is at:	14.55 m	dome at 45°
Location 11 is at:	16.13 m	dome apex

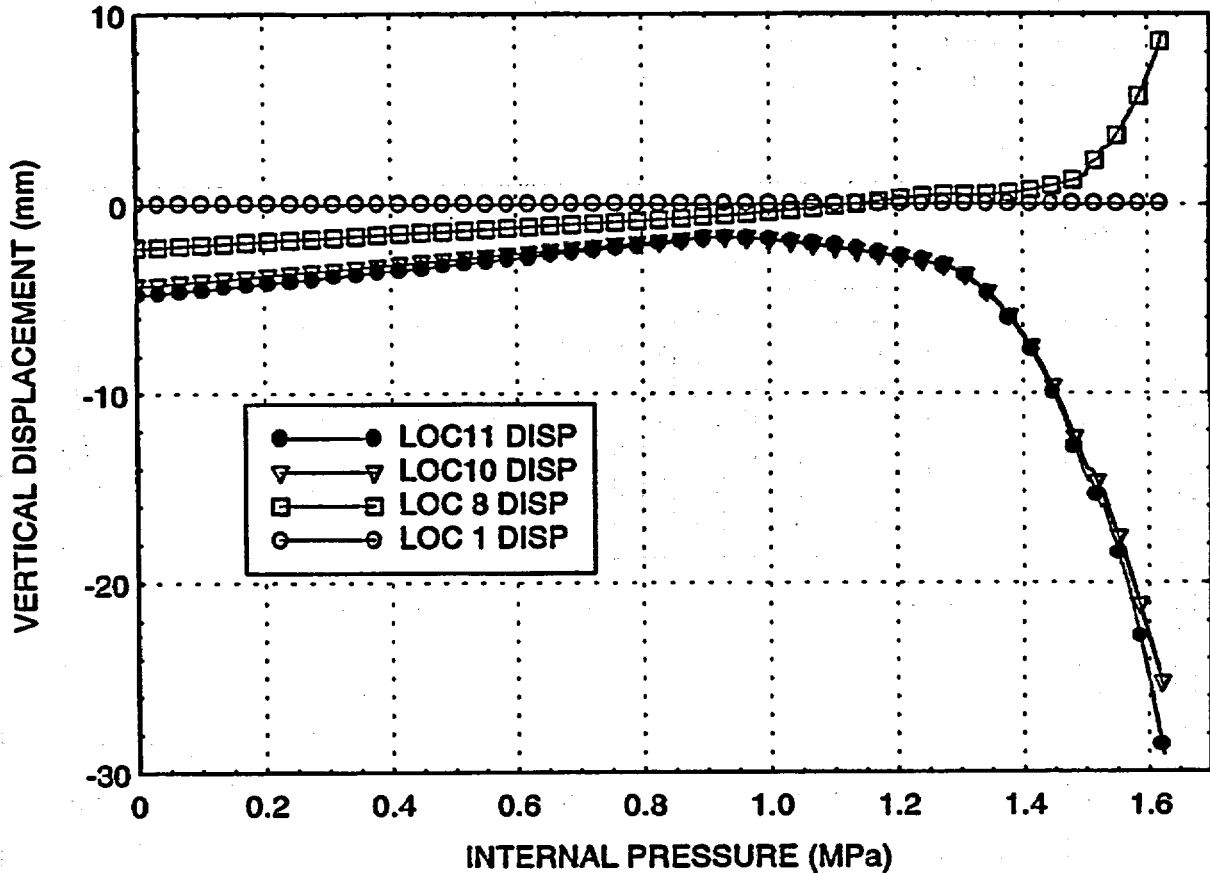


Figure 9. Vertical Displacement versus Internal Pressure at Standard Output Locations

The vertical displacements are much smaller than the radial displacements presented in Fig. 8. Location 1 is zero, because of the modeling assumption of the basemat-wall juncture, in which a fixed condition (i.e. no translations or rotations) was prescribed. Location 10 and 11 indicate the dome will move upward as the pressure is increased, but will begin to move downward around 1.0 MPa (145.0 psig) of internal pressure.

The rebar meridional strains for standard output locations 16, 17, 18, 19, 20 and 21 are shown in Figure 10.

Location 16 is at:	0.05 m	base of cylinder (inner layer)
Location 17 is at:	0.05 m	base of cylinder (outer layer)
Location 18 is at:	0.25 m	base of cylinder (inner layer)
Location 19 is at:	0.25 m	base of cylinder (outer layer)
Location 20 is at:	1.43 m	base of cylinder (inner layer)
Location 21 is at:	1.43 m	base of cylinder (outer layer)

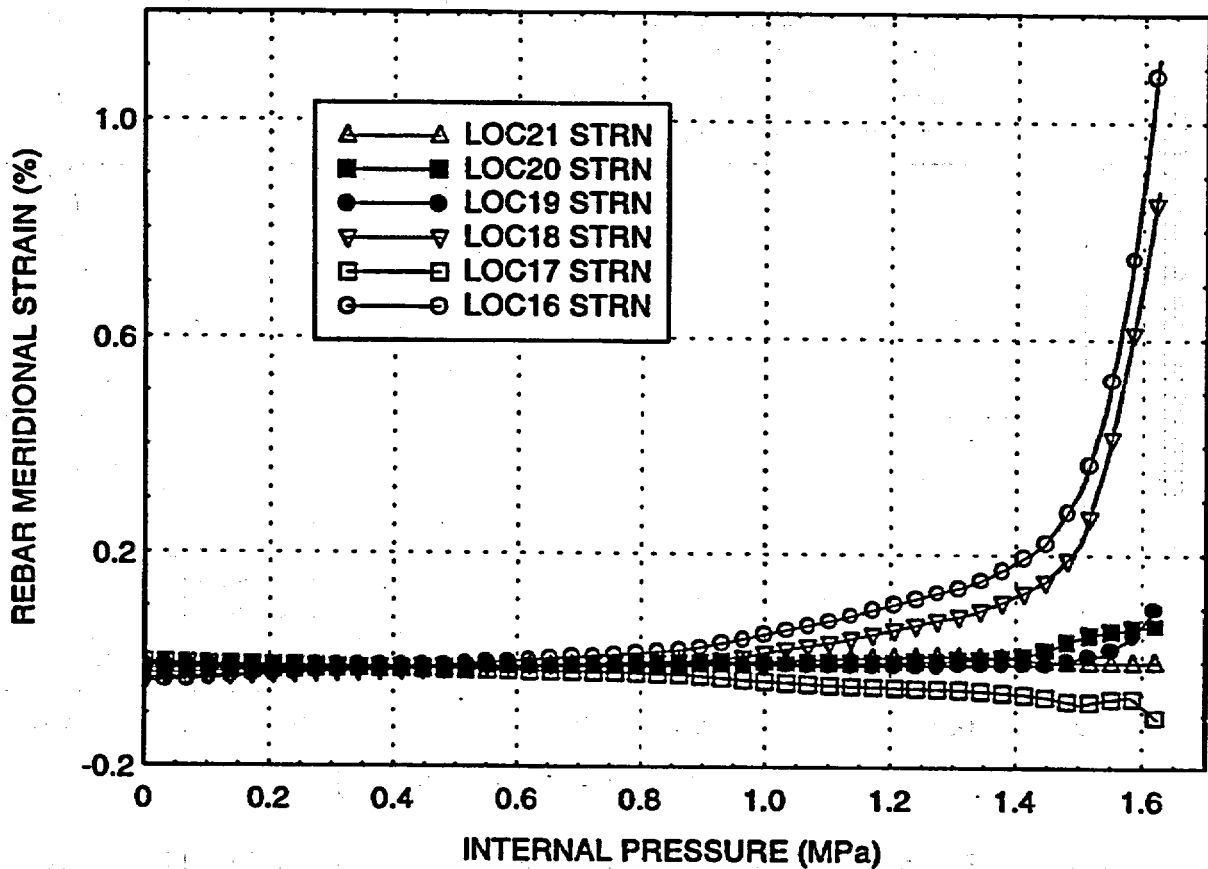


Figure 10. Rebar Meridional Strains versus Internal Pressure at Standard Output Locations

Locations 16, 17, 18 and 19 are near the basemat-wall juncture where a large moment will occur during vessel pressurization. Thus, the inner layer of rebars (location 16 and 18) will be in tension and the outer layers (location 17 and 19, except near the failure pressure for location 19) are in compression. Since the concrete will crack from the tension stresses, the rebar strains in tension will be greater than the compression rebar strains, because the concrete can develop significant compressive stresses. As the distance is increased from the basemat-wall juncture, the meridional rebar strain decrease.

The rebar hoop strains for standard output locations 22, 24 and 27 are shown in Figure 11.

Location 22 is at:	6.20 m	midheight of cylinder (outer layer)
Location 24 is at:	10.75 m	springline (outer layer)
Location 27 is at:	14.55 m	dome at 45° (outer layer)

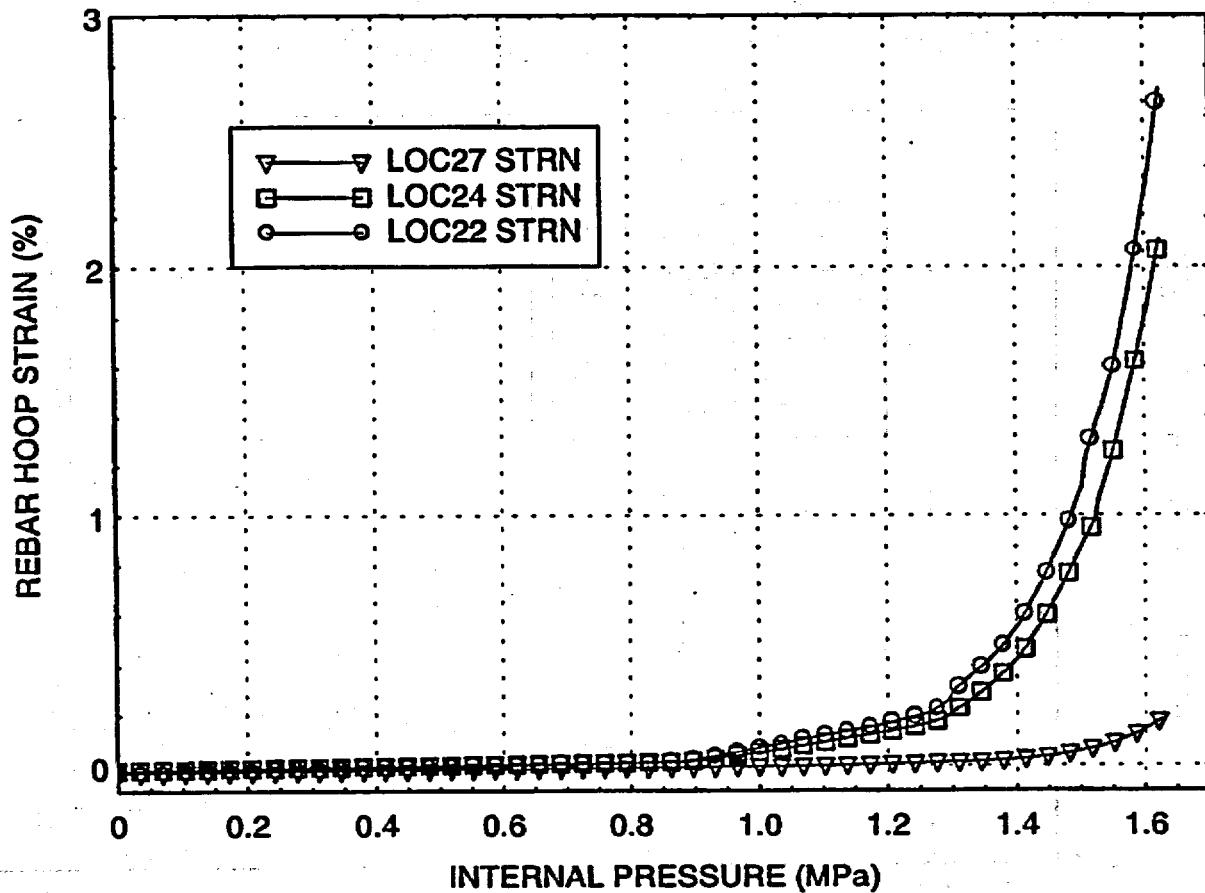


Figure 11. Rebar Hoop Strains versus Internal Pressure at Standard Output Locations

As indicated in Fig. 8, the largest radial displacements occur near the midheight of the vessel; thus, the maximum hoop strain will be at location 22. The other locations (24 and 27) have lower hoop rebar strains.

The rebar meridional strains for standard output locations 23, 25, 26, 28 and 29 are shown in Figure 12.

Location 23 is at:	6.20 m	midheight of cylinder (outer layer)
Location 25 is at:	10.75 m	springline (inner layer)
Location 26 is at:	10.75 m	springline (outer layer)
Location 28 is at:	14.55 m	dome at 45° (inner layer)
Location 29 is at:	14.55 m	dome at 45° (outer layer)

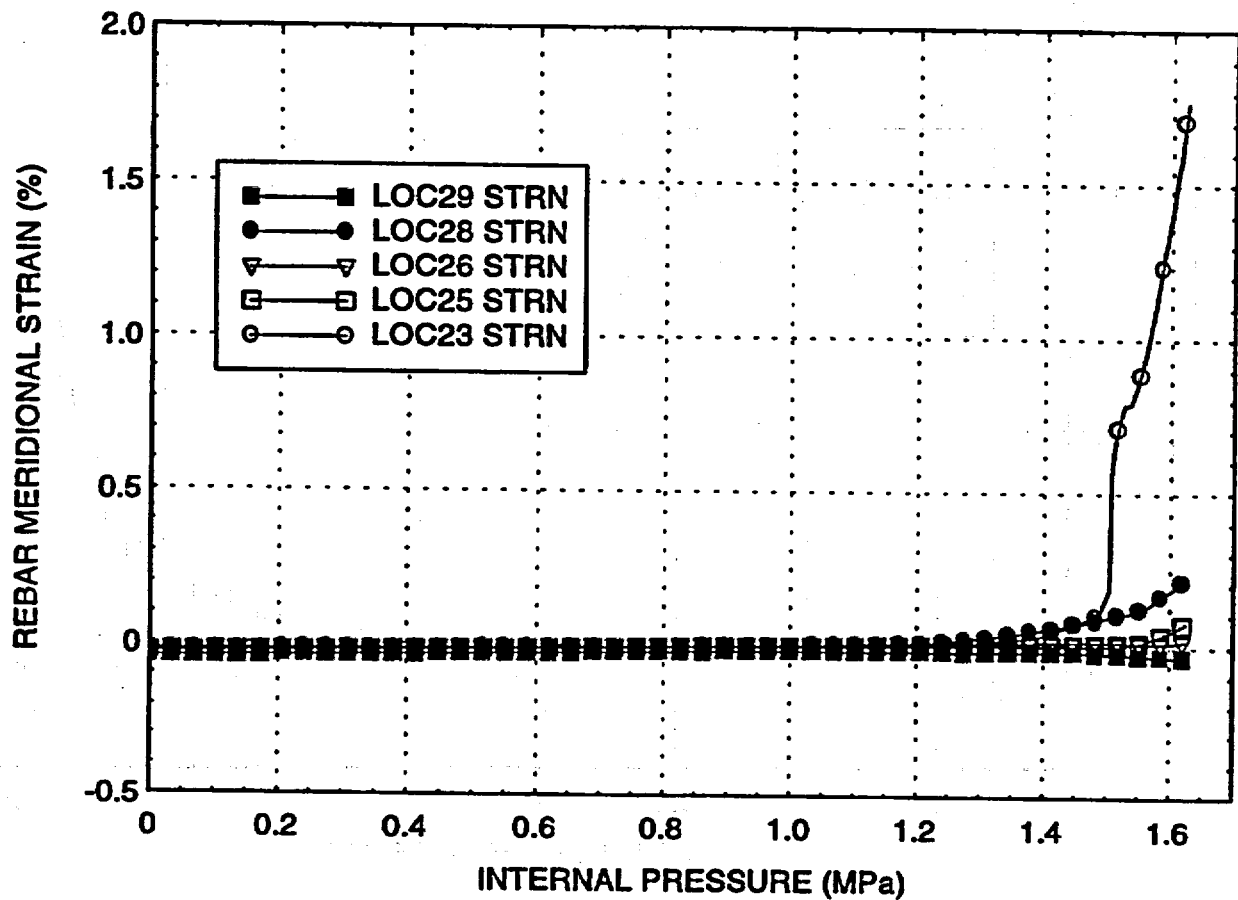


Figure 12. Rebar Meridional Strains versus Internal Pressure at Standard Output Locations

Location 23 is the largest rebar meridional strain from Figs. 10 and 12. However, the strain is not close to the failure strain (i.e. rebar coupler failure) of 6.9% strain, as shown in Fig. 3.

The liner meridional strains for standard output locations 36, 38, 40 and 42 are shown in Figure 13.

Location 35 is at:	0.01 m	base of cylinder (outside)
Location 36 is at:	0.25 m	base of cylinder (inside)
Location 38 is at:	6.20 m	midheight of cylinder (inside)
Location 40 is at:	10.75 m	springline (inside)
Location 42 is at:	16.13 m	dome apex (inside)

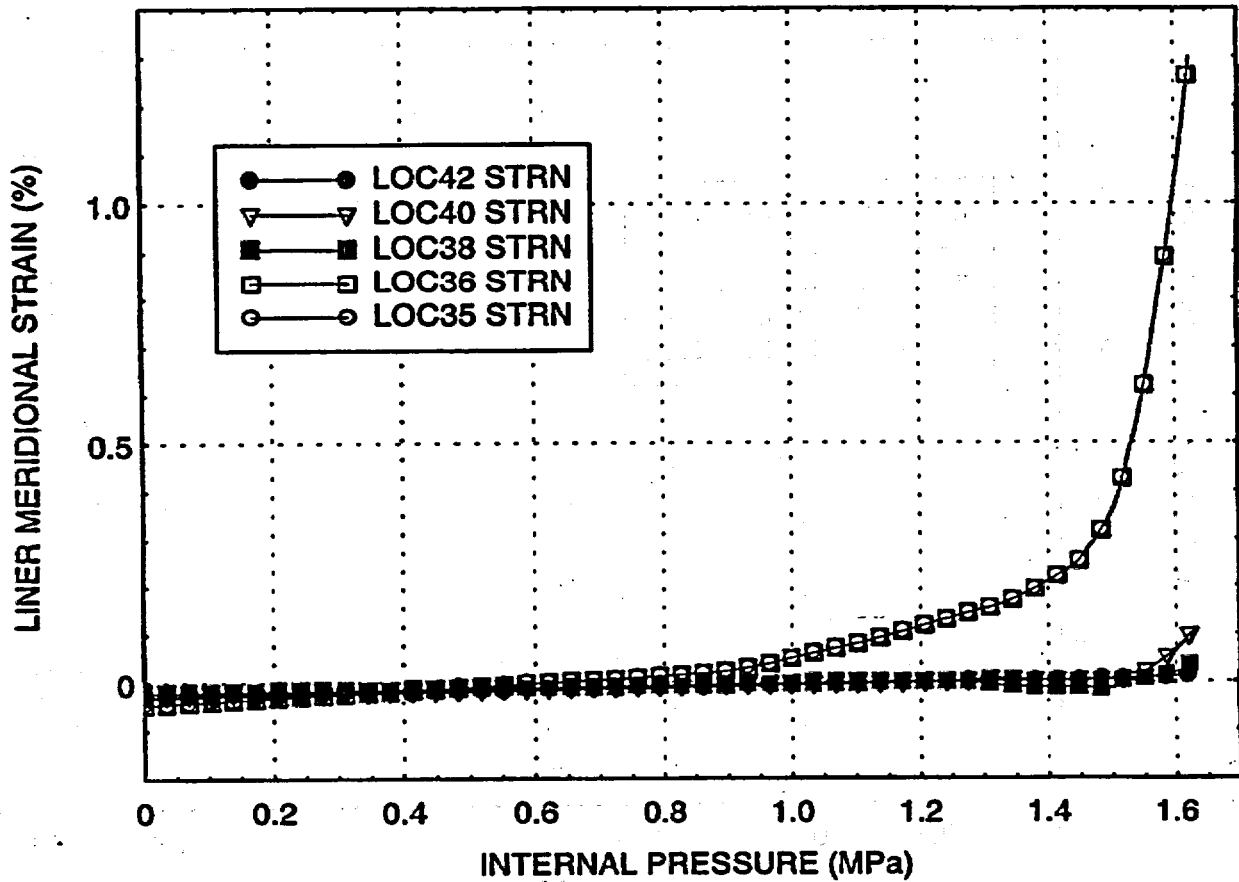


Figure 13. Liner Meridional Strains versus Internal Pressure at Standard Output Locations

Location 35 and 36 indicate the maximum liner meridional strain occurs near the basemat-wall juncture. However, these strains are smaller than the liner hoop strains presented in Fig. 14.

The liner hoop strains for standard output locations 37, 39 and 41 are shown in Figure 14.

Location 37 is at:	0.25 m	base of cylinder (inside)
Location 39 is at:	6.20 m	midheight of cylinder (inside)
Location 41 is at:	10.75 m	springline (inside)

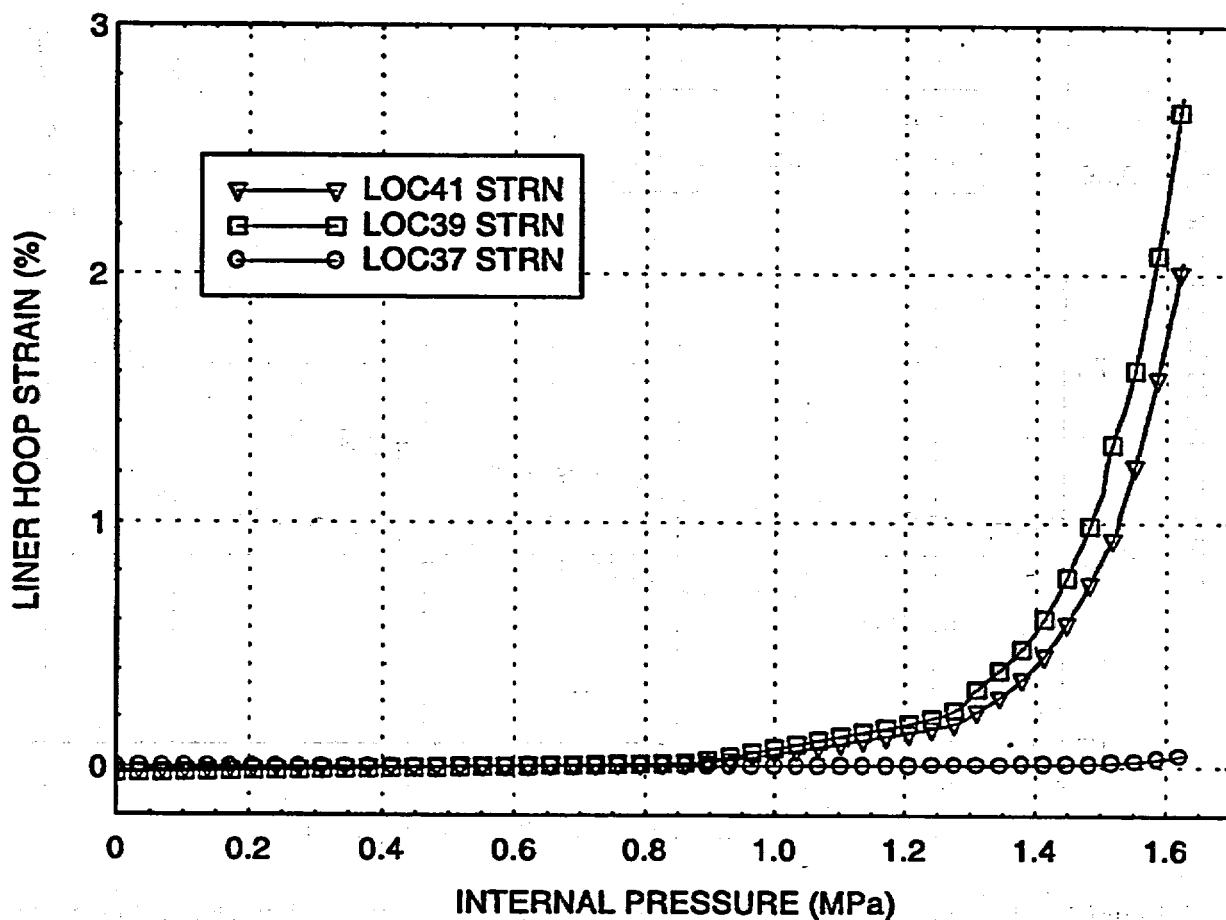


Figure 14. Liner Hoop Strains versus Internal Pressure at Standard Output Locations

The maximum liner hoop strain is at the midheight of the cylinder, the other hoop strains decrease towards the springline and the basemat-wall juncture.

The hairpin (meridional) tendon strains for standard output locations 48 and 49 are shown in Figure 15.

Location 48 is at: 15.60 m tendon apex
Location 49 is at: 10.75 m tendon springline

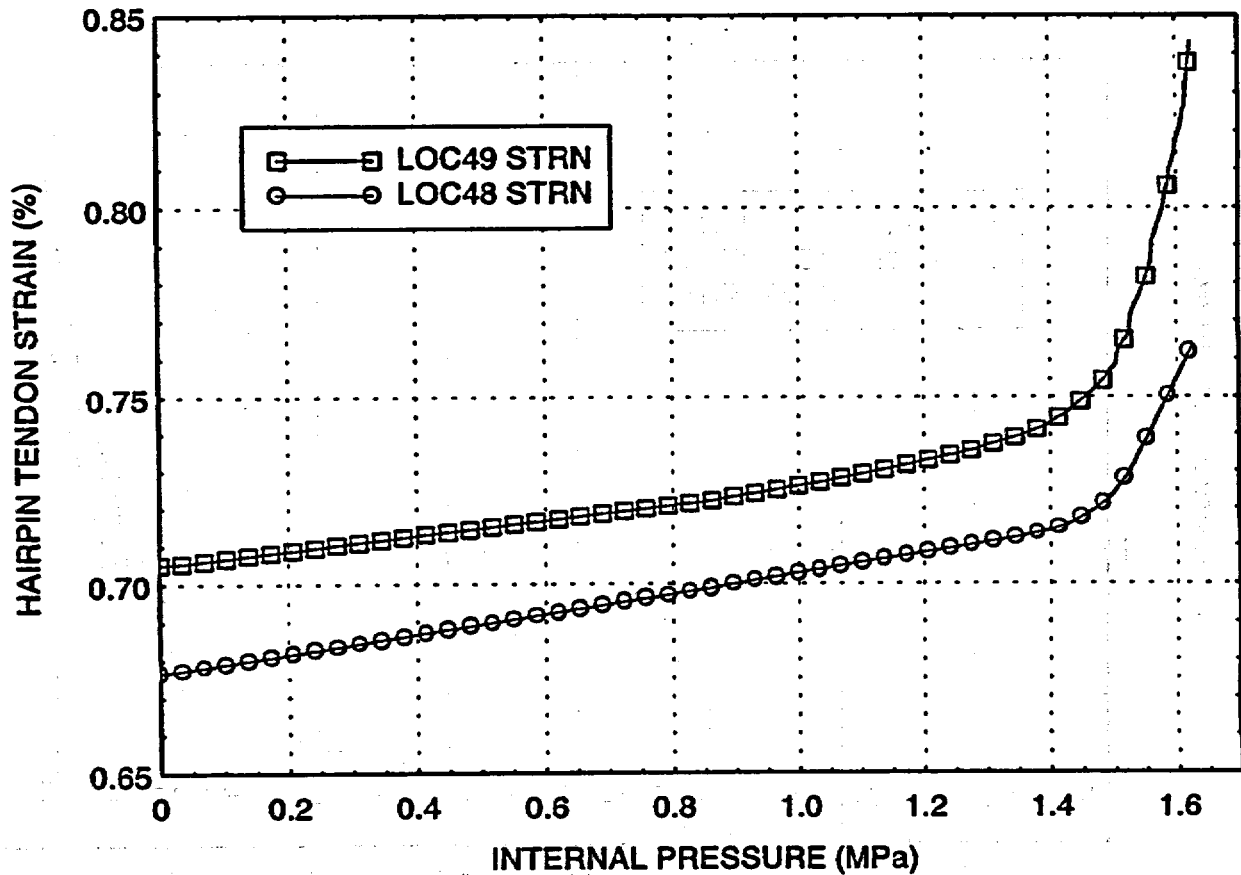


Figure 15. Hairpin Tendon Strains versus Internal Pressure at Standard Output Locations

There is a reduction of approximately 4% in strain for the hairpin tendon as indicated in Fig.15. Even though no friction was used in the computational model, a reduction in the hairpin tendon was observed.

The hoop tendon strains for standard output locations 52 and 53 are shown in Figure 16.

Location 52 is at: 6.58 m tendon near midheight of cylinder at buttress
Location 53 is at: 4.57 m tendon between E/H and A/L

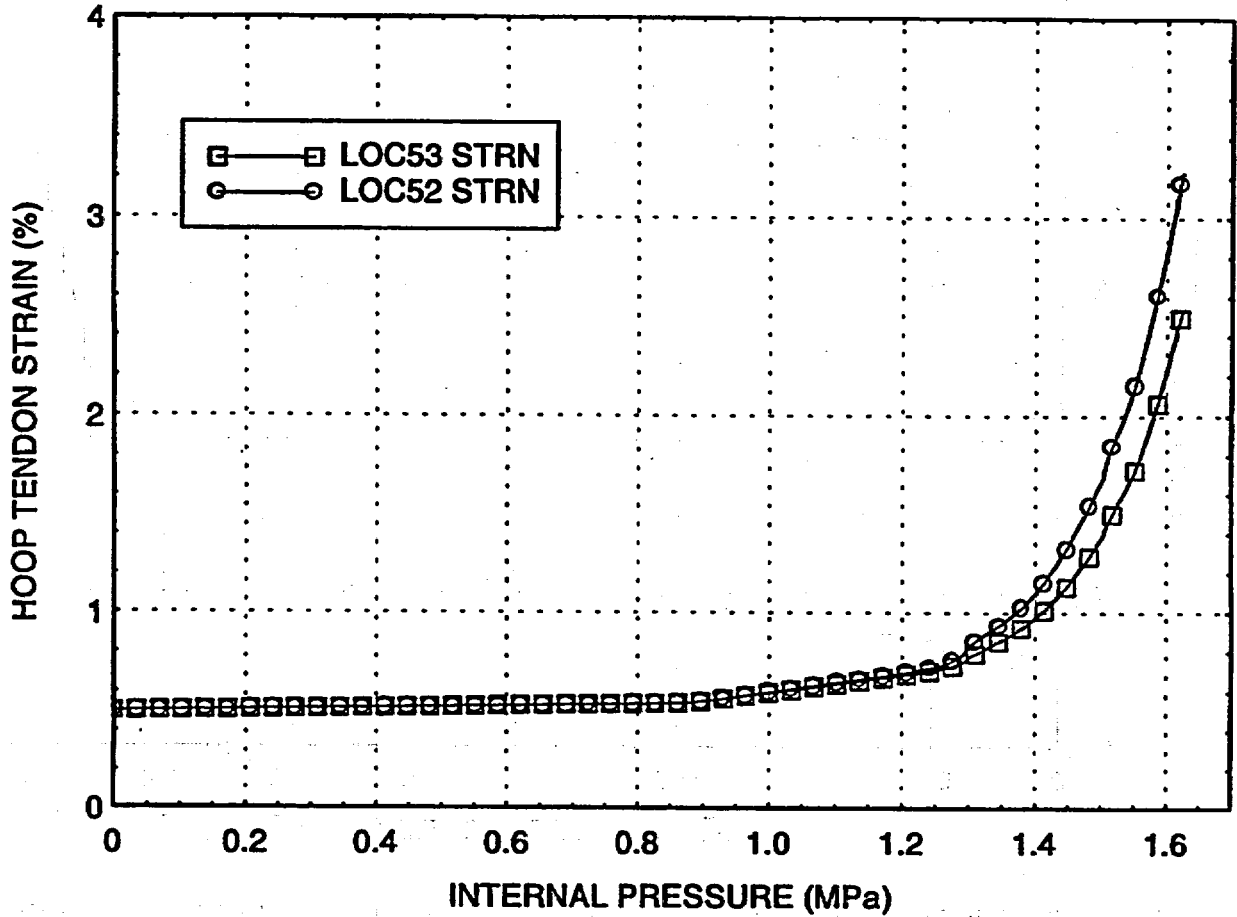


Figure 16. Hoop Tendon Strains versus Internal Pressure at Standard Output Locations

The tendon strains shown above, indicate that structural failure (i.e. hoop tendon reaching its ultimate strain of 3.25%) will occur near the midheight of the vessel.

The hairpin (meridional) tendon force for standard output location 54 is shown in Figure 17.

Location 54 is at: 0.0 m tendon gallery

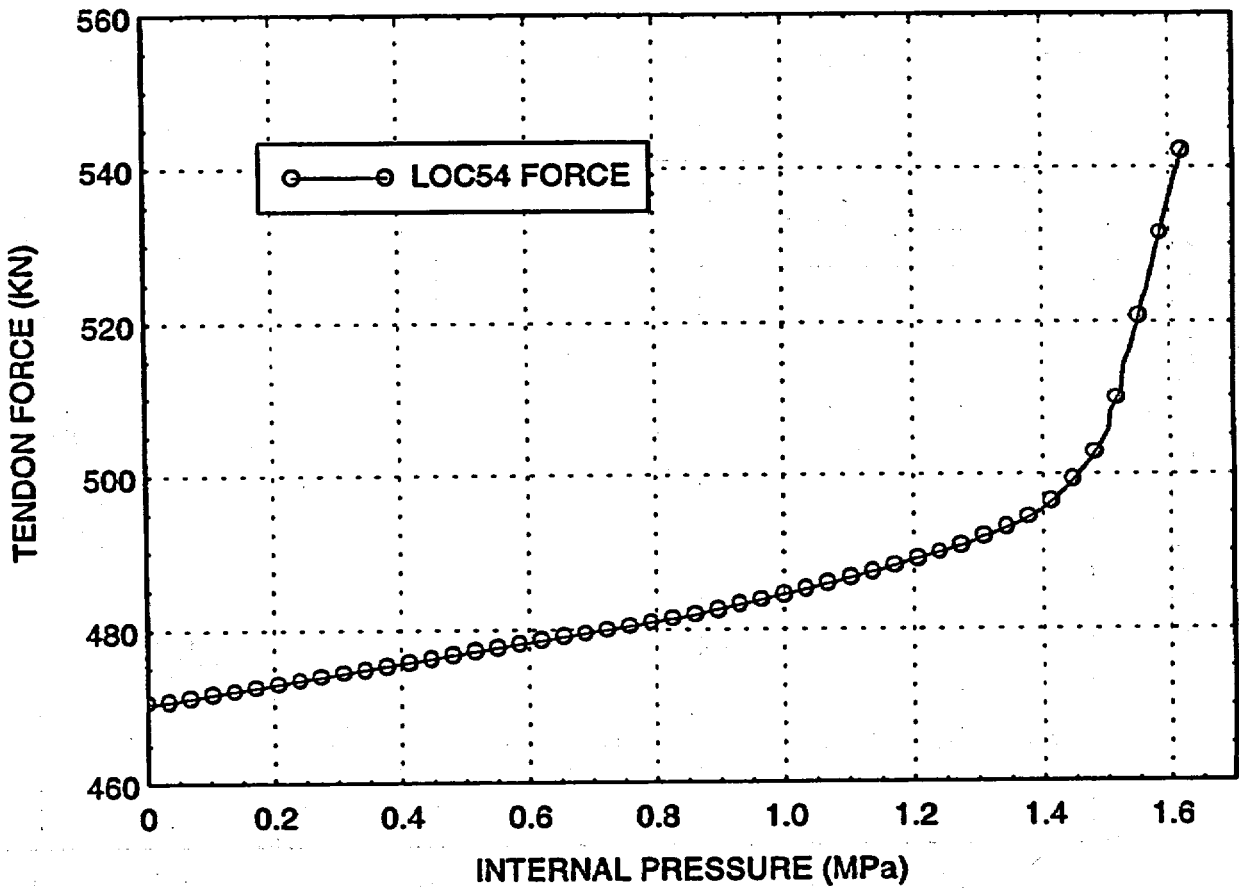


Figure 17. Hairpin Tendon Force versus Internal Pressure at the Standard Output Location

The results above indicate the tendon force will increase as the internal pressure is raised. As the failure pressure of the model is reached, the force increase accelerates, but is below the failure force, which is approximately 582.0 kN.

The displacements and strains depicted in Figs. 8 – 16 include the initial deflection/strain from the prestressing of the PCCV. This is why at zero pressure, a displacement or strain is present in some of the pressure history responses.

The effect of pressuring the vessel leads to the following events:

	Gage Pressure	
	(MPa)	(psig)
First cracking of concrete in the cylinder due to hoop stresses:	0.86	124.5
First cracking of concrete in the cylinder due to meridional stress:	0.75	109.5
First yielding of hoop rebar in cylinder:	1.25	182.0
First yielding of meridional rebar in wall basemat juncture:	1.45	210.0
First cracking of dome concrete above 45° dome angle:	1.18	171.0
First cracking of dome concrete below 45° dome angle:	0.88	127.0
Hoop tendons in cylinder reaching 1 % strain (at mid cylinder):	1.37	199.0
Hoop tendons in cylinder reaching 2 % strain (at mid cylinder):	1.54	223.0
Hoop tendons in cylinder reaching 3 % strain (at mid cylinder):	1.61	233.5

Analysis 2: Prestress Loss

The analysis assumes that a prestress loss was present in the model in a free field location. A value of 30% reduction was estimated for the average hoop tendon load in the free field location of the containment vessel. The estimate was determined by the friction loss and set loss given in Ref. [11], Appendix II, Ancillary Test Reports, "Tendon Friction Coefficient and Set Loss Verification Test", JPN-18-T4. The estimate was based on the loss due to friction from the angle change (99% of loss) and the loss due to tendon length friction. At a location of 90° from the buttress, the tendon force is 71% of the applied tendon force at the buttress. Note, only the hoop tendon in the finite element model were reduced by 30%, the hairpin (meridional) tendon forces were not reduced.

The pressure history plots of the analysis (i.e. Analysis 2: Prestress Loss) are given in Figures 18 through 33 at the standard plot locations for the free field response (i.e. azimuth angle of 135 degrees in the PCCV model). Additionally, these plots compare the prestress loss results to the results obtained from the first analysis (i.e. Analysis 1: No Prestress Loss).

The radial displacements for standard output locations 2, 3 and 9 are shown in Figure 18 for the analysis of a prestress loss and no prestress loss.

Location 2 is at:	0.25 m	base of cylinder
Location 3 is at:	1.43 m	base of cylinder
Location 9 is at:	14.55 m	dome at 45°

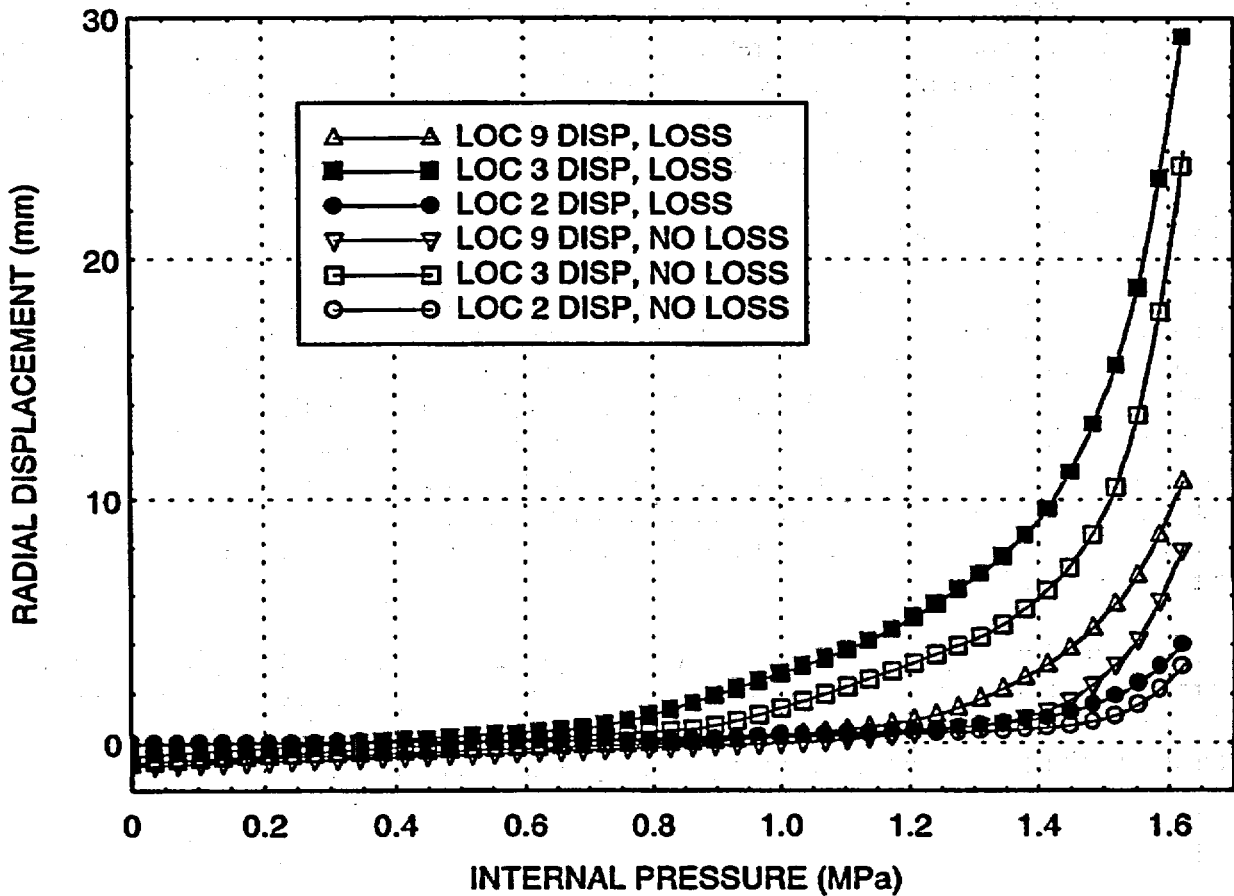


Figure 18. Radial Displacements versus Internal Pressure at Standard Output Locations

The radial displacements for standard output locations 4 and 5 are shown in Figure 19 for the analysis of a prestress loss and no prestress loss.

Location 4 is at: 2.63 m base of cylinder
 Location 5 is at: 4.68 m E/H elevation

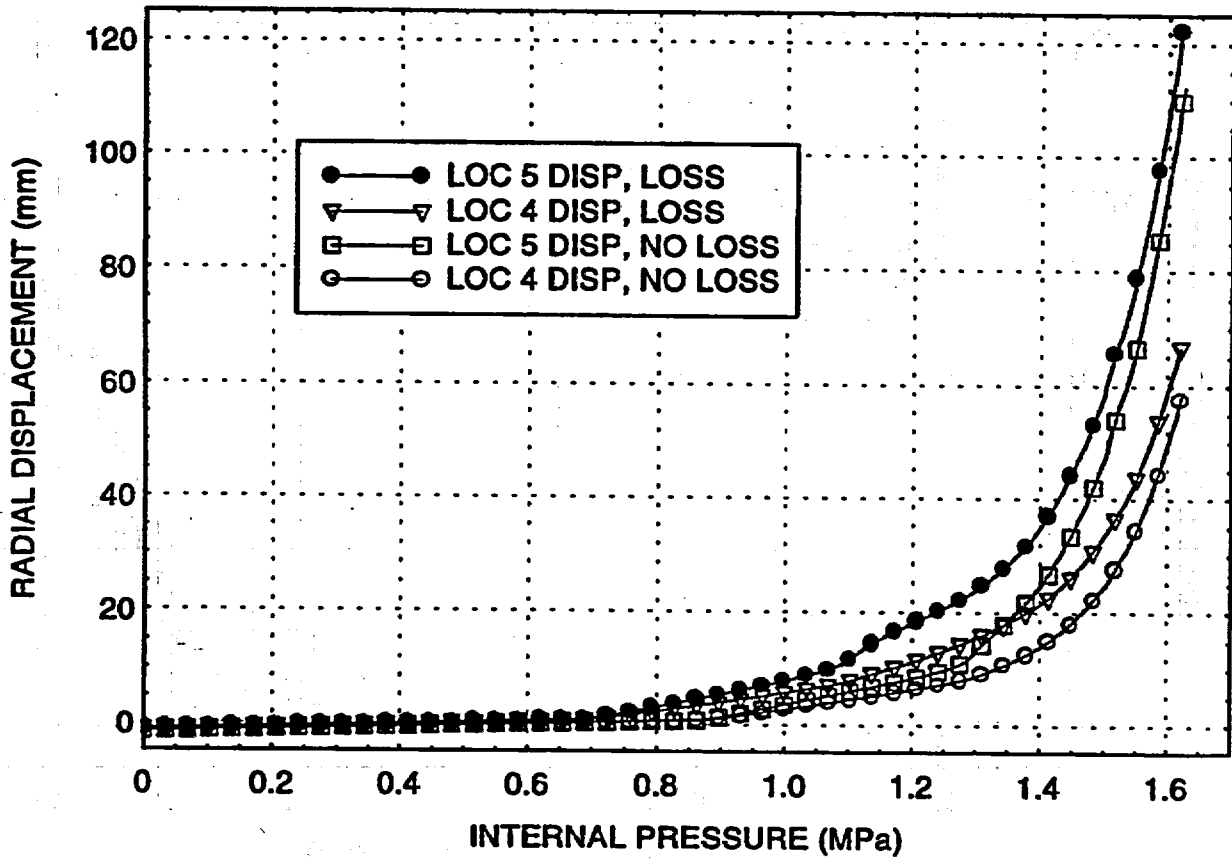


Figure 19. Radial Displacements versus Internal Pressure at Standard Output Locations

The radial displacements for standard output locations 6 and 7 are shown in Figure 20 for the analysis of a prestress loss and no prestress loss.

Location 6 is at: 6.20 m Midheight of cylinder
 Location 7 is at: 10.75 m springline

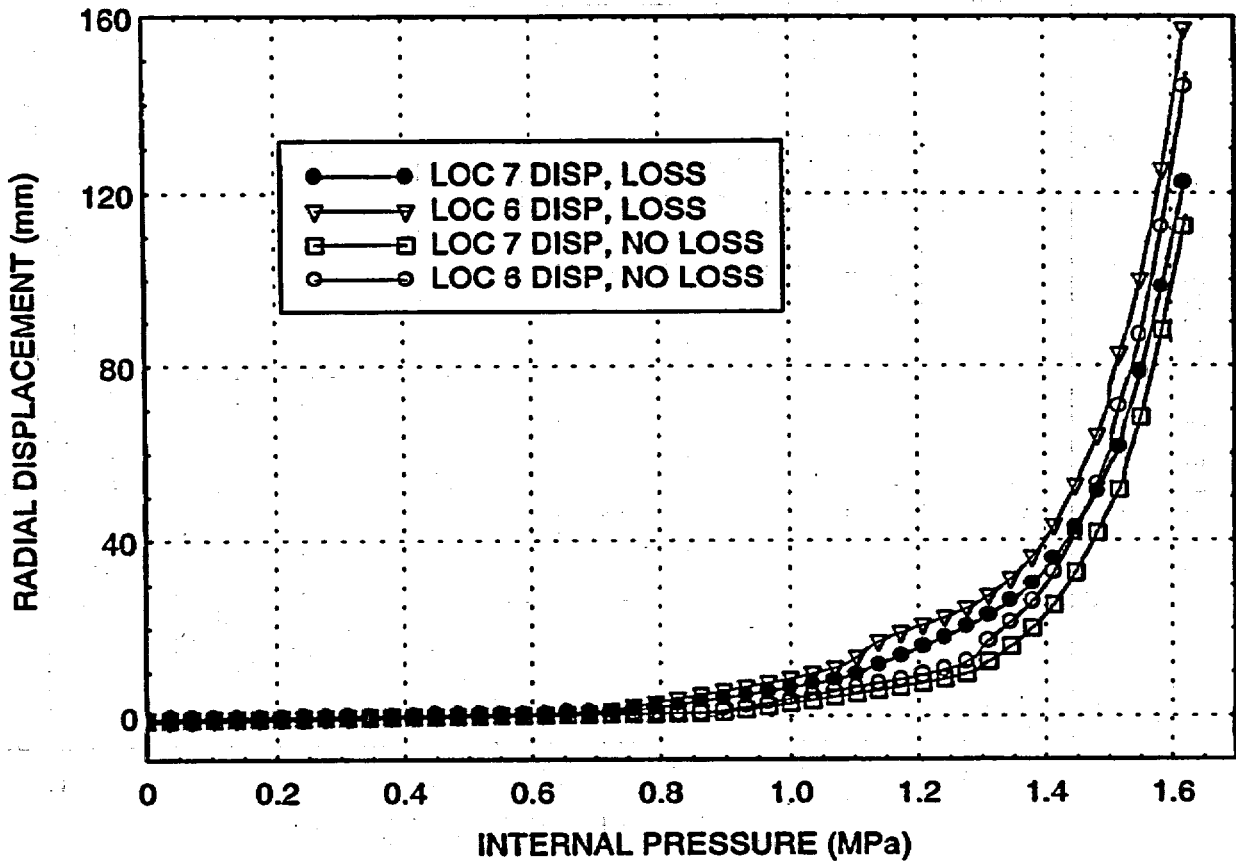


Figure 20. Radial Displacements versus Internal Pressure at Standard Output Locations

The radial displacements given in Figures 18 - 20 indicate a prestress loss will cause the nonlinear response to occur at a lower pressure. Thus, the results are shifted to the left by approximately 0.1 to 0.15 MPa when compared to the analysis of no prestress loss, depending on the location.

The vertical displacements for standard output locations 8, 10 and 11 are shown in Figure 21 for the analysis of a prestress loss and no prestress loss.

Location 8 is at:	10.75 m	springline
Location 10 is at:	14.55 m	dome at 45°
Location 11 is at:	16.13 m	dome apex

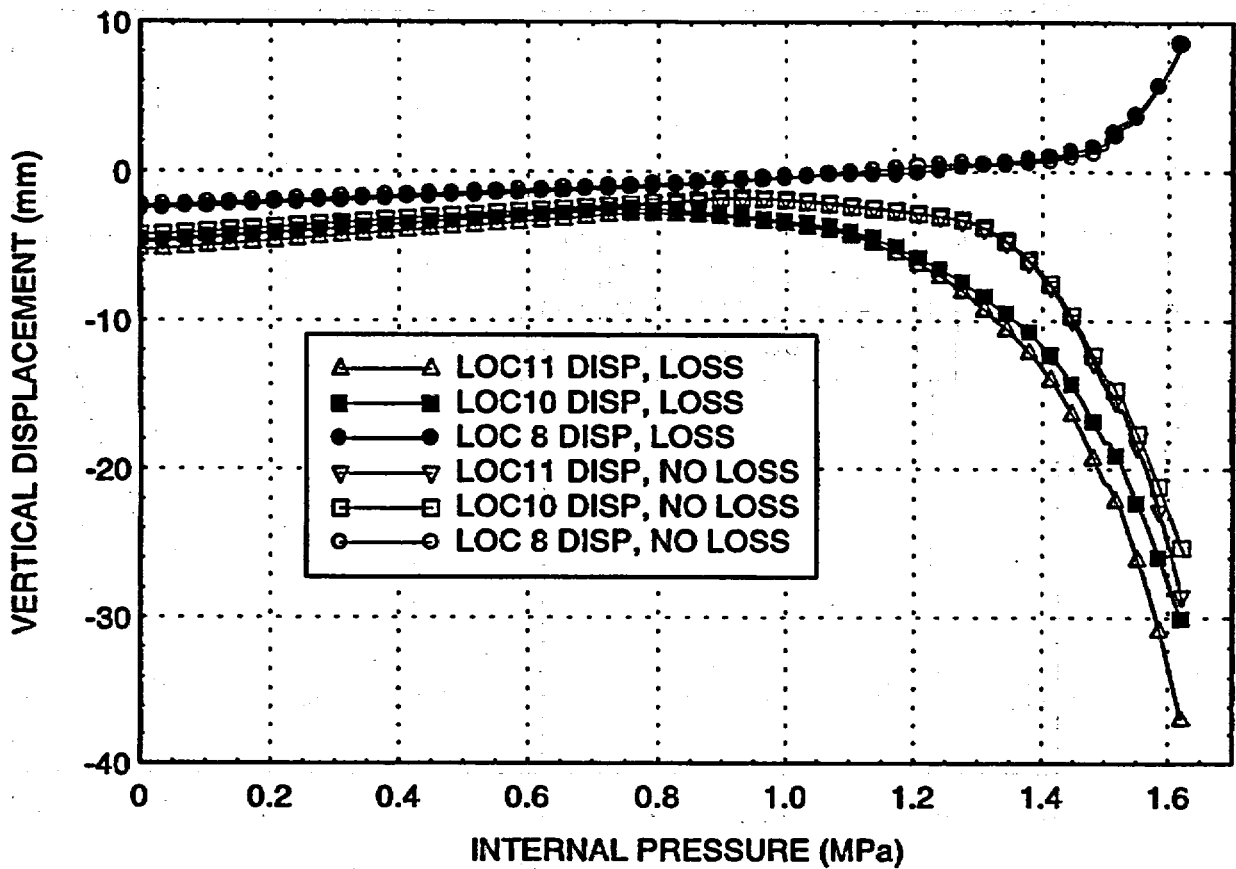


Figure 21. Vertical Displacement versus Internal Pressure at Standard Output Locations

The vertical displacement for Location 1, at elevation 0.00 m, was not provided in the above plot due to a zero displacement. This occurs because the finite element model assumes the basement-wall juncture is infinitely rigid, i.e. fixed support boundary condition. The effect of the prestress loss on the vertical displacements is smaller when compared to the radial displacements responses in Figures 18 - 20.

The rebar meridional strains for standard output locations 16 and 17 are shown in Figure 22 for the analysis of a prestress loss and no prestress loss.

Location 16 is at: 0.05 m base of cylinder (inner layer)
 Location 17 is at: 0.05 m base of cylinder (outer layer)

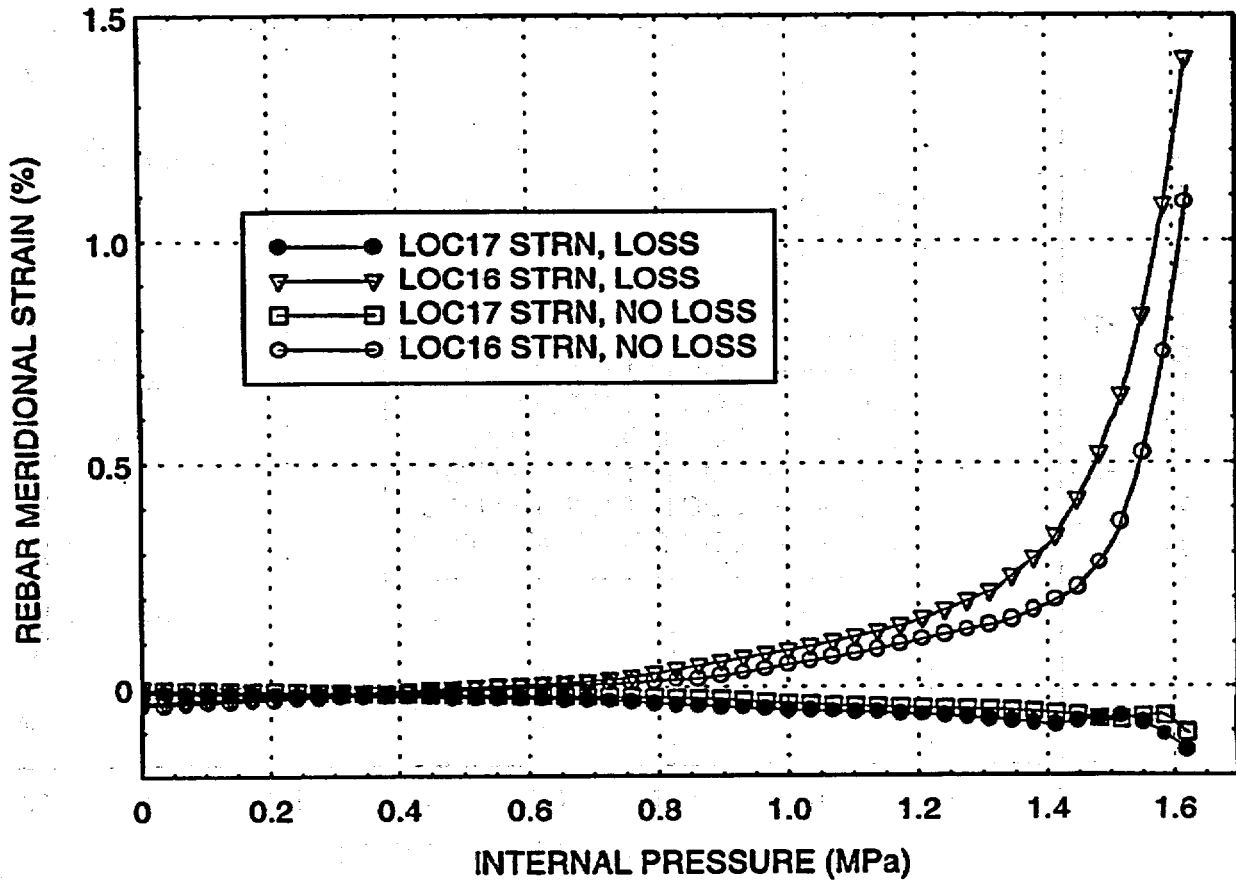


Figure 22. Rebar Meridional Strains versus Internal Pressure at Standard Output Locations

The prestress loss effect at location 16 (tension rebar response) is more significant when compared to the compression rebar response at location 17.

The rebar meridional strains for standard output locations 18 and 19 are shown in Figure 23 for the analysis of a prestress loss and no prestress loss.

Location 18 is at: 0.25 m base of cylinder (inner layer)
 Location 19 is at: 0.25 m base of cylinder (outer layer)

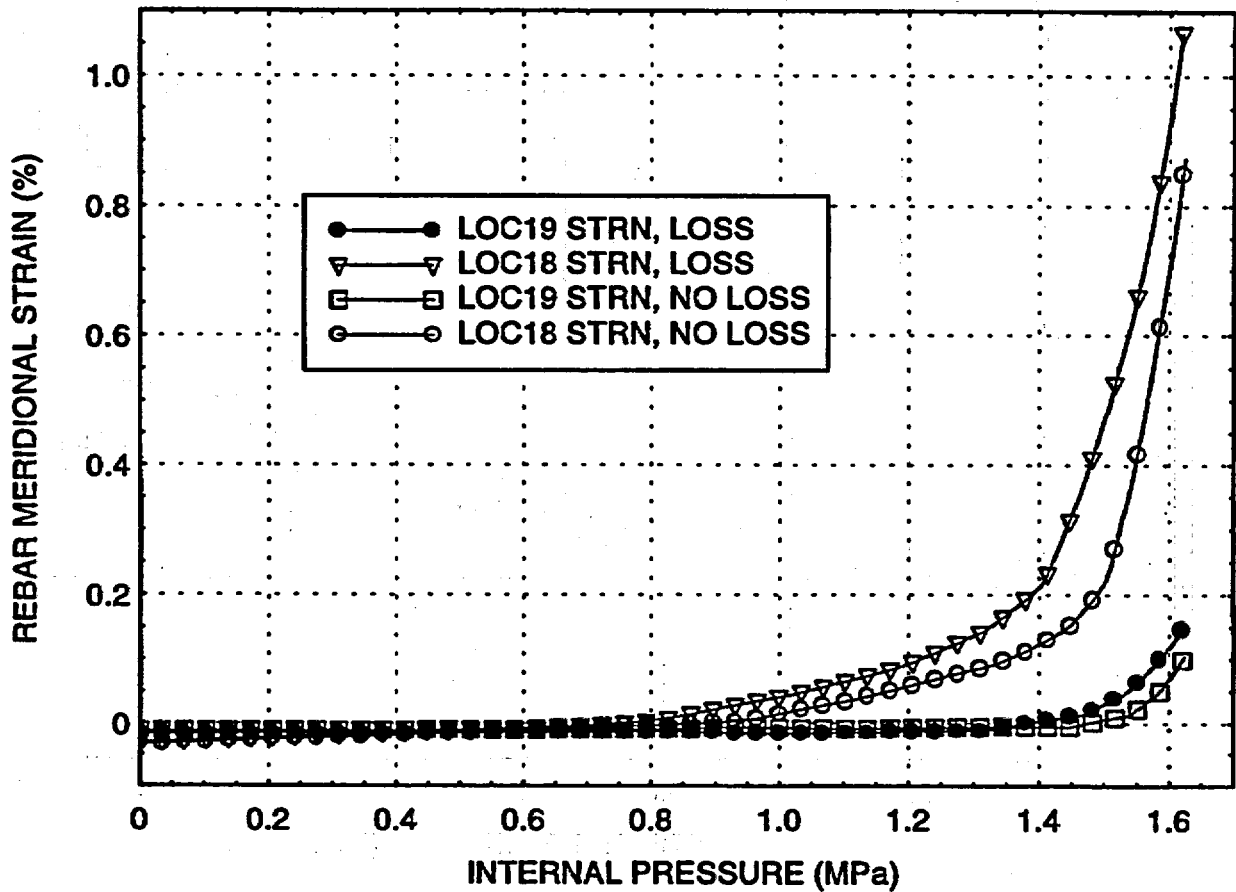


Figure 23. Rebar Meridional Strains versus Internal Pressure at Standard Output Locations

The prestress loss effect is similar to Figure 22 for the tension rebar at location 18.

The rebar meridional strains for standard output locations 20 and 21 are shown in Figure 24 for the analysis of a prestress loss and no prestress loss.

Location 20 is at: 1.43 m base of cylinder (inner layer)
 Location 21 is at: 1.43 m base of cylinder (outer layer)

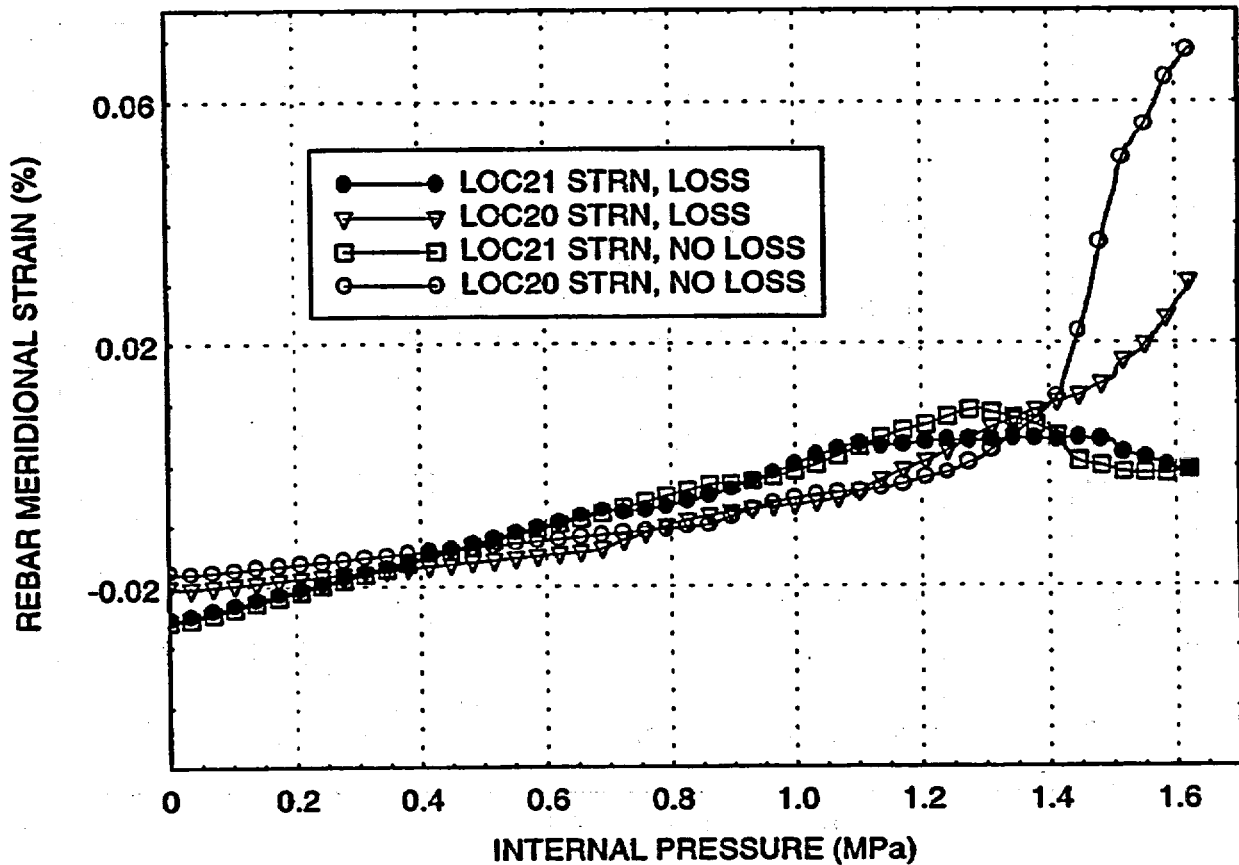


Figure 24. Rebar Meridional Strains versus Internal Pressure at Standard Output Locations

The rebar strains are small (below yield) when compared to the other meridional rebar strain in Figures 22 and 23. The effect of the prestress loss is not significant at these locations.

The rebar hoop strains for standard output locations 22, 24 and 27 are shown in Figure 25 for the analysis of a prestress loss and no prestress loss.

Location 22 is at:	6.20 m	midheight of cylinder (outer layer)
Location 24 is at:	10.75 m	springline (outer layer)
Location 27 is at:	14.55 m	dome at 45° (outer layer)

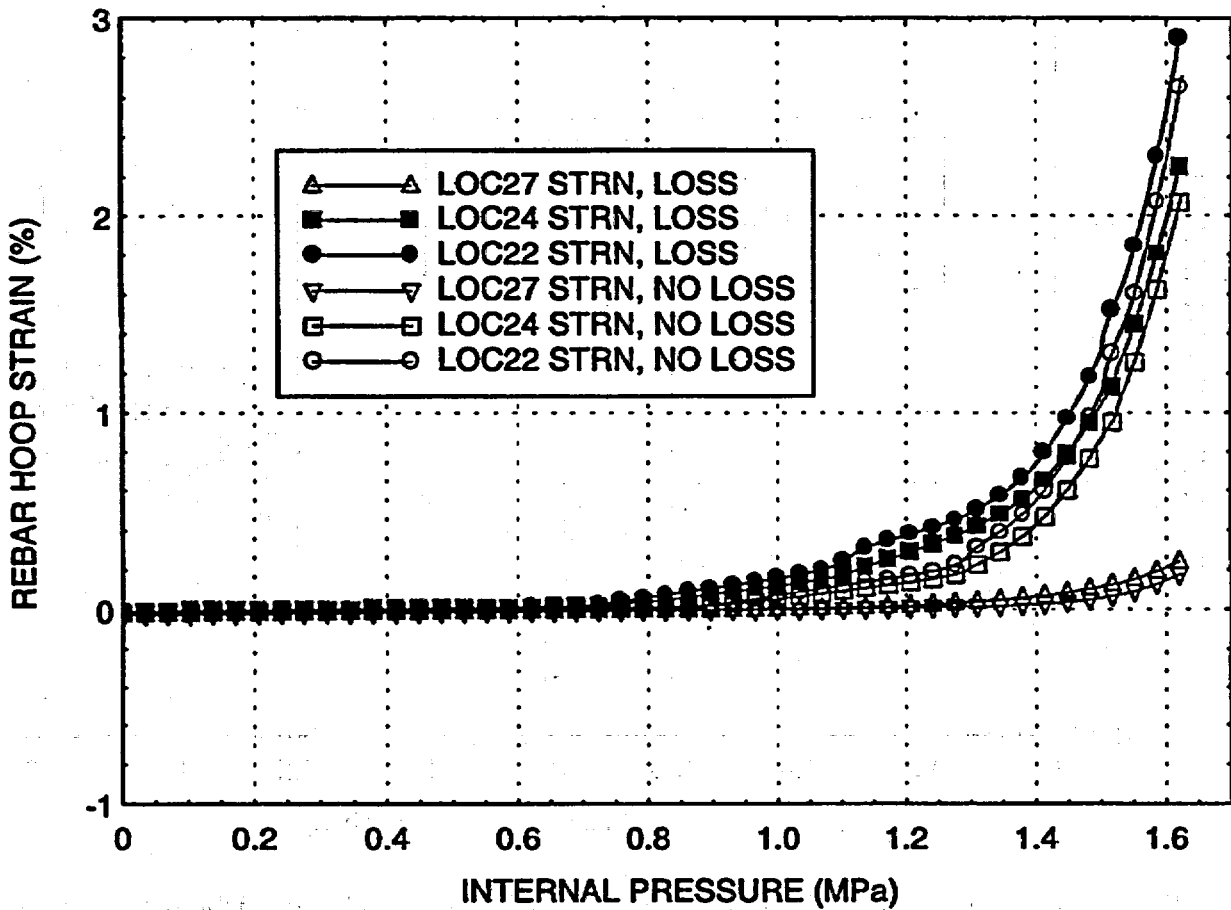


Figure 25. Rebar Hoop Strains versus Internal Pressure at Standard Output Locations

The effect of the prestress loss is more significant in the cylinder locations when compared to the dome location. The same effect can be observed in the radial displacement plots in Figures 18 – 20.

The rebar meridional strains for standard output locations 25 and 26 are shown in Figure 26 for the analysis of a prestress loss and no prestress loss.

Location 25 is at: 10.75 m springline (inner layer)
 Location 26 is at: 10.75 m springline (outer layer)

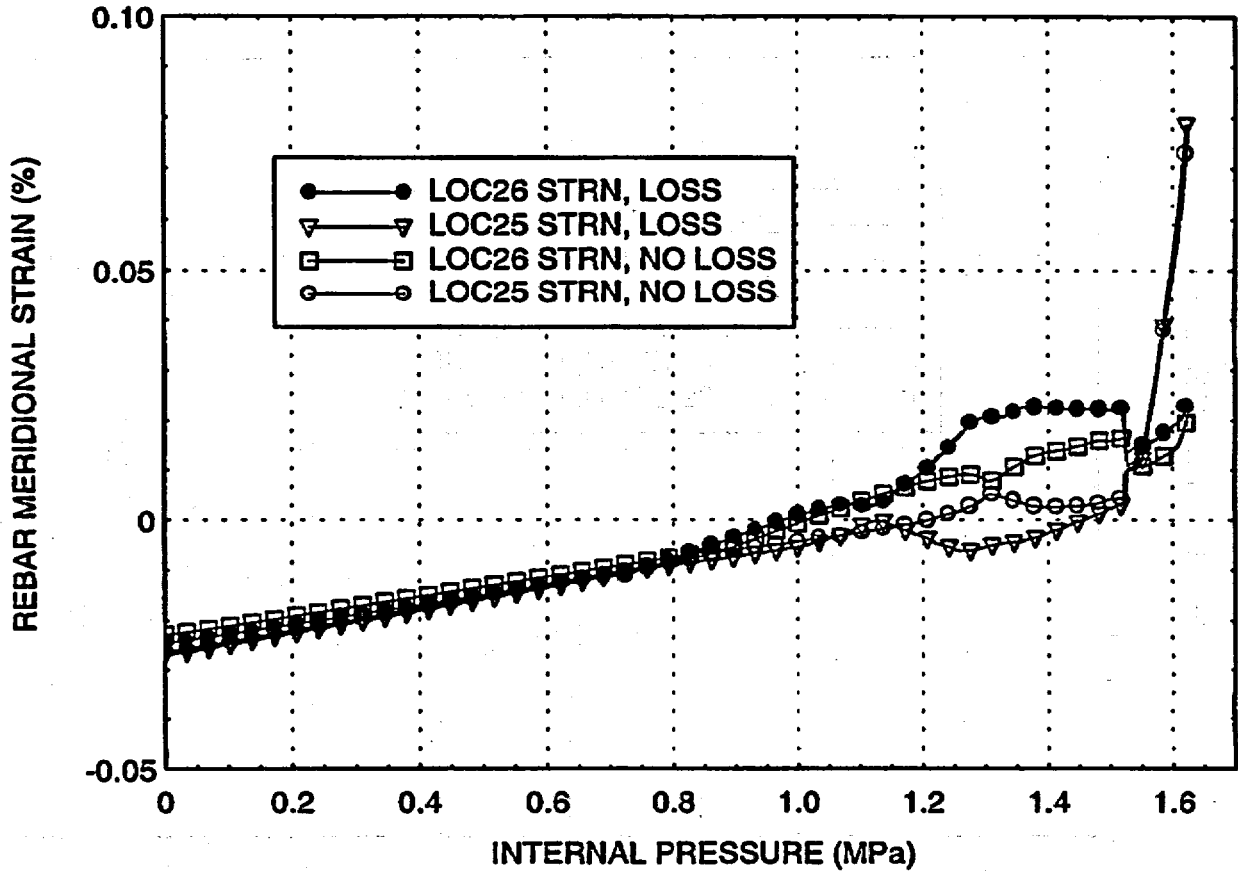


Figure 26. Rebar Meridional Strains versus Internal Pressure at Standard Output Locations

The effect of the prestress loss at these locations is minor, because of the small rebar meridional strains (below yield) at the springline.

The rebar meridional strains for standard output locations 23, 28 and 29 are shown in Figure 27 for the analysis of a prestress loss and no prestress loss.

Location 23 is at:	6.20 m	midheight of cylinder (outer layer)
Location 28 is at:	14.55 m	dome at 45° (inner layer)
Location 29 is at:	14.55 m	dome at 45° (outer layer)

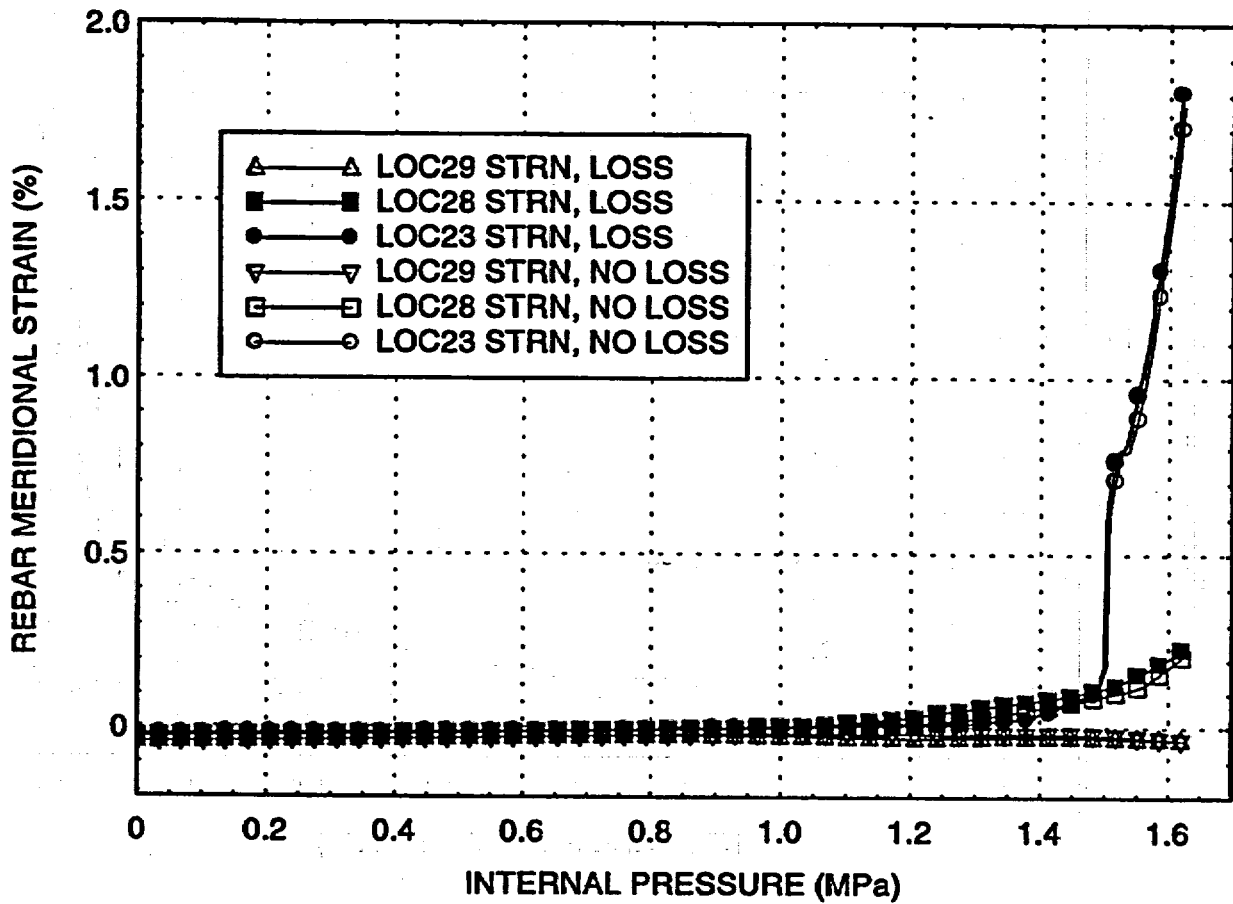


Figure 27. Rebar Meridional Strains versus Internal Pressure at Standard Output Locations

The effect of the prestress loss is hardly noticeable at these locations for the meridional rebar strains.

The liner meridional strains for standard output locations 36 and 38 are shown in Figure 28 for the analysis of a prestress loss and no prestress loss.

Location 36 is at: 0.25 m base of cylinder (inside)
 Location 38 is at: 6.20 m midheight of cylinder (inside)

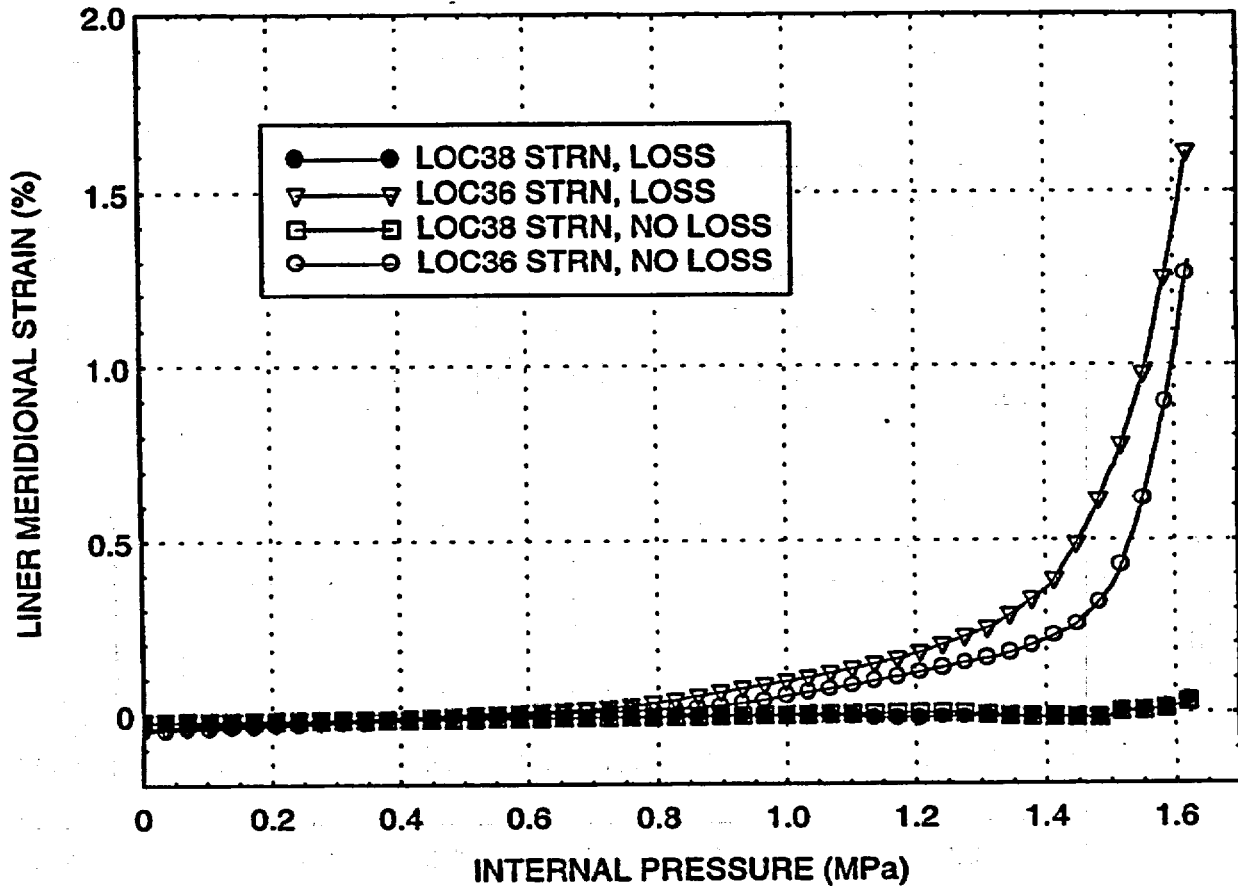


Figure 28. Liner Meridional Strains versus Internal Pressure at Standard Output Locations

The effect of prestress loss, given above, is similar to the prestress loss effect on the rebar meridional strains, as depicted in Figures 22 and 27. The prestress loss reduces the pressure by 0.1 MPa for the nonlinear response at location 36, but had no effect at location 38.

The liner meridional strains for standard output locations 40 and 42 are shown in Figure 29 for the analysis of a prestress loss and no prestress loss.

Location 40 is at: 10.75 m springline (inside)
 Location 42 is at: 16.13 m dome apex (inside)

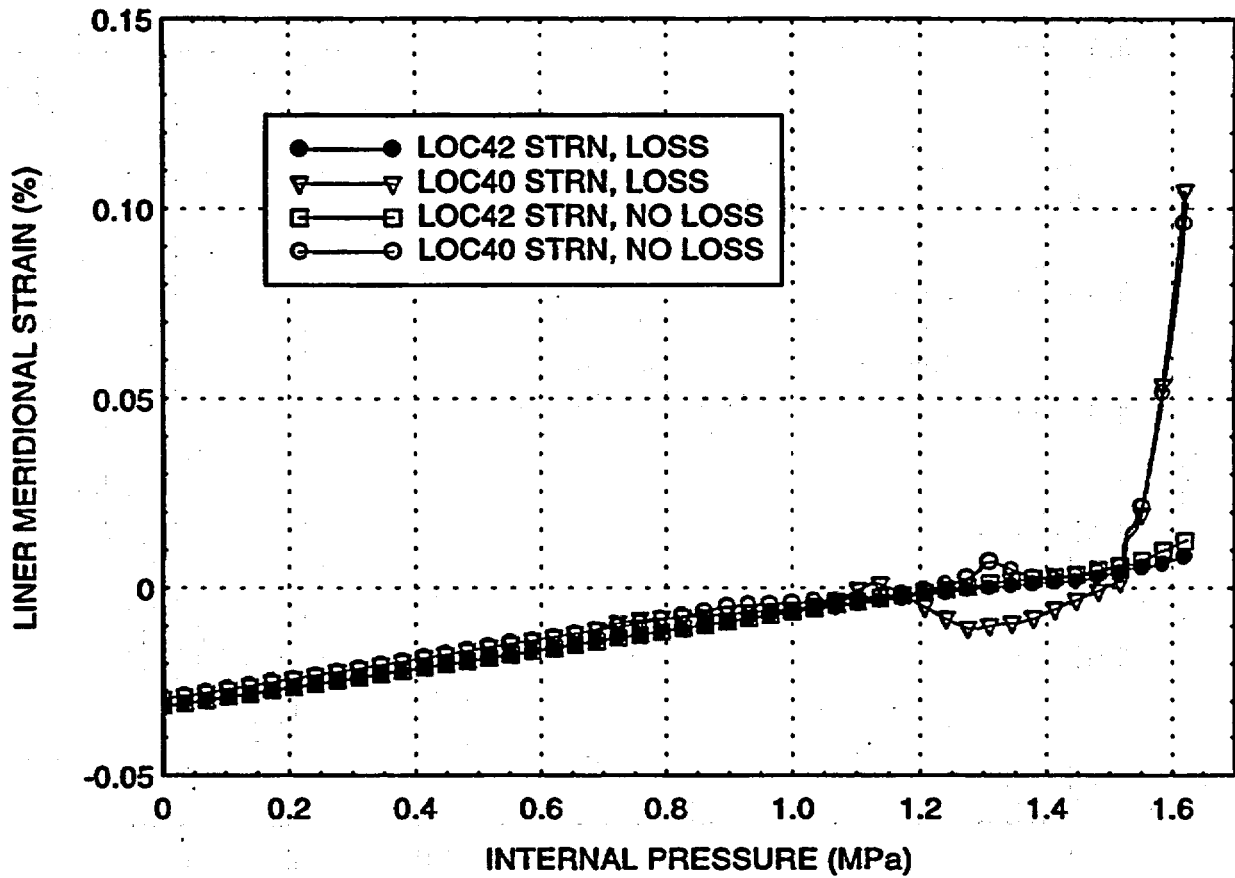


Figure 29. Liner Meridional Strains versus Internal Pressure at Standard Output Locations

The effect of the prestress loss is very small for liner strain at and above the springline in the dome.

The liner hoop strains for standard output locations 37, 39 and 41 are shown in Figure 30 for the analysis of a prestress loss and no prestress loss.

Location 37 is at:	0.25 m	base of cylinder (inside)
Location 39 is at:	6.20 m	midheight of cylinder (inside)
Location 41 is at:	10.75 m	springline (inside)

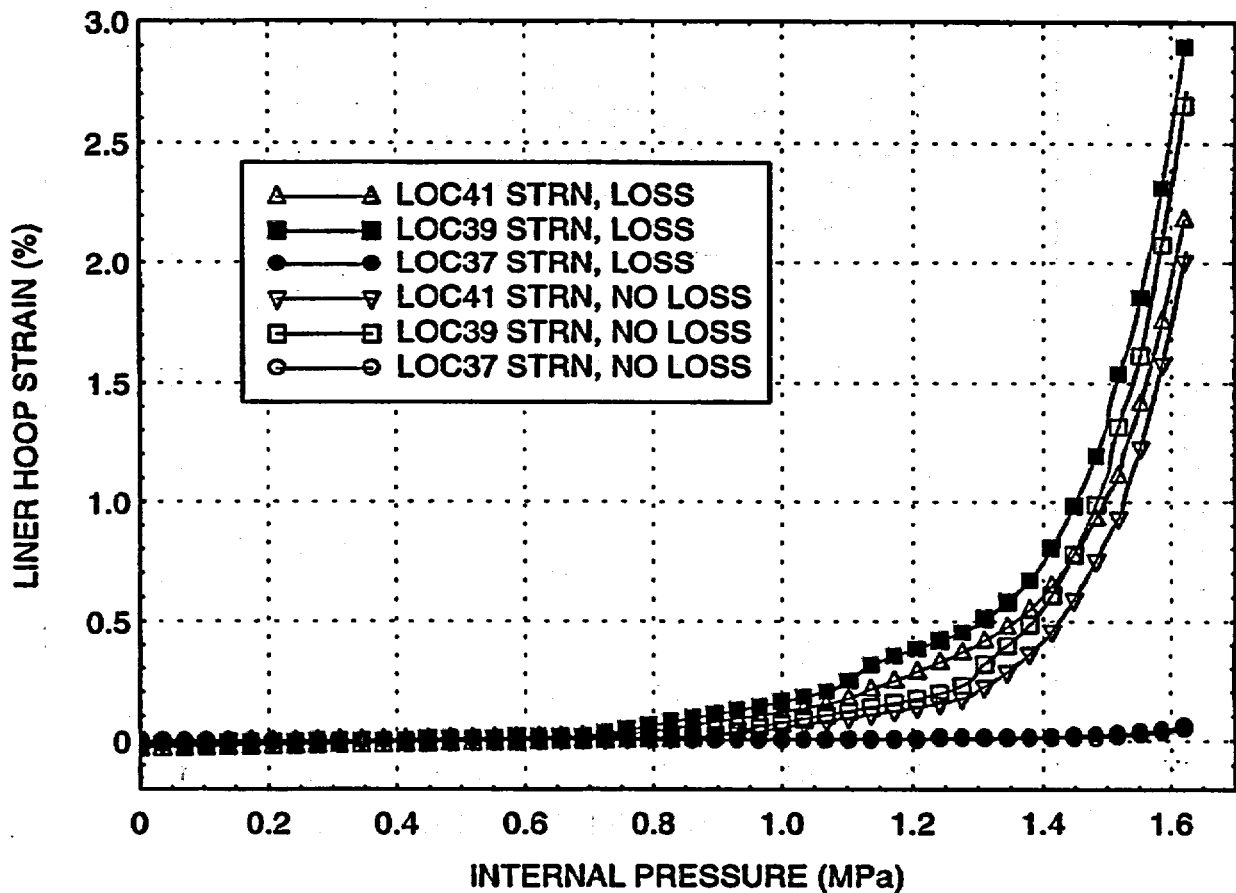


Figure 30. Liner Hoop Strains versus Internal Pressure at Standard Output Locations

The effect of the prestress loss, given above, is similar to the radial displacement responses given in Figures 18 – 20. The nonlinear response occurs at a lower pressure, by approximately 0.1 to 0.15 MPa when the prestress loss is accounted for.

The hairpin (meridional) tendon strains for standard output locations 48 and 49 are shown in Figure 31 for the analysis of a prestress loss and no prestress loss.

Location 48 is at: 15.60 m tendon apex
 Location 49 is at: 10.75 m tendon springline

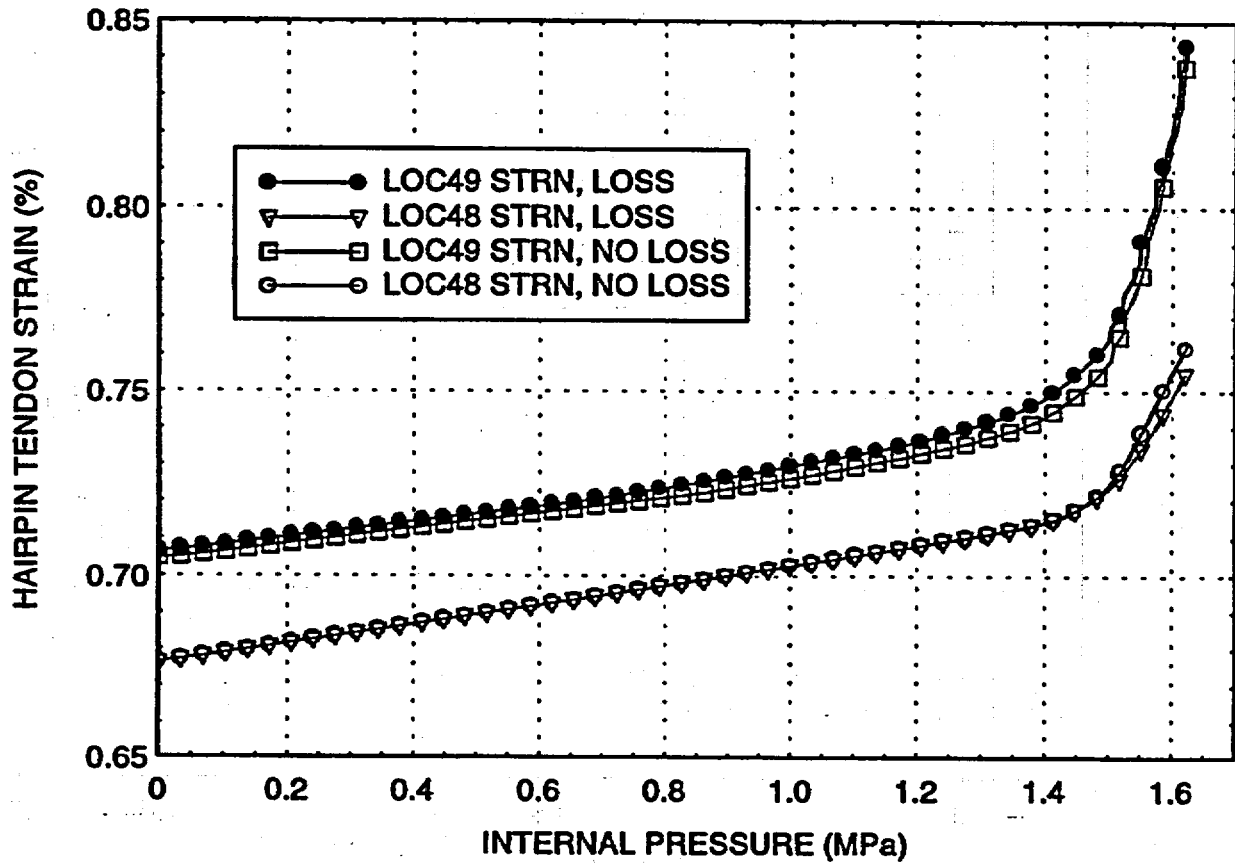


Figure 31. Hairpin Tendon Strains versus Internal Pressure at Standard Output Locations

The effect of the hoop prestress loss has little or no effect on the meridional (hairpin) tendon response.

The hoop tendon strains for standard output locations 52 and 53 are shown in Figure 32 for the analysis of a prestress loss and no prestress loss.

Location 52 is at: 6.58 m tendon near midheight of cylinder at buttress
 Location 53 is at: 4.57 m tendon between E/H and A/L

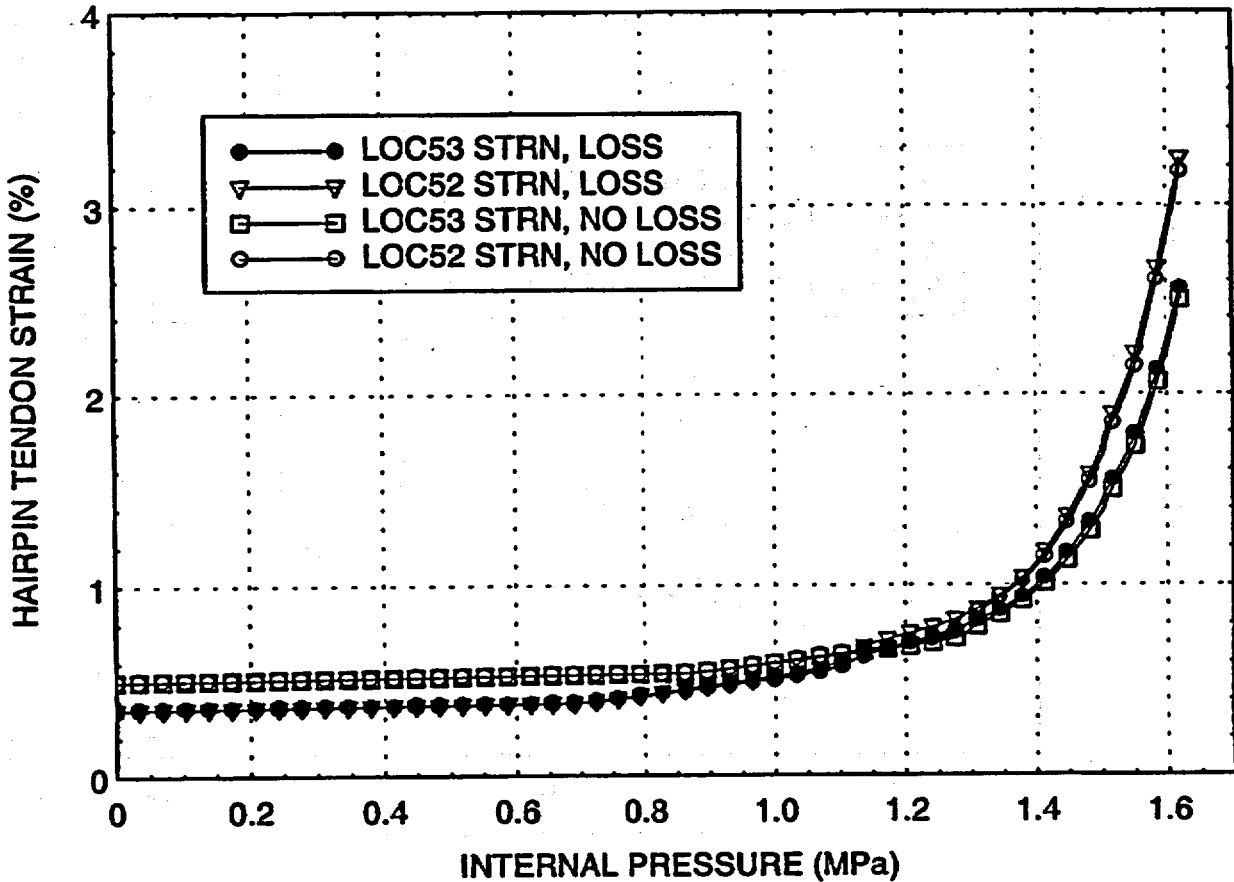


Figure 32. Hoop Tendon Strains versus Internal Pressure at Standard Output Locations

The hoop prestress loss is evident by the vertical shift downwards at zero pressure loading (i.e. 30% reduction), but the response is very similar to the results of Analysis 1 (no prestress loss). At internal pressures above 1.0 MPa, the results for the two analyses are virtually the same.

The hairpin (meridional) tendon force for standard output location 54 is shown in Figure 33 for the analysis of a prestress loss and no prestress loss.

Location 54 is at: 0.0 m tendon gallery

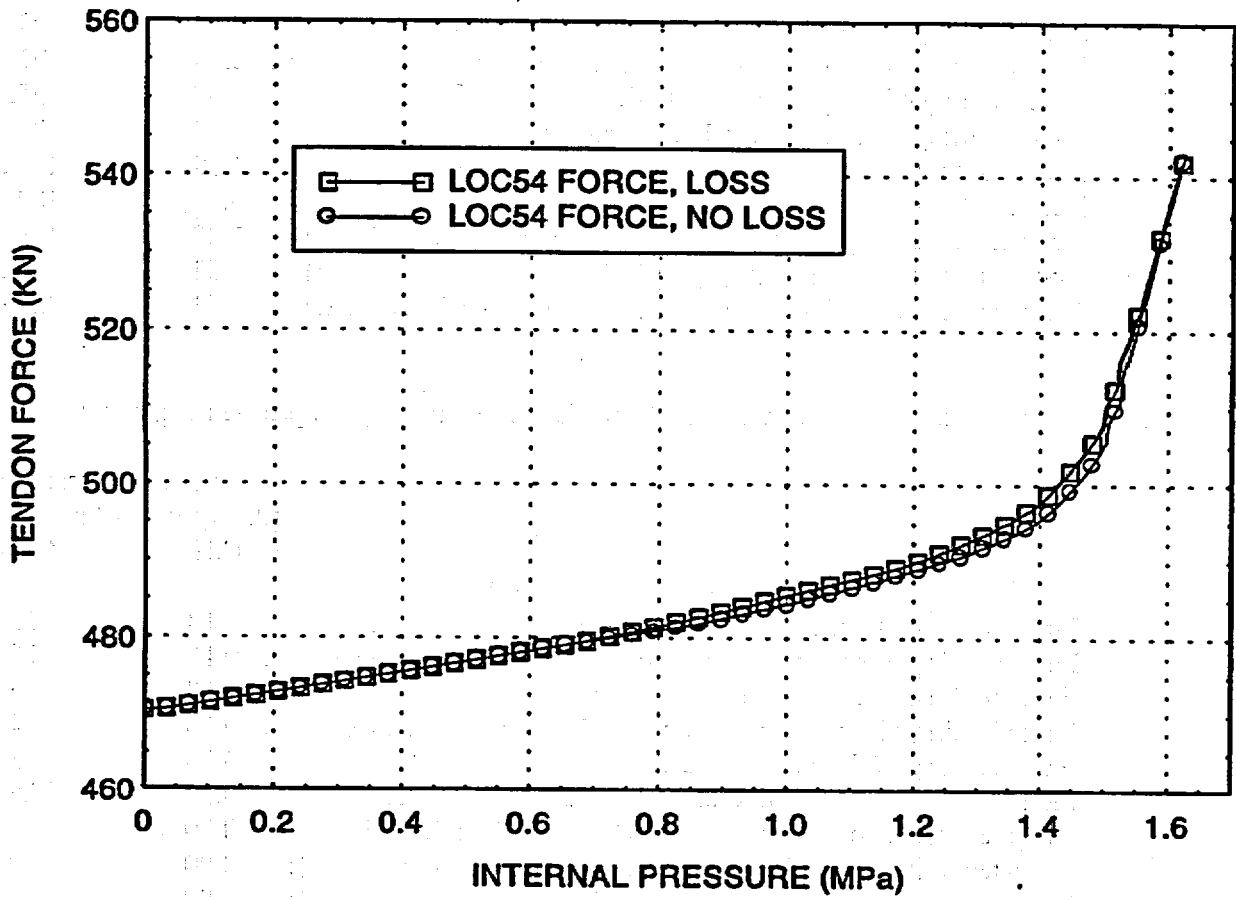


Figure 33. Hairpin Tendon Force versus Internal Pressure at the Standard Output Location

The effect of the prestress loss has little or no effect on the meridional (hairpin) tendons. Similar results were presented in Figure 31 for the hairpin tension strains.

The displacements and strains depicted in Figs. 18 – 33 include the initial deflection/strain from the prestressing of the PCCV. This is why at zero pressure, a displacement or strain is present in some of the pressure history responses.

The effect of pressuring the vessel leads to the following events:

	Gage Pressure (MPa)	(psig)
First cracking of concrete in the cylinder due to hoop stresses:	0.68	98.5
First cracking of concrete in the cylinder due to meridional stress:	0.64	93.5
First yielding of hoop rebar in cylinder:	1.07	155.5
First yielding of meridional rebar in wall basemat juncture:	1.35	195.5
First cracking of dome concrete above 45° dome angle:	1.09	157.5
First cracking of dome concrete below 45° dome angle:	0.70	102.0
Hoop tendons in cylinder reaching 1 % strain (at mid cylinder):	1.37	198.5
Hoop tendons in cylinder reaching 2 % strain (at mid cylinder):	1.53	222.5
Hoop tendons in cylinder reaching 3 % strain (at mid cylinder):	1.61	233.0

The above results are compared with the Analysis 1, in which the full prestressing was applied.

	Pressure Difference [Analysis 1 – Analysis 2]	
	(MPa)	(psig)
First cracking of concrete in the cylinder due to hoop stresses:	0.18	26.5
First cracking of concrete in the cylinder due to meridional stress:	0.11	16.0
First yielding of hoop rebar in cylinder:	0.18	26.5
First yielding of meridional rebar in wall basemat juncture:	0.10	14.5
First cracking of dome concrete above 45° dome angle:	0.09	15.5
First cracking of dome concrete below 45° dome angle:	0.17	25.0
Hoop tendons in cylinder reaching 1 % strain (at mid cylinder):	0.00	0.5
Hoop tendons in cylinder reaching 2 % strain (at mid cylinder):	0.00	0.5
Hoop tendons in cylinder reaching 3 % strain (at mid cylinder):	0.00	0.5

Thus, the hoop prestress loss lowers the onset of concrete cracking, yielding of rebar, and yielding of the liner by approximately 0.1 to 0.2 MPa of internal pressure in the PCCV model. Additionally, the hoop prestress tendon loss does cause the nonlinear response of the radial displacements and hoop strains (rebar and liner) to occur at a lower pressure, by approximately 0.1 to 0.15 MPa. However, the hoop prestress loss has little or no effect on the hoop and hairpin tendon response to internal pressure.

FAILURE PRESSURE OF MODEL

Two failure mechanisms were determined for each analysis case, 1 and 2. The first is a structural failure, in which a hoop tendon will fail due to reaching its ultimate strain in tension.

Several failure modes were investigated during the analysis, such as hoop rebar coupler failure, meridional coupler failure, hoop tendon failure and hairpin tendon failure. The most plausible structural failure was hoop tendon failure near midheight of the vessel cylinder.

The second failure mechanism is a local failure of the liner at approximately midheight of the vessel cylinder, where liner strain concentrations will occur due to the penetrations (i.e. equipment hatch, air lock, other ports, etc.) thickened liner plates, weldments, and liner stud interactions. The local failure pressure predicted was lower than the structural failure pressure.

Structural failure was determined in each of the analysis cases. The failure was the same mode and approximately the same location for each analysis case, which was hoop tendon failure at a location, which is slightly above the midheight of the cylinder. Figure 34 depicts the displaced shape of the vessel just prior to failure in analysis case 1, i.e. last load step at which static equilibrium is maintained. Figure 35 is the displaced shape of the vessel just prior to failure in analysis case 2.

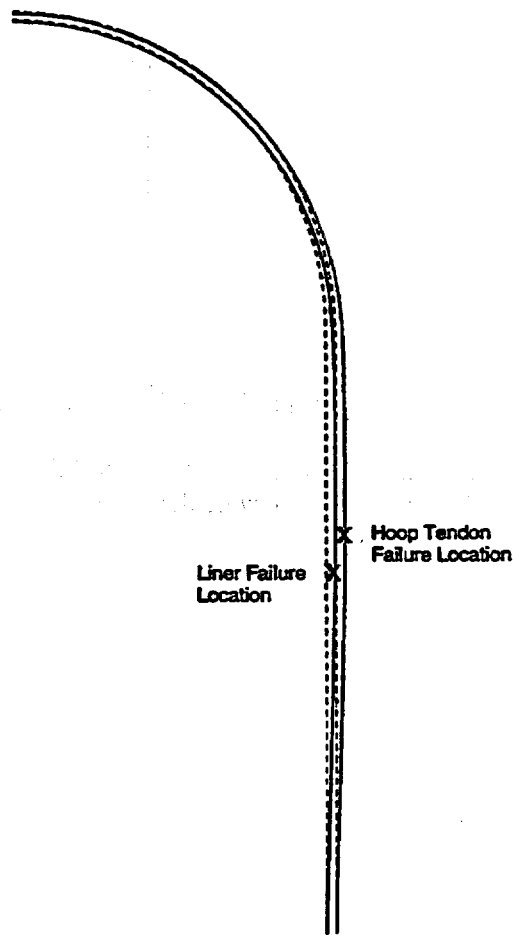


Figure 34. Vessel Displacements at Impending Failure Pressure for Analysis 1.

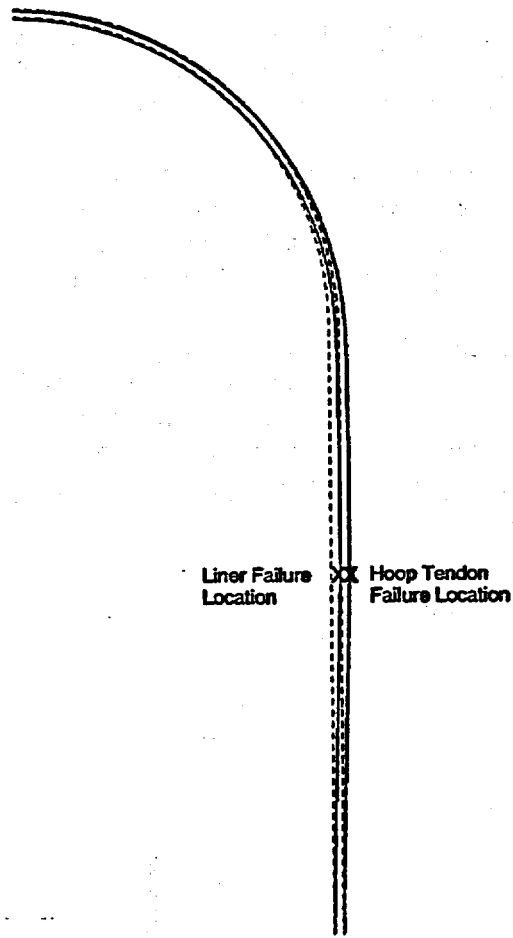


Figure 35. Vessel Displacements at Impending Failure Pressure for Analysis 2.

The main difference between the results of Figure 34 and 35 is the location of the hoop tendon failure. Figure 36 shows the pressure history of the hoop tendon that fails for the two analyses and Table 2 summarizes the results.

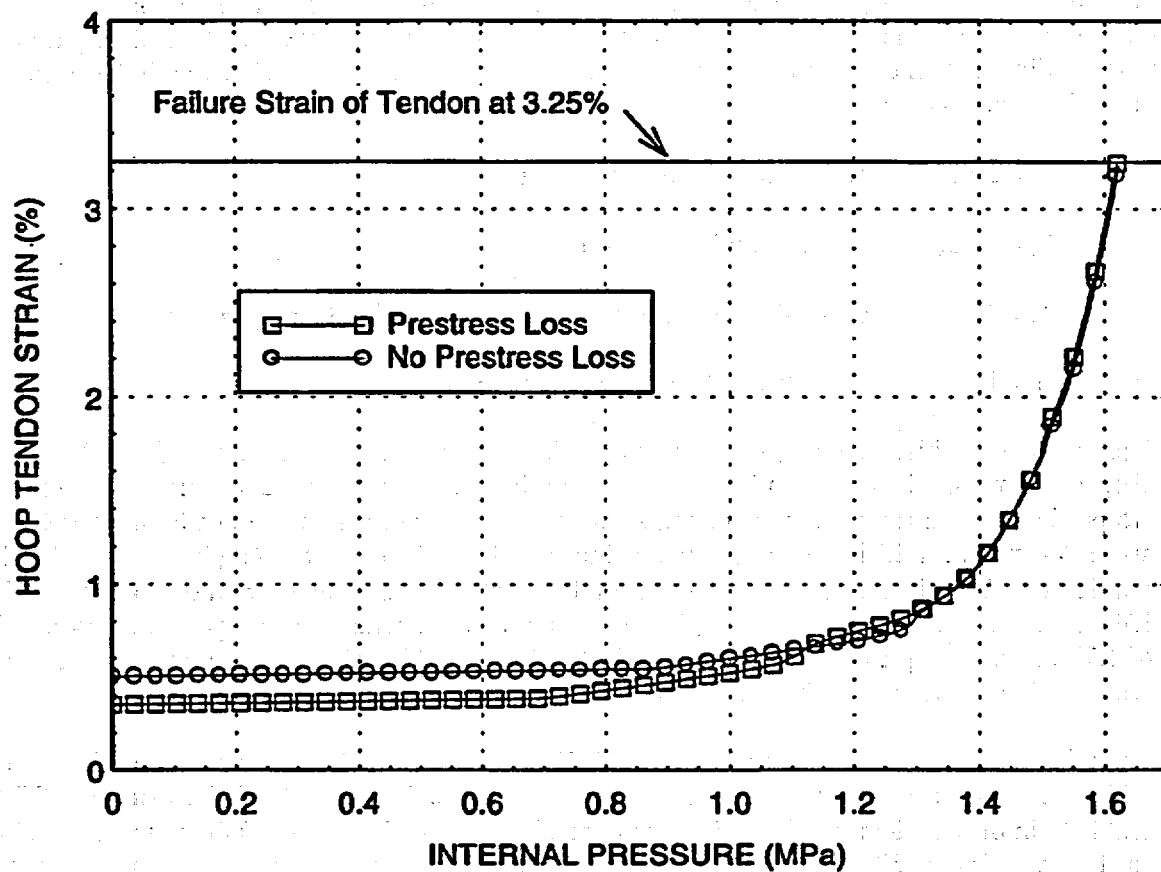


Figure 36. Maximum Hoop Tendon Strain versus Internal Pressure near Cylinder Mid-Height

Table 2. Structural Failure of Hoop Tendon near Cylinder Mid-Height

Analysis Case	Prestress Loss	Elevation of Tendon	Failure Pressure
1	No	7.1 m (277.8 in.)	1.624 MPa (235.5 psi)
2	Yes	6.4 m (251.3 in.)	1.620 MPa (235.0 psi)

The effect of prestress loss for the prediction of this structural failure has little or no consequences on the failure pressures, and a slight effect on the location of failure (0.7 m lower when prestress loss is present).

The liner of the vessel was determined to have a local failure due to the global strains provided in the axisymmetric analyses. The local failure mechanism is described in Eq. 5, in which a reduced failure strain is estimated. The location of the liner was approximately mid-height of the vessel cylinder at an elevation of 6.4m. The knockdown factor was calculated with the following individual factors:

- $K_1 = 5.0$, for the analysis sophistication
- $K_2 = 1.25$, for the as-built condition
- $K_3 = 1.74$, for the liner material condition, i.e. weld joint strength
- $F_T = 1.8$, for the triaxial ductility reduction

The analysis sophistication was chosen to be 5, which is the maximum recommended value, because only global strains can be obtained from the axisymmetric model utilized. Strains that are produced from liner studs, weldments, and thickened liner plates can not be modeled. The as-built factor of 1.25 is a conservative estimate. The welded joint strength given in the data provided by SNL indicates a failure strain of 19% with a liner failure strain of 33%, thus $K_3 = 33\%/19\% = 1.74$. The biaxial state of stress in the liner elements were proportioned by a factor of 1.77 for internal pressures of 1.51 MPa (219 psi) to 1.54 MPa (223 psi), i.e. meridional stress / hoop stress = 1.87, and results in $F_T = 1.8$.

Thus, the total knockdown factor $KF_T = K_1 K_2 K_3 F_T = 19.6$, which gives a reduced failure strain of 1.69% for a liner material failure strain of 33% (Figure 7 depicts the failure strain). With a yield strain of 0.16% in the liner, this would result in a effective plastic failure strain of 1.53%, as shown in Figure 37. The effective plastic strain is based on a uniaxial stress-strain response for a multi-axial state of stress. The results of the local failure analyses are summarized in Table 3, with both load cases indicating local liner failure at an elevation of 6.38m. The reduced prestress load has a minimal effect (1.8% reduction) on the estimated failure pressure. The estimated global failure strain of 1.69% is in a agreement with past concrete containment vessel experiments, i.e. 1/6 scale reinforced concrete containment vessel test at SNL. Ref. [6] provides similar global strains (average axisymmetric global strains of 1.73% in the free field for local liner failure at vessel cylinder mid-height) to the estimated failure strain calculated above.

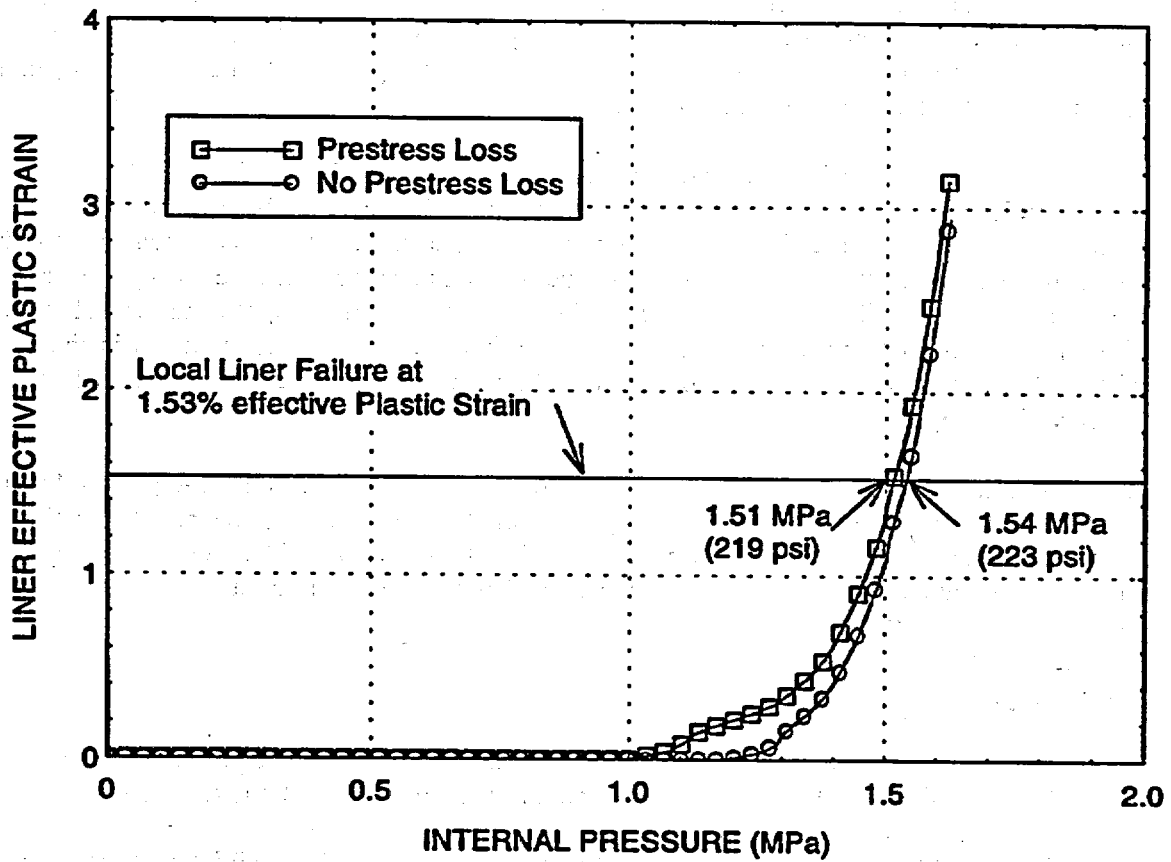


Figure 37. Maximum Liner Effective Plastic Strain versus Internal Pressure at an Elevation of 6.38m

Table 3. Local Liner Failure at Cylinder Mid-Height, Elevation 6.38m

Analysis Case	Prestress Loss	Failure Pressure
1	No	1.54 MPa (223 psi)
2	Yes	1.51 MPa (219 psi)

SUMMARY

Two analyses were performed using an axisymmetric model of the PCCV scaled test. The first analysis used the full hoop tendon force and the second analysis use a reduced hoop tendon force. The reduced tendon force was an approximation of what the actual free field of the vessel model will experience, in regards to the hoop tendons. The reduced tendon force resulted in an earlier onset of concrete cracking, yielding of rebar and yielding of the liner. The difference in

internal pressure was about 0.1 MPa to 0.2 MPa for cracking and yielding to occur. However, the predicted failures did not decrease significantly with a prestress loss, approximately 1.8% maximum reduction. There was no change in the internal pressure to cause yielding of the tendons, when the two analyses are compared.

Two failure modes were investigated, structural failure and local liner failure. The structural failure predicted is a hoop tendon failing, which in turn will cause the liner to rip and allow the internal pressure to escape through the cracked concrete vessel wall. The local liner failure occurs at a lower pressure and will also allow the internal pressure to escape through the cracked concrete vessel wall. Both failures occur at a location near the mid-height of the vessel cylinder with an elevation of between 6.4m to 7.1m. Note that the liner and hoop strains in the vessel cylinder from an elevation of 5.5m to 7.5m are almost constant, thus the failures could occur in this elevation range.

The displacements, strains and forces provided to SNL for inclusion in the composite plots (i.e. comparisons with the other round robin participants) were based on the results obtained in Analysis 2, which had the hoop prestressing loss. These results would be more representative of the displacements and strains of the actual PCCV model in the free field response, where a prestress loss will exist.

In summary:

Local liner failure is estimated at 1.51 MPa (219 psi) internal pressure near the mid-height of the vessel cylinder, where local liner strain concentrations are present.

Structural failure of hoop tendons estimated at 1.62 MPa (235 psi) internal pressure near the mid-height of the vessel cylinder.

Best estimate of static failure pressure is 1.51 MPa (219 psi) near the mid-height of the vessel cylinder, due to a local liner failure that results from a liner strain concentration. This pressure is approximately 3.8 times the design pressure.

Minimum pressure reachable with a 90% confidence level (i.e. PCCV will most likely reach this pressure): 1.36 MPa (197 psi) based on an estimate of 90% certainty for the lowest failure pressure predicted.

Maximum pressure reachable with a 90% confidence level (i.e. PCCV will never reach this pressure): 1.62 MPa (235 psi).

ACKNOWLEDGMENT

This work was performed under the auspices of the U.S. Department of Energy, Office of International Nuclear Safety and Cooperation, under Contract W-31-109-Eng-38.

REFERENCES

- [1] Marchertas, A. H., and Kulak, R. F., "Numerical Modeling of Concrete Under Thermal Loads," Nuclear Engineering and Design, Vol. 68, No. 2, 1981, pp. 225-236.
- [2] Marchertas, A. H., and Kulak, R. F., "Response Simulation of Concrete Structures to High Temperatures," Proceedings of the workshop on Containment Integrity, Vol. 1, NUREG/CP-0033, SAND82-1659, Sandia National Laboratories, Albuquerque, NM, October 1982, pp. 193-212.
- [3] Marchertas, A. H., Kennedy, J. M., and Pfeiffer, P. A., "Reinforced Flexural Elements for the TEMP-STRESS Program," Nuclear Engineering and Design, Vol. 106, 1988, pp. 87-102.
- [4] Pfeiffer, P. A., et al., "Pretest Analysis of a 1:6-Scale Reinforced Concrete Containment Model Subject to Pressurization," Nuclear Engineering and Design, Vol. 115, 1989, pp. 73-89.
- [5] Pfeiffer, P. A., et al., "Thermal Effects in the Overpressurization Response of Reinforced Concrete Containment," Nuclear Engineering and Design, Vol. 120, 1990, pp. 25-34.
- [6] Pfeiffer, P. A., et al., "Posttest Analysis for the Nonlinear Response of an Internally Pressurized 1:6-Scale Reinforced Concrete Containment Model," Nuclear Engineering and Design, Vol. 133, February 1992, pp. 143-157.
- [7] Hsieh, S. S., Ting, E. C., and Chen, W. F., "A Plastic-Fracture Model for Concrete," Int. J. Solids Structures, Vol. 18, No. 3, 1985, pp. 181-197.
- [8] Bazant, Z. P., and Oh, B. H., "Crack Band Theory for Fracture of Concrete," Materiaux et Constructions, Vol. 16, No. 93, pp. 155-177.
- [9] Flanders, H. E., "Strain Limit Criteria to Predict Failure," Proceedings of the 5th DOE Natural Phenomena Hazards Mitigation Conference, Organized by LLNL, November 13-14, 1995, Denver Colorado, pp. 164-168.
- [10] Manjoine, M. J., "Ductility Indices at Elevated Temperatures," Journal of Material Technology (Transactions of the ASME), 1975.
- [11] Luk, V. K., "PCCV Round Robin Analysis - Release of Design Package," Sandia National Laboratories, SO-97-047, Nov. 17, 1997.

APPENDIX D

CEA

**COMMISSARIAT A L'ÉNERGIE ATOMIQUE
FRANCE**

Appendix A, Composite Plots, comprises test data compiled and plotted from all organizations that participated in the Prestressed Concrete Containment Vessel (PCCV) Round Robin Pretest Analysis. To avoid duplicating the composite information, individual sets of data and/or plots have been omitted from participants' reports. In some cases this action resulted in disconnects between callouts and content and in the numbering of figures, tables, and pagination in some reports.

In Appendix D, "CEA, Commissariat a l'Energie Atomique, France," discontinuity arises from omitting the following material:

Table 1

PCCV Pretest Analysis Report

Table of Contents

1. INTRODUCTION.....	2
2. FINITE ELEMENT MODEL AND BOUNDARY CONDITIONS.....	3
3. RESULTS OF PRESSURE LOADING CALCULATION.....	6
4. CONCLUSION.....	7
REFERENCES.....	8
Table 1. PCCV Standard Output Locations (8/27/98) (from [3]).....	9
FIGURES	
Fig. 1. Outline sketch of PCCV model (from ref. [2]).....	10
Fig. 2. Overall view of the prestressing cables.....	11
Photo by Sandia National Laboratories	
Fig. 3. Concrete mesh.....	12
Fig. 4. Longitudinal rebars.....	13
Fig. 5. Hoop rebars.....	14
Fig. 6. Prestressing tendons.....	15
Fig. 7. Portion of containment considered for prestressing phasis.....	16
Fig. 8. Uniaxial response of concrete under traction load.....	17
Fig. 9. Stress-strain curve for D10 steel.....	18
Fig. 10. Stress-strain curve for D13 steel.....	18
Fig. 11. Stress-strain curve for D16 steel.....	19
Fig. 12. Stress-strain curve for D19 steel.....	19
Fig. 13. Stress-strain curve for D22 steel.....	20
Fig. 14. Stress-strain curve for tendons steel.....	20
Fig. 15. Radial displacement versus pressure.....	21
Fig. 16. Vertical displacement versus pressure.....	22
Fig. 17. Hoop cracking strains in concrete for $p = 0.8$ MPa.....	23
Fig. 18. Meridional cracks for $p = 0.8$ MPa.....	24
Fig. 19. Meridional cracking pattern for various pressure levels.....	25
Fig. 20. Maximum hoop strain in cylinder, versus pressure.....	26

1. INTRODUCTION

This report presents the model used by CEA/DMT/LM2S for the predictive calculation of the 1 : 4 scale model of a prestressed concrete containment vessel (PCCV) for pressurized water reactors, in the framework of an international round robin exercise, organized by the Sandia National Laboratories (USA). The aim of these calculations is to predict the failure loading as well as the failure mode of the PCCV model, when subjected to an increasing internal pressure, beyond design pressure. Such exercises have been already carried out in the past on reinforced concrete containment vessels [1]. The originality here is the fact that the containment is prestressed and therefore one might expect some catastrophic structural failure before a significant leakage of the containment.

The main dimensions of the PCCV are shown on figure 1, and the layout of the prestressing cables as installed, at the date of October 1998 is shown on figure 2. From these two figures, it is clear that the model is definitely not axisymmetric. As far as geometrical features are concerned, it can be observed on figure 1 that the 135° azimuth, which is located furthest from the various penetrations, may be chosen as representative for an axisymmetric model, even though the overall deformation of the containment will not show an axisymmetric shape, in particular because of the equipment hatch. In fact, as summarized in table 1, many results required from the pretest analysis are concerning azimuth 135°. An axisymmetric modelisation of the prestressing cables is more problematic because of the cables arrangement in the dome. In fact, a most straightforward approach is to describe the prestressing cables as they are, leading thus to a three dimensional model of the containment, or a part of it, by means of solid or even shell elements.

The main difficulty of such an approach lies in the preparation of the geometrical model which leads to a very important time and amount of data, more than in the modeling choices. Moreover, the computer resources needed are also very important, in terms of CPU time as well as storage disks. Therefore, because of our limited resources in terms of manpower and computer, we have decided to restrict ourselves to an axisymmetric analysis even though it leads to two major difficulties :

- ⇒ the results can not be provided as required at the 55 standard output locations but only at 34 locations (corresponding to azimuth 135° on table 1),
- ⇒ some approximations must be done in the modeling of the prestressing cables in the dome, leading thus to an approximate state of stresses and strains in that part of the structure.

The following parts of this report describe the finite element model, the material data as well as the boundary conditions as used in the computation, and the main results obtained.

2. FINITE ELEMENT MODEL AND BOUNDARY CONDITIONS

In order to have a systematic description, as much as possible in the framework of an axisymmetric model, of the various rebars and cables, we have represented the various steel components leading thus to the mesh of the concrete, in particular in the basemat. The elements used for the concrete are linear quadrilateral elements. The elements used for the liner as well as the longitudinal rebars and prestressing cables, are two node shell elements, and the elements used for hoop rebars and prestressing cables are 1 node circular elements.

In the upper half to the dome, the non axisymmetric prestressing cables have been modeled by means of an equivalent shell. The same applies to the orthogonal non axisymmetric rebars in the basemat. Figures 3 to 6 show the various meshes of the concrete, longitudinal and hoop rebars, and prestressing tendons in the containment. The total number of elements is as follows : 2604 elements for the concrete, 1521 elements for the longitudinal rebars, 471 elements for the hoop rebars, 305 elements for the prestressing tendons and 204 elements for the liner.

In the calculation, the rebars nodes are tied to the concrete ones. Concerning the prestressing tendons, they are first considered as unbounded, during the prestressing phases and then tied to the concrete nodes. This means that under the internal pressure loading, there will be no possible sliding movement of the tendons with regards to the concrete. Of course, this is not representative of reality, but we think that these relative movements will not be so important during the pressure loading phase, compared to the prestressing phase. Concerning the boundary conditions, the radial displacements are prevented on the axisymmetry axis, a zero vertical movement is prescribed to the point below the basemat on this axis, while all the other vertical displacements at the bottom of the basemat are subjected to unilateral constraints : they can move upwards (authorizing thus an uplift movement of the basemat) but they cannot move downwards.

The loading sequence of the containment has been decomposed into four phases :

- a. *First phasis* : Calculation of the incomplete containment (see figure 7), without prestressing, under dead weight.
- b. *Second phasis* : Prestressing of the incomplete containment.
- c. *Third phasis* : Calculation of the full containment, under dead weight of the added portion.
- d. *Fourth phasis* : Calculation of the full containment under increasing internal pressure.

We have considered that the experimental results are being recorded during this fourth phasis, and therefore, the end of the third phasis is considered as our initial state from which we supply displacements and strains.

The calculations are performed using the finite element Code Castem 2000 (ref. [4]), which is a general purpose object oriented F.E. Code. The non linear equilibrium equations are solved using a classical modified Newton-Raphson technique. Various non linear material models are available for concrete as well as steel.

Material modeling

a) Concrete

In this study, we have used for concrete the classical elastoplastic fracturing model proposed by Ottosen in the literature. It is based on the smeared crack approach, in which the discontinuity induced by cracking is accounted for by means of the material model at each Gauss point within an element. As far as cracking is concerned, up to three orthogonal cracks may form at one point. The cracking criterion is a maximum principal stress criterion. Once a crack is formed, the response of the concrete becomes anisotropic, and the direction of the crack is memorized. The uniaxial stress-strain in the direction perpendicular to a crack is as shown on figure 8.

Upon unloading, the material follows a path corresponding to a damaged modulus. When the ultimate strain ε_u is reached then the concrete can not sustain a traction load any more along this direction.

For the computation, in view of the uncertainties on the concrete properties, as measured from the yard, we have considered some mean properties, with reference to field curing, as follows :

- Young's modulus : $E_c = 27\ 000\ \text{MPa}$
- Poisson's ratio : $\nu = 0.18$
- Compressive strength : $f'_c = 44\ \text{MPa}$
- Traction strength : $f'_t = 3.45\ \text{MPa}$

$$\varepsilon_r = 7 \cdot \frac{f'_t}{E_c} = 8.94 \cdot 10^{-3}$$

b) Rebars

The rebars are modeled using an elastoplastic with isotropic hardening material model. The uniaxial curves depicted on figures 9 to 13 have been used to identify the hardening properties of the various kinds of rebars.

The nominal sections of the rebars have been used as such or as data to calculate the equivalent thicknesses of shell elements when needed. In all cases, the thickness is calculated on the basis of an equivalence of quantity of steel.

The rebars sections used as input data are (in m^2) :

$$SD\ 10 = 71.33\ 10^{-6}$$

$$SD\ 13 = 126.7\ 10^{-6}$$

$$SD\ 16 = 198.6\ 10^{-6}$$

$$SD\ 19 = 286.5\ 10^{-6}$$

$$SD\ 22 = 387.1\ 10^{-6}$$

The corresponding Young's modula are (in Pa) :

$$E_s\ 10 = 1.82\ 10^{11}$$

$$E_s\ 13 = 1.83\ 10^{11}$$

$$E_s\ 16 = 1.83\ 10^{11}$$

$$E_s\ 19 = 1.84\ 10^{11}$$

$$E_s\ 22 = 1.91\ 10^{11}$$

The horizontal orthogonal rebars in the basemat are modeled by means of an equivalent isotropic shell, with Poisson's ratio equal to 0.3. The vertical rebars are modeled by means of shells having unidirectional properties.

The hoop rebars, represented by one node circular element, by construction, have resistance only along the hoop direction.

c) *Liner*

The liner is also modeled by means of an elastoplastic material model, with isotropic hardening. Its thickness is 1.6 mm and its stress-strain relation follows D16 steel curve (figure 11).

d) *Prestressing tendons*

As already mentioned, the longitudinal prestressing cables are modeled in the cylinder and in the lower half of the dome by shell elements having unidirectional properties, and in the upper half of the dome by an equivalent isotropic shell. For both, we used an elastoplastic material model with isotropic hardening identified from the stress-strain curve displayed on figure 14.

The equivalent shell in the dome has a uniform thickness $e = 4.18$ mm and a Poisson's ratio set equal to 0. The basic data considered for the thicknesses and sections of prestressing tendons is the section of a tendon, which has been taken as 339.3 mm^2 .

One important aspect is the prestressing phasis. As specified, the tendons are prestressed from both ends, one after the other, and according to a well defined sequence. In our axisymmetric calculation, we could not follow this sequence (which results in various stress redistributions), and we applied the prestressing loads in one operation.

For this purpose, we performed separate additional calculation on full single tendons (longitudinal and circular) in order to calculate the distributions of stresses along the tendons due to the various losses (friction, set loss due to pull back).

Then, these stress distributions have been transferred to our axisymmetric model, without modification for the longitudinal tendons and using mean value for the circular tendon (Indeed, the circumferential variation of the stress is not compatible with our axisymmetry hypothesis, and therefore we considered a mean value of 269 kN).

In the upper half of the dome, identical prestress was assumed in the two principal directions of the equivalent shell.

3. RESULTS OF PRESSURE LOADING CALCULATION

The fourth phasis of the calculation consisted in applying an internal increasing pressure, with steps of 0.1 MPa. The calculation was run up to 1.6 MPa. For 1.7 MPa, no equilibrium state could be reached which means that our prediction of the limit pressure sustainable by the containment is between 1.6 MPa and 1.7 MPa. This is confirmed by the analysis of some displacements at some locations in the containment which show a rapid increase at 1.6 MPa, as shown on figures 15 and 16, which present the radial and vertical displacements at some points of the containment.

The first cracking of concrete, in the cylinder and in the hoop direction does occur for an internal pressure of 0.7 MPa and it further develops in nearly all the cylinder between 0.7 MPa and 0.8 MPa, leading to the discontinuity of the radial displacement, visible on figure 15.

Figure 17 shows a plot of the iso hoop cracking strains in the concrete, for an internal pressure of 0.8 MPa.

The first cracking of concrete in the cylinder in a meridional plane, does occur for an internal pressure of 0.5 MPa. It is localized at the junction between the cylinder and the basemat. It does

not evolve much until the pressure reaches 0.8 MPa. For this value, the cracks start also in the dome, mostly below 45°. The figure 18 shows the state of the cracks in a meridional plane, for $p = 0.8$ MPa. The repartition of the cracks in the dome is due to a bending deformation of the dome.

Then for $p = 0.9$ MPa, the dome is entirely cracked, and some cracks also develop in the lower part of the cylinder. The meridional cracking of concrete is nearly complete for $p = 1$ MPa. Figure 19 shows the meridional crack pattern for $p = 0.9$ MPa, 1 MPa and finally 1.6 MPa. For this last pressure level, the basemat portion located between the cylinder and the tendon prestressing gallery is highly sheared, leading to inclined cracks. Moreover, at the junction between the cylinder and the basemat, the concrete is cracked in two directions, leading to a sort of plastic hinge.

The evolution of the maximum strain in cylinder tendons, versus pressure is shown on figure 20. The 1 % value will be reached for a pressure level comprised between 1.6 MPa and 1.7 MPa. Note that this figure is consistent with the evolution of the radial displacement versus pressure, as already shown on figure 15.

4. CONCLUSION

We have performed a simplified axisymmetric analysis for the prediction of the limit load and failure mode of the PCCV make-up, for economy's reasons. Of course, such a model is not fully appropriate, since the real structure is not axisymmetric, because of geometrical features and prestressing tendons lay-out. Therefore, the model necessarily implies additional hypothesis, which may induce differences with regards to a prediction using a full three dimensional analysis. This is particularly true for the non linear behavior of the dome. Another source of discrepancy is the assumption of perfect bonding between the prestressing tendons and the concrete, once the prestressing forces have been applied. This assumption may lead to an over stiff behavior of the containment and therefore an overestimated limit load. However, we think that our calculation should give a good first approximation of this limit load, which, according to our calculation, should be comprised between 1.6 MPa and 1.7 MPa, the corresponding failure mode being an excessive radial displacement at the mid height of the cylinder, leading to a prestressing tendons rupture and probably to a tearing of the liner in this region.

REFERENCES

- [1] Claus D.B., 1987.
« Round Robin pretest analysis of a 1 : 6 scale reinforced concrete containment model subject to static internal pressurization ».
SAND 87 - 0891, NUREG/CR-4913.
- [2] PCCV Round Robin Analysis.
Release of Design Package. SO-97-047.
- [3] PCCV Round Robin Analysis.
Updated Information Package. SO-98-052.
- [4] P. VERPEAUX, A. MILLARD, T. CHARRAS, A. COMBESCURE
« A modern approach of large computer codes for structural analysis ». Proc. of SMIRT 10 Conference, Ed. Hadjian, Los Angeles, 1989.

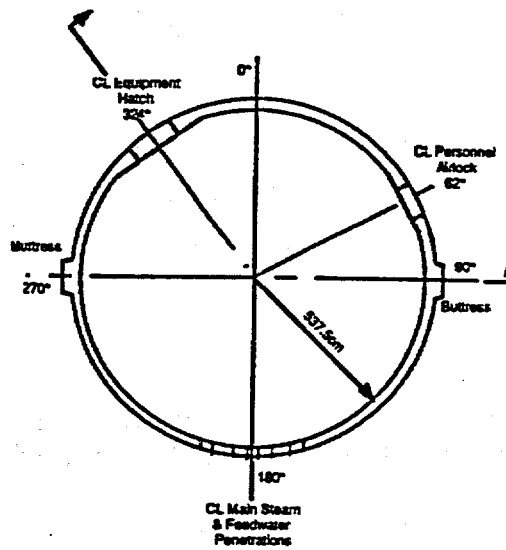
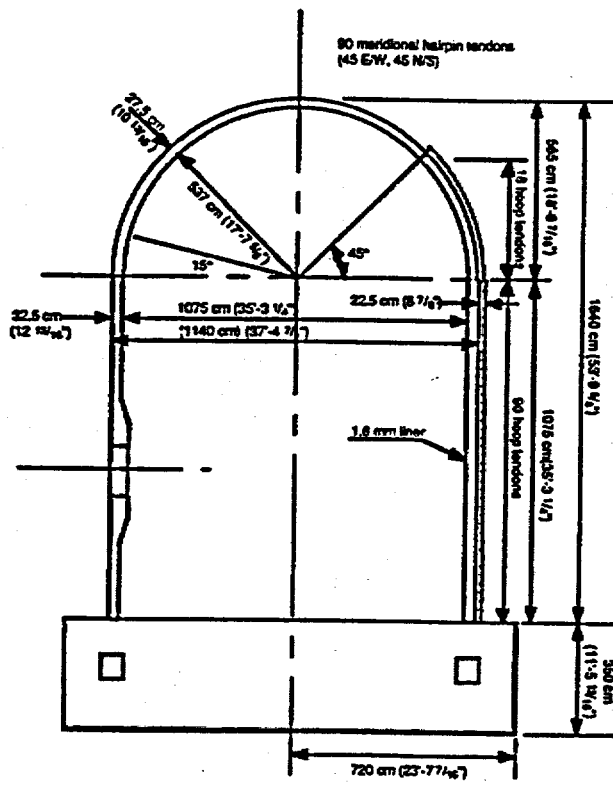


Fig. 1. Outline sketch of PCCV model (from ref. [2])

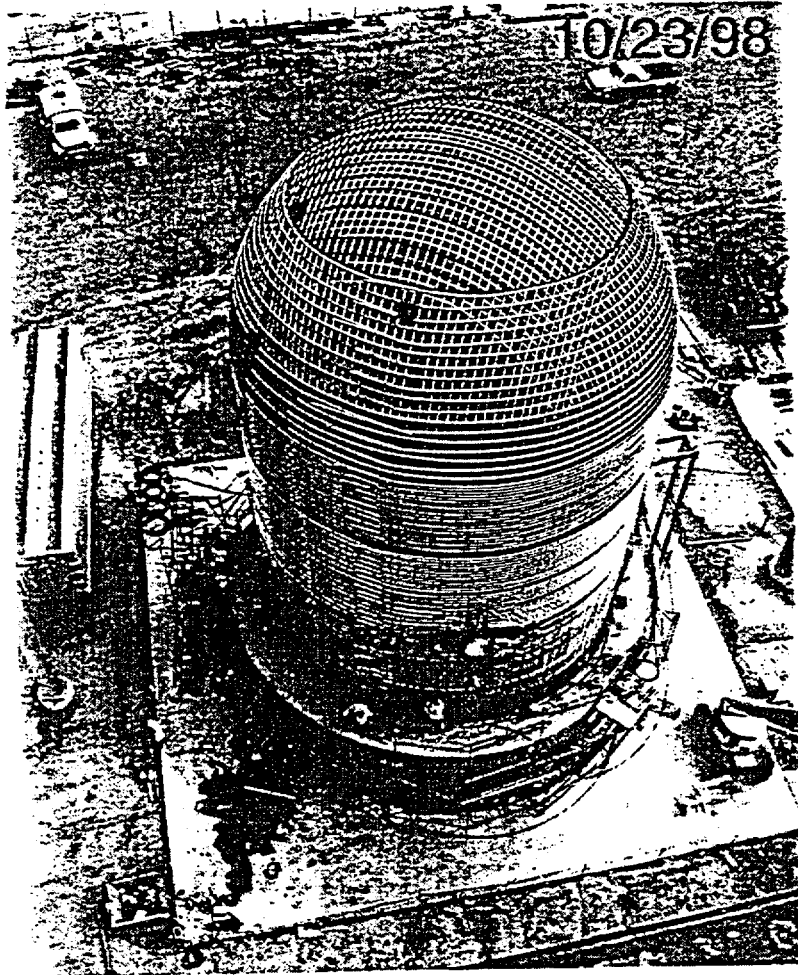


Fig. 2. Overall view of the prestressing cables
Photo by Sandia National Laboratories

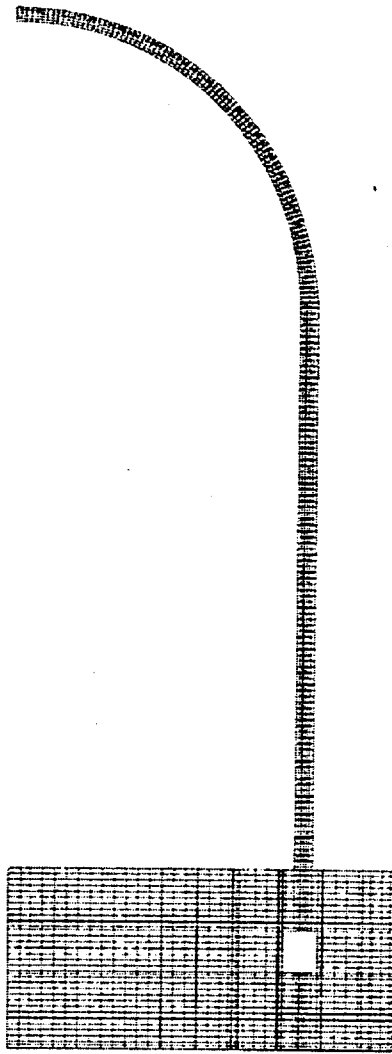


Fig. 3. Concrete mesh

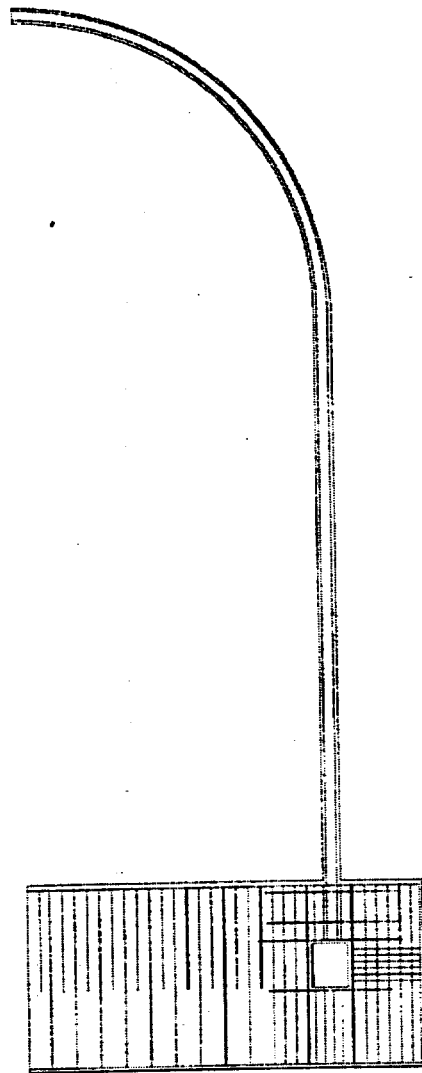


Fig. 4. Longitudinal rebar

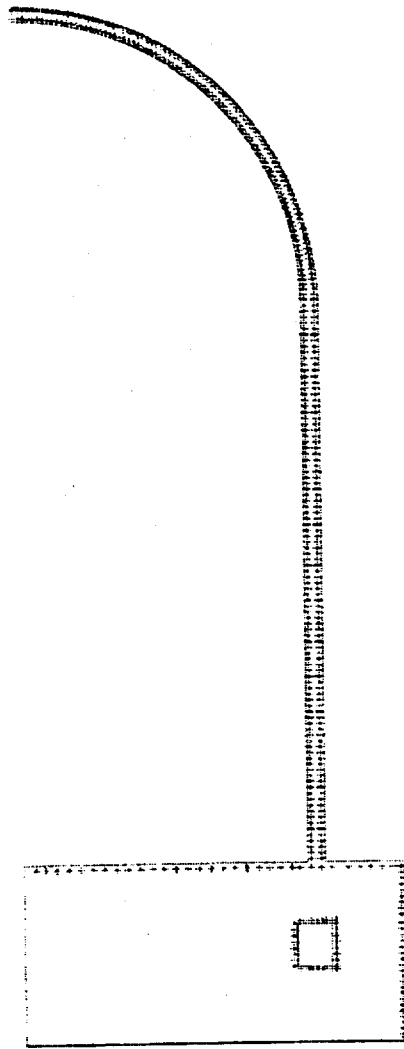


Fig. 5. Hoop rebars

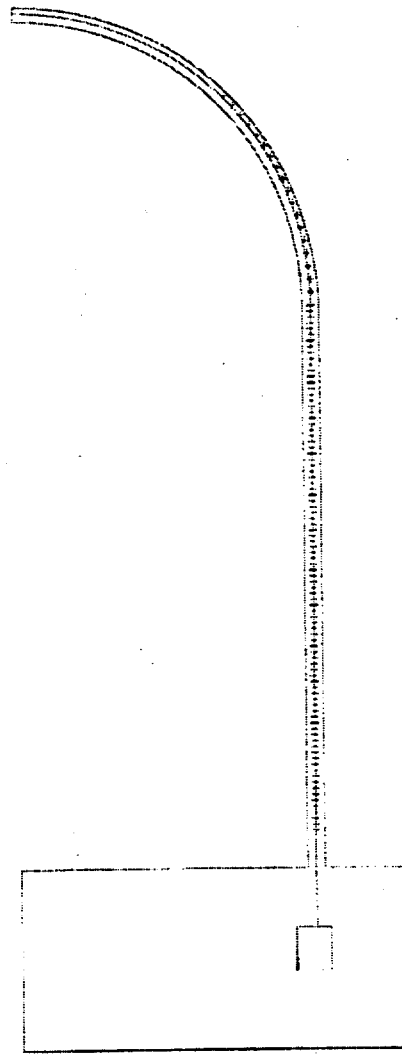


Fig. 6. Prestressing tendons

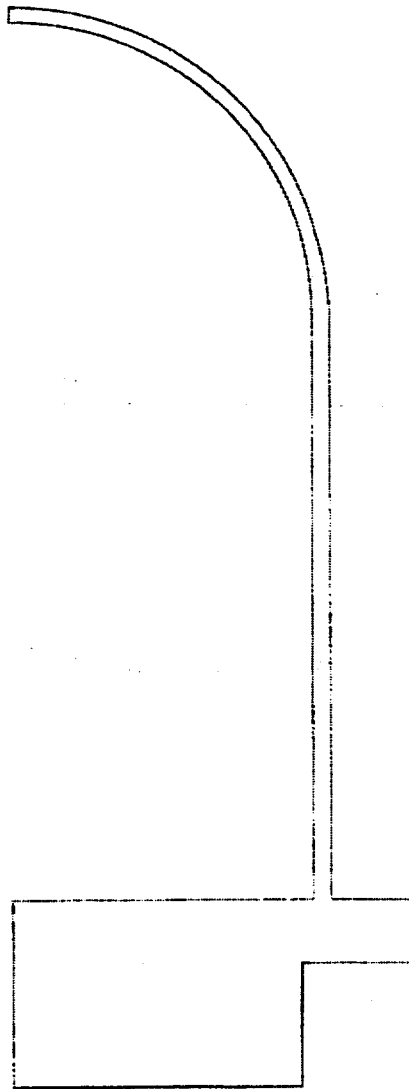


Fig. 7. Portion of containment considered for prestressing phasis

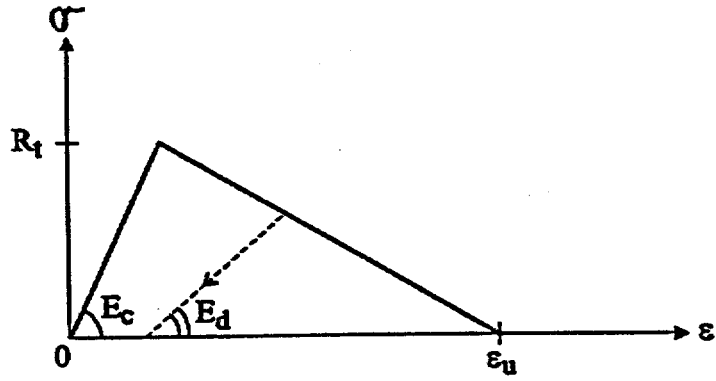


Fig. 8. Uniaxial response of concrete under traction load

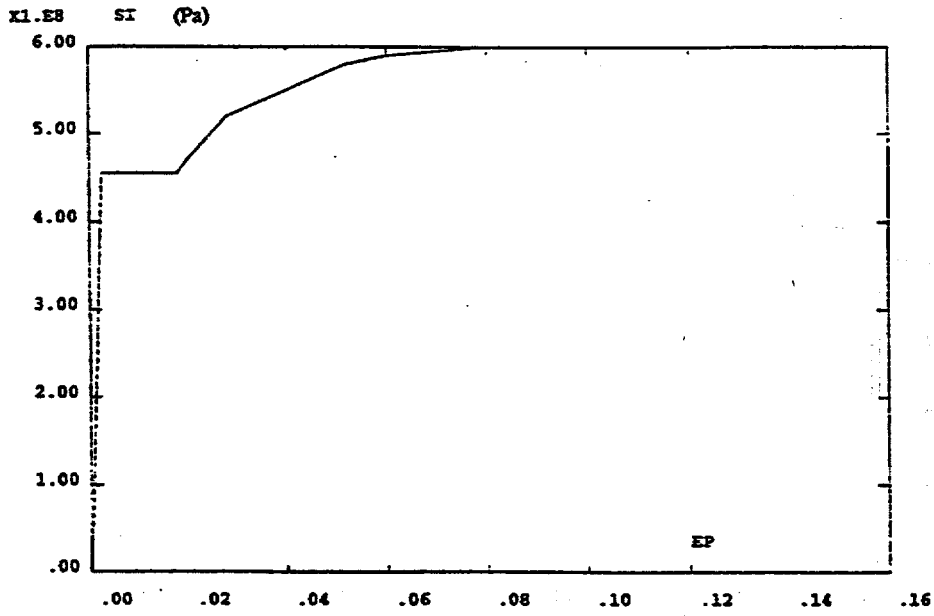


Fig. 9. Stress-strain curve for D10 steel

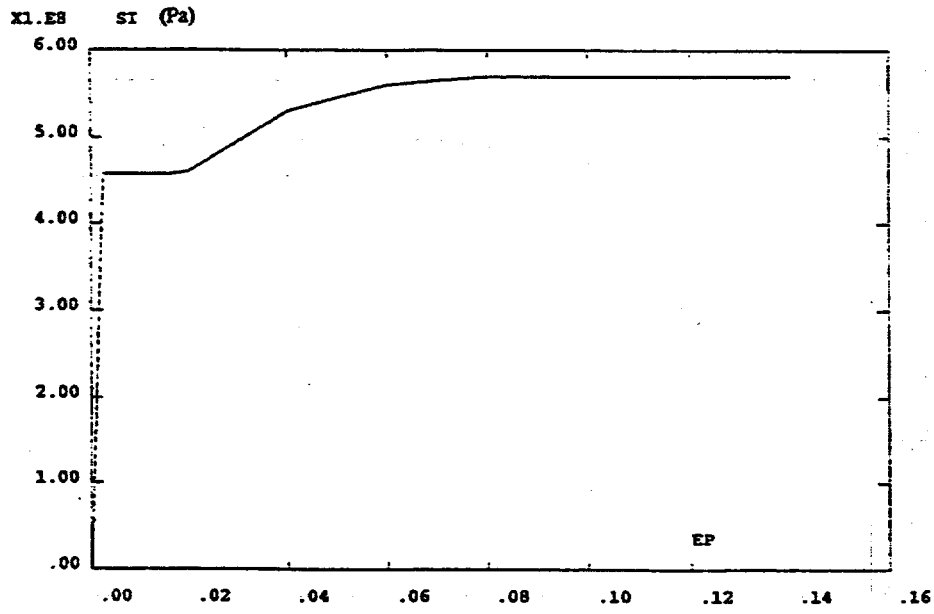


Fig. 10. Stress-strain curve for D13 steel

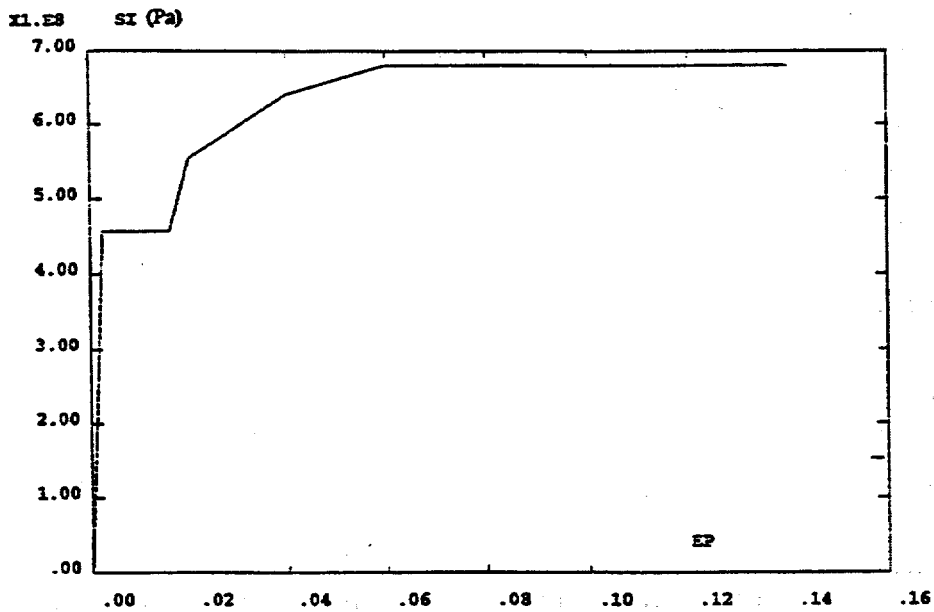


Fig. 11. Stress-strain curve for D16 steel

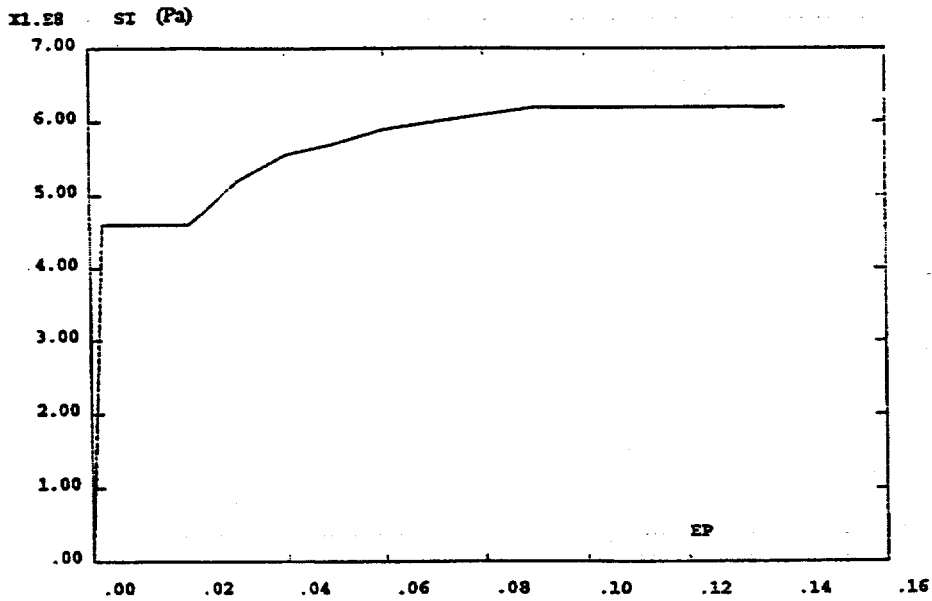


Fig. 12. Stress-strain curve for D19 steel

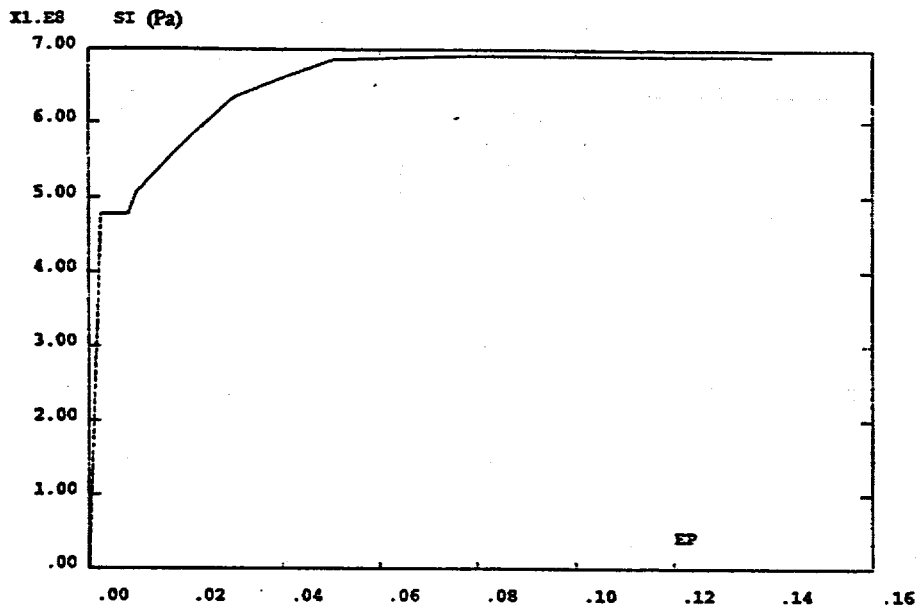


Fig. 13. Stress-strain curve for D22 steel

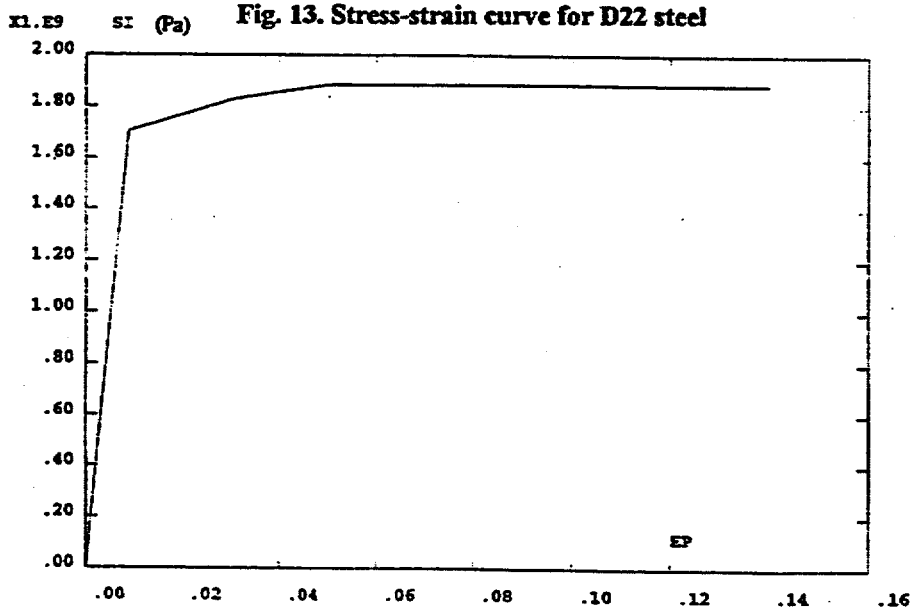


Fig. 14. Stress-strain curve for tendons steel

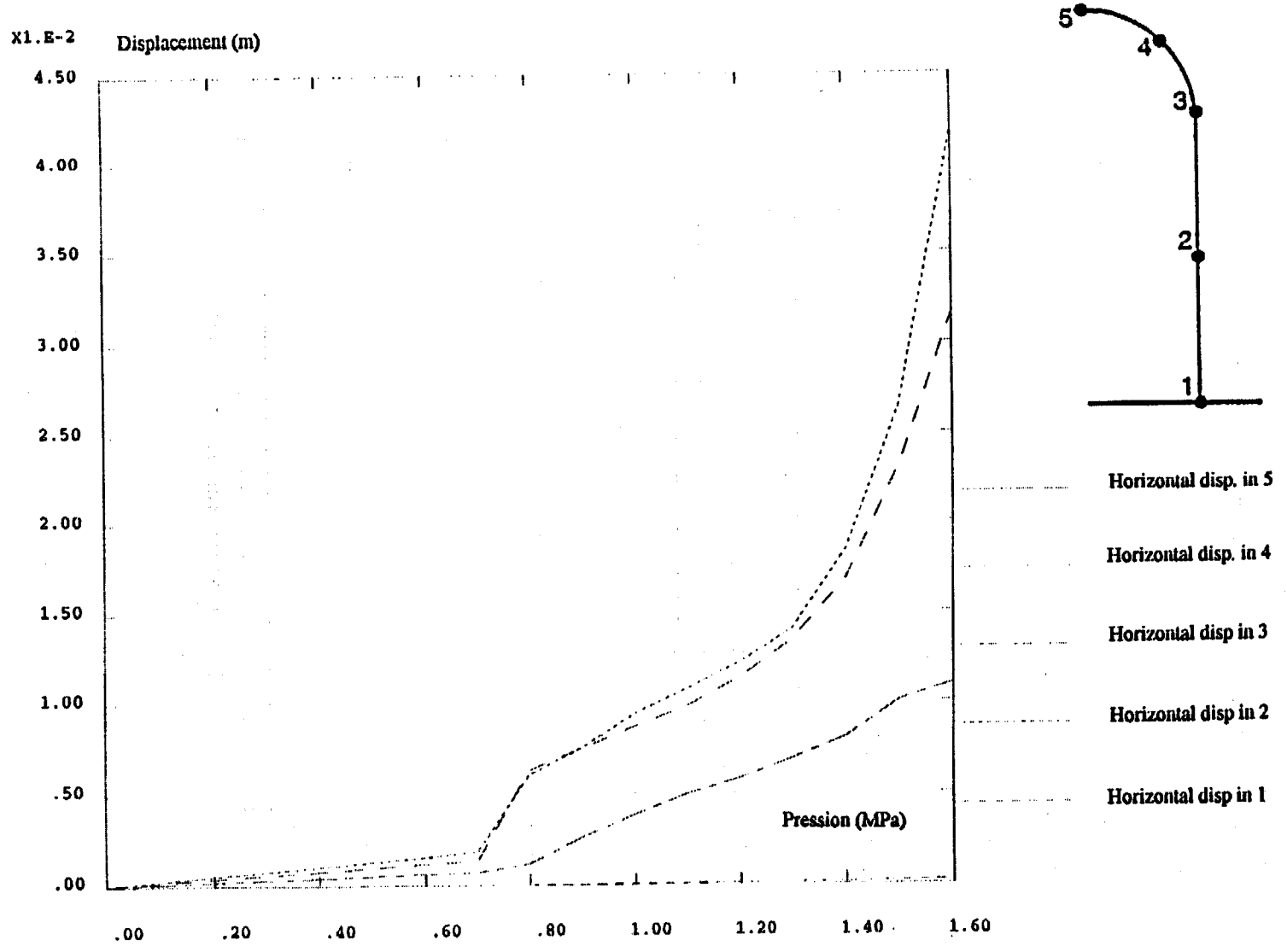


Fig. 15. Radial displacement versus pressure

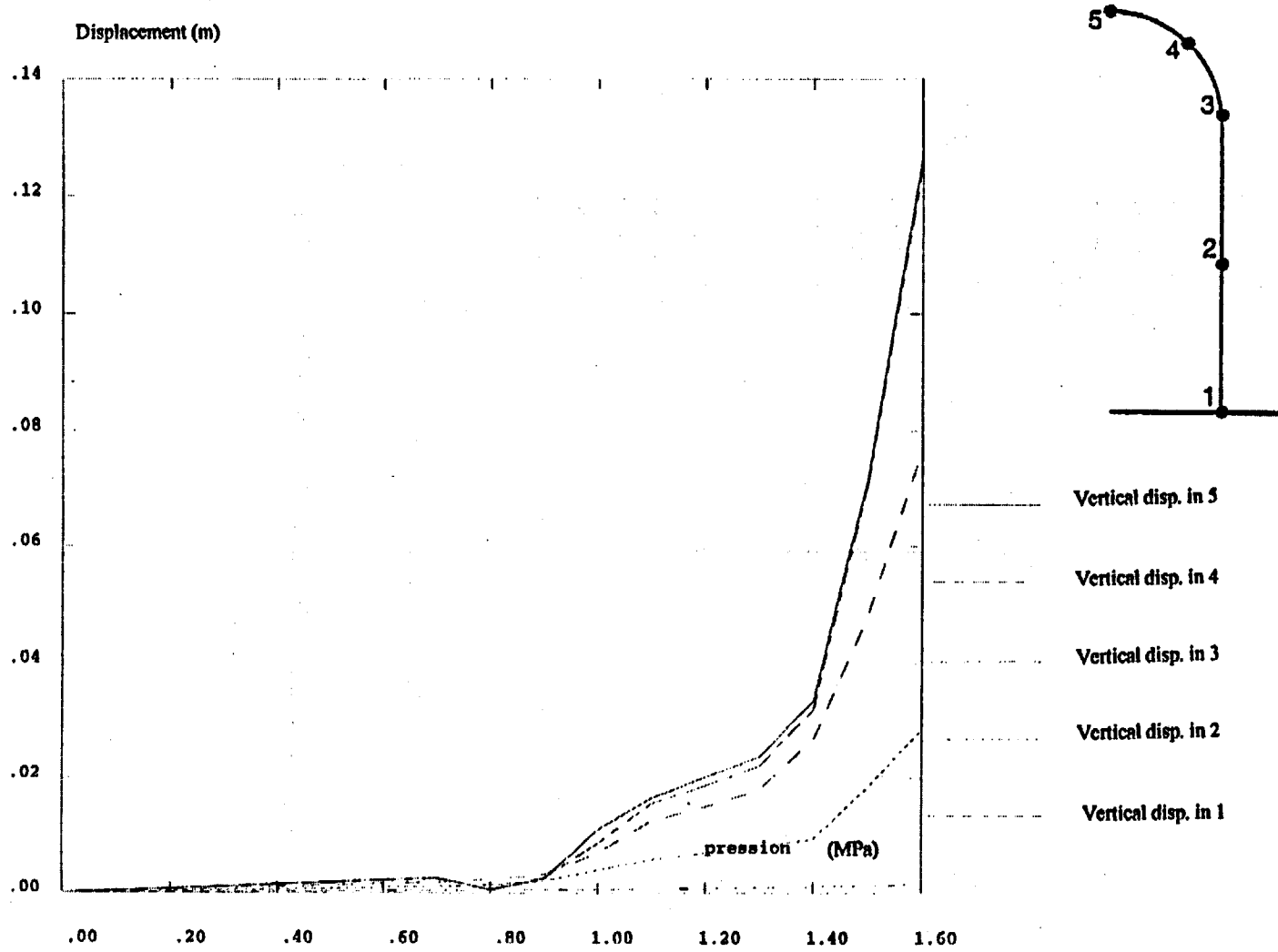


Fig. 16. Vertical displacement versus pressure

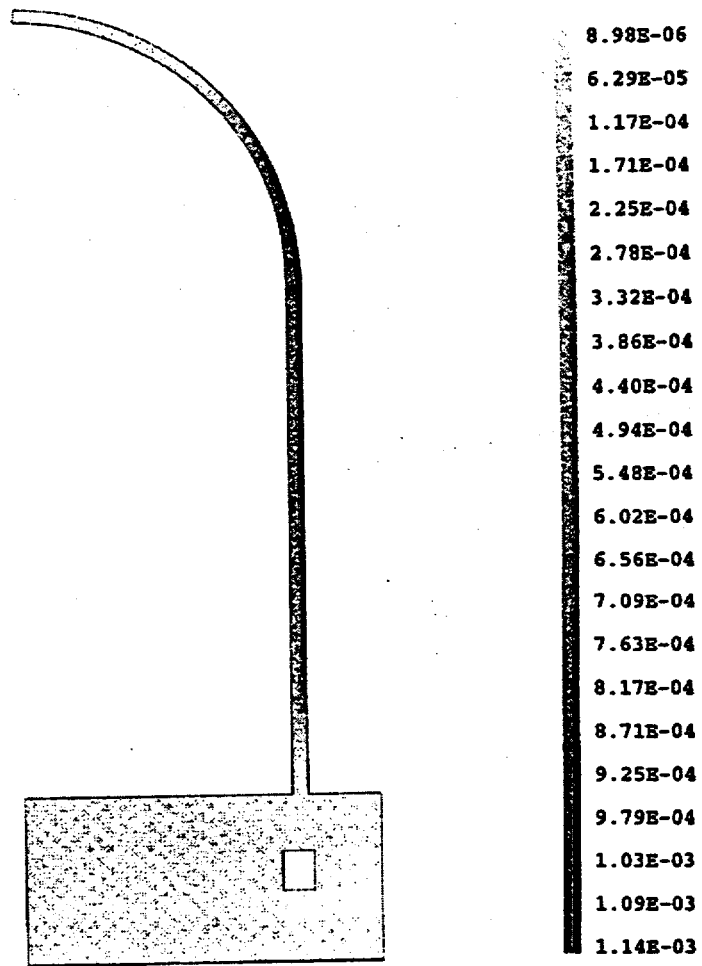


Fig. 17. Hoop cracking strains in concrete for $p = 0.8 \text{ MPa}$

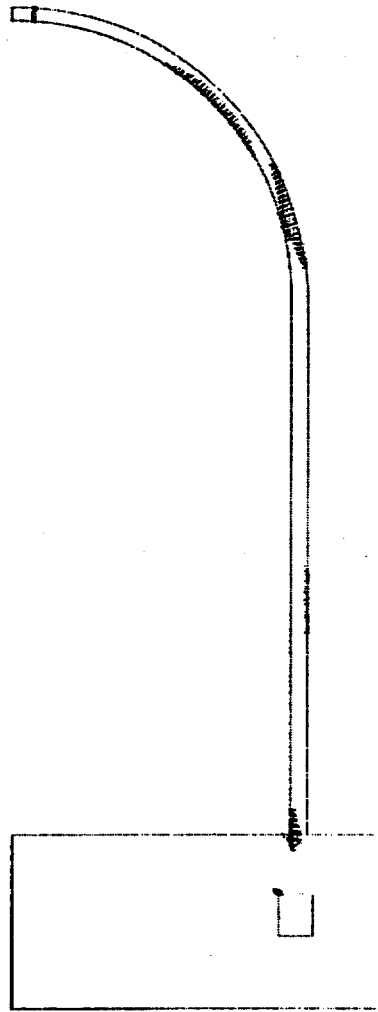


Fig. 18. Meridional cracks for $p = 0.8$ MPa

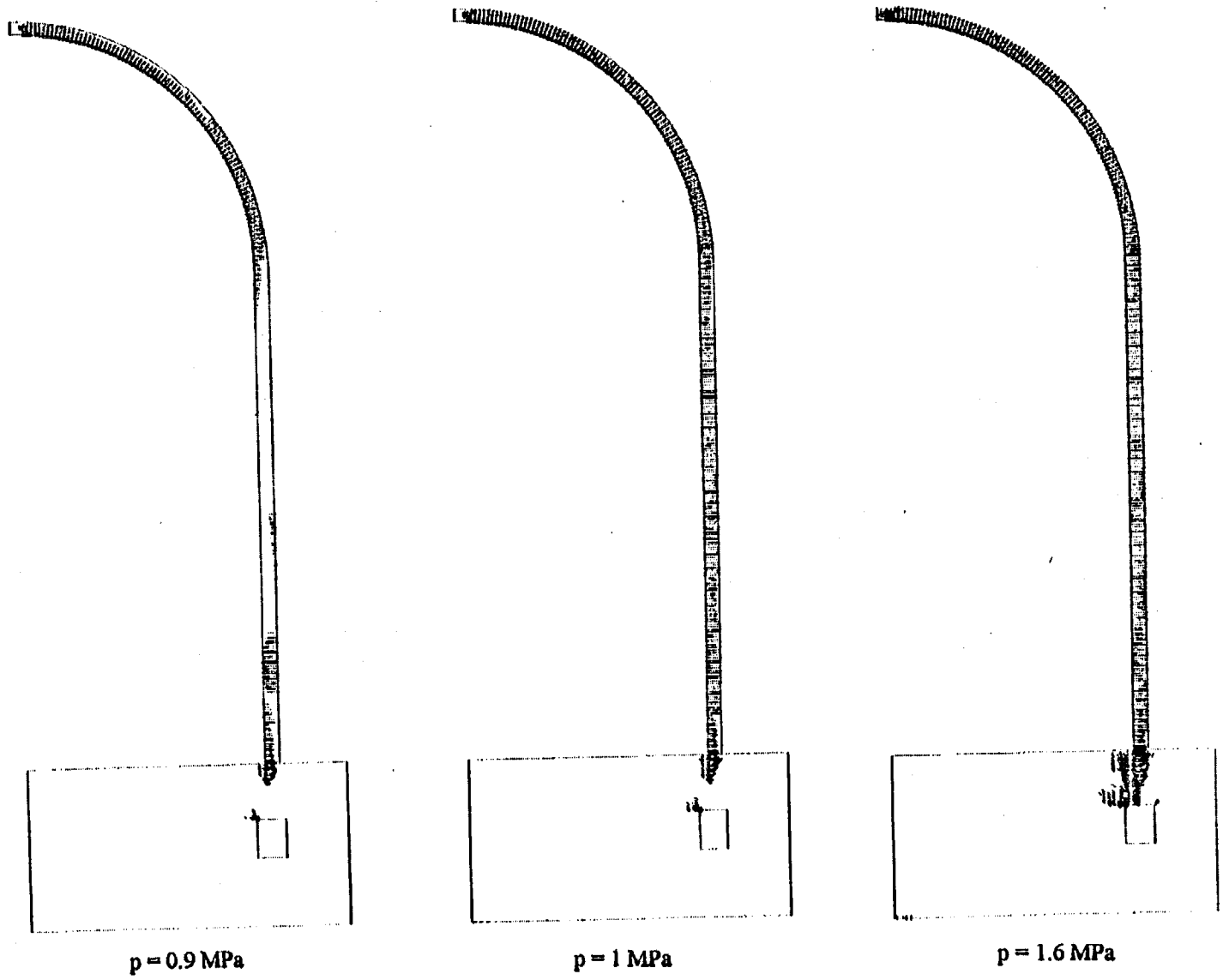


Fig. 19. Meridional cracking pattern for various pressure levels

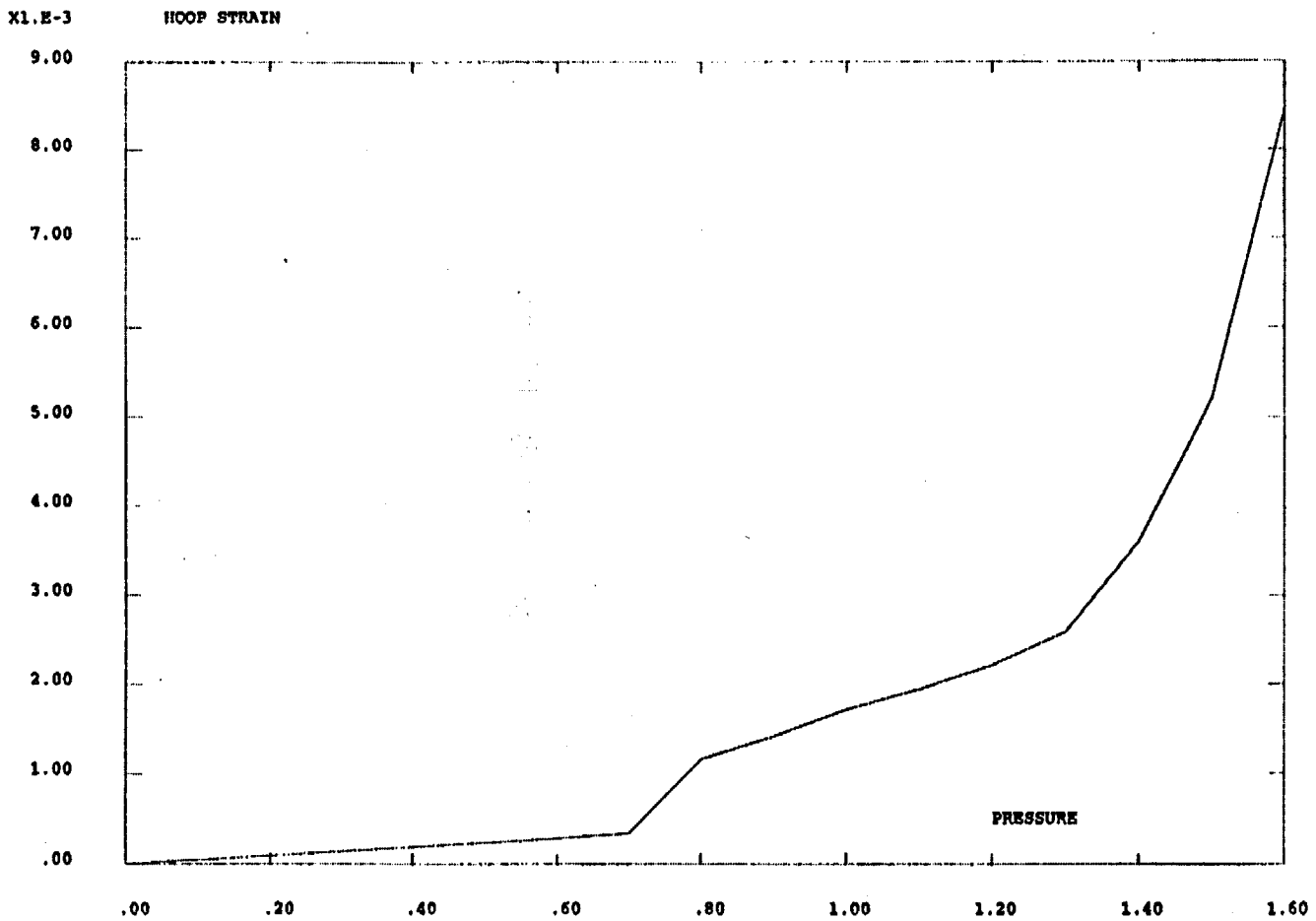


Fig. 20. Maximum hoop strain in cylinder, versus pressure

Page intentionally left blank.

APPENDIX E

EDF

**ÉLECTRICITÉ DE FRANCE
FRANCE**

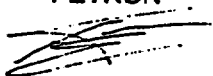
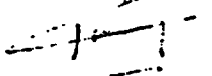
Appendix A, Composite Plots, comprises test data compiled and plotted from all organizations that participated in the Prestressed Concrete Containment Vessel (PCCV) Round Robin Pretest Analysis. To avoid duplicating the composite information, individual sets of data and/or plots have been omitted from participants' reports. In some cases this action resulted in disconnects between callouts and content and in the numbering of figures, tables, and pagination in some reports.

In Appendix E, "EDF, Électricité de France, France," discontinuity arises from omitting the following material:

standard output location data tables and associated plots
Appendix 3

**SANDIA II
ANALYSIS OF THE AXISYMMETRIC MODEL
PRETEST ANALYSIS RESULTS**

6060	Document # 02	Revision B
------	---------------	------------

Preparation	Check	Approval	Date	Revision
J. CHANTRON-PEYRON 	P. BISCH 	P. BISCH 	08/11/99	B

LIST OF MODIFICATIONS

REVISION	DATE	SUBJECT AND SOURCE
A	07/06/99	First issued
B	08/11/99	Completed with hand calculations which take into account the good assumption : the tendons are tensioned from both ends
C		
D		

0. REFERENCE DOCUMENTS

• Documents :

- [1] PCCV Round Robin Analysis – Design Package
- [2] "Modelization of non-linear reinforced concrete in the ASTER computer code" (see Appendix 1)

• Drawings :

- [3] PCCV Round Robin Analysis – Design Package

List of Drawings

NUMBER	DATE	REV	DESCRIPTION
PCCV-QCON-01	12/20/96	2	Model-General Arrangement Basemat Rebar Arrangement
PCCV-QCON-02	12/20/96	1	Basemat Tendon Gallery Access Tunnel Rebar Arrangement
PCCV-QCON-03	12/20/96	1	Prestressing Tendon General Arrangement
PCCV-QCON-04	12/20/96	1	Cylinder Prestressing Tendon Arrangement
PCCV-QCON-05	12/20/96	1	Cylinder Prestressing Tendon Arrangement
PCCV-QCON-06	12/20/96	1	Cylinder Prestressing Tendon Arrangement
PCCV-QCON-07	12/20/96	1	Prestressing Tendon Details (E/H) (Vertical Dome)
PCCV-QCON-08	12/20/96	1	Prestressing Tendon Details (E/H) (HOOP)
PCCV-QCON-09	12/20/96	1	Prestressing Tendon Details (A/L)
PCCV-QCON-10	12/20/96	1	Prestressing Tendon Details (M/S F/W)
PCCV-QCON-11	12/20/96	1	Dome Prestressing Tendon Arrangement-Prestressing System
PCCV-QCON-12	12/20/96	1	Cylinder & Dome Rebar General Arrangement (1)
PCCV-QCON-13	12/20/96	1	Cylinder & Dome Rebar General Arrangement (2)
PCCV-QCON-14	12/20/96	1	Cylinder & Dome Rebar Details
PCCV-QCON-15	12/20/96	2	Butress Rebar Details
PCCV-QCON-16	12/20/96	1	Opening Rebar Details (E/H)
PCCV-QCON-17	12/20/96	2	Opening Rebar Details (A/L)
PCCV-QCON-18	12/20/96	3	Penetration Rebar Details (M/S F/W)
PCCV-QCON-19	12/20/96	2	Crane Bracket Rebar Details Rebar Arrangement Standards
M1-ZCD1001A	12/20/96	3	Liner General Arrangement
M1-ZCD1002A	12/20/96	0	Cylinder Liner Anchor Details
M1-ZCD1006A	12/20/96	0	Liner Plate Block Layout of Cylinder Portion
M1-ZCD1007A	12/20/96	2	Cylinder Liner Anchor Details #2-5 Blocks (0-90 Degrees)
M1-ZCD1008A	12/20/96	2	Cylinder Liner Anchor Details #2-5 Blocks (90-270 Degrees)
M1-ZCD1009A	12/20/96	2	Cylinder Liner Anchor Details #2-5 Blocks (270-360 Degrees)
M1-ZCD1010A	12/20/96	0	Cylinder Liner Anchor Details #2-5 Blocks (E/H)
M1-ZCD1011A	12/20/96	0	Cylinder Liner Anchor Details #2-5 Blocks (A/L)
M1-ZCD1012A	12/20/96	0	Cylinder Liner Anchor Details #2-5 Blocks (M/S)
M1-ZCD1013A	12/20/96	0	Cylinder Liner Anchor Details #2-5 Blocks (F/W)
M1-ZCD1014A	12/20/96	0	Cylinder Liner Anchor Details Pals Crane Bracket Details
M1-ZCD1015A	09/22/97	1	Liner Plate Block Layout of Dome
M1-ZCD1016A	12/20/96	0	Stud Layout of Dome
M1-ZCD1025A	04/14/97	1	Base Liner Plate Detail

- *Regulations :*

[4] BPEL 91 : French Technical rules for design and calculations relating to prestressed concrete structures and building using the limit states method (July 92 issue)

- *Computer code :*

ASTER, non-linear finite element program, developed by ELECTRICITE DE FRANCE/Research and Development Division, NEWS version

1. SCOPE

This document deals with the analysis of the Prestressed Concrete Containment Vessel (PCCV) model test.

The SANDIA II model is currently under construction in the Sandia National Laboratories (ALBUQUERQUE - New Mexico - USA).

This model is a uniform 1:4 scale model representative of an existing pressurized water reactor (PWR) prestressed concrete containment vessel in Japan. It will be pressure tested up to its ultimate capacity.

The purpose of this document is to describe the modeling approaches, to provide the main basic data chosen by EDF in order to conduct its axisymmetric pretest analysis and to present the numerical results obtained.

Compared to the last version, this document is completed with a hand calculation which takes into account the right assumption for the prestressing : the tendons are tensioned from both ends.

The ASTER calculation have not been modified since the last version (they always take into account the wrong assumption, which is that the tendons are tensioned only from one end).

The presentation and the results of the hand calculations are given in a specific chapter (chapter 7).

The synthesis of the main results, especially the comparison between the hand calculations (with the wrong and good assumption concerning the prestressing) and the ASTER analysis, are given in the next chapter, called "Synthesis".

2. SYNTHESIS

2.1 COMPARISON CURVES

We can compare the different following results :

- those obtained thanks to ASTER calculation at the node N620 (with the wrong assumption : tendons are tensioned only from one end),

F_H : horizontal prestressing force in the cylinder
 $F_H = 1,544 \text{ MN/ml}$

F_V : vertical prestressing force in the cylinder
 $F_V = 1,479 \text{ MN/ml}$

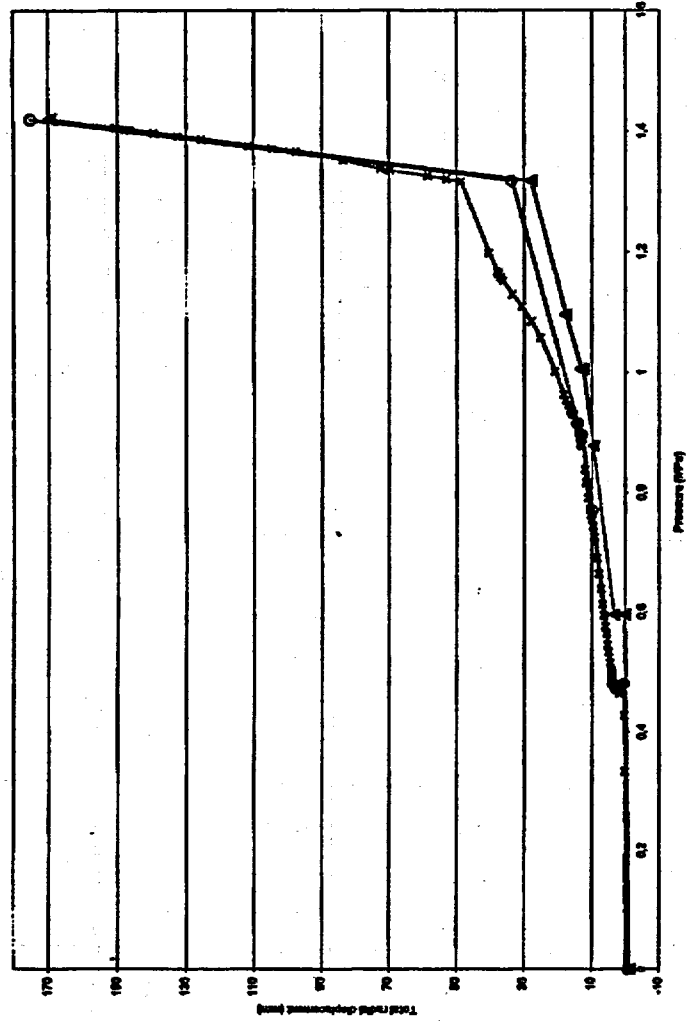
- those obtained thanks to hand calculation at medium height of the cylinder (with the wrong assumption),

- those obtained thanks to hand calculations at medium height of the cylinder (with the good assumption : tendons are tensioned from both ends).

$F_H = 2,121 \text{ MN/ml}$
 $F_V = 1,949 \text{ MN/ml}$

The last results, which take into account the good assumption, can be compared to those obtained for the location # 6 and should be included into the composite plots already presented for this location.

Comparison curves - $D = f(P)$



—○— Hyp. 1
- - -□- - Hyp. 2
- - -△- - AFTER evolution - Hyp. 1

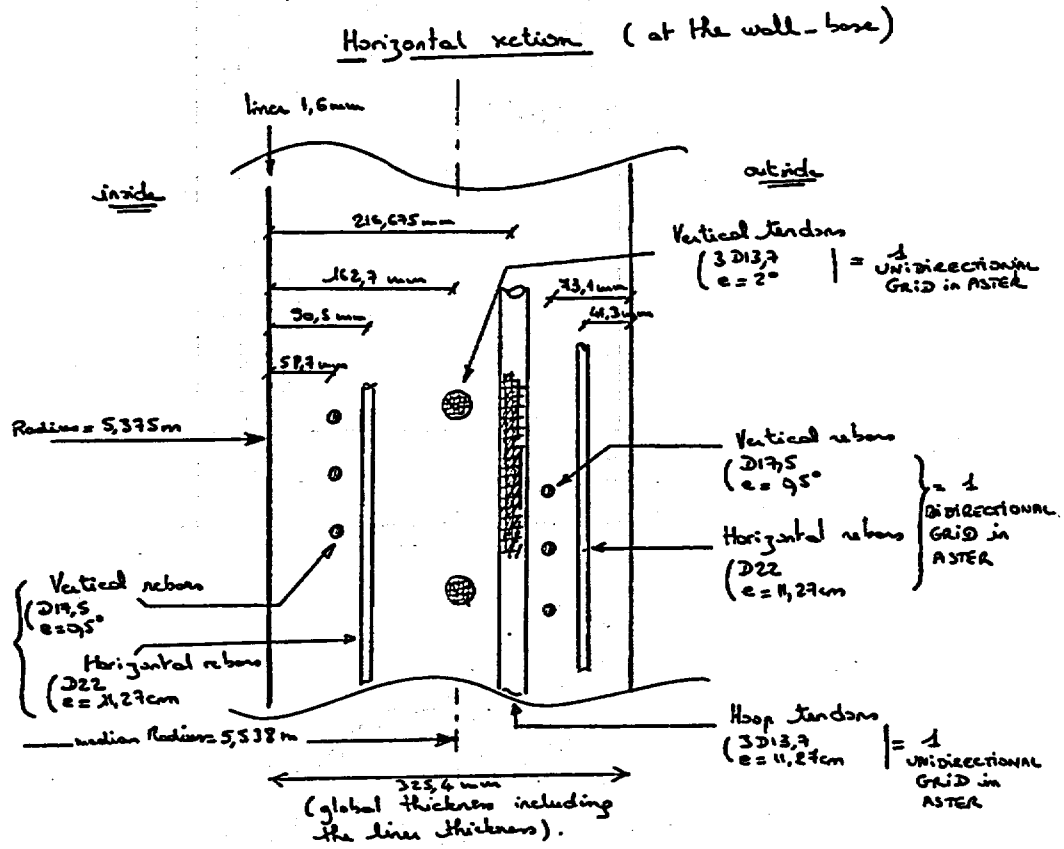
Hyp. 1 : the tendons are tensioned from one end
Hyp. 2 : the tendons are tensioned from both ends

2.2 SYNTHESIS TABLE

EVENTS	Wrong assumption : tendons are tensioned only from one end			True assumption : tendons are tensioned from both ends (analytic results)	
	P : PRESSURE LEVELS (*) (absolute values in Mpa)	SOURCE	RATIO P / Pd Pd = 0,39 Mpa	P : PRESSURE LEVELS (absolute values in Mpa)	RATIO P / Pd Pd = 0,39 Mpa
1. First cracking of concrete in cylinder due to hoop stresses	0,47	Aster calc.	1,2	0,59	1,5
2. First cracking of concrete in cylinder due to meridional stresses	due to flexion at the basemat juncture [0,47 ; 0,50]	Aster calc.	[1,2 ; 1,3]	×	×
	cracking at medium height of the cylinder [0,53 ; 0,86]	Aster calc.	[1,4 ; 2,2]	1,10	2,8
3. First yield of hoop rebar in cylinder	0,88	Aster calc.	2,3	1,00	2,8
4. First yield of meridional rebar in wall-basemat juncture	1,03	Aster calc.	2,6	×	×
5. First cracking of dome concrete above 45° dome angle	0,57	Aster calc.	1,5	×	×
6. First cracking of dome concrete below 45° dome angle	0,48	Aster calc.	1,2	×	×
7. Hoop tendons in cylinder reaching 1% strain	1,34	Aster calc.	3,4	1,32	3,4
8. Hoop tendons in cylinder reaching 2% strain	1,38	Aster calc.	3,5	1,36	3,5
9. Hoop tendons in cylinder reaching 3% strain	1,41	Aster calc.	3,6	1,40	3,6
10. Best estimate of static failure pressure	1,45	Analytic calc.	3,7	1,42	3,6
11. Minimum pressure reachable with 90% confidence level	1,27	Analytic calc.	3,3	1,25	3,2
12. Maximum pressure reachable with 90% confidence level	1,65	Analytic calc.	4,2	1,61	4,1

(*) : Pressure levels are defined by interpretation of designs of cracking schemes and isovalues of stresses : values chosen take into account a significant local appearance of the event

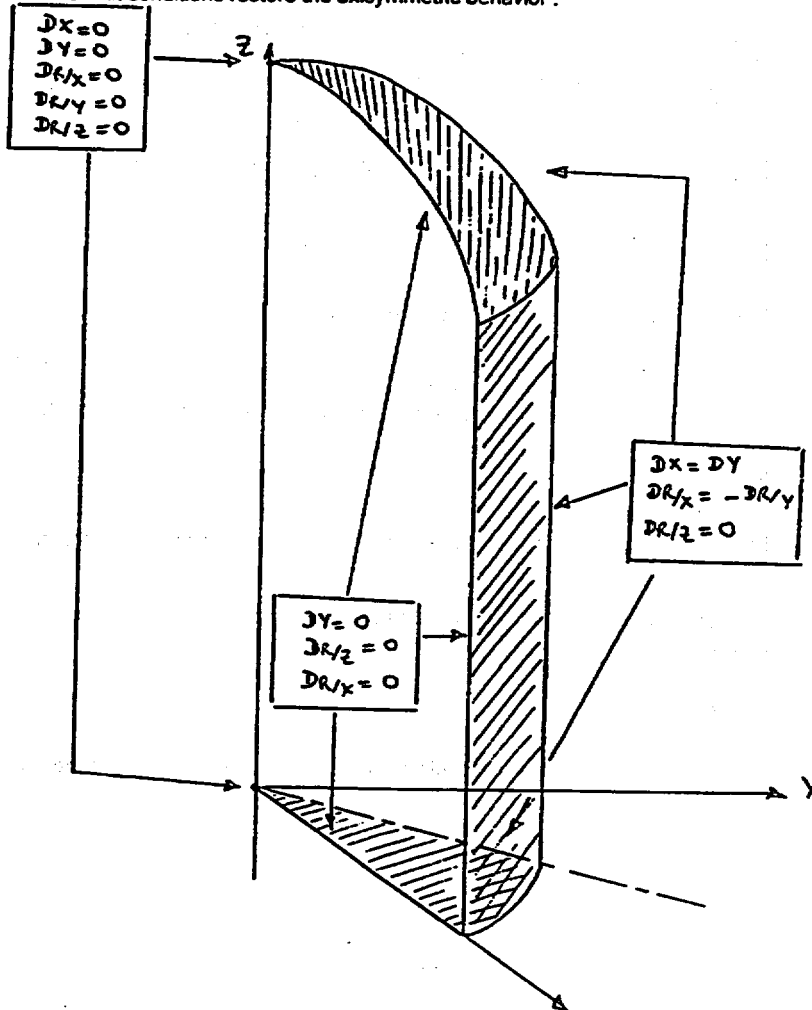
Thickness of a typical section of the model
 Typical horizontal cross-section of the model



4. ASSUMPTIONS AND BOUNDARY CONDITIONS

4.1 CHOICE OF THE MODEL

- The azimuth of 135° is considered to be the best location to describe the free-field behavior of the model. Consequently, only 1/8 of the PCCV model is represented : a "slice" between the 135° azimuth and the 180° azimuth. This specific choice allows restitution of all the symmetries of the problem, such as the formwork, the rebars and the prestressing of the dome.
- The limit conditions restore the axisymmetric behavior :



- In order to take into account the possible uplift of the basemat, we have performed a more detailed study of this point.
It appears that boundary conditions on the basemat are not fully restrained since there is a peripheral uplift from $P = 1,2$ MPa (this test is made with an elastic model of the concrete ; the loads are the internal pressure P and the dead load). However, since the uplift appears only for high pressures, it has been decided not to take into account this feature in the modeling approach : the basemat is modeled with thick shell elements on which the boundary condition is $DZ = 0$.
- Finally, there is a possible sliding due to shear force at the wall-base juncture ; this sliding, which is characterized by a cracking in the basemat, appears only under high internal pressure so it does not seem to be useful to model it thanks to a special element.

Those two last points constitute special assumptions which have been taken in order to simplify the analysis and the modeling ; but it is obvious that the current model could be improved by considering unilateral bearings under the basemat and a special element to link the wall nodes to the basemat nodes.

4.2 CHOICE OF FINITE ELEMENTS AND CONSTITUTIVE RELATIONSHIPS

4.2.1 CONCRETE

The concrete is modeled with DKT shell elements.

The model is "NADAI_B" : multi-layered shell elements (in-plane stresses), with a Drucker-Prager criteria under compression and an uniaxial orthotropic relation in the cracking directions under tensile forces (see documentation of the NADAI_B model in Appendix 1).

4.2.2 REBARS

The rebars are modeled with grid elements (orthotropic grids) which are properly set in the vessel thickness.

The constitutive relationship is "Von Mises" with isotropic hardening (elastoplastic behavior with bilinear work hardening).

4.2.3 LINER

The liner is modeled with an excentric grid (the constitutive relationship is the same as rebars).

4.2.4 PRESTRESSING

- *Hoop tendons (wall and portion of the dome) :*

The median prestressing level is calculated at the 135° azimuth ; the prestressing losses such as anchoring set losses, friction losses and delayed strains are taken into account according to BPEL code.

In the ASTER code, the prestressing level of tendons is obtained due to a negative temperature applied to tendons.

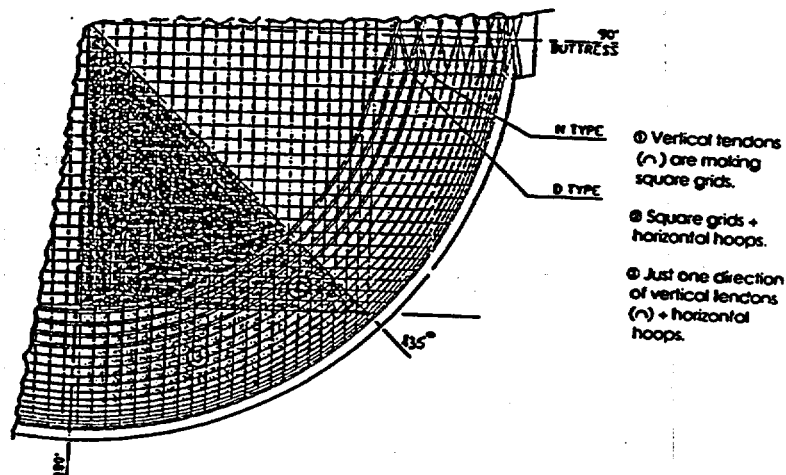
The stiffness of the tendons is modeled by using unidirectional grid elements with bilinear elastoplastic constitutive relationship.

- *Vertical tendons in the wall :*

A median prestressing is calculated and is modeled in the same way as the horizontal prestressing.

- *Prestressing in the dome :*

Three zones are defined : each one has a typical type of prestressing.



For each zone, the prestressing is calculated and obtained by applying a negative temperature to tendons.

As far as the stiffness is concerned, it is modeled with unidirectional or bidirectional grid elements.

4.3 MATERIAL PROPERTIES

(calculated by the material test data given in the ref. [1])

4.3.1 CONCRETE

Compressive Strength = $(60,21 + 48,84)/2 = 54,52$ MPa
(an average between "Fields" values and "Standard" values)

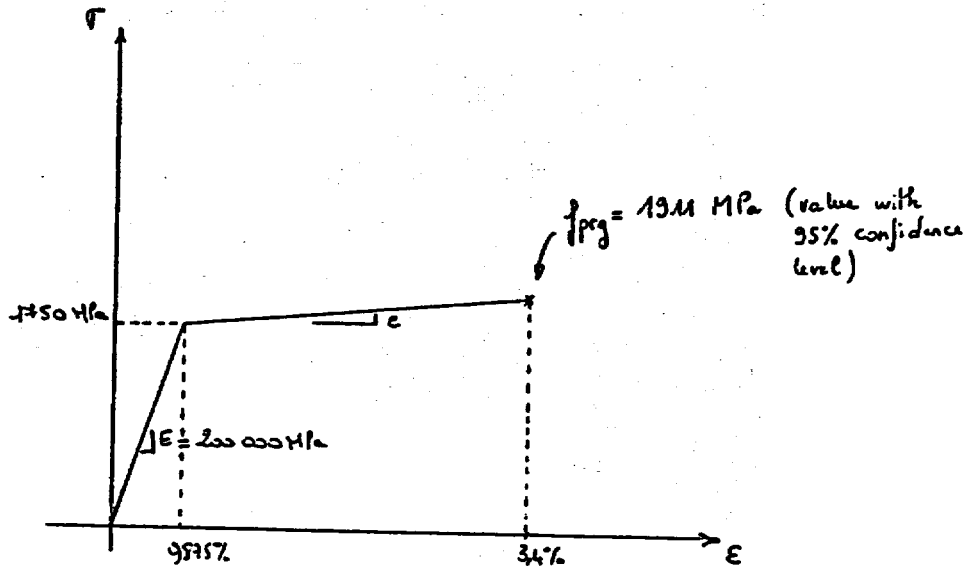
Young's Modulus = $(31\ 970 + 26\ 970)/2 = 29\ 470$ MPa

Poisson's Ratio = 0,19

Density = 2,225 t/m³

Tensile Strength = $(2/3) * (4,21 + 3,45)/2 = 2,55$ MPa

4.3.2 TENDONS



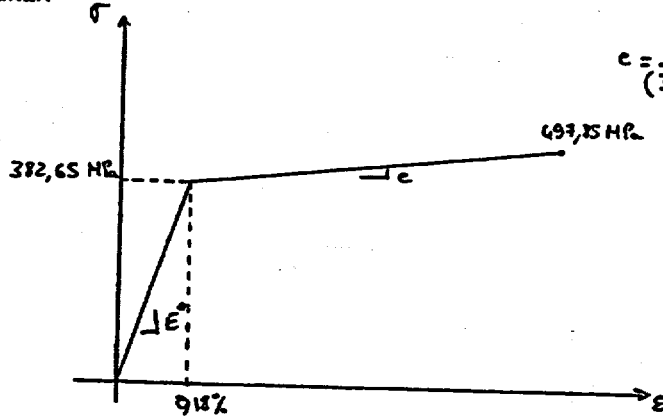
$$\nu = 0,3$$

$$\alpha = 10^{-5}$$

$$c = \frac{1911 - 1750}{(3,4 - 9,875) \times 10^{-2}} = 6376 \text{ MPa}$$

4.3.3

LINER



$$E^* = \frac{\sigma_{\text{linear}}}{\epsilon} = 233\,608 \text{ MPa}$$

$$c = \frac{497,25 - 382,65}{(33,2 - 9,11) \times 10^{-2}} = 349 \text{ MPa}$$

$$\nu = 0,3$$

$$\alpha = 10^{-5}$$

4.3.4

REBARS

(The properties depend on the diameters of the rebars → see Table 2 page 31 ref. [1])

The hoop and the vertical rebars are modeled with the same grid.

As a consequence, the material properties are chosen in order to best reconstitute the stiffness : in all the cases, $E = E_{\text{hoop}}$ and ρ_1/ρ_2 is modified in order to reestablish the right vertical stiffness (ES).

(With ρ_1 = ratio of rebars in the direction 1,
and ρ_2 = ratio of rebars in the direction 2)

(See an example of calculation in Appendix 2)

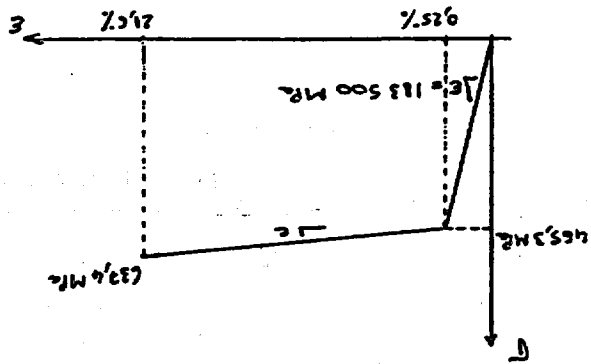
As far as the strength parameters are concerned (such as the elastic limit, σ_e and ϵ_e), the horizontal direction (hoops) is privileged.

For the SANDIA modeling, the different types of grids are :

③

Hoop rebars: D19-D16
Vertical rebars: D16

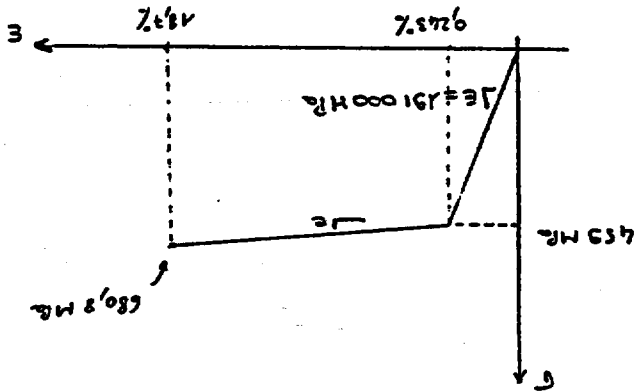
→ see ②



$$e = \frac{637.4 - 465.3}{(21.6 - 0.25) \times 10^2} = 306 \text{ MPa}$$

②

Hoop rebars: D19-D16
Vertical rebars: D19

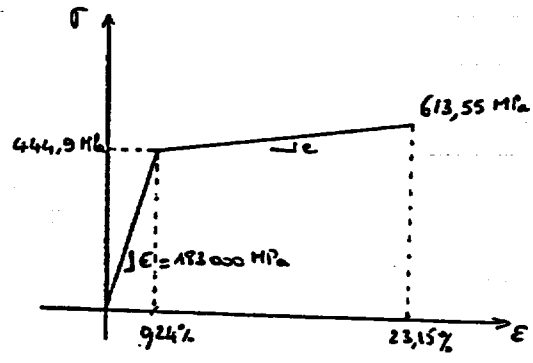


$$e = \frac{680.8 - 459}{(18.7 - 0.443) \times 10^2} = 1202 \text{ MPa}$$

①

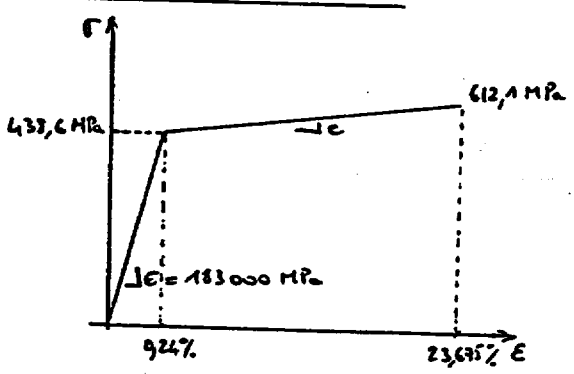
Hoop rebars: D22
Vertical rebars: D19-D16

④ Hoop rebar: 2D16-D13
Vertical rebar: D16.



$$c = \frac{613,55 - 444,9}{(23,15 - 0,24) \times 10^{-2}} = 730 \text{ MPa}$$

⑤ Hoop rebar: 1D16-3D13
Vertical rebar: D13



$$c = \frac{612,1 - 433,6}{(23,695 - 0,24) \times 10^{-2}} = 740 \text{ MPa}$$

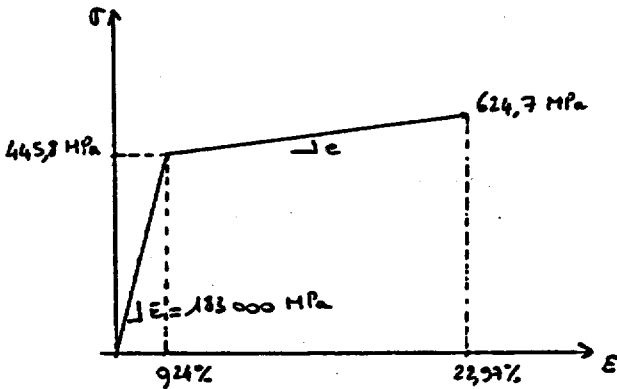
⑥ Hoop rebar: 3D16-D13 → see ④
Vertical rebar: D13

⑦ Hoop rebar: 1D16-3D13 → see ⑤
Vertical rebar: D13

⑧ Hoop rebar: 2D16-D13 → see ④
Vertical rebar: 1D13-2D10

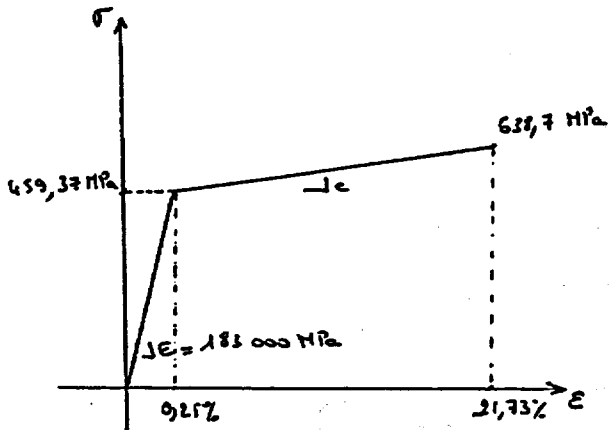
⑨ Hoop rebars: $\frac{1D16-3D13}{1D13-2D10}$ → see ⑤
 Vertical rebars: $1D13-2D10$

⑩ Hoop rebars: $\frac{1D13-2D10}{1D13-2D10}$
 Vertical rebars: $1D13-2D10$



$$e = \frac{624.7 - 445.8}{(23.97 - 9.24) \times 10^{-2}} = 777 \text{ MPa}$$

⑪ Hoop rebars: $\frac{1D13-2D10}{1D13-2D10}$
 Vertical rebars: $1D13-2D10$

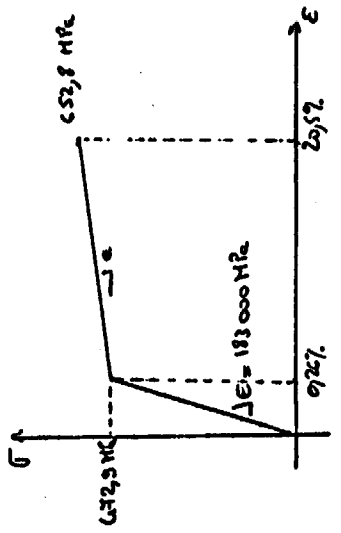


$$e = \frac{638.7 - 459.37}{(21.73 - 9.25) \times 10^{-2}} = 835 \text{ MPa}$$

12) Hoop stress: $\frac{1.713 - 2.710}{2.710}$
 Vertical stress: $\frac{2.710}{2.710}$

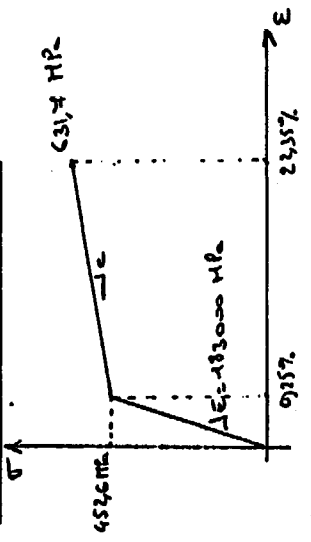
see 11

13) Hoop stress: $\frac{3.710}{2.710}$
 Vertical stress: $\frac{2.710}{2.710}$



$$e = \frac{652.8 - 672.9}{(2.05 - 0.72) \times 10^{-2}} = 885 \text{ MPa}$$

14) Hoop stress: $\frac{1.713 - 1.710}{1.710}$
 Vertical stress: $\frac{2.710}{1.710}$



$$e = \frac{631.7 - 652.6}{(2.35 - 0.72) \times 10^{-2}} = 810 \text{ MPa}$$

15) Hoop stress: $\frac{2.710}{2.710}$
 Vertical stress: $\frac{2.710}{2.710}$

see 13

5. ANALYSIS DESCRIPTION

The model is submitted to a pressure test sequence which is described page 29 of ref. [1].

In fact, for $P = 1,125 P_d$, all the materials are still elastic so we have just applied the high pressure testing on our model. The point is to study its response and estimate as precisely as possible the different critical phases till the failure.

The loading cases are :

- the dead load,
- the prestressing forces,
- the internal pressure.

6. ANALYSIS RESULTS

Two types of results are given :

- Plots of pressure history for strain, displacement at every standard output location (in fact, results are taken for nodes which best represent those location → see locations in Appendix 3).
- Description of pressure levels corresponding to the following events milestones and an explanation of how they were derived :
 - first cracking of concrete in cylinder due to hoop stresses,
 - first cracking of concrete in cylinder due to meridional stresses,
 - first yield of hoop rebar in cylinder,
 - first yield of meridional rebar in wall-basemat juncture,
 - first cracking of dome concrete above 45° dome angle,
 - first cracking of dome concrete below 45° dome angle,
 - hoop tendons in cylinder reaching 1 % strain,
 - hoop tendons in cylinder reaching 2 % strain,
 - hoop tendons in cylinder reaching 3 % strain,
 - best estimate of static failure pressure,
 - minimum pressure reachable with 90 % confidence level
(this is the pressure that the participant is at least 90 % certain that the model will reach),
 - maximum pressure reachable with 90 % confidence level
(this is the pressure that the participant is at least 90 % certain that the model will never exceed).

EVENTS	P : PRESSURE LEVELS (*) (absolute values in Mpa)	SOURCE	RATIO P/Pd (Pd = 0,39 Mpa)
1. First cracking of concrete in cylinder due to hoop stresses	0,47	Aster calculation	1,2
2. First cracking of concrete in cylinder due to meridional stresses	due to flexion at the basemat juncture [0,47 ; 0,50]	Aster calculation	[1,2 ; 1,3]
	cracking at medium height of the cylinder [0,53 ; 0,86]	Aster calculation	[1,4 ; 2,2]
	first cracking (extracos) through cracking		
3. First yield of hoop rebar in cylinder	0,88	Aster calculation	2,3
4. First yield of meridional rebar in wall-basemat juncture	1,03	Aster calculation	2,6
5. First cracking of dome concrete above 45° dome angle	0,57	Aster calculation	1,5
6. First cracking of dome concrete below 45° dome angle	0,48	Aster calculation	1,2
7. Hoop tendons in cylinder reaching 1% strain	1,34	Aster calculation	3,4
8. Hoop tendons in cylinder reaching 2% strain	1,38	Aster calculation	3,5
9. Hoop tendons in cylinder reaching 3% strain	1,41	Aster calculation	3,6
10. Best estimate of static failure pressure	1,45	Analytic result	3,7
11. Minimum pressure reachable with 90% confidence level	1,27	Analytic result	3,3
12. Maximum pressure reachable with 90% confidence level	1,65	Analytic result	4,2

(*) : Pressure levels are defined by interpretation of designs of cracking schemes and isovalues of stresses : values chosen take into account a significant local appearance of the event

7. PRESENTATION AND RESULTS OF THE HAND CALCULATION

7.1 AIMS OF ANALYTICAL ANALYSIS

Those complementary calculations are performed to provide a good reference to calibrate numerical results.

The calculation is made for a point located at medium height of the cylinder, on the 135th azimuth. The results obtained for this point are comparable to those obtained for the location # 6.

Those hand calculation have already been made with the first and wrong assumption concerning the prestressing (the assumption which is still the one used in the ASTER calculations): the tendons are tensioned only from one end.

These hand calculations have been made again with the good assumption: the tendons are tensioned from both ends.

7.2 PRINCIPLES OF THE HAND CALCULATION

The calculations are performed by giving an estimation of axisymmetric strains and stresses at mid-height and mid-thickness of the cylinder.

For each layer, at each characteristic stage of the behaviour, there is an estimation of the stiffness :

For instance : yield of horizontal cables (event # 7)

Horizontal prestressing :

$$\epsilon_{med} = - (2,121/10415) = - 0,2036 \times 10^{-3}$$

(2,121 MN/ml : prestressing force

10415 MN/ml : total stiffness of the layers except cables)

$$\epsilon_{cables} = 2,121/602 = 3,523 \times 10^{-3}$$

(horizontal)

(602 MN/ml : stiffness of the horizontal cables)

$$\epsilon_i = 8,75 \times 10^{-3}$$

Strain of the cables since the prestressing :

$$(8,75 - 3,523) \times 10^{-3} = 5,227 \times 10^{-3}$$

$$\rightarrow \text{displacement } w_7 = 5,227 \times 10^{-3} \times 5592 = 29,2 \text{ mm}$$

(5592 mm : radius of the cables).

Strain of other layers : $(5,227 - 0,2036) \times 10^{-3} = 5,02 \times 10^{-3}$

Layer	Stresses (MPa)	Section (mm ²)	Force (kN)
Liner	$382,65 + (5,02 - 1,8) \times 10^{-3} \times 349 = 383,77$	1 600	614
Int. rebars	$444,9 + (5,02 - 2,4) \times 10^{-3} \times 736 = 446,83$	1 443	645
Ext. rebars	$438,6 + (5,02 - 2,4) \times 10^{-3} \times 740 = 440,54$	1 284	566
Cables	1 750	3 008	5 264
		Total	7 089

→ Corresponding pressure : $P_7 = 7089/5,375 = 1\,319$ kPa

7.3 MAIN RESULTS FOR EACH HAND CALCULATION

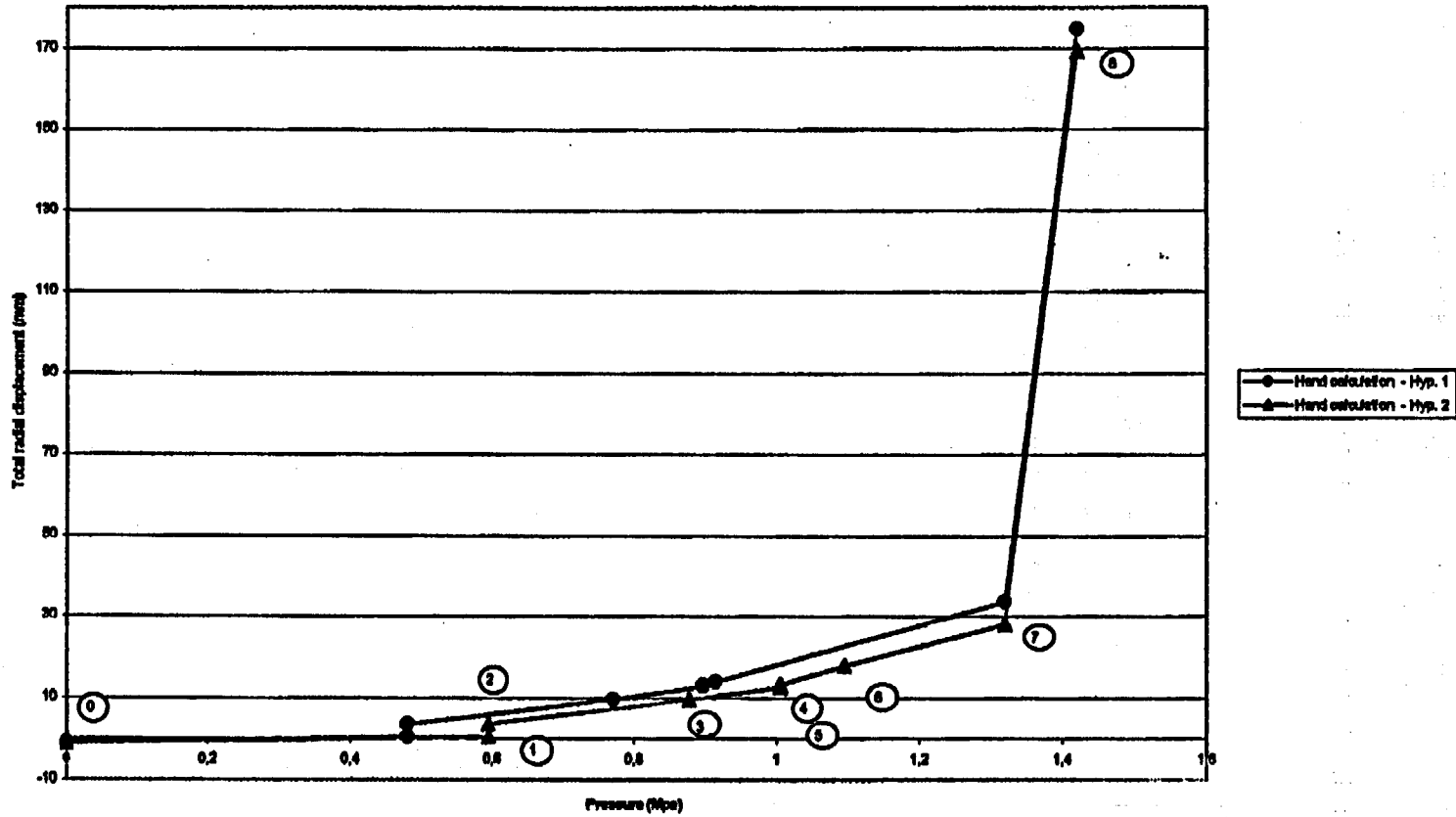
- First calculation : The tendons are tensioned only from one end (= WRONG ASSUMPTION)

Event	0	1	2	3	4	5	6	7	8
Description	Prestressing	Beginning of the cracking of concrete due to σ_{99}	Total cracking of concrete due to σ_{99}	Yield of liner	Yield of internal hoop rebars	Yield of external hoop rebars	Cracking of concrete due to σ_{zz}	Yield of horizontal cables	Rupture of horizontal cables
Total displacement (mm)	- 0,821	1,262	4,363	10,472	13,752	13,927	14,825	34,576	175,766
Pressure (MPa)	0	0,481	0,481	0,770	0,897	0,897	0,915	1,319	1,421

- Second calculation : The tendons are tensioned from both ends (= RIGHT ASSUMPTION)

Event	0	1	2	3	4	5	6	7	8
Description	Prestressing	Beginning of the cracking of concrete due to σ_{99}	Total cracking of concrete due to σ_{99}	Yield of liner	Yield of internal hoop rebars	Yield of external hoop rebars	Cracking of concrete due to σ_{zz}	Yield of horizontal cables	Rupture of horizontal cables
Total displacement (mm)	- 1,128	1,560	4,885	10,770	13,752	14,230	18,856	29,213	170,403
Pressure (MPa)	0	0,595	0,595	0,877	1,005	1,005	1,096	1,319	1,421

Evolution $D=f(P)$ - Comparison between both hand calculations



Hyp. 1 : the tendons are tensioned from one end
Hyp. 2 : the tendons are tensioned from both ends

- **Comments on the curves $D = f(P)$**

(0)-(1) This is the elastic straight line, its slope is determined by the stiffness of all the elements.

Stage (1)-(2) Its position depends on the prestressing force.

(2)-(3)

(3)-(4)

(4)-(6)

(5)

(6)-(7)

(7)-(8)

The slopes of the different segments are determined thanks to the successive stiffnesses (they are not influenced by the initial prestressing).

(8) The strain at the rupture is lower if the initial prestressing is higher.

Appendix 1
Modelization of non-linear reinforced concrete in the ASTER
computer code

I Concrete model

The concrete model is based upon the plasticity theory for uncracked concrete with isotropic hardening and associated flow. Cracked concrete is treated by uncoupled uniaxial laws which are written for general cyclic load path.

I-1 Uncracked concrete

The cracking surface is composed of two surfaces, respectively for compression and tension (Figure 1). The mathematical expressions of these surfaces, proposed by Nadai, are :

$$\left\{ \begin{array}{l} f_{comp}(\sigma_{oct}, \tau_{oct}) = \frac{\tau_{oct} + a \cdot \sigma_{oct}}{b} - f'_c = 0 \\ \sigma_1 < 0 \text{ and } \sigma_2 < 0 \end{array} \right. \quad \text{in compression, and}$$

$$\left\{ \begin{array}{l} f_{comp}(\sigma_{oct}, \tau_{oct}) = \frac{\tau_{oct} + c \cdot \sigma_{oct}}{d} - f'_c = 0 \\ \sigma_1 > 0 \text{ and / or } \sigma_2 > 0 \end{array} \right. \quad \text{in tension.}$$

With :

$$\sigma_{oct} = I_1 / 3 \quad \text{and} \quad \tau_{oct} = \sqrt{\frac{2J_2}{3}} = \sqrt{\frac{2}{9}} \sigma_{equ}$$

$$a = \sqrt{2} \frac{\beta - 1}{2\beta - 1}, \quad b = \frac{\sqrt{2}}{3} \frac{\beta}{2\beta - 1}$$

$$c = \sqrt{2} \frac{1 - \alpha}{1 + \alpha}, \quad d = \frac{2\sqrt{2}}{3} \frac{\alpha}{1 + \alpha}$$

σ_{equ} : Von Mises equivalent stress

$$\beta = f_c / f_{cc} \approx 1.16$$

$$\alpha = f_t / f_c \approx 0.1$$

f_t : uniaxial tensile resistance

f_c : uniaxial resistance in compression

f_{cc} : biaxial resistance in compression

$$I_1 = \sigma_x + \sigma_y$$

$$J_2 = \frac{1}{2} (S_x^2 + S_y^2 + S_z^2) + \tau_{xy}^2$$

$$S_x = \sigma_x - \frac{I_1}{3}; \quad S_y = \sigma_y - \frac{I_1}{3}; \quad S_z = \sigma_z - \frac{I_1}{3}$$

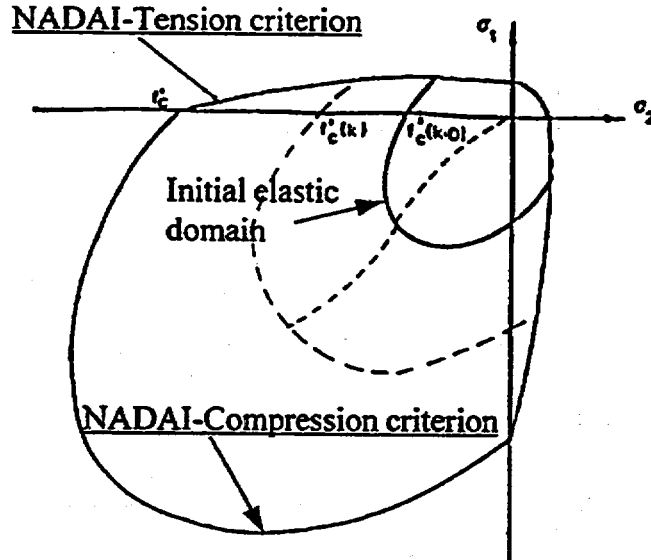


Figure 1: NADAI's criterion.

The load surface is deduced from the surface of rupture by replacing in the expression of the compression cracking criterion the ultimate resistance under uniform compression by the equivalent uniaxial stress, which controls the evolution of the actual elasticity domain. It is written as follows:

$$\left\{ \begin{array}{l} f(\sigma, \kappa) = \frac{\tau_{act} + a \cdot \sigma_{act}}{b} - \tau(\kappa)_c = 0 \\ \sigma_1 < 0 \text{ and } \sigma_2 < 0 \text{ or} \\ \sigma_1 < 0 \text{ and } \sigma_2 > 0 \end{array} \right.$$

The evolution of this surface is determined by the cumulative plastic strain κ . The hardening modulus "h" corresponds to the slope of the uniaxial (stress-plastic strain) curve (Figure 2). The mathematical expression of this curve is:

$$\left\{ \begin{array}{l} \tau = f_c \left[\theta + (1 - \theta) \sqrt{1 - \left(\frac{\kappa - \kappa_{pic}}{\kappa_{rupt}} \right)^2} \right] \quad \text{for } 0 < \kappa < \kappa_{pic} \\ \tau = \frac{f_c}{\kappa_{rupt} - \kappa_{pic}} (0.95 \cdot \kappa + 0.05 \cdot \kappa_{pic} - \kappa_{rupt}) \quad \text{for } \kappa_{pic} \leq \kappa \leq \kappa_{rupt} \\ \tau = 0.05 \cdot f_c \quad \text{for } \kappa > \kappa_{rupt} \end{array} \right.$$

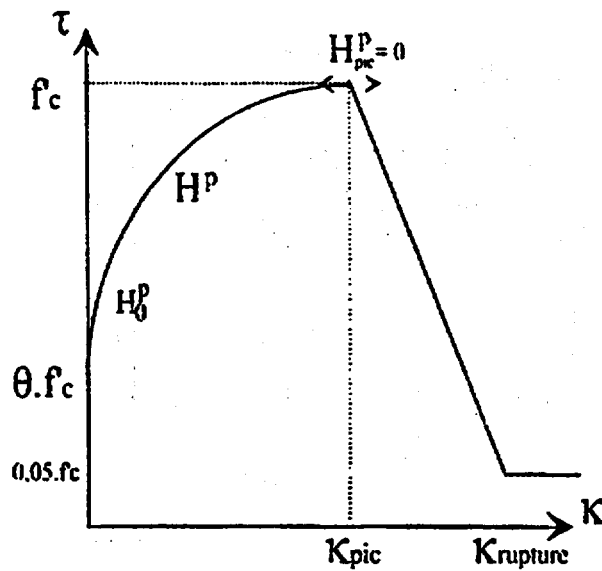


Figure 2: Stress/plastic strain curve.

I-2 Cracked concrete

When the ultimate surface is reached in tension, a crack is created perpendicularly to the principal direction of maximum tension, and its orientation is considered as fixed subsequently. The behaviour is then modelled by an orthotropic law whose orthotropy directions are normal and parallel to the crack (Figure 3). During the increment which generates the cracking at an integration point, the switching from the biaxial elastoplastic model to the uncoupled orthotropic model requires a specific processing. The strains are broken down into a part coming from the continuum located on both sides of the crack and a part coming from the opening of the crack. The state of strain is written in the reference linked to the crack:

$$\varepsilon_i = \varepsilon_i^{\text{cont}} + \varepsilon_i^{\text{fiss}} \quad \text{with } i=x,y$$

The continuum follows a linear elastic law after cracking:

$$\varepsilon_i^{\text{cont}} = \frac{\sigma_i}{E_0} - \frac{\nu}{E_0} \sigma_j \quad j \neq i$$

and $\varepsilon_i^{\text{fiss}}$ follows a unidimensional law (the dilatancy effect is neglected) this allows to create plastic strains perpendicular to the crack (crack opening). Therefore:

$$\varepsilon_i = \varepsilon_i^{\text{fiss}} + \frac{\sigma_i}{E_0} - \frac{\nu}{E_0} \sigma_j . \quad \text{By posing: } \varepsilon'_i = \varepsilon_i^{\text{fiss}} + \frac{\sigma_i}{E_0} = \varepsilon_i + \frac{\nu}{E_0} \sigma_j$$

From the strain ε_i along a direction i , the corresponding stress can be calculated: $\sigma_i = f(\varepsilon'_i)$.

Each direction is then processed independently by a cyclic uniaxial law, and the stress tensor in the local reference is completed by the shear stress, elastically calculated with a reduced shear modulus to account for the effect of interlocking. In the crack reference:

$$\{\Delta\sigma\} = \begin{cases} \Delta\sigma_x = f_u(\varepsilon'_{0x}, \sigma_{0x}, \Delta\varepsilon'_x) \\ \Delta\sigma_y = f_u(\varepsilon'_{0y}, \sigma_{0y}, \Delta\varepsilon'_y) \\ \Delta\sigma_{xy} = \mu \cdot G \cdot \Delta\varepsilon_{xy} \end{cases}$$

With ε'_{0x} , ε'_{0y} , σ_{0x} , σ_{0y} being the strains and stresses at the beginning of the increment

- $\Delta\sigma$ the plastically admissible stress increment;
- $\Delta\varepsilon'$ the strain increment elastically calculated;
- f_u the uniaxial law described below;
- μ the shear transfer factor;
- G the initial shear elastic modulus.

Therefore, a second crack can only form perpendicularly to the first one.

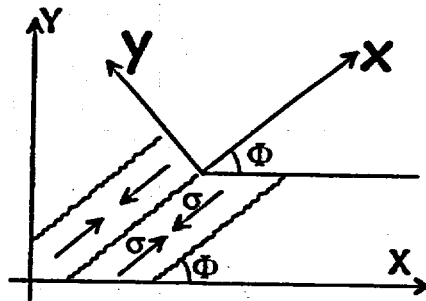


Figure 3 : Reference linked to the crack.

I-3 Cyclic uniaxial law

The uniaxial law implemented in each of the directions is identical to the one used in the frame work of a multi-fiber modelling. It allows to account for the main phenomena observed during a loading composed of a small number of alternated cycles. Because of this original feature, it deserves to be detailed. The experiments on which the model is based are listed in reference of [1].

Let us first consider in figure 4 the behaviour of a point initially under tension which completely cracks prior to undergoing a reverse loading in compression. Being elastic until it reaches the resistance under uniform tension: f_t (path 1), the concrete cracks afterwards according to a negative stiffness (Slope E_{ts} , Path 2) up to a strain ϵ_{tm} . Beyond, the crack opening occurs with a nil stress (Path 3).

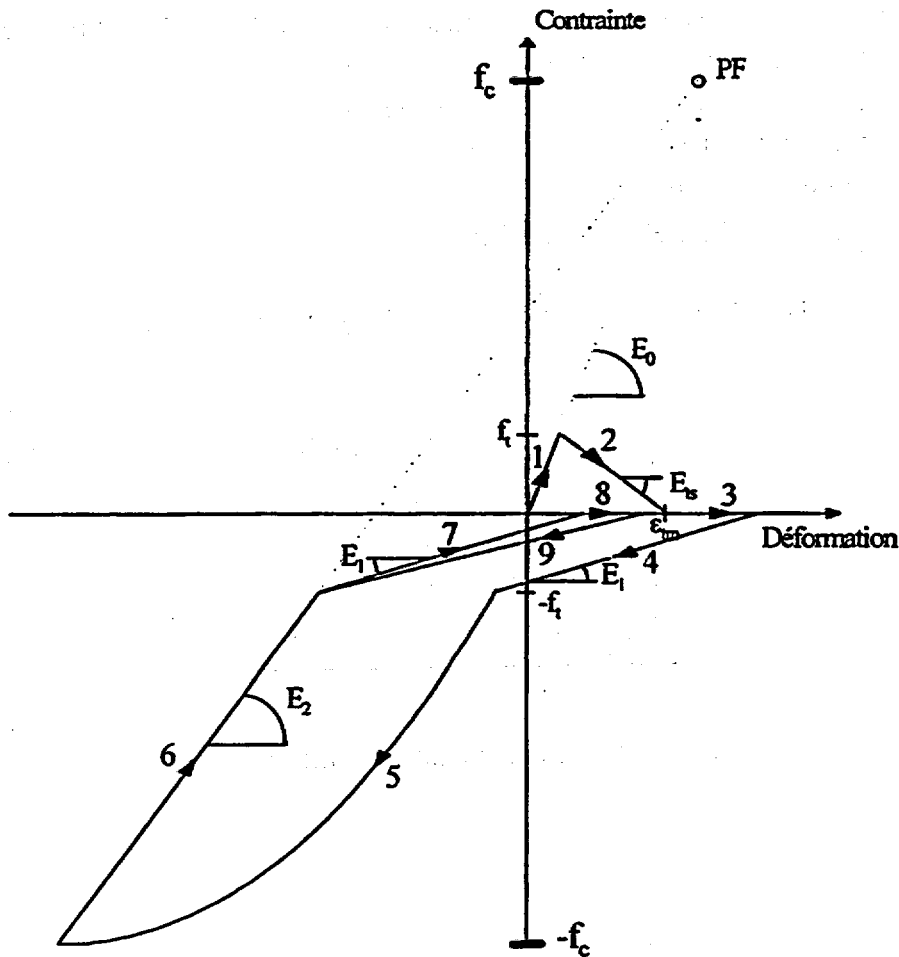


Figure 4 : Concrete uniaxial model: point initially in tension.

When the load changes direction, an increasing compression stress is necessary to progressively close back the crack (Slope $E_1 \neq E_0$, Path 4). The crack is considered as completely closed for a stress smaller than $-f_t$, level from which the stiffness is fully restored (Path 5). Description of Path 4 is based on experiments that show that the facing lips of a crack do not coincide and deform under the action of a stress which tends to close the crack back, and that the stiffness of the sound concrete is restored only once the crack has completely closed back. However, the closing of the crack occurs under a nil stress as long as the strain is greater than a certain threshold: $3 \cdot \epsilon_{tm}$.

Path 5 follows the nonlinear law of concrete under uniform compression up to a new load inversion which generates an unloading according to a straight line of slope E_2 (Path 6) and which passes through a focal point $(f_t; \epsilon_0)$, as suggested by Mander *et al.* [2] and Park [3]. Indeed, the experiments show that the modulus during unloading is different from the initial one due to the deterioration of concrete in compression.

When stress exceeds $-f_t$ (Path 7), the modulus E_1 corresponding to the closing of the crack is met again. Paths 8 and 9 follow the same rules as Paths 3 and 4.

Now, let us follow on figure 5 the history of an initially compressed point. The essential difference is the new resistance in tension which, as the unloading modulus, is damaged by the compression it underwent (Paths 3 and 4). This resistance is thus modified as suggested by Morita and Kaku [4]:

$$\left\{ \begin{array}{ll} f'_t = f_t \left(1 - \frac{\epsilon_r}{\epsilon_c} \right) & \text{Si } \epsilon_r > \epsilon_c \\ f'_t = 0 & \text{Si } \epsilon_r \leq \epsilon_c \end{array} \right. \quad \begin{array}{l} \text{With: } f_t : \text{Resistance under uniform tension;} \\ \epsilon_r : \text{Residual strain;} \\ \epsilon_c : \text{Strain in compression at the peak } (\sigma = -f_c). \end{array}$$

As far as the residual strain is concerned, it is obtained by considering the damaged stiffness of unloading, and is given by the following relation:

$$\epsilon_r = \epsilon_d - \frac{(\epsilon_d - \epsilon_0)}{\sigma_d - E_0 \epsilon_0} \cdot \sigma_d$$

With σ_d and ϵ_d being the stress and the strain at the instant of the compression unloading.

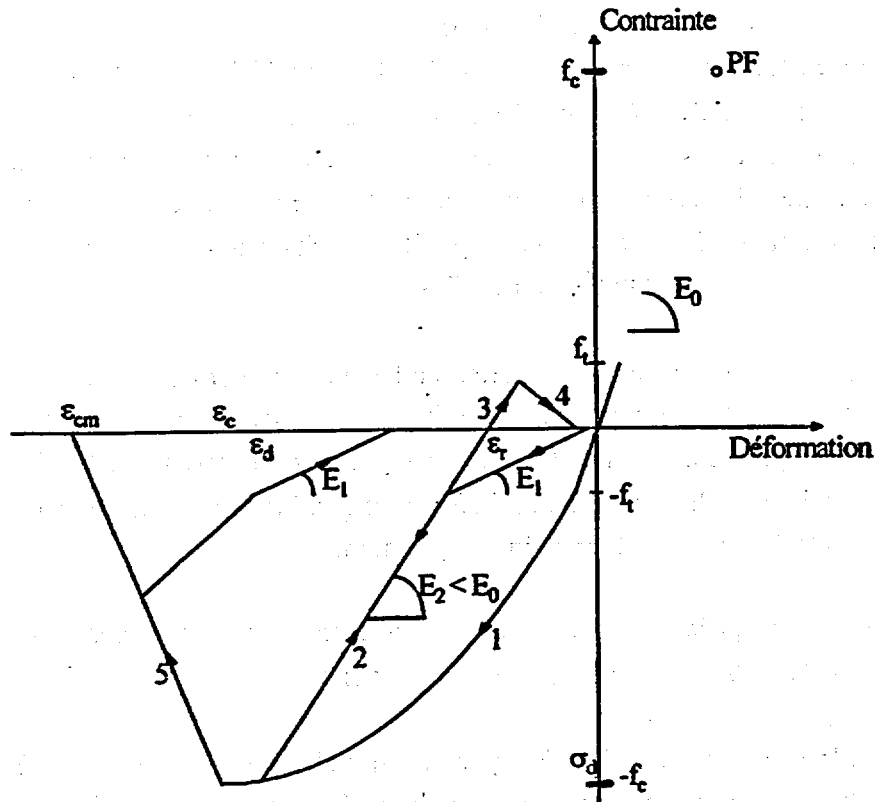


Figure 5 : Concrete uniaxial model: point initially in compression.

Path 5 corresponds to the concrete softening in compression. The slope of the descending branch is simply obtained from the ultimate strain of the material under uniform compression and the strain at the peak.

REFERENCES

- [1] MERABET, O; DJERRROUD, M.; CHAHROUR, I.; REYNOUARD, J.M.
Développement d'un modèle semi global pour le calcul des systèmes de poutres en béton armé sous chargements alternés cyclés. Comportement cyclique et dynamique des structures en béton armé. CNRS, rapport scientifique édité par J.M Reynouard, Aussois, 1991, p. 417-420.

- [2] MANDER, J.B.; PRIESTLEY, M.J.N, PARK, R.
Theoretical stress-stain model for confined concrete. *Journal of structural engineering*, 1988, Vol. 114, N°8, p. 1804-1825.

- [3] PARK, Y.S
Fatigue of concrete under random loadings. *Journal of structural engineering*, 1990, Vol. 116, N°11, p. 3228-3235.

- [4] MORITA, S.; KAKU, T.
Cracking and deformation of reinforced concrete beams subjected to tension. *Liege colloquium inter-association*, 1975.

Appendix 2

**Example of calculation of the rebar characteristics
applied to the grids**

①

Hoop rebars: D22, $e = 11,27 \text{ cm}$.
 Vertical rebars: D19-D16, $e = 0,5$.

INNER REBARS

Hoop rebars: $A_1 = 387,10 \text{ mm}^2 \rightarrow S_1 = \frac{387,10}{0,1127} = 3435 \text{ mm}^2/\text{m}$

Vertical rebars: $A_2 = \frac{280,5 + 198,6}{2} = 242,55 \text{ mm}^2$

$R_{\text{vertical rebars}} = 5,375 + 0,0587 = 5,434 \text{ m}$

$\alpha R = 1 \text{ ml}$

$\hookrightarrow \alpha = \frac{1}{R} = \frac{1}{5,434} = 10,54^\circ$

for 1ml, $n = \frac{10,54}{0,5} = 21 \text{ vertical rebars}$

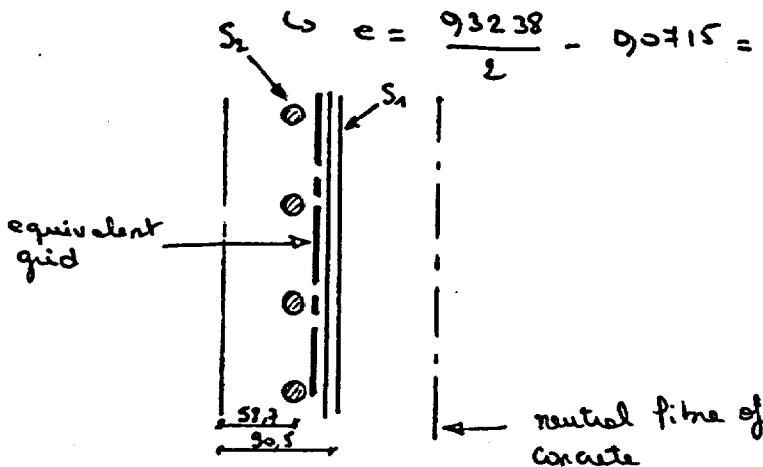
$\rightarrow S_2 = 242,55 \times 21 = 5094 \text{ mm}^2/\text{m}$

$P_1 = 1$

$P_2 = \frac{E_2 S_2}{E_1 S_1} = \frac{183500 \times 5094}{191000 \times 3435} = 1,42 \text{ (equivalence of stiffness)}$

Eccentricity: $e_{\text{int}} = \frac{0,0587 \times 5094 + 0,0905 \times 3435}{5094 + 3435} = 0,0715 \text{ m}$

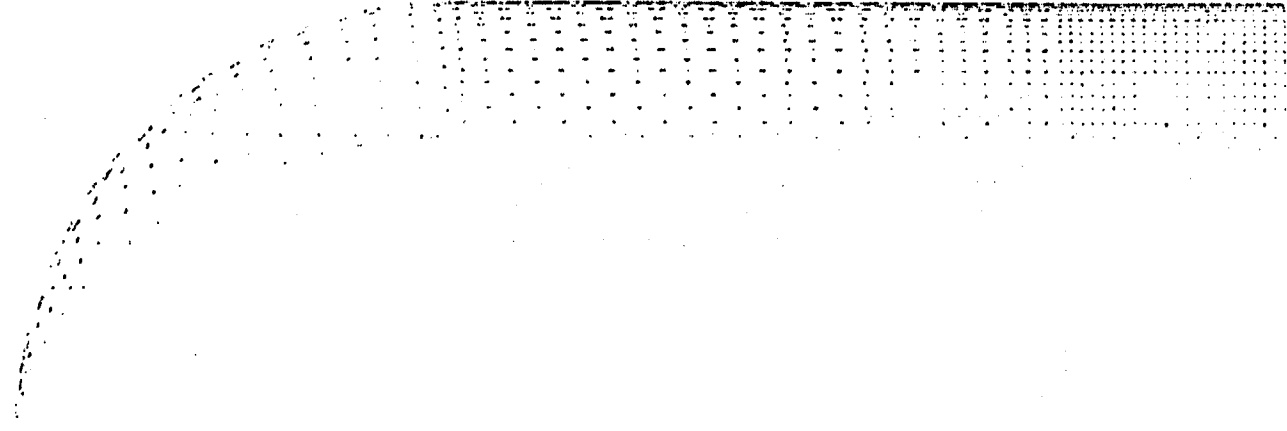
$e = \frac{93238}{2} - 0,0715 = 0,0304 \text{ m}$



Appendix 4

**Design of the model
(finite element mesh)**

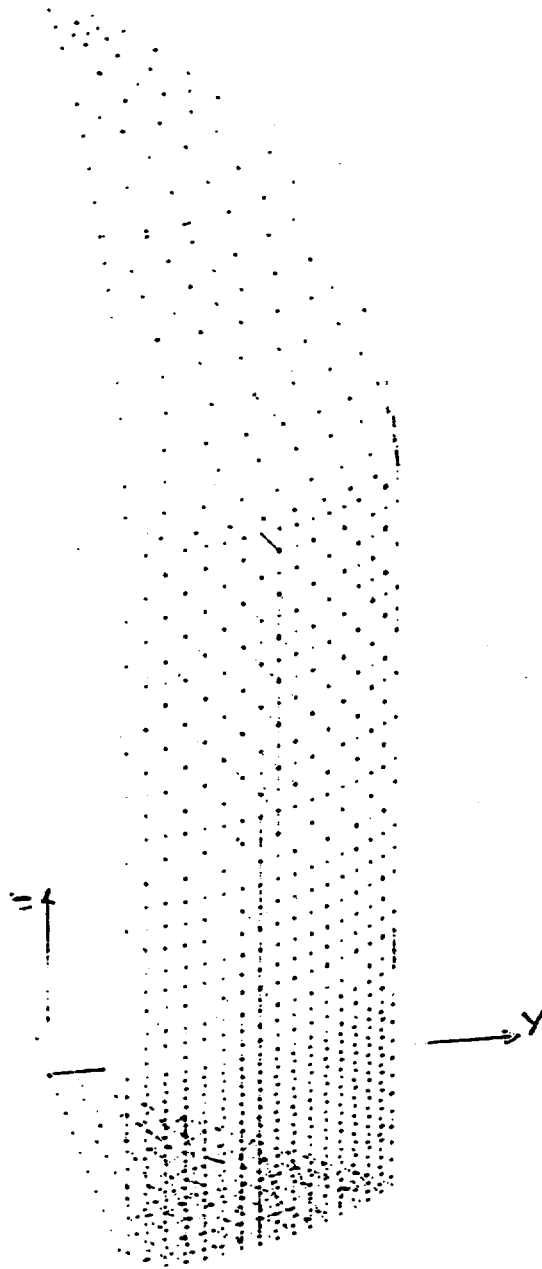
General view of the finite element mesh



GIBI FECIT



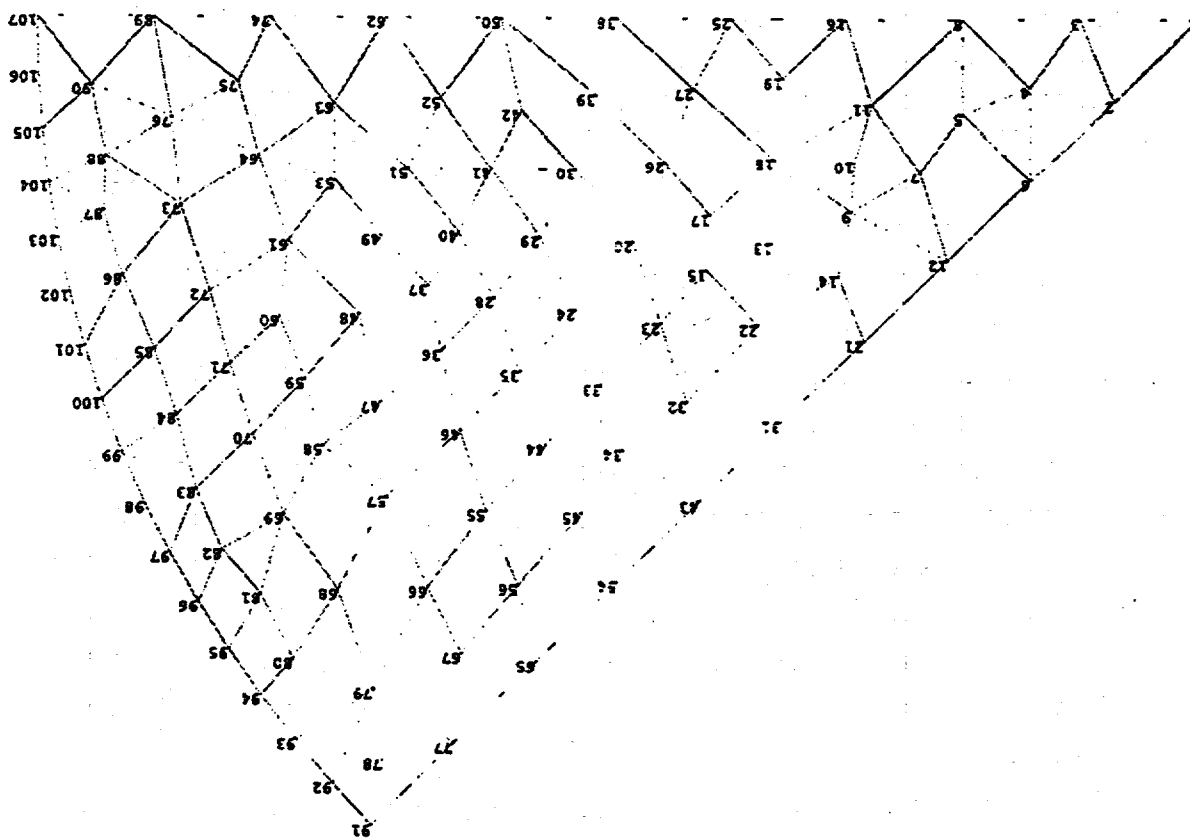
**General view of the finite element mesh
Definition of the axis**



JIBI PECIP

X

GRID POINT



Basemat

NODES

NODES

First part of the wall (bottom)

532	531	530	529	528	527	526	525	524	523	522	521	520	519	518	517	516
515	514	513	512	511	510	509	508	507	506	505	504	503	502	501	500	99
498	497	496	495	494	493	492	491	490	489	488	487	486	485	484	483	482
481	480	479	478	477	476	475	474	473	472	471	470	469	468	467	466	465
464	463	462	461	460	459	458	457	456	455	454	453	452	451	450	449	448
447	446	445	444	443	442	441	440	439	438	437	436	435	434	433	432	431
430	429	428	427	426	425	424	423	422	421	420	419	418	417	416	415	414
413	412	411	410	409	408	407	406	405	404	403	402	401	400	399	398	397
396	395	394	393	392	391	390	389	388	387	386	385	384	383	382	381	380
379	378	377	376	375	374	373	372	371	370	369	368	367	366	365	364	363
362	361	360	359	358	357	356	355	354	353	352	351	350	349	348	347	346
345	344	343	342	341	340	339	338	337	336	335	334	333	332	331	330	29
328	327	326	325	324	323	322	321	320	319	318	317	316	315	314	313	312
311	310	309	308	307	306	305	304	303	302	301	300	299	298	297	296	295
294	293	292	291	290	289	288	287	286	285	284	283	282	281	280	279	278
277	276	275	274	273	272	271	270	269	268	267	266	265	264	263	262	261
260	259	258	257	256	255	254	253	252	251	250	249	248	247	246	245	244
243	242	241	240	239	238	237	236	235	234	233	232	231	230	229	228	227
226	225	224	223	222	221	220	219	218	217	216	215	214	213	212	211	210
209	208	207	206	205	204	203	202	201	200	199	198	197	196	195	194	193
192	191	190	189	188	187	186	185	184	183	182	181	180	179	178	177	176
175	174	173	172	171	170	169	168	167	166	165	164	163	162	161	160	59
158	157	156	155	154	153	152	151	150	149	148	147	146	145	144	143	142
141	140	139	138	137	136	135	134	133	132	131	130	129	128	127	126	25
124	123	122	121	120	119	118	117	116	115	114	113	112	111	110	109	108
107	106	105	104	103	102	101	100	99	98	97	96	95	94	93	92	91

GIBI FECIT

NODES

Second part of the wall (top)

890.891 892.893 895.896 897.894 898.899 900.901 902.903 904.905 906
874.873 876.875 879.878 880.877 882.881 884.883 886.885 888.887 889
856.858 857.859 862.861 864.863 866.865 868.867 870.869 872.871
840.839.842 841.844 843.845 845.848 847.850 849.852 851.855 854.853
822.824.823 825.828 827.830 829.832 831.834 833.838 837.835
806.805.808 810.809 812.811 814.813 816.815 821.820 818.817
788.790 789.792 791.794 792.796 795.798 797.804 803.802 801.800 799
772.771.774 776.775 778.777 780.779 787.786 785.784 783.782 781
754.756.755 757.760 759.762 761.770 769.768 767.766 765.764 763
738.737.740 742.741 744.743 753.752 751.750 749.748 747.745 745
720.722 721.724 723.726 725.736 735.734 733.732 731.730 729.727
704.703.706 708.707 713 718.717 716.715 714.713 712.711 710.709
686.688.687 689.702 701.700 699.698 697.696 695.694 693.692 691
670.669.672 685.684.683 682.681.680.679.678.677.676.675.674.673
653.652.655 664.668 667.666 665.664 663.662 661.660 659.658 657.656
635.637 636.639 650.649 649.647 646.645 644.643 642.641 640.639 638
619.618.634 633.632.631.630 629.628.627.626.625.624.623.622.621.620
602.601.617 616.615.614.613 612.611.610.609.608.607.606.605.604.603
585.584.600 599.598.597.596 595.594.593.592.591.590.589.588.587.586
567.583 582.581 580.579.578.577.576.575.574.573.572.571.570.569.568
550.566.565.564.563.562.561.560.559.558.557.556.555.554.553.552.551
549.548 547.546 545.544.543 542.541.540.539.538.537.536.535.534.533
532.531.530 529.528 527.526 525.524 523.522.521.520.519.518.517.516

GIBI FECIT

NODES

Dome

1035
1034¹⁰³³
1031¹⁰³²1030
1029¹⁰²⁸1025
1026¹⁰²⁴1023
1019 1020
1021 1022 1015 1014
1016
1017 1018 1012.1008
1007
1013 1006
1009 1010 1011 1001 1000
1003 1005 1004 994
996 1002 999 998 997
990 995 993 992 991 988
983 981 982 987 985 984 980
974 973 979 978 977 975
964 969 970 976 967 968 965 972
956 953 971 966 957 959 958 962
955 954 961 960 948 949 952 953
946 947 951 950 943 944 945
937 938 942 941 940 939 943 934 935
928 931 932 930 929 933 934 925
918 923 921 922 919 923 924 926 917
907 908 909 911 910 912 913 915 916 906
890 891 892 893 895 896 897 894 898 899 900 901 902 903 904 905

GIBI FECIT

APPENDIX F

GLASGOW

UNIVERSITY OF GLASGOW

UNITED KINGDOM

Appendix A, Composite Plots, comprises test data compiled and plotted from all organizations that participated in the Prestressed Concrete Containment Vessel (PCCV) Round Robin Pretest Analysis. To avoid duplicating the composite information, individual sets of data and/or plots have been omitted from participants' reports. In some cases this action resulted in disconnects between callouts and content and in the numbering of figures, tables, and pagination in some reports.

In Appendix F, "Glasgow, University of Glasgow, United Kingdom," discontinuity arises from omitting the following material:

figures 11 through 37, Response Histories Standard Locations

Table of Contents

(1) DESCRIPTION OF THE MATHEMATICAL MODEL	2
(2) MATERIAL PROPERTIES	2
(2.1) Linear Elastic Material Properties	2
(2.2) Nonlinear Material Properties	3
(3) ANALYSIS RESULTS	4
(4) REVIEW OF MILESTONE PRESSURE LEVELS	4
(5) REFERENCES	5
FIGURES 1-6, FE MESH DETAILS	6-11
FIGURES 7-10, DEFORMED SHAPES, CONTOURS	12-15
FIGURES 11-37, RESPONSE HISTORIES STANDARD LOCATIONS	16-29

(1) DESCRIPTION OF THE MATHEMATICAL MODEL

PCCV was modelled using the DIANA Finite Element Analysis, developed by the TNO Building and Construction Research, Delft, Netherlands. The adopted model comprises a total of 2480 eight noded solid elements HX24L (8 node bricks), used to model the concrete cylinder and buttresses, as well as the internal steel liner. There are a total of 3246 nodes (each with three dof's) forming the main mesh. Tendons are modelled as embedded, fully bonded, bar elements, whereas the reinforcement is modelled through an embedded grid elements. An additional number of nodes is created (with tied degrees of freedom), where the tendons intersect the solid elements - the total number of nodes is 7728, where the translation dofs of the 3246 nodes are the main variables of the problem.

Buttresses are modelled by two extra layers of solid elements. The assumption is made that the main cylinder is fully clamped into the basemat, which is considered rigid and therefore excluded in the discretisation process. In order to avoid the influence of unrealistic stress concentrations near the basemat boundary, the first bottom ring of solid elements (both for concrete and liner) is modelled as a linear elastic material with a reduced modulus (reduction factor 2/3). All other solid elements follow the nonlinear constitutive relationship as given below. In addition, no provision is made within the mathematical model for the hatch or opening geometry details, i.e. the departure from structural axi-symmetry stems from the buttresses and the hairpin tendon layout. The dome apex is modelled as not fully closed, in order to allow the discretisation with 8 noded brick elements. Various FE mesh details are illustrated in Figs 1-6

(2) MATERIAL PROPERTIES

(2.1) Linear Elastic Material Properties

Concrete

Modulus of Elasticity	38100 MPa
Poisson Ratio	0.20

Steel Liner

Modulus of Elasticity	224000 MPa
Poisson Ratio	0.25

Reinforcement

Modulus of Elasticity	183000 MPa
Poisson Ratio	0.25

Tendons

Modulus of Elasticity	38100 MPa
Poisson Ratio	0.25

(2.2) Nonlinear Material Properties

Concrete

Cracking Model in DIANA (CRACK 2) with tension cut off

Tensile strength f_t 3.40 MPa

Compressive Strength f_c 44.13 MPa

Nonlinear Exponential Tension Softening Model (DIANA, TENSION option 5, Hordijk et al)

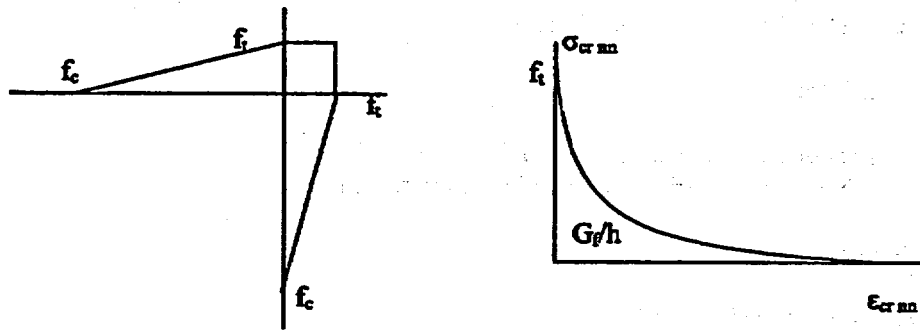
Tensile strength f_t 3.40 MPa

Fracture Energy Release Rate G_f 0.10 N/mm

Crack Band (one element size) h_c 1000 mm

Default c_1 and c_2 parameters for Hordijk et al exponential softening model

Constant shear retention factor 0.2



Hordijk et al Nonlinear Softening Model for Concrete

Steel Liner

von Mises plasticity model

Yield Limit 398 MPa

Reinforcement

von Mises plasticity model

Yield Limit 470 MPa

Tendons

von Mises plasticity model

Yield Limit 1750 MPa

(3) ANALYSIS RESULTS

Plots of deformed shapes and contours of cracking strains are included in Figs 7-10, whereas pressure histories for strain, displacement and tendon force at selected standard output location are included in Figs 11 - 37. Analysis results clearly indicate significant change in structural behaviour corresponding to the internal pressure gauge of 0.95 MPa.

(4) REVIEW OF MILESTONE PRESSURE LEVELS

(4.1) First cracking of concrete in cylinder primarily in the hoop direction
(appeared in both hoop and meridional direction at the same time)

0.95 MPa

(4.2) first cracking of concrete in cylinder primarily in the meridional direction
(appeared in both hoop and meridional direction at the same time)

0.95 MPa

(4.3) first yield of hoop rebar in cylinder
(estimated as the level of the second plateau in the P-delta diagram)

1.05 MPa

(4.4) first yield of meridional rebar in wall-basemat juncture
(could not have been evaluated as the model is assumed fully fixed)

N/A

(4.5) first cracking of dome concrete above 45° dome angle
first cracking occurred at the dome apex (near the artificial top opening) and is therefore ignored as a sensible result. Dome cracking will probably appear at the same pressure level as in the wall.

0.95 MPa

(4.6) first cracking of dome concrete below 45° dome angle
(same time as the cracking in the cylinder wall appears)

0.95 MPa

(4.7) first hoop tendon in cylinder reaching 1 % strain

Analysis never reached the stage where tendon strains are of that level (max 0.9 %)

greater than 1.4 MPa

(4.8) first hoop tendon in cylinder reaching 2 % strain

Analysis never reached the stage where tendon strains are of that level (max 0.9 %)

greater than 1.4 MPa

(4.9) first hoop tendon in cylinder reaching 3 % strain

Analysis never reached the stage where tendon strains are of that level (max 0.9 %)

greater than 1.4 MPa

(4.10) Qualitative assessment of the lower and upper limits of the PCCV model failure pressure

- **minimum pressure reachable with 90 % confidence level**
 - this is the predicted pressure, with a high degree of confidence, that the model will achieve without failing
 -
 - 0.95 MPa, 2.435 times the design pressure**

- **maximum pressure reachable with 90 % confidence level**
 - this is the predicted pressure, with a high degree of confidence, that the model will not exceed
 -
 - 2.50 MPa**

(5) REFERENCES

1. **DIANA User's Manual, Nonlinear Analysis, Release 6.1, eds de Witte and Feenstra, TNO Building and Construction Research, Delft, The Netherlands, 1996**
2. **Cornelissen, H. A. W., Hordijk, D. A., Reinhardt, H. W., Experimental determination of crack softening characteristics of normalweight and lightweight concrete, Heron 31 (2), 1986**

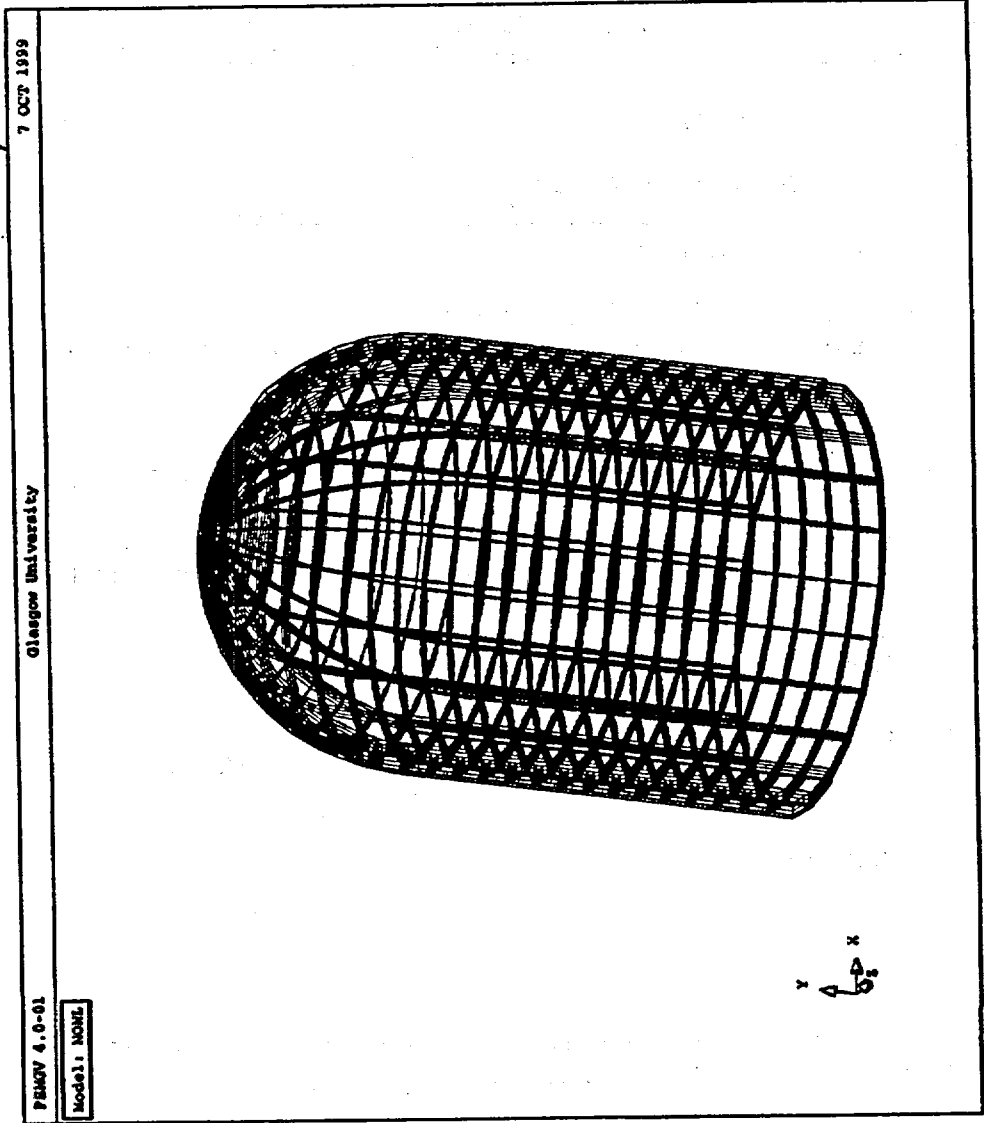


Fig 1 - DIANA Main FE Mesh (Concrete Cylinder + Buttresses)

7 OCT 1999

Glasgow University

FR9V 4.0-01

Model: NOME

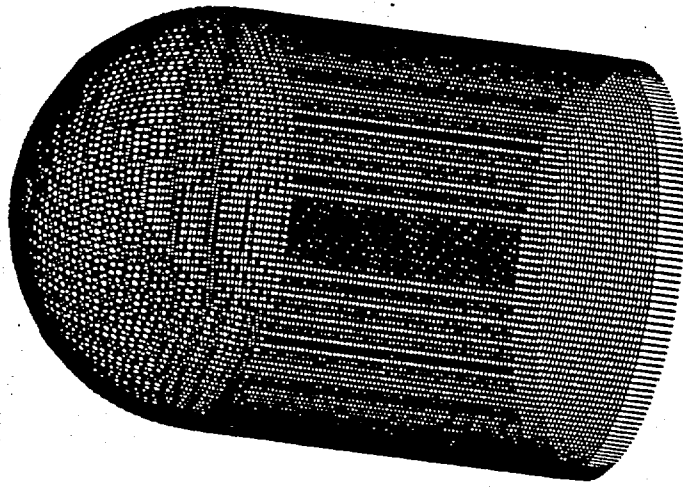


Fig 3 - DIANA Main FE Mesh - Hairpin and Hoop Tendons

7 OCT 1989

Glasgow University

FRANV 4.0-01

Model: N0001

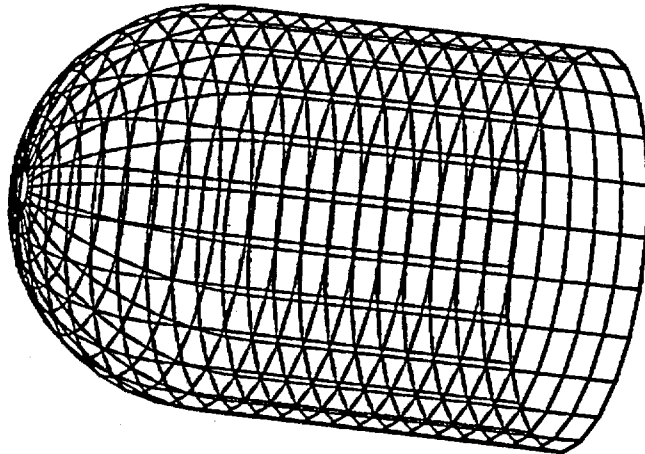


Fig 2 - DIANA FE Mesh (Steel Liner)

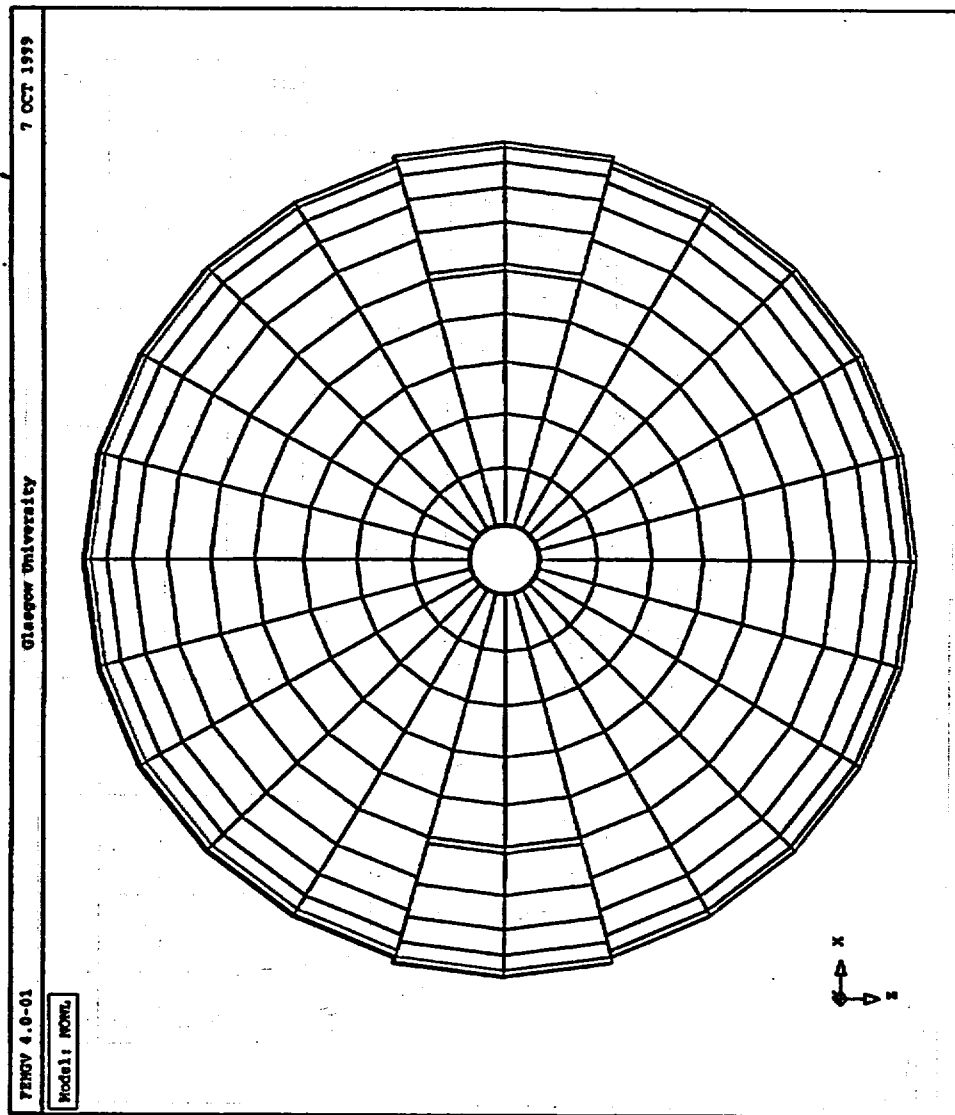


Fig 4 - DIANA FE Mesh - Top View (hidden lines removed)

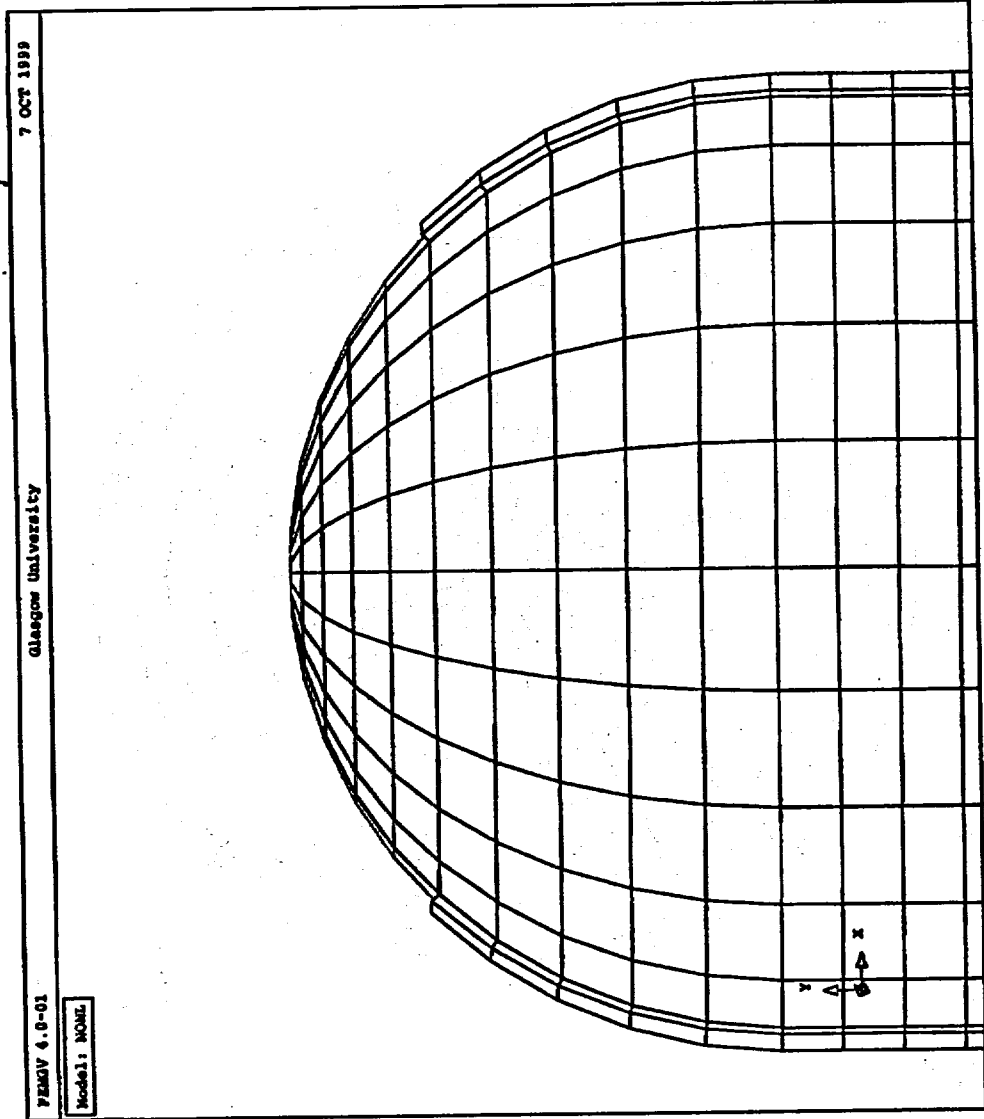


Fig 5 - DIANA FE Mesh (Top side view, hidden lines removed)

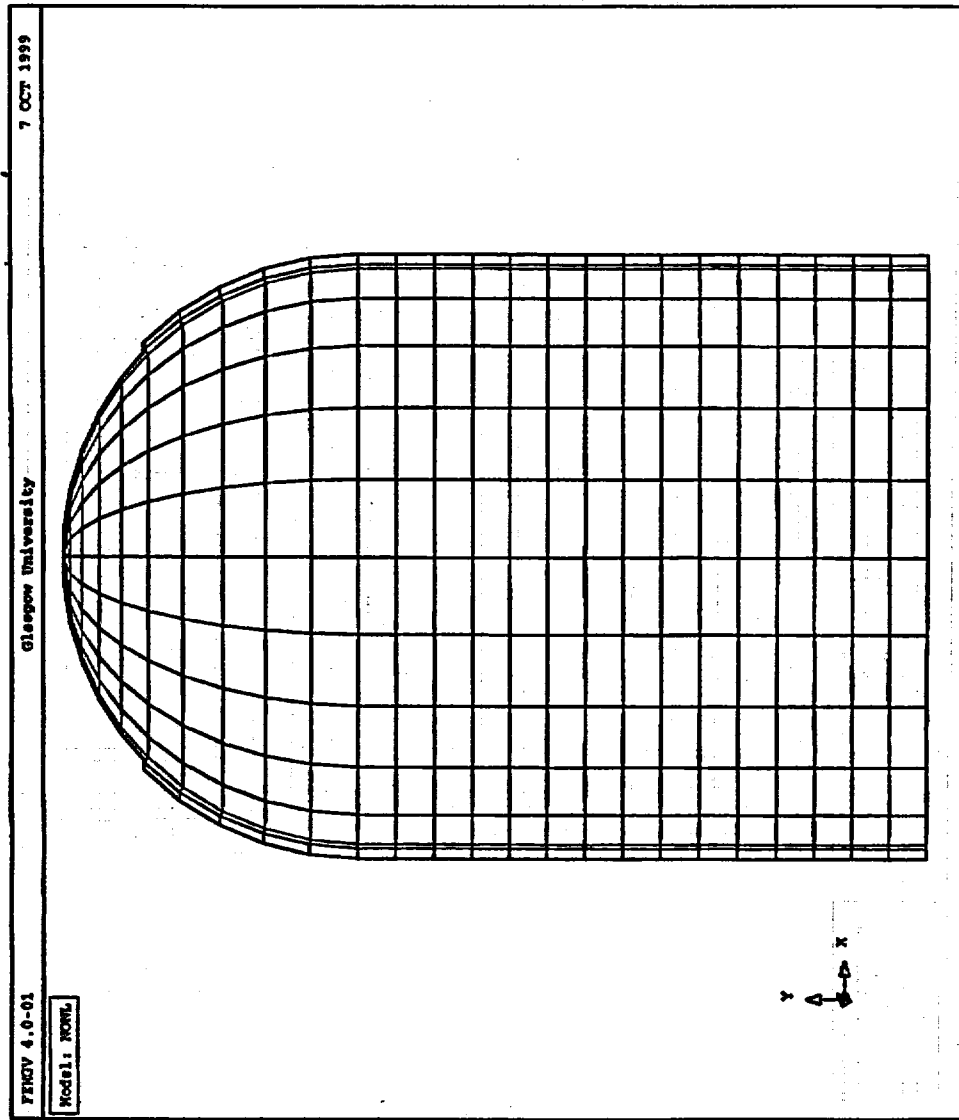


Fig 6 - DIANA FE Mesh (Side View, 180°)

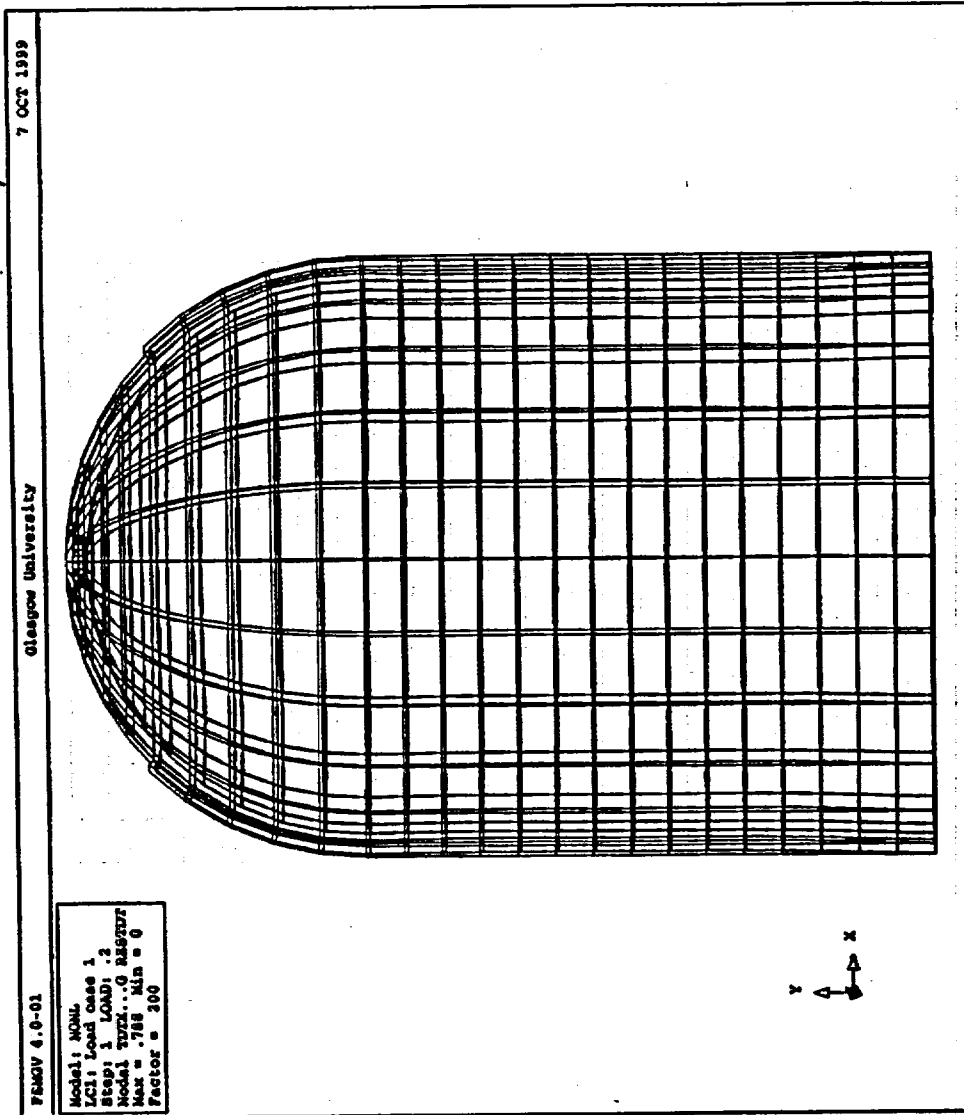


Fig 7 - Deformed Shape at Working Pressure, DIANA Main FE Mesh (Side View)

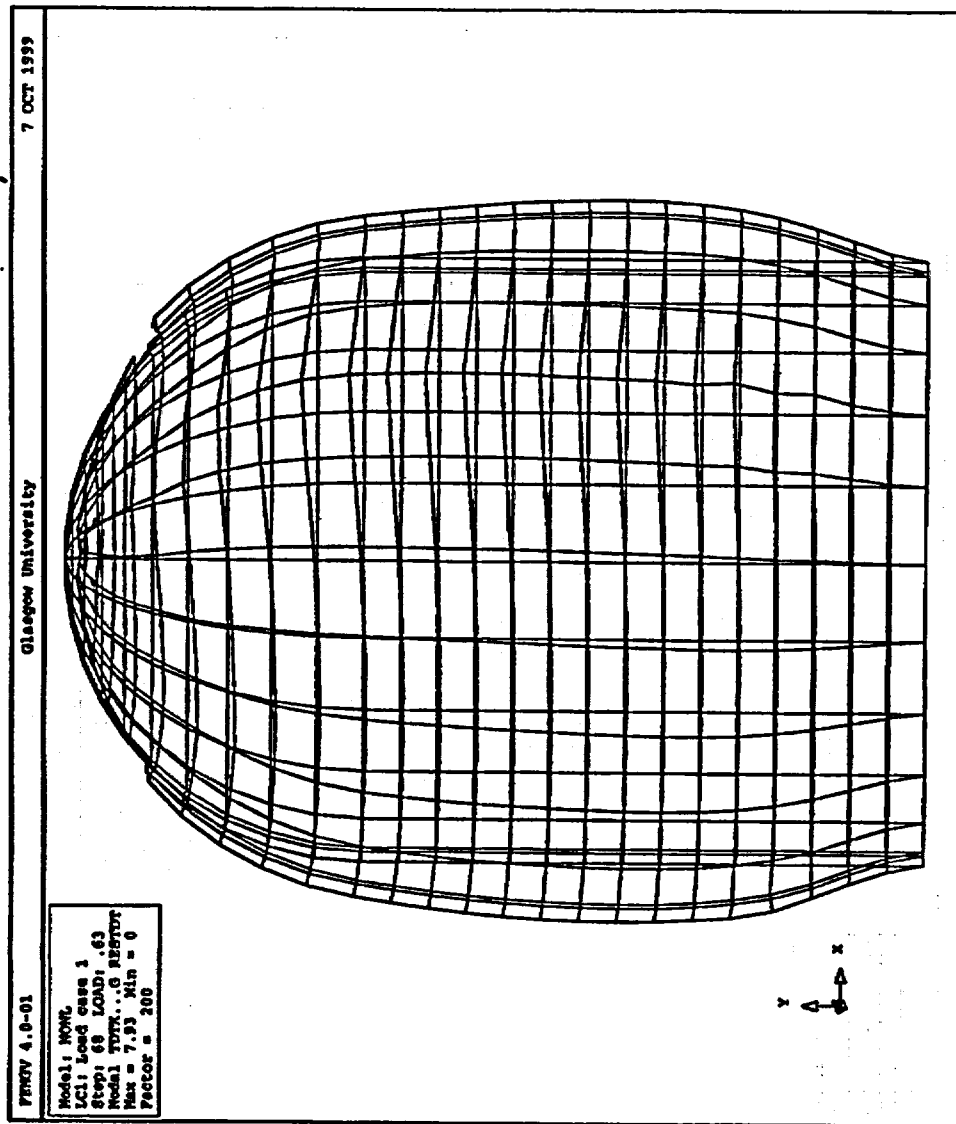


Fig 8 - Deformed Shape at the End of Analysis, DIANA Main FE Mesh (Side View)

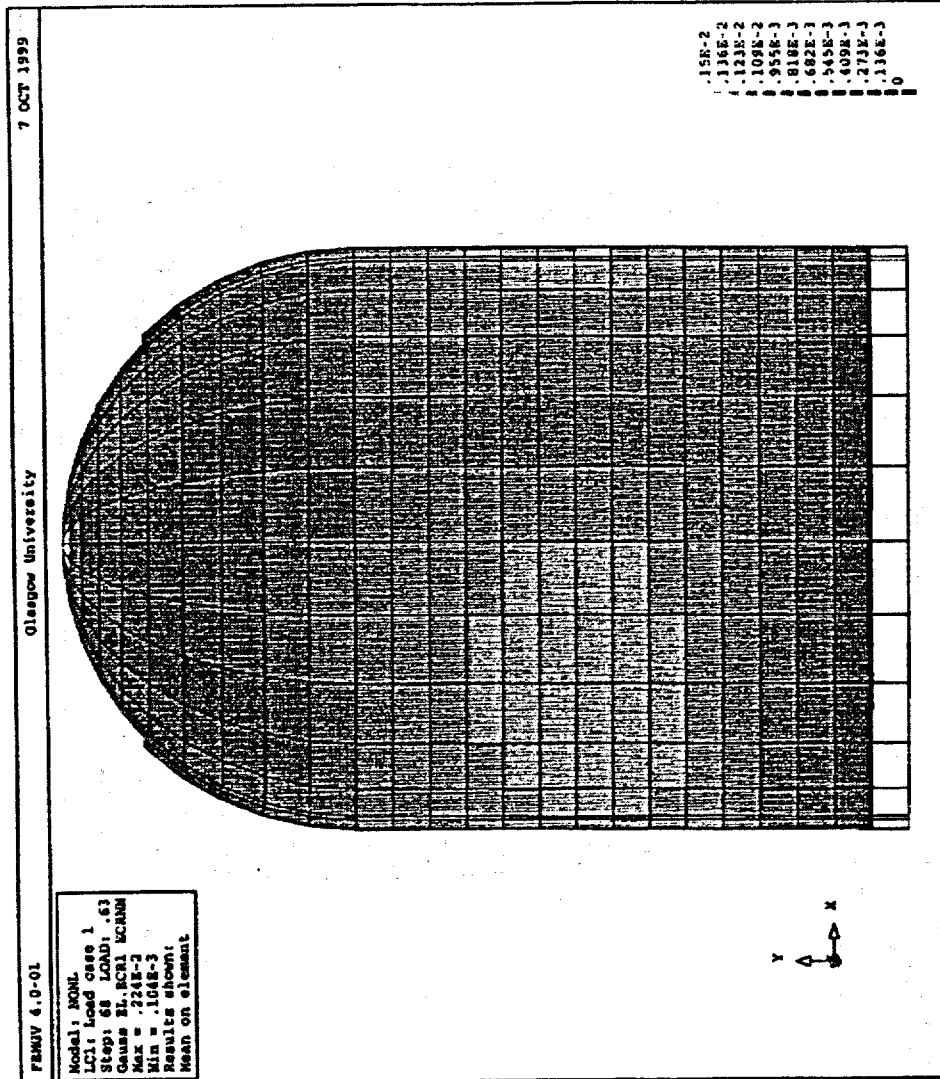


Fig 9 - Cracking Strain at the End of Analysis, DIANA Main FE Mesh (Side View)

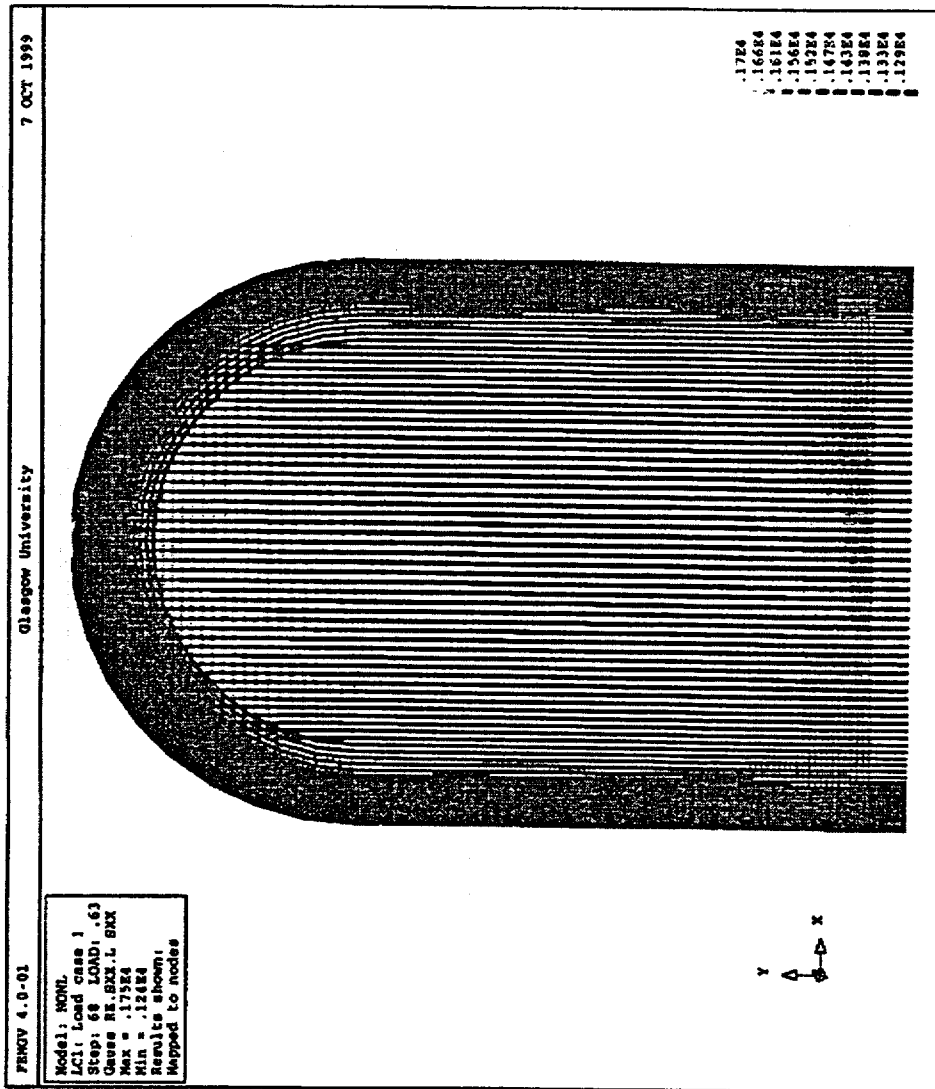


Fig 10 - Tendon Forces at the End of Analysis (Side View)

APPENDIX G

HSE

**HEALTH AND SAFETY EXECUTIVE
UNITED KINGDOM**

Appendix A, Composite Plots, comprises test data compiled and plotted from all organizations that participated in the Prestressed Concrete Containment Vessel (PCCV) Round Robin Pretest Analysis. To avoid duplicating the composite information, individual sets of data and/or plots have been omitted from participants' reports. In some cases this action resulted in disconnects between callouts and content and in the numbering of figures, tables, and pagination in some reports.

However, Appendix G, "HSE, Health and Safety Executive, United Kingdom," contains none of these discontinuities.



Adding value through knowledge

DOCUMENT ISSUE RECORD (Engineering Documents)

Document Title: HSE/NNC Pretest Analysis Report On 1/4 Scale PCCV Model - Summary Report
Project: CS769

Purpose of Issue: Issue to client
Security Class: Unclassified

Issue	Description of Amendment	Originator/ Author	Checker	Approver	Date
01	First Issue	<i>[Signature]</i> NK Prinja V Kante	<i>[Signature]</i> J Outley	<i>[Signature]</i> B V Day	9/11/99

Previous issues of this document shall be destroyed or marked **SUPERSEDED**

© NNC Limited 1999

All rights reserved. No part of this document or any information or descriptive material within it may be disclosed, loaned, reproduced, copied, photocopied, translated or reduced to any electronic medium or machine readable form or used for any purpose whatsoever without the written permission of the Company.

Distribution: Sandia Labs, HSE (D J Shepherd), Job File, NKP

HSE/NNC Pretest Analysis Report On ¼ Scale PCCV Model – Summary Report

Contents

		Page No.
1	Introduction	6
2	Modelling features of the PCCV scale model	6 - 7
3	FE models	7
4	Description of the full 3D finite element model	7
4.1	Cylinder wall and dome	8
4.2	Basemat	8
4.3	The cylinder wall penetrations	9
4.4	The post-tensioning tendons	9
4.5	Internal liner and liner anchorage	9 - 10
4.6	Concrete reinforcements	10
4.7	Derivation of post-tensioning tendon loads	10 - 11
4.8	Soil foundation	11
4.9	Boundary conditions	11
4.10	Material properties	11 - 12
5	Analysis	12
5.1	Analysis of full 3D global model	12 - 14
5.2	Analysis using 3D sector models	14 - 15
6	Pressure histories	15 - 16
7	Failure analysis	16 - 17

Contents (cont'd)

	Page No.
7.1 PCCV failure criterion	17
7.2 Prediction of failure using local models	17 - 19
8 Confidence level	19
9 Summary of main results	19 - 20
10 References	20
11 List of tables and figures	20 - 21

List of Tables

Table	Title	Page No.
1	Material data used in FE analysis	T1 - 2

List of Figures

Figure	Title	Page No.
1	Finite element representation of the PCCV	F1
2	Detail view of the PCCV dome model	F2
3	The PCCV basemat model	F3
4	Detailed view of equipment hatch penetration model	F4
5	Detailed view of the airlock penetration model and liner anchorage	F5
6	Detailed view of the main steam and feedwater penetrations model	F6
7	PCCV vertical tendons model	F7
8	Internal vessel liner, with details around the equipment hatch and airlock penetrations and the basement in view	F8
9	Equipment hatch penetration lining and cover plate with critical buckling mode prediction	F9
10	Deformed shape of cylinder and dome after post-tensioning	F10
11	Plan section through cylinder after post-tensioning	F11
12	Variation of hoop tendon load around vessel after transfer	F12
13	Deformed shape of cylinder due to internal pressure	F13
14	3D sector models of free field area and buttress/airlock area	F14
15	Reduced modulus due to concrete cracking	F15
16	Model of liner at junction of thin/thick plate	F16

1 Introduction

NNC Limited is acting as a round robin participant on behalf of the Health and Safety Executive (HSE) in the United Kingdom. This work has been carried out under HSE contract PC/GNSR/129. General purpose finite element computer code ABAQUS (Ref 1) has been used for analysis.

2 Modelling Features of the PCCV Scale Model

It was appreciated that a realistic representation of the vessel could only be obtained through the explicit representation of the prime structural components. The following are the structural components, whose representation determine the nature of the finite element model.

- (i) The cylinder wall penetrations are potential locations of failure initiation due to the stress concentration occurring around the structural discontinuities created by the penetrations. Further, the penetration areas are more heavily reinforced than the general free-field cylinder area rendering the vessel non-axisymmetric. Consequently, all the cylinder wall penetrations are represented in the model.
- (ii) The post-tensioning tendons are important structural elements as they subject the concrete to an initial compressive stress. Failure of the tendon would result in the relief of the compressive stress, which may precipitate the onset of cracking in the concrete. The tendons are to be left un-grouted after tensioning. Thus, in the tendon axial direction, they are capable of sliding relative to the surrounding duct. The vertical tendons are modelled explicitly while the hoop tendons are modelled as reinforcements embedded in the surrounding concrete. It is expected that the overall global response of the vessel at high pressures will be in part governed by the tendon behaviour.
- (iii) Although the basemat is a relatively rigid structure, its contribution to the flexural behaviour at the cylinder/basemat junction is not known prior to the test. Further, the stress concentration occurring at this junction due to the geometric discontinuity presents a potential area of vessel failure. Therefore, a full representation of the basemat is necessary to capture the behaviour at the cylinder/basemat junction.
- (iv) Although the internal vessel liner plays a minor structural role, its integrity determines the leak-tightness of the vessel. The limit state capacity of the vessel may be determined by the integrity of the liner as it may not be possible to pressurise the vessel above a certain rate if it is significantly breached. Therefore, to predict the possibility of liner tearing the entire internal liner has been modelled.

- (v) The two buttresses are stiffer than the surrounding cylinder wall. Nonuniform radial expansion is expected at these locations.
- (vi) There are 55 pre-defined standard output locations around the vessel at which the vessel's instrumented outputs are to be recorded. These recorded results are to be compared against the predictions from numerical models. Therefore, an appropriate numerical model must have discrete representation of these standard output locations to allow direct comparison with measured results.

In light of these considerations, it was concluded that only a full three-dimensional representation of the PCCV could accurately predict the behaviour of the vessel at the low pressure and limit load states. A description of the numerical model employed to study the behaviour of the PCCV is presented in the following sections. The general purpose finite element code ABAQUS (Ref 1) has been employed in this work.

3 FE Models

Five separate FE models have been developed and used to predict the behaviour of the PCCV.

- 3D full global model
- 3D sector model of free field
- 3D extended sector model from buttress to penetration
- local liner plate model
- penetration cover plate model.

The full global model was required to take account of the asymmetry in the structure caused mainly by the penetrations, buttresses and the layout of the vertical tendons. The full model was used to identify the critical areas and the remaining four models to study local details.

4 Description of the Full 3D Finite Element Model

Concrete components of the vessel are simulated with eight-noded solid elements C3D8 and include steel reinforcements. At a minority of locations, due to meshing requirements, six-node linear prism element (C3D6) were used. Six-node prism elements do not support reinforcement capability. Within the cylinder, all the solid elements are fully integrated, while basemat and dome solid elements are reduced integration. Figure 1 shows the full global model which has 140662 elements and 492948 DOFs.

4.1 Cylinder Wall and Dome

The mesh density of the cylinder wall and dome in the circumferential direction was driven by the requirement to model the vertical post-tensioning tendons explicitly. Three elements were employed in the wall-thickness direction of the cylinder and dome. For the fully integrated elements, this gives a total of six integration points through the wall to provide adequate information in areas of high bending. To allow for the explicit representation of each vertical tendon, 184 solid elements were arranged around the circumference of the vessel. The resulting layout consists of a cylinder and dome wall mesh with elements at approximately 2 degrees intervals in the circumferential direction.

The mesh density in the vertical direction was influenced by the specification of the hoop tendons in the concrete elements. The cylinder hoop tendons were arranged at vertical intervals of 112.7 mm. The solid element nodes are meshed vertically to correspond with the spacing of the hoop tendons.

The height of the elements in the lower half of the dome is based on the vertical spacing of the dome hoop tendons. The dome elements are uniformly meshed up to a height of 14690 mm, the location of the uppermost hoop tendon. The meshing of the dome (see Fig 2) in the hoop direction was dictated by the vertical plane of the tendons through the dome. In the dome apex region, a refined solid element mesh allows meshing of the vertical tendon where they intersect at the vessel crown.

The buttresses at the 90° and 270° azimuths are reinforced columns onto which the hoop tendons are anchored. The stiffness of the cylinder and the dome at the 90° and 270° azimuths is enhanced by the restraining effect of the buttresses. The reinforcement scheme of the buttresses comprises vertical, radial U bars and trim rebars. Additional stiffening is provided by the steel plates at the tendon anchorage end-blocks. The buttresses and their reinforcement have been explicitly modelled.

4.2 Basemat

The basemat is a thick concrete reinforced slab supporting the vessel superstructure within which the vertical tendons are anchored. It is heavily reinforced at its top and bottom surfaces. The top surface reinforcement consists of a layer of hoop rebars sandwiched between two grids of radially spanning rebars. The bottom surface is reinforced with a rectangular grid of cross rebars. Additional reinforcement is provided in the vicinity of the tendon anchorage gallery. The flexural reinforcements were defined within each solid element. The basemat shear reinforcements were not modelled. Figure 3 shows a view of the basemat model.

4.3 The Cylinder Wall Penetrations

The cylinder wall penetrations and their immediate vicinity have been explicitly modelled. Structural features within the penetration area that are represented explicitly in the model are the enhanced reinforcement stiffening, thickened wall section (airlock and equipment hatch penetrations), steel plates lining the penetration cavity, the penetrations cover plates, the vertical and hoop tendons, internal vessel liner and the liner anchorage. The finite element meshes of the airlock, equipment hatch, main steam and feed water penetrations are shown in Fig 4, 5 and 6.

4.4 The Post-Tensioning Tendons

The post-tensioning tendons have been modelled using two different approaches. The vertical tendons were modelled explicitly using the two-node, linear truss element T3D2. For each tendon, nodes have been generated coincident to the solid element concrete nodes along the tendon path. Typically, in the non-penetrated areas a vertical tendon consists of up to 220 elements, depending on its location within the vessel. Each vertical tendon node lying within the cylinder of the vessel is constrained in the horizontal degrees of freedom (i.e., the X and Z directions) to the coincident concrete nodes. The vertical degree of freedom of tendon nodes within the cylinder were left unconstrained, allowing relative sliding of the tendons and concrete in the vertical direction. Within the cylinder friction at the concrete/tendon interface is assumed to be negligible and has not been modelled. However, within the dome, the curved trajectory of the tendon causes appreciable friction at the concrete tendon interface, resulting in a non-uniform variation of load in the tendon. Although interface behaviour has not been explicitly modelled, the non-uniform distribution of load in the vertical tendons over the dome is allowed for by constraining all coincident tendon and concrete nodal degrees of freedom. The vertical tendon mesh is shown in Fig 7.

The hoop tendons are modelled as single rebars embedded within concrete elements (Ref 1). The concrete elements were defined such that an element edge lies along the path of the hoop tendon as this facilitated the placement of the hoop tendons within the elements. Each hoop tendon starts at one face of the buttress, completes a 360 degree loop round the vessel and is anchored at the opposite face on the same buttress. Alternative tendons are anchored at opposite buttresses. Interface behaviour between the concrete and the tendon has not been modelled.

4.5 Internal Liner and Liner Anchorage

The internal vessel steel liner has been modelled using the reduced integration membrane element M3D4R. The thicker insert plates surrounding the main steam and feed water penetrations are simulated with the shell element S4R. The liner elements are meshed around nodes defined independently but coincident with adjacent concrete nodes. The internal liner

mesh is shown in Fig 8. The mesh of the plate lining the EH penetration cavity is presented in Fig 9. The lining at the other penetrations used similar model.

The liner-to-concrete anchorage was modelled by connecting the liner node to the corresponding coincident concrete node with three linear spring elements at each node, representing the radial, hoop and axial anchorage plate stiffness. Given that the pitch of the horizontal and vertical liner anchorage plates is not uniform, no attempt was made to simulate the anchorage plates at their exact locations. The spring stiffness are derived from test results for the pull-out of anchorage plates in tensile and shear modes, Ref 3.

4.6 Concrete Reinforcements

The grid of reinforcing bars in the vessel have been represented as rebar (Ref 1) smeared within the parent solid elements. The orientation, cross-sectional area, spacing and material properties are taken from the construction drawings.

The duct-supporting steel frame construction is modelled as single rebars within the parent solid elements.

4.7 Derivation of Post-Tensioning Tendon Loads

The vertical and hoop tendons are tensioned to the desired tensile load using hydraulic jacks and are anchored at the tendon gallery and the buttresses. Neither the sequence of tensioning nor the tensioning process is being represented in the numerical model. The model represents the scenario immediately following the transfer of the tensioning load from the jacks onto the tendon, with the tendon load being reacted at the anchorage.

Due to frictional forces mobilised between the tendons and ducts during tendon tensioning, the load distribution within a tendon is non-uniform. For each tendon, the maximum load occurs at the anchored ends. The post-tensioning stress along the tendon length varies according to the exponential law.

$$P_1 = P_0 e^{(\alpha L - 0.001L)}$$

1

Where P_0 = stress at the tensioning end
 α = Change of angle from tensioning end
 P_1 = stress at α from tensioning end
 L = length of tendon.

P_0 was taken as the tendon load at transfer which the designers has specified as 350 kN and 471 kN for the hoop and vertical tendons respectively. For each tendon element, the average value of the change of angle from the anchor was computed from the element nodal co-ordinates and the post-tensioning stress evaluated using equation 1.

The stresses were then applied to the tendon elements as an initial condition using the option *INITIAL CONDITION. Reduction of the tendon load due to anchorage relaxation has not been taken into account.

4.8 Soil Foundation

The basemat is constructed on a 150 mm thick un-reinforced slab which itself is supported on an engineered sand and gravel subgrade. The soil stiffness was characterised as exhibiting a settlement less than 25 mm due to a bearing pressure of 35 Ton/m².

The soil was represented using the grounded spring element SPRING1. Each node on the bottom surface of the basemat was supported on a spring element. The spring stiffness was computed based on the influence area of each spring node.

4.9 Boundary Conditions

The global model is supported in the vertical direction by grounded springs. The vessel was constrained to eliminate rigid body translations and rotations at four nodal positions on the top surface of the basemat in the horizontal degrees of freedom.

4.10 Material Properties

Material data for the liner, steel reinforcing bars, tendons and concrete has been derived from material tests. The true elastic-plastic stress/strain curve for the liner, reinforcements and tendons was specified in the finite element model.

Concrete has been modelled using a combination of linear elastic and non-linear smeared cracking material models. The linear concrete elastic model cannot account for the degradation of material due to cracking and crushing. However, the non-linear smeared cracking model in ABAQUS (Ref 1) is capable of simulating cracking by using a damaged elasticity approach. This smeared cracking model requires careful calibration specific to the concrete used in construction. Further, ill-conditioning may arise due to the development of locally confined cracking.

In view of these considerations, the smeared cracking model has been employed only in regions of the vessel where the development of cracks is expected to appreciably effect the global response of the vessel. Thus, the non-linear smeared cracking concrete model was

specified for the cylinder elements while the linear elastic model was specified for the dome and basemat elements.

Concrete creep and shrinkage was not considered in the finite element analysis as it was thought that their effect on the overall behaviour of the vessel would be negligible.

The material constants used in the analysis are presented in Table 1.

5 Analysis

The vessel is to undergo a series of pressure tests at low pressure defined as follows.

- (i) Instrumentation functionality test, IFT, (0.039 MPa).
- (ii) Structural integrity test, SIT, (0.439 MPa).
- (iii) Integrity leak rate test, ILRT, (0.351 MPa).
- (iv) Design pressure test, DPT, (0.390 MPa).

The low pressure test will be followed by a limit state test in which the vessel will be pressurised until failure. The analysis steps are as follows:

- Gravity
- Gravity + prestress
- Gravity + prestress + pressurisation.

The actual test includes the effect of gravity but the instrumentation will record only the effect of prestress and pressurisation. Therefore, for the pressure history data, the stresses due to gravity alone have been subtracted from the results from the third step.

5.1 Analysis of Full 3D Global Model

5.1.1 Gravity + Prestress

An initial load step in which the vessel is brought into static equilibrium with the initial post-tensioning tendon loads and the vessel self-weight was established. The weight of the embedded steel reinforcements and hoop tendons has not been included as part of the total vessel weight. The load step establishes static equilibrium of the vessel for the initial vessel loads.

Figure 10 shows the deformed shape of the vessel dome and cylinder for the self-weight and post-tensioning load step. The deformed shape plots indicate that the vessel is deforming inward due to the effect of the hoop tensioning stress.

The deformed shape plot of a slice of cylinder around the penetrations level is shown Fig 11. This clearly shows that the response of the vessel is non-symmetric, with the buttress providing radial restraint to the cylinder wall. The restraining effect of the buttress is reinforced with the absence of the anchorage concentrated loads, a consequence of modelling the hoop tendons as embedded rebars.

Increased vessel displacements are observed local to the airlock and equipment hatch penetration region. The equipment hatch penetration is observed to deform radially inward rather more than any other region of the vessel, even though this region is stiffer than the rest of the cylinder wall. Further, a change in the curvature of the wall surface is also observed. This phenomenon is the result of the concentration of the hoop tendons in the region above and below the penetration. The tendons create high components of forces acting radially inwards on the vessel. This region is analogous to a pressurised plate with a hole. The immediate vicinity of the penetration deforms more, causing the change in curvature. The cylinder wall on either side of the penetration block is observed to undergo significant bending deformation. This phenomenon is not observed at the main steam/feed water penetration region because the hoop tendon paths are less concentrated and the penetrations are much smaller.

An average settlement of the vessel of 4.8 mm was observed. The vertical downward deformation of the apex of the dome relative to the settlement of the vessel was computed as 4.0 mm.

Figure 12 shows the variation of hoop tendon load with tendon length around the vessel. This indicates that at the end of the self weight and post-tensioning load step, the variation of hoop tendon load around the vessel is reasonably consistent with the distribution of load given by equation 1.

5.1.2 Analysis of Internal Pressurisation

A uniform pressure was applied to the faces of the concrete elements that comprise the internal surface of the vessel. Because the liner is more coarsely meshed than the concrete enclosure the internal pressure has been applied to the concrete surface rather than the liner surface. Consequently, the liner is loaded by the deformation of the concrete enclosure to which it has been tied using spring elements. The internal pressure was also applied to the penetrations cover plates. The analysis was restarted from the end of the selfweight and post-tensioning load step.

The analysis progressed up to an internal pressure of 0.60 MPa whereupon numerical problems were encountered due to cracking of the concrete. Cracking was confined mainly to the entire column of elements at the cylinder/butresses junction. The number of cracked elements was such that the solution becomes singular due to loss of stiffness in these elements. The analysis was terminated at a pressure of 0.60 MPa, a load 54% higher than the design pressure, 0.39 MPa.

Deformed shape of the cylinder is shown in Fig 13. It is evident that the enhanced stiffening of the cylinder wall in the penetration regions and buttresses caused differential radial deformation of the vessel, with the less reinforced free-field areas deforming more than the heavily reinforced areas. This phenomenon is more pronounced at the equipment hatch area.

Examination of the deformed shape plot around the buttresses revealed that they provided significant restraint against the outward radial expansion of the cylinder wall. The cylinder wall on both sides of the buttress column was observed to deform more than the buttress area. This created a change in the direction of curvature of the internal surface of the cylinder at the buttressed region.

The hoop tendon anchorage is set at an inclination of 13.6° from the circumferential tendon trajectory. For a load at transfer of 350 kN, each hoop tendon exerts a horizontal shear force of 165 kN at the buttress, in the direction radially inward to the vessel. Thus, the meridional section at the buttress junction is subject to concentrated shear forces from the tendon anchorage. The combination of shear load and bending at the buttress region may explain the early prediction of cracking in the buttress region.

There is high stress concentration in the liner at the region between the airlock penetration and the buttress at azimuth 90° . The high strain gradient at this region is also seen at the output location 44. This results from the local bending of the wall around the buttress.

5.2 Analysis Using 3D Sector Models

Due to the numerical problems with the non-linear smeared cracking models for pressures exceeding 0.60 MPa, two sector models of the vessel were used to assist in gaining an insight into the vessel behaviour at higher pressures. The following sections described the 3D sector models of the PCCV.

5.2.1 3D Sector Model of Free Field

A 3D model of a sector of the vessel was extracted from the global model in the vicinity of azimuth 135° , the free-field area. This is a 10° sector model consisting of five solid concrete elements and one membrane liner element in the hoop direction. The model includes six vertical tendons modelled using truss elements. Hoop tendons are modelled as embedded steel

reinforcements. The cylinder vertical tendons are as defined for the global model. However, within the dome they run radially towards the apex of the dome. The vertical tendon constraints, initial tendon loads, liner anchorage and soil springs are as defined for the global model. Constraints were applied at the sector edges in the circumferential degrees of freedom. The finite element mesh for the sector model is depicted in Fig 14.

The analysis comprises two load steps; an initial load step for static equilibrium of the vessel under the post-tensioning loads and self-weight, and then an internal pressurisation load step.

This model was first analysed using the concrete material model in ABAQUS. Due to convergence problems after onset of cracking, the model was re-analysed using reduced modulus technique in which Young's Modulus was varied with pressure in accordance with the relationship shown in Fig 15.

5.2.2 Extended Sector Model

This model is similar to the smaller free field sector model but it covers the sector from azimuth 62° (centre line of Air lock) to 90° (centre line of buttress). The 3D global model analysis indicated that this region experiences high strain gradients. The model was analysed to upto 1.0 MPa using the reduced modulus approach described in section 5.2.1. The model is depicted in Fig 14.

6 Pressure Histories

Variation in the physical quantities measured at all the 55 standard output has been obtained in form of pressure histories obtained from the full 3D global model. Since the global model was analysed to only 0.60 MPa, the pressure histories were extended by using the results from the two sector models.

Location 1 pressure history shows the vertical displacement of a point on the top surface of the basemat. This indicates a linear response with a maximum displacement of the order of 1.5 mm for an internal pressure of 0.60 MPa.

Location 2 to 15 are displacement predictions taken from the inside surface of the liner at various locations within the vessel. These plots indicate a linear deformation response consistent with a state of internal pressurisation of the vessel.

The rebar strain predictions at output locations 16 to 33 indicate that at the end of the post-tensioning, the rebars are subject to compressive strains. The strains in the inner meridional rebars at the cylinder/basemat junction becoming less negative while the outer rebar strains become more compressive with internal pressurisation.

All but one of the strain predictions indicate linear behaviour up to 0.60 MPa. However, the curve for location 32 shows that non-linear behaviour initiates at about 0.57 MPa. This is for a mid-height hoop rebar around the buttress at azimuth 90°. The high strain gradients observed after 0.58 MPa suggests that this region is a potential zone for initiation of structural failure.

The liner strains predictions are given in the curves for locations 34 to 47. At the start of internal pressurisation the liner is in a state of compressive stress due to the effects of post-tensioning. With internal pressurisation, a linear strain response up to a pressure of about 0.60 MPa is observed for all but one of the output locations. Non-linear behaviour initiates at about 0.57 MPa at location 44, the azimuth 90° buttress area.

The tendon output predictions are presented in histories of location 48 to 55. A linear tendon response is observed for locations 48, 49, 51 and 52 at location 53 a non-linear variation of tendon strain is observed at pressures less than the design pressure. At higher pressures there is reduced rates of increase in the tendon strain. This is thought to be caused by the modelling of the hoop tendons as embedded rebars. This output location is for a hoop tendon position at azimuth 0°. The cylinder wall at azimuth 0° and a height of 4.57 m is a zone of local bending caused by the interaction of the equipment hatch and airlock penetrations. With the tendon modelled as an embedded rebar, it attracts some bending deformation since there is no allowance for hoop slippage.

7 Failure Analysis

A number of structural failure mechanisms are possible for the vessel. These are extensive cracking/crushing of the containment concrete, yielding of steel reinforcing bars, yielding of tendons, loss of liner anchorage due to cracked concrete, rupture of steel liner and loss of tendon anchorage at buttresses due to damaged concrete.

It is envisaged that cracking of concrete is the first stage of failure. Progressive damage to the integrity of the concrete would inhibit its ability to sustain load. Thus, the proportion of load previously carried by the concrete is redistributed to the other structural components. The transference of load to the other structural components is likely to lead to the onset of other failure modes.

Within the finite element model, the propensity for failure can be assessed by examining the stress/strain output for each component. The global model gives an insight into vulnerable areas of the vessel. However, the model has limited capacity for simulating the interaction of the failure modes following the onset of cracking. For the liner and tendon anchorage failure modes, only qualitative judgements on their occurrence can be made from an examination of the state stress in the neighbouring concrete.

The following failure modes have been investigated:

- Liner tear
- Rebar rupture
- Tendon rupture
- Buckling of cover plates.

7.1 PCCV Failure Criterion

The limit load is determined by the inability of the vessel to retain pressure and this is dependent on the integrity of the steel liner. Consequently, the failure criterion of the vessel is defined as the breach of the pressure boundary (i.e. liner).

The liner has the lowest ductility at a welded joint where an average rupture strain of 19% is was observed in the tests, Ref 3. The numerical and test data is subject to a number of uncertainties which have not been fully quantified. These are variabilities in material test data, eccentricities at liner plate joints and numerical modelling uncertainties plus triaxiality factor. Given these uncertainties it was decided to reduce the liner rupture strain by factor of 2 to a notional value of 11%.

From an assessment of construction features of the liner, a number of sites were identified as potential locations for liner rupture. Welded joints at geometric discontinuities were identified as particularly vulnerable areas. These include the liner joints at basemat/cylinder junction, the dome/cylinder junction, liner around wall penetrations and welded joints between the thick insert plate and thin liner plate in the main steam/feed water penetration region.

Examination of the results from the 3D global model analysis did not indicate that the basemat/cylinder and dome/cylinder junctions were subject to high strain gradients as was originally thought. The liner plate around the airlock and equipment hatch penetration openings were subject to high strain gradients. Further the global model analysis results indicate that the liner plate region between the airlock penetration and the buttress at the 90° azimuth was a region of high strain concentration.

7.2 Prediction of Failure Using Local Models

7.2.1 2D Liner Plate Model

The intensification of strain at the thick insert plate/liner junction was studied with a 2D plate model. A section of the internal lining around the main steam penetration was developed using the shell element S4R. The vertical liner anchorage spacing in this region is 150 mm.

The liner anchorages are modelled as springs set at 150 mm spacing in the hoop direction. The extent of plate modelled is adequate to ensure the junction is not influenced by boundary conditions. The curvature of the liner plate has been ignored. The finite element mesh is shown in Fig 16.

An equivalent plastic strain contour plot depicted in Fig 16 shows the extent of strain concentration at the liner thick/thin junction. A 3% strain in the free field can cause up to 11% strain at the thick/thin junction.

It has been assumed that straining of the liner leading to strain intensification is predominantly in the uni-axial direction. Straining of the liner plate model was caused by applying a displacement between the section of plate enclosing the thick plate and the section simulating the thin plate. The differential displacements were applied at the spring nodes in the direction corresponding to the vessel hoop direction.

Successive differential displacements were applied until a value was found giving the predicted rupture strain of 11% at the plate junction. This state of strain at the junction was associated with a differential displacement of 5.1 mm at the anchorage on either side of the junction.

Considering the internal radius of the vessel of 5375 mm, a uniform hoop expansion of 5.1 mm is consistent with a uniform radial expansion of 182 mm of the cylinder at the mid-height region. Given the enhancement of wall stiffness by the buttresses and the local heavily reinforced penetration regions, the cylinder is unlikely to deform uniformly. However, no account has been made of the non-uniform deformation behaviour of the cylinder on the computation of liner rupture strain.

7.2.2 3D PCCV Sector Model

The numerical difficulties arising from concrete cracking precluded the analysis of the global and the 3D sector models beyond internal pressures of 0.60 MPa and 1.02 MPa respectively.

Due to the difficulties experienced with the concrete cracking material model an alternative approach of modelling the degradation of concrete was considered. This consisted of modelling the concrete as a linear elastic material, with the elastic modulus varying as a function of the applied load. The elastic modulus, E , of concrete is held constant until a pressure of 0.7 MPa, at which point substantial cracking would have occurred. Beyond 0.7 MPa, the elastic modulus is reduced linearly to one-tenth of its undamaged value at a pressure of 1.5 MPa. Beyond 1.5 MPa it is further degraded linearly to a thousandth at a pressure of 2.5 MPa as shown in Fig 15.

This analysis is useful in providing insights into the mechanism of load re-distribution from the concrete to the other structural components as the concrete modulus is reduced at high

pressures. The assertion is made here that at high pressures the response of the vessel is entirely dictated by the behaviour of the reinforcements and tendons. The concrete serves as a soft matrix into which the reinforcement and tendons are embedded. The trend of the loading of the rebars, tendons and liner with softening of the concrete is indicated in the pressure history curves for locations 16 to 21, 36, 38, 39, 40, 51 and 54. Rupture of the rebars and/or tendons leading to catastrophic failure of the PCCV is not likely to occur before the liner rupture.

It is evident that for the 'softened' concrete, there is rapid increase in the straining of the other structural components. At about mid-height a radial displacement of 182 mm at a pressure of 1.98 MPa was obtained. The strain field in the liner at this region was of the order of 3%. Assuming uniform radial deformation around the vessel circumference, a strain of 3% in the free-field area is magnified at the junction of the thick/thin insert plate to a strain of about 11%. Thus at an internal pressure of 1.98 MPa the liner is deemed to have ruptured at the welded junction of the thick insert plate and thin liner, leading to de-pressurisation of the vessel.

7.2.3 Buckling of Penetration Cover Plates

Critical buckling modes of the cover plates of the air lock and equipment hatch penetrations were obtained using detailed shell element models. A typical mode is shown in Fig 9. It was found that the cover plates had adequate buckling strength with the critical buckling pressure exceeding 10 MPa which is far in excess of the design pressure.

8 Confidence Level

Attempt has been made to model the as-built condition of the PCCV. However, there are a large number of uncertainties which cannot be accounted for in a single deterministic analysis. Since the failure or the limit load of the PCCV is most likely going to be dictated by a rupture in the liner, the strength of the lines at the welded joints becomes an important issue. Two main variables have been considered in predicting the 90% confidence level: modelling uncertainty measured as actual strength/predicted strength of welded panels and variability in lines rupture strain. Modelling uncertainty was assumed to have log normal distribution with mean of 1.22 and standard deviation of 0.122. The variability in the liner rupture strain was assumed to follow normal distribution with mean of 11% and standard deviation of 0.79%. The combined effect gave the 90% confidence interval (mean \pm 1.28 standard deviation) of 2.16 MPa to 1.78 MPa.

9 Summary of Main Results

A summary of the main results drawn from the 3D global and sector models are presented.

- (i) Extensive concrete crack was first observed at a pressure of 0.57 MPa at the cylinder/buttress junction.

- (ii) Inner meridional rebars at cylinder/basemat junction yields at a pressure of 1.7 MPa.
- (iii) First yield of vertical tendon occurs at a pressure of 2 MPa.
- (iv) Cylinder hoop tendon reaches 1% strain at about 1.6 MPa.
- (v) Cylinder hoop tendon reaches 2% strain at about 1.75 MPa.
- (vi) Cylinder hoop tendon reaches 3% strain at about 1.95 MPa.
- (vii) Minimum pressure reachable with 90% confidence is 1.78 MPa.
- (viii) Maximum pressure not exceedable with 90% confidence is 2.16 MPa.

The limit load of the PCCV model is dictated by rupture of the liner at the welded joints following extensive cracking of the concrete at the buttress/cylinder wall joint.

10 References

Ref	Title
1	ABAQUS 5.8-1 Standard Users' Manual. Hibbitt, Karlsson & Sorensen, Inc 1998
2	Sandia National Laboratory PCCV Design Package, Material Properties Report.

11 List of Tables and Figures

Table	Title
1	Material data used in FE analysis

Fig	Title
1	Finite element representation of the PCCV
2	Detail view of the PCCV dome model
3	The PCCV basemat model
4	Detailed view of equipment hatch penetration model
5	Detailed view of the airlock penetration model and liner anchorage

Fig	Title
6	Detailed view of the main steam and feedwater penetrations model
7	PCCV vertical tendons model
8	Internal vessel liner, with details around the equipment hatch and airlock penetrations and the basement in view
9	Equipment hatch penetration lining and cover plate with critical buckling mode prediction
10	Deformed shape of cylinder and dome after post-tensioning
11	Plan section through cylinder after post-tensioning
12	Variation of hoop tendon load around vessel after transfer
13	Deformed shape of cylinder due to internal pressure
14	3D sector models of free field area and buttress/airlock area
15	Reduced modulus due to concrete cracking
16	Model of liner at junction of thin/thick plate

Table 1 – Material data used in FE analysis

Soil spring properties

Description of soil region	Spring stiffness (N/mm)
Densely defined region of mesh at centre of basemat	110
Region of basemat mesh corresponding with cylinder meshing	250
Coarser general region of basemat mesh	2270

Spring stiffness derived from soil stiffness of 0.014 MPa/mm

Anchorage properties

Description of spring	Stiffness (N/mm)
Liner tensile pull-out stiffness	3680000
Liner shear stiffness	1820000
Penetration lining anchor spring	581000

Concrete properties

Description	
Elastic modulus	27950 N/mm ²
Poisson's ratio	0.18
Compressive strength	88 N/mm ² (*)
Tensile strength	4 N/mm ²
Density	2.21 x 10 ⁻⁹ tonnes/mm ³

Note: The compressive strength was increased by a factor of two to avoid convergence problem with the smeared cracking model.

Table 1 (cont'd)**Reinforcing rebar properties**

Type	Elastic modulus (N/mm ²)	Poisson's ratio	Yield stress (N/mm ²)	Rupture strain (%)
Pre-stressing Tendon	224230	0.30	1740	3.83
Rebar SD345-D6	169000	0.30	370	30.4
Rebar SD345-D10	182000	0.30	370	23.8
Rebar SD390-D10	183000	0.30	477	20.5
Rebar SD390-D13	183000	0.30	440	24.2
Rebar SD390-D16	183000	0.30	450	22.1
Rebar SD390-D19	184000	0.30	470	22.1
Rebar SD390-D22	191000	0.30	465	25.9
Rebar SD490-D10	187000	0.30	500	21.4
Rebar SD490-D13	184000	0.30	548	16.4
Rebar SD490-D16	185000	0.30	490	17.1
Rebar SD490-D19	186000	0.30	514	17.8
Tendon sheath frame	205000	0.30		-

Internal steel liner properties

Description	
Elastic modulus	219650 N/mm ²
Poisson's ratio	0.30
Yield strength	382 N/mm ²
Rupture strain	11%
Density	7.85 x 10 ⁻⁹ tonnes/mm ³

Size
140662 elements
206896 nodes
492948 DOFs

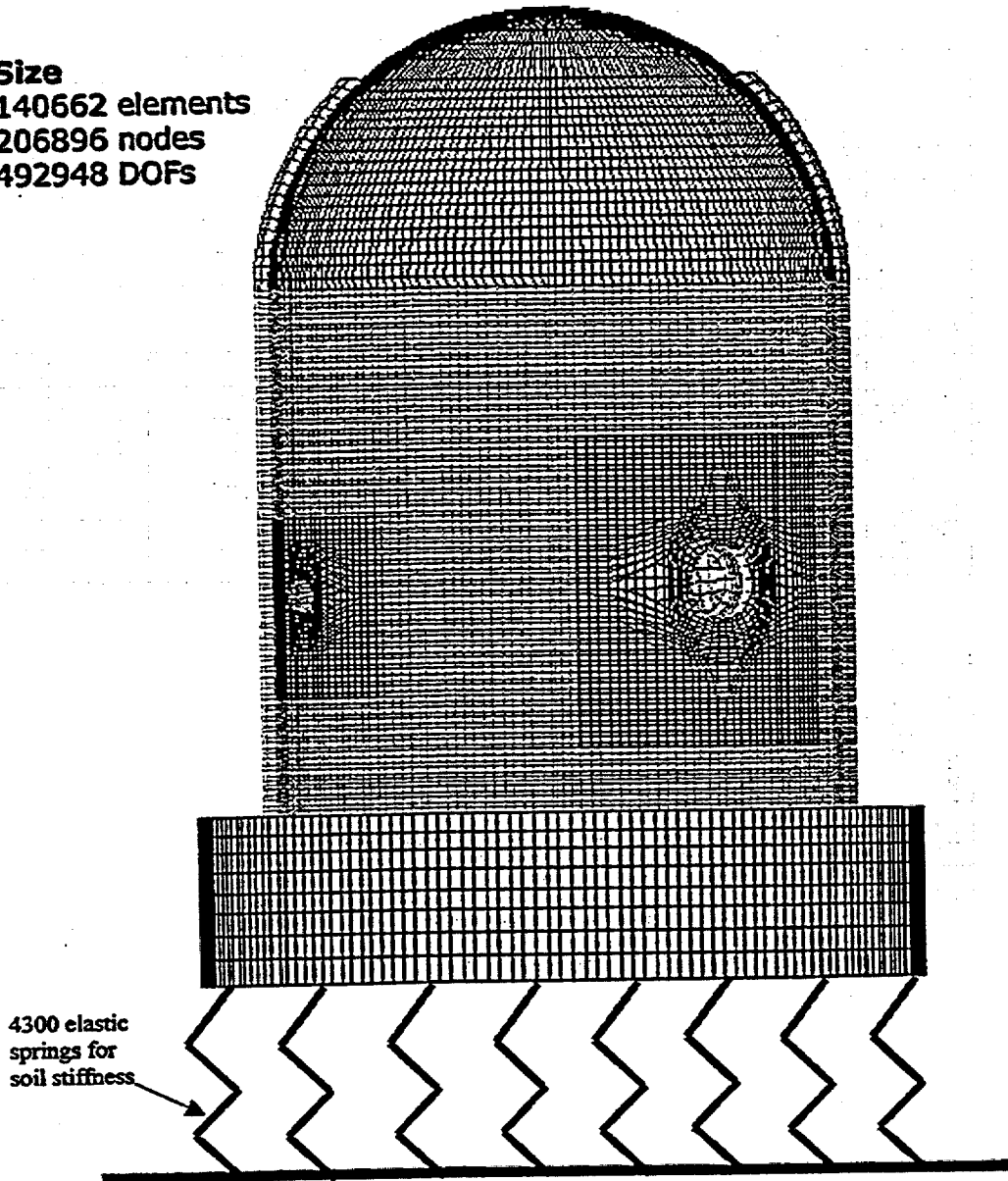


Figure 1 – Finite element representation of the PCCV

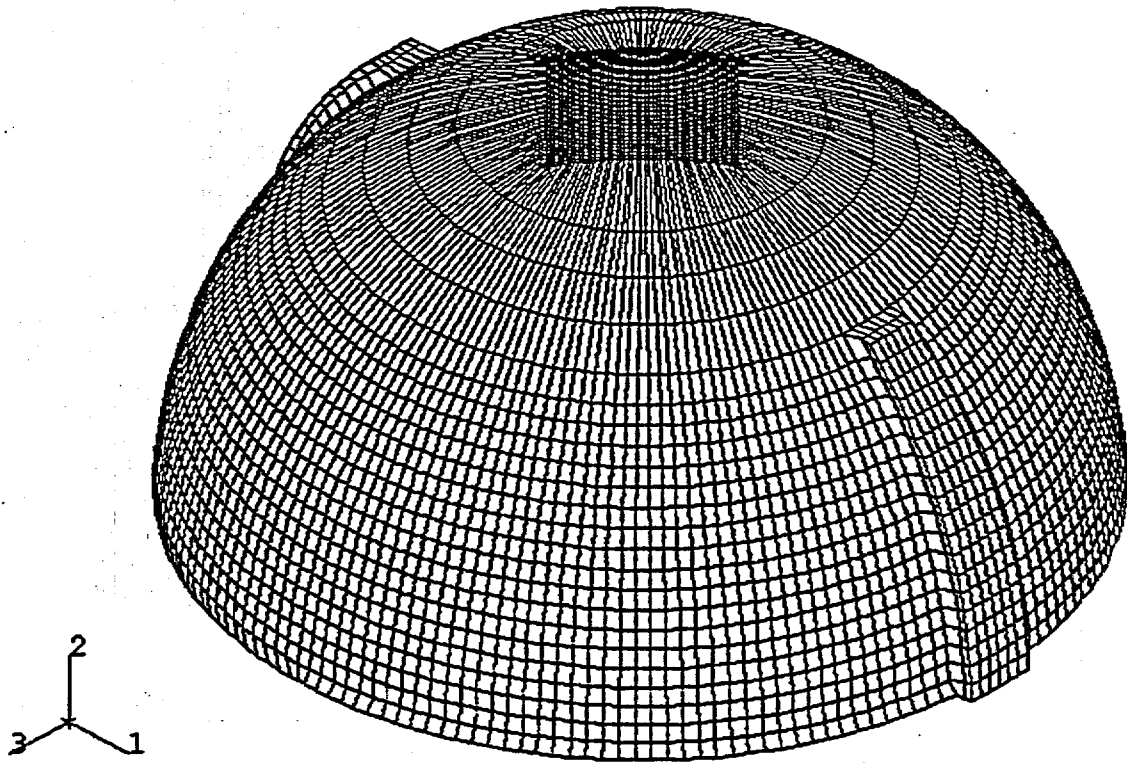
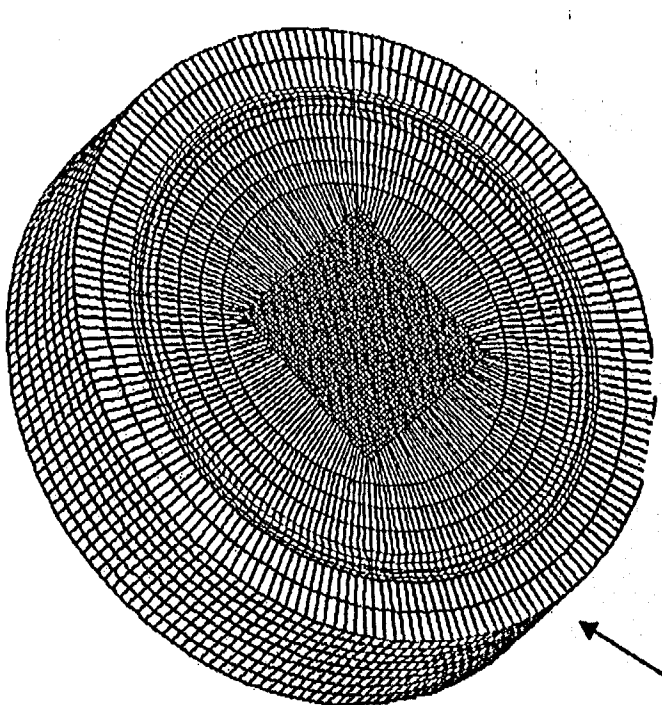
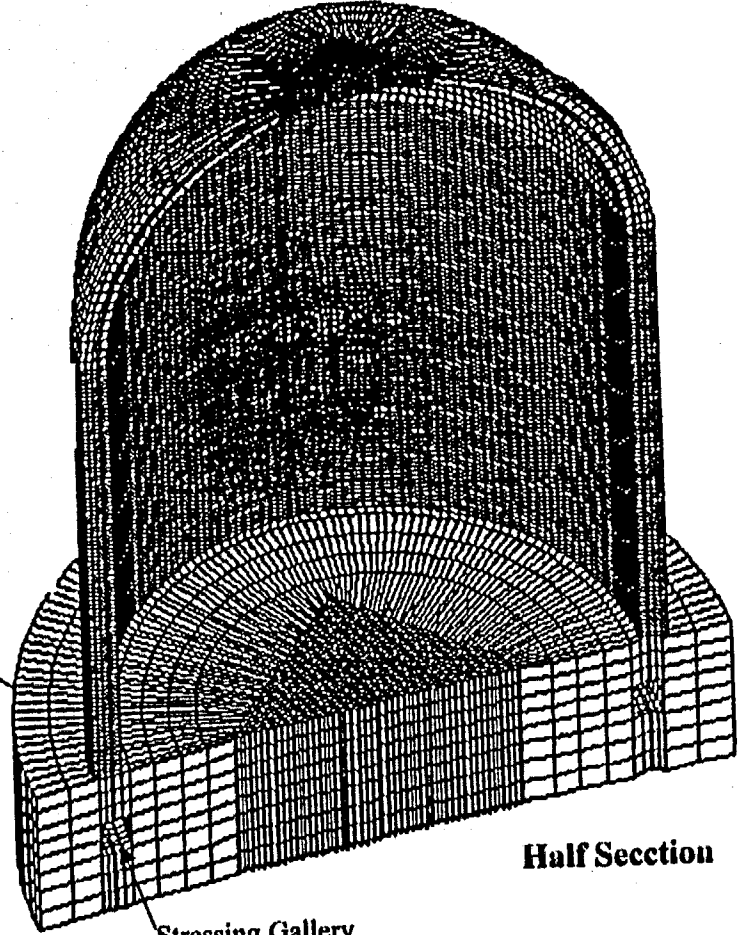


Figure 2 - Detail view of the PCCV dome model



Base slab



Half Section

Stressing Gallery

Figure 3 – The PCCV basemat model

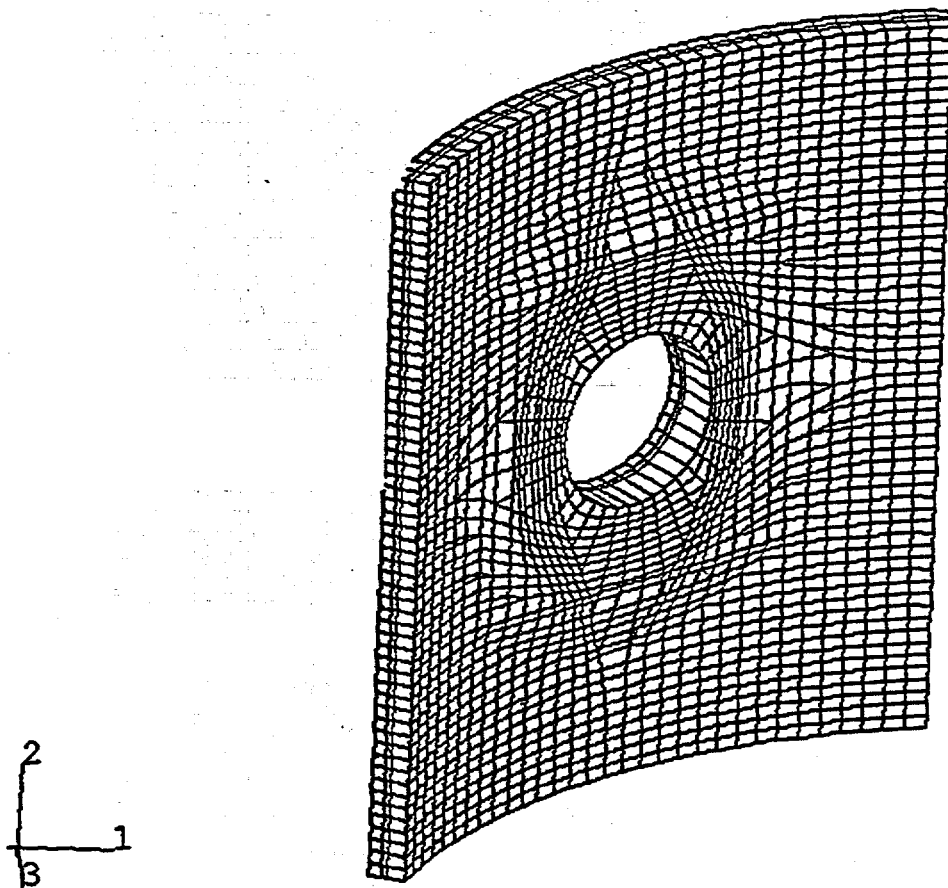
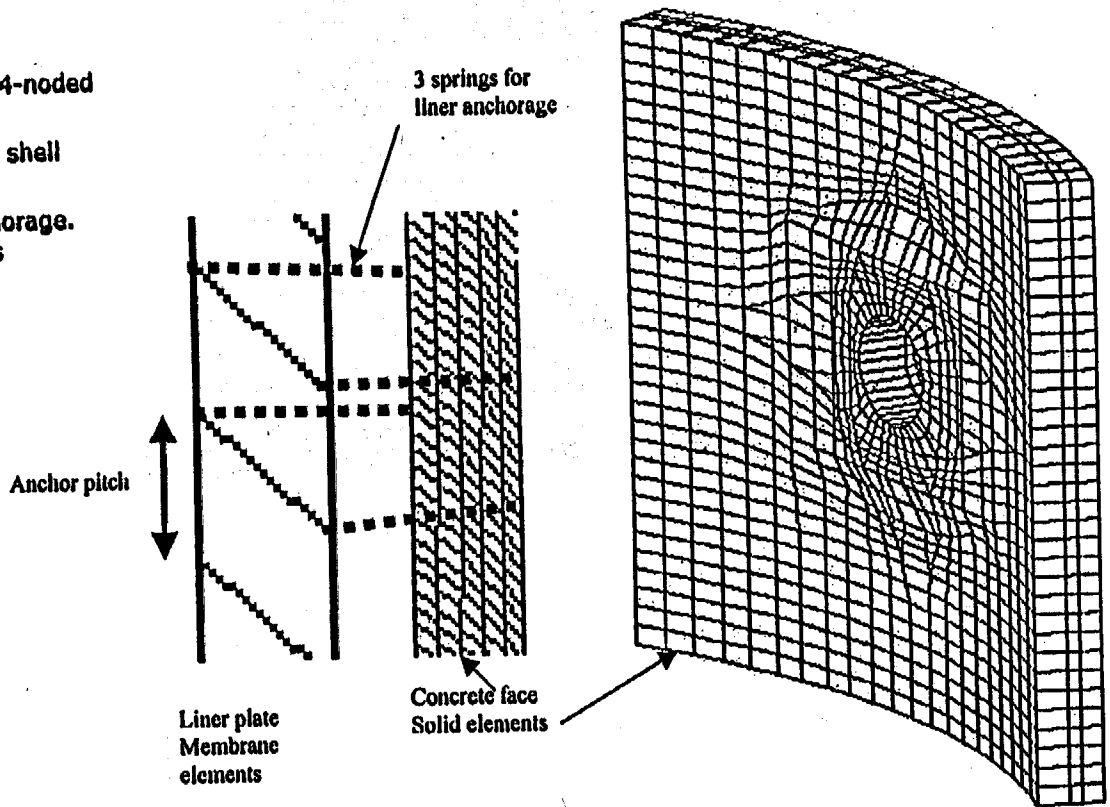


Figure 4 – Detailed view of equipment hatch penetration model

Figure 5 – Detailed view of the airlock penetration model and liner anchorage

- Liner as reduced integration 4-noded membrane element
- Insert plates as 4-noded shell elements
- Three linear springs for anchorage. Stiffness obtained from tests
 - Pull out 3.68 MN/mm
 - Shear 1.82 MN/mm



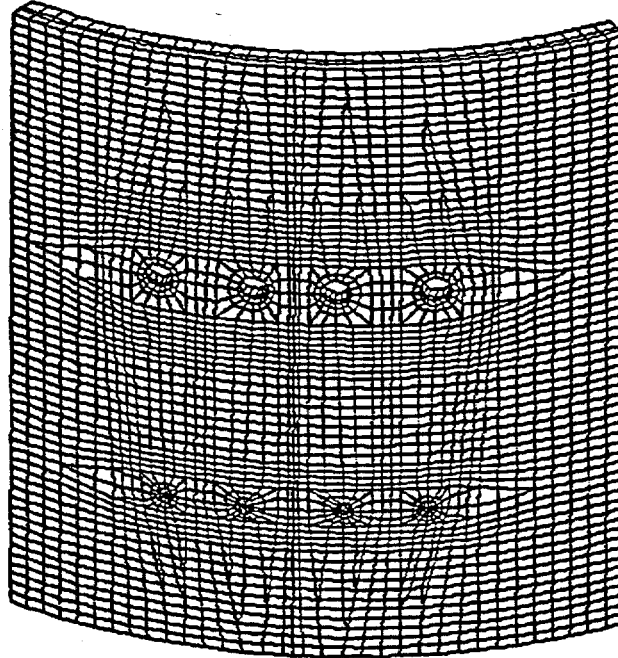
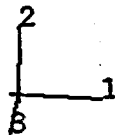


Figure 6 – Detailed view of the main steam and feedwater penetrations model

3
2
1

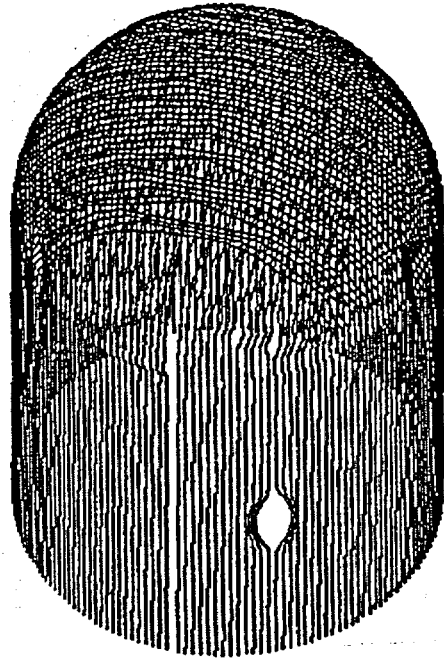


Figure 7 – PCCV vertical tendons model

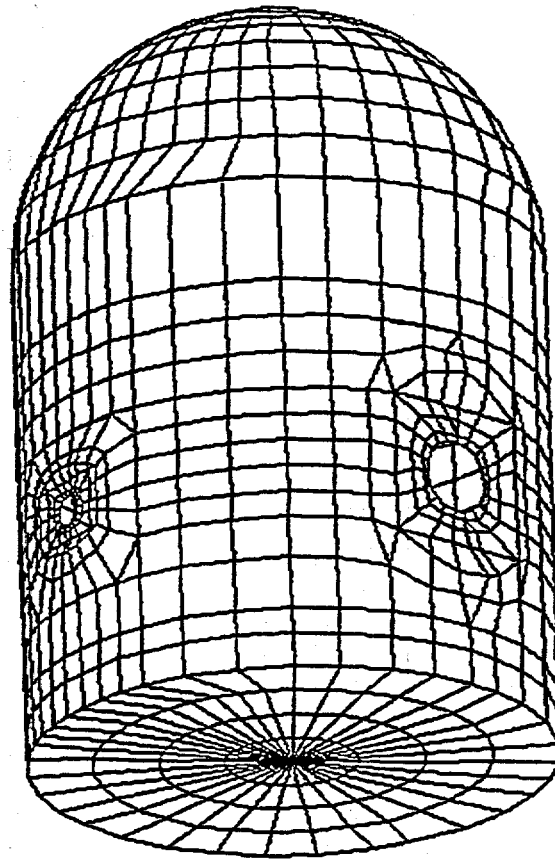
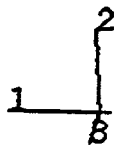
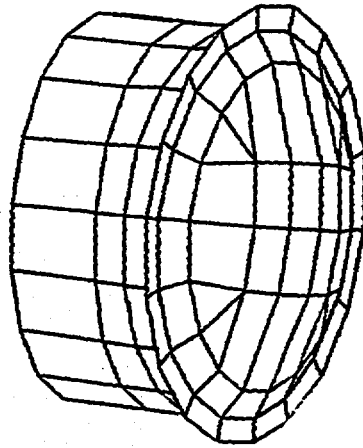
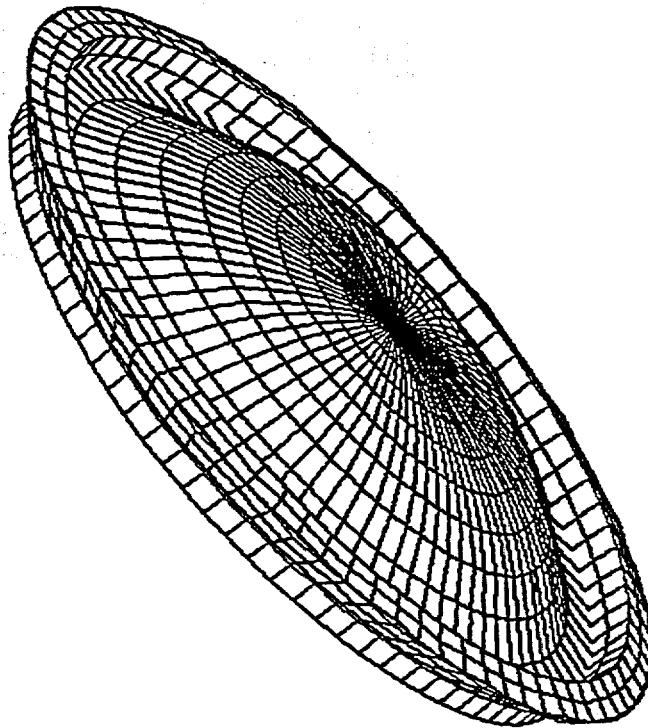


Figure 8 – Internal vessel liner, with details around the equipment hatch and airlock penetrations and the basement in view



(a) FE mesh of cover plate and penetration lining



(b) Deformed shape of cover plate

Figure 9 - Equipment hatch penetration lining and cover plate with critical buckling mode prediction

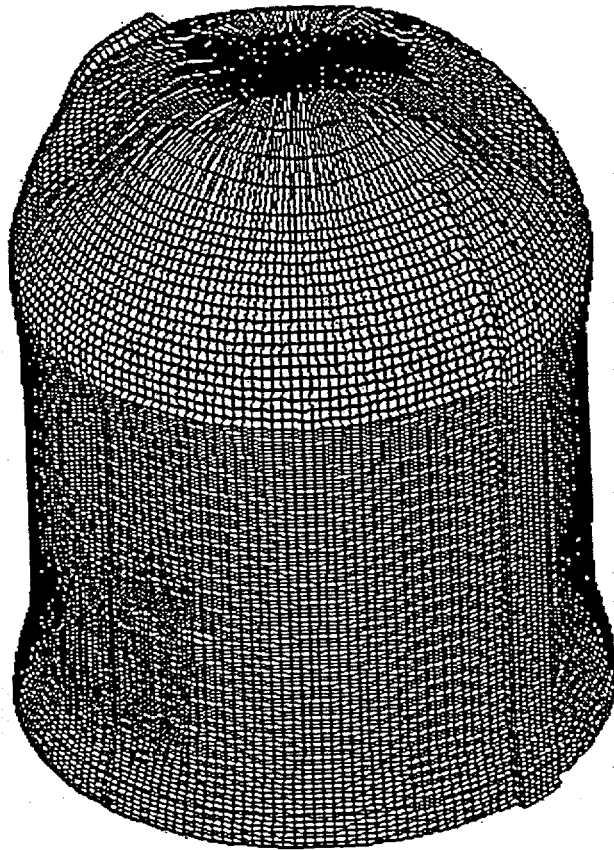


Figure 10 – Deformed shape of cylinder and dome after post-tensioning

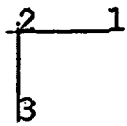
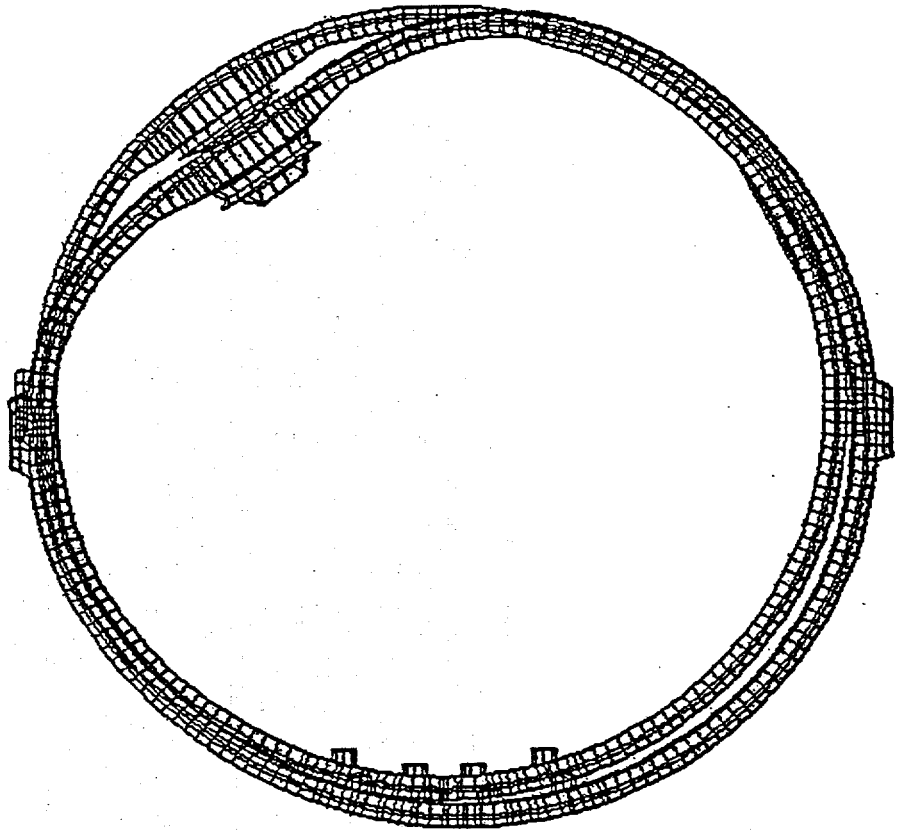
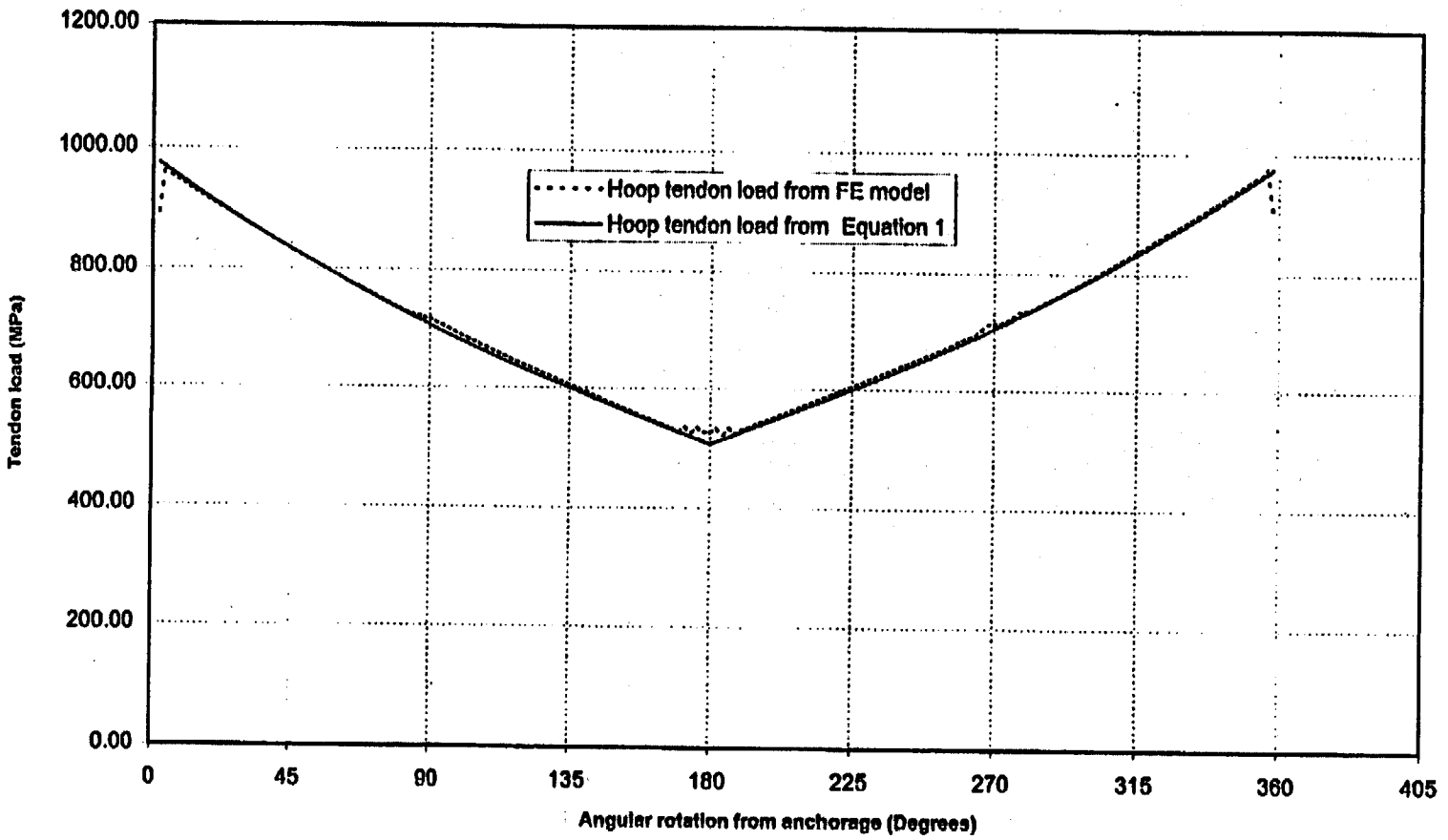


Figure 11 – Plan section through cylinder after post-tensioning

Figure 12 – Variation of hoop tendon load around vessel after transfer



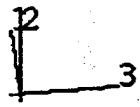
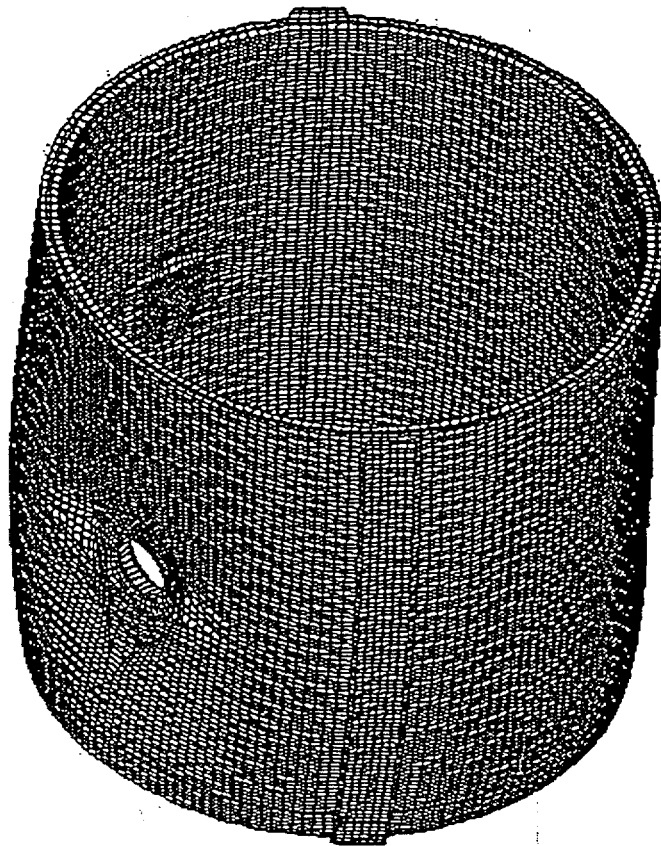


Figure 13 – Deformed shape of cylinder due to internal pressure

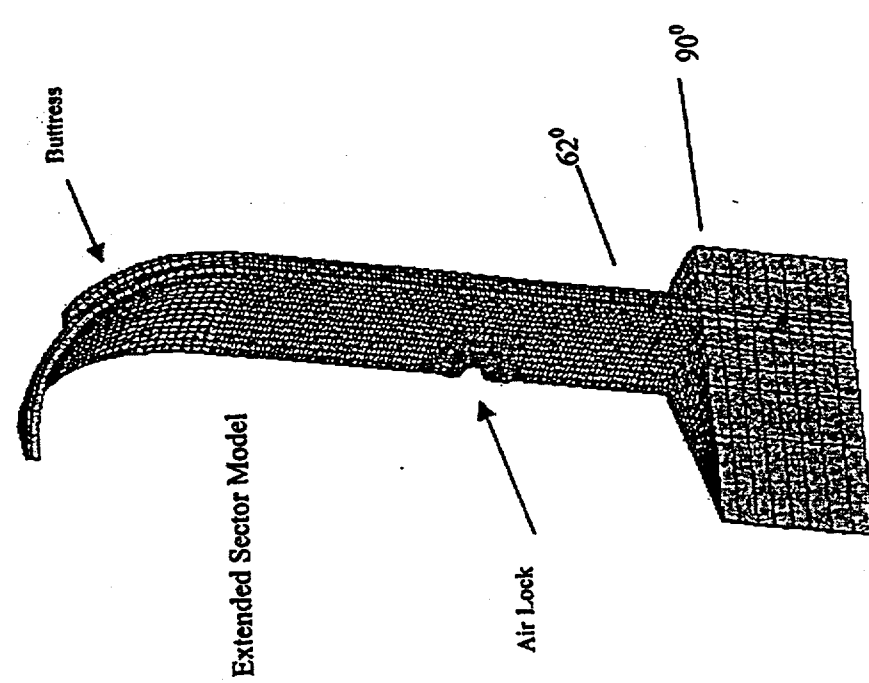
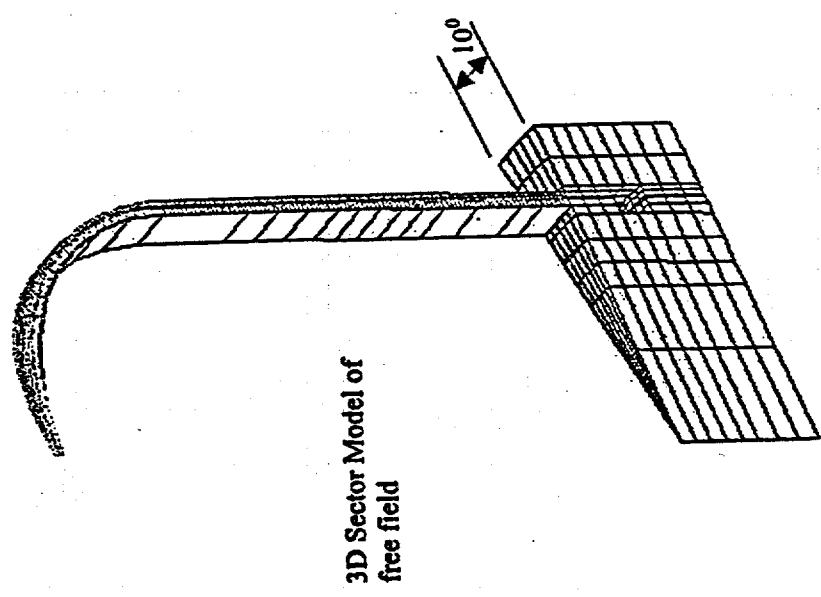


Figure 14 – 3D sector models of free field area and buttress/airlock area

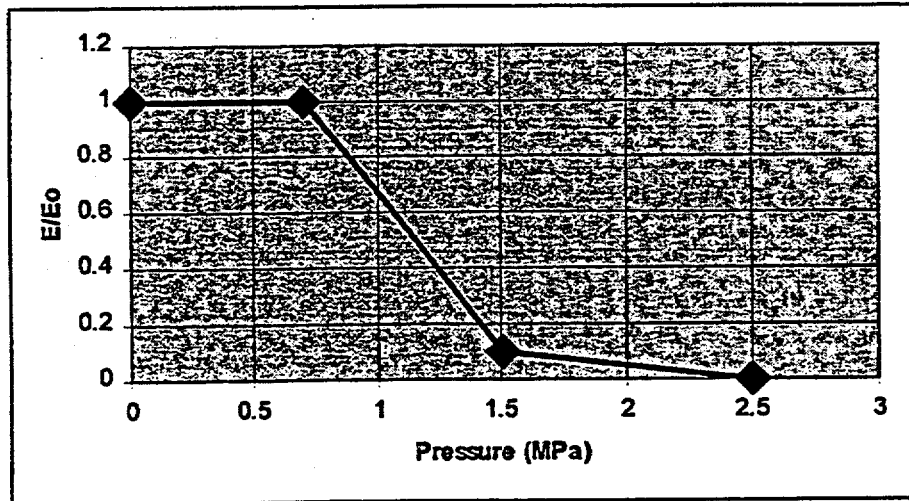
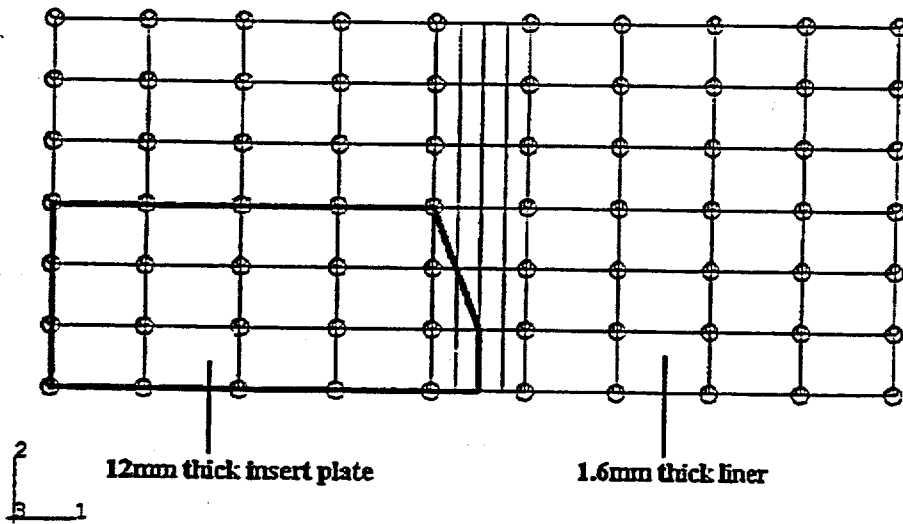
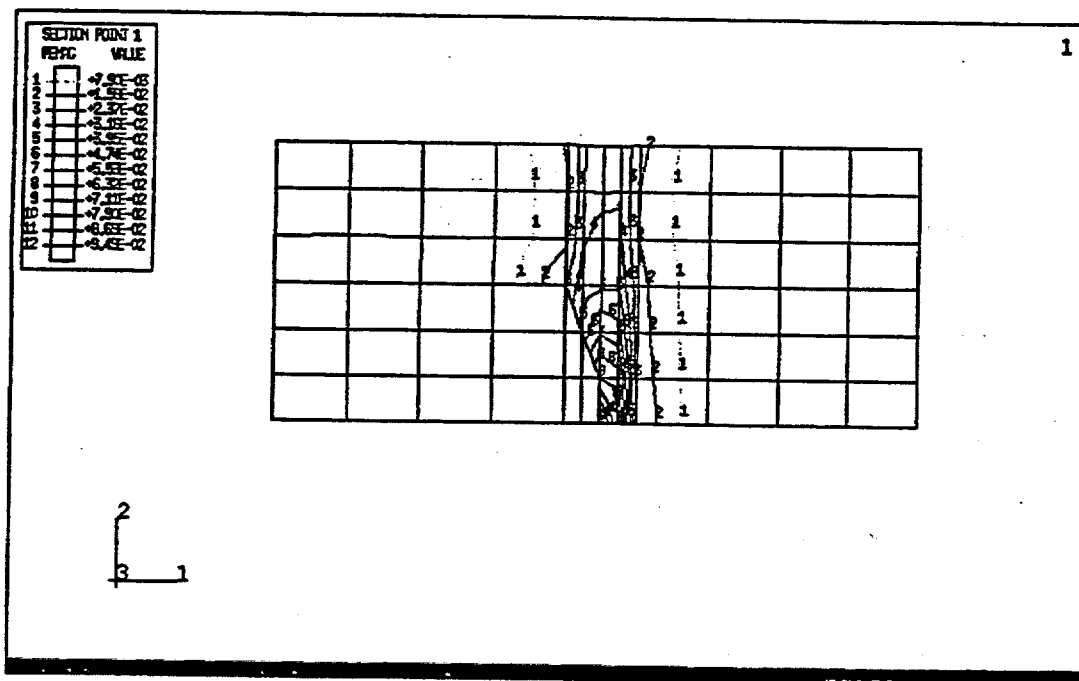


Figure 15 – Reduced modulus due to concrete cracking



(a) FE model at junction of thin/thick plate



(b) Strain contour at junction

Figure 16 – Model of liner at junction of thin/thick plate

APPENDIX H

IBRAE

**NUCLEAR SAFETY INSTITUTE
RUSSIA**

Appendix A, Composite Plots, comprises test data compiled and plotted from all organizations that participated in the Prestressed Concrete Containment Vessel (PCCV) Round Robin Pretest Analysis. To avoid duplicating the composite information, individual sets of data and/or plots have been omitted from participants' reports. In some cases this action resulted in disconnects between callouts and content and in the numbering of figures, tables, and pagination in some reports.

In Appendix H, "IBRAE, Nuclear Safety Institute, Russia," discontinuity arises from omitting the following material:

figures 4-1 through 4-45, standard output location plots

Contents:

1. Description of the Finite Element Calculated Model	H-5
2. Characteristics of Materials Specified in Calculations	H-20
3. Description of the Accident Model Used in the Analysis	H-21
4. Results of Calculating SSS of the Containment Model	H-22
5. Pressure Levels Corresponding to the Following Events:	H-22

List of Tables:

Table 1. Thickness of Layers Simulating Common Reinforcement	H-8
--	-----

List of Figures:

Figure 1-1. Data used as base to account for containment reinforcement.	H-11
Figure 1-2. Three-dimensional calculated model of Sandia containment, one-fourth scale	H-12
Figure 1-3. One-fourth part of the containment used in calculations	H-13
Figure 1-4. Fragment of the calculated model in the area of containment cylinder - 3D base structure connection	H-14
Figure 1-5. Scheme of the model of containment Sandia (on a scale $\frac{1}{4}$ at the height from 1552 to 2913 mm)	H-16
Figure 1-6. Scheme of the model of containment Sandia (on a scale the dome part $\frac{1}{4}$ and between the angles 30 and 45°)	H-17
Figure 1-7. The calculation model fragment of the containment Sandia (cylindrical part) on a scale $\frac{1}{4}$ at the height from 1552 mm to 2913 mm	H-18
Figure 1-8. The calculation model fragment of the containment Sandia (the dome part) on a scale $\frac{1}{4}$ between the angles 30 and 45°	H-19

1. Description of the Finite Element Calculated Model

Calculations were carried out with the application of CONT-routine complex destined to perform numerical simulation of stress strain states (SSS) of different NPP-type containments under both static operational and off-normal mode loads. The procedure is founded on mathematical relationships of the finite element method. With the aim to increase both the efficiency of the calculated algorithm and the possibilities of its application when calculating SSS of complex full-scale structures, the traditional finite-element procedure was supplemented with a superstructure in the form of a super-element algorithm allowing: calculations of SSS of structures by stages and a consideration of reiteration of the geometry of individual fragments. As a result, a considerable decrease of computer resource consumption as well as a possibility of the software installation in PCs were obtained.

The structure of «Sandia» containment model at the one-fourth scale is axially symmetric as a whole excluding the thickened zone around the big technological penetration on the containment inner surface and the areas of pilaster location.

Such a structure allows the application of the calculation procedure in the axially symmetric statement when calculating: impact of inner pressure, own structure weight, several thermal load types. In such a case the thickened zones can be isolated in the form of individual fragments to which forces are applied (these forces are determined starting from axially symmetric calculations of the containment).

The containment loading with the base load of prolonged effect from forces of prestressed reinforcements is rather nonuniform. Not axial-symmetry of the load from the prestressed state of the structure is observed within the dome zone (this is a consequence of applying an orthogonal-loop scheme of arrangement of the stressed reinforcements) and within the cylindrical part of the containment wherein asymmetric nonuniformities of considerable extent appear when going round large technological penetrations. Consequently, correct calculated analyses of the stressed state of the containment are more objective under the three-dimensional statement of the problem. However when calculating the containment with consideration for nonlinear properties of reinforced concrete, an axially symmetric calculated model can be used.

It should be also considered that: - in parallel with prestressed reinforcements considerable quantities of standard not-stressed ones are positioned in walls and in the dome of the containment and - all the

inner containment surface possesses a metal liner. The impact of these structure elements on the stress strain state of the containment is considerable, and it should be taken into account in calculations.

In this connection a three-dimensional finite-element model and a procedure of calculating the prestressed reinforced concrete containment in 3D statement were developed. The procedure took into account the following characteristic properties:

1. Load action from a prestress of tendons. In this case the following factors were considered:

- in the calculated model loads from each tendon were simulated separately, since the value of forces in tendons was different as a result of different radii of bending within the dome area and the cylindrical part (in the opening area);
- actual tendon trajectories with consideration for their arrangement within both the uniform zone and the area of large technological penetration;
- loads from prestressed tendons were determined having regard to the factors responsible for prestress losses within them; namely, a decrease of forces along the length of tendons depending on: - the value of friction coefficient between tendons and polyethylene tubes (containing tendons) and - the angle of tendon bend;
- increment of forces in tendons at their lengthening under the impact of inner pressure.

2. Load effect from the own structure weight. Though no considerable impact of this factor on the final result has been expected, with the aim to consider in full the tensions acting in full-scale structure, along with other loads a consideration of the own structure weight seems to be profitable.

3. Inner pressure impact on the structure.

The containment calculated models were developed on the basis of: geometrical parameters, mechanical characteristics of materials used, reinforcement type, see Reference [1]. The data presented in Figure 1-1 were used as the base to account for the containment reinforcement.

The three-dimensional containment model is presented in Figure 1-2. At this stage of our investigations calculations with consideration for concrete cracking were performed for 1/4th part of the containment (see Figure 1-3). In Figure 1-4 a fragment of the calculated model representing the cylinder-3D base structure connection area is given. The calculated model is fulfilled with the application of linear 8th-unit final elements. The total number of elements equals 24508, of units 28404.

In Figure 1-5 and Figure 1-6 the schemes of reinforcing the containment wall from an elevation of 1552 to 2913 mm (cylinder part) and between 30 and 45° angles (dome part) are presented. The corresponding fragments of the model are given in Figure 1-7 and Figure 1-8. Common reinforcement was taken into account in the calculated model in the form of thin steel layers with orthotropic properties (in one direction the layers simulating reinforcements possessed properties of steel, in another direction of concrete). In the calculated model an increase/decrease of the reinforcement section area throughout the containment height was controlled by modifying the thickness of both steel layer and the adjacent concrete layer.

Throughout the wall thick the containment model contains 12 layers of materials within the cylinder and the dome parts (see Figure 1-7 and Figure 1-8). R in Figure 1-7 represents the radius of cylinder bending, and R in Figure 1-8 is the radius of bending of the containment dome area. In these figures the layers n°3 and n°9 simulate the reinforcement in the form of a thin steel cover with a cross-section area corresponding to the reinforcement section area in meridian direction, and the layers n°5 and n°11 simulate hoop-direction reinforcement.

In Table 1 the thickness of layers simulating common reinforcement is presented.

The calculated axially symmetric model is fulfilled with the application of linear 4-unit axially symmetric elements. The total number of elements equals 2700, of units 3400. In the containment-base connection zone an embedment throughout the whole bottom boundary is accepted.

Within the axially symmetric calculated model the reinforcement stressed was taken into consideration through the application of loads on boundaries of the elements positioned on R_1 and R_2 radii (Figure 1-7 and Figure 1-8). When performing calculations this load was adjusted in accordance with the value of the mentioned element deformations. It is worth noting that the reinforcement in question has not been included into the model as an element of the section rigidity. Below a substantiation of forces in tendons specified when performing calculations in the axially symmetric statement is presented.

Justification of forces specified in tendons

According to Reference [1] p.40, the force at pull sides of tendons is 50 tons. To calculate the stress-strain state of the containment in an axially symmetric formulation, it is necessary to determine the mean force in hoop tendons and force in meridional tendons which works for the hole height from the basemat up to the dome top.

Table 1. Thickness of Layers Simulating Common Reinforcement

Z-coordinate [mm]	Inner meridian reinforcement	Inner hoop reinforcement	Outer hoop reinforcement	Outer meridian reinforcement
-1175<Z<0	5.31	-	-	5.31
0<Z<800	5.31	3.37	3.37	5.31
800<Z<999	3.054	2.208	2.208	5.31
999<Z<1552.5	3.054	2.208	2.208	3.054
1552.5<Z<2912	3.02	2.16	2.16	2.01
2912<Z<3127.3	3.054	2.208	1.351	2.252
3127.3<Z<3578.1	3.054	2.208	1.351	1.972
3578.1<Z<3916.3	2.252	2.208	1.351	1.972
3916.3<Z<4487.8	2.252	2.208	1.351	1.415
4487.8<Z<5152	2.252	1.526	1.351	1.415
5152<Z<5491	1.415	1.526	1.351	1.415
5491<Z<6502.3	1.415	1.526	1.351	1.030
6502.3<Z<10750	1.03	1.526	1.351	1.030
In the penetration zone (1540 mm in diameter)	3.67	4.33	5.31	4.33

Shortening of a tendon during anchoring makes up 4.7 mm (due to the Table 1, p.46). Friction coefficient on the curved section of a tendon equals to $\mu=0.21$, friction coefficient along the length of a tendon equals to $\lambda=0.001$.

Determination of a force mean value in hoop tendons

The mean force in tendons is calculated taking into account the length of an active section assumed by analogy with rig tests, it is equals to 3.5 m.

For this purpose, let's determine the force losses in tendons after their anchoring. The change of tendons deformation on a linear section is equal to: $\Delta\epsilon=\Delta l/l=4.7/3500=0.00134$.

The tension in tendons will decrease. The decrease of tension will be equal to:

$$\Delta\sigma=\Delta\epsilon \times E =0.00134 \times 2000000=2686 \text{ kg/cm}^2 ,$$

where E is the elasticity modulus of a tendon.

The value of tension decrease will make up:

$$\Delta N=\Delta\sigma \times F =2686 \times 3.39=9104 \text{ kg} ,$$

where F is the area of a tendon section.

Let's determine the force losses in tendons due to the friction against the walls of the channels. In the middle part of the tendon the force will make up:

$$N_1 = N_0 \cdot e^{-(\mu \cdot \alpha + \lambda \cdot l)} \quad \text{Eqn. (1)}$$

N_0 - the force on the pull end;

N_1 - the force in the middle part of a tendon;

μ - friction coefficient when the angle is changed;

α - the change of an angle, radian;

λ - friction coefficient along the length of a tendon;

l - the length of a tendon, m;

$$N_1 = 50 \cdot e^{-(0.21 \cdot 3.14 + 0.001 \cdot 16.88)} = 25.4 \text{ tons.}$$

The total force from two adjacent tendons makes up:

$$N_{sum} = (N_0 - \Delta N) + N_1 = (50 - 9.104) + 25.4 = 66.3 \text{ tons.}$$

The mean force in a hoop tendon is:

$$N_{mid} = N_{sum} / 2 = 33.15 \text{ tons.}$$

Calculations of force values in meridian tendons

Now let us calculate force losses in tendons after their anchoring. Since the value of meridian tendon shortening after their anchoring is not given in (1), this parameter is accepted to be equal to that in the case of hoop tendons.

The length of rectilinear meridian tendon section with consideration for anchoring within the bottom hoop gallery equals 12 m. Variations of tendon deformations within the rectilinear section is equal to:

$$\Delta \epsilon = \Delta l / l = 4.7 / 12000 = 0.00039$$

The value of tension lowering equals:

$$\Delta \sigma = \Delta \epsilon \times E = 0.0039 \times 20000000 = 783 \text{ kg/sm}^2.$$

The value of force decrease makes up:

$$\Delta N = \Delta \sigma \times F = 783 \times 3.39 = 2654 \text{ kg.}$$

Within the anchoring area the forces in meridian tendons equal 47.35 t.

Besides, the forces in tendons will decrease due to the losses by friction along the length of the tendon from the basemat of the containment up to the zone of connection of a cylinder with the dome. The forces value in this zone will make up:

$$N_1 = N_0 \cdot e^{-(\lambda \cdot l)} = N_1 = 50 \cdot e^{-(0.00112)} = 49.4 \text{ tons.}$$

In the end the force in the tendons in the zone of connection will make up $49.4 - 2.65 = 46.75$ tons.

The value of forces in tendons will decrease due to the dependence (1) beginning from the line of a cylinder connection with the dome up to the dome top.

It should be mentioned, that in a given work stage, the decrease of forces in tendons due to concrete shrinkage and creeping and reinforcement relaxation wasn't taken into account.

Not Available

Figure 1-1. Data used as base to account for containment reinforcement

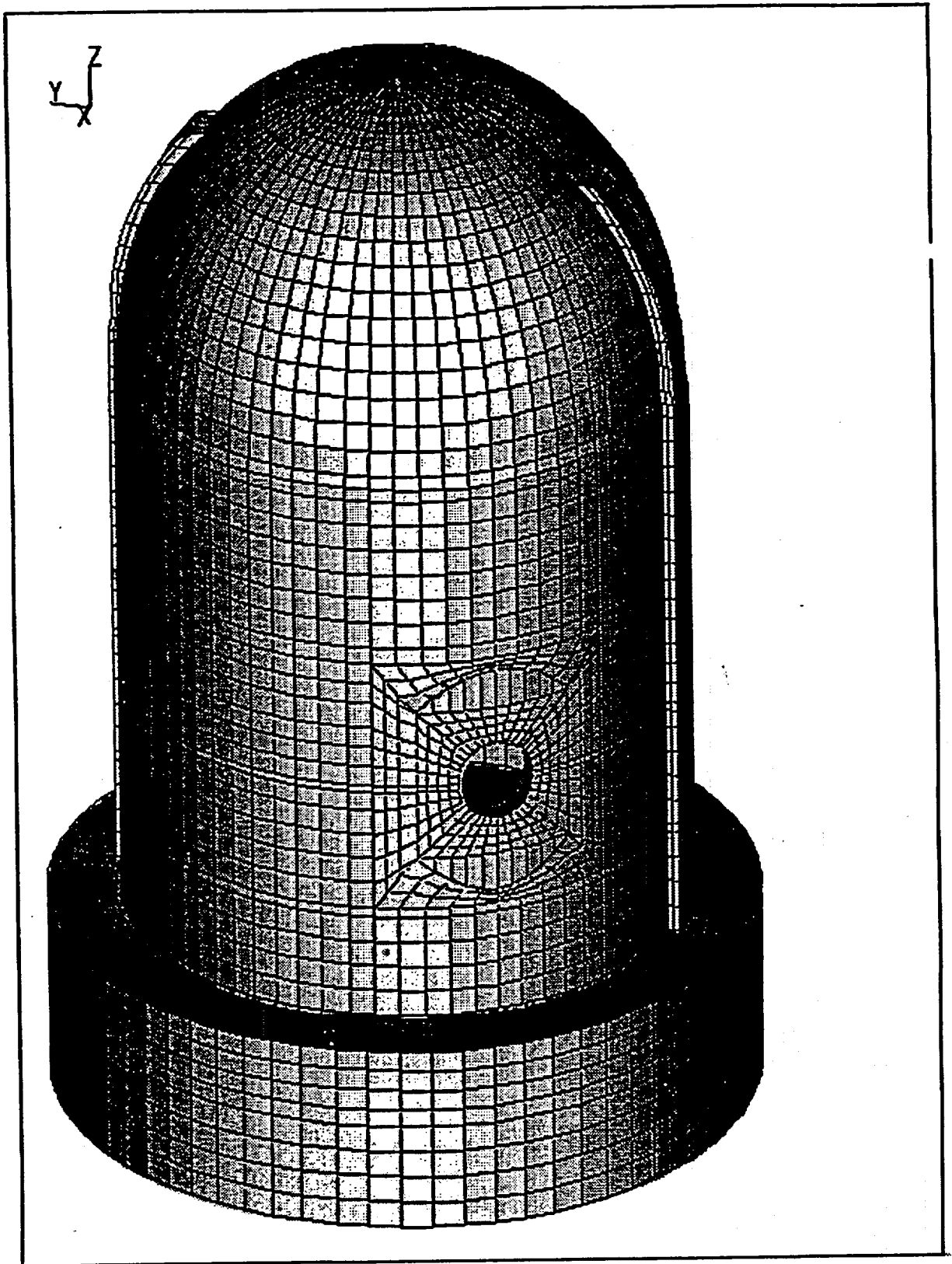


Figure 1-2. Three-dimensional calculated model of Sandia containment, one-fourth scale

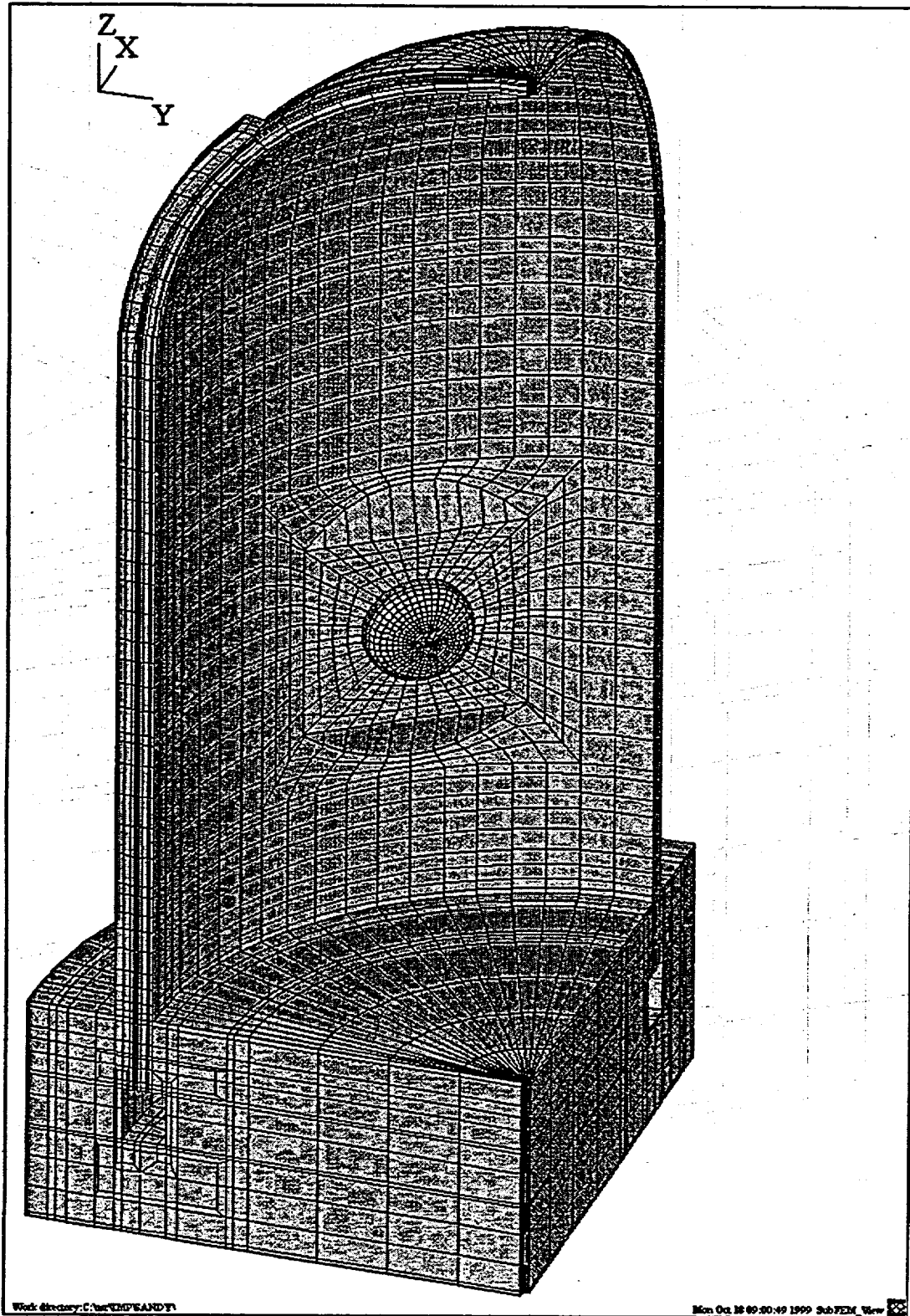


Figure 1-3. One-fourth part of the containment used in calculations

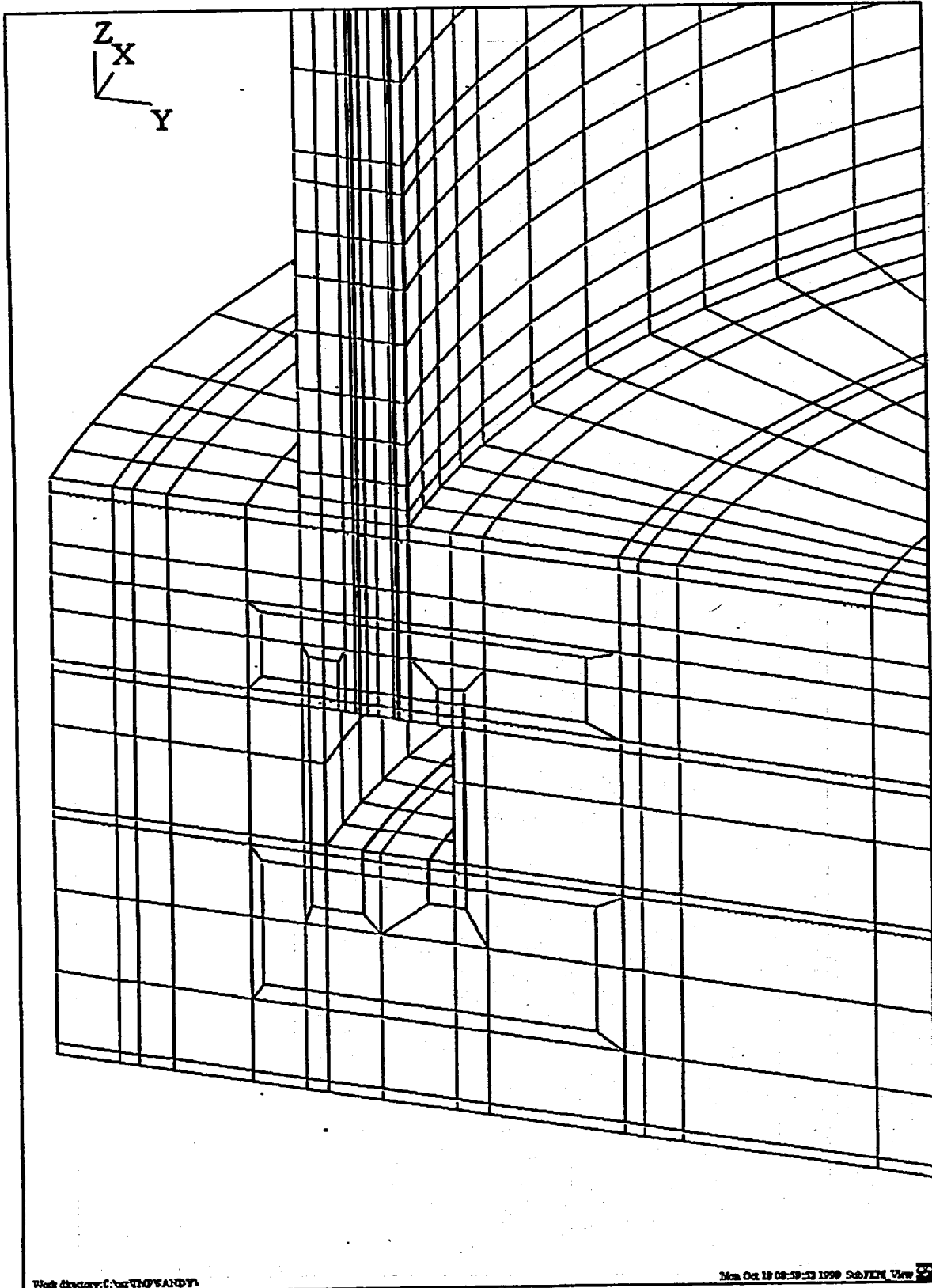


Figure 1-4. Fragment of the calculated model in the area of containment cylinder - 3D base structure connection

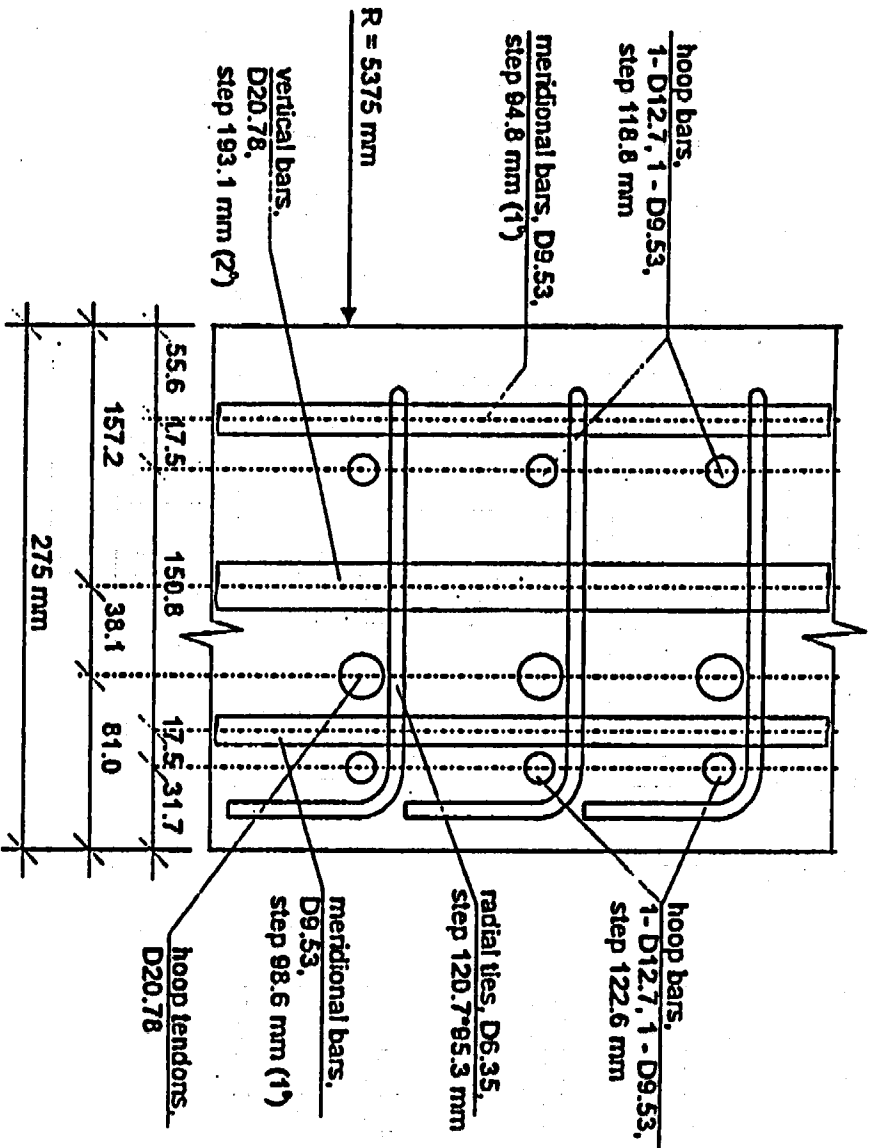


Figure I-5 Scheme of the model of containment Sandia (on a scale $\frac{1}{4}$ at the height from 1552 to 2913 mm)

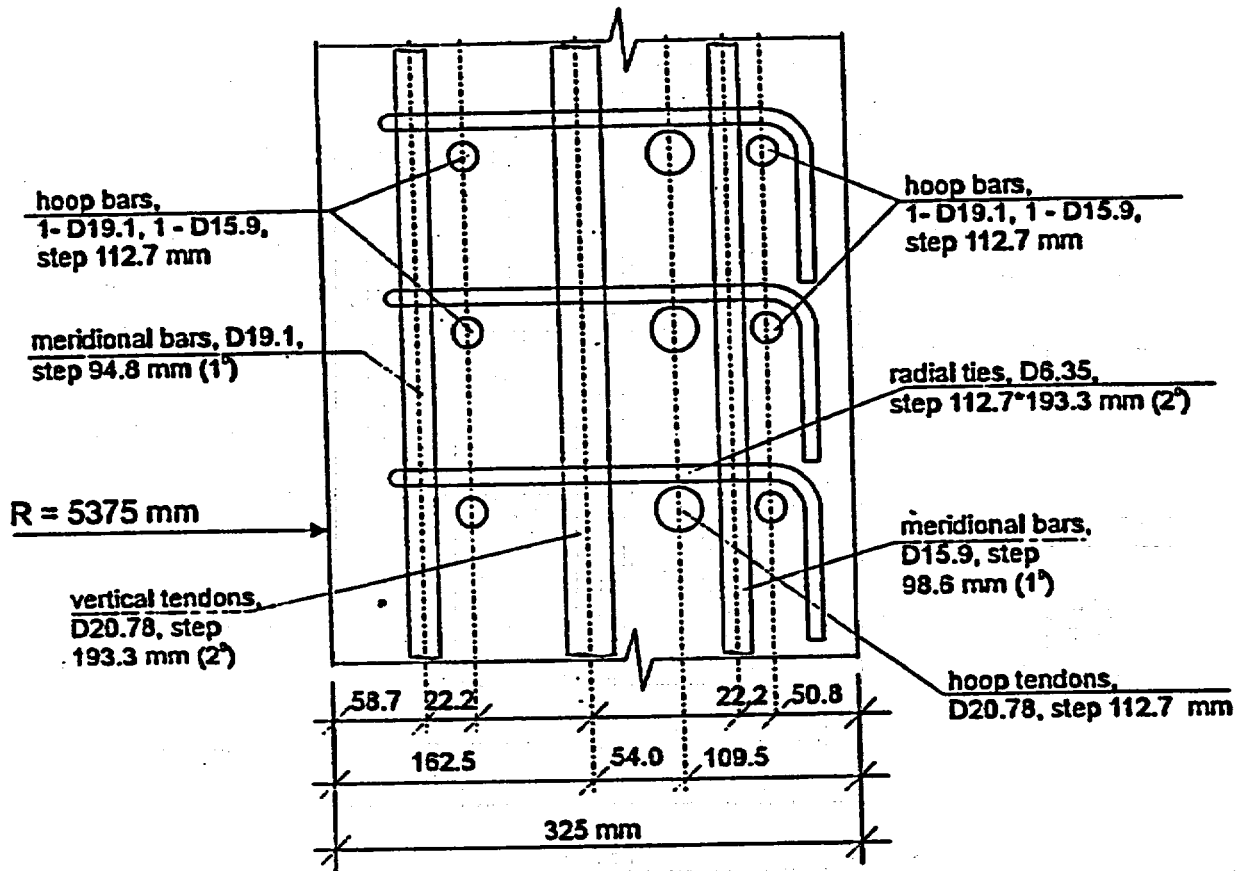


Figure 1-6 Scheme of the model of containment Sandia (on a scale the dome part $\frac{1}{4}$ and between the angles 30 and 45°)

Table 1-2. Section Characteristics

N of layer	Material	Thickness of layer, mm	N of layer Reduced modulus of elasticity, E, merid. direction (MPa)	Reduced modulus of elasticity, E, hoop direction (MPa)
1	Met.liner	1.6	210 000	210 000
2	Concrete	57.1	27 000	27 000
3	Meridional bars	3.02	185 000	27 000
4	Concrete	19.8	27 000	27 000
5	Hoop ties	2.16	27 000	185 000
6	Concrete	79.44	27 000	27 000
7	Concrete	54.0	27 000	27 000
8	Concrete	35.5	27 000	27 000
9	Meridional bars	2.01	185 000	27 00
10	Concrete	20.19	27 000	27 000
11	Hoop ties	2.16	27 000	185 000
12	Concrete	48.64	27 000	27 000

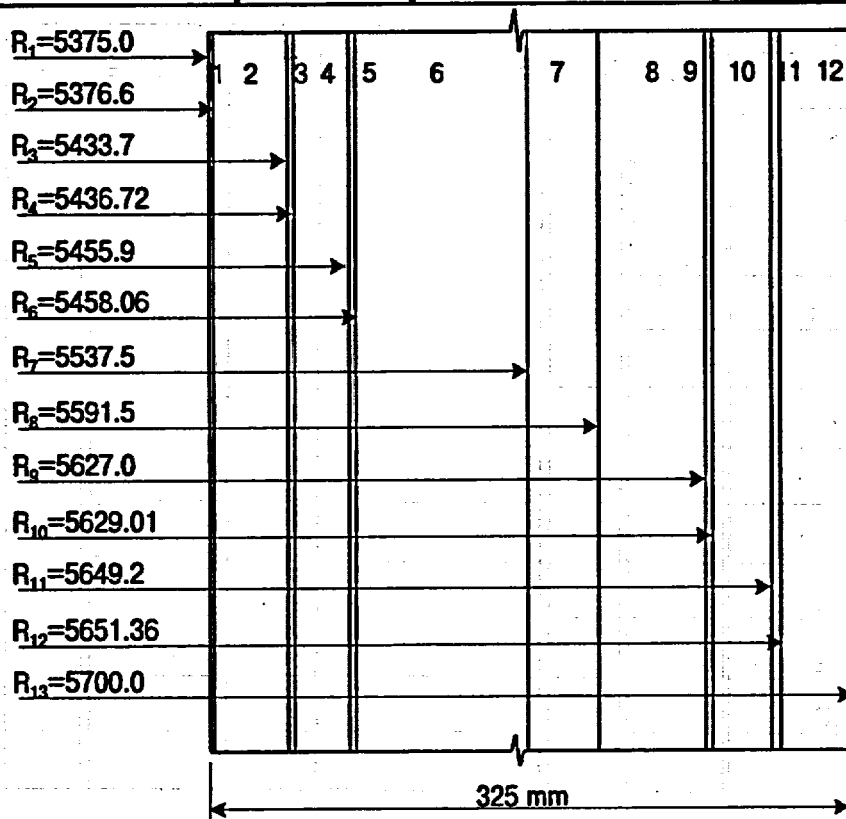


Figure 1-7. The calculation model fragment of the containment Sandia (cylindrical part) on a scale 1/4 at the height from 1552 mm to 2913 mm

Table 1-3. Section Characteristics

N of layer	Material	Thickness of layer, mm	Reduced modulus of elasticity, E, merid. direction (MPa)	Reduced modulus of elasticity, E, hoop direction (MPa)
1	Met.liner	1.6	210 000	210 000
2	Concrete	54.0	27 000	27 000
3	Meridional bars	0.75	185 000	27 000
4	Concrete	16.75	27 000	27 000
5	Hoop ties	0.83	27 000	185 000
6	Concrete	83.37	27 000	27 000
7	Concrete	36.8	27 000	27 000
8	Concrete	31.8	27 000	27 000
9	Meridional bars	0.72	185 000	27 000
10	Concrete	16.78	27 000	27 000
11	Hoop ties	0.81	27 000	185 000
12	Concrete	30.79	27 000	27 000

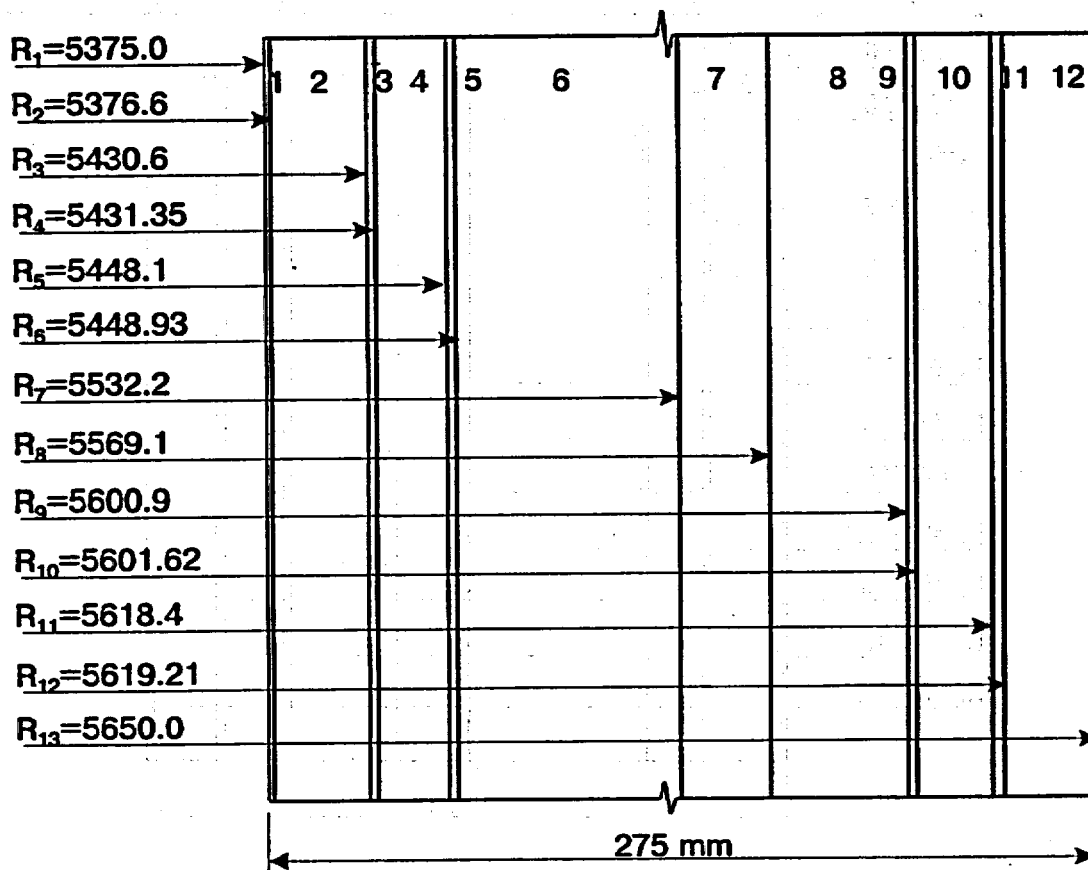


Figure 1-8. The calculation model fragment of the containment Sandia (the dome part) on a scale 1/4 between the angles 30 and 45°

2. Characteristics of Materials Specified in Calculations

The following mechanical characteristics of the materials applied were adopted.

For the concrete:

The initial elasticity modulus $E_b = 27000$ MPa

Poisson's ratio $\nu_b = 0.18$

Concrete one-axis tension strength $R_{bt} = 3.45$ MPa

Concrete one-axis compressive strength $R_b = 40$ MPa

For the lining:

Elasticity modulus $E_s = 210000$ MPa

Poisson's ratio $\nu_s = 0.3$

Yield point $R_s = 380$ MPa

Ultimate strength $R_{su} = 498$ MPa

Ultimate breaking strength $\varepsilon_{su} = 33$ %

For the reinforcement:

Elasticity modulus $E_s = 185000$ MPa

Poisson's ratio $\nu_s = 0.1$

Yield point $R_s = 450$

Ultimate strength $R_{su} = 600$ MPa

Ultimate breaking strength $\varepsilon_{su} = 20$ %

The following mechanical characteristics were assumed for the stressed reinforcement:

Elasticity modulus $E_s = 200000$ MPa

Yield point $R_s = 1700$ MPa

Ultimate strength $R_{su} = 1900$ MPa

Ultimate breaking strain $\varepsilon_{su} = 3.3 \%$

Tendons section area = 339 mm^2

* - in brackets characteristics of materials used when performing calculations in axially symmetric statement are indicated.

Radial reinforcement installed within the containment model has not been taken into account in calculations.

3. Description of the Accident Model Used in the Analysis

The problem of displacements, deformations and stresses was solved by the iteration method during some steps of the load change due to the inner pressure influence. A system of equilibrium equations was formed and solved at every step of loading. Elastic model was used with the analysis of the plasticity beginning separately in meridional and circumferencial directions for the ordinary reinforcement layers and with the Hubera-Mizesa equation for the lining.

Concrete cracking was simulated with the help of iteration process, when the stresses in "concrete" elements reached their critical value in meridional and circumferencial direction on the next iteration decreased in correspondence with the coefficient of a normal rigidity decrease which was equal to 0.0001. Concrete properties in radial direction remained the same. In the elements of reinforcement adjacent to the cracked concrete elements, the reduced elasticity modulus E_{sb} was introduced, its value is determined by the following dependence:

$$E_{sb} = \frac{1}{1 - \frac{\varepsilon_{s,cr}}{\varepsilon_s} \cdot \beta}, \quad \text{Eqn. (2)}$$

where $\varepsilon_{s,cr}$ - deformations in the reinforcement at the moment just after the cracks formation;

ε_s - deformations in the reinforcement at the observed moment of loading;

β - coefficient which is assumed to be equal to 0.5.

To solve the elastic problem, a method of consistent approximations with variable parameters of elasticity was used. At the same time, for the points of the model, where the stresses went over the

yield point, the secant elasticity modulus was specified in correspondence with the obtained values of plastic deformation. Meridional and circumferencial directions were analyzed separately for the reinforcement. Besides, with the account of the values of plastic deformation tensor components, we corrected the steel yield point in accordance with the specified hardening modulus. Iterations stopped when in all points of a body the stresses values were below the yield point or differed from it by no more than $\epsilon = 0.005 \sigma_c$.

Simultaneously, elongations of tendons were determined on every iteration; and on the next iteration the increase of stresses in them connected with the elongation was taken into account.

When critical value of tensile stress in concrete reaches R_{bc} value, it is assumed to be a criterion of cracks formation.

Achievement by the stresses and deformations in non-stressed reinforcement, lining or tendons the critical values R_{su} and ϵ_{su} , was assumed as the criterion of destruction.

In the course of the calculations, the stress-strain state of the containment under the effect of prestress was determined. Then the load from the inner pressure was applied. The value of the inner pressure on the first step was 0.39 MPa. The value of the inner pressure increased by 0.0195 MPa at every following step.

When performing calculations in the three-dimensional formulation the first pitch inner pressure value equaled 0.2 MPa. Then, up to the value of 0.7 MPa the load increment at every pitch equaled 0.1 MPa; at values over 0.7 MPa an increase of inner pressure by 0.04 MPa at every pitch was observed, at the last two pitches by 0.06 MPa.

It is worth noting that at the present stage of our investigations the impact of concrete creepage and shrinkage as well as of temperature factors on SSS of the structure has not been taken into consideration.

4. Results of Calculating SSS of the Containment Model

In the chapter presented plots of variations of: displacements, deformations and forces under the impact of inner pressure for standard positions are demonstrated.

In the course of our investigations characteristics of the materials used were modified. The containment calculations were performed: - in the axially symmetric statement with initial

properties, - in the three-dimensional one using refined data. Moreover, both the axially symmetric and the three-dimensional calculation models possess their own distinguishing features. Therefore it makes sense to present the results of both the axially symmetric and the three-dimensional calculations.

5. Pressure Levels Corresponding to the Following Events:

The first crack in the cylinder concrete due to hoop strains appears:

at a pressure = 0.7 MPa: cracks within the large penetration area $\Phi=324^\circ$;

at a pressure = 0.74 MPa: cracks within the small penetration area $\Phi=62^\circ$;

at a pressure = 0.86 MPa: cracks within the pilaster area $\Phi=90^\circ$; $\Phi=270^\circ$;

at a pressure of = 0.9 MPa: almost full cracking of the cylinder part is observed.

The first crack in the cylinder concrete due to meridian strains appears:

at a pressure of = 0.78 MPa near the base in the connection area with the base plate.

The onset of plastic deformations of hoop reinforcements in the cylinder takes place:

at a pressure of = 1.22 MPa.

The first crack in the concrete of the dome over (above) 45° angle appears:

at a pressure of = 0.94-0.98 MPa.

The first crack in the concrete of the dome under (below) 45° angle appears:

at a pressure of = 0.9 MPa;

Hoop tendons reach 1 % deformation:

at a pressure of = 1.15 MPa;

Hoop tendons reach 2 % deformation:

at a pressure of = 1.206 MPa.

Hoop tendons reach 3 % deformation:

at a pressure of = 1.25 MPa.

Containment destruction (i.e. reaching the strength limit by hoop tendons) occurs:

at a pressure of = 1.26 MPa.

Reference:

1. PCCV Round Robin Analysis - Release of Design Package. Sandia National Laboratories, P. O. Box 5800. Albuquerque, New Mexico 87185 - 0744 USA. SO-97-047.